WOODHEAD PUBLISHING SERIES IN ELECTRONIC AND OPTICAL MATERIALS

Sensor Technologies for Civil Infrastructures

Volume 1: Sensing Hardware and Data Collection Methods for Performance Assessment

Edited by M. L. Wang, J. P. Lynch and H. Sohn

WP
WOODHEAD
PUBLISHING

VISIT…

LANZAROTE
Caliente.com

Sensor Technologies for Civil Infrastructures

Related titles:

Handbook of terahertz technology for imaging, sensing and communications
(ISBN 978-0-85709-235-9)

Ultrasonic transducers
(ISBN 978-1-84569-989-5)

MEMS for automotive and aerospace applications
(ISBN 978-0-85709-118-5)

Woodhead Publishing Series in Electronic and Optical Materials:
Number 55

Sensor Technologies for Civil Infrastructures

Volume 1: Sensing Hardware and Data Collection Methods for Performance Assessment

Edited by
M. L. Wang, J. P. Lynch
and H. Sohn

AMSTERDAM • BOSTON • CAMBRIDGE • HEIDELBERG • LONDON
NEW YORK • OXFORD • PARIS • SAN DIEGO
SAN FRANCISCO • SINGAPORE • SYDNEY • TOKYO
Woodhead Publishing is an imprint of Elsevier

Woodhead Publishing is an imprint of Elsevier
80 High Street, Sawston, Cambridge, CB22 3HJ, UK
225 Wyman Street, Waltham, MA 02451, USA
Langford Lane, Kidlington, OX5 1GB, UK

Copyright © 2014 Woodhead Publishing Limited. All rights reserved

No part of this publication may be reproduced, stored in a retrieval system or transmitted in any form or by any means electronic, mechanical, photocopying, recording or otherwise without the prior written permission of the publisher.
Permissions may be sought directly from Elsevier's Science & Technology Rights Department in Oxford, UK: phone (+44) (0) 1865 843830; fax (+44) (0) 1865 853333; email: permissions@elsevier.com. Alternatively you can submit your request online by visiting the Elsevier website at http://elsevier.com/locate/permissions, and selecting Obtaining permission to use Elsevier material.

Notice
No responsibility is assumed by the publisher for any injury and/or damage to persons or property as a matter of products liability, negligence or otherwise, or from any use or operation of any methods, products, instructions or ideas contained in the material herein. Because of rapid advances in the medical sciences, in particular, independent verification of diagnoses and drug dosages should be made.

British Library Cataloguing-in-Publication Data
A catalogue record for this book is available from the British Library

Library of Congress Control Number: 2014931602

ISBN 978-0-85709-432-2 (print)
ISBN 978-0-85709-913-6 (online)
ISBN 978-1-78242-244-0 (two-volume set – print)
ISBN 978-1-78242-428-4 (two-volume set – online)

For information on all Woodhead Publishing publications
visit our website at http://store.elsevier.com/

Typeset by Newgen Knowledge Works Pvt Ltd, India

Printed and bound in the United Kingdom

ELSEVIER
Book Aid International
Working together
to grow libraries in
developing countries
www.elsevier.com • www.bookaid.org

Contents

Contributor contact details *xiii*

Woodhead Publishing Series in Electronic and Optical Materials *xvii*

Preface *xxiii*

1 Introduction to sensing for structural performance assessment and health monitoring 1

M. L. Wang, Northeastern University, USA, J. P. Lynch, University of Michigan, USA and H. Sohn, Korea Advanced Institute of Science and Technology, Republic of Korea

1.1 Introduction 1

1.2 Introduction to this book 5

1.3 Overview of sensors and sensing system hardware 5

1.4 Overview of sensor data interrogation and decision making 9

1.5 Overview of application of sensing systems to operational infrastructure 11

1.6 Future trends 13

1.7 Conclusion 17

1.8 References 20

2 Sensor data acquisition systems and architectures 23

M. D. Todd, University of California San Diego, USA

2.1 Introduction 23

2.2 Concepts in signals and digital sampling 30

2.3 Analog-to-digital conversion 34

2.4 Digital-to-analog conversion 39

2.5 Data acquisition systems 41

2.6 Optical sensing DAQ system 47

2.7 Conclusion and future trends 54

2.8 References 56

3 Commonly used sensors for civil infrastructures and their associated algorithms 57

N. C. Yoder, Whistle Labs Inc., USA and D. E. Adams, Vanderbilt University, USA

3.1 Introduction 57
3.2 Brief review of commonly used sensing technologies 58
3.3 Associated algorithms 69
3.4 Examples of continuous monitoring systems 78
3.5 Conclusions and future trends 79
3.6 References 80

4 Piezoelectric transducers for assessing and monitoring civil infrastructures 86

Y-K. An, Southeast University, China, and M. K. Kim and H. Sohn, Korea Advanced Institute of Science and Technology (KAIST), Republic of Korea

4.1 Introduction 86
4.2 Principle of piezoelectricity 87
4.3 Piezoelectric materials and the fabrication of piezoelectric transducers 92
4.4 Piezoelectric transducers for SHM applications 95
4.5 Bonding effects 97
4.6 Limitations of piezoelectric transducers 98
4.7 SHM techniques using piezoelectric transducers 99
4.8 Applications of piezoelectric transducer-based SHM 105
4.9 Future trends 110
4.10 Conclusion 112
4.11 References 113

5 Fiber optic sensors for assessing and monitoring civil infrastructures 121

K. J. Peters, North Carolina State University, USA, and D. Inaudi, SMARTEC S.A. Switzerland

5.1 Introduction 121
5.2 Properties of optical fibers 123
5.3 Common optical fiber sensors 130
5.4 Future trends 145
5.5 Sources for further information and advice 150
5.6 Conclusions 150
5.7 References 150

6 Acoustic emission sensors for assessing and monitoring civil infrastructures 159
M. Meo, University of Bath, UK

6.1 Introduction 159
6.2 Fundamentals of acoustic emission (AE) technique 160
6.3 Interpretation of AE signals 161
6.4 AE localization methods 162
6.5 Severity assessment 166
6.6 AE equipment technology 169
6.7 Field applications and structural health monitoring using AE 171
6.8 Future challenges 175
6.9 Conclusion 176
6.10 References 176

7 Nonlinear acoustic and ultrasound methods for assessing and monitoring civil infrastructures 179
M. Meo, University of Bath, UK

7.1 Introduction 179
7.2 Fundamentals of nonlinear acousto-ultrasound techniques 181
7.3 Harmonic and subharmonic generation 182
7.4 Nonlinear wave modulation 185
7.5 Nonlinear resonance ultrasound spectroscopy 191
7.6 Future trends 196
7.7 Conclusions 197
7.8 References 197

8 Radar technology: radio frequency, interferometric, millimeter wave and terahertz sensors for assessing and monitoring civil infrastructures 201
D. Huston, University of Vermont, USA and D. Busuioc, DB Consulting, USA

8.1 Introduction 201
8.2 Brief history of ground penetrating radar (GPR) systems 203
8.3 Current challenges and state of the art systems 208
8.4 Fundamentals of operation 209
8.5 Electromagnetic interactions with materials 217
8.6 Transmitter and receiver design 219
8.7 Signal processing 224
8.8 Laboratory and field studies 227
8.9 Conclusions and future trends 232
8.10 References 234

9 Electromagnetic sensors for assessing and monitoring civil infrastructures 238
M. L. WANG, Northeastern University, USA and G. WANG, Chicago Bridge and Iron, USA

9.1 Introduction to magnetics and magnetic materials 238
9.2 Introduction to magnetoelasticity 242
9.3 Magnetic sensory technologies 245
9.4 Role of microstructure in magnetization and magnetoelasticity 249
9.5 Magnetoelastic stress sensors for tension monitoring of steel cables 253
9.6 Temperature effects 256
9.7 Eddy current 258
9.8 Removable (portable) elastomagnetic stress sensor 259
9.9 Conclusion and future trends 262
9.10 References 262

10 Micro-electro-mechanical-systems (MEMS) for assessing and monitoring civil infrastructures 265
D. OZEVIN, University of Illinois at Chicago, USA

10.1 Introduction 265
10.2 Sensor materials and micromachining techniques 266
10.3 Sensor characteristics 273
10.4 MEMS sensors for SHM 279
10.5 Application examples 284
10.6 Long term technical challenges 285
10.7 Conclusion and future trends 286
10.8 Sources of further information and advice 288
10.9 References 289

11 Multifunctional materials and nanotechnology for assessing and monitoring civil infrastructures 295
K. J. LOH and D. RYU, University of California-Davis, USA

11.1 Introduction 295
11.2 Properties of carbon nanomaterials 296
11.3 Cementitious-based composites 299
11.4 Fiber-reinforced polymer composites 303
11.5 Polymer-based thin films 306
11.6 Conclusion and future trends 316
11.7 References 317

12 **Laser-based sensing for assessing and monitoring civil infrastructures** **327**
T-Y. Yu, University of Massachusetts Lowell, USA

12.1 Introduction 327
12.2 Laser principles 329
12.3 Laser interferometry or electronic speckle pattern interferometry 333
12.4 Laser digital shearography 335
12.5 Laser scanning photogrammetry 337
12.6 Laser Doppler vibrometry 339
12.7 Laser-ultrasound 342
12.8 Other laser-based techniques 346
12.9 Civil infrastructure applications 348
12.10 Laser safety 351
12.11 Conclusion 352
12.12 References 352

13 **Corrosion sensing for assessing and monitoring civil infrastructures** **357**
A. Poursaee, Clemson University, USA

13.1 Introduction 357
13.2 Principles of corrosion 358
13.3 Corrosion evaluation techniques 361
13.4 Corrosion sensors for field monitoring 372
13.5 Conclusion and future trends 377
13.6 References 378

14 **Vision-based sensing for assessing and monitoring civil infrastructures** **383**
Y. F. Ji, Tongji University, China and C. C. Chang, Hong Kong University of Science and Technology, Hong Kong

14.1 Introduction 383
14.2 Vision-based measurement techniques for civil engineering applications 386
14.3 Important issues for vision-based measurement techniques 388
14.4 Applications for vision-based sensing techniques 396
14.5 Conclusions 405
14.6 Acknowledgment 406
14.7 References 406

15 Robotic sensing for assessing and monitoring civil infrastructures 410
H. Myung, H. Jeon and Y-S. Bang, Korea Advanced Institute of Science and Technology (KAIST), Republic of Korea and Y. Wang, Georgia Institute of Technology, USA

15.1 Introduction 410
15.2 Vision-based robotic sensing for structural health monitoring (SHM) 414
15.3 Remote robotic sensing for SHM 419
15.4 Vibration-based mobile wireless sensors 424
15.5 Conclusions and future trends 436
15.6 References 439

16 Design and selection of wireless structural monitoring systems for civil infrastructures 446
M. B. Kane, C. Peckens and J. P. Lynch, University of Michigan, USA

16.1 Introduction 446
16.2 Overview of wireless networks 450
16.3 Hardware design and selection 456
16.4 Wireless sensor network software 464
16.5 Conclusion and future trends 471
16.6 Acknowledgments 472
16.7 References 472

17 Permanent installation of wireless structural monitoring systems in infrastructure systems 480
C. A. Peckens, M. B. Kane, Y. Zhang and J. P. Lynch, University of Michigan, USA

17.1 Introduction 480
17.2 Case study I – The Golden Gate Bridge, San Francisco, California, USA 482
17.3 Case study II – The Stork Bridge, Winterthur, Switzerland 487
17.4 Case study III – Jindo Bridge, Haenam/Jindo, South Korea 492
17.5 Case study IV – New Carquinez Bridge, Vallejo/Crockett, California, USA 497
17.6 Conclusion 505
17.7 Acknowledgments 505
17.8 References 506

18 Energy harvesting for infrastructure sensing systems 510

J. T. Scruggs, University of Michigan, USA

18.1 Introduction 510
18.2 Harvester dynamic modeling 514
18.3 Power availability and the optimal harvesting admittance 518
18.4 Power extraction circuits 525
18.5 Ongoing advancements and future directions 532
18.6 References 534

Index *537*

Contributor contact details

(* = main contact)

Editors and Chapter 1

M. L. Wang
Northeastern University
360 Huntington Ave
Boston, MA 02115, USA

E-mail: Mi.Wang@neu.edu

J. P. Lynch
Department of Civil and Environmental Engineering
University of Michigan
Ann Arbor, MI 48109–2125, USA

E-mail: jerlynch@umich.edu

H. Sohn
Korea Advanced Institute of Science and Technology (KAIST)
291 Daehak-ro
Yuseong-gu
Daejeon, 305–701, Republic of Korea

E-mail: hoonsohn@kaist.ac.kr

Chapter 2

M. D. Todd
University of California San Diego
Department of Structural Engineering
9500 Gilman Drive 0085
La Jolla, CA 92093–0085, USA

E-mail: mdtodd@ucsd.edu

Chapter 3

N. C. Yoder*
Whistle Labs, Inc.
3180 18th Street
Suite 102
San Francisco, CA 94110, USA

E-mail: nyoder@gmail.com

D. E. Adams
Vanderbilt University
Laboratory for Systems Integrity & Reliability (LaSIR)
2301 Vanderbilt Place
PMB 351831
267 Jacobs Hall
Nashville, TN 37235–1831, USA

E-mail: douglas.adams@vanderbilt.edu

Chapter 4

Y-K. An
International Institute for Urban
System Engineering (IIUSE)
Southeast University (SEU)
2 Sipailou Street, Nanjing
Jiangsu, China, 210096

E-mail: ayk2028@gmail.com

M. K. Kim and H. Sohn*
Department of Civil and Environmental Engineering
Korea Advanced Institute of Science and Technology (KAIST)
291 Daehak-ro Yuseong-gu
Daejeon, 305–701, Republic of Korea

E-mail: hoonsohn@kaist.ac.kr

Chapter 5

K. J. Peters*
Department of Mechanical and Aerospace Engineering
North Carolina State University
911 Oval Drive
Raleigh
NC, 27695, USA

E-mail: kjpeters@ncsu.edu

D. Inaudi
SMARTEC S.A.
Via Pobiette 11
Manno, CH-6928, Switzerland

E-mail: daniele.inaudi@smartec.ch

Chapters 6 and 7

M. Meo
Department of Mechanical Engineering
University of Bath
Bath, BA2 7AY, UK

E-mail: m.meo@bath.ac.uk

Chapter 8

D. Huston
The University of Vermont
Burlington, VT 05405, USA

E-mail: dryver.huston@uvm.edu

D. Busuioc
DB Consulting
USA

Chapter 9

M. L. Wang*
Northeastern University
360 Huntington Ave
Boston, MA 02115, USA

E-mail: Mi.Wang@neu.edu

G. Wang
Chicago Bridge and Iron
14105 S. Route 59
Plainfield, IL 60544, USA

E-mail: gordonwang15@aol.com

Chapter 10

D. Ozevin
University of Illinois at Chicago
Civil and Materials Engineering
842 W Taylor Street ERF 3073
Chicago, IL 60607, USA

E-mail: dozevin@uic.edu

Chapter 11

K. J. Loh* and D. Ryu
Department of Civil & Environmental Engineering
University of California-Davis
1 Shields Avenue
Davis, CA 95616–5294, USA

E-mail: kjloh@ucdavis.edu

Chapter 12

T-Y. Yu
Department of Civil and Environmental Engineering
University of Massachusetts Lowell
Falmouth 107C

One University Avenue
Lowell, MA 01854, USA

E-mail: TzuYang_Yu@uml.edu

Chapter 13

A. Poursaee
Glenn Department of Civil Engineering
316 Lowry Hall
Clemson University
Clemson, SC 29634, USA

E-mail: amire@clemson.edu

Chapter 14

Y. F. Ji*
Department of Bridge Engineering
Tongji University
1239 Siping Road
Shanghai, Peoples Republic of China

E-mail: betoneyji@tongji.edu.cn

C. C. Chang
Department of Civil and Environmental Engineering
Hong Kong University of Science and Technology
Clear Water Bay
Kowloon, Hong Kong

E-mail: cechang@ust.hk

Chapter 15

H. Myung,* H. Jeon and Y-S. Bang
Dept. of Civil & Env. Engg. / Robotics Program,
Korea Advanced Institute of Science and Technology (KAIST)
291 Daehak-ro
Yuseong-gu
Daejeon, 305–701, Republic of Korea

E-mail: hmyung@kaist.ac.kr

Y. Wang
School of Civil and Environmental Engineering,
Georgia Institute of Technology,
790 Atlantic Dr
NW Atlanta, GA 30332–0355, USA

E-mail: yang.wang@ce.gatech.edu

Chapter 16

M. B. Kane, C. A. Peckens and J. P. Lynch*
Department of Civil and Environmental Engineering
University of Michigan
Ann Arbor, MI 48109–2125, USA

E-mail: jerlynch@umich.edu

Chapter 17

C. A. Peckens, M. B. Kane, Y. Zhang and J. P. Lynch*
Department of Civil and Environmental Engineering
University of Michigan
Ann Arbor, MI 48109–2125, USA

E-mail: jerlynch@umich.edu

Chapter 18

J. T. Scruggs
Department of Civil and Environmental Engineering
University of Michigan
Ann Arbor, MI 48109–2125, USA

E-mail: jscruggs@umich.edu

Woodhead Publishing Series in Electronic and Optical Materials

1 **Circuit analysis**
J. E. Whitehouse
2 **Signal processing in electronic communications: For engineers and mathematicians**
M. J. Chapman, D. P. Goodall and N. C. Steele
3 **Pattern recognition and image processing**
D. Luo
4 **Digital filters and signal processing in electronic engineering: Theory, applications, architecture, code**
S. M. Bozic and R. J. Chance
5 **Cable engineering for local area networks**
B. J. Elliott
6 **Designing a structured cabling system to ISO 11801: Cross-referenced to European CENELEC and American Standards Second edition**
B. J. Elliott
7 **Microscopy techniques for materials science**
A. Clarke and C. Eberhardt
8 **Materials for energy conversion devices**
Edited by C. C. Sorrell, J. Nowotny and S. Sugihara
9 **Digital image processing: Mathematical and computational methods Second edition**
J. M. Blackledge
10 **Nanolithography and patterning techniques in microelectronics**
Edited by D. Bucknall
11 **Digital signal processing: Mathematical and computational methods, software development and applications Second edition**
J. M. Blackledge
12 **Handbook of advanced dielectric, piezoelectric and ferroelectric materials: Synthesis, properties and applications**
Edited by Z.-G. Ye
13 **Materials for fuel cells**
Edited by M. Gasik

14 **Solid-state hydrogen storage: Materials and chemistry**
Edited by G. Walker
15 **Laser cooling of solids**
S. V. Petrushkin and V. V. Samartsev
16 **Polymer electrolytes: Fundamentals and applications**
Edited by C. A. C. Sequeira and D. A. F. Santos
17 **Advanced piezoelectric materials: Science and technology**
Edited by K. Uchino
18 **Optical switches: Materials and design**
Edited by S. J. Chua and B. Li
19 **Advanced adhesives in electronics: Materials, properties and applications**
Edited by M. O. Alam and C. Bailey
20 **Thin film growth: Physics, materials science and applications**
Edited by Z. Cao
21 **Electromigration in thin films and electronic devices: Materials and reliability**
Edited by C.-U. Kim
22 ***In situ* characterization of thin film growth**
Edited by G. Koster and G. Rijnders
23 **Silicon-germanium (SiGe) nanostructures: Production, properties and applications in electronics**
Edited by Y. Shiraki and N. Usami
24 **High-temperature superconductors**
Edited by X. G. Qiu
25 **Introduction to the physics of nanoelectronics**
S. G. Tan and M. B. A. Jalil
26 **Printed films: Materials science and applications in sensors, electronics and photonics**
Edited by M. Prudenziati and J. Hormadaly
27 **Laser growth and processing of photonic devices**
Edited by N. A. Vainos
28 **Quantum optics with semiconductor nanostructures**
Edited by F. Jahnke
29 **Ultrasonic transducers: Materials and design for sensors, actuators and medical applications**
Edited by K. Nakamura
30 **Waste electrical and electronic equipment (WEEE) handbook**
Edited by V. Goodship and A. Stevels
31 **Applications of ATILA FEM software to smart materials: Case studies in designing devices**
Edited by K. Uchino and J.-C. Debus

32 **MEMS for automotive and aerospace applications**
Edited by M. Kraft and N. M. White
33 **Semiconductor lasers: Fundamentals and applications**
Edited by A. Baranov and E. Tournie
34 **Handbook of terahertz technology for imaging, sensing and communications**
Edited by D. Saeedkia
35 **Handbook of solid-state lasers: Materials, systems and applications**
Edited by B. Denker and E. Shklovsky
36 **Organic light-emitting diodes (OLEDs): Materials, devices and applications**
Edited by A. Buckley
37 **Lasers for medical applications: Diagnostics, therapy and surgery**
Edited by H. Jelínková
38 **Semiconductor gas sensors**
Edited by R. Jaaniso and O. K. Tan
39 **Handbook of organic materials for optical and (opto)electronic devices: Properties and applications**
Edited by O. Ostroverkhova
40 **Metallic films for electronic, optical and magnetic applications: Structure, processing and properties**
Edited by K. Barmak and K. Coffey
41 **Handbook of laser welding technologies**
Edited by S. Katayama
42 **Nanolithography: The art of fabricating nanoelectronic and nanophotonic devices and systems**
Edited by M. Feldman
43 **Laser spectroscopy for sensing: Fundamentals, techniques and applications**
Edited by M. Baudelet
44 **Chalcogenide glasses: Preparation, properties and applications**
Edited by J.-L. Adam and X. Zhang
45 **Handbook of MEMS for wireless and mobile applications**
Edited by D. Uttamchandani
46 **Subsea optics and imaging**
Edited by J. Watson and O. Zielinski
47 **Carbon nanotubes and graphene for photonic applications**
Edited by S. Yamashita, Y. Saito and J. H. Choi
48 **Optical biomimetics: Materials and applications**
Edited by M. Large
49 **Optical thin films and coatings**
Edited by A. Piegari and F. Flory

50 **Computer design of diffractive optics**
Edited by V. A. Soifer
51 **Smart sensors and MEMS: Intelligent devices and microsystems for industrial applications**
Edited by S. Nihtianov and A. Luque
52 **Fundamentals of femtosecond optics**
S. A. Kozlov and V. V. Samartsev
53 **Nanostructured semiconductor oxides for the next generation of electronics and functional devices: Properties and applications**
S. Zhuiykov
54 **Nitride semiconductor light-emitting diodes (LEDs): Materials, technologies and applications**
Edited by J. J. Huang, H. C. Kuo and S. C. Shen
55 **Sensor technologies for civil infrastructures**
Volume 1: Sensing hardware and data collection methods for performance assessment
Edited by M. Wang, J. Lynch and H. Sohn
56 **Sensor technologies for civil infrastructures**
Volume 2: Applications in structural health monitoring
Edited by M. Wang, J. Lynch and H. Sohn
57 **Graphene: Properties, preparation, characterisation and devices**
Edited by V. Skákalová and A. B. Kaiser
58 **Silicon-on-insulator (SOI) technology**
Edited by O. Kononchuk and B.-Y. Nguyen
59 **Biological identification: DNA amplification and sequencing, optical sensing, lab-on-chip and portable systems**
Edited by R. P. Schaudies
60 **High performance silicon imaging: Fundamentals and applications of CMOS and CCD sensors**
Edited by D. Durini
61 **Nanosensors for chemical and biological applications: Sensing with nanotubes, nanowires and nanoparticles**
Edited by K. C. Honeychurch
62 **Composite magnetoelectrics: Materials, structures, and applications**
G. Srinivasan, S. Priya, and N. Sun
63 **Quantum information processing with diamond: Principles and applications**
Edited by S. Prawer and I. Aharonovich
64 **Advances in non-volatile memory and storage technology**
Edited by Y. Nishi
65 **Laser surface engineering: Processes and applications**
Edited by J. Lawrence, C. Dowding, D. Waugh and J. Griffiths

66 **Power ultrasonics: A handbook of materials, design and applications of high power ultrasound transducers**
Edited by J. A. Gallego-Juárez
67 **Advances in delay-tolerant networks (DTNs): Architectures, routing and challenges**
Edited by J. Rodrigues
68 **Handbook of flexible organic electronics: Materials, manufacturing and applications**
Edited by S. Logothetidis
69 **Machine-to-machine (M2M) communications: Architecture, performance and applications**
Edited by C. Anton-Haro and M. Dohler
70 **Ecological design of smart home networks: Technologies, social impact and sustainability**
Edited by N. Saito and D. Menga
71 **Industrial tomography: Systems and applications**
Edited by M. Wang
72 **Vehicular communications and networks: Architectures, protocols, operation and deployment**
Edited by W. Chen
73 **Modeling, characterization, and production of nanomaterials: Electronics, photonics and energy applications**
Edited by V. Tewary and Y. Zhang
74 **Reliability characterisation of electrical and electronic systems**
Edited by J. Swingler
75 **Handbook of industrial wireless sensor networks: Monitoring, control and automation**
Edited by R. Budampati and S. Kolavennu
76 **Epitaxial growth of complex metal oxides: Techniques, properties and applications**
Edited by G. Koster and G. Rijnders
77 **Semiconductor nanowires: Materials, synthesis, characterization and applications**
Edited by J. Arbiol and Q. Xiong

Preface

The oldest of all of the engineering disciplines, Civil Engineering, enjoys a proud history of providing society with infrastructure systems to ensure economic prosperity and a high quality of life. In recent years, a number of grand challenges have emerged that fundamentally jeopardize the profession's ability to continue designing and maintaining infrastructure with the high level of performance as experienced in the past. For example, structures in urban environments are seeing unprecedented levels of demand from growing populations leading to higher levels of deterioration occurring at faster rates. This is an especially demanding issue for civil engineers in developed nations who are now dealing with a growing number of infrastructure components exceeding their intended design lives (typically half a century). It is costlier to maintain the safe operating condition of aging infrastructure. Another challenge for civil engineers is the need to continue to improve the design of their infrastructure to withstand extreme loadings associated with natural hazard events including earthquakes and tropical storms. An especially pressing challenge is the frequent occurrence of failures at points of interconnection between two or more interdependent infrastructure systems. Unfortunately, functional interdependencies create the potential for cascading failures that can result in systemic disasters. A case in point was the progression of infrastructure system failures that occurred during both Hurricane Katrina (2005, New Orleans) and the Tohoku Earthquake (2011, Japan). The breaching of the levees in New Orleans led to cascading failures that ultimately crippled an entire city; to this day, New Orleans has not fully recuperated from this natural disaster. The Tohoku Earthquake offered another case of cascading failures with the failure of a protective sea wall setting off a chain reaction of failures leading to the meltdown of the Fukushima nuclear reactors; Fukushima remains an ongoing disaster with major public health implications for the coming century.

The civil engineering community is facing yet another grand challenge in how to innovatively design and construct more durable and safer infrastructure systems while being responsible stewards of the natural environment. The field is now exploring new ways of designing resilient infrastructure with lower levels of embodied energy, while emitting lower levels of greenhouse gasses during construction.

The magnitude and scale of these challenges are necessitating new approaches to learning how infrastructure systems behave under both normal and extreme load conditions. Sensors are a key technology that allows civil engineers unprecedented levels of observation of operational infrastructure systems. Surveillance and observation are the main elements that aid professions to appropriately model their systems, improve system designs, and optimize future operations and maintenance processes. Concurrent to the growing demand for sensing, there has been a proliferation of new enabling technologies to improve capabilities of sensing systems while lowering their costs and simplifying their deployments. The creation of new, micro-scale sensors through the adoption of micro-electro-mechanical systems (MEMS) has led to a new generation of sensors with compact forms and low costs. In addition, the adoption of low power microprocessors that benefit from Moore's Law has helped create a class of 'intelligent and smart' sensors with computing autonomy. Similar to Moore's Law, Eldholm's Law is projecting continued improvement in wireless communications. The result has been scalable, high rate wireless communication standards that have been optimized for wireless communications within sensor networks. Undoubtedly, these trends have improved the sensing arsenal available to civil engineers to observe their systems while lowering traditional barriers to adoption including cost and ease of use.

At the outset, the editors felt there was a pressing need to create an authoritative reference of established and emerging sensing technologies impacting the field's ability to monitor its infrastructure systems. With that goal in mind, the editors invited the leaders of the field to provide detailed overviews of sensing hardware in Volume 1 of the two volume set. Specifically, Volume 1 concentrates on describing explicit sensor types and data acquisition methods relevant to the civil infrastructure domain. Sensors have the potential to generate unprecedented amounts of data; this can create a bottleneck in the decision-making process of engineers. In order to aid decision makers responsible for the operation and upkeep of infrastructure, data analysis systems are direly needed to process growing amounts of sensor data. The experts in the domain of data interrogation and decision support systems were invited to author chapters in Volume 2 of the book. Furthermore, Volume 2 showcases how sensors and sensing systems are already being used to observe specific infrastructure system types. The editors home these case studies provided the basis for others to implement impactful sensing systems of their own.

At the beginning of this book project, the editors felt there was an equally pressing need for a comprehensive reference that could be used to educate students. Specifically, graduate programs in civil engineering have begun to add new disciplinary concentrations that are intended to train students to be the thought leaders that will usher in the solutions required to solve some of the aforementioned grand challenge problems. For example, many universities across the globe are now offering a specialization in 'infrastructure systems' with the goal of training students to approach infrastructure system problems with a 'systems' perspective. Sensors are a key enabling technology required to observe operational infrastructure systems. For this reason, these new graduate programs now offer courses in sensors, sensing systems, and data processing using sensor data. This book has been designed to offer educators a reference book that offers students a complete review of the fundamental operational principles of current and future sensor technologies (Volume 1) and showcasing the use of these sensing technologies to observe real-world systems (Volume 2). The book is written assuming students are upper-level undergraduates or at the post-graduate level.

When undertaking a project of this scale, it should be acknowledged that the project was only possible due to the support and encouragement of the editors' peers in the international research community. The pace of technological development that has occurred over the past quarter century has been fueled by the intellectual vitality and camaraderie of the research community engaged in sensing technologies for infrastructure monitoring. The editors are grateful that this community was willing and eager to contribute to this book. The result is a reference that accurately represents the state-of-the-art of the field and the impact sensing technologies has in solving emerging problems in the field of civil infrastructure systems. Enjoy reading!

Ming L. Wang, PhD
Boston, MA

Jerome Lynch, PhD
Ann Arbor, MI

Hoon Sohn, PhD
Daejeon, Korea

1

Introduction to sensing for structural performance assessment and health monitoring

M. L. WANG, Northeastern University, USA, J. P. LYNCH,
University of Michigan, USA and H. SOHN, Korea Advanced
Institute of Science and Technology, Republic of Korea

DOI: 10.1533/9780857099136.1

Abstract: Over the past 50 years, the role of sensors and sensing systems has grown considerably in the design, construction, and management of civil infrastructure systems. Growth in the application of sensors to monitoring operational structures has occurred due in large part to the rapid transformation of sensors into high-performance measurement devices capable of measuring the behavior of structures at global and local scales. These attributes have led to the adoption of sensing systems to track the progress of infrastructure construction, evaluate the design of innovative structures, and to monitor the health of structures. In transforming structural monitoring systems into structural *health* monitoring systems, sensing systems support the automated execution of data interrogation methods that diagnose damage including its location and severity. This book has been written to provide both novice and expert readers with an encyclopedic summary of current state-of-the-art sensors and sensing systems for civil infrastructure monitoring. The book is divided into three parts: Volume 1 – Sensing hardware and data collection methods for performance assessment, Volume 2/Part I – Sensor data interrogation and decision making, and Volume 2/Part II – Case studies in assessing and monitoring specific structures. This chapter begins with a historical perspective on the development and use of sensors for civil infrastructure monitoring followed by an overview of each part of the book. The chapter concludes with a summary of the open challenges that remain in the field of infrastructure monitoring including the need for new sensors and improved methods of data interrogation for civil infrastructure management.

Key words: sensors, sensing systems, civil engineering, infrastructure, structural health monitoring, asset management, damage detection.

1.1 Introduction

Infrastructure systems including bridges, roads, pipelines, dams, and power grids are vital resources that provide basic services to society. Given the vital role infrastructure plays in providing society with a high quality-of-life,

© 2014 Woodhead Publishing Limited

monitoring these assets using sensors is an important step towards verifying design assumptions, tracking structural performance over a structure's life, and rapidly identifying unsafe structural conditions originating from damage and deterioration. The past half century has witnessed an explosive growth in the availability of powerful new sensors that can be adopted to monitor the behavior, performance, and health of large-scale, operational civil infrastructure systems. This growth has been fueled in part by industry and government. For example, government-funded research programs have been initiated and sustained in academic settings to scientifically advance sensing technologies in the laboratory. Concurrently, industry has made strategic investments aimed at translating promising laboratory-based technologies into reliable, field-ready sensing components and systems. A direct beneficiary of these long-term investments has clearly been the civil engineering field, which today is at the cutting-edge in terms of the advancement and deployment of sensing systems tailored for monitoring complex and massive structural systems. Adoption of sensing systems to monitor operational civil infrastructure systems has undergone three major phases over the past 50 years: (i) sensors were first used in special case studies centered on assessing structures with revolutionary design concepts; (ii) sensors were later used more widely to monitor structures exposed to extreme loads to determine structural performance and the limits of performance under such harsh load conditions; and (iii) today, interest in sensing systems has grown in response to the need for sensed data to assess the structural health of a system monitored.

Early examples of permanent structural monitoring date as far back as the 1940s. An early example of a monitoring system installed on an operational civil engineering structure was the installation of ten Hall accelerometers on the Golden Gate Bridge between 1945 and 1946 to monitor vertical deck accelerations under wind excitation (Vincent, 1958; Abdel-Ghaffar and Scanlan, 1985). Hall accelerometers were large single degree-of-freedom mass systems that wrote their measurements to paper on a rotating drum. The installation of the Hall accelerometers on the Golden Gate Bridge was optimized to illuminate the behavior of the long, slender bridge structure under strong wind loading. Installation of the system was in response to the dramatically catastrophic failure of the Tacoma Narrows Bridge that same year. This monitoring system was kept in continuous operation until 1954 (Abdel-Ghaffar and Scanlan, 1985). The decision to install permanent monitoring systems, like that deployed on the Golden Gate Bridge, were extremely rare and typically reserved for 'special' structures with unique designs that required verification of design assumptions.

By the early 1960s, digital data acquisition systems were beginning to emerge with the advent of the personal computer. For example, IBM introduced the IBM 1710 personal computer and IBM 7700 data acquisition system in 1961 and 1963, respectively (Border, 1990). Based on analog interfaces, digital data acquisition systems rapidly matured for both laboratory and field use over the three decades following the introduction of the first IBM data acquisition systems. Specifically, improved functionality (e.g., higher digitalization resolutions, higher sample rates, more channels) and hardware ruggedization all allowed digital data acquisition systems to be deployed to the field for reliable operation in civil infrastructure systems. Due to the availability of digital data acquisition systems, civil engineers began to deploy monitoring systems more widely to assess the response of infrastructure systems during extreme load events (e.g., earthquakes, hurricanes) in order to determine if structures were operating in a manner that placed the public at risk. Unfortunately, the high costs of the systems only justified their use in critical structures operating in extreme load environments. Examples include monitoring systems in bridges (Peeters and DeRoeck, 2001; Wong, 2004; Ko and Ni, 2005; Brownjohn *et al.,* 2010) and buildings (Celebi, 2000; Nayeri *et al.*, 2008) exposed to seismic and wind loads, and offshore oil platforms (Tidewell and Ilfrey, 1969) exposed to extreme sea states and subject to fatigue. The seismic monitoring of civil structures has been a particularly strong driver of monitoring system adoption. For example, in the United States, 60 bridges, 170 buildings, and 20 dams have been instrumented since 1972 through the California Strong Motion Instrumentation Program (CSMIP, 2013). Other strong ground motion instrumentation programs in Japan, Taiwan, China, and Europe have led to similar instrumentation efforts in their respective nations and regions.

Beginning with the 1970s, the structural engineering field sought to do more with sensors and sensing systems deployed to the field. Specifically, attention was turned to expanding the role of monitoring systems to track the behavior of structural systems over their complete life-cycles so as to assess their long-term performance and health (i.e., structural health monitoring (SHM)). Two technological advances fueled strong interest in SHM. First, new classes of sensors began to emerge that offered new measurement modalities and more convenient means of data acquisition at lower cost. For example, microelectromechanical systems (MEMS) sensors were beginning to be marketed that miniaturized sensor packages while reducing sensor unit costs (Petersen, 1982; Liu, 2011). Other disruptive, new sensing technologies included fiber optic sensors (Ansari, 1993; Glisic and Inaudi, 2007), wireless sensors (Straser and Kiremidjian, 1998; Lynch, 2002; Spencer *et al.,* 2004; Lynch and Loh, 2006), and piezoelectric surface sensors (Raghavan and Cesnik, 2007), among others. Second, data management and health-based data interrogation methods began to emerge that allowed measurement data to be analyzed to infer structural conditions (i.e., assess if a structure is damaged or deteriorated)

(Sohn and Oh, 2010). As early as the 1970s, the offshore oil and aerospace industries began to study the use of vibration-based damage assessment methods to assess the health of offshore platforms and aerospace systems, respectively. In the 1980s, the civil infrastructure community started to use vibration-based approaches as monitoring tools for bridges and buildings (Salane *et al.,* 1981; Salawu, 1994; Doebling *et al.*, 1996; Sohn *et al.,* 2004). Modal properties and global quantities derived from these characteristics, such as mode shape curvature and dynamic flexibility, have been the primary features used to identify the existence of damage in structures. To enhance the sensitivity of damage detection methods to identify the location, type and severity of structural damage, nondestructive detection techniques (NDT) such as impact echo, magnetic particles, ultrasonic inspection, acoustic emission, thermography, and ground penetration radar, to name just a few, have been considered for use in SHM systems (Chong *et al.,* 1994, 2003; Chong and Liu, 2003). While data interrogation methods for damage detection are still in their early stages of development, great strides have been made in recent years making automated SHM a potentially viable technology for asset management of civil infrastructure systems.

Today, the civil infrastructure field is fortunate to have deployed a large number of sensing systems to operational civil engineering structures. Prior to 2000, the monitoring systems deployed had largely been commercial monitoring systems installed by owners to either improve their asset management methods (as was the case for offshore structures, where owners sought means of managing fatigue accumulation in their structures) or to be compliant to local regulations (as was the case for building owners in California, who were required to install seismic monitoring systems in large structures by the state building code). Academic researchers also play increasingly greater roles in the deployment of monitoring systems in operational civil engineering structures with many systems now including experimental, non-commercial components. Specifically, many researchers engaged in the technological development of sensors and sensing systems to view full-scale, operational structures as the ultimate test of their technologies. For example, the reliability of wireless monitoring systems must be tested at full-scale in the field because environmental variations in the wireless communication channel cannot be accurately simulated in a laboratory setting. Academia–industry collaborations have also impressively led to prolific adoption of structural monitoring systems on newly constructed critical infrastructure systems including long-span bridges. This is especially true in developing countries, such as China where more than 70 newly constructed bridges have been instrumented with dense networks of sensors and sophisticated data acquisition systems since 2000.

1.2 Introduction to this book

The objective of this book is to introduce and showcase the many sensors, sensing systems (i.e., monitoring systems), and data processing techniques recently proposed and validated in real operational civil infrastructure systems. These systems have as their primary goal the assessment of the performance, operation, and physical health of a monitored structure. Since the authors' interest and expertise lie in civil engineering, our discussion mainly focuses on infrastructure systems such as high-rise buildings, signature bridges, wind turbines, nuclear power plants, electrical distribution systems, pipelines, dams, roads, communication networks, and railroad systems, among others. We have selected three major areas that will serve as focal points for this two volume book: Volume 1 - Sensing hardware and data collection methods for performance assessment, Volume 2/Part I - Sensor data interrogation and decision making, and Volume 2/Part II - Case studies in assessing and monitoring specific structures.

In Volume 1, sensing hardware (i.e., sensors, data acquisition systems) is the primary focus. The sensors presented in this book have been used for performance assessment of civil infrastructure systems ranging from commonly used sensors (e.g., accelerometers, strain gages) to new wireless, noncontact, robotic sensors. Furthermore, sensing data acquisition systems and energy harvesting issues are also discussed, given their important relationship to sensors installed in operational infrastructure systems. Readers will find this section particularly useful, since several intriguing sensing techniques specific to civil engineering systems are introduced. In Part I of Volume 2, the book explores how data acquired from various sensors can be processed and transformed into valuable information that owners and asset managers can utilize to understand the characteristics of a structure, evaluate its condition, identify damage, and predict future performance. Key data interrogation and decision-making methods are presented, including statistical inference, data fusion methods, and decision analysis techniques. In Part II of Volume 2, case studies of the technologies presented in the earlier chapters are highlighted. This section includes successful examples of structural monitoring systems deployed in various civil engineering systems ranging from conventional buildings, bridges, tunnels, and dams to lifeline systems, roads, and offshore structures.

1.3 Overview of sensors and sensing system hardware

The fundamental building block of structural monitoring systems is the sensing transducer. The quality and completeness of the data set collected for a given structure largely depends upon the capabilities and quality of the transducers used to record structural responses. To date, a plethora of sensor types are available for installation in civil infrastructure systems. Traditional transducers widely used in bridge and building monitoring were largely macroscopic sensors: accelerometers (e.g., force-balance, piezoelectric, piezoresistive, and capacitive), linear variable displacement transducers, strain gages (e.g., metal foil, semiconductor), tilt meters, ground positioning system (GPS), anemometers, and geophones. Many of these sensing transducers have enjoyed decades of successful field deployments and have proven valuable for measuring static and dynamic structural responses to loading. The objective of Volume 1 is to review currently available sensing and data acquisition technologies that are being used to assess current structural conditions.

First, the basic operational principles of data acquisition system architectures used to collect measurement data are presented in Chapter 2 of Volume 1 by Todd. This chapter presents an overview of important concepts related to the process of getting (i.e., data acquisition) and processing of data (i.e., data reduction). It includes many potent subjects, such as time/frequency domain signal analysis, probability, uncertainty analysis, analog-to-digital (A/D) and digital-to-analog (D/A) conversions, sampling theory, multiplexing, filtering, and aspects of hardware design. With the basics of data acquisition introduced, Chapter 3 of Volume 1 by Yoder and Adams reviews and describes some commonly used traditional sensors (which are mature and often inexpensive sensors) for long-term monitoring of infrastructure systems. The measurements made using these sensors are well correlated to the physical characteristics of a structure or to its operating condition. This chapter also identifies commonly used algorithms for processing the data originating from these sensors.

In general, sensors designed for structural monitoring are ‘passive’ components; in other words, such sensors record the response of the system without acting directly on the structure itself. In contrast, ‘active’ sensors described in Chapter 4 of Volume 1 by An *et al.* introduce controlled excitations into the structure and measure the corresponding structural response. The advantage of using active sensors for SHM is that they can be used to introduce controllable and repeatable excitations. This chapter deals with the basic operational principles of piezoelectric transducers and the characteristics of piezoelectric materials. Several active sensing techniques used for defect detection such as guided waves, impedance spectroscopy, and acoustic emission are introduced.

In recent years, fiber-optic-based strain sensors, especially long-gage strain sensors and displacement sensors, have received much attention because of their high sensitivity and immunity to environmental factors such as electromagnetic interference and resistance to chemical attack. Chapter 5 of Volume 1 by Peters and Inaudi describes many different fiber optic sensor technologies, defines their ranges of performance, and presents their suitability for monitoring civil infrastructure systems.

Chapter 6 of Volume 1 by Meo provides an overview of acoustic emission techniques for fatigue detection in civil infrastructure systems. Basic principles are followed by techniques for acoustic source localization and defect quantification. Field application is introduced to validate its effectiveness. Chapter 7 by the same author goes further and presents nonlinear acoustic and ultrasonic techniques.

Chapter 8 of Volume 1 by Huston and Busuioc presents a comprehensive overview of radar technology to detect the subsurface condition of a structure. It includes probing subsurface conditions in concrete, detecting cracks and corrosion in concrete decks, assessing asphalt pavement depth along with its overall layer properties, and detecting delamination of reinforcement inside concrete and debonding between concrete and asphalt layers. An important feature of radar sensing is that disturbances in the magneto-elastic (EM) field serves as both a probe for measurement and a signal transmitter.

Despite the increasing popularity of cable-stayed bridges, accurate yet simple methods are still needed to directly measure stresses (forces) in stay cables. The measurement of cable force is important for monitoring excessive wind or traffic loadings, gaging the redistribution of forces present after seismic events and other natural disasters, and for detecting corrosion via loss of the cable cross section. Wang and Wang in Chapter 9 of Volume 1 present a state-of-the-art technique using the magneto-elastic (EM) sensor to measure stress or force in high-strength steel strands and cables. EM techniques are used to determine forces in all sizes of a prestressed steel cable or tendon. Applications include stress measurement of strands in prestressed concrete members during or after construction, and stress measurement in cable-stayed bridges and in hanger cables and anchorage strands for suspension bridges. Additional applications include monitoring of cable anchors for retaining walls and tunnels, as well as in monitoring cable-based support systems of dome structures.

Chapter 10 of Volume 1 by Ozevin discusses advances in MEMS as a sensing tool for monitoring of civil infrastructure systems. Sensors can now be miniaturized using the same operational principles as their traditional counterparts yet have circuitry for signal processing and computation included on the same silicon die. To date, the greatest success of MEMS has been in the design and fabrication of accelerometers (e.g. Analog Devices, MEMSIC, STMicro, VTI). MEMS-based transducers also have been produced to sense such parameters as relative humidity, temperature, pressure of all types, magnetic field (compass), tilt, twist (gyroscope), strain, corrosion, and gaseous compounds such as CO, NO_x, methane, and sarin. Closely related to MEMS are nano-engineered systems. In Chapter 11 of Volume 1 by Loh and Ryu, multifunctional materials and nanocomposites are presented for use in sensing strain of structural elements. Multifunctional materials are designed to perform multiple functions such as sensing, actuation, energy harvesting, mechanical reinforcement, and energy dissipation. Technological breakthroughs allow a plethora of new materials to be created through controlled assembly of different molecular components.

Laser-based sensing for displacement field measurement is discussed in Chapter 12 of Volume 1 by Yu. This chapter provides an overview of current laser-based sensing techniques for engineering applications. It includes descriptions of laser interferometry or electronic speckle pattern interferometry (ESPI), digital shearography, scanning photogrammetry, and laser Doppler vibrometry (LDV).

Corrosion sensing is discussed in Chapter 13 of Volume 1 by Poursaee. Numerous sensor technologies exist for monitoring corrosion effects on steel. These technologies can be categorized as electrochemical or mechanical methods. Since corrosion of steel reinforcement is an electrochemical process, such sensors either measure electrical fields at the concrete surface or measure main corrosion factors such as chloride content and pH of pore fluids. In recent years, a number of researchers have begun to explore means of integrating wireless read-out mechanisms for corrosion sensors to make their use more attractive to bridge managers. Physical approaches include fiber optic corrosion sensors and magneto-elastic corrosion sensors. Additional technologies include the use of resistance probes, guided waves, among others.

Ji and Chang in Chapter 14 of Volume 1 describe vision-based measurement techniques for deformation monitoring. Results from the laboratory as well as from the field are obtained to demonstrate the accuracy and the potential for applications to infrastructure systems. Deformation measurement of large-scale infrastructure, including bridges, has always been a demanding task. However, deformation data can be used for design validation, performance monitoring, as well as for structural safety and integrity assessment.

Myung *et al.* in Chapter 15 of Volume 1 use robotic technology to remotely inspect and monitor structural systems. A prototype robotic system carrying various sensing technologies such as a camera, optical sensors, laser sensors, and wireless sensors, is used to inspect a structure and to detect defects remotely. There is a growing concern with the disruption of regular traffic due to human inspection processes; remote and robotic sensing can offer an alternative to this growing problem.

Comprehensive discussion on wireless sensing platforms for monitoring civil engineering systems is presented in Chapters 16 and 17 of Volume 1 by Kane *et al.* and Peckens *et al.*, respectively. Traditionally, SHM is performed at a global level, with a limited number of sensors distributed over a relatively large area of a structure. Such sensing systems, with gross spatial resolution, can only detect major damage conditions. Wireless sensor networks offer engineers the opportunity to deploy dense networks of sensors at reduced cost. As discussed in Chapter 17 of Volume 1, wireless sensors have made an especially major impact in the monitoring of operational bridge structures.

Chapter 18 of Volume 1 by Scruggs gives an overview of some of the fundamental design issues arising in vibrating energy harvesting systems for sensing applications. It focuses primarily on piezoelectric and electromagnetic transducers. A number of basic electronic circuits for extracting power from harvesters are discussed, including the standard diode bridge rectifier, DC/DC converters, and synchronized switch harvesting on inductor (SSHI) circuits.

In conclusion, traditional sensors to measure strain, stress, acceleration, velocity, temperature, and displacement are reviewed in Volume 1. These sensors offer tremendous possibilities for the monitoring of various infrastructure system types subjected to external load conditions. Additional new technologies, such as fiber optic sensors and MEMS sensors, offer various possibilities of sensing and defect detection under severe environmental constraints. Acoustic and ultrasound sensors in the form of piezoelectric elements are also introduced to more aggressively assess current structural conditions. Electromagnetic sensors are introduced to measure the forces in steel cables and to detect the breakage of cables. Ground penetrating radar (GPR) is used to locate and determine the extent of corrosion of reinforcement steel or prestressing tendons buried inside concrete elements or covered by asphalt pavements. Robotic sensing, remote sensing, and wireless sensing platforms including energy harvesting are emerging as powerful new additions to the sensing arsenal of the civil engineer for long-term health monitoring of infrastructure.

1.4 Overview of sensor data interrogation and decision making

Structural monitoring and SHM systems deploy sensors to collect measurements of structural responses, assess the current state of a structure, and assist decision-makers with making informed and ideally optimal decisions. The second major section of the book (Volume 2/Part I) focuses on sensor data interrogation and decision-making technologies and is intended to serve as a linkage between the data collected from sensors (covered primarily in Volume 1) to decision making so that the information inferred from the measurement data can be utilized for structural health assessments, life-cycle assessment and management, and long-term resource allocation for infrastructure repair, rehabilitation and replacement, just to name a few. The objective of this section of the book is to cover, in detail, the current state-of-the-art in the management of sensor data including the interrogation of sensor data for decision making.

The first part of Volume 2 of this book (Chapters 1 through 6) is reserved for presenting the current data management methods associated with structural monitoring. Specifically, Chapter 1 of Volume 2 by Law *et al.* summarizes key data management issues including data collection and storage at the site, data communication, and transfer of data to off-site facilities for storage. In particular, the discussion focuses on: (i) data processing and management at wireless sensor nodes (sensor-level) with special attention on energy consumption reduction; (ii) in-network communication issues such as wireless communication range, robust communication protocol design; and (iii) system- and database-level persistent data management and retrieval by means of a wind turbine monitoring system as an illustrative example.

Chapter 2 of Volume 2 by Zonta presents Bayesian logic as a mathematical framework to formulate the inference problem, in attempting to gain information on the target structure based on sensor readings, particularly accounting for data and model uncertainties. Next, since monitoring systems often produce a variety of data from distributed sensors, common data reduction techniques including principal component analysis (PCA), probabilistic PCA, multidimensional scaling, and kernel PCA are introduced to reduce computational efforts and to enhance inference performance. Furthermore, sensor- and temporal-level data fusion techniques are discussed based on Bayesian and alternative non-probabilistic models.

Chapter 3 of Volume 2 by Bernal builds on Chapter 2 by further exploring statistical inference and PCA for vibration-based damage detection and localization as one step in infrastructure decision making. Novelty detection, which is one class of statistical inference, is used for damage identification, particularly under a situation where environmental variations are not measured. Examples of damage detection using statistical subspace system identification, Kalman filtering, and cumulative sum charts are presented in sufficient detail to allow implementation by users.

Other types of vibration-based damage detection techniques are introduced in Chapter 4 of Volume 2 by Nagarajaiah *et al.* focusing on modal parameter identification using output-only signals. These output-only system identification techniques are particularly attractive for civil infrastructure systems because large-scale civil systems are often subjected to temporally and spatially distributed unknown system inputs. Furthermore, time varying characteristics of systems are captured using time-frequency analysis techniques such as the short-time Fourier transform, empirical mode decomposition, wavelet transforms, and blind source separation techniques.

In Chapter 5 of Volume 2 by Frangopal and Kim, the prediction of structural performance based on monitoring data using the Bayesian approaches described in Chapter 2 of Volume 2 are presented. However, the chapter goes much further, in showing how the data can also be utilized for cost-effective

SHM planning, life-cycle performance analysis, and cost analysis. In particular, probability- and statistics-based decision-making approaches are presented to effectively treat epistemic uncertainty for rational performance assessment and prediction. Furthermore, measured data are used to reduce uncertainties in prognosis. Finally, the effects of SHM on life-cycle assessment and approaches for efficient integration of SHM into life-cycle analysis of civil infrastructure systems are discussed.

Finally, Chapter 6 of Volume 2 by Birken *et al.* focuses on a detailed case study to highlight the vexing challenges associated with large-scale data management in the field. Based on the Versatile Onboard Traffic-Embedded Roaming Sensors (VOTERS) project, a roaming sensing system is introduced where a group of sensors are mounted onto a survey vehicle to inspect the conditions of roads' surfaces and bridge decks. A group of heterogeneous sensors are employed to capture the full and coherent picture of surface and subsurface defects over large spatial areas. Challenges and solutions associated with data uploading and storage, correlating spatially and temporally distributed data, and fusion and rapid processing of large amounts of bulk data are discussed in detail.

1.5 Overview of application of sensing systems to operational infrastructure

The application of sensors and sensing systems to specific infrastructure system types is presented in Chapters 7 through 21 of Volume 2. Each chapter focuses on only one infrastructure system type, in order to ensure a detailed and complete summary is presented to the readers. These application-specific chapters are designed to build upon the content contained in Volume 1 (i.e., sensing hardware and data collection methods) and Chapters 1 through 6 (i.e., sensor data interrogation and decision making) of Volume 2, with minimal overlap presented. Each application chapter begins with an introduction that provides the reader with the motivation for sensing in the defined field of application, followed by a brief summary of prior approaches (if any) to monitoring and assessing system performance and health. A summary of the sensors previously used in monitoring each application is provided with a description of how their operational attributes fit the application. Where appropriate, laboratory validations performed prior to deployment in the field will be described. Each chapter devotes a significant portion of its focus to specific case studies that provide a representative picture of how sensors and sensing systems are deployed and how sensing data are used to aid structure owners and managers in their decision-making processes. Finally, each chapter concludes with a summary of the lessons learned in each case study, with key findings generalized for future technology development and field deployment.

The following infrastructure systems have been selected for coverage in this book: bridges, seismically-excited buildings, super-tall towers, dams, tunnels, roads, wind turbines, pipelines, underwater systems offshore structures, railroad tracks, nuclear power plants, subsurface utilities, power systems, and levees. In Chapter 7 of Volume 2, Brownjohn *et al.* describe the current state of art in the deployment of long-term monitoring systems in bridges. The chapter both describes the sensors successfully used in this application and presents an extensive case study in which the sensors have been used to monitor the performance of the Tamar Bridge in Saltash, England. Equally impressive are the various monitoring systems deployed to monitor buildings. In particular, buildings in seismic areas have garnered the most instrumentation, given the extreme load that buildings are exposed to during earthquakes. Chapter 8 of Volume 2 by Mita highlights the deployment of sensing systems for seismic monitoring of high-rise structures. This chapter provides a broad overview before describing various case studies in Japan. Chapter 9 of Volume 2 by Ni describes the importance of structural monitoring and health monitoring for super-tall towers such as marquee TV towers located outside seismic areas.

Large earth structures have benefited from long-term deployments of sensors and sensing systems as presented in Chapters 10 through 13 of Volume 2. For example, Chapter 10 by Loh describes the deployment of a permanent monitoring system to the Fei-Tsui arch dam located in Taiwan. A major contribution of this chapter is an extensive description of data processing of the dam response data for system identification. Chapter 11 by Hoult and Soga introduce sensors commonly used for monitoring existing tunnels and those under construction. Their chapter covers the application of long-term monitoring of tunnels in both soft ground and rock, which come with very different sensing system requirements. Chapter 12 by Birken and Oristaglio presents a detailed overview of the sensing methods required to explore subgrade structures including buried pipes. The chapter has a very specific focus on the use of electromagnetic geophysical sensing arrays that are applied on a mobile platform. Chapter 13 by Inaudi explores the application of fiber optic sensors as a distributed sensing platform for monitoring the stability of levees, sinkholes, and landslides. In a similar manner, Chapter 14 by Glisic applies similar fiber optic sensors to monitor buried pipeline systems.

Transportation systems are also very important systems to monitor because of their vast spatial distribution. These systems often require mobile sensing strategies where sensors are based on a movable platform that can be moved through the system to collect data. Both road and rail transportation systems are considered in Volume 2. Chapter 15 by Wang and Birken explores the application of sensing technologies and nondestructive evaluation (NDE) methods to monitor the integrity of road systems including asphalt pavements and concrete bridge decks. Similarly, Chapter 16 by Rizzo explores the development of sensing systems for monitoring extensive lengths of railroad tracks. Eddy current, thermography, and ultrasonic methods are just a few of the key methods presented for rail road health assessment.

Chapters 17 and 18 of Volume 2 focus on sensing systems designed for the monitoring of offshore structures. Chapter 17 by Rizzo provides a broad overview of the sensing systems available for structures situated underwater, which is an inherently harsh environment for sensors. Chapter 18 by Kim and Lee goes into greater depth in the application of sensing systems for the hull monitoring of ships and offshore oil platforms.

Finally, Chapters 19 through 21 of Volume 2 are devoted to the application of sensing and monitoring systems to monitor the operation and performance of energy systems. Specifically, Chapter 19 by Rolfes *et al.* describes the application of monitoring systems to monitor the structural integrity of large wind turbine systems sited on- and offshore. Chapter 20 by Sohn *et al.* focuses on the demanding sensing requirements of the nuclear industry to monitor the structural performance of heavy nuclear containment structures. Finally, Chapter 21 by Hiskens is an overview of the monitoring systems employed by the power industry to monitor the operation of national energy grids.

1.6 Future trends

The application of sensors and sensing systems to operational civil infrastructure systems has blossomed in recent years. Permanent structural monitoring systems have been successfully deployed on operational bridges, dams, pipelines, and offshore structures, among other structures. These permanent monitoring systems have been deployed to collect data related to the performance of these structures under normal load conditions as well as during extreme load events. It is clear that bridges and buildings have been the greatest beneficiaries of structural monitoring systems, especially those located in seismically active areas. For example, most of the large buildings and bridges in the western United States, as well as in Japan, have been instrumented with a minimal number of accelerometers through various regional strong ground motion programs. Wireless communications is currently ushering in a major paradigm-shift in the structural monitoring field. Wireless sensors offer infrastructure owners a lower-cost option for instrumentation thereby allowing more structures to be economically monitored. In addition, the ease of installation of wireless sensors is also driving higher sensor densities in a single structure, which in turn offers more quantitative data on structural performance and health. The trend of adoption of wireless telemetry in structural monitoring applications will continue unabated into the future; this is a promising trend that will lead to a proliferation of monitoring systems for civil infrastructure.

Other key sensing technologies that are equally paradigm-shifting include fiber optic sensors for distributed sensing and ultrasonic measurements. Fiber optic sensors have had a particularly high impact in the realm of large, continuous structures whose dimensions span miles, including pipelines, levees, and geotechnical systems (e.g., landfills, sink holes). Ultrasonic sensors and associated NDE methods used to be limited to manual operation when needed. However, technological developments are moving these powerful sensors into the realm of continuous, permanent monitoring. In addition to permanent monitoring systems, classical NDE methods have undergone a revolution in technology development as well as in deployment. As previously mentioned, NDE sensors are being developed for both permanent installation in structures as well as for more automated (and less manual) use in the field. For example, the use of NDE methods such as GPR has proven to be a powerful means of assessing continuous pavement systems found in roads and tarmacs (Saarenketo and Scullion, 2000). In this application domain, research and development have primarily focused on how to transition these powerful sensing techniques into platforms that allow them to sense large swaths of infrastructure systems as quickly and as cost-effectively as possible.

While sensors and sensing systems have made great strides toward offering structure owners valuable information that they can use for the assessment of their structures, there are a number of technological challenges that must be resolved to ensure that the full benefit of structural monitoring is realized for those structure owners who elect to procure such systems. The remainder of this section explores some of the more urgent and vexing challenges that remain ahead for the field.

1.6.1 New sensors for monitoring material processes

The durability of critical infrastructure systems is largely at risk due to material degradation. Such phenomena occur at the fundamental length scale of the material (i.e., the molecular-scale). Cross-disciplinary research is needed between structural engineers and material scientists to hypothesize how materials degrade over the life-cycle of a structure. To provide empirical data to feed such work, sensors are needed to monitor the chemical aging processes of structural materials used in harsh field conditions. Numerous sensor technologies exist for monitoring the chemical properties of building materials, but unfortunately most are based on large-scale laboratory-grade scientific equipment that are impossible to take to the field. As such, there is an absence of compact sensor technologies that can be deployed for long-term *in situ* installation in large-scale civil structures. With recent advances in the field of micro- and nano-electromechanical sensors (MEMS and NEMS, respectively), there is an unprecedented opportunity to formulate novel sensing methods that can be deployed for monitoring chemical properties of construction materials. MEMS and NEMS are especially important because these small-scale systems would be properly scaled to molecular scales, are low-cost when fabricated in batch, and are highly compact allowing for possible inclusion directly within structural material without interfering with structural function. Already many MEMS devices have been proposed for measuring the presence of chemical species (e.g., chloride ions) in structural elements (Chui *et al.,* 2001; Huang and Choi, 2007). New chemical sensors developed for assessment of material chemical properties will likely need to be embedded directly into the material itself. For instance, a concrete bridge structure in a harsh environment (e.g., a saltwater coastal area) would represent a sufficiently challenging environment to assess the performance of nascent chemical sensors.

1.6.2 New sensors for displacement measurements

Current transducers typically measure relative displacement over short distances (e.g., linear variable displacement transducers). With the growing acceptance of performance-based design (largely based on structural displacements), the need for accurate absolute displacement sensing has grown. The practice of double integrating accelerometer data does not yield accurate or detailed results (Clinton and Heaton, 2002), so new technology avenues need to be explored. For example, the measurement of the absolute displacement of bridge decks and tower settlement is of great significance for assessing the bridge condition, estimating the bridge influence line for design verification, and predicting the abnormal internal force redistribution caused by uneven settlement. Likewise, the monitoring of horizontal displacement at pier bases is important for evaluating the consequences after incidents such as earthquakes, ship collisions, and traffic accidents. Laser- and vision-based sensing for displacement monitoring are emerging as viable techniques that complement existing displacement measurement techniques.

1.6.3 Development of robust damage models for structural health assessment

Perhaps the next major challenge in health monitoring of civil engineering structures lies in developing robust damage (or condition) models. Because damage is generally well defined (locations and symptoms) and understood in typical mechanical and aerospace structures, this allows sensors to be optimally developed for measuring and monitoring structural conditions and detecting damage. Conversely, for most civil engineering structures under hazard or normal (aging) conditions, there are no 'equivalent' damage models. It is difficult to identify needs in sensor technology research without knowing where, under what measurement conditions, and for what kind of damage we must contend. After we know how to properly define archetypical damage states of civil structures, we will be in a stronger position to address what to measure and how to directly interpret or relate measured signals to the condition of the instrumented structure. These are some of the issues that civil engineers should address before they consult with the sensor experts.

1.6.4 Data inundation and information extraction

As witnessed throughout the book, current technology trends suggest that there will be an increasing number of sensors deployed in the field for short- and long-term monitoring of civil infrastructure systems. In addition, the diversity of the sensors deployed will also increase allowing more heterogeneous sensor data sets to be collected. In particular, the advancement of wireless sensors, moving and roaming sensing systems, and noncontact scanning devices is expected to exponentially increase the amount of data that sensors can produce. The increase in the amount of sensor data will impose unprecedented challenges in the storage and interrogation of data for effective decision making. These challenges are not an isolated trend witnessed only in infrastructure monitoring, but is happening across almost all engineering and scientific disciplines. The treatment of the plethora of data for discovering information and drawing decision has become a hot research topic in recent years and has been discussed in the context of 'big data' analysis and a ubiquitously interconnected world (i.e., the 'internet-of-things'). For example, data transmission, scalable data storage, data fusion, and rapid processing become common issues as the availability of larger data sets grow. However, when it comes to life-span monitoring of large-scale and distributed infrastructure systems, the magnitude of the problem with big data analysis is significantly amplified. Therefore, more progress is direly needed in this field.

Specific issues with data interrogation include the measurement and treatment of nonstationary and nonlinear system responses. There seems to be a general consensus among researchers that nonstationary and nonlinear system behavior should be fully explored to better understand the dynamic characteristics of structural systems and to detect incipient local defects. Furthermore, it is critical to measure and comprehend the real environmental and operational conditions that operational civil infrastructure systems are exposed to over their life-cycles (Sohn, 2007). This is one of the unique challenges that set infrastructure monitoring apart from many other condition-based monitoring systems, and why civil infrastructure SHM (specifically, damage detection) is more difficult than the monitoring of in-house mechanical systems. Although larger data sets tend to reduce uncertainties in the assessment of system responses and properties, significant uncertainty, particularly epidemic uncertainty, will inevitably remain. Therefore, it is expected that data interrogation and decision making will be cast in the context of statistical and probabilistic frameworks moving forward.

Many statistical inference, pattern recognition, and machine learning approaches are being developed or adapted from other disciplines to assist in autonomously transforming data recorded from civil infrastructure systems into information. Sensing data measured from civil infrastructure have been used for system identification, condition assessment, and damage detection. Recently, sensor data are also being used for performance prediction, life-cycle cost analysis, and resource allocation for infrastructure maintenance and replacement. However, little work has been accomplished in terms of how to integrate measurement data with heuristic knowledge. In addition, there is a need to transfer data and knowledge gained from one specific monitored structural system to another structure. These issues remain as challenging issues since every single civil infrastructure system is unique.

1.7 Conclusion

Unquestionably, the future for sensors and sensing systems for the assessment of civil infrastructure systems has a very bright future. With the adoption of sensors in the infrastructure management field accelerating, future infrastructure will be better designed, easier to manage cost-effectively, and safer for the public to use. This book seeks to provide a single reference for both the novice and expert reader alike, with a detailed review of sensors, sensing systems, data management approaches, and field applications. While every attempt has been made to produce a book with great breadth, interested readers may also consult a number of other references that would give them deeper knowledge. The following list provides a number of references external to this book that may aid in the cultivation of deeper knowledge in sensors and their application to civil infrastructure systems. Enjoy!

Journals

- *AIAA Journal*, American Institute of Aeronautics and Astronautics
- *Cement and Concrete Research,* Elsevier
- *Composites Part B-Engineering,* Elsevier
- *Composites Science and Technology,* Elsevier
- *Composite Structures*, Elsevier

- *Computer-Aided Civil and Infrastructure Engineering,* Wiley
- *Earthquake Engineering & Structural Dynamics,* Wiley
- *Engineering Structures*, Elsevier
- *Experimental Mechanics*, Springer
- *IEEE Sensors Journal*, Institute of Electrical and Electronics Engineers
- *IEEE Signal Processing Magazine*, Institute of Electrical and Electronics Engineers
- *Journal of Engineering Mechanics*, American Society of Civil Engineers
- *Journal of Intelligent Material Systems and Structures*, Sage
- *Journal of Nondestructive Evaluation*, Springer
- *Journal of Sound and Vibration*, Elsevier
- *Journal of Structural Control and Health Monitoring*, Wiley
- *Journal of Structural Engineering*, American Society of Civil Engineers
- *Journal of the Acoustical Society of America*, Acoustical Society Of America
- *Measurement Science & Technology*, Institute of Physics
- *Mechanical Systems and Signal Processing*, Elsevier
- *NDT & E International*, Elsevier
- *Smart Materials & Structures*, Institute of Physics
- *Smart Structures and Systems*, Techno Press
- *Structural Health Monitoring – An International Journal*, Sage
- *Ultrasonics*, Elsevier

Books

Achenbach, J. D. (1975), *Wave Propagation in Elastic Solids*, North-Holland Publishing Company.

Adams, D. E. (2007), *Health Monitoring of Structural Materials and Components: Methods with Applications*, John Wiley & Sons.

Ansari, F. (2005), *Sensing Issues in Civil Structural Health Monitoring*, Springer.

Balageas, D., Fritzen, C.-P. and Guemes, A. (2006), *Introduction to Structural Health Monitoring*, ISTE.

Blitz, J. and Simpson, G. (1996), *Ultrasonic Methods of Non-destructive Testing*, Chapman & Hall.

Culshaw, B. (1996), *Smart Structures and Materials*, Artech House.

Ettouney, M. M. and Alampalli, S. (2011), *Infrastructure Health in Civil Engineering*, Taylor and Francis.

Farrar, C. R. and Worden, K. (2013), *Structural Health Monitoring: a Machine Learning Perspective*, Wiley.

Fraden, J. (1996), *Handbook of Modern Sensors: Physics, Designs, and Applications*, 4th Edn., Springer.

Gandhi, M. V. and Thomson, B. S. (1992), *Smart Materials and Structure*, Chapman & Hall.

Giurgiutiu, V. (2008), *Structural Health Monitoring with Piezoelectric Wafer Active Sensors*, Elsevier.

Glisic, B. and Inaudi, D. (2007). *Fibre Optic Methods for Structural Health Monitoring*, Wiley.

Huston, D. (2011). *Structural Sensing, Health Monitoring, and Performance Evaluation*, CRC Press.

Karbhari, V. M and Ansari, F. (2009*). Structural Health Monitoring of Civil Infrastructure Systems*, Woodhead Publishing Limited.

Kundu, T. (2003), *Ultrasonic Nondestructive Evaluation: Engineering and Biological Material Characterization*, Woodhead Publishing Limited.

Liu, G. R. and Han, X. (2003), *Computational Inverse Techniques in Nondestructive Evaluation*, Woodhead Publishing Limited.

Meijer, G. (2008), *Smart Sensor Systems*, John Wiley & Sons.

Rose, J. L. (1999), *Ultrasonic Waves in Solid Media*, Cambridge University Press.

Schwartz, M. M. (2002), *Encyclopedia of Smart Materials*, John Wiley & Sons.

Staszewski, W., Boller, C. and Tomlinson, G., (2004), *Health Monitoring of Aerospace Structures: Smart Sensor Technologies and Signal Processing*, John Wiley & Sons.

Wang, Z. L. and Kang, Z. C. (1998), *Functional and Smart Materials: Structural Evolution and Structure Analysis*, Plenum Press.

Wenzel, H. (2009), *Health Monitoring of Bridges*, Wiley.

Wilson, J. S. (2005), *Sensor Technology Handbook*, Elsevier.

Conferences

ASCE Engineering Mechanics (annually)

Asia-Pacific Symposium on Structural Reliability and its Applications (every 4 years)

Asia-Pacific Workshop on SHM (bi-annually)

European Workshop on SHM (bi-annually)

International Conference on Bridge Maintenance, Safety and Management (bi-annually)

International Conference on Structural Health Monitoring of Intelligent Infrastructures (bi-annually)

International Conference on Structural Safety & Reliability (every 4 years)

International Conference on Smart Structures and Systems (bi-annually)

International Conference ‘Smart Materials, Structures and Systems’(bi-annually)

International Modal Analysis Conference (annually)

International Symposium on Innovation and Sustainability of Structures in Civil Engineering (bi-annually)

International Workshop on Advanced Smart Materials and Smart Structures Technology (annually)

International Workshop on Structural Health Monitoring (bi-annually)

Review of Progress in Quantitative NDE (annually)

SPIE Smart Structures/NDE (annually)

World Conference on Non-Destructive Testing (every 4 years)
World Conference on Structural Control and Monitoring (every 4 years)

Educational programs

Asia-Pacific Summer School on Smart Structures Technology (APSS)
https://sites.google.com/site/apss2013kaist
International Summer School on Smart Materials & Structures
http://events.unitn.it/en/smartstructures2013
Nondestructive Testing (NDT) Education
http://www.ndt-ed.org
IEEE Seasonal Schools in Signal Processing (S3P)
http://www.signalprocessingsociety.org/community/seasonal-schools/
The Los Alamos Dynamics Summer School (LADSS)
http://institutes.lanl.gov/ei/dynamics-summer-school

1.8 References

Abdel-Ghaffar, A. M. and Scanlan, R. H. (1985), 'Ambient vibration studies of golden gate bridge: I. Suspended structure', *Journal of Engineering Mechanics*, *ASCE*, **111**(4), pp. 463–482.

Ansari, F. (1993), *Applications of Fiber Optic Sensors in Engineering Mechanics: A Collection of State-Of-The-Art Papers in the Applications of Fiber Optic Technologies*, American Society of Civil Engineers (ASCE), Reston, VA.

Border, G. C. (1990), 'Digital computer based data acquisition and control software packages', *Proceedings of the IEEE 42nd Conference on Electrical Engineering Problems in the Rubber and Plastic Industries*, Akron, OH, pp. 29–31.

Brownjohn, J. M. W., Magalhaes, F., Caetano, E. and Cunha, A. (2010), 'Ambient vibration re-testing and operational modal analysis of the humber bridge', *Engineering Structures*, **32**(8), pp. 2003–2018.

Celebi, M. (2000), 'Seismic Instrumentation of Buildings', United States Geological Survey, Report 00–157, Menlo Park, CA.

Chong, K. P., Carino, N. J. and Washer, G. (2003), 'Health monitoring of civil infrastructures', *Smart Materials and Structures*, **12**(3), pp. 483–493.

Chong, K. P., Dillon, O. W., Scalzi, J. B. and Spitzig, W. A. (1994), 'Engineering research in composite and smart structures', *Composites Engineering*, **4**(8), pp. 829–852.

Chong, K. P. and Liu, S. C. (Eds.) (2003). *Intelligent Structures*, Elsevier Applied Science, London, New York.

Chui, Y., Wei, Q., Park, H. and Lieber, C. M. (2001), 'Nanowire nanosensors for highly sensitive and selective detection of biological and chemical species', *Science*, **293**(5533), pp. 1289–1292.

Clinton, J. F. and Heaton, T. H. (2002), 'Potential advantages of a strong-motion velocity meter over a strong-motion accelerometer', *Seismological Research Letters*, **73**(3), pp. 332–342.

CSMIP (2013), California Geological Survey – About CSMIP (California Strong Motion Instrumentation Program). Department of Conservation, State of California, http://www.conservation.ca.gov/cgs/smip/Pages/about.aspx.

Doebling, S. W., Farrar, C. R., Prime, M. B. and Shevitz, D. W. (1996). *Damage Identification and Health Monitoring of Structural and Mechanical Systems from Changes in Their Vibration Characteristics: A Literature Review*, Report LA-13070-MS, Los Alamos National Laboratory, Los Alamos, NM.

Glisic, B. and Inadui, D. (2007), *Fibre Optic Methods for Structural Health Monitoring*, Wiley, Hoboken, NJ.

Huang, X. -J., and Choi, Y. -K. (2007), 'Chemical sensors based on nanostructured materials', *Sensors and Sctuators, B: Chemical*, **122**(2), pp. 659–671.

Ko, J. M. and Ni, Y. Q. (2005), 'Technology developments in structural health monitoring of large-scale bridges', *Engineering Structures*, **27**(12), pp. 1715–1725.

Liu, C. (2011), *Foundations of MEMS*, Prentice Hall, Upper Saddle River, NJ.

Lynch, J.P. (2002), 'Decentralization of Wireless Monitoring and Control Technologies for Smart Civil Structures', John A. Blume Earthquake Engineering Center, Stanford, CA.

Lynch, J. P. and Loh, K. J. (2006), 'A summary review of wireless sensors and sensor networks for structural health monitoring', *Shock and Vibration Digest*, **38**(2), pp. 91–130.

Nayeri, R. D., Masri, S. F., Ghanem, R. G. and Nigbor, R. L. (2008), 'A novel approach for the structural identification and monitoring of a full-scale 17-story building based on ambient vibration measurements', *Smart Materials and Structures*, **17**(2), 025006.

Peeters, B. and DeRoeck, G. (2001), 'One year monitoring of the Z24-bridge: Environmental influences versus damage events', *Earthquake Engineering and Structural Dynamics*, **30**(2), pp. 147–171.

Petersen, K. F. (1982). 'Silicon as a mechanical material,' *Proceedings of the IEEE*, **70**(5), pp. 420–457.

Raghavan, A. and Cesnik, C. E. S. (2007), 'Review of guided-wave structural health monitoring', *Shock and Vibration Digest*, **39**(2), pp. 91–116.

Saarenketo, T. and Scullion, T. (2000), 'Road evaluation with ground penetrating radar', *Journal of Applied Geophysics*, **43**(2–4), pp. 119–138.

Salane, H. J., Baldwin, J. W. and Duffield, R. C. (1981). 'Dynamics approach for monitoring bridge deterioration,' *Transportation Research Record*, **832**, pp. 21–28.

Salawu, O.S. (1994). 'Nondestructive evaluation of constructed facilities using vibration testing,' *Insight*, **36**(8), pp. 611–615.

Sohn H., Farrar, C. R., Hemez, F. M., Shunk, D. D., Stinemates, D. W., Nadler, B. R. and Czarnecki, J. J. (2004), 'A review of structural health monitoring literature: 1996–2001', Los Alamos, New Mexico: Los Alamos National Laboratory.

Sohn, H. and Oh, C.K. (2010), 'Applications of statistical pattern recognition paradigms to structural health monitoring,' a book chapter of *Encyclopedia of Structural Health Monitoring* (Editors: Profs C. Boller, F.K. Chang and Y. Fujino), John Wiley & Sons.

Sohn, H. (2007) 'Effects of environmental and operational variability on structural health monitoring,' *a Special Issue of Philosophical Transactions of the Royal Society A on Structural Health Monitoring*, **365**, pp. 539–560.

Spencer, B.F., Ruiz-Sandoval, M. E. and Kurata, N. (2004), 'Smart sensing technology: Opportunities and challenges', *Journal of Structural Control and Health Monitoring*, **11**(4), pp. 349–368.

Straser, E. and Kiremidjian, A. S. (1998), *Modular, Wireless Damage Monitoring System for Structures*, John A. Blume Earthquake Engineering Center, Stanford, CA.

Tidewell, D. R. and Ilfrey, W. T. (1969). 'Developments in marine drilling riser technology,' *Proceedings of the American Society of Mechanical Engineers (ASME)*.

Vincent, G. S. (1958). 'Golden gate bridge vibration studies', *Journal of the Structural Division*, *ASCE*, **84**(1817), pp. 1–42.

Wong, K. Y. (2004), 'Instrumentation and health monitoring of cable-supported bridges', *Structural Control and Health Monitoring*, **11**(2), pp. 91–124.

2

Sensor data acquisition systems and architectures

M. D. TODD, University of California San Diego, USA

DOI: 10.1533/9780857099136.23

Abstract: This chapter describes key topics in the design and operation of conventional data acquisition systems used for structural health monitoring. These systems are discussed by four sub-system modules: (1) the sensor module, which consists of the physical element(s) that interact with the system-under-test to sense the physical process(es) and convert that information into a detectable signal form (e.g., an electrical voltage); (2) the signal conditioning module, which may have any number of functions, which could be further subdivided into analog functions (voltage amplification, some types of filtering, and possibly telemetry) and digital functions (timekeeping, digitization, triggering, master control); (3) the output module, which provides an actual indication, in an appropriate form, of the measurement(s) desired; and (4) the control module, which contains some form of an active controller that interprets the output and feeds back that information to an actuator that can manipulate the physical process (only present in active sensing systems). In the discussion of each module, the relevant hardware and signal processing components that comprise its operation and function are described, and the chapter concludes with a short summary of key concepts and observation of trends in data acquisition for structural health monitoring.

Key words: sampling, signals, analog-to-digital conversion, sensor metrics.

2.1 Introduction

This book considers sensing technologies for civil infrastructure monitoring and health management, the scope of which was addressed in Chapter 1. Any such monitoring activity inevitably requires getting a measurement (more likely, many measurements) of some physically-observable behavior of the structural system e.g., the system's vibration, strain, temperature, etc. This chapter will present an overview of important concepts related to the process of getting such measurements ('data acquisition'), the primary issues associated with this process, and the most common architectures used to execute this process. A fairly comprehensive list of important topics in this chapter includes time/frequency domain signal analysis,

© 2014 Woodhead Publishing Limited

probability, uncertainty analysis, analog-to-digital conversion (and digital-to-analog conversion (DAC)), sampling theory, transducer design, multiplexing/demultiplexing, filtering, and many aspects of hardware design. A number of excellent books on these subjects are available for example Kay (1993); Figliola and Beasley (2000); Doeblin (2003); Ayyub and Klir (2006); Beckwith *et al*. (2006); Bendat and Piersol (2010). Each of these topics warrants an entire literature collection by itself, so the primary objective of this chapter will be to present relevant information about the most important of these topics, defined to be the ones of salient interest to the engineer interested in civil infrastructure monitoring applications. As such, this chapter begins with an overview of what measurement systems generally 'look like,' then considers a number of background concepts in signal processing, and subsequently discusses the specific realizations of the components and their properties that comprise typical voltage-based measurement systems. The chapter then concludes with some of the differences found in digital input/output and in optical-based measurement systems.

2.1.1 General measurement system

A very general schematic of a measurement system is shown in Fig. 2.1. The schematic shows the bridge between the physical process being detected (e.g., acceleration vibration of a structure) and the analyzer (the engineer

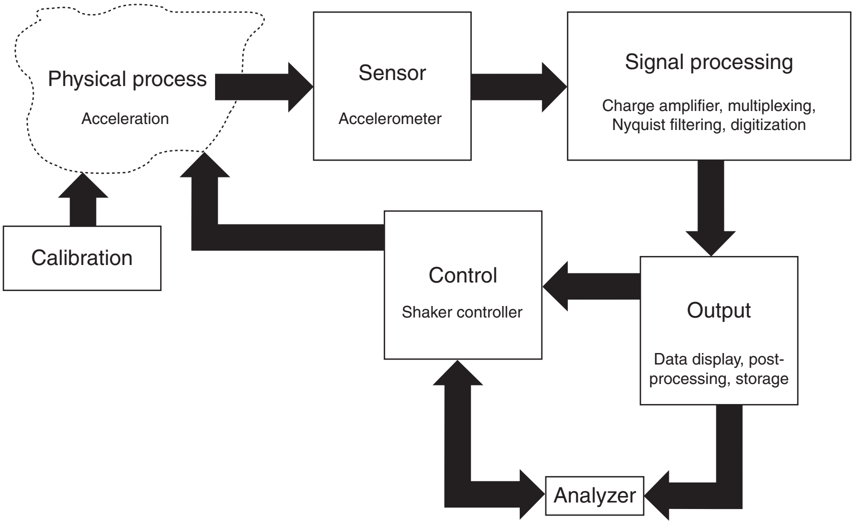
Physical process
Acceleration
Sensor
Accelerometer
Signal processing
Charge amplifier, multiplexing, Nyquist filtering, digitization
Calibration
Control
Shaker controller
Output
Data display, post-processing, storage
Analyzer

2.1 A very general schematic of measurement systems: a sensor module, a signal processing module, and output module, and (possibly) a control module.

who reads and interprets output from the measurement system) as several modules. The first module is the *sensor module*, which consists of the physical element(s) that somehow interact with the system to sense the physical process and convert that information into a detectable signal form (e.g., an electrical voltage). For example, in a structural vibration application, the sensing module might consist of an accelerometer mounted to the structure; the accelerometer contains an inertial mass that moves in response to the host structure motion, and this inertial mass motion induces stress in some piezoelectric material, which causes an electric potential (voltage difference) to develop.

Information from the sensing module proceeds to a *signal conditioning module*, which may have any of a number of functions that could be subdivided into analog functions (voltage amplification, some types of filtering, and possibly telemetry) and digital functions (timekeeping, digitization, triggering, master control). The signal conditioning module in this conception may be thought of as the 'brain' of the measurement system, as it is primarily responsible for taking raw information from the sensing module and converting it to a form suitable for display and analysis by the engineer (analyzer). In the accelerometer example, the signal conditioning module would contain a charge amplifier (the voltage differences produced by the piezoelectric effect are very small), a noise filter (to get rid of very high-frequency random processes), a Nyquist filter (tuned to the desired sampling frequency of the system), a multiplexing unit (for appropriately managing multiple accelerometer channels in simultaneous signal detection), some form of analog-to-digital converter, and a controller with analog or digital trigger input/output, a buffer, and a master clock. Digital data are then sent to the *output module*, which provides an actual indication, in an appropriate form, of the measurement. The simplest module might be a digital word read-out of the measurement value on a display, although more commonly the digitized words are stored (either in RAM or on a digital storage medium) for interface with a personal computer. The most sophisticated output modules integrate post-digitization data analysis (see Part I 'Sensor data interrogation and decision making' in Volume 2), usually with external software.

Finally, data from the signal processing module may also interact with a *control module*, which contains some form of an active controller that interprets the output and feeds back that information to an actuator that can manipulate the physical process. This module is only present in active sensing applications; in the context of the accelerometer measurement, if part of the civil infrastructure application was to mitigate excessive levels of vibration, then some sort of control module would be present whereby acceleration signals are used as feedback to, say, hydraulic dampers, to actively reduce the acceleration. This control module is not meant to be confused with a number of activities that the signal conditioning module performs in controlling the data acquisition process such as timekeeping, filter setting, and so forth; all applications will have some sort of signal conditioning module that controls the data acquisition process, but only active sensing applications will have the additional separate control module that directs actions that explicitly affect the physical process being measured.

2.1.2 Sensing module

While this chapter will focus primarily on the signal conditioning module and system-level architectures, a few words must be included on sensing. The sensing module itself depends primarily upon what physical process must be detected and/or controlled, and many of the chapters after this one treat major sensing categories in detail. One element common to all sensors is that they convert kinematic, kinetic, or thermal information to a measurable and controllable quantity, such as a voltage or current, which is then processed, either in hardware or software, to obtain information that supports decision-making e.g., structural health management. The main point here is that all sensors are themselves dynamic systems, and it is generally very useful to model their output, $y(t)$, as such, e.g.:

$$c_n \frac{d^n y}{dt^n} + c_{n-1} \frac{d^{n-1} y}{dt^{n-1}} + \rightleftharpoons + c_1 \frac{dy}{dt} + c_0 y = F(t), \tag{2.1}$$

where $F(t)$ is the physical process being monitored (assumed time-dependent), and the c_i are coefficients that characterize the sensor. The order of the highest derivative required to accurately describe the sensor's response to the physical input is the *sensor order*; as an example, consider a piezoelectric accelerometer and its equivalent dynamic system model (Fig. 2.2). If the absolute displacement of the inertial mass inside the housing is defined as y and the input to the accelerometer is defined as x, the system may be readily described by its equivalent dynamic model as:

$$\underbrace{m \frac{d^2 y}{dt^2} + c \frac{dy}{dt} + ky}_{\text{'output'}} = \underbrace{c \frac{dx}{dt} + kx}_{\text{'input'}}, \tag{2.2}$$

and by noting that the relative motion of the inertial mass, $z = y - x$, is what will affect the piezoelectric element, the input/output model may be written as:

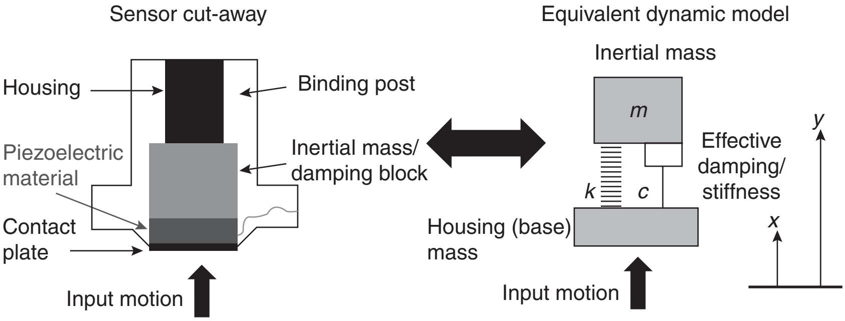
Sensor cut-away
Housing
Binding post
Piezoelectric material
Inertial mass/ damping block
Contact plate
Input motion
Equivalent dynamic model
Inertial mass
m
Effective damping/ stiffness
k
c
y
x
Housing (base) mass
Input motion

2.2 A piezoelectric accelerometer cut-away (left), compared to its equivalent second-order spring/mass/damper dynamic system representation (right).

$$m\frac{d^2z}{dt^2}+c\frac{dz}{dt}+kz=\underbrace{-m\frac{d^2x}{dt^2}}_{F(t)}, \tag{2.3}$$

which directly relates the kinematic output (z) to the input (x). Clearly, in this case, the accelerometer is a second-order sensor. If the second-order case of Equation [2.1] is divided through by c_0, the resulting coefficient ratios $c_2/c_0 \equiv 1/\omega^2$, which will always have units of time squared (e.g., s^2), and $c_1/c_0 \equiv \tau$, which will always have units of time (e.g., s), completely define the dynamic behavior of the sensor to the physical process input. Similarly, the ratio $F(t)/c_0$, which always has units of output field units divided by input field units, defines the *sensitivity* of the sensor. In particular, the reciprocal $1/c_0 \equiv K$ is known as the *static sensitivity* of the sensor, and that value, along with the two previous ratios defined, determine the complete behavior of the second-order sensor.

The static sensitivity simply relates static input change to static output change, and zero-order sensors are completely characterized by this value since the higher-order constants are zero. For a zero-order sensor, such as a simple piston-style tire pressure gage, if the static pressure were $F(t) = \Delta P$ where ΔP was the pressure difference inside the gage and outside, then the sensor would read $K\Delta P$, where by simple physical modeling one could find that $K = A/k$, where k is the piston spring stiffness and A is the cross-sectional area of the gage chamber.

The static sensitivity, however, does not completely characterize the input/output relationship for a dynamic signal input. Dynamic signals cause a first-order response in a sensor due to a capacitive ('storage') element; thus the constant τ now governs the sensor's response to inputs. This constant is known as the *time constant* of the sensor, and the general solution to first-order linear sensor systems is an exponential decay. The response to any input *F(t)* for a first-order sensor is given by:

$$y(t) = \underbrace{y_0 e^{-t/\tau}}_{\substack{\text{transient}\\ \text{response}}} + \underbrace{\int_{T=0}^{t} F(T)(K/\tau)e^{-(t-T)/\tau}\,dT}_{\substack{\text{steady-state}\\ \text{response}}}, \qquad [2.4]$$

where the sensor now has a transient response (whose duration is governed by τ) and a steady-state response that depends on the input itself (as well as τ). A bulb thermometer is an excellent example of a first-order sensor. First-order sensor responses to dynamic input are noted for a time lag before reaching steady-state (due to the time constant τ) and both phase and magnitude change between input and output (depending also upon τ).

Finally, second-order sensors, such as the accelerometer first introduced, are characterized not only by a static sensitivity and time constant but also by a characteristic natural frequency, ω, related to the second-order constant above. The general response of a second-order sensor is given by:

$$\begin{aligned} y(t) &= e^{-\xi\omega t}\underbrace{\left[y_0 \cos \omega\sqrt{1-\xi^2 t + \left(\frac{\dot{y}_0 + y_0\omega\xi}{\omega\sqrt{1-\xi^2}}\right)}\sin \omega\sqrt{1-\xi^2 t}\right.}_{}, \\ &+ \underbrace{\int_{T=0}^{t} F(T)(K\omega/\sqrt{1-\xi^2} e^{-\xi\omega(t-T)} \sin\left[\omega\sqrt{1-\xi^2}(t-T)\right]dT}_{\substack{\text{steady-state}\\ \text{response}}} \end{aligned} \qquad [2.5]$$

where $\xi = \omega\tau/2$ is the sensor's damping value. Depending on the relative values of the parameters K, τ, and ω, a second-order sensor will either oscillate or exponentially decay to the steady-state input, with a magnitude and phase offset from the input dependent upon all these parameters. If the input occurs at time scales commensurate with ω, the phenomenon of sensor resonance occurs, where very large outputs (i.e., significantly different from the static sensitivity K) are achieved per unit input. As $\omega \to 0$, a second-order sensor responds with static sensitivity K, as expected, but the resonant effect changes the dynamic sensitivity of the sensor significantly, effectively reducing the frequency band over which it is a useful sensor.

As a consequence of sensor module dynamics, several performance metrics are usually defined that are important to consider when selecting a sensor type for a given application. These performance metrics are summarized here:

1. *Sensitivity*. This is the fundamental scaling relationship that the sensor obeys in transferring input (what is desired to be measured) to output (what is actually measured). This metric is usually given by the static sensitivity K, or in the case of dynamic sensors, augmented by the time constant τ and (in the case of second-order sensors), the operable frequency band that avoids sensor resonance.
2. *Cross-axis sensitivity*. This metric describes how much the sensor responds to inputs not aligned with the primary sensing direction, given in the same units as the sensitivity above or possibly a fraction or percentage of the main sensitivity. Single-axis accelerometers typically have a non-zero cross-axis sensitivity, and this value can be verified by mounting the accelerometer on its side to a shaker and measuring its output per unit input.
3. *Resolution*. This metric quantifies the minimal detectable value of input and is usually given in terms of an amplitude or power spectral density e.g., volts^2/Hz. A common way to estimate resolution is to isolate the sensor from any inputs, measure a long time history of its response to this nominally quiescent state, and compute the average amplitude or power spectral density of the time history. Bendat and Piersol (2010) describe the concept of spectral density estimation in great detail.
4. *Dynamic range*. This metric describes the full operating range over which the sensor behaves as intended (linearly with static sensitivity K, distortion-free, etc.) and is usually defined as a logarithmic ratio between maximum measurable value and minimum measurable value (thus expressed in decibels (dB)). Sometimes, sensor manufacturers report also a percent linearity metric, which shows how much departure from expected linear response could be expected. As a side note, while less common, dynamic range can occasionally refer to operating frequency bandwidth, some care must be taken to understand context of the value.
5. *Sensitivity to extraneous measurands*. This metric quantifies how the sensor responds to unintended inputs and is usually expressed as a static or dynamic sensitivity. The classic example is the thermal sensitivity of a strain gage sensor, as it is well-known that strain gages respond to thermal strain as well as mechanical strain. Accelerometers also may have thermal sensitivity that must be quantified in order either to use the accelerometer only in an appropriate temperature range or otherwise to correct the output.

These fundamental performance metrics are useful in the selection, calibration, and operation of any sensor. Fundamentally, the output from the sensor module is an analog voltage that will be sent to the signal conditioning module for suitable transformation into digital information. In the following section, some fundamental concepts in signals and sampling are presented to facilitate understanding of this module's functionality and operation.

2.2 Concepts in signals and digital sampling

This section provides a general context for fundamental concepts in the nature of analog signals and their digital sampling. It will establish a general signal model and then review relevant sampling requirements and the representation of digitally-sampled signals.

2.2.1 Sampling criteria

The sensor module outputs $y(t)$ are inevitably analog voltages, and while analog waveforms are continuous in time and amplitude, they do not lend themselves to easy storage and subsequent processing. Inevitably, digitized representation of the measured outputs is required, which involves appropriate *sampling* of the waveform. The most important sampling parameter is the sampling frequency, f_s, which determines the rate at which the analog voltage is recorded; the time between each sample Δt is the inverse of the sampling frequency, or $\Delta t = 1/f_s$. Figure 2.3 shows a 1 s-long 5 Hz sinusoidal waveform sampled at four different sampling frequencies, 95 Hz, 45 Hz, 15 Hz, and 7 Hz. Each point represents the value recorded at that instant in time; clearly, the larger the sampling rate, the more closely-spaced the samples are, and the analog waveform is more accurately approximated. Clearly the sinusoid is not very accurately portrayed in either amplitude or frequency as the sampling frequency gets too low (connect the dots with straight lines in Fig. 2.3 to visualize what the engineer would observe). In the case of sampling at 7 Hz, it appears that the engineer is not even observing a 5 Hz waveform anymore, but rather something distorted at a lower frequency.

One way to better visualize what is happening is to transform the time series y to the frequency domain Y via a discrete Fourier transform (DFT),

$$Y_k = \frac{1}{f_s}\sum_{n=0}^{N-1} y_n e^{-2\pi ikn/N}, \qquad [2.6]$$

where the discretized voltage $y(t)$ is now a sequence of points y_n, $n = 1, \ldots, N$, and the corresponding DFT is discretized at each frequency, $k = 1, \ldots, N$. The time between samples Δt corresponds to a frequency width of $\Delta f = 1/N\Delta t = f_s/N$. Figure 2.4 shows the magnitude of the DFT for each corresponding time series of Fig. 2.3. As expected, a peak is observed at 5 Hz for each sample rate that

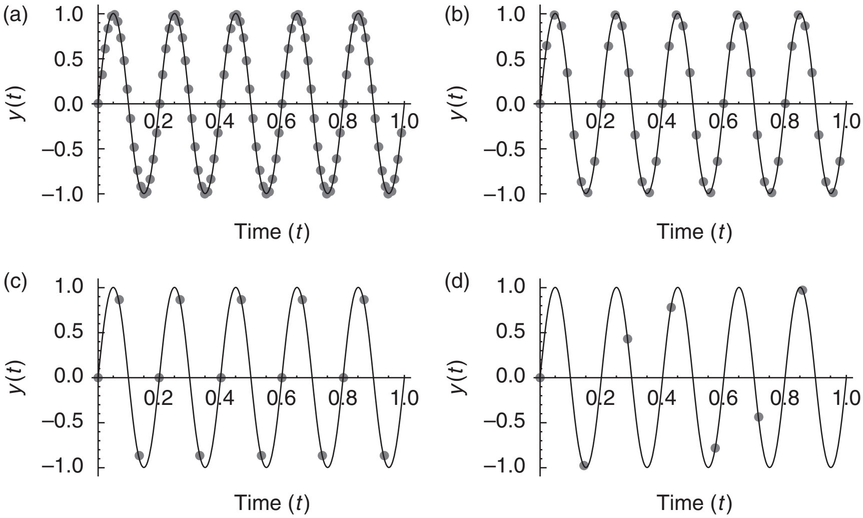

2.3 A 5 Hz sinusoid waveform sampled at (a) 95 Hz, (b) 45 Hz, (c) 15 Hz, and (d) 7 Hz.

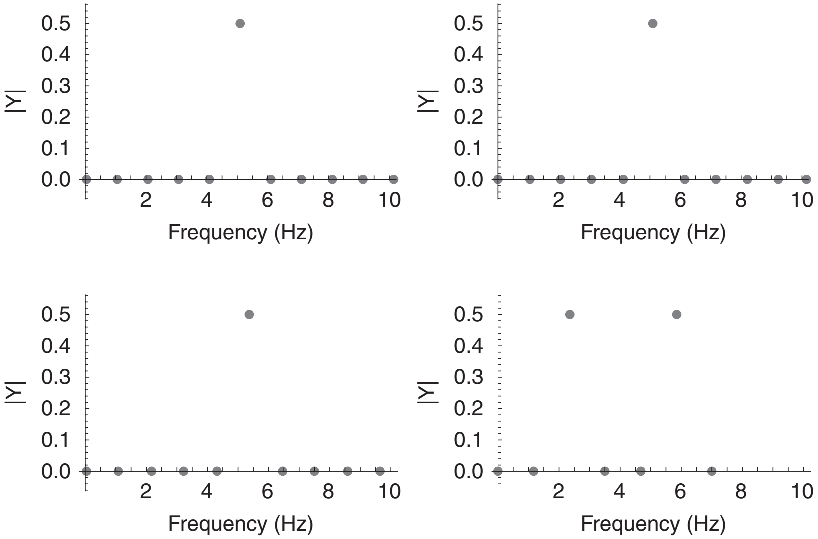

2.4 The DFT of each of the waveforms of Fig. 2.3.

is at least twice that of the waveform; however, when the 5 Hz waveform was sampled at 7 Hz, spurious frequencies known as *aliasing* frequencies appear due to the fact that the sample rate is not fast enough to capture the oscillation. The *Nyquist sampling criterion* thus states a condition for minimum sampling to avoid aliasing: one must choose $f_s > 2f_{\max}$, where $f_{\max}$ is the highest expected frequency contained in the measured waveform. The *Nyquist frequency* is then defined to be half the sampling used, $f_N = f_s/2$, and this represents the frequency above which any frequencies in the analog waveform will be aliased. If the Nyquist sampling criterion is followed, the frequencies estimated by the DFT procedure will be accurate. Otherwise, false alias frequencies will be folded back into the spectrum and interfere with actual frequencies such that they cannot be distinguished, creating false information or masking true information. The alias frequencies f_a corresponding to any given frequency f are $f_a = |f - nf_s|$, where $n > 0$. In the case of sampling at 7 Hz, the first alias frequency for the 5 Hz waveform is $|5–7| = 2$ Hz, and a 2 Hz peak is observed in the spectrum. Thus, this 5 Hz waveform sampled at 7 Hz is not different from a 2 Hz waveform sampled at 7 Hz. The peak near 6 Hz is just a consequence of the symmetry of DFTs about f_N. In the general (and typical) case of sampling a signal of unknown frequency content, the only way to avoid aliasing is to low-pass filter the signal with an analog filter (prior to discretization) at f_N.

The waveforms of Fig. 2.3 were all sampled in such a way that the total number of samples was an integer number of the fundamental period (0.2 s), and the amplitudes predicted by the DFT were correct (the sinusoid had an amplitude of unity, and the DFT gave an amplitude of 0.5, as a full double-sided DFT will always give amplitudes at half the value, except at DC and Nyquist frequencies, due to the symmetry of the spectrum). Consider the same 5 Hz waveform sampled at 95 Hz again (well above the Nyquist criterion minimum sampling frequency) at different record lengths. Figure 2.5 shows this waveform and its corresponding DFT for different record lengths. One can see in the time series that an exact number of cycles is not being sampled, and in the DFT, distortion is appearing near the peak at 5 Hz; this is known as *leakage*, and it occurs as a result of the discontinuity in the waveform that the DFT effectively sees, since DFT estimation assumes periodicity of the measured waveform. Leakage may be minimized prior to digitization only by varying the desired frequency resolution, Δf, and observing statistics on the estimated waveform. The smaller the frequency resolution, the more that any leakage will be minimized. Post-discretization leakage suppression may also be performed via windowing prior to DFT estimation, whereby the discretized waveform y_n is multiplied by a discrete window w_n that tapers the finite data record to be zero (or at least periodically equivalent) at the boundaries. A number of windows exist e.g., a Hanning or half-cosine window $w_n = (1/2)(1 - \cos 2\pi n/N)$, and an excellent detailed discussion of the trade-offs among windows may be found in Oppenheim *et al.* (1999). In

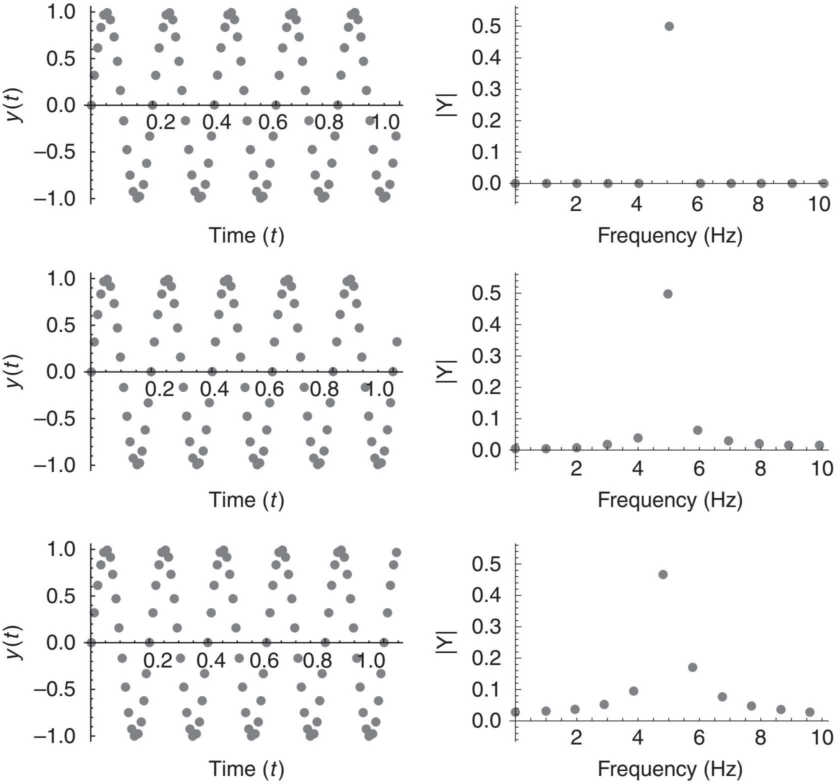

2.5 A 5 Hz waveform (left) and its corresponding DFT (right) sampled at different record lengths.

summary, by adherence to the Nyquist sampling criterion and by varying Δf appropriately, one will obtain the best sampling frequency and record length to establish discretization of the analog waveform in terms of optimal accurate frequency and amplitude information.

2.2.2 Digitization and encoding

The process of discretization of the analog voltage waveform involves encoding the voltage in some finite, digital representation. Nearly all measurement systems employing digitization of analog data employ some variation on *binary encoding*, which is just a number system using base-2 (instead of the usual decimal, or base-10, system most engineers work with). Binary encoding uses the binary digit, or *bit*, as the fundamental unit of information, and a bit may only be a ‘0’ or a ‘1’ (only two possibilities since it is a binary-encoded system). By combining bits, numbers larger than 0 or 1 may be represented, and these bit collections are called *words*. Eight-bit words have a special name historically, known as *bytes*.

The word length – the number of bits used to comprise the word – defines the maximum number that the word can represent. The N individual bits that comprise an N-bit word can be arranged to produce 2^N different integer values; for example, a two-bit word would be expected to have $2^2 = 4$ combinations, and those four combinations are 00, 01, 10, and 11. The decimal numerical value of these words is computed by moving from the right-most bit to the left-most bit, so the decimal equivalents to these 2-bit words are 0, 1, 2, and 3, respectively. Thus, an N-bit word can represent all decimal integers from 0 to 2^N-1 (e.g., a 16-bit word can represent any integer 0–65,535). The left-most bit (bit $N-1$) is known as the most significant bit (MSB), since it contributes the most to the overall value of the word, and the right-most bit (bit 0) is the least-significant bit (LSB). This is known as *straight binary code*.

Because all of the numerical values are of the same sign in straight binary code, it is a unipolar encoding. *Offset binary code* is a variant on this where the MSB is used as a sign, effectively converting an N-bit word's evaluation range from $-2^{N-1}-1$ to $+2^{N-1}-1$, resulting in a bipolar encoding. Thus a 4-bit word in straight binary code has an evaluation between 0 and 15, while the offset binary code for the same 4-bit word has an evaluation between −7 and +7. There are also ones- and twos-complement binary codes, which simply move bits around in the word to change the positioning of the zero; twos-complement encoding is very popular in personal computers. As a comparative example, the 4-bit word 1010 has a straight binary evaluation of 10, an offset binary evaluation of 2, a twos-complement evaluation of −6, and a ones-complement evaluation of −5. Other such encodings exist; one important variant that is often used for digital device communications is *binary coded decimal* (BCD). In this code, each digit individually is encoded in straight binary. For example, the number 149 encoded in BCD would be 0001 0100 1001 (a binary 1, a binary 4, a binary 9). The advantage of BCD is that each binary number has to be only 4 bits in order to span the range 0–9. As the full value of the number being encoded goes beyond 9 (say, to 10), it just engages the next higher-order word.

2.3 Analog-to-digital conversion

Given the signal model considerations in the previous section, this section considers issues associated with the digitization of these signals. The section first considers issues (such as quantization error) associated with the digitization process, and then presents fundamental analog-to-digital converter architectures in common practice.

2.3.1 Quantization and quantization error

The bits that comprise digital words may be thought of as electrical switches, where the 0 and 1 may indicate the ‘off’ and ‘on’ position, respectively. By forming words from the bits, a *switch register* is created that conveys the numerical of value through the various individual bit switch settings. This switch register is connected to a voltage source such that the ‘on’ position (bit value of 1) corresponds to some reference, nominally labeled ‘HIGH’ voltage (for example, +5 V) and the ‘off’ position (bit value of 0) corresponds to a ‘LOW’ voltage (for example, 0 V). This is standard *transistor-transistor logic* (TTL) design, where the switch is expressed by a flip-flop circuit (Fortney, 1987). Figure 2.6 shows such a simple switch realization on the left side of the schematic. Control logic dictates whether the switch is open or closed, which consequently results in either a HIGH or LOW reading at the switch output. The middle part of the schematic shows a 4-bit switch register specifically showing the binary value 1001 (the MSB and LSB are HIGH, and the two interior bits are LOW). The right side of the figure shows the actual output voltage series, where each output is sampled at the sampling

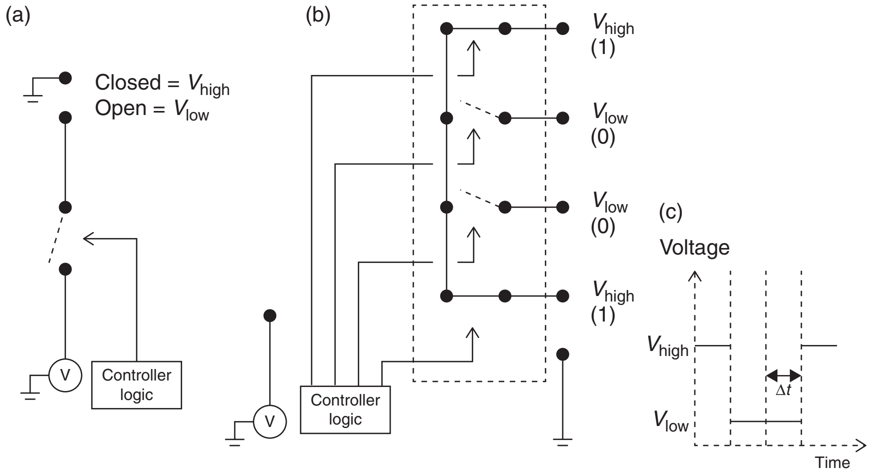

2.6 A simple switch (a), a 4-bit switch register (b) in the configuration 1001, and the TTL output from the 4-bit switch register (c).

time Δt specified. This is the fundamental architecture by which electrical devices indicate binary code.

The analog voltage outputs from the sensor module must be encoded into the binary form for further processing, as just described. The basic process is called *analog-to-digital* (A/D) *conversion*, and this conversion is generally some form of *quantization*. A/D converters are designed to operate over some voltage range, V_R. Typical designs include unipolar converters between 0 and 10 V or bipolar converters between −10 to +10 V or even −25 to +25 V. An N-bit A/D converter, as described in the encoding discussion of Section 2.2.2, produces N-bit words that can convey 2^N total binary values between 0 and 2^N-1. Thus, the resolution V_{res} of the A/D converter is just the ratio of total available voltage range divided by total available digital range, or

$$V_{\text{res}} = \frac{V_R}{2^N}. \qquad [2.7]$$

Consider a 0–4 V unipolar, 3-bit A/D converter. This device will have a resolution $V_{\text{res}} = 0.5$ V, which means that errors may occur between the actual input voltage and the binary encoding of that voltage by the A/D converter. For example, an input voltage of 0 V would result in the same binary encoding as 0.45 V (namely 000), yet an input of 0.51 V (much closer to 0.45 than 0 V) would result in a higher binary encoding, 001. This is called *quantization error*, and thus the resolution of the converter represents the value of its LSB. Figure 2.7 shows the A/D conversion process for this A/D converter. The resolution is 0.5 V, so the binary output is constant for 0.5 V increments in the input voltage. A common design tool is to spread quantization error symmetrically about the input voltage, as opposed to the biased way Fig. 2.7 indicates. As such, a bias voltage equivalent to ½ LSB is usually added to the input voltage internally within the A/D converter so that the error (in this example) would be ±0.25V. The dashed line shows ideal conversion for comparison; clearly, as V_{res} gets smaller, ideal conversion is asymptotically achieved.

Wagdy and Ng (1989) derived a formula for the variance of the quantization noise, which depends on the magnitude of the signal (assumed harmonic), here expressed somewhat differently as a fraction α of the A/D resolution V_{res}

$$\sigma^2 = \frac{V_{res}^2}{12} + \frac{V_{res}^2}{\pi^2}\sum_{n=1}^{\infty}\frac{(-1)^n J_0(2\pi n\alpha)}{n^2}, \qquad [2.8]$$

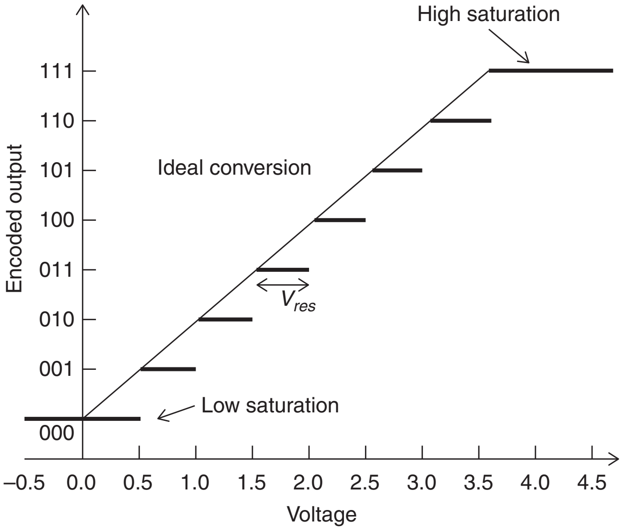

2.7 Quantization of voltage by a 3-bit digitizer.

where J_0 is a zero-order Bessel function of the first kind. For signals that are large compared to the resolution (the most common scenario), i.e., $\alpha \gg 1$, the summation term drops out, and the variance approaches the usual variance associated with a uniform probability distribution over the resolution range, $V_{res}^2/12$. The quantization-limited signal-to-noise (SNR) ratio in dB for a harmonic signal that fills the entire available range is given by:

$$\begin{aligned}\mathrm{SNR} &= 10\log\frac{V_R^2}{\sigma^2} = 10\log\left[\frac{2^{2N}V_{res}^2}{V_{res}^2\left(1/12+\sum_{n=1}^{\infty}\left((-1)^n J_0(2\pi n\alpha)/n^2\pi^2\right)\right)}\right]\\ &= 10\log\left[\frac{12\cdot 2^{2N}}{1+12\sum_{n=1}^{\infty}\left((-1)^n J_0(2\pi n\alpha)/n^2\pi^2\right)}\right]\\ &= 10\log 12\cdot 2^{2N}\,(\text{if } \alpha \gg 1)\end{aligned} \qquad [2.9]$$

Equation [2.9], for sufficiently large signals, is plotted in Fig. 2.8; each bit adds about 6.02 dB of SNR capability. Most converters in today's A/D markets are at least 16-bit, resulting in a quantization error nearly 100 dB below

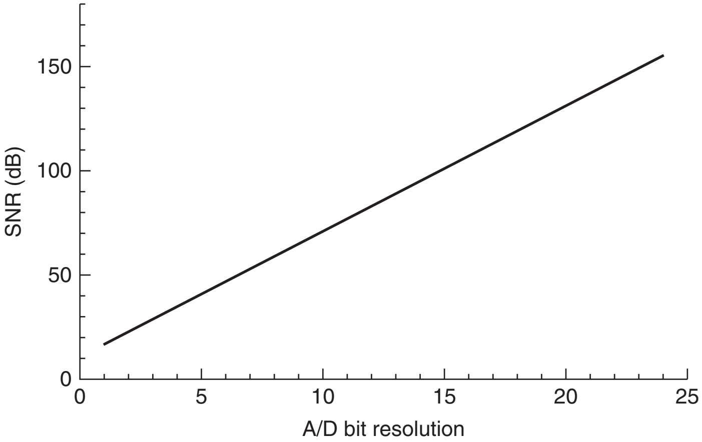

2.8 Signal-to-noise ratio referenced to quantization error as a function of A/D word-length capacity.

a unit signal. Increasingly, 24-bit converters are becoming more and more common.

At small signal levels (α small), distortion can happen due to the nonlinear dependence upon the signal (Equation [2.8]), and this distortion comes after any anti-aliasing, so the detected signal may have significant degradation. One common remedy for minimizing distortion is by dithering. *Dithering* is a process where random noise at least twice the amplitude of V_{res} is deliberately added, and the effect is to 'noise shape' the quantization error in such a way that the distortion is eliminated at the expense of slight SNR decrease. Most A/D systems automatically dither input voltage signals.

Errors can also occur at the extremes of the voltage range of the A/D. If the input voltage drops below 0 V, the A/D converter is low-saturated and will continue to encode the voltage as 000 regardless of the actual input voltage. Similarly, if the input voltage goes above 4 V, the A/D converter is high-saturated and will continue to encode the voltage as 111 regardless of the actual input voltage. These saturation errors result in the familiar phenomenon of *clipping* in the observed digital time history; a clipped zero-mean sinusoid would have flattened peaks for the portions of the trace that exceed the A/D voltage range.

2.3.2 Analog-to-digital converter architectures

A number of different designs for implementing the general A/D conversion (ADC) process described above exist (Kester, 2005). Four are in most common practice: Flash ADC, Successive approximation ADC, Ramp converter

ADC, and Sigma-delta ADC. *Flash ADC*s are known as direct ADCs, as they have a series of comparators that sample the input signals in parallel in the switch register, resulting in very fast direct voltage encoding (on the order of GHz sampling rates), but typically are low-resolution (e.g., 8 bits or less), because the number of comparators needed doubles with each required bit, resulting in very large circuits.

*Successive approximation ADC*s, one of the most common methods, estimate the input voltage essentially on a trial-and-error basis, as the name suggests. A comparator is used to reject voltage ranges, finally settling on the proper voltage range through a feedback circuit from a digital-to-analog converter (DAC) (discussed later) that provides the guess from a shift register. The sign of the comparator essentially chooses which bit value to converge to per clock cycle. Unlike Flash ADC, each bit desired requires one clock cycle, so an 8-bit successive approximation ADC would require eight times longer to obtain an 8-bit word than the Flash ADC. However, the quantization noise is better controlled, and successive approximation ADCs are much less costly to build. As such, the cost/speed trade-off has favored their deployment for many commercial systems.

*Ramp converter ADC*s generate a sawtooth (piece-wise linear ramp) voltage signal and use a comparator, integrator, and capacitor (sample/hold) network to discern the input voltage level. A clock governs the voltage ramp changes, and the time is noted when equality occurs. Ramp converters have, typically, the least number of logic gates, and the approach results in some of the highest accuracy, particularly for low signal levels (sub-millivolt). However, the local oscillator used to generate the ramp is often sensitive to the ambient thermal environment, and its linearity (and thus accuracy) can be compromised. Ramp converters are relatively slow due to the oscillator as well, although some nonlinear ramp converters have been implemented that reduce the sample/hold latencies (Figliola and Beasley, 2000).

Finally, *sigma-delta ADC*s simply oversample the input voltage significantly, filter the desired measurement band, and convert at a much lower bit count via Flash ADC. This signal, along with any quantization error from the flash, is fed back into the filter, and this has the effect of suppressing the noise of the flash. Then, a digital filter is applied to downsample the flash conversion, remove unwanted noise, and increase resolution. Sigma-delta ADCs are primarily digital devices and are very cost-effective and energy-efficient, and this type of ADC is particularly common in audio digital media (CD, DVD).

2.4 Digital-to-analog conversion

In many measurement applications, particularly if there is a control module, and even in the design of some A/D systems (see previous section), there is

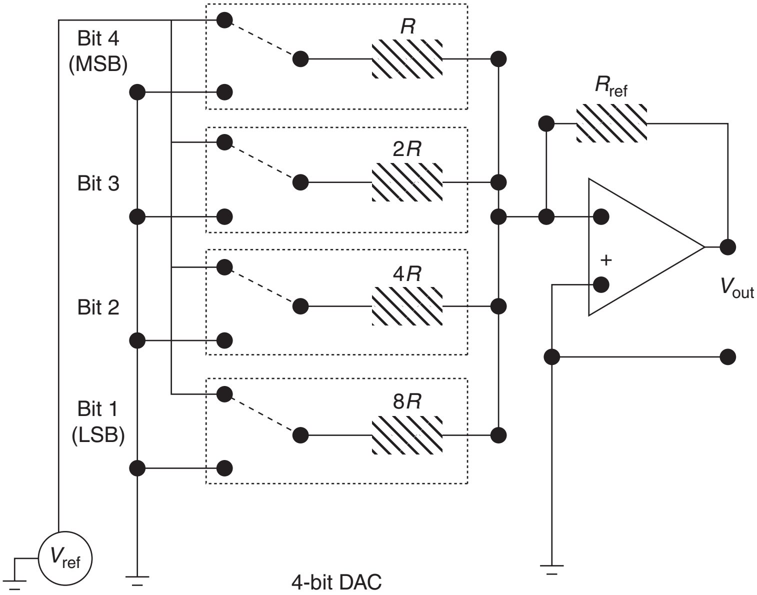

2.9 Schematic of a 4-bit DAC system.

a need to convert digital information back to analog information (D/A conversion), e.g., most commonly a voltage. The simplest way to envision most DAC is shown in Fig. 2.9, where a 4-bit DAC is drawn. The network consists of four resistors having a common summing junction, with each resistor doubling in size starting at the MSB. At the operational amplifier output, the voltage V_{out} is easily computed to be

$$V_{\text{out}} = V_{\text{ref}} \sum_{n=1}^{4} \frac{b_n R_{\text{ref}}}{2^{n-1} R}, \tag{2.10}$$

where the b_n is either 0 or 1 depending on the n-th bit value that controls that switch. A clock controls when each bit value is latched until the next clock cycle, and the effect is that the current V_{out} is held during that cycle; this results in a piece-wise constant output, similar to the A/D quantization in Fig. 2.7. This 'stairstepping' results in some potentially unintended high harmonic content being generated, which must be analog filtered before the waveform is sent to whatever device requires it. This is very important to understand if the DAC is being used to generate precise control inputs for feedback purposes.

2.5 Data acquisition systems

A *data acquisition system (DAQ)* is the integration of several components within the signal conditioning module, the sensing module, the output/display module, and sometimes the control module that leads to stored, manipulable digital data representations of the sensor measurements. This integration is accomplished in a compact DAQ board that easily interfaces with a personal computer. A very general schematic for DAQ systems used for centralized wired-sensor configurations is shown in Fig. 2.10, where a single central controller is assumed.

2.5.1 Analog signal considerations

Analog sensor voltages are sent first into a conditioning unit that could serve several purposes. One of the first subcomponents in this unit is a bank of shunt circuits; the actual raw output from many sensors (e.g., piezoceramic accelerometers) is a current rather than a voltage, and a *shunt circuit* uses Ohm's law to convert this current to a voltage suitable for use with the DAQ system. DAQ systems either have separate current/voltage inputs or switches that engage shunt circuits in analog input channels when needed. Not all voltages from the sensors, however, are suitable for the voltage limitations (V_R) of the DAQ components (such as the ADC). Thus, many analog voltage signals need either amplification or attenuation to avoid the

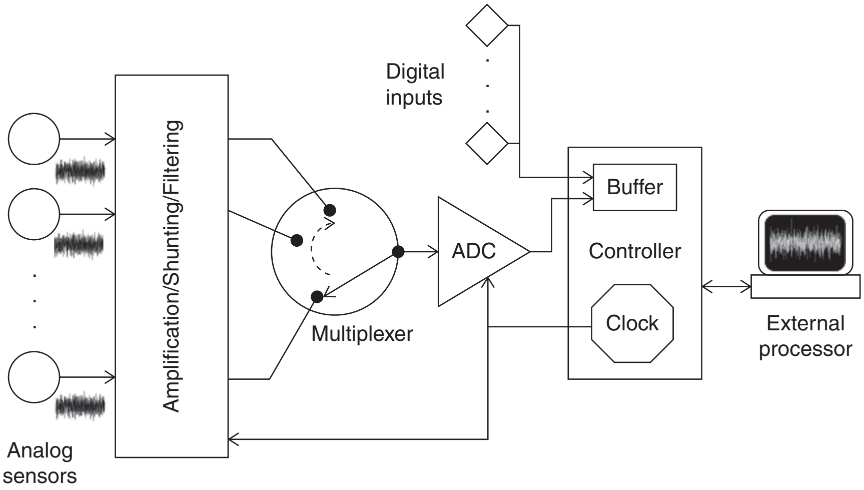

2.10 A general schematic of a conventional wired-sensor data acquisition process.

saturation effects shown in Fig. 2.7. Amplifier gains in most modern DAQ systems are controllable individually on each channel via switch logic that engages variable resistor banks (for amplification) or engage variable resistor voltage divider networks (for attenuation).

The specific form of the wired connections to the DAQ unit typically are either single-ended or differential. *Single-ended connections* use one line from the sensor as the active input to the amplifier and reference the other to ground, which must be common for all of the analog sensor channels. The common ground point is external, usually provided by the DAQ board. If all the sensors cannot be wired to common ground, or if a separate ground source exists at some source point (power supply for the sensors, for example) that cannot be common-grounded, the possibility for a common-mode voltage exists, which will combine unpredictably with the true input signals to cause interference. Conversely, *differential-ended connections* allow voltage differences to be measured among variably-grounded sensors and/or other voltage sources. Here, the second sensor line is attached to the amplifier without any ground junction, and the voltage measured is the difference across the amplifier; hence it is often called a 'floating' measurement because it is not measured relative to a fixed ground. Differential connections are usually required for systems taking in many diverse voltage/current sources, and they have the ability to measure very small voltage signals more accurately, provided a large resistor is dropped between the amplifier's second input and ground. Most modern DAQ boards allow software-programmable switching between single-ended and differential conditions as the specific measurement situation warrants.

After voltage conditioning, analog filtering is another very common action. Although not present on all DAQ boards, anti-aliasing filters with cut-off frequencies set to the Nyquist frequency, as described in Section 2.2.1, remove irrelevant high-frequency information that could wrap into the measurement band. In customized systems, special analog filters that serve to either high-, low-, or band-pass the voltages, may be present in the design prior to sampling and digitization. For conventional strain gage or other resistance-based sensors, special resistor bridges (e.g., a Wheatstone bridge) may be present for noise rejection, and for thermocouple temperature measurements, cold-junction compensation units may exist for measurement stabilization to as low as 0.25°C.

After signal conditioning, each sensor output has to be multiplexed. Multiplexers are basically integrated circuits that use parallel flip-flops to rapidly select individual lines and pass along the information, allowing a multi-channel system to share common telemetry and ADC. This drastically reduces cost in DAQ systems. The trade-off for some applications is that inevitably there is an *interchannel delay* induced by the multiplexer as it individually selects each channel, leading to lags in the absolute synchrony of data recorded across several channels. True simultaneous sampling may be achieved without a multiplexer, but as long as the inter-channel delay is negligible compared to the overall sampling frequency, the phase errors that result will also be negligible. Finally, the analog data are sent to the ADC for digitization, as already described in detail in Section 2.3.

A central controller, or central processing unit (CPU), governs the entire DAQ process, as shown in Fig. 2.10, and its primary functions are timing control and information buffering, including often interfacing with some form of external personal computer, although these controllers can operate independent of a personal computer. The CPU's processing speed depends on its internal clock speed and the design of the various buses in the DAQ system. *Buses* are just electrical pathways through which information and commands are sent among the CPU, memory, the ADC, any other peripherals including digital input/outputs, and the personal computer. Most DAQ systems have a central bus through which many other devices/components interact through other buses. Figure 2.11 shows such a schematic. Essentially, the central bus contains three information pathways: an address lane, a data lane, and a control lane. As data are to be moved around the DAQ system, the address lane contains a digital description of the locations of the two components between which the data are to be exchanged ('Where are we going to and coming from?'), the data lane contains the data information itself ('What data are going or coming?'), and the control lane contains the status information regarding logistics and control of data movement ('How and when do we send the data?'). When data, or information, are being sent over the central bus, the control lane sends a 'busy' flag so that other information flows do not interfere, and a 'ready' flag when the process is finished;

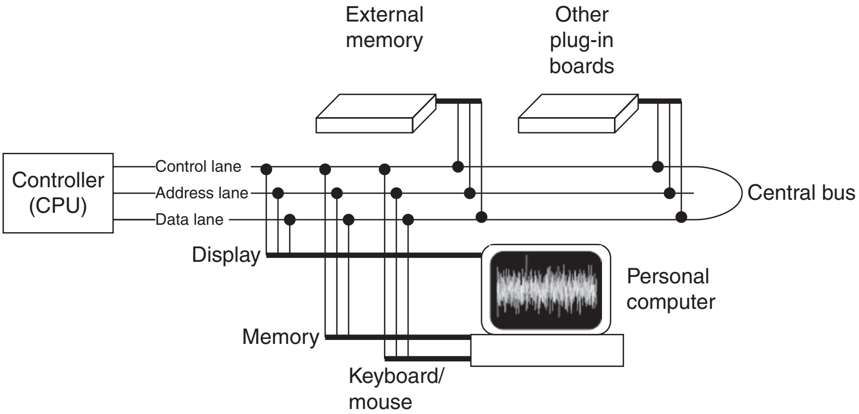

2.11 A central bus architecture showing typical connectivities.

in this way, the same lanes may be used for many different types of operations that execute at different speeds. This is called 'handshaking.'

Memory is a mechanism for data and information storage and retrieval, and, regardless of specific type, basically consists of registers for storing digital information. Most memory types are classified as either non-volatile (does not require power to retain/store information) or volatile (does require power to retain/store information). Common types of non-volatile memory include basic *read-only memory* (ROM), *flash memory*, and older personal computer peripheral magnetic storage devices (e.g., floppy disk or zip disk). ROM is physically unchangeable information (microcode) typically used in firmware or hardware for dedicated processes. Flash memory is a very common storage mechanism today because it may be easily erased and reprogrammed via dense NAND or NOR gate architectures (both functionally complete logic gates, meaning any binary operation may be performed by combining NAND and/or NOR gates). Flash is found in common universal serial bus (USB) flash drives, solid state external hard disks, smart phones, and audio/video systems. Some DAQ systems employ flash memory in assisting the transport of data across different devices with different speeds, known as buffers. *Buffers* consist of some pre-allocated memory storage space where data may reside without interruption to other system processes until the receiving device sends a 'ready' flag over the control lane. Data stored in most buffers follows a first-in, first-out (FIFO) protocol, where data that were the first to enter the buffer are also the first data to leave, preserving the original ordering of the data.

One important class of non-volatile memory is the electrically-erasable programmable read-only memory (EEPROM). Unlike flash memory, which cannot effectively be overwritten in small (byte-level) amounts, EEPROMs are large arrays of floating-gate transistors that may be modified (written to) by increasing the voltage levels as determined by the user. Modern EEPROMs have a life cycle measured near 10^6 reprogramming cycles, and this often is the design limit for systems that use them. EEPROMs are used in DAQ operations for functions such as device configuration and complex, varying computation on post-digitized data.

Volatile memory is typically classified as either *static random access memory* (SRAM) or *dynamic random access memory* (DRAM). The terms 'static' and 'dynamic' fundamentally differentiate between whether the semiconductor needs to be periodically refreshed (dynamic) or not (static). Each bit in SRAM requires four cross-coupled inverting transistors for storage and two more transistors for control; conversely, DRAM stores each bit on a capacitor with a single transistor for control, but the capacitor needs periodic recharging (hence, the term 'dynamic'). Thus, DRAM footprints are much smaller and allow much denser circuit design, resulting in significant cost savings; DRAM is subsequently the most common memory type found in personal computers. However, SRAM uses less power, does not suffer some of the bandwidth limitations that DRAM does, and is much easier to interface over buses; so many DAQ systems employ SRAM architectures for some memory requirements.

2.5.2 Digital communications

Much of the multifunctionality that is required for modern DAQ systems has been integrated into compact 'plug-and-play' boards. Figure 2.12 shows a generic schematic of such a multifunctional plug-and-play board. These boards contain several analog and digital communications, processing, and control functions. As already seen in Section 2.5.1, digital signals play a critical role in a number of CPU, control, triggering, signal processing, and A/D operations in a DAQ system. Generally speaking, digital (TTL-compatible) signals communicate with devices in serial (bit by bit) or in parallel (in words).

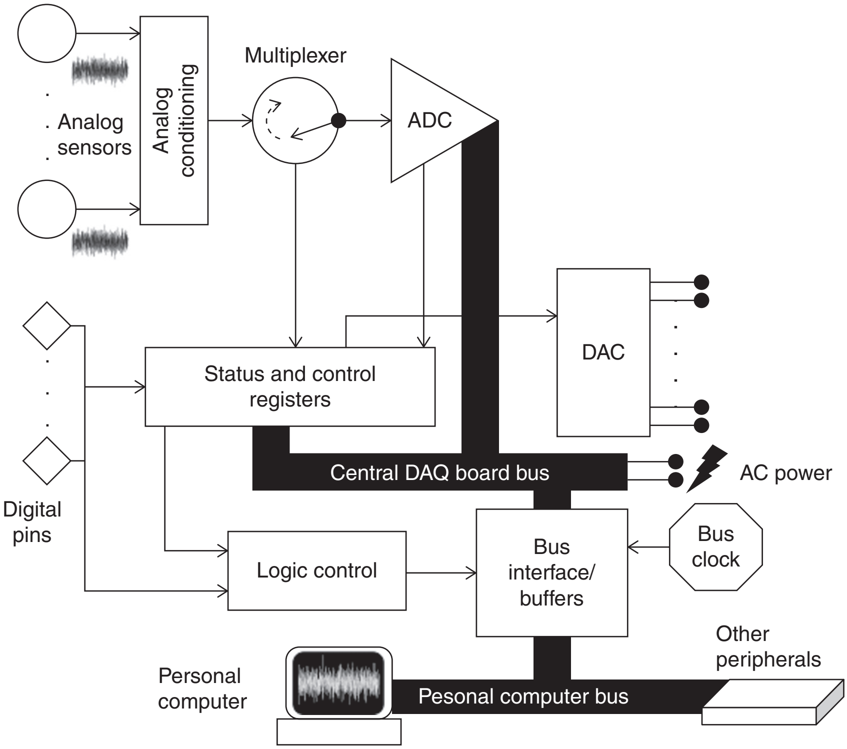
Analog sensors
Analog conditioning
Multiplexer
ADC
DAC
Status and control registers
Digital pins
Central DAQ board bus
AC power
Logic control
Bus interface/ buffers
Bus clock
Other peripherals
Personal computer
Pesonal computer bus

2.12 A general DAQ system plug-and-play architecture for multipurpose functionality.

Standards have been established by which these digital communications are achieved. One of the fundamental serial communications standards was RS-232C, originally used for telephone/modem communications. This protocol allows for either 9-pin or 25-pin connections for two-way communications via two single-ended lines (transmit, or T/X, and receive, or R/X) and a ground line. The remaining wires are related to handshaking. The data are sent in successive streams, one bit at a time, where each bit is represented by an analog voltage pulse, with 0 and 1 being represented by a voltage of opposite polarity (usually in the 3.2–25 V range). Transmission streams generally are composed of a start bit, 7–8 information bits, a parity bit (sometimes), and a stop bit; the start and stop bits work together to execute proper handshaking. Parity just involves counting the number of 1's in a word, and the addition of a '1' as a parity bit makes the number of 1's predetermined either even or odd. Some devices can effectively do simple error checking by checking for the parity bit. A newer serial standard suite, RS-422A (with further standard modifications), allows for 37 differentially-connected pins for noise reduction and uses 0 V and +5 V signals for 0 and 1, respectively. Up to 255 devices on a single RS-485 (one of the later modifications of RS-422A) could be accommodated, with 2 million bit/s (2 Mbit/S) transfer rates over 50 m cable lengths.

A more modern (and now, far more common) serial protocol is the USB, which has become the standard in personal computers. The USB architecture is a tiered-star topology (hubs and branches), allowing up to 128 devices to interconnect between 1.5–12 Mbit/s over 5 m cable lengths (version 1.0, 1995). A host computer might connect to a root hub on which up to four other devices may be connected, including other hubs that themselves can have daughter device connections (hence, the 'tiered-star' terminology). Each individual cable configuration consists of two data wires: a power wire and a ground wire. The USB standard allows *in situ* enumeration and initialization when a USB device is connected to a host or hub, allowing instant digital communications without powering anything down. The host directs all traffic routing through the tiered-star network. In USB 2.0 (2000), speeds were significantly increased to 480 Mbit/s and improved sleep/wake performance for connected devices (better power management). USB 3.0 (2008) brought speeds up to 4 Gbit/s and has been appearing since 2010 in some host personal computers and peripherals. Beginning with USB 2.0 and increasing with USB 3.0, DAQ architectures have increasingly used this protocol for communications, particularly with personal computers serving as hosts.

In addition, parallel communication protocols have been in use for dedicated instrument buses. By far the most common and widely-accepted standard was IEEE-488, the General Purpose Interface Bus (GPIB). GPIB is an 8-bit parallel bus. The bus uses eight ground lines and 16 signal lines, eight for bi-directional data transfer, three for handshake, and five for bus management. GPIB, however, was not really intended for direct connection to personal computers for the multifunctional DAQ capability implied by the schematic in Fig. 2.12, and other bus designs were developed. One of the most common is the Peripheral Component Interconnect (PCI) bus, first introduced in 1992, with 58 or 60 pin connections, depending on specific architecture. General specifications included 33 MHz clock with synchronous (parallel execution) transfers, a 32-bit bus width, and either 32-bit or 64-bit memory address space. PCI-X was developed as a newer parallel bus in 1998 with up to 533 MHz clocks.

PCI-E (also known as PCI-Express) was developed as a serial bus in 2004 that substantially improved throughput (16 GB/s in a 16-lane bus) and reduced the number of pin connections, since it is based on point-to-point topology; a 4-lane PCI-E bus has the same peak transfer rate as a 64-bit PCI-X device (both about 1 GB/s), but the PCI-E will ultimately perform better when multiple devices are transferring data, due to the serial architecture. Parallel bus architectures, particularly when loaded fully, suffer from *timing skew*, which is the phenomenon whereby parallel signals transmitted simultaneously arrive at their destination at slightly different times due to the unique length of each signal's path.

2.6 Optical sensing DAQ system

Sections 2.1–2.5 have presented overviews of the relevant signal processing and hardware architectures used in most conventional, wired DAQ systems that interrogate sensors inherently producing voltage or current analog waveforms that are proportional to the physical field being measured. Optical sensing inherently takes advantage of modulated properties of light – intensity (power), wavelength, polarization state, or phase – to deduce changes to the measured field. In fiber optic sensing architectures (the kinds used most commonly for structural health monitoring applications), the light is completely contained, until detection by a photodetector; in an optical fiber, a cylindrical waveguide that uses refractive mismatches to exploit total internal reflection and coherently propagate the light over very long distances (km in the case of infrared-wavelength light). In this way, fiber optic sensing strategies are self-telemetered; the 'power source' and the sensing mechanism are contained within the fiber, which makes for far less cabling and electronics equipment required near the sensing field itself. Additionally, since all information is optical at the sensor sites, the susceptibility to extraneous measurands is often reduced, particularly in the case of electromagnetic interference. Three fiber sensing references with specific application to practical sensing considerations include the comprehensive Lopez-Higuera (2002), Yeh (1990), and Todd (2005).

Chapter 5 considers specific optical sensing architectures in greater detail, but fundamentally almost every fiber optic sensing approach requires (1) a source of light generation, (2) exploitation of some optical property modulated in a fiber, and (3) photodetection. Thus, fiber optic DAQ requires both optical components and non-optical components, and Fig. 2.13 depicts a general fiber optic sensing schematic. Depending on the sensing principle, light is generated by a laser (narrowband) or diode (broadband), transmitted to the sensing regions of the fiber where sensing is accomplished via intensity, phase, or wavelength modulation, and the modulated light is detected by a photodetector. A piezoelectric element may be present for some sensing architectures in order to control a tunable optical filter on the optical side. Photodiodes, photodetectors, and tunable filters will be discussed in turn.

2.6.1 Photodiodes

Semiconductor-based optical sources are a very common and practical choice for most sensing applications, mainly due to their compactness, long service life, and relatively low cost. This section will be limited to light-emitting

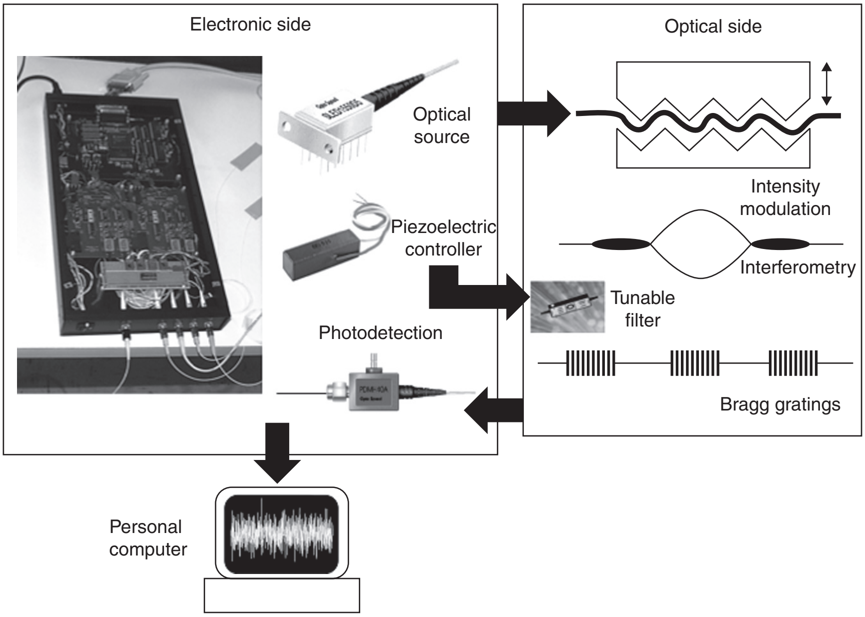
Electronic side
Optical side
Optical source
Piezoelectric controller
Photodetection
Intensity modulation
Interferometry
Tunable filter
Bragg gratings
Personal computer

2.13 A general fiber optic measurement system schematic.

diodes (LEDs), although laser diodes are very commonly used as well. Light emission in LEDs is based on electron transition from an occupied state in the conduction band to an unoccupied state (hole) in the valence band, which is called *spontaneous emission*: the electron–hole recombination process is a radiative process that emits a photon. This process is only possible if occupied states in the conduction band have the same wavenumbers as holes in the valence band. This is not an equilibrium state, and pumping of electrons from the valence band to the conduction band is required from some external source. Because semiconductors are also susceptible to absorption processes (where a photon transfers its energy from a valence band electron to promote it to the conduction band), the electron-pumping rate must overcome this to achieve a positive gain. The non-equilibrium state required to achieve emission is stimulated by voltage-biasing a p-n junction diode. The electrical field produced by the bias voltage induces electron drift from the n-side to the p-side and hole drift in the opposite direction. At the junction region, where concentrations of electrons and holes are very high, recombinations promote spontaneous optical emission in all directions, and even stimulated emission once an optical field is produced. A variety of materials and substrates have been employed to produce light at wavelengths from as low as 400 nm up to 25 000 nm; typical materials include In, Al, Zn, GaASP, or InGaAs with GaAs, GaP, or InP substrates. The optical bandwidth of the emissions depends on wavelength and temperature and typically ranges between 30–150 nm. Since each spontaneous emission event is uncorrelated, so are the emitted photons with respect to phase, direction, and polarization. With surface-emitting diodes, photon emission is through the substrate, perpendicular to the junction (see Fig. 2.14a). The substrate is etched, and a circular ring acts as the contact with the fiber placed as closely as possible to the active emission region. With edge-emitting LEDs (ELEDs), light is emitted from the side (parallel to the junction), which results in higher extraction efficiency (Fig. 2.14b). ELEDs are better for long-distance, higher bit-rate transmission, but they are more sensitive to temperature fluctuations than surface-emitting diodes. Typical maximum optical power outputs, depending on wavelength region, vary from about 0.015–8 mW.

2.6.2 Photodetectors

In 2.6.1, the concept of spontaneous emission was mentioned in conjunction with the operating principle of LEDs. The reverse, but very similar, process is absorption, where incoming photons transmit their energy to valence band electrons that subsequently are promoted to the conduction band. This is the process behind the operation of photodetectors, which may be defined as devices in which photons are converted to electric charge carriers. The effect

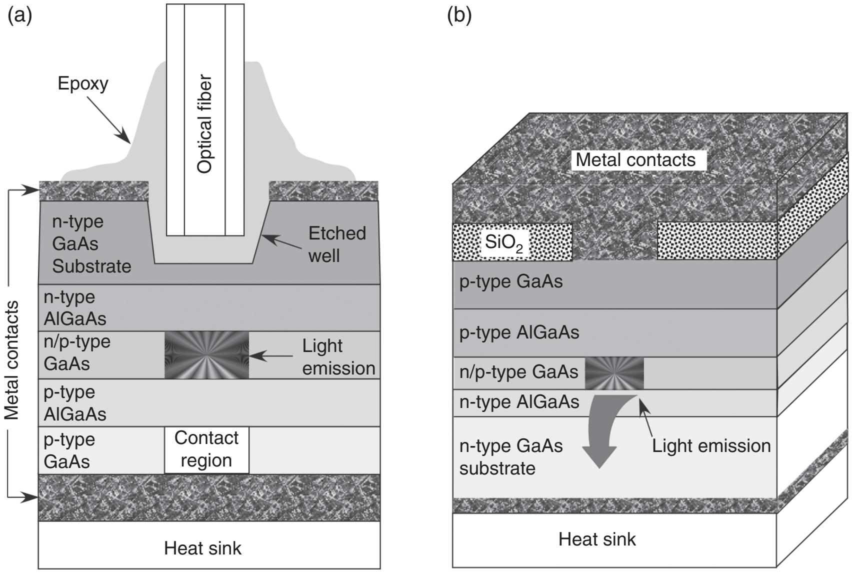
(a)
Epoxy
Optical fiber
n-type
GaAs
Substrate
Etched
well
n-type
AlGaAs
n/p-type
GaAs
Light
emission
p-type
AlGaAs
p-type
GaAs
Contact
region
Metal contacts
Heat sink
(b)
Metal contacts
SiO_2
p-type GaAs
p-type AlGaAs
n/p-type GaAs
n-type AlGaAs
n-type GaAs
substrate
Light emission
Heat sink

2.14 Surface-emitting (a) and edge-emitting (b) diode light source cross-sections.

of the electric charge carriers is measured by applying voltage with a load resistor to generate a current. The amount of current generated by the electric charge carriers is often called the photocurrent, but even when no light is incident upon the device, a current is still produced by the polarization circuit (called the dark current). This feature should be kept as low as possible for SNR optimization. The primary performance metric of photodetectors is the responsivity, defined to be the ratio of the output photocurrent (in amperes) to the power of the incident light (in watts). Responsivity is a function of both the incident optical wavelength and the device's efficiency at converting the light to current. Different materials respond with different efficiencies across the optical wavelength spectrum, and in some cases, they do not respond at all. The materials typically used in photodetectors are Si, GaAs, Ge, and InP, similar to LEDs.

One common type of photodetector is a p-i-n photodiode, as shown in Fig. 2.15a. This device is very similar to the LED structures presented previously, except that an intrinsic semiconductor is inserted between the p and n layers. In addition, these layers have been highly doped (denoted by '+' signs in the figure), which increases the electric field in the transition zone and reduces the concentration of minority carriers. A reverse bias voltage is applied (on the order of a few volts) to establish the polarization current. Reverse bias photodetectors are inherently very linear devices with regard to

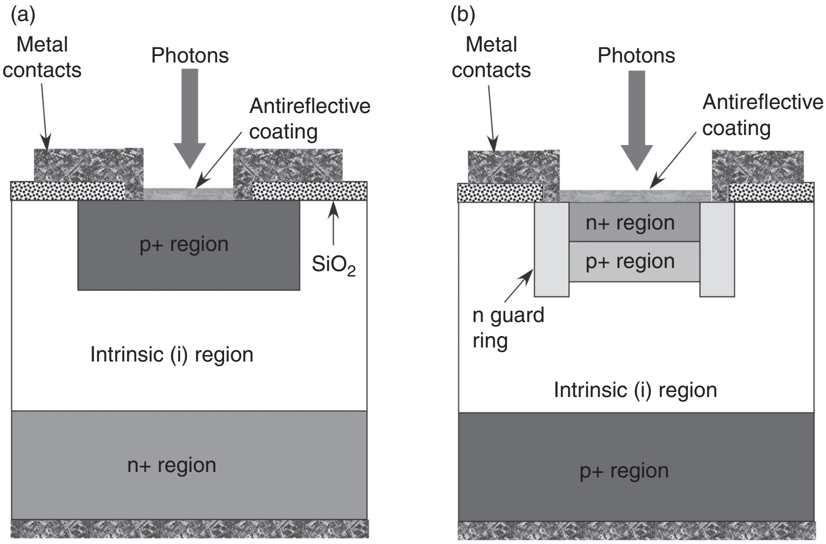
(a)
Metal contacts
Photons
Antireflective coating
p+ region
SiO$_2$
Intrinsic (i) region
n+ region
(b)
Metal contacts
Photons
Antireflective coating
n+ region
p+ region
n guard ring
Intrinsic (i) region
p+ region

2.15 PIN (a) and avalanche (b) photodiode cross-sections.

responsivity over wide dynamic ranges (up to 60 dB) up to saturation, which typically occurs at about 1 mW of input power. Typical fiber sensing systems as well as communications applications do not require nearly this high a power level, so saturation is rarely an issue. The performance of the photodiode is most affected by the thickness of the detector active area and the detector time constant.

A second type of photodiode is the avalanche photodiode (APD), shown in Fig. 2.15b. The overall structure is similar to a p-i-n photodiode, but a large reverse bias (on the order of hundreds of volts) is applied that causes the electrons generated by the photon incidence to accelerate as they move through the active region. These carriers tend to collide with other electrons, inducing some of them to join the photocurrent, initiating an avalanche process that continues until the electrons are outside the active region. This process results in a large gain factor that multiplies the responsivity; this gain factor may be increased by increasing the reverse bias voltage, but this is done at the expense of increased dark current (and thus noise). Furthermore, since not every electron undergoes the same avalanche multiplication, this becomes a source of noise, so a limit is placed on the usable gain factor. The same factors that affect the design of the p-i-n photodiode affect the APD, with the additional time required to execute the avalanche multiplication process. Trade-offs between using p-i-n photodiodes or APDs depend on the relative importance of responsivity, resolution, stabilization requirements, and cost. APDs have internal gain due to the avalanche effect, so they are more responsive, but have higher noise properties. Since this gain factor also depends on temperature, thermal compensation is almost always required for proper use of APDs. In addition, APDs cost more and have much larger voltage and stabilized source requirements than p-i-n photodiodes.

2.6.3 Tunable optical filters

Wavelength-specific acceptance or rejection (filtering) of light propagating in a fiber has many sensing applications, particularly if wavelength is used as a multiplexing strategy in a sensor network. Tunable, in-line filtering is realized mostly with resonator cavities such as a fiber Fabry–Pérot (FFP) tunable filter. The most commonly used form employs a fiber-coupled Fabry–Pérot tunable filter as a bandpass filter. Tunable FFPs make use of a Fabry–Pérot etalon, shown schematically in Fig. 2.16. Two fiber ends with partially reflecting dielectric mirrors implanted inside are brought some distance *d* together with an air gap between them. When light is incident upon this gap, multiple reflections will be established, and the reflections will constructively or destructively interfere dependent upon the spacing *d* (and the wavelength λ). For an incident optical wave, the phase delay it undergoes after each round trip is given by $\phi = 4\pi nd / \lambda$, where *n* is the refractive index in the gap. If the mirrors have the same transmission *T* and reflection *R* properties, the transfer function *H* of the ratio of the power transmitted out of the etalon to the incident power is given by:

$$H = \frac{1 - R^2}{1 - R^2 + 4R\sin^2 \phi}, \qquad [2.11]$$

where a 360° shift, not explicitly shown, is assumed accrued at each reflection boundary (dielectric reflection boundary condition), and scattering losses have been ignored. This function is plotted as a function of phase angle for various values of *R* in Fig. 2.16. The transfer function has pi-periodic windows of maximum transmission with a transition sharpness dependent upon the reflectivity. The larger that *R* is, the sharper the transmission peaks will be.

Two performance metrics for FFPs are important: the free spectral range (FSR), or the distance between transmission peaks, and the finesse, defined to be the ratio of the FSR to the full width of the transmission peak at half of maximum value (FWHM). These metrics are typically expressed in terms of the wavelength, so conversion from phase to wavelength is employed through Equation [2.11]. They may be summarized by:

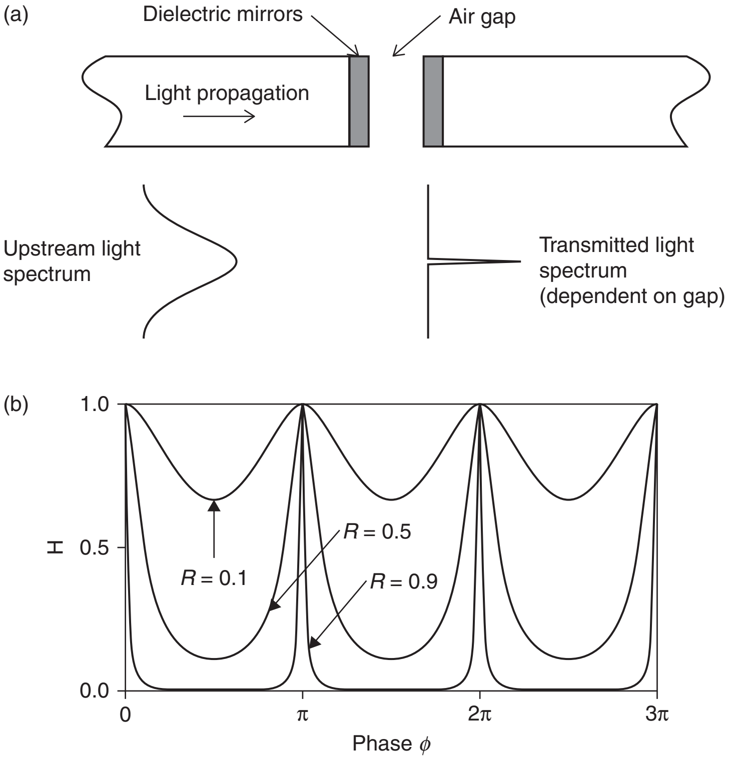
(a)
Dielectric mirrors
Air gap
Light propagation
Upstream light spectrum
Transmitted light spectrum (dependent on gap)
(b)
1.0
0.5
0.0
H
R = 0.1
R = 0.5
R = 0.9
0
π
2π
3π
Phase ϕ

2.16 An etalon-based tunable Fabry–Pérot optical filter (a) and its transfer function (b).

$$\begin{aligned} \mathrm{FSR} &= \frac{\lambda^2}{4nd} \\ \text{finesse} &= \frac{\pi}{2\sin^{-1}\sqrt{(1-R^2)/4R}} \end{aligned} \qquad [2.12]$$

The finesse is only dependent upon the reflectivity of the mirrors. For filtering applications, a wide FSR may be desirable, but this also implies a wider bandwidth for a given finesse, which is undesirable for sensing applications. Commercial FFPs typically have FSRs between 40 and 80 nm (at 1550 nm), passband bandwidths of about 0.2–0.5 nm, and a finesse of 100–200. The tunability of the passband center wavelength is controlled by varying *d*, which is typically done by incorporating a piezoelectric element with voltage control at the micron-level of displacement (Fig. 2.16). Such filters are used in a variety of fiber Bragg grating-based and interferometric-based sensor architectures, both of which are discussed in greater detail in Chapter 5.

2.7 Conclusion and future trends

This chapter presented an overview of important concepts related to the process of obtaining and processing measurements of relevant kinematic or kinetic behavior of structures, the primary issues associated with this process, and the most common architectures used to execute this process. Specific focus was placed upon conventional, wired data acquisition processes for making voltage measurements. A fairly comprehensive list of important topics in this chapter included time/frequency domain signal analysis, filtering, probability and uncertainty analysis, analog-to-digital conversion, DAC, sampling theory, transducer design, multiplexing/demultiplexing, and important sensor-level and system-level aspects to selecting DAQs for a given application. This chapter also presented an overview of digital data acquisition (including common protocols such as USB) and presented common architectural components for fiber optic-based data acquisition (with far more detail on this topic presented in Chapter 5 of this book). The references provided at the end of this chapter were carefully selected to provide more information in each of these topical areas. The objective of this chapter was to give an engineer tasked with a structural health monitoring application the most relevant information required for obtaining voltage-based measurements (and fiber optic measurements, to some degree), understanding how they get processed in preparation for conversion into useful information, and the issues and challenges associated with such data acquisition.

While the conventional wired data acquisition architectures and fiber optic sensing architectures discussed here certainly still dominate most structural health monitoring applications, primarily due to their proven reliability, robustness, and regulation certification acceptance where required (such as the aerospace industry), there are a number of trends in data acquisition that are substantially advancing the field. First and foremost, beginning in the 1990s, was the wireless revolution. Key data acquisition components described in this chapter (D/A, A/D, signal processing) were integrated with microcontrollers, software/firmware 'micro' operating systems, and wireless antennas into much smaller platforms called *nodes*. Chapter 15 describes the general architectures of wireless nodes, and gives some deployment examples, but the primary revolution in this advancement was taking data acquisition from a centralized construction (where each sensor's raw data are streamed individually over wires to the central acquisition/processing unit, where A/D, demultiplexing, sampling control, and appropriate signal processing are governed) to a distributed construction, where each sensor node now may perform many of these operations locally and wirelessly broadcast reduced information sets rather than raw data (decreasing bandwidth requirements and providing potential redundancy in the information movement chain).

Somewhat concurrent with this wireless trend, fueled by the telecommunications industry's development of smartphones in the mid to late 2000s, is a trend toward low-power components (powered at 0.5 V and operating in the mW range, compared to powered at 5–10 V and consuming several W). As data acquisition components achieve lower power usage requirements, energy harvesting strategies (Chapter 17) become much more feasible, and as such energy harvesting – defined to be any strategy that seeks to convert otherwise wasted or unused non-electrical energy sources into useful electrical energy – has become a big research and development topic. In particular, since wireless sensor nodes require a local power source such as a battery, energy harvesting could provide alternative means of powering such nodes to create an energy-neutral platform with increased autonomy. Not surprisingly, autonomy in general has been another important sensing/data acquisition trend, and Chapters 13 and 14 discuss some important developments in robotic and vision-based sensing that support this trend. In fact, it is becoming increasingly clear overall that sensing and data acquisition are moving toward increased autonomy, increased intelligence, and even sensor system self-awareness and adaptability. Figure 2.17 shows this taxonomy, evolving from where the field

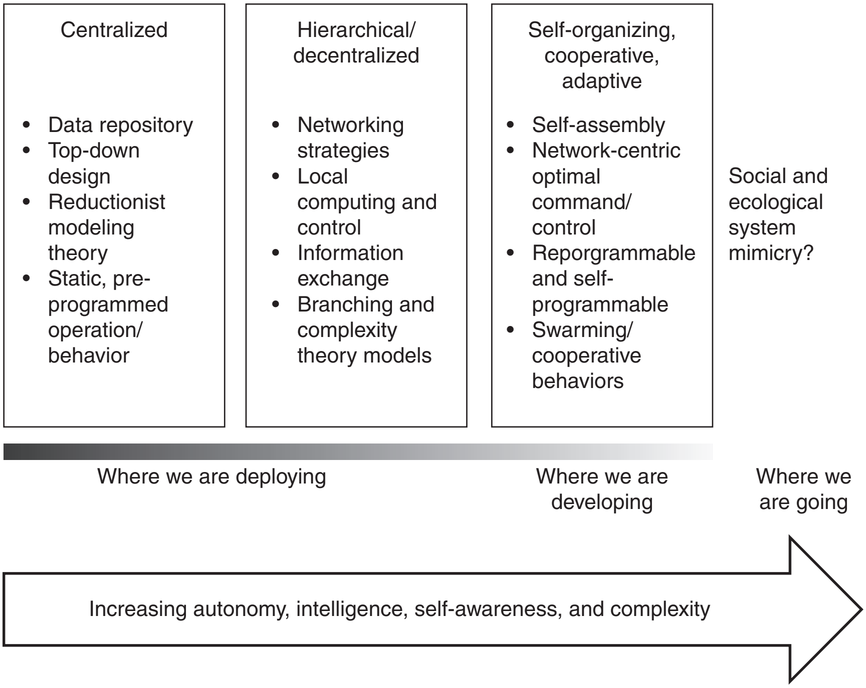
Centralized
• Data repository
• Top-down design
• Reductionist modeling theory
• Static, pre-programmed operation/behavior
Hierarchical/decentralized
• Networking strategies
• Local computing and control
• Information exchange
• Branching and complexity theory models
Self-organizing, cooperative, adaptive
• Self-assembly
• Network-centric optimal command/control
• Reporgrammable and self-programmable
• Swarming/cooperative behaviors
Social and ecological system mimicry?
Where we are deploying
Where we are developing
Where we are going
Increasing autonomy, intelligence, self-awareness, and complexity

2.17 A schematic of sensor and data acquisition taxonomic evolution moving toward increased autonomy, intelligence, self-awareness, and overall complexity.

has been (centralized architectures) to the current state-of-the-art (hierarchical and decentralized) to the near future (self-assembled, self-aware, cooperative networks) and even beyond (mimicry of complete socio-ecological systems). These very advanced sensor networking and programming concepts are, at the time of writing, very much at the cutting edge of sensor network research and development.

2.8 References

Ayyub B M and Klir G J (2006), *Uncertainty Modeling and Analysis in Engineering and the Sciences*, Boca Raton, Chapman & Hall/CRC.

Beckwith T G, Marangoni R D and Lienhard J H (2006), *Mechanical Measurements 6th Edition*, Upper Saddle River, NJ, Prentice-Hall.

Bendat J S and Peirsol A G (2010), *Random Data: Analysis and Measurement Procedures,* Hoboken, NJ, John Wiley and Sons.

Doeblin E R (2003), *Measurement Systems: Application and Design*, New York, McGraw-Hill.

Figliola R S and Beasley D E (2000), *Theory and Design for Mechanical Measurements*, New York, John Wiley and Sons.

Fortney L (1987), *Principles of Electronics: Analog and Digital*, New York, Harcourt Brace Jovanovich.

Kay S (1993), *Fundamentals of Statistical Signal Processing*, Upper Saddle River, NJ, Prentice-Hall.

Kester W ed. (2005), *The Data Conversion Handbook*, New York, Elsevier: Newnes.

Lopez-Higuera J-M ed. (2002), *Handbook of Optical Fibre Sensing Technology*, Chichester, UK, John Wiley and Sons.

Oppenheim A V, Schafer R W and Buck J A (1999), *Discrete-Time Signal Processing*, Upper Saddle River, NJ, Prentice Hall.

Todd M (2005), 'Optical-based sensing', in Inman D J, Farrar C R, Lopes V and Steffen V, *Damage Prognosis*, Chichester, UK, John Wiley and Sons, 343–362.

Wagdy M F and Ng WM (1989), 'Validity of uniform quantization error model for sinusoidal signals without and with dither,' *IEEE Transactions on Instrumentation and Measurement*, **38**(3), 718–722.

Yeh C (1990), *Handbook of Fiber Optics: Theory and Applications*, San Diego, Academic Press.

3

Commonly used sensors for civil infrastructures and their associated algorithms

N. C. YODER, Whistle Labs Inc., USA and D. E. ADAMS,
Vanderbilt University, USA

DOI: 10.1533/9780857099136.57

Abstract: As health monitoring technologies for civil infrastructure transition from research to practice, several leading sensor technologies and associated algorithms have emerged. The rationale for choosing a given sensor type in a specific health monitoring installation depends on many factors, but they are generally inexpensive, robust, and mature technologies. Furthermore, while a large variety of advanced algorithms have been developed for health monitoring applications, the majority of these algorithms share commonalities in the features that are extracted from the data. This chapter will classify and describe the sensor technologies that are used most frequently in recent monitoring installations and will identify commonalities in the algorithms that are used to process the data from these sensors.

Key words: sensors, civil infrastructure, monitoring, algorithms, damage detection.

3.1 Introduction

Because of its potential to increase public safety while decreasing maintenance costs, health monitoring has attracted a significant amount of attention and has resulted in many books, journal articles, and conference papers about new and existing sensors and algorithms. Each new type of sensor aims to address technical challenges that are confronted in the transition of health monitoring from the research laboratory to the field. While many of these technologies may eventually prove instrumental in the widespread implementation of health monitoring, to date there is a relatively small subset of sensor technologies and associated algorithms that are widely used in health monitoring systems. Although the exact reasons for the preponderance of these traditional sensors across the wide variety of monitoring system are difficult to quantify and are likely influenced by the familiarity

© 2014 Woodhead Publishing Limited

of practitioners with these sensors, by looking across multiple installations it is apparent that the most commonly used sensor types consist of relatively inexpensive, robust, and mature technologies. In addition to the relatively long history that each of these sensor technologies has had operating reliably in the field, there is also an extensive and robust set of algorithms that have been developed to extract damage sensitive features from these sensor measurements.

Because of the large amount of research and publications devoted to new sensing techniques and advanced algorithms for health monitoring, it is worthwhile for both new and experienced researchers to review the utility and practicality of traditionally used sensors. In an effort to summarize the attributes of this family of commonly used sensors, this chapter will review sensing techniques that are commonly used for the health monitoring of civil infrastructure as well as the algorithms that are commonly used in combination with them. A brief review of the physical principles that are behind the operation of each type of sensor will first be given. Then several algorithms that utilize these types of sensors will be described with an emphasis on the underlying commonalities between the algorithms and how they exploit the unique attributes of each sensing technology. The algorithms that are explored focus heavily on health monitoring techniques using accelerometer measurements because the preponderance of global damage identification methodologies have used them extensively and utilized other sensors for local monitoring or data-normalization purposes. Several brief examples of continuous monitoring systems that exploit the described technologies will then be described and the chapter will conclude by describing some of the major trends in this area.

3.2 Brief review of commonly used sensing technologies

While there are a wide array of different sensing technologies that are widely used throughout the civil and aerospace industries for health monitoring purposes, this chapter focuses on four general types of measurements that are widely used as part of health monitoring systems: displacement, strain, acceleration, and environmental parameters. For each of these measurement types, two or three different types of traditional sensors that are commonly used in practice are then described. Although additional sensors could be included in this list, only those sensors that were found to be the most commonly used in the literature for monitoring civil structures with a focus on bridges have been included here. Furthermore, the inclusion of sensor types in this list of ‘traditional’ technologies does not indicate that there are no longer innovations or advancements in each of these types of sensors. In each of these areas, new advancements continue to be made as the sensors are made smaller, less expensive, and more robust and the algorithms associated with them are improved.

3.2.1 Displacement

One sensing modality that is commonly used in monitoring bridges, dams, and other large civil structures is relative displacement measurement. While these measurements are not commonly used for health monitoring of aerospace structures, they can prove useful in monitoring civil infrastructure because of the much larger scales and geometric changes that can occur during a civil structure's lifecycle. While technologies such as the global positioning system (GPS) offer the capability to measure global changes in position, traditional displacement measurements are typically made using linear variable differential transformers (LVDTs) or potentiometers, which are connected to two locations on or at the boundary of the structure of interest in order to measure relative displacements.

Linear variable differential transformers

LVDTs are a type of two-part inductive sensor in which a ferromagnetic armature moves within an outer transformer consisting of one primary and two secondary coils. The secondary coils are located on either side of the primary coil and are wound in opposite directions. The primary coil is excited with an alternating current (AC) excitation and the magnetic flux that is developed is coupled to the secondary windings through the ferromagnetic core. Due to the opposite windings of the two secondary coils, when the core is positioned in the magnetic center of the transformer the two secondary coils cancel one another and no voltage is measured at the output. However, when the core moves away from this central position the amount of induced flux that is coupled into the two secondary coils becomes unequal, which creates a voltage differential in the circuit. While the core remains within the operating range of the LVDT, the amount of output voltage is linearly related to the displacement of the core (Fraden, 2010).

LVDTs are attractive for measuring displacement for several reasons. Because there is no mechanical contact between the sensing elements, there are no frictional forces to distort the readings and the sensors are highly robust because there are no mechanical connections that could suffer fatigue failures. This lack of mechanical connection also means that the minimum resolution of the sensor is based solely upon the noise in the signal conditioning and data acquisition systems, and consequently high resolutions can be achieved (Fraden, 2010). However, because the sensor relies on this lack of contact between the core and the body, transverse motion must be minimized to avoid internal rubbing. Another possible drawback to the use of LVDTs is that the sensor's operating range is limited by the size of the sensor itself, since the core must remain within the coils for the system to operate correctly.

Potentiometers

Potentiometers come in many shapes and sizes but are typically predicated on relating changes in resistance to changes in rotational or linear position. This change in resistance is typically accomplished by moving a pot wiper along a length of wire causing a linear change in the resistance between the excitation source and the wiper (Fraden, 2010). As previously stated, although there are many forms of potentiometers, one of the most common is a string potentiometer in which a measuring cable is wound around a spool. The spool has a torsional spring to maintain tension in the measurement wire and the length of string that has come out of the sensor can be calculated using the rotational potentiometer on which the spool is mounted.

One reason why string potentiometers can be attractive for measuring displacements is because, unlike LVDTs, they can measure displacements that are significantly larger than the sensor itself because the measurement wire is wound around the spool. This allows them to be relatively lightweight while still being able to measure ranges of over 50 meters. However, because of their mechanical connections most string potentiometers have limits on their frequency range, lifetime, and accuracy. Furthermore, while it is not typically an issue on large civil structures, the tension in the cable can affect the measurement for smaller structures that are more sensitive to external loads.

3.2.2 Strain

Strain measurements are used for a variety of health monitoring techniques because they are a direct measurement of the structure's relative deformation under the applied load. While these measurements can provide valuable information about a given component, they are also related to the, often unknown, load that the structure is undergoing. Despite this fact, both piezoresistive and vibrating-wire strain gages are often used in monitoring systems for large civil structures.

Piezoresistive

Resistive strain gages are utilized widely on both aerospace and civil structures. These simple sensors are bonded to the structure of interest so that the deformation of the structure causes the sensor to elongate or contract as well. Deformations of less than approximately 2% can be related to the resistance of the gage through the equation:

$$R = R_0\left(1 + S_e\varepsilon\right) \tag{3.1}$$

where R is the resistance of the deformed gage, R_0 is the resistance of the gage with no stress applied, S_e is the gage factor of the conductor (approximately 2 for many metals) and ε is the strain across the gage (Fraden, 2010). These changes in resistance are typically converted to an absolute voltage using a Wheatstone bridge circuit (Boyes, 2010).

While piezoresistive strain gages are small and consequently have relatively negligible mass loading effects on the structure, their response is dominated by localized effects such as stress concentrations. For large structures this means that strain gages should be restricted to monitoring 'hot spots' where damage is expected to occur or on critical components because large areas will require extensive numbers of sensors for global monitoring. Dense instrumentation with piezoresistive strain gages can be problematic because good installation is essential to obtain high quality measurements from a strain gage and installation is a labor-intensive process that is best performed by those with the expertise. Piezoresistive strain gage measurements can also be affected by changes in temperature, and it can be difficult to detect slowly varying strains using them due to sensor drift (Boyes, 2010).

Vibrating-wire

Vibrating-wire strain gages are an alternative type of strain gage that is commonly used on large civil structures such as bridges but are not extensively used in the aerospace industry. Vibrating-wire strain gages are based on the principle that if a wire is pinned at both ends and put under tension, the natural frequency of the vibration of its first mode is:

$$f = \frac{1}{2l}\sqrt{\frac{T}{m}} \tag{3.2}$$

where l is the length of the wire, T is the tension in the wire, and m is the mass per unit length of the wire. By bonding the locations at which the wire is fixed to the structure of interest, the strain across the length of the wire can be determined by monitoring the natural frequency of the wire. This is typically done by utilizing a ferromagnetic material for the wire and exciting the wire at the middle of its span with a solenoid in order to ensure that the first mode of the wire is excited. A typical vibrating-wire strain gage has a wire diameter of 0.25 mm and a nominal operating frequency of 1 kHz (Boyes, 2010).

Vibrating-wire strain gages are typically much larger than piezoresistive strain gages and are often between 50 and 250 mm in length. The gages themselves are often attached by welding them directly to the structure of interest or, in the case of concrete, can be directly embedded in the material. In the case of strain gages on concrete, the relatively large size of vibrating-wire strain gages is advantageous because it averages the strain over a sufficient distance to average out much of the local inhomogeneities that are inherent in the concrete. While these gages are sensitive to temperature, like piezoresistive strain gages, when they are carefully installed and used at room temperature they have been found to be very stable and exhibit drift of less than one microstrain over several months (Boyes, 2010).

3.2.3 Acceleration

Acceleration measurements are among the most commonly used measurements in health monitoring of both civil and aerospace structures. One reason for this is that they are well understood and contain information about both the local and the global characteristics of the structure. Because of their widespread use in health monitoring applications, three different types of accelerometers are described in this section: force-balance, capacitive, and piezoelectric accelerometers.

Force-balance

A force-balance, or servo, accelerometer utilizes an active feedback control system to control the position of the proof mass, and the feedback required to keep the mass stationary is used to calculate the acceleration that the system is undergoing. The system works as follows. When the sensor housing is accelerated, the proof mass inside the sensor attempts to remain stationary with respect to the inertial frame of reference. This causes the proof mass to move away from its nominal position in the sensor housing. This relative motion is detected using a displacement sensor (often capacitive), which produces an error signal in the control system. This causes current to flow through the force generating element that balances the force due to the acceleration. Then, by relating the current to the applied force, the acceleration can be calculated using the known proof mass and properties of the forcing system (Boyes, 2010).

Force-balance accelerometers can be attractive for monitoring civil structures because they are very sensitive and have very good resolution at low frequency. Furthermore, they are relatively insensitive to thermal effects and have relatively low nonlinearities. However, the major drawback of force-balance accelerometers is the control mechanism itself, which makes the sensor more expensive than other accelerometers and limits the bandwidth of the sensor to relatively low frequencies.

Capacitive

A capacitive accelerometer utilizes the displacement of a proof mass with respect to the housing of the accelerometer in order to determine the acceleration that the sensor is experiencing. In a capacitive accelerometer, the motions of the proof mass are relatively small (less than 20 μm) so the proof mass is typically suspended between two plates, one of which is above it and one of which is below it. The two capacitors that are formed between the mass and the top and bottom plates are then utilized in a differential mode so that small drifts and interferences can be compensated for in the measurement (Fraden, 2010).

Capacitive accelerometers are advantageous for monitoring large structures because they are able to acquire measurements across a wide frequency range including static acceleration while generally having superior stability, sensitivity, and resolution to piezoresistive accelerometers. However, they are somewhat susceptible to temperature and humidity variations and are relatively fragile compared to piezoelectric accelerometers.

Piezoelectric

Piezoelectric accelerometers are highly utilized in both the civil and aerospace industries. These accelerometers are based upon the piezoelectric effect in which certain crystalline materials generate an electric change that is proportional to the net force acting on the piezoelectric material (Boyes, 2010). Piezoelectric accelerometers typically utilize one of three different configurations, namely the shear mode, flexural mode, or compression mode configurations, to measure the applied acceleration. In a shear mode accelerometer the piezoelectric material is sandwiched between a rigid post and a cylindrical proof mass as shown in Fig. 3.1, so that as the proof mass moves relative to the rigid post in the sensing direction, it generates a shear stress in the piezoelectric material. In flexural mode accelerometers, a beam-shaped crystal is used that is supported on a fulcrum so that accelerations directly induce strains in the piezoelectric beam. This type of piezoelectric accelerometer is best suited for low-frequency, low-amplitude applications. Compression mode accelerometers use tensile and compressive loads to generate forces in the piezoelectric material. While early designs preloaded the piezoelectric material against the base of the sensor, it was found that this approach made the accelerometer very sensitive to base strains and temperature variations. Therefore, new designs isolate the crystal by either placing it at the top of the sensor or isolating it using a washer (Newman, 2010).

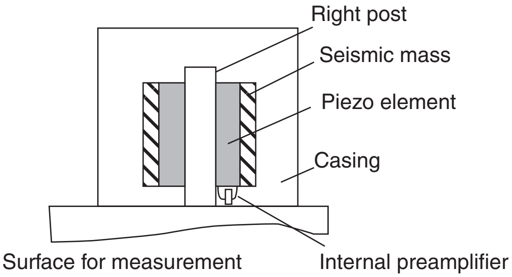

3.1 Diagram of a shear mode piezoelectric accelerometer (Adams, 2007). (*Source*: Reproduced by permission of Wiley.)

Piezoelectric accelerometers have gained such wide use in large part because they can be used in a wide variety of environments and are relatively robust. They have a long service life because there are no moving components in the sensor and they can be applied across a wide frequency and possess good linearity across a large dynamic range. However, these sensors typically have a minimum frequency at which they can be used and are, therefore, unable to measure static accelerations in contrast to capacitive or piezoresistive accelerometers.

3.2.4 Environment

Because most civil infrastructures operate in widely varying environments the preponderance of health monitoring systems typically include several types of traditional sensors to measure the current environmental conditions. While these measurements may not be used to directly calculate the health of the structure, they are essential for monitoring the loads on the structure and for the data-normalization process that is a necessary part of detecting changes in the sensor's measurements due to damage from changes due to variations in the structure's environment (Farrar and Worden, 2007).

Anemometers

For large civil structures such as buildings and bridges, wind speed can be of particular interest as it can significantly excite the structure. This is even more critical for bridges in which improper design can lead to aerodynamic self-excitation, as was the case with the famous Tacoma Narrows bridge (Billah and Scanlan, 1991). Lastly, anemometers are also of great interest in wind turbines since the entire operation of the structure is based on wind speed and these measurements can be used to help normalize the response of the structure. While a variety of different types of anemometers exist, perhaps the most widely used is the cup anemometer, which typically consists of three or four cups mounted on the end of horizontal arms that are fixed to a common vertical shaft. The cup anemometer is a drag-driven device that turns because the drag on the smooth back surface of the cup is less than that on the open face of the cup. This imbalance in drag results in rotational speed of the cups being proportional to the average wind speed (Tong, 2010).

Thermocouples and resistive thermometers

For large and relatively flexible structures such as bridges or even buildings, temperature changes can have a large effect on the response characteristics of the structure and can easily mask changes in the structure due to damage or result in false indications of damage. For example, Alampalli (1998) found that freezing in the supports of a bridge caused changes in the natural frequencies of the structure that were more than ten times more significant than the changes in the natural frequencies due to damage. However, perhaps even more interesting was Farrar *et al.*'s (1997) finding that the first mode of the Alamosa Canyon bridge varied by approximately 5% throughout a single day, and that rather than being correlated with the overall ambient temperature of the structure this change was correlated with the temperature gradient across the bridge deck. This influence of temperature gradients has resulted in the widespread application of temperature sensors including thermocouples and resistance thermometers with as many as 388 temperature sensors being installed on a single bridge (Wong and Ni, 2009).

Resistance thermometers utilize the principle that the resistance of metals increases with temperature. Platinum is typically utilized for resistance thermometers because it has the highest possible coefficient of resistivity, which is indicative of its high purity, and the slight changes in its resistance with temperature can be measured using a Wheatstone bridge (Boyes, 2010). Thermocouples, on the other hand, use the fact that if two different metal wires are connected, the voltage that is produced in the vicinity of their connection is dependent on the temperature difference between the connectors and other parts of those wires. A wide variety of different thermocouples are produced utilizing a range of different alloys depending on the specific temperature range in which the sensor will be operating (Boyes, 2010).

3.2.5 Prevalence of commonly used sensors in SHM systems

To determine which sensors are most commonly used in health monitoring installations, a literature review was performed to identify some

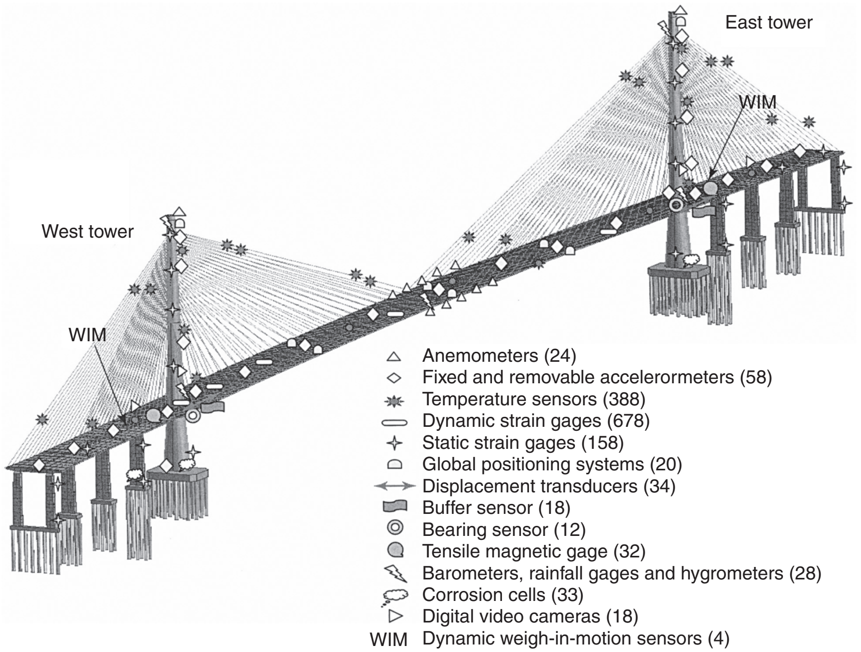
East tower
WIM
West tower
WIM
△ Anemometers (24)
◇ Fixed and removable accelerormeters (58)
✱ Temperature sensors (388)
▭ Dynamic strain gages (678)
✧ Static strain gages (158)
⌓ Global positioning systems (20)
↔ Displacement transducers (34)
▬ Buffer sensor (18)
◎ Bearing sensor (12)
● Tensile magnetic gage (32)
Barometers, rainfall gages and hygrometers (28)
Corrosion cells (33)
▷ Digital video cameras (18)
WIM Dynamic weigh-in-motion sensors (4)

3.2 Sensor layout for Stonecutters Bridge in Hong Kong (Wong and Ni, 2009). (*Source*: Reproduced by permission of Wiley.)

instances of installed health monitoring systems and the types of sensors that are used within them. Some of the installed instrumentation and the number of gages of each type are listed in Table 3.1. As an illustration of the complexity of some of these systems, Fig. 3.2 shows an instrumentation diagram for the Stonecutters Bridge in Hong Kong. For each installation listed in Table 3.1, the number of traditional gages for each of the investigated measurement types is listed, along with the total percentage of installed sensors that are one of the 'traditional' sensors as defined above. Despite the fact that the total number and distribution of sensors in each installation vary significantly, it is clear that, in general, the most up-to-date installed health monitoring systems rely heavily on the traditional sensing technologies that have just been described. This list is largely composed of bridge health monitoring systems, because those were the types of installations that were the most prominent in the literature, but also include systems that have been implemented on several buildings and have even been designed to monitor wind turbine rotor blades.

Table 3.1 Health monitoring systems found installed in the literature with the type and number of sensors installed

Structure	Percent 'traditional' sensors	Displacement	Strain	Acceleration	Wind speed	Temperature
Vanke Center (Teng *et al.*, 2011)	43%	0	154	14	0	0
Shenzhen Bay Stadium (Teng *et al.*, 2011)	95%	0	108	8	2	102
24-story steel frame building (Celebi *et al.*, 2004)	100%	0	0	30	0	0
UCLA Louis Factor Building (Skolnik *et al.*, 2006)	100%	0	0	72	0	0
Humber Bridge (Brownjohn, 2007)	59%	6	0	16	13	2
Samcheonpo Bridge (Koh *et al.*, 2009)	77%	4	0	44	2	5
Sunrise Bridge (Catbas *et al.*, 2010)	83%	0	94	40	0	0
Namhae Bridge (Koh *et al.*, 2009)	87%	4	54	18	2	0
Stonecutters Bridge (Wong and Ni, 2009)	89%	34	836	58	24	388
Tsing Ma Bridge (Wong and Ni, 2009)	91%	2	110	19	6	115
Shenzhen Western Corridor (Wong and Ni, 2009)	92%	4	212	44	8	118
Seohae Bridge (Koh *et al.*, 2009)	94%	10	94	36	2	14
Yongjong Bridge (Koh *et al.*, 2009)	94%	4	297	52	4	33

(*Continued*)

Table 3.1 Continued

Structure	Percent 'traditional' sensors	Displacement	Strain	Acceleration	Wind speed	Temperature
Gwangan Bridge (Koh *et al.*, 2009)	95%	5	4	20	4	70
Øresund Bridge (Peeters, 2009)	96%	0	19	66	2	14
Kap Shui Mun Bridge (Wong and Ni, 2009)	96%	2	30	3	2	224
Little Mystic Span of Tobin Memorial Bridge (Brenner *et al.*, 2010)	97%	0	96	6	1	6
Ting Kau Bridge (Wong and Ni, 2009)	97%	2	88	45	7	83
Fairview Road On-Ramp Overcrossing (Fen *et al.*, 2006)	98%	1	19	21	0	3
Kings Stormwater Channel Bridge (Guan *et al.*, 2006)	99%	4	20	63	0	1
Jamboree Road Bridge (Fen *et al.*, 2006)	100%	1	0	14	0	0
Neka Railway Bridge (Ataei *et al.*, 2005)	100%	20	42	27	0	0
New Cape Girardeau Bridge (Celebi, 2006)	100%	0	0	84	0	0
CX-100 SMART Rotor (Adams *et al.*, 2011, Berg *et al.*, 2011)	48%	0	21	24	0	0

Note: The total percent of installed sensors that have been deemed 'traditional' is listed in the second column while the remaining columns have the number of traditional sensors of each type that were installed on each structure.

3.3 Associated algorithms

Despite the widespread use of the above sensors as part of health monitoring systems, none of those sensors, or any other sensor for that matter, can directly measure damage (Worden *et al.*, 2007). Instead, these sensors measure the response of the structure to its operational and environmental input and then the health of the structure must then be inferred using a damage feature that is obtained from the acquired data. Each sensor type, however, has specific characteristics that can lend itself to a specific type of data feature or damage identification algorithm. Therefore, this portion of this chapter briefly describes how each of the traditional types of sensors can be utilized as part of a health monitoring system and what unique capabilities they lend to the performance of the system. Because of their extensive use in damage identification methodologies, algorithms created primarily for acceleration measurements will be described in greater detail than those for other sensing modalities. Emphasis is placed on identifying the underlying commonalities of the algorithms and data source from which each of the damage features were obtained.

3.3.1 Displacement sensors

Displacement sensors are most commonly utilized to monitor large bulk changes in a structure and, therefore, have typically been used as part of straightforward algorithms to assist in monitoring the health of the structure. For instance, in a bridge they may be used to measure the maximum deflection at certain spans (Guan *et al.*, 2007), and then simple level crossing or peak holding methodologies can be used to detect anomalous events. Similar measurements of peak displacements can also be useful for monitoring inter-story drift in buildings during earthquakes, but are difficult to make in real-world structures where long distances must be spanned and there are numerous partition walls (Skolnik *et al.*, 2008). While this is a measurement of the transient geometry of the structure, displacement sensors are also commonly used to monitor the geometry of the structure due to changes that occur over longer time scales, such as those due to temperature and material creep (Wong and Ni, 2009).

Another way in which displacement sensors have been used is to directly monitor cracks and crack opening displacements (Issa *et al.*, 2005). Because of the long-term stability of most displacement sensors such as LVDTs and potentiometers, crack opening displacements can be measured directly to determine the long-term degradation of the structure (Lovejoy, 2007). Furthermore, because these measurements are relatively insensitive to temperature changes, they can be used in conjunction with temperature measurements to differentiate crack opening displacements due to temperature changes from those due to operational loading such as traffic on a bridge (Wang, 2009). The relative stability of these measurements also allows them to be used on large civil structures to estimate average moduli, which may then be tracked using more statistically rigorous methods such as bootstrapping to identify significant changes in the structure (Lloyd *et al.*, 2003).

3.3.2 Strain gages

Strain gages have received fairly broad attention because they are relatively inexpensive and can provide good engineering insight into the local behavior of the structure (Yu and Ou, 2006). This is one reason why they have been used widely to monitor fatigue in fixed-wing aircraft. In this application, strain gages are commonly used to measure fatigue critical loads due to external forces like gust and buffeting as well as abrupt maneuvers. However, in order to fully utilize these measurements, because the strain gages are so highly influenced by the local behavior of the structure, their location must be chosen carefully to either monitor hot spots where damage is likely to occur or to monitor the dominant fatigue loads acting on the structure (Buderath, 2009). The same need to place strain gages in critical locations is also present in civil structures to ensure that the measurements can be used effectively in algorithms such as strain-based mode-shape algorithms (Kiremidjian *et al.*, 1997). In addition to damage identification methodologies derived from dynamic strain measurements such as those mentioned above, a damage identification methodology has recently been developed by Jang *et al.* (2008), who utilized static strain measurements to detect and locate damage on a simple truss system even when the strain in the damage truss member was not directly measured.

Strain gages may be most useful for the monitoring of loads in a component or substructure, particularly when that structure has well defined load paths that can be directly measured using a relatively small number of sensors. One example of this in the aerospace industry is monitoring of landing gear loads and fatigue using strain gages mounted on the gear that can be used to infer the ground loads imparted on the gear (Schmidt and Sartor, 2009). The operational environment of prestressed concrete pressure vessels that are used in nuclear power plants is also evaluated using vibrating-wire strain gages in conjunction with thermocouples to ensure that the operating conditions are within safe ranges and the plant is functioning as expected (Smith, 1996). Therefore, while strain gages are usually not used in order to monitor entire civil structures, they can be successfully utilized as part of a full monitoring system because of the physical insight they provide into loads in specific components.

3.3.3 Accelerometers

Accelerometers have been the most widely used type of sensor for damage identification and health monitoring algorithms because of their ease of use, robustness, relatively low cost, and ability to detect changes in both local and global properties. This widespread use is due in part to their ability to measure relatively small motions over a wide frequency band. Good broadband performance is important in health monitoring because, in general, low-frequency responses are more global in nature while high frequency responses contain more localized information about the structure and may, therefore, be more sensitive to damage (Friswell, 2007). Furthermore, accelerometers are generally robust, easy to install, and relatively inexpensive. This combination of factors has led to the development of an extremely wide variety of different algorithms that utilize acceleration measurements to monitor the health of structures.

A summary of a small subset of these methods that were found in the literature and showed promising results on an experimental structure are listed in Table 3.2. Also listed in that table is the main data source from which each method's damage feature and the level of damage identification that it provided was calculated. The level of damage identification provided by the algorithm refers to the levels of (1) determination that damage is present, (2) determination of the geometric location of the damage, and (3) quantification of the severity of the damage (Rytter, 1993). If the reader would like a more in-depth description of health monitoring algorithms, there are several excellent reviews in that area including articles by Doebling and Farrar (1998), Carden and Fanning (2004), Montalvao *et al.* (2006), and Fan and Qiao (2011).

Changes in modal parameters

One of the most commonly used ways in which accelerometers have been used in an attempt to monitor civil infrastructure for damage is through the calculation of modal parameters including natural frequencies and mode shapes, despite the general lack of sensitivity that modal parameters have shown to localized structural damage. However, this approach has been commonly used because it is a convenient data reduction technique (Farrar and Doebling, 1997) that is familiar to most researchers and is clearly tied back to the physics of the structure (Carden and Fanning, 2004).

The first form of a modal-based health monitoring method that drew significant attention was the detection of damage through changes in natural frequencies. A review on this method was published by Salawu (1997) that documented over 60 instances of its use. One such use was the detection of the decrease in the natural frequencies of a multi-pile offshore platform

Table 3.2 Accelerometer based damage identification algorithms, the intrinsic damage feature they utilize, the structure on which they were demonstrated, and the level of damage identification that they provide

Method	Damage feature source	Structure investigated	Level 1: detection	Level 2: location	Level 3: quantification
Decreased natural frequencies (Brinker *et al.*, 1995)	Natural frequencies	Multi-pile offshore platform	X		
Compensated changes in natural frequency (De Roeck *et al.*, 2000)	Natural frequencies	Z24 Bridge	X		
Changes in modal curvature (Abdel Wahab and De Roeck, 1999) (Gul, 2009)	Mode shapes	Z24 Bridge	X	X	
Modal strain energy method (Farrar and Doebling, 1999)	Mode shapes	I-40 Rio Grande Bridge	X	X	
Transfer function pole migration (Lynch, 2005)[a] (Swarts and Lynch, 2008)[b]	Modal properties	IASC-ASCE experimental Benchmark[a], Z24 Bridge[b]	X		
Minimum rank model updating (Doebling, 1996)	Modal properties	NASA 8-Bay cantilevered truss	X	X	
Bayesian FE model updating (Ching and Beck, 2004)[a] (Skolnik *et al.*, 2006)[b]	Modal properties	IASC-ASCE experimental Benchmark[a], UCLA factor building[b]	X	X	X
Direct stiffness calculation (Maeck and De Roeck, 2003)	Modal Properties	Z24 Bridge	X	X	X
FE model updating (Teughels and De Roeck, 2004)	Modal Properties	Z24 Bridge	X	X	X
Damage locating vector (Gao *et al.*, 2004)	Modal properties	Experimental small-scale truss	X	X	

Operating shape local curvature (Sampai *et al.*, 1999)	FRFs	Experimental bridge structure	X	X	
Interpolation damage detection method (Limongelli, 2010)	FRFs	I-40 Rio Grande Bridge	X	X	
FRF PCA for neural networks (Ni *et al.*, 2006)	FRFs	Scale building model	X	X	
Linear and nonlinear frequency domain ARX models (Adams and Farrar, 2002)	Frequency domain input–output models	Unistrut frame structure	X		X
Transmissibility functions (Johnson *et al.*, 2004)	FRFs	Unistrut frame structure, rotorcraft fuselage	X	X	
Embedded sensitivity functions (Yang *et al.*, 2008)	FRFs	Metallic composite panel	X	X	X
Two-tier AR and ARX models (Lu *et al.*, 2008)	Response time histories	Two-story RC frame structure	X		
ARX model parameters (Gul and Catbas, 2011)	Response time histories	Z24 Bridge	X	X	X
Optimized neural-wavelets (Taha, 2010)	Response time histories	IASC-ASCE experimental Benchmark	X		X

Note: The superscript letters denote which reference refers to which structure.

FRF: frequency response function; RC: reinforced concrete.

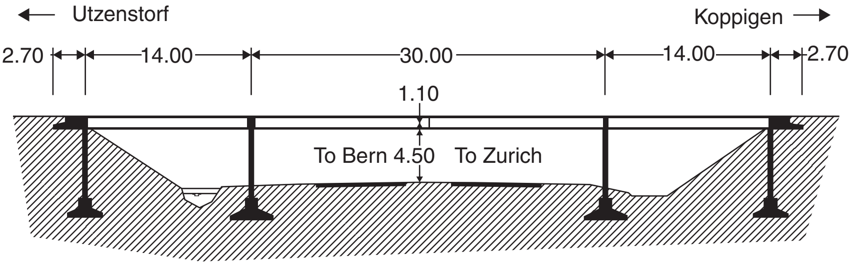

3.3 Schematic of the Z24 Bridge with distances listed in meters (Reynders and De Roeck, 2009). Data from the bridge while it was progressively damaged has been used by many researchers to demonstrate different health monitoring algorithms. (*Source*: Reproduced by permission of Wiley.)

throughout a year of operation (Brinker *et al.*, 1995) that may have been caused by an accumulation of damage. However, recent research has suggested that the detection of damage in realistic structures in the field using frequency shifts is difficult, in part because of variations in the natural frequencies caused by environmental factors (Carden and Fanning, 2004). One way in which this problem can be addressed is by measuring and modeling the influence of these external parameters on the natural frequencies of the structure. For example, De Roeck *et al.* (2000) utilized an auto-regressive, exogenous input (ARX) model to account for the influence of temperature on the Z24 Bridge (Fig. 3.3). This model successfully helped to distinguish between damage- and temperature-induced variations in the natural frequencies of the structure.

Another methodology that has been utilized to monitor structures for damage focuses on changes in the mode shape of the structure. One reason why several researchers have moved to detecting changes in mode shapes rather than natural frequencies is because mode shapes are less sensitive to global temperature changes than natural frequencies (Farrar and James, 1997), although temperature gradients in the structure can still distort the mode shape. Abdel Wahab and De Roeck (1999) applied a modal curvature-based methodology to the data from the Z24 Bridge and found that, by calculating the difference in curvature across multiple modes, they were able to detect and locate the damage. Farrar and Doebling (1999) utilized the mode shapes from an I-40 bridge over the Rio Grande to detect and locate damage using the Damage Index Method developed by Stubbs *et al.* (1995). This method is based on the detection of changes in the strain energy of the mode shape before and after damage.

One health monitoring technique that utilizes multiple modal parameters was developed by Lynch (2005) and tracks transfer function poles in the complex plane to detect damage. The poles of the transfer function are a combination of the natural frequencies and modal damping values of the structure. Damage in the IASC-ASCE experimental benchmark data was detected by the changes in the poles of the system in five different damaged conditions (Lynch, 2005). Swartz and Lynch (2008) extended this method by creating an algorithm to compare the poles with the appropriate baseline condition and then calculate damage based on the system's pole locations. The methodology allows for local processing on a distributed network of sensors and was able to detect most of the progressive damage tests that were performed on the Z24 Bridge (Swartz and Lynch, 2008).

Algorithms for both detecting and locating damage have also been developed that utilize both natural frequencies and mode shapes. Many of these algorithms utilize experimental measurements along with finite element models of the structure to detect, locate, and possibly even quantify the level of damage. Doebling (1996) utilized modal properties along with an optimal updating methodology to identify and locate damage in a small-scale cantilevered truss. Ching and Beck (2004) developed a Bayesian finite element model updating methodology that they applied to the IASC-ASCE experimental benchmark data to identify damage. This methodology was also applied by Skolnik *et al.* (2006) to a 15-story building on the University of California Los Angeles' campus. In this case, because the structure could not be damaged, the methodology was demonstrated by updating a model that was used to assess the likelihood of damage from an earthquake. Lastly, Teughels and De Roeck (2004) used finite element model updating using data from the Z24 Bridge tests and quantified the decrease in bending and torsional stiffness along the length of the bridge in several cases.

Another methodology that uses both mode shape and natural frequency information, but not a finite element model, was developed by Gao *et al.* (2004) who utilized mode shape and natural frequency estimates from a 4.5 m long 3-D truss structure to detect, locate, and quantify the loss in stiffness in an element of the truss using the Damage Locating Vector method. This methodology was developed by Bernal (2002) and it utilizes the modal properties of the structure before and after damage to calculate the flexibility matrix at the sensor locations. Then, using these flexibility matrices, the method calculates a static load vector that when applied to the structure induces no stress in the damaged components. The developed methodology was also applied to another slightly larger truss structure to demonstrate that the methodology could be used to detect multiple damaged elements simultaneously (Tran *et al.*, 2008). Another damage detection methodology that utilized changes in both natural frequencies and mode shapes to detect, locate, and quantify damage is the Direct Stiffness Calculation method, which was used by Maeck and De Roeck (2003) to calculate the loss in stiffness along the length of the Z24 Bridge due to progressively induced damage. This methodology is applicable to beamlike structures and is based on the relation between the bending and torsional stiffness in each section. It is interesting to note that for several of the damage states, the loss in bending stiffness calculated by this method compared well to the values calculated using finite element model updating (Reynders and De Roeck, 2009).

Changes in input–output models

Perhaps the most commonly used system level model of the input–output behavior of a structure is the frequency response function (FRF). In order to use FRFs for health monitoring purposes, they usually need to be reduced to a damage feature of smaller dimensionality. However, modal parameters are not the only method that can be used for data reduction purposes on FRFs. Ni *et al*. (2006) applied principal component analysis to FRFs and used the resulting data as an input to a neural network in order to detect damage in a 1/20 scale building. Rather than using FRFs directly, Adams and Farrar (2002) utilized linear and nonlinear frequency domain ARX models to characterize the input–output behavior of a possibly nonlinear structure and demonstrated that such a model could successfully detect and quantify the presence of loose bolts in a three-story unistrut frame building.

In a manner similar to how mode shapes were used to detect and locate damage, spatial variations in FRFs have also been used for health monitoring purposes. For instance, Sampaio *et al*. (1999) used changes in the spatial variations of FRFs to detect damage. At each measurement location the local curvature of the operational deflection shapes at a specific frequency was calculated and changes in these values allowed for the detection and localization of damage in a bridge. Another method that utilizes the spatial variations in FRFs is the interpolation damage detection method, which was used by Limongelli (2010) to detect damage on the I-40 Rio Grande Bridge despite the presence of temperature variations. This method assumes that damage introduces a discontinuity in the deformation shape of the structure and detects this discontinuity by comparing each experimentally measured FRF to the FRF that is interpolated at that location by spline fitting the remaining FRFs.

FRFs may also be transformed in order to create functions that can be utilized more directly for damage detection purposes. Transmissibility functions were demonstrated to be valuable for the detection and localization of damage in a three-story unistrut frame structure (Johnson *et al*., 2004) because they are functions of the transfer function zeros, which are more sensitive to local changes of the structure than poles (Johnson, 2002). Another transformation of FRFs that has been utilized to aid in health monitoring is the calculation of embedded sensitivity functions. These functions use the assumption that physical properties are lumped at certain degrees of freedom (DOF) to calculate partial derivatives with respect to lumped stiffness and mass properties (Yang *et al.*, 2004). Using this methodology, changes in the mass and stiffness of a metallic composite panel on standoffs was detected, located, and quantified in terms of stiffness and mass changes (Yang *et al.*, 2008).

Changes in time response based models

The last set of health monitoring algorithms considered here are typically computed from the error in time series models or from transformed versions of the acceleration measurements themselves. For instance, Lu *et al.* (2008) utilized a database of auto-regressive models for data-normalization purposes so that the parameters from ARX models could be compared more directly to one another for each sensor. This methodology was able to successfully detect changes due to high-level shake table excitations of a two-story RC frame structure using a wireless sensing system (Lu *et al.*, 2008). Gul and Catbas (2011) utilized ARX models to predict the output of one sensor using a cluster of other sensors. The model was trained on the baseline data set. By tracking the changes in the prediction error in the models, the presence, location, and some comparative information about the magnitude of the damage on the Z24 Bridge was obtained (Gul and Catbas, 2011). Another time series methodology was developed by Taha (2010) and applied to the IASC-ASCE experimental benchmark. This method utilized the wavelet transform for data reduction purposes and an optimized neural network for the detection and quantification of damage. However, this methodology did not detect the specific location of the damage, and, therefore, the quantification corresponded only to a description of the severity of the damage and no estimates of the size or type of damage could be made.

3.3.4 Environmental measurements

Environmental measurements are not typically used for health monitoring of a structure directly, but recent experience has shown that they are an important part of any health monitoring system because environmental changes can have a large influence on the behavior of the structure being monitored. This is a vast and quickly expanding area of research and only a brief overview of some methodologies is given here. The interested reader is encouraged to read Sohn's (2007) excellent review on the topic for more information.

One example of the use of temperature measurements for compensating for environmental changes was already described in which De Roeck *et al.* (2000) utilized an ARX model to eliminate temperature effects from the changes in the natural frequencies of the Z24 Bridge so that the effects of damage could be detected. Sohn *et al.* (1999) took a similar approach to the problem by using a linear model to predict changes in both the first and second natural frequencies of the I-40 Rio Grande Bridge. Temperature compensation methods also apply principal component analysis to vibration features such as natural frequencies directly (Yan *et al.*, 2005a) or after they have been clustered (Yan *et al.*, 2005b). Both of these methods showed promise in compensating for the temperature variations observed on the Z24 Bridge.

3.4 Examples of continuous monitoring systems

In large part because of the decreasing costs, increasing reliability, and advanced algorithms designed for many of the aforementioned sensing technologies, continuous health monitoring systems have begun to be developed and deployed for civil infrastructure. One example of such a system for a building has been implemented on the Burj Khalifa Tower in Dubai, which is the tallest manmade structure in the world (Abdelrazaq, 2012). This system utilizes the building's existing network for the transmission of data and monitors the structure using modal properties estimated using time, frequency, or time–frequency techniques (Kwon *et al.*, 2010). A system has also been deployed on the Guangzhou New TV Tower and has recorded the building's vibrations during several types of dynamic events such as earthquakes and typhoons (Ni, 2010).

However, the preponderance of vibration monitoring systems that have currently been deployed is on bridges, not buildings (Brownjohn *et al.*, 2011). One example of such a system is the Stonecutters Bridge in Hong Kong (Wong, 2010), which has over 1500 sensors on it. As was shown in Table 3.1, 388 of these sensors were temperature measurements. One reason for this large number of temperature measurements is that they can be used as part of correlation models to help account for changes in the modal frequencies of the bridge due to changes in the environment (Ni, 2010). However, the majority of the sensors on the Stonecutters Bridge are strain sensors. The large number of strain sensors was likely influenced by the successful use of strain sensors on the Tsing Ma Bridge to monitor the performance of the bridge deck under operational loading, detect the presence of local damage using a strain energy formulation, and assess the fatigue life of the bridge using the daily stress spectra and modeled stress concentration factors (Ni, 2010).

Several other noteworthy examples of continuous monitoring systems include the Øresund Bridge and the Bill Emerson Memorial Bridge. While the Øresund Bridge monitoring system has a variety of sensors installed (see Table 3.1), many of the monitoring methodologies rely on accelerometer readings to monitor key aspects of the bridge's performance. For instance, the accelerometer readings are utilized for the operational modal analysis of the bridge including its deck, towers, and cables (Peeters *et al.*, 2003). If the influence of environmental variations on the modal parameters of the bridge are properly accounted for, changes in the bridge's modes of vibration that are dominated by the motion of the deck and tower can be used to monitor the overall health of the bridge while cable modes can be used to monitor the tension in any supporting cables (Peeters et al., 2003). The Bill Emerson Memorial Bridge also relies on accelerometers in its monitoring system (Celebi, 2006). This monitoring system has been utilized to assess the performance of the bridge against design parameters and has been utilized to analyze the response of the bridge to several earthquakes (Celebi, 2006).

Despite these examples of deployed health monitoring systems, the industry has still been relatively resistant to the deployment of health monitoring systems and new technologies (Brownjohn *et al.*, 2011). While there are many reasons for this slow transition from research to practice, one reason for this is that these systems are currently relatively expensive to install and deploy. For example, the system on the Bill Emerson Memorial Bridge reportedly cost approximately $1.3 million dollars or over $15 000 per channel (Spencer *et al.*, 2011). As advances continue to be made in both traditional and novel sensor technologies and data acquisition systems, these costs will be reduced and continuous monitoring systems for civil infrastructure will likely become far more prevalent.

3.5 Conclusions and future trends

Despite the fact that the majority of literature on structural health monitoring may focus on new and novel sensors and algorithms, traditional sensors and their associated algorithms continue to play a major role in the transition of health monitoring systems from the laboratory to the field. While one significant reason for this trend may be the practitioner's previous experience with these sensing technologies, these sensors have also demonstrated that they are relatively inexpensive, robust, and complement each other well. For instance, displacement and strain gages are well suited for monitoring local phenomena for specific types of damage such as crack opening displacements or loads in specific components. Accelerometer measurements, on the other hand, contain significant global information as well and have had a plethora of different algorithms developed for them to use this information to detect, locate, and even quantify damage that may be a considerable distance from the sensors. While the number of different algorithms is large, the algorithms are formulated around several different sets of damage features, which are intrinsically linked back to the structure's dynamic response. Because a structure's response is influenced by external factors other than damage, however, environmental measurements are a necessary part of almost any health monitoring system. These environmental measurements can then be used, along with physical or statistical models, to compensate for their influence on the structure's dynamics so that the changes due to damage can be reliably detected.

As health monitoring technology continues to progress and begins to become an accepted part of new structural designs, there are several trends that are likely to continue to gain prominence. One such trend is that as sensing technologies continue to mature and become less expensive, there will likely be even higher sensor densities on large civil structures. This will not only involve the sensing elements but also wireless sensing modules and the requisite distributed data acquisition and analysis architecture. As more sensors are placed on the structure, algorithms and methodologies that utilize sensor fusion techniques to synthesize health indicators from multiple measurement modalities will become an essential part of health monitoring systems. For instance, temperature measurements are already being used in concert with vibration measurements to account for environmental changes, but the simultaneous use of strain, vibration, and displacement measurements for increased sensitivity and robustness to the authors' knowledge has not yet been fully implemented. This type of data synthesis will become more important as new sensing technologies emerge, and is just one example of how algorithms will likely evolve and help drive advances in health monitoring. Regardless of the new algorithms or sensors that are developed, because of their long history and well-established use in health monitoring, it will likely be a long time before traditional sensors are no longer an integral part of long-term health monitoring systems.

3.6 References

Abdel Wahab M M and De Roeck G (1999), 'Damage detection in bridges using modal curvatures: application to a real damage scenario', *J. Sound Vib.*, **226**(2), 217–235.

Abdelrazaq A (2012), 'Validating the structural behavior and response of Burj Khalifa: synopsis of the full scale structural health monitoring programs', *Int. J. High-Rise Build.*, **1**(1), 37–51.

Adams D E (2007), '*Health Monitoring of Structural Materials and Components: Methods with Applications*', England, John Wiley & Sons Ltd.

Adams D E and Farrar C R (2002), 'Classifying linear and nonlinear damage using frequency domain ARX models', *Struct. Health Monit.*, **1**(2), 185–201.

Adams D E, White J, Rumsey M and Farrar C R (2011), 'Structural health monitoring of wind turbines: method and application to a HAWT', *Wind Energy*, **14**(4), 603–623.

Alampalli S (1998), 'Influence of in-service environment on modal parameters', *Proc. IMAC*, **16**, 111–116.

Ataei S, Aghakouchak A A, Marefat M S and Mohammadzadeh S (2005), 'Sensor fusion of a railway bridge load test using neural networks', *Expert Syst. Appl.*, **29**, 678–683.

Berg D, Berg J, Wilson D, White J, Resor B and Rumsey M (2011), 'Design, fabrication, assembly and initial testing of a SMART rotor', *Proceedings of the 29th ASME Wind Energy Symposium*, Orlando, Florida, USA.

Bernal D (2002), 'Load vectors for damage localization', *J. Eng. Mech.-ASCE*, **128**(1), 7–14.

Billah K Y and Scanlan R H (1991), 'Resonance, Tacoma Narrows bridge failure, and undergraduate physics textbooks', *Am. J. Phys.*, **59**(2), 118–124.

Boyes W (2010), *Instrumentation Reference Book*, Boston, Elsevier.

Brenner B, Bell E S, Sanayei M, Pheifer E and Durack W (2010), 'Structural modeling, instrumentation, and load testing of the Tobin Memorial bridge in Boston, Massachusetts', *Proceedings of Structures Congress 2010*, 729–740.

Brinker R, Kirkegaard P H, Andersen P and Martinez M E (1995), 'Damage detection in an offshore structure', *Proc. SPIE*, **2460**(2), 661–667.

Brownjohn J M W (2007), 'Structural health monitoring of civil infrastructure', *Phil. Trans. R. Soc. A*, **365**(1925), 589–622.

Brownjohn J M W, De Stefano A, Xu Y L, Wenzel H and Aktan A E (2011), 'Vibration-based monitoring of civil infrastructure: challenges and successes', *J. Civil Struct. Health Monit.*, **1**(3–4), 79–95.

Buderath M (2009), 'Fatigue monitoring in military fixed-wing aircraft', in Boller C, Chang F K, and Fujino Y, *Encyclopedia of Structural Health Monitoring*, Chichester, Wiley.

Carden E P and Fanning P (2004), 'Vibration based condition monitoring: a review', *Struct. Health Monit.*, **3**(4), 355–378.

Catbas F N, Gul M, Zaurin R, Gokce H B, Terrell T, Dumlupinar T and Maier D (2010). Long term bridge maintenance monitoring demonstration on a movable bridge: A framework for structural health monitoring of movable bridges, Florida Department of Transportation, Final Report BDK78 977-07.

Celebi M (2006), 'Real-time seismic monitoring of the New Cape Girardeau Bridge and preliminary analyses of recorded data: an overview', *Earthq. Spectra*, **22**(3), 609–630.

Celebi M, Sanli A, Sinclair M, Gallant S and Radulescu D (2004), 'Real-time seismic monitoring needs of building owner and the solution: a cooperative effort', *Earthq. Spectra*, **20**(2), 333–346.

Ching J and Beck J L (2004), 'Bayesian analysis of the phase II IASC-ASCE structural health monitoring experimental benchmark data', *J. Eng. Mech.*, **130**(10), 1233–1244.

De Roeck G, Peeters B and Maeck J, (2000), 'Dynamic monitoring of civil engineering structures', in *Computation Methods for Shell and Spatial Structural IASS-IACM* Crete, Greece.

Doebling S W and Farrar C R (1998), 'A summary review of vibration-based damage identification methods', *Shock Vib. Dig.*, **30**(2), 91–105.

Fan W and Qiao P (2011), 'Vibration-based damage identification methods: a review and comparative study', *Struct. Health Monit.*, **10**(1), 83–111.

Farrar C R and Doebling S W (1997), 'An overview of modal-based damage identification methods, in *Proceedings of the DAMAS Conference*, Sheffield, UK.

Farrar C R and Doebling S W (1999), ‘Damage detection II: field applications to large structures’, in Silva J M M and Maia N M M, *Modal Analysis and Testing*, Dordrecht, Kluwer Academic Publishers.

Farrar C R, Doebling S W, Cornwell P J and Straser E G (1997), ‘Variability of modal parameters measured on the Alamosa Canyon bridge’, *Proc. SPIE*, **3089**, 257–263.

Farrar C R and James G H (1997), ‘System identification from ambient vibration measurements on a bridge’, *J. Sound Vib.*, **205**(1), 1–18.

Farrar C R and Worden K (2007), ‘An introduction to structural health monitoring’, *Phil. Trans. R. Soc. A*, **365**(1851), 303–315.

Feng M Q, Fukuda Y, Chen Y, Soyoz S and Lee S (2006), ‘Long-term structural performance monitoring of bridges phase II: development of baseline model and methodology for health monitoring and damage assessment’, *California Department of Transportation*.

Fraden J (2010), *Handbook of Modern Sensors: Physics, Designs, and Applications*, New York, Springer.

Friswell M I (2007), ‘Damage identification using inverse methods’, *Phil. Trans. R. Soc. A*, **365**(1855), 393–410.

Gao Y, Spencer B F and Bernal D (2004), ‘Experimental verification of the damage locating vector method’, *Proceedings of the 1st International Workshop on Advanced Smart Materials and Smart Structures Technology*, Honolulu, Hawaii, 12–14 January.

Guan H, Karbhari V M and Sikorsky C S (2006), ‘Web-based structural health monitoring of an FRP composite bridge’, *Comput.-Aided Civ Infrastruct. Eng.*, **21**, 39–56.

Guan H, Karbhari V M and Sikorsky C S (2007), ‘Long-term structural health monitoring system for a FRP composite highway bridge structure’, *J. Intel. Mat. Syst. Str.*, **18**(8), 809–823.

Gul M and Catbas F N (2011), ‘Damage assessment with ambient vibration data using a novel time series analysis methodology’, *J. Struct. Eng.-ASCE*, **137**(12), 1518–1526.

Issa M A, Shabila H I and Alhassan M (2005), ‘Structural health monitoring systems for bridge decks and rehabilitated precast prestress concrete beams’, in Ansari F *Sensing Issues in Civil Structural Health Monitoring*, Dordrecht, Springer.

Jang S A, Sim S H and Spencer B F (2008), ‘Structural damage detection using static strain data’, in Spencer B F, Tomizuka M, Yun C B, Chen W M, and Chen R W, *Proceedings of the World Forum on Smart Materials and Smart Structures Technology*, London, Taylor & Francis Group.

Johnson T J (2002), ‘Analysis of dynamic transmissibility as a feature for structural damage detection’, Masters’ Thesis, Purdue University, Lafayette, Indiana, United States.

Johnson T J, Brown R L, Adams D E and Schiefer M (2004), ‘Distributed structural health monitoring with a smart sensor array’, *Mech. Syst. Signal Pr.*, **18**(3), 555–572.

Kiremidjian A S, Straser E G, Meng T, Law K and Soon H (1997), ‘Structural damage monitoring for civil structures’, *Proceedings of the International Workshop on Structural Health Monitoring*, Stanford, California, 18–20 September, 371–382.

Koh H M, Lee H S, Kim S and Choo J F (2009), 'Monitoring of bridges in Korea', in Boller C, Chang F K and Fujino Y, *Encyclopedia of Structural Health Monitoring*, Chichester, Wiley.

Kwon D, Kijewski-Correa T and Kareem A (2010), 'SmartSync: an integrated real-time monitoring and SI system for tall buildings', *2010 Structures Congress*, 3176–3185.

Lei Y, Kiremidjian A S, Nair K K, Lynch J P, Law K H, Kenny T W, Carryer E and Kottapalli A (2003), 'Statistical damage detection using time series analysis on a structural health monitoring benchmark problem', *Proceedings of the 9th International Conference on Applications of Statistics and Probability in Civil Engineering*, San Francisco, CA, 6–9 July.

Limongelli M P (2010), 'Frequency response function interpolation for damage detection under changing environment', *Mech. Syst. Sig. Process.*, **24**(8), 2898–2913.

Lloyd G M, Wang M L, Wang X and Halvonik J (2003), 'Bootstrap analysis of long-term global and local deformation measurements of the Kishwaukee bridge', *Proceedings of the 4th International Workshop on Structural Health Monitoring*, Stanford, California, 15–17 September, 163–171.

Lovejoy S (2007), 'Applications of structural health monitoring to highway bridges', *Western Bridge Engineers' Seminar 2007*.

Lu K C, Loh C H, Yang Y S, Lynch J P and Law K H (2008), 'Real-time structural damage detection using wireless sensing and monitoring system', *Smart Struct. Syst.,* **4**(6), 759–778.

Lynch J P (2005), 'Damage characterization of the IASC-ASCE structural health monitoring benchmark structure by transfer function pole migration', *Proceedings of the 2005 ASCE Structures Congress.*

Maeck J and De Roeck G (2003), 'Damage assessment using vibration analysis on the Z24-bridge', *Mech. Syst. Sig. Process.*, **17**(1), 133–142.

Montalvao D, Maia N M M and Ribeiro A M R (2006), 'A review of vibration-based structural health monitoring with special emphasis on composite materials', *Shock Vib. Dig.*, **38**(4), 295–324.

Newman E S (2010), 'Piezoelectric accelerometers in structural health monitoring', University of Massachusetts Lowell, United States.

Ni Y Q (2010), 'Structural health monitoring for civil infrastructure systems: from research to application', *Proceedings of the Fifth European Workshop on Structural Health Monitoring*, Naples, Italy, 28 June–4 July, 6–17.

Ni Y Q, Zhou X T and Ko J M (2006), 'Experimental investigation of seismic damage identification using PCA compressed frequency response functions and neural networks', *J. Sound Vib.*, **270**(1–2), 1–14.

Peeters B, Couvreur G, Razinkov O, Kundig C, Van der Auweraer H and De Roeck G (2003), 'Continuous monitoring of the Øresund Bridge: system and data analysis', *Proceedings of the 21st International Modal Analysis Conference*, Kissimmee, Florida, February.

Peeters B (2009), 'Continuous Monitoring of the Øresund Bridge: data Acquisition and Operational Modal Analysis', in Boller C, Chang F K and Fujino Y, *Encyclopedia of Structural Health Monitoring*, Chichester, Wiley.

Reynders E and De Roeck G (2009), 'Continuous vibration monitoring and progressive damage testing on the Z24 bridge', in Boller C, Chang F K and Fujino Y, *Encyclopedia of Structural Health Monitoring*, Chichester, Wiley.

Rytter A (1993), 'Vibration based inspection of civil engineering structures', Ph.D. Dissertation, Aalborg University, Denmark.

Salawu O S (1997), 'Detection of structural damage through changes in frequency: a review', *Eng. Struct.*, **19**(9), 718–723.

Sampaio R P C, Maia N M M and Silva J M M (1999), 'Damage detection using the frequency-response-function curvature method', *J. Sound Vib.*, **226**, 1029–1042.

Schmidt R K and Sartor P (2009), 'Landing Gear', in Boller C, Chang F K, and Fujino Y, *Encyclopedia of Structural Health Monitoring*, Chichester, Wiley.

Skolnik D A, Ying L and Yu E and Wallace J W (2006), 'Identification, model updating, and response prediction of an instrumented 15-story steel frame building', *Earthq. Spectra*, **22**(3), 781–802.

Skolnik D A, Kaiser W J and Wallace J W (2008), 'Instrumentation for structural health monitoring: measuring interstory drift', *Proceedings of the 14th World Conference on Earthquake Engineering*, Beijing, China, 12–17 October, 1–7.

Smith L M (1996), 'In-service monitoring of nuclear-safety-related structures', *Struct. Eng.*, **74**(12), 210–211.

Sohn H, Dzwonczyk M, Straser E G, Kiremidjian A S, Law K H and Meng T (1999), 'An experimental study of temperature effect on modal parameters of the Alamosa canyon bridge', *Earthq. Eng. Struct.*, **28**(8), 879–897.

Spencer B F, Cho S and Sim S H (2011), 'Wireless monitoring of civil infrastructure comes of age', *Structure*, October 2011, 12–16.

Stubbs N., Kim J T and Farrar C R (1995), 'Field verification of a nondestructive damage localization and severity estimation algorithm', *Proceedings of the 13th International Modal Analysis Conference*, Nashville, Tennessee, 13–16 February.

Swartz R A and Lynch J P (2008), 'Damage characterization of the Z24 bridge by transfer function pole migration', *Proceedings of the 26th International Modal Analysis Conference*, Orlando, Florida, 4–7 February.

Taha, M M R (2010), 'A neural-wavelet technique for damage identification in the ASCE benchmark structure using phase II experimental data', *Adv. Civil Eng.*, **2010**(675927), 1–13.

Teng J, Xiao Y, Peng X, Yao S, Lu W and Li C (2011), 'Intelligent structural health monitoring system theory and engineering applications', *Proceedings of the 6th International Workshop on Advanced Smart Materials and Smart Structures Technology*, Dalian, China.

Tong W (2010), *Wind Power Generation and Wind Turbine Design*, Boston, WIT Press.

Tran V A, Duan W H and Quek S T (2008), 'Structural damage assessment using damage locating vector with limited sensors', *Proceedings of SPIE Sensors and Smart Structures Technologies for Civil, Mechanical, and Aerospace Systems*, **6932**(2), 1–11.

Wang M L (2009), 'Loads and temperature effects on a bridge', in Boller C, Chang F K and Fujino Y, *Encyclopedia of Structural Health Monitoring*, Chichester, Wiley.

Wong K Y (2010), 'Structural health monitoring and safety evaluation of Stonecutters Bridge under the in-service condition', *Proceedings of the Fifth International IABMAS Conference*, 521.

Wong K Y and Ni Y Q (2009), 'Modular architecture of SHM system for cable-supported bridges', in Boller C, Chang F K, and Fujino Y, *Encyclopedia of Structural Health Monitoring*, Chichester, Wiley.

Worden K, Farrar C R, Manson G and Park G, (2007), 'The fundamental axioms of structural health monitoring', *Proc. R. Soc. A*, **463**(2082), 1639–1664.

Yan A M, Kerschen G, De Boe P and Golinval J C (2005a), 'Structural damage diagnosis under varying environmental conditions – part I: a linear analysis', *Mech. Syst. Signal Pr.*, **19**(4), 847–864.

Yan A M, Kerschen G, De Boe P and Golinval J C (2005b), 'Structural damage diagnosis under varying environmental conditions – part II: local PCA for non-linear cases', *Mech. Syst. Signal Pr.*, **19**(4), 865–880.

Yang C, Adams D E, Yoo S W and Kim H J (2004), 'An embedded sensitivity approach for diagnosing system-level vibration problems', *J. Sound Vib.*, **269**(3–5), 1063–1081.

Yang C, Adams D E, Derriso M and Gordon G (2008), 'Structural damage identification in a mechanically attached metallic panel using embedded sensitivity functions', *J. Intel. Mat. Syst. Str.*, **19**(4), 475–485.

Yu Y and Ou J P (2006), 'Integration and tests of wireless strain sensor applied to structural local monitoring', in Ou J P, Li H, and Duan Z D, *Structural Health Monitoring and Intelligent Infrastructure, Vol **1***, London, Taylor & Francis Group.

4

Piezoelectric transducers for assessing and monitoring civil infrastructures

Y-K. AN, Southeast University, China, and M. K. KIM and
H. SOHN, Korea Advanced Institute of Science and Technology
(KAIST), Republic of Korea

DOI: 10.1533/9780857099136.86

Abstract: Piezoelectric transducers are being commonly used for sensing and actuation applications for smart structural systems. In particular, they are widely used for structural health monitoring (SHM) thanks to such attractive characteristics as multi-functionality, nonintrusivity, light weight, low cost, rapid response time, and high repeatability. This chapter first deals with the basic principles of piezoelectric transducers and the characteristics of piezoelectric materials. Subsequently, various piezoelectric transducer-based SHM methodologies including guided wave, impedance, and acoustic emission techniques are summarized. Then, their state-of-the-art applications to SHM fields are presented. Future trends are also discussed in this chapter.

Key words: piezoelectric transducers, structural health monitoring, guided wave, impedance, acoustic emission.

4.1 Introduction

This chapter deals with the characteristics of piezoelectric materials, the basic principles of the piezoelectric transducer, and its state-of-the-art applications. In particular, there is focus on applications of the piezoelectric transducers to SHM fields.

Over the last several decades, piezoelectric transducers have been widely used for sensing and actuation applications in smart structural systems, thanks to their versatility. The key characteristic of the piezoelectric transducer is piezoelectricity. When a piezoelectric material is squeezed or stretched, an electric charge is generated across the material, which is called ‘direct piezoelectricity.’ Conversely, a piezoelectric material mechanically deforms when subjected to electric voltage, which is called ‘converse piezoelectricity’(Cady, 1964).

The piezoelectricity phenomenon was first discovered by brothers, Pierre and Jacques Curie in 1880 (Curie and Curie, 1880). While

© 2014 Woodhead Publishing Limited

investigating the characteristics of a number of natural crystals, they realized that some materials, such as quartz and tourmaline, have an ability to transform energy of a mechanical input into an electrical output. This unique characteristic of the piezoelectric materials have been widely applied to various fields. In the early 1900s, several breakthroughs were made. In 1917, Langevin developed a piezoelectric transducer composed of a quartz and steel sandwich for ultrasonic generation (Jan *et al.*, 2010). In 1921, Cady proposed the piezoelectric resonator as an electrical oscillator to achieve frequency stability (Cady, 1922). This piezoelectric resonator made a great contribution in the field of broadcasting systems. Further applications of piezoelectric materials include watches, crystal and ceramic filters, underwater acoustic devices, and speakers (Jan *et al.*, 2010). In recent years, the application fields of piezoelectric transducers have been widened into SHM (Staszewski *et al.*, 2004a; Balageas *et al.*, 2006; Boller *et al.*, 2009).

4.2 Principle of piezoelectricity

This section first introduces the basic principles of piezoelectricity and piezoelectric materials.

4.2.1 Definition and categorization of piezoelectricity

Electric charge is created between two electrodes of piezoelectric materials when the materials are exposed to an external mechanical strain. On the other hand, when voltage is applied to the piezoelectric materials, it expands or contracts, creating mechanical strain. The former effect is called the direct piezoelectric effect, as shown in Fig. 4.1a, and the latter is the converse piezoelectric effect, as described in Fig. 4.1b. Based on these unique characteristics of piezoelectric materials, various types of actuators and sensors have been developed.

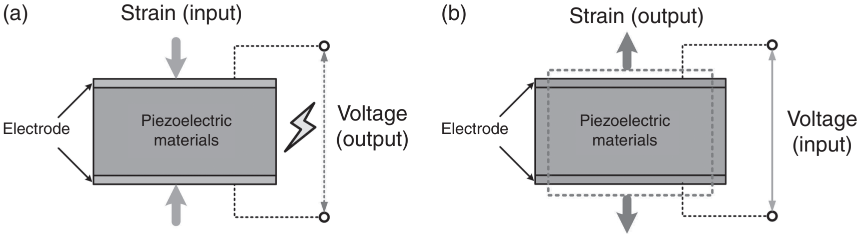

4.1 Piezoelectric effects: (a) direct piezoelectric effect and (b) converse piezoelectric effect.

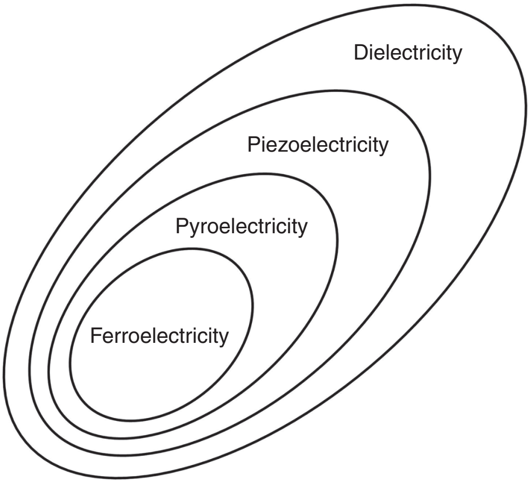

4.2 Categorization of piezoelectricity (Zhang *et al.*, 2009).

The piezoelectricity can be categorized as shown in Fig. 4.2 (Zhang *et al.*, 2009). Dielectricity is defined as the characteristic where dipoles within an insulated material can be polarized when an electric field is applied. The piezoelectricity as a subgroup of dielectricity is the material property where the polarization can be changed by mechanical perturbation. As a subgroup of piezoelectricity, the polarization of pyroelectric materials can be altered by temperature variation. Finally, ferroelectricity is the material characteristic in which spontaneous polarization can exist with zero electric field, once polarization is achieved by a sufficiently strong electric field (Damjanovic, 1998).

Although ferroelectricity is a subgroup of dielectricity, polarization behavior is different. Figure 4.3 conceptually compares the polarizations of dielectric and ferroelectric materials under a varying electric field. The polarization of the dielectric material shows a linear relationship with the electric field, as shown in Fig. 4.3a. Here, P and E denote the polarization and electric field, respectively. On the other hand, the ferroelectric materials show a hysteresis behavior under the changing electric field, as shown in Fig. 4.3b. The electric field is applied to the ferroelectric material until the maximum polarization (P_{max}) is achieved. Then, the material exhibits a remanent polarization (P_r) even when the electric field is removed. To eliminate P_r, a reverse electric field is applied in the opposite direction. This hysteresis nature of ferroelectric materials has been widely employed for nonvolatile memories (Bertotti and Mayergoyz, 2005). The information is stored when the polarization is in positive or negative remanent polarized state, and the stored information is kept before the reverse electric field is applied.

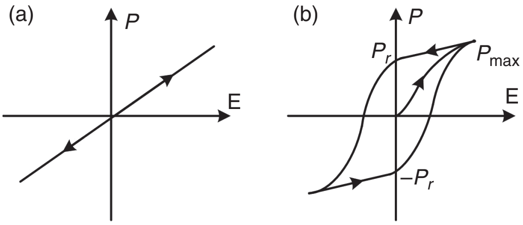

4.3 Comparison of the polarizations of dielectric and ferroelectric materials under a varying electric field: (a) dielectric polarization and (b) ferroelectric polarization (*P*, *E*, P_r, and P_{max} denote the polarization, electric field, remanent polarization, and maximum polarization, respectively). (*Source*: Reproduced from Jaffe, 1971.)

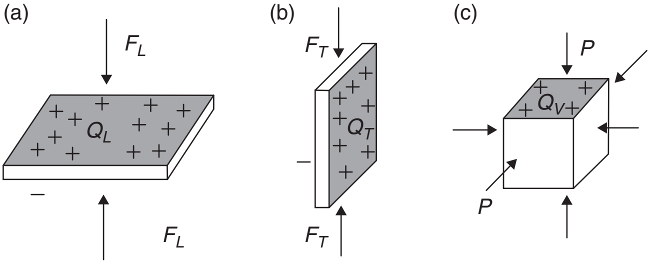

4.4 Operational principle of piezoelectric materials: (a) longitudinal effect, (b) transverse effect, and (c) volume effect. (*Source*: Reproduced from Jon, 2005.)

4.2.2 Operational principle of piezoelectric materials

The operational principle of piezoelectric materials depends on the direction of applied external loads to the piezoelectric materials. Figure 4.4 displays three different effects, i.e. longitudinal, transverse, and volume effects (Jon, 2005). For these three effects, the relationships between the induced charge (Q) and the applied longitudinal force (F_L), transverse force (F_T), and volumetric pressure (P) can be summarized as follows, respectively:

$$\begin{aligned} Q_L &= d_L \cdot F_L \\ Q_T &= d_T \cdot F_T \cdot R_S = d_T \cdot F_T \cdot A_Q / A_F \\ Q_V &= (d_L \cdot P + 2 \cdot d_T \cdot P) \cdot A_Q \end{aligned} \qquad [4.1]$$

where d_L is the longitudinal piezoelectric coefficient and d_T is the transverse piezoelectric coefficient. A_Q and A_F are the surface areas where Q and F_T are applied, respectively.

For the longitudinal effect, the induced charge (Q_L) and the applied longitudinal force (F_L) share the same surface as shown in Fig. 4.4a. Thus, Q_L is proportional to F_L. For the transverse effect, the transverse force (F_T) is applied to the perpendicular surface of Q_T as shown in Fig. 4.4b, and Q_T becomes proportional to the product between F_T and the surface ratio (R_S). For the volume effect shown in Fig. 4.4c, the volumetric coefficient depends on the combination of the longitudinal and transverse coefficients when the pressure (P) is applied to all surfaces of the element. These three effects are used independently or collectively to manufacture various types of piezoelectric transducers. For example, the longitudinal and shear effects are utilized for manufacturing surface-mounted pressure and shear wave transducers, respectively (Jon, 2005).

4.2.3 Constitutive equations of piezoelectric materials

The piezoelectric constitutive relations between the electrical and mechanical parameters are expressed as follows (IEEE Standard, 1987):

$$D_i = \varepsilon_{ij}^T E_j + d_{im}^d T_m \quad [4.2]$$

$$S_k = d_{jk}^c E_j + s_{km}^E T_m \quad [4.3]$$

where D_i is the electric displacement (C/m^2), S_k is the strain, E_j is the applied electric field (V/m), and T_m is the stress (N/m^2). Here $\varepsilon_{ij}{}^T$ and s_{km}^E denote the dielectric permittivity (F/m) and the elastic compliance (m^2/N), respectively. The superscripts T and E denote that these quantities are measured at zero stress and zero electric field, respectively. Then, d_{im}^d and d_{jk}^c are the piezoelectric coefficients (C/N or m/V), respectively. Here, the superscripts c and d represent the converse and direct piezoelectric effects, respectively, and d_{im}^d and d_{jk}^c are numerically identical. For a typical sheet of piezoelectric material, the poling direction is usually along the thickness (3-axis), and the 2- and 3-axes denote the plane of the sheet, as shown in Fig. 4.5.

The constitutive relations can be rewritten in a matrix form (Sirohi and Chopra, 2000):

$$\begin{bmatrix} \mathbf{D} \\ \mathbf{S} \end{bmatrix} = \begin{bmatrix} \boldsymbol{\varepsilon}^T & \mathbf{d}^d \\ \mathbf{d}^c & \mathbf{s}^E \end{bmatrix} \begin{bmatrix} \mathbf{E} \\ \mathrm{T} \end{bmatrix} \quad [4.4]$$

The applied electric field matrix **E** and the corresponding electric displacement matrix **D** are

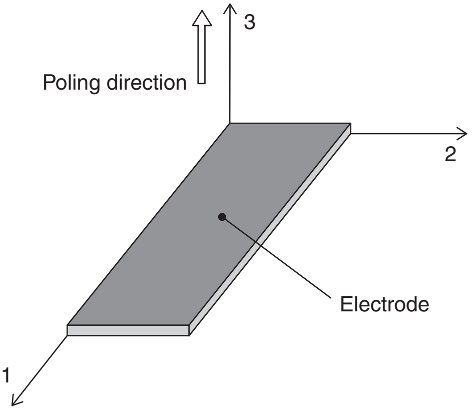

4.5 Typical piezoelectric material sheet. (*Source*: Reproduced from Sirohi and Chopra, 2000.)

$$\mathbf{E} = \begin{bmatrix} E_1 \\ E_2 \\ E_3 \end{bmatrix} \mathbf{D} = \begin{bmatrix} D_1 \\ D_2 \\ D_3 \end{bmatrix} \quad [4.5]$$

where D_i denotes the electric displacement in the i direction when the electric field E_j is applied in the j direction.

Then, the permittivity matrix $\boldsymbol{\varepsilon}^T$ is

$$\boldsymbol{\varepsilon}^T = \begin{bmatrix} \varepsilon_{11}^T & 0 & 0 \\ 0 & \varepsilon_{22}^T & 0 \\ 0 & 0 & \varepsilon_{33}^T \end{bmatrix} \quad [4.6]$$

where the electric permittivities ε_{11}^T, ε_{22}^T, and ε_{33}^T denote the measurement of the polarizability in the 1, 2, and 3 directions, respectively, when an electric field is applied in the corresponding directions.

The **d** matrix can be expressed as

$$\mathbf{d} = \begin{bmatrix} 0 & 0 & d_{31} \\ 0 & 0 & d_{32} \\ 0 & 0 & d_{33} \\ 0 & d_{24} & 0 \\ d_{15} & 0 & 0 \\ 0 & 0 & 0 \end{bmatrix} \quad [4.7]$$

where the piezoelectric coefficients $d_{31,}$ d_{32}, and d_{33} represent the normal strains in the 1, 2, and 3 directions due to the electrical poling in the 3 direction (E_3), respectively. The coefficients d_{15} and d_{24} are the shear strain in the 1–3 plane due to the field E_1 and the shear strain in the 2–3 plane due to the field E_2, respectively.

The stress and strain matrices, **T** and **S**, can be written as

$$\mathbf{T} = \begin{bmatrix} \sigma_1 \\ \sigma_2 \\ \sigma_3 \\ \sigma_4 \\ \sigma_5 \\ \sigma_6 \end{bmatrix} \quad \mathbf{S} = \begin{bmatrix} S_1 \\ S_2 \\ S_3 \\ S_4 \\ S_5 \\ S_6 \end{bmatrix} \qquad [4.8]$$

where σ_1, σ_2, and σ_3 are the normal stresses, and S_1, S_2, and S_3 are the corresponding normal strains. σ_4, σ_5, and σ_6 are the shear stresses in the 2–3, 3–1, and 1–2 planes, and S_4, S_5, and S_6 represent the corresponding shear strains, respectively.

The compliance matrix $\mathbf{S}^E$ is

$$\mathbf{S}^E = \begin{bmatrix} s_{11} & s_{12} & s_{13} & 0 & 0 & 0 \\ s_{12} & s_{22} & s_{23} & 0 & 0 & 0 \\ s_{13} & s_{23} & s_{33} & 0 & 0 & 0 \\ 0 & 0 & 0 & s_{44} & 0 & 0 \\ 0 & 0 & 0 & 0 & s_{55} & 0 \\ 0 & 0 & 0 & 0 & 0 & s_{66} \end{bmatrix} \qquad [4.9]$$

where the six elastic compliances from s_{11} to s_{33} denote the ratio of the normal strain to the normal stress in each direction under a constant electric field, respectively. For example, s_{12} is the ratio of the normal strain in the 2 direction to the normal stress in the 1 direction. The remaining three elastic compliances from s_{44} to s_{66} indicate the ratio of the shear strain to the shear stress in each direction.

Equation [4.2] is a sensing equation representing the direct piezoelectric effect, while Equation [4.3] is an actuating equation corresponding to the converse piezoelectric effect. Based on these constitutive equations, sensors and actuators are analytically modeled. Then, the analytical models can be used to fabricate and optimize piezoelectric transducers and to simulate their effects for actuation or sensing applications (Roundy and Wright, 2004; Park *et al.,* 2010a).

4.3 Piezoelectric materials and the fabrication of piezoelectric transducers

Now, the characteristics of piezoelectric materials and the fabrication process of piezoelectric ceramics are described in this section.

4.3.1 Piezoelectric materials

Natural piezoelectric materials such as quartz (SiO_2) and Rochelle salt ($NaKC_4H_4O_{6\text{–}4}H_2O$) have been widely used for piezoelectric transducers. Quartz, shown in Fig. 4.6a, has been the most favorable material for many years, and is still popular for pressure measurement because of its high mechanical strength of 2–3 GPa, high-voltage sensitivity, and thermal resistance up to 400°C (Jon, 2005). Rochelle salt is also used to manufacture various types of transducers due to its high piezoelectricity. However, its applications are often limited due to its vulnerability to liquid and high temperature.

To overcome the limitations of these natural piezoelectric materials and improve the piezoelectric performance, synthesized piezoelectric materials have been developed for the last two decades. For example, piezoelectric ceramics such as barium titanate ($BaTiO_3$), lead titanate ($PbTiO_3$), and lead zirconate titanate (PZT) ($PbZrTiO_3$) exhibit much higher piezoelectric and piezoelectric voltage constants than quartz, making them attractive for transducer manufacturing. Table 4.1 compares the material properties between APC850-type PZT and quartz (American Piezo Ceramics Inc.). Other widely used synthesized piezoelectric materials include lithium niobate ($LiNbO_3$) and lithium tantalite ($NiTaO_3$), which have the characteristics of insolubility and thermal resistance up to 650° C. Moreover, these materials have high electromechanical coupling factors compared to natural piezoelectric materials. Thus, they have been widely used for surface acoustic wave devices (Ikeda, 1996).

4.3.2 Fabrication of piezoelectric ceramics

The fabrication of the piezoelectric ceramics starts with mixing raw materials such as lead oxide (PbO), zirconium (Zr), and titanium (Ti) with chemically

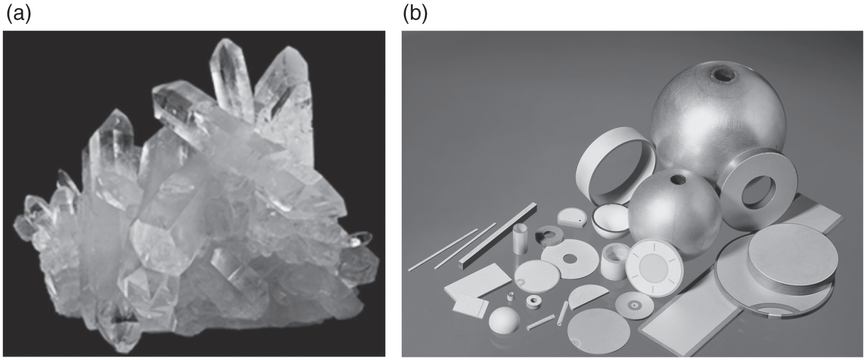

4.6 Piezoelectric materials: (a) natural piezoelectric crystal materials: Quartz (SiO_2) and (b) synthesized piezoelectric ceramics from American Piezo Ceramics Inc. (http://americanpiezo.com).

Table 4.1 Typical properties of piezoelectric ceramic (American Piezo Ceramics Inc.)

Property	Symbol	APC850-type PZT	Quartz
Curie point(°C)	T_C	360	573
Elastic modules (10^{10} N/m)	Y^E	6.3	7.7
Dielectric constant (Unitless)	$\varepsilon/\varepsilon_0$	1200	4.5
Piezoelectric constant (pC/N)	d	175	2.3
Piezoelectric voltage constant (Vm/N)	g	12.4	0.5
Electromechanical coupling factor (Unitless)	k	0.36	0.10
Frequency constant (Hz.m)	N	1500	2800
Poisson ratio (Unitless)	υ	0.35	0.17
Density (kg/m^3)	ρ	7600	2650

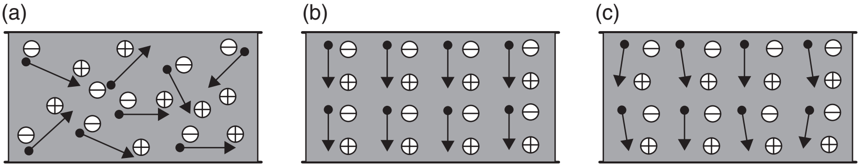

4.7 The poling process of a piezoelectric ceramic: (a) a crystalline material is heated up near its Curie temperature, (b) the applied electric field aligns the dipoles along the electric field lines, and (c) the polarization is permanently maintained after cooling. (*Source*: Reproduced from Fraden, 1996.)

correct proportions. Then, the mixture is heated around 800–1000°C to accelerate the reaction of the components (Sirohi and Chopra, 2000). This blending and heating process creates the piezoelectric powder. Subsequently, the piezoelectric powder is mixed with a binder and sintered into the desired shape, resulting in the ceramic material. After this material is cooled down, the crystalline structure is formed. Then, conductive electrodes are bonded to the ceramic surface. Here, metallic silver is commonly used as the electrode (Jaffe, 1971).

Next, the poling process is performed, as shown in Fig. 4.7. The crystalline material, which has randomly oriented dipoles, is warmed up slightly below its Curie temperature as shown in Fig. 4.7a (Fraden, 1996). Then, an electric field is applied to the unit cell so that the dipoles strongly align along the electric field lines, as shown in Fig. 4.7b. Finally, the material is cooled down while the electric field is maintained, and the electric field is removed. Figure 4.7c shows that the polarization permanently remains as long as the poled material is maintained below the Curie temperature. Note that if excessive mechanical stress, large input voltage, or high temperature over the Curie temperature is applied to the material, it can lose its polarization.

4.4 Piezoelectric transducers for SHM applications

This section deals with various types of piezoelectric transducers used for SHM applications as displayed in Fig. 4.8. PZT shown in Fig. 4.8a is one of the most widely utilized transducer types for SHM applications, because of its light weight, low cost, and a fast electromechanical response. However, PZT has limited conformity to curved surfaces due to its brittleness. To overcome this limitation, flexible piezoelectric polymers and composites have been developed.

Macro-fiber composite (MFC) is an innovative flexible transducer offering high-performance at a competitive cost. MFC was first developed at NASA Langley Research Center in 1996 to enhance the flexibility of piezoelectric transducers, as shown in Fig. 4.8b (High and Wilkie, 2003). Figure 4.9a shows the structure of MFC composed of rectangular fibers sandwiched between adhesive layers and electrode polyimide films (Smart Materials Inc.). With great flexibility, MFCs were used as a guided wave generator in a pipeline structure (Lee and Sohn, 2012). In addition, Wait and Todd (2007) utilized MFCs as a strain sensor through dynamic strain tests on an aluminum specimen.

Another widely used flexible piezoelectric transducer is active fiber composite (AFC) developed by Massachusetts Institute of Technology (Bent *et al.*, 1995). Figure 4.9b depicts the structure of AFC composed of thin and conformable piezoelectric fibers with orthotropic materials. It was initially developed for actuators for structural control, but it also has been used for SHM applications. Williams *et al.* (2002) used AFCs to suppress the vibration of helicopter rotor blades, and Birchmeier *et al.* (2009) investigated the generation of the fundamental Lamb wave modes using AFCs.

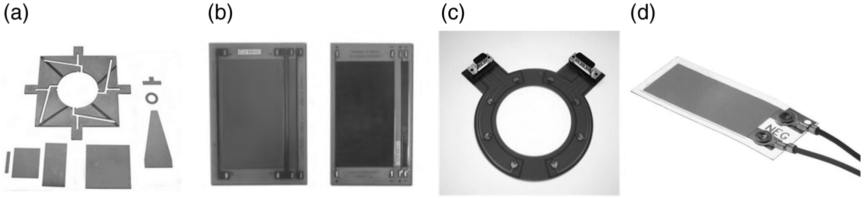

4.8 Various piezoelectric transducers: (a) piezoelectric ceramics from Piezo Systems Inc. (http://www.piezo.com), (b) MFC from Smart Materials Inc. (http://www.smart-material.com), (c) smart layer from Acellent technologies Inc. (http://64.105.143.179/types.asp), and (d) PVDF sensor from Measurement Specialties Inc. (http://www.meas-spec.com/).

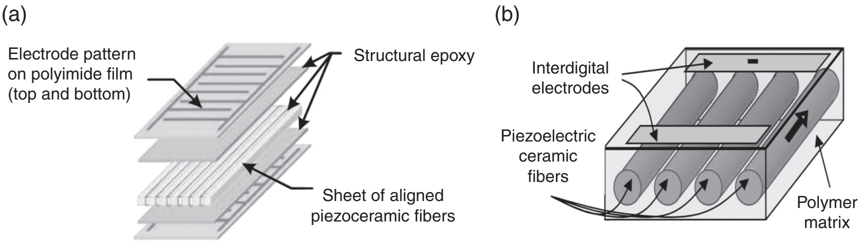
(a)
Electrode pattern on polyimide film (top and bottom)
Structural epoxy
Sheet of aligned piezoceramic fibers
(b)
Interdigital electrodes
Piezoelectric ceramic fibers
Polymer matrix

4.9 Schematic configurations of AFC and MFC: (a) MFC from Smart Materials Inc. (http://www.smart-material.com) and (b) AFC from Piezodevices Inc. (http://www.piezodevices.com).

An integrated network of distributed piezoelectric transducers, called the 'smart layer,' has been introduced by Lin and Chang (2002). The smart layer is a thin dielectric film with embedded piezoelectric transducers, as shown in Fig. 4.8c. Since the smart layer is fabricated using thin and flexible printed circuits, it can also be used for curved surface structures or complex structures. Qing *et al*. (2007) utilized the smart layer for monitoring of a composite bottle structure.

Polyvinylidene fluoride (PVDF) is another popular piezoelectric polymer because of its flexibility. PVDF developed by Kawai has been employed for SHM applications including curved structures and high-strain spots (Kawai, 1969). Lin and Giurgiutiu (2006) applied PVDF to a long rod for ultrasonic measurement, and Yi and Liang (2008) utilized PVDF for the deformation measurement of automotive tires. Matsumoto *et al.* (2004) utilized PVDF as a strain sensor to evaluate the surface strain distribution of a rectangular plate. Table 4.2 compares the material properties of PVDF and other typical piezoelectric materials. Since the piezoelectric voltage constant of PVDF is much higher than those of the other materials, it is frequently used for headphones and speakers. However, PVDF is generally not suitable for actuation, due to its relatively small elastic modulus. Thus, it is generally limited to sensing applications (Sirohi and Chopra, 2000; Lin and Giurgiutiu, 2006). In addition, its performance highly depends on thermal and poling conditions.

Another newly developed piezoelectric transducer is the polymer-based piezoelectric paint sensor, as shown in Fig. 4.10a. The piezoelectric paint sensor developed by Klein *et al*. (1986) is composed of tiny piezoelectric composite films. The benefits of the piezoelectric paint sensors are compactness, flexibility, and controllability of piezoelectric properties. White *et al*. (2004) investigated the applicability of the piezoelectric paints as vibration sensors, and Zhang (2006) employed the piezoelectric paints for fatigue crack detection.

Table 4.2 Properties of piezoelectric materials at 20°C

Property	PVDF	PZT	$BaTiO_3$	Quartz
Density (10^3 kg/m^3)	1.78	7.5	5.7	2.65
Dielectric constant (Unitless)	12	1200	1700	4.5
Elastic modules (10^{10} N/m)	0.3	8.3	11	7.7
Piezoelectric voltage constant (Vm/N)	216	10	5	0.5
Piezoelectric constant (pC/N)	20	110	78	2.3
Electromechanical coupling constant (%)	11	30	21	10
Acoustic impedance (10^6 kg/m^{2}s)	2.3	25	25	14.3

Source: Reproduced from Giurgiutiu, 2008.

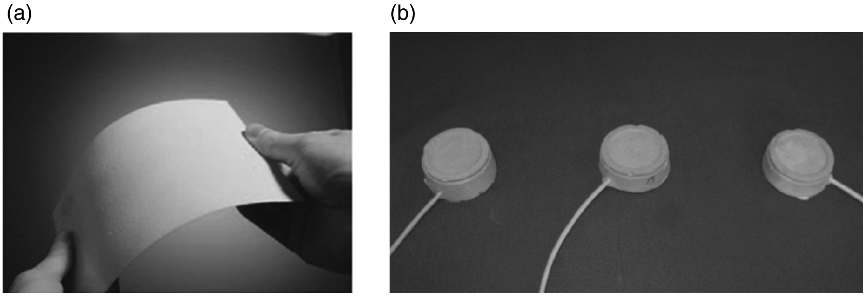

4.10 Additional piezoelectric transducers: (a) piezoelectric paint sensor (Zhang, 2006) and (b) smart aggregate (Song *et al.*, 2008).

Smart aggregate is a new piezoceramic device developed for concrete structure monitoring as shown in Fig. 4.10b (Song *et al.*, 2008). The smart aggregate is composed of a waterproof piezoelectric patch with lead wires embedded in a small concrete block. The devices are then embedded in concrete structures during casting. One smart aggregate is used as an actuator to generate a desired input signal, while the other smart aggregates are used as sensors to detect the corresponding responses. They are used for early-age strength monitoring (Gu *et al.*, 2006), crack detection (Song *et al.*, 2007a), and impact detection and evaluation (Song *et al.*, 2007b).

4.5 Bonding effects

Figure 4.11 shows the bonding layer between the piezoelectric transducer and the host structure. In typical SHM applications, the piezoelectric transducers are assumed to be perfectly bonded with a host structure via an adhesive. In reality, however, the adhesive forms an interfacial layer of finite thickness between the piezoelectric element and the host structure,

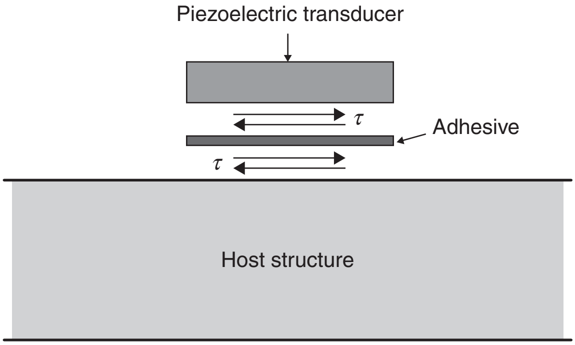

4.11 Bonding layer between a piezoelectric transducer and a host structure: τ denotes interfacial shear stress between the piezoelectric transducer, bonding layer, and the host structure.

and this adhesive layer significantly affects the shear stress (τ) transfer between the transducer and the host structure (Rabinovitch and Vinson, 2002). Crawley and de Luis (1987) first proposed a shear spring model of the adhesive effect. Their analytical model assumed that the shear stress in the adhesive is proportional to the longitudinal relative deformation between the piezoelectric transducer and the host structure. The shear lag effect becomes more dominant with a lower shear modulus and a thicker adhesive layer, resulting in less effective shear transfer between the piezoelectric transducer and the host structure. Bhalla and Soh (2004) formulated electromechanical impedance considering the shear lag effect, and Qing *et al*. (2006) experimentally investigated the effects of adhesive thickness and its modulus on the performance of bonded piezoelectric elements. Sohn and Lee (2010) tuned the conventional Lamb wave tuning curve analyzing the bonding layer effect.

4.6 Limitations of piezoelectric transducers

Piezoelectric transducers generally have limited temperature of operation, maximum applicable voltage without causing depolarization, and mechanical strain that the transducers can measure or mechanically sustain. Around 200–300°C, phase transition of piezoelectric materials occurs, resulting in the loss of piezoelectricity (Akiyama *et al*., 2009). For instance, it is reported that polycrystalline ($Bi_4Ti_3O_{12}$) loses its piezoelectricity around 675°C by the depolarizing phenomenon (Damjanovic, 1998). The piezoelectric transducers can also be depolarized when a strong electric field, about 500–1000 V/mm, is applied with the polarity opposite to the original poling direction (Piezo Systems Inc. (2013)). Piezoelectric transducers also have their maximum measurable strain level, normally 500 μ (Piezo Systems Inc.). In reality, piezoelectric transducers attached on a target structure are often exposed to high-stress and -strain concentrations under operating conditions of the target structure.

4.7 SHM techniques using piezoelectric transducers

This section extensively summarizes piezoelectric transducer based on various SHM methodologies including guided wave, impedance, acoustic emission, and self-diagnosis techniques.

4.7.1 Guided wave techniques

Guided wave techniques using piezoelectric transducers are one of the most popular SHM techniques. These techniques are attractive because guided waves, defined as elastic waves confined by the boundaries of a structure, can travel a long distance with little signal attenuation and high sensitivity to small structural damages (Cawley and Alleyne, 1996; Staszewski *et al.*, 2004a). Figure 4.12 depicts two typical modes of guided wave measurement (Raghavan and Cesnik, 2007). When an electrical voltage is applied to PZT mounted on a plate-like target structure, guided waves are generated and propagate along the target structure. Then, the corresponding responses can be measured by the same PZT in a pulse–echo mode or by the other PZT in a pitch–catch mode. The guided waves traveling through a structural discontinuity produce scattering, reflection, and mode conversion, making it possible to identify structural damage. Alleyne and Cawley (1992) investigated the interactions of guided waves with a variety of structural damage through finite element analysis and experiment. Then, Rose (1999) theoretically estimated the quantity of guided wave mode conversions produced by thickness variations of waveguides.

Guided waves are, however, also sensitive to environmental and operational variation, often resulting in false alarms (Sohn, 2007). To minimize these effects on the guided wave techniques, reference-free guided wave techniques have been proposed. In conventional guided wave techniques, structural damage is often identified by simple comparison between baseline data obtained from the pristine condition of the target structure and the current data measured from current state of the target structure. On the other hand, the reference-free techniques utilize only current data for damage diagnosis, thus making them less sensitive to environmental and operational variations.

One of the first proposed reference-free techniques is based on a time reversal process (TRP). The basic assumption of the TRP method is that the

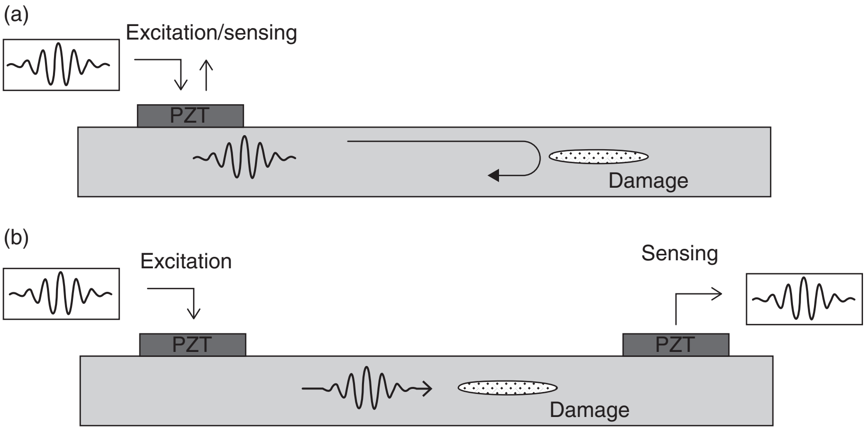

4.12 Two modes of guided wave measurements: (a) pulse–echo mode and (b) pitch–catch mode.

elastodynamic reciprocity is broken when damage occurs along a guided wave propagating path. Park *et al*. (2006a) and Sohn *et al*. (2007) developed the TRP-based damage detection techniques and applied them to composite structures. Kim and Sohn (2007) proposed another reference-free technique based on the polarization characteristics of piezoelectric transducers. This reference-free technique identifies cracks by extracting crack-induced mode conversion signals using PZT transducers attached to both sides of a thin metal plate. Sohn and Kim (2010) also developed a reference-free technique using newly designed dual PZT transducers so that mode conversion signals can be isolated using the PZT transducers attached only to a single surface of a target structure. Then, An and Sohn (2010) examined the performance of the reference-free techniques under varying temperature and external loading conditions.

Guided wave imaging techniques using piezoelectric transducers have been developed for damage localization as well as identification. In order to construct guided wave images, guided wave tomography techniques, using the data obtained from a sparse array of piezoelectric transducers, have been developed. Hutchins *et al*. (1993) detected defects in aluminum plates by constructing guided wave tomography images using noncontact air coupled and electromagnetic acoustic transducers. Leonard *et al*. (2002) used the guided wave tomography technique to construct a quantitative Lamb wave map. This tomography technique, however, requires solution of a complex inverse problem to build a guided wave image with high spatial resolution.

Another guided wave imaging technique is a phased array technique. It employs a dense transducer array that can sequentially generate guided

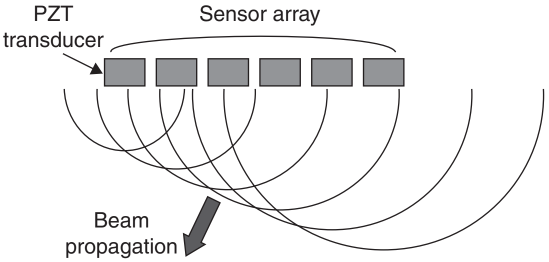

4.13 Principle of a phased array technique.

waves to obtain guided wave images based on interference patterns. Figure 4.13 shows an example of beam forming toward a specific direction using a phased array. This technique can identify and localize damage in a wide area by adjusting the excitation time delay. Giurgiutiu and Bao (2004) utilized the phased arrays to localize damages in thin-wall structures, and Banchet *et al*. (2004) used phase arrays to detect crack defects in a lap joint structure. Fromme *et al*. (2006) proposed a prototype phased array to detect corrosion damage in large plate-like structures. Luo and Rose (2007) used a phase array focusing method to perform pipe inspection. This method shows an improved signal-to-noise ratio and better sensitivity that enables detection of small defects in pipeline network. However, the use of this phase array technique is often limited, because the instrumentation is expensive and performance of the whole system is governed by each piezoelectric transducer of the system.

4.7.2 Impedance techniques

Impedance techniques using piezoelectric transducers have been developed to detect local damages in complex structures (Liang *et al*., 1994). In the impedance technique, an electromechanical impedance signal is measured by applying an electric voltage to PZT and measuring the corresponding output current when the PZT is attached to a host structure, as shown in Fig. 4.14. Since the electrical impedance of the PZT is coupled with the mechanical impedance of the host structure, potential damage can be manifested by monitoring the change of the measured impedance signal. The electromechanical impedance can be written as follows:

$$Z_{\text{total}}(\omega) = \left[i\omega C \left(1 - k_{31}^2 \frac{Z_s(\omega)}{Z_a(\omega) + Z_s(\omega)} \right) \right]^{-1} \quad [4.10]$$

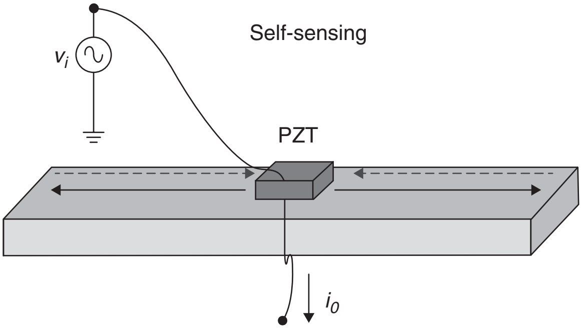

4.14 Scheme of the impedance technique.

where Z_{total} is the electromechanical impedance measured by the PZT, Z_s is the mechanical impedance of the host structure, Z_a is the mechanical impedance of the PZT, ω is angular frequency, C is the zero-loaded capacitance of the PZT, and k_{31} is the electromechanical coupling coefficient of the PZT, respectively.

The impedance technique is attractive for local damage detection because it is sensitive to even small damage and can be applied to complex structures (An *et al.*, 2012). However, impedance measurements become difficult with highly damped materials such as carbon fiber reinforced polymer (CFRP) and glass fiber reinforced polymer (GFRP) or large-scale structures with high mechanical impedance, because PZT transducers cannot produce excitation forces large enough to create standing waves, which are a requisite to obtain impedance signal (Kim *et al.,* 2011a).

A number of PZT-based impedance SHM applications have been reported. For crack detection, several numerical and experimental studies have been successfully carried out (Giurgiutiu, 1999; Soh *et al.*, 2000; Park *et al.*, 2006b). For bolt loosening detection, bolt joint connections of airplane and bridge structures have been investigated (Chaudhry *et al.,* 1995; Min *et al.,* 2010a). For delamination detection, a few numerical and experimental implementations have been conducted on composite structures (Bois and Hochard, 2004; Yan *et al.,* 2011). It is worth noting that the sensitivity of the impedance technique to each damage type is different. An and Sohn (2011) investigated the sensitivity of the impedance technique to three different types of damages, i.e., crack, bolt loosening, and delamination.

In the impedance technique, one of the most challenging issues is that the impedance signals are also sensitive to environmental variations, such as temperature and loading changes as well as structural damages. To minimize these effects, temperature compensation techniques have been developed by several researchers. Temperature variation often causes a horizontal frequency shifting of impedance signals, and this temperature induced shifting is compensated by Koo *et al*. (2009) using a cross-correlation coefficient. Lim *et al*. (2011) also proposed a data normalization technique using Kernel principal component analysis to minimize false alarms caused by temperature and static/dynamic loading variations. Furthermore, Kim *et al*. (2011b) proposed reference-free impedance technique for crack detection in plate-like structures. This reference-free technique identifies cracks by extracting converted modes from the impedance signals measured from only current state of the target structure, thus making it robust against environmental variations.

4.7.3 Acoustic emission techniques

Acoustic emission (AE) is defined as 'transient elastic stress waves produced by a release of energy from a localized source' (Weng *et al.,* 1982). An AE sensor composed of a thick piezoelectric element shown in Fig. 4.15a converts the mechanical energy caused by elastic waves into an electrical signal. The AE sensors have a high sensitivity near a narrowband of frequencies, because the piezoelectric element is designed to have a mechanical resonance at a specific target frequency (typically 60 kHz to 1 MHz). Also, preamplifier-embedded AE sensors are often used to obtain AE signals with high sensitivity. Figure 4.15b shows the basic working principle of the AE-based damage detection technique. When a load applied to a structure gradually increases, some microscopic deformations may occur, resulting in elastic waves propagating through the target surface. Then, these elastic waves are detected and converted to voltage signals by an AE sensor mounted on the structure's surface. In addition, the location of damage can be identified using multiple AE sensors based on the differences in the arrival times of the AE signals. The AE techniques have been used to detect

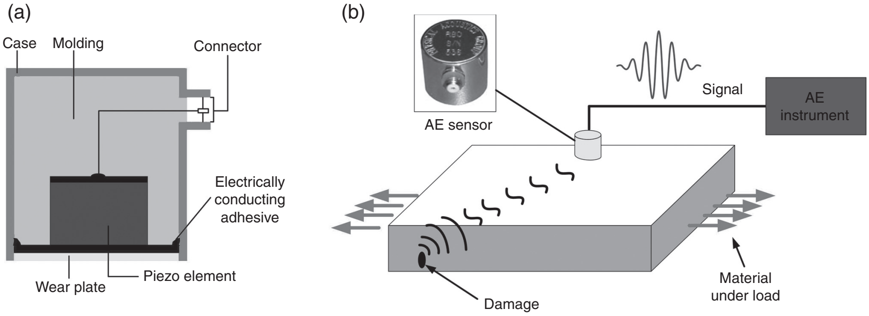

4.15 Overview of acoustic emission technique: (a) structure of an AE sensor from Vallen System Inc. (http://www.vallen.de) and (b) scheme of acoustic emission technique for damage detection.

damage in metallic and composite structures (Mazille *et al.,* 1995; Carlyle *et al.,* 1999; Prosser *et al.,* 1999). More recently, they have also been applied to evaluate deterioration of concrete structures (Shiegeishi *et al.*, 2001; Carpinteri *et al.*, 2007). In the context of localization applications, Carpinteri *et al.* (2006) conducted an experiment on RC structures to localize micro-crack sources using spatially distributed AE sensors, and McLaskey *et al.* (2010) proposed a new concept called 'Acoustic Emission Array Processing' for AE source localization using AE sensor arrays.

Analogous to the AE techniques, impact localization techniques using piezoelectric transducers have been broadly studied by the SHM community. Osmont *et al.* (2001) developed a network of a small number of piezoelectric transducers to detect and localize impacts in carbon/epoxy composite plates. Kim *et al.* (2005a) used PVDFs and PZTs for monitoring of impact damage initiation and propagation in composite laminates. More recently, Sohn *et al.* (2011a) developed an impact localization technique based on a TRP for aircraft fuselage monitoring using surface-mounted PZTs and a scanning laser Doppler vibrometer (SLDV). Perelli *et al.* (2012) proposed an impact localization technique based on dispersion compensation of guided waves using sparse PZTs mounted on an aluminum plate.

4.7.4 Piezoelectric transducer self-diagnosis techniques

Piezoelectric transducers used for SHM systems themselves often become the weakest link within the entire SHM system due to harsh environments (Saint-Pierre *et al.*, 1996; Overly *et al.*, 2009; Lee and Sohn, 2010). To tackle this issue, a number of self-diagnosis techniques have been developed. Saint-Pierre *et al.* (1996) observed the phenomenon that the PZT debonding causes the shift of the PZT resonant frequency. Overly *et al.* (2009) proposed PZT debonding and cracking diagnosis techniques using admittance signals. More recently, Lee and Sohn (2010) proposed a TRP-based PZT self-diagnosis technique to detect the cracking and debonding of the PZT.

Figure 4.16 shows an overview of the TRP-based PZT debonding detection procedure. First, a symmetric toneburst input signal is applied to a PZT, and the response reflected off from the boundaries is measured at the same PZT. Then, the measured response is scaled and reversed in the time domain, and re-emitted to the PZT. Finally, the corresponding response, which is named as the reconstructed signal, is measured again at the same PZT. According to TRP, it can be shown that the shape of the reconstructed signal's main peak should be identical to that of the original input signal, and also symmetric as long as there is no PZT debonding. However, this symmetry breaks down when PZT debonding occurs. For

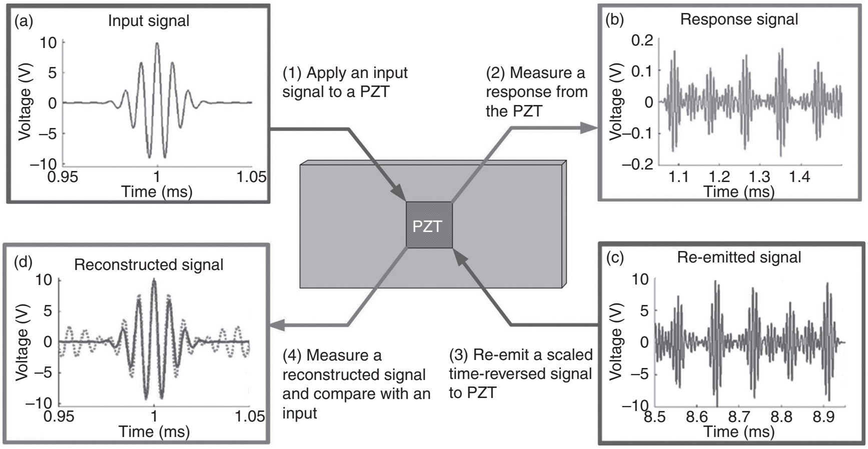
(a)
Input signal
Voltage (V)
10
5
0
−5
−10
0.95
1
1.05
Time (ms)
(1) Apply an input signal to a PZT
(2) Measure a response from the PZT
(b)
Response signal
Voltage (V)
0.2
0.1
0
−0.1
−0.2
1.1
1.2
1.3
1.4
Time (ms)
PZT
(d)
Reconstructed signal
Voltage (V)
10
5
0
−5
−10
0.95
1
1.05
Time (ms)
(4) Measure a reconstructed signal and compare with an input
(3) Re-emit a scaled time-reversed signal to PZT
(c)
Re-emitted signal
Voltage (V)
10
5
0
−5
−10
8.5
8.6
8.7
8.8
8.9
Time (ms)

4.16 Piezoelectric transducer self-diagnosis technique based on a TRP for PZT debonding detection (Lee and Sohn, 2010): (a) a toneburst input signal is applied to a PZT, (b) the corresponding response is measured at the same PZT, (c) the measured signal is scaled and reversed in the time domain, and re-emitted to the PZT, and (d) the corresponding response named as the reconstructed signal is measured and compared with the original input signal. When PZT is debonded, the symmetry of the reconstructed signal breaks down.

PZT crack detection, the mechanical response power (MRP) index defined as the total energy of the response signal normalized by the input signal energy is used. The basic premise of the MRP index is that the energy that the PZT can exert on the structure, and consequently the energy of the corresponding response, is a function of the driving frequency at a given PZT size. Therefore, the relationship between the MRP index and the driving frequency is altered when the PZT size changes. This technique has a merit of robustness against changing temperature and loading conditions, because the signals are obtained only from the current state of the monitored PZT without relying on baseline signals.

4.8 Applications of piezoelectric transducer-based SHM

Piezoelectric transducers have been mostly used for local damage detection, and there is increasing interest in integrating these local nondestructive testing (NDT) techniques with global vibration monitoring techniques for improved SHM of civil, mechanical, and aerospace systems. In this section, state-of-the-art examples of piezoelectric transducer applications to SHM are presented.

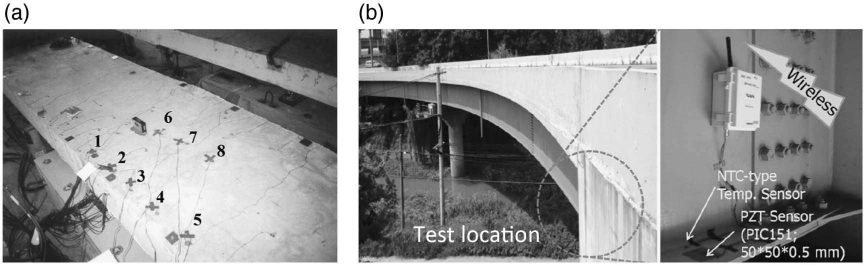

4.17 Applications to bridge structures: (a) surface crack detection in a scaled-prototype RC bridge (Soh *et al.*, 2000) and (b) bolt loosening detection in a full-scale steel box bridge (Min *et al.*, 2010b).

4.8.1 Bridge structures

The demands for bridge monitoring are triggered by past historical bridge incidents (Lichtenstein, 1993; Cho *et al.,* 2001; Hao, 2010). To meet these demands, global bridge monitoring techniques have been widely investigated. However, the global monitoring techniques are often insensitive to local incipient damage. To overcome this limitation, local bridge monitoring techniques using piezoelectric transducers have been studied. Soh *et al.* (2000) carried out crack monitoring of a scaled-prototype RC bridge using electromechanical impedance signals obtained from the embedded PZTs, as shown in Fig. 4.17a. Popovics *et al.* (2000) investigated surface-breaking cracks in a concrete structure using surface waves generated and measured from surface-mounted PZTs. Park *et al.* (2006c) investigated the applicability of the guided wave and impedance techniques using PZTs to steel bridge components. More recently, Min *et al.* (2010b) investigated the applicability of the impedance technique to detection of bolt loosening at a real steel box bridge site using wireless impedance sensor nodes as shown in Fig. 4.17b. In addition, An *et al.* (2013) investigated the applicability of the reference-free techniques to two *in situ* bridge sites under varying temperature, and static and dynamic traffic loading conditions.

The piezoelectric transducer-based bridge monitoring, however, still has a number of challenges to be overcome. First, the durability issue of piezoelectric transducer itself is critical. In general, piezoelectric transducers embedded for local bridge monitoring may deteriorate faster than the target bridge structure. To improve their durability, An *et al.* (2013) examined the ruggedness of packaged PZTs over two years at *in situ* bridge sites. Second, the wiring often becomes the weakest link in the monitoring system, and electric cabling can be labor-intensive and time consuming. To overcome these limitations, there are several approaches to integrating a wireless telemetry system with PZTs (Lynch and Loh, 2006; Park *et al.*, 2010; Zhou *et al.,* 2010). However, the full validation of this emerging technique for *in situ* bridge site monitoring is still warranted. Third, advanced signal processing techniques are needed. Since the responses obtained from piezoelectric transducers are sensitive to environmental conditions, such as temperature and loading variations, the development of novel signal processing techniques is necessary to be able to distinguish damage effects from environmental effects. Finally, a new type of piezoelectric transducer needs to be developed that can be placed near critical regions with high-stress and high-strain concentrations. Conventional piezoelectric transducers can be impaired or their responses can be saturated when they are subjected to excessive strain.

4.8.2 Aerospace structures

Piezoelectric transducer-based local SHM techniques are also actively studied by the aerospace community because incipient damage in an aircraft structure can lead to a catastrophic disaster. In particular, a large volume of SHM studies, which utilize guided wave and impedance measurements, have been reported, because many aircraft components are fundamentally thin plate-like structures. Chaudhry *et al.* (1995) investigated the applicability of the impedance technique to local damage detection in a full-scale aircraft using PZTs. Giurgiutiu *et al.* (2002) utilized PZT-based impedance and guided techniques for monitoring of fatigue cracks and corrosions in an aging aircraft. Zhao *et al.* (2007) conducted experiments on a full-scale aircraft wing for damage identification and localization using a PZT sensor array as shown in Fig. 4.18a. Di Scalea *et al.* (2007) studied the monitoring of

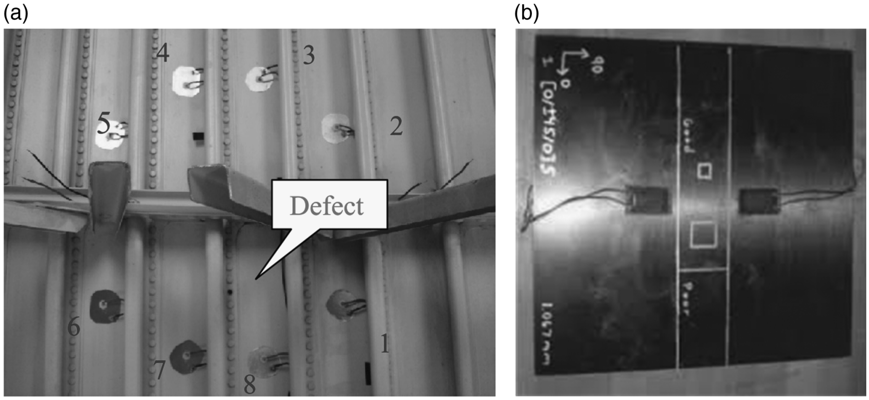

4.18 Applications to aerospace structures: (a) PZT array attached at the inner surface of the aircraft wing panel for defect monitoring (the numerals in the panel denote the PZT numbers) (Zhao *et al.*, 2007) and (b) MFCs attached to the composite wing skin-to-spar joint for debonding detection (Di Scalea *et al.*, 2007).

the composite wing skin-to-spar joint in an unmanned aerial vehicle using guided waves obtained from a pair of MFCs, as shown in Fig. 4.18b. More recently, An *et al.* (2012) investigated the feasibility of the integrated impedance and guided wave (IIG) technique for monitoring a full-scale aircraft wing structure under temperature and external loading variations. The unique characteristics of piezoelectric transducer SHM of aerospace systems are that (1) piezoelectric transducers should often be embedded inside aircraft, (2) the embedded piezoelectric transducer network should be designed with redundancy because the embedded transducers cannot be easily replaced or repaired, (3) weight of the transducers, wires, onboard data acquisition devices should be minimized, and (4) SHM systems should be designed with caution to avoid interference with existing onboard communications.

4.8.3 Pipeline structures

Piezoelectric transducers have been also used for pipeline monitoring. Lowe *et al.* (1998) estimated the defect size using a piezoelectric transducer-based guided wave technique in a pipeline structure. Harley *et al.* (2009) utilized a piezoelectric transducer array for TRP-based pipeline monitoring. Davies and Cawley (2009) developed a guided wave imaging technique for pipeline monitoring using circumferential array of piezoelectric shear transducers, and the effectiveness of the proposed method was numerically and experimentally validated. The uniqueness of pipeline SHM applications is that (1) the conformability of piezoelectric transducers is important, (2) guided waves can travel relatively longer distances than other applications since the energy is confined within the pipe, and (3) often a long range data and power transmission is necessary.

4.8.4 Nuclear power plants

Nuclear energy is seen as one of the most promising alternative energy sources to oil, and monitoring of nuclear power plants (NPPs) is another area where piezoelectric transducers can be potentially exploited. In response to this interest, there have been several preliminary studies where the applicability of piezoelectric transducers to NPP monitoring has been investigated. Stepinski *et al.* (1998) developed a sensor array made of piezoelectric composites for assessing the structural integrity of nuclear waste fuel. Machado *et al.* (2000) developed a specially designed PVDF sensor for the monitoring of nuclear fuel assemblies, and their sensors have been tested using a prototype of fuel assembly. More recently, Ai *et al.* (2010) used piezoelectric AE sensors to detect fatigue cracks in a main cooling pipe system. The biggest challenge for NNP applications is that sensors often need to be embedded for online monitoring, and should be designed to withstand high temperature and radiation. To the best knowledge of the authors, currently there are no commercially available piezoelectric transducers that can meet these stringent requirements imposed by NNPs.

4.8.5 Wind turbines

The monitoring of wind turbine structures has just begun to germinate, in response to the recent energy crisis and demands of clean energy (Schulz and Sundaresan, 2006). Sundaresan *et al.* (2002) utilized a PZT-based guided wave technique to investigate excessive load-induced damage in a wind turbine blade under static loading conditions. Joosse *et al.* (2002) also monitored a rotor blade to identify and localize damage from a series of static and fatigue tests using an AE technique. Pitchford *et al.* (2007) validated the applicability of the PZT- and MFC-based impedance techniques for wind blade monitoring through actual blade testing. For online wind blade monitoring, it is imperative to embed sensors inside wind blades so that they do not interfere with the aerodynamic characteristics of blades. Furthermore, the power and data transmission between the blades and the base monitoring station becomes a daunting test. On the other hand, the repeated global vibration caused by the rotating blades offers an opportunity for combined global and local techniques, such as a vibro-acoustic technique where high-frequency ultrasonic signals generated by an embedded piezoelectric transducer are modulated by the global low-frequency excitation generated by the rotating blades when certain types of damage appear (Duffour *et al.,* 2006).

4.8.6 Other fields

Piezoelectric transducers have been widely utilized in the fields of high-precision and vibration controls. For high-precision control applications, Kim *et al.* (2005b) developed a micro-tensile testing machine using PZT actuators. Fleming and Leang (2010) developed a nano-positioning platform using piezoelectric transducers, as shown in Fig. 4.19a. Examples of commercial applications to high-precision controls are available at Physik Instrumente Inc. (http://www.physikinstrumente.com/). As for vibration control, Vautier and Meheimani (2005) used PZT patches to reduce undesirable vibration in an aluminum beam, as shown in Fig. 4.19b.

Another growing area of application is energy harvesting. To name a few, Choi *et al.* (2005) developed a thin-film PZT-based energy harvesting microelectromechanical systems (MEMS) device for long-term SHM applications. Ericka *et al.* (2005) modeled an energy harvesting generator using piezoelectric membranes. Wang and Xu (2007) invented an energy harvesting

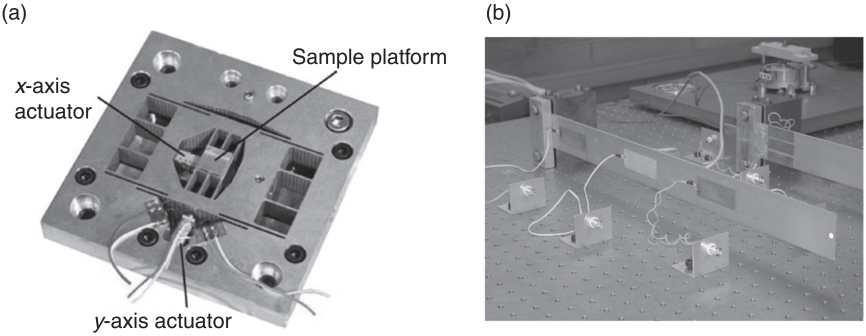

4.19 Applications to high-precision and vibration control: (a) high-speed nano-positioning platform (Fleming and Leang, 2010) and (b) structural vibration control system (Vautier and Meheimani, 2005).

device based on air-spaced piezoelectric cantilevers. Traditionally, energy harvesting using piezoelectric transducers has been limited to a relatively high-frequency range (kHz), but recently there have been several studies where energy was harnessed using piezoelectric transducers from low-frequency vibrations (Priya, 2007).

4.9 Future trends

As shown in the previous section, the application of piezoelectric transducers to the SHM field is increasing. However, there are still many challenging technical hurdles that have to be overcome before piezoelectric transducers can be widely accepted for SHM applications. In this section, new research trends, and novel ongoing efforts that might be able to address some of the current technical difficulties, are briefly introduced.

4.9.1 High-temperature piezoelectric transducers

High-temperature piezoelectric transducers have great potential application, such as NPP monitoring. However, the piezoelectricity of typical piezoelectric transducers deteriorates as temperature increases. To overcome this limitation, researchers have investigated alternative piezoelectric materials that retain their piezoelectricity even at high temperature. Materials such as lithium niobate ($LiNbO_3$), ferroelectric crystals ($Sr_2Nb_2O_7$ and $La_2Ti_2O_7$), and aluminum nitride films have turned out to have great thermal stability and resistivity (Turner *et al.,* 1994). For example, Kobayashi *et al.* (2010) developed an ultrasonic transducer operating up to 500°C using the same material and successfully tested up to 500°C. However, the manufacturing cost of these compounds is high, due to their high melting points.

4.9.2 High-strain piezoelectric transducers

Piezoelectric transducers often need to be placed near structurally critical areas where expected stress and strain levels are high. However, typical piezoelectric transducers become less responsive when they are subjected to high strain. For this reason, the development of high-strain piezoelectric transducers is necessary for SHM applications. For actuation, high-strain piezoelectric transducers that can endure high-temperature environments have been developed (Donnelly *et al*., 2007; Kurihara and Masao, 2008). However, the performance of these high-strain piezoelectric transducers for sensing is still questionable. Therefore, the development of high-strain piezoelectric transducers not only for actuation but also for sensing is a future requirement for building a robust SHM system.

4.9.3 Integration with optic-based SHM techniques

Recently, a number of optic-based SHM techniques using piezoelectric transducers have been reported. First, an optic-based wireless PZT excitation and sensing system using laser and optoelectronic devices was proposed by Park *et al.* (2010). In this system, the input waveform for PZT excitation as well as the power required for wireless sensing is remotely transmitted via a continuous laser source. Second, optic-based hybrid systems combining piezoelectric transducers for guided wave generation and fiber-optic for sensing have been proposed (Betz *et al.,* 2003; Takeda *et al.,* 2005). These hybrid systems are less susceptible to noise and capable of multi-point sensing. Third, a combination of piezoelectric transducer and laser for either noncontact sensing or excitation has been proposed and successfully validated by several researchers (Staszewski *et al.,* 2004b; Leong *et al.,* 2005; Sohn *et al.,* 2011b). In these systems, excitation is done by a piezoelectric transducer and sensing is done by noncontact laser, or inversely the excitation can be achieved by laser and sensing by a piezoelectric transducer. The main advantage of these systems is that wavefield visualization with high spatial and temporal resolution can be achieved by laser scanning, making it possible to identify and localize damage without solving a complex inverse problem.

4.9.4 Nano-piezoelectric transducers

There is an increased interest in developing nano-scaled piezoelectric transducers due to the advantages of its ultra-compactness and meticulous precision control. Nano-scaled piezoelectric powders, which are central to the nano-piezoelectric transducers, have been developed for versatile precision control applications (Reddy *et al.*, 2002; Lee *et al.*, 2006; Sinha *et al.*, 2009). These studies have revealed that the nano-scaled piezoelectric transducers have comparable piezoelectric coefficients to bulk piezoelectric transducers, although their elastic modulus is lower than that of the bulk transducers. Then, Chen *et al.* (2010) developed a new piezoelectric nano-fiber transducer for mechanical energy harvesting. However, applications of nano-piezoelectric transducers to SHM community have not been much focused on. Thus, further study on the utilization of nano-piezoelectric transducers to SHM field is warranted.

4.9.5 Multi-functional piezoelectric sensing

As described in this chapter, piezoelectric transducers are widely used for damage detection techniques based on guided wave, impedance, and AE measurement. Naturally, there is a strong desire to design a single multi-functional piezoelectric transducer that can be used for simultaneous measurements of these different types of signals and corresponding damage detection techniques. The advantage of this multi-functional sensing might be that the number of necessary sensors can be reduced, and information gained from various signal measurements and damage detection algorithms can be synergistically combined for improved SHM diagnosis. The difficulty here is that measurements of guided wave, impedance, and AE signals are based on different principles and require different constraints for transducer designs. Therefore, it becomes difficult to design a single piezoelectric transducer that can meet all these various design requirements. For example, it is typically desirable to increase the transducer size for actuation applications. On the other hand, the smaller transducer achieves higher sensing sensitivity. Song *et al.* (2008) developed a multi-functional piezoelectric device, i.e., smart aggregates, to use in early-age concrete strength monitoring, impact detection, and health monitoring of concrete structures. For the multi-functional PZT sensing, An and Sohn (2011) proposed an IIG technique to improve the detectability of various types of damages such as cracking, bolt loosening, and delamination.

4.10 Conclusion

In this chapter, the working principles and characteristics of piezoelectric transducers are described first, and then their fabrication process and applications are introduced. In particular, their applications to state-of-the-art SHM are highlighted. The direct and converse piezoelectricity effects of piezoelectric materials allow them to be used both for actuation and sensing applications, setting them apart from most conventional passive sensors.

With the excitation at our full disposal, not only can signal-to-noise ratio be improved but also subsequent signal processing, signal interpretation, and system identification become much straightforward. Furthermore, the nonintrusive nature, low cost, light weight, and good repeatability of the piezoelectric transducers make them attractive for SHM applications, where sensors often need to be permanently installed. However, when it comes to permanent installation and embedded sensing, future research should focus on addressing the long-term ruggedness, miniaturization, increased flexibility, and applications under high-temperature, high-strain, and high-radiation environments.

4.11 References

Acellent technologies, Inc. (2013), Available from: http://64.105.143.179/types.asp (Accessed 11 September 2013).

Ai Q, Liu C, Chen X, He P and Wang Y (2010), 'Acoustic emission of fatigue crack in pressure pipe under cyclic pressure', *Nucl Eng Des*, **240**(10), 3616–3620.

Akiyama M, Kamohara T, Kano K, Teshgahara A, Takeuchi Y and Kawahara N (2009), 'Enhancement of piezoelectric response in scandium aluminum nitride alloy thin films prepared by dual reactive cosputtering', *Adv Mater*, **21**(5), 593–596.

Alleyne D and Cawley P (1992), 'The interaction of Lamb waves with defects', *IEEE T Ultrason Ferr*, **39**(3), 381–397.

American Piezo Ceramics, Inc. (2013), Available from: http://americanpiezo.com (Accessed 11 September 2013).

An Y, Kim M and Sohn H (2012), 'Aircraft wing structure monitoring using integrated impedance and guided wave measurements', *Struct Control Hlth*, **19**(7), 592–604.

An Y, Lim H, Kim M, Yang J, Sohn H and Lee C (2013), 'Investigation of applicability of local reference-free damage detection techniques to *in-situ* bridges', *J Struct Eng-ASCE*, doi: 10.1061/(ASCE)ST. 1943–541X. 0000846.

An Y and Sohn H (2010), 'Instantaneous crack detection under varying temperature and static loading conditions', *Struct Control Hlth*, **17**(7), 730–741.

An Y and Sohn H (2011), 'Integrated impedance and guided wave based damage detection', *Mech Syst Signal Pr*, **28**(1), 50–62.

Balageas D, Fritzen C P and Guemes A (2006), *Structural Health Monitoring,* London, ISTE Ltd.

Banchet J, Sicard R, Chahbaz A and Goyette J (2004), 'Phased array for guided waves and crack detection for airframe structures', *P AIP*, **700**, 826–833.

Bent A, Hagood N and Rodgers J (1995), 'Anisotropic actuation with piezoelectric fiber composites', *J Intel Mat Syst Str*, **6**(3), 338–349.

Bertotti G and Mayergoyz I (2005), *The Science of Hysteresis*, New York, Academic Press.

Betz D, Thursby G, Culshaw B and Staszewski W (2003), 'Acousto-ultrasonic sensing using fiber Bragg gratings', *Smart Mater Struct*, **12**(1), 122–128.

Bhalla S and Soh C (2004), 'Electromechanical impedance modeling for adhesively bonded piezo-transducers', *J Intel Mat Syst Str*, **15**(12), 955–972.

Bois C and Hochard C (2004), 'Monitoring of laminated composites delamination based on electro-mechanical impedance measurement', *J Intel Mat Syst Str*, **15**(1), 59–67.

Birchmeier M, Gsell D, Juon M, Brunner A, Paradies R and Dual J (2009), 'Active fiber composites for the generation of Lamb waves', *Ultrasonics*, **49**(1), 73–82.

Boller C, Chang F and Fujino Y (2009), *Encyclopedia of Structural Health Monitoring*, Cambridge, John Wiley & Sons, Ltd.

Cady G (1922), 'The piezo-electric resonator', *P Ire*, **10**(2), 83–114.

Cady G (1964), *Piezoelectricity*, New York, Dover.

Carlyle J, Bodine H, Henley S, Dawes R, Demeski R and Hill E (1999), 'Practical AE methodology for use on aircraft, Acoustic Emission: standards and technology update', *ASTM Sp Tech P*, **1353**, 191–205.

Carpinteri A, Lacidogna G and Niccolini G (2006), 'Critical behaviour in concrete structure and damage localization by acoustic emission', *Key Eng Mat*, **312**(1), 305–310.

Carpinteri A, Lacidogna G and Pugno N (2007), 'Structural damage diagnosis and life-time assessment by acoustic emission monitoring', *Eng Fract Mech*, **74**(1–2), 273–289.

Cawley P and Alleyne D (1996), 'The use of Lamb waves for the long range inspection of large structures', *Ultrasonics*, **34**(2–5), 287–290.

Chaudhry Z, Joseph T, Sun F and Rogers C (1995), 'Local-area health monitoring of aircraft via piezoelectric actuator/sensor patches', *PSPIE*, **2443**, 268–276.

Chen X, Xu S, Yao N and Shi Y (2010), '1.6 V Nanogenerator for mechanical energy harvesting using PZT nanofibers', *Nano Lett*, **10**(1), 2133–2137.

Cho H, Lim J and Choi H (2001), 'Reliability-based fatigue failure analysis for causes assessment of a collapsed steel truss bridge', *Eng Fail Anal*, **8**(4), 311–324.

Choi W, Jeon Y, Jeong J, Sood R and Kim S (2005), 'Energy harvesting MEMS device based on thin film piezoelectric cantilevers', *J Electroceram*, **17**(2–4), 543–548.

Crawley E and de Luis J (1987), 'Use of piezoelectric actuators as elements of intelligent structures', *AIAA J*, **25**(10), 1373–1385.

Curie J and Curie P (1880), 'Développement par pression de l'électricitépôlairedans les cristauxhermièdres à faces inclines', *Cr Acad Sci*, **91**(1), 294.

Damjanovic D (1998), 'Ferroelectric, dielectric and piezoelectric properties of ferroelectric thin films and ceramics', *Rep Prog Phys*, **61**(9), 1267–1324.

Davies J and Cawley P (2009), 'The application of synthetic focusing for imaging crack-like defects in pipelines using guided waves', *IEEE T Ultrason Ferr*, **56**(4), 759–771.

Di Scalea F, Matt H, Bartoli I, Coccia S, Park G and Farrar C (2007), 'Health monitoring of UAV wing skin-to-spar joints using guided waves and macro fiber composite', *J Intel Mat Syst Str*, **18**(1), 373–388.

Donnelly N, Shrout T and Randall C (2007), 'Addition of a Sr, K, Nb (SKN) combination to PZT (53/47) for high strain applications', *J Am Ceram Soc*, **90**(2), 490–495.

Duffour P, Morbidini M and Cawley P (2006), 'A study of the vibro-acoustic modulation technique for the detection of cracks in metals', *J Acoust Soc Am*, **119**(3), 1463–1475.

Ericka M, Vasic D, Costa F, Poulin G and Tliba S (2005), 'Energy harvesting from vibration using a piezoelectric membrane', *J Phys IV Fr*, **128**(1), 187–193.

Fleming A and Leang K (2010), 'Integrated strain and force feedback for high-performance control of piezoelectric actuators', *Sensor Actuat A-Phys*, **161**(1–2), 256–265.

Fraden J (1996), *Handbook of Modern Sensors: Physics, Designs, and Applications*, 2nd Edition, New York, AIP Press.

Fromme P, Wilcox P, Lowe M and Cawley P (2006), 'On the development and testing of a guided ultrasonic wave array for structural integrity monitoring', *IEEE T Ultrason Ferr*, **50**(6), 699–709.

Giurgiutiu V (1999), 'Experimental investigation of E/M impedance health monitoring for spot-welded structural joints', *J Intel Mat Syst Str*, **10**(10), 802–812.

Giurgiutiu V (2008), *Structural Health Monitoring with Piezoelectric Wafer Active Sensors*, San Diego, Elsevier.

Giurgiutiu V and Bao J (2004), 'Embedded-ultrasonics structural radar for *in situ* structural health monitoring of thin-wall structures', *J Intel Mat Syst Str*, **3**(2), 121–140.

Giurgiutiu V, Zagrai A and Bao J (2002), 'Piezoelectric wafer embedded active sensors for aging aircraft structural health monitoring', *J Intel Mat Syst Str*, **1**(1), 41–61.

Gu H, Song G, Dhonde H, Mo Y and Yan S (2006), 'Concrete early-age strength monitoring using embedded piezoelectric transducers', *Smart Mater Struct*, **15**(6), 1837–1845.

Hao S (2010), 'I-35W bridge collapse', *J Bridge Eng*, **15**(5), 608–614.

Harley J, O'Donoughue N, Jin Y and Moura J (2009), 'Time reversal focusing for pipeline structural health monitoring', *P Meetings Acoust*, **8**, 1–8.

High J and Wilkie W (2003), *Method of Fabricating NASA-Standard Macro-Fiber Piezocomposite Actuators*, NASA/TM-2003–212427, ARL TR 2833.

Hutchins D, Jansen D and Edwards C (1993), 'Lamb-wave tomography using non-contact transduction', *Ultrasonics*, **31**(2), 97–103.

Ikeda T (1996), *Fundamentals of Piezoelectricity*, New York, Oxford University Press.

IEEE Standard on Piezoelectricity (1987), ANSI/IEEE. Std. 176.

Jaffe B (1971), *Piezoelectric Ceramics*, New York, Academic Press Inc.

Jan T, Firi E, Erwin K and Jana P (2010), *Fundamentals of Piezoelectric Sensorics: Mechanical, Dielectric, and Thermodynamical Properties of Piezoelectric Materials*, New York, Springer.

Jon S (2005), *Sensor Technology: Handbook*, Oxford, Elsevier.

Joosse P, Blanch M, Dutton A, Kouroussis D, Philippidis T and Vionis P (2002), 'Acoustic emission monitoring of small wind turbine blades', *J Sol Energ- T ASME*, **124**(4), 446–454.

Kawai H (1969), 'The piezoelectricity of poly (vinylidene Fluoride)', *Jpn J Appl Phys*, **8**(1), 975–976.

Kim I, Lee H and Kim J (2005a), 'Impact damage detection in composite laminates using PVDF and PZT sensor signals', *J Intel Mat Syst Str*, **16**(11–12), 1007–1013.

Kim S, Lee H, Lee N, Han C and Hwang J (2005b), 'Development and verification of PZT actuating micro tensile tester for optically functional materials', *Int J Control Autom*, **3**(3), 477–485.

Kim E, Kim M, Sohn H and Park H (2011a), 'Investigating electro-mechanical signals from collocated piezoelectric wafers for the reference-free damage diagnosis of a plate', *Smart Mater Struct*, **20**(6), 065001.

Kim M, Kim E, An Y, Park H and Sohn H (2011b), 'Reference-free impedance-based crack detection in plates', *J Sound Vib*, **330**(24), 5949–5962.

Kim S and Sohn H (2007), 'Instantaneous reference-free crack detection based on polarization characteristics of piezoelectric materials', *Smart Mater Struct*, **16**(6), 2375–2387.

Klein K, Safari R, Newnham R and Runt J (1986), 'Composite piezoelectric paints', *P IEEE 6th Int Symp Appl Ferroelectrics (ISAF-86)*, **1**, 285–287.

Kobayashi M, Jen C, Bussiere J and Wu K (2010), 'High-temperature integrated and flexible ultrasonic transducers for nondestructive testing', *NDT&E Int*, **42**(2), 157–161.

Koo K, Park S, Lee J and Yun C (2009), 'Impedance-based automated structural health monitoring incorporating effective frequency shift for compensating temperature effects', *J Intel Mat Syst Str*, **20**(4), 367–377.

Kurihara K and Masao K (2008), 'High-strain piezoelectric ceramics and application to actuators', *Ceram Int*, **34**(4), 695–699.

Lee C, Tai N and Hsieh S (2006), 'Synthesis of nano-sized polycrystalline PZT powders using molecular building blocks by designed chemical route', *J Nanopart Res*, **8**(2), 287–292.

Lee S and Sohn H (2010), 'Piezoelectric transducer self-diagnosis under changing environmental and structural conditions', *IEEE T Ultrason Ferr*, **57**(9), 2017–2027.

Lee H and Sohn H (2012), 'Damage detection for pipeline structures using optic-based active sensing', *Smart Struct Syst*, **9**(5), 461–472.

Leonard K, Malyarenko E and Hinders M (2002), 'Ultrasonic Lamb wave tomography', *Inverse Probl*, **18**(6), 1795–1808.

Leong W, Staszewski W, Lee B and Scarpa F (2005), 'Structural health monitoring using scanning laser vibrometry: III. Lamb waves for fatigue crack detection', *Smart Mater Struct*, **14**(6), 1387–1395.

Liang C, Sun F and Rogers C (1994), 'An impedance method for dynamic analysis of active material systems', *J Vib Acoust*, **116**(1), 120–128.

Lichtenstein A (1993), 'The silver bridge collapse recounted', *J Perform of Constr Fac*, **7**(4), 249–261.

Lim H, Kim M, Sohn H and Park C (2011), 'Impedance based damage detection under varying temperature and loading conditions', *NDT&E Int*, **44**(8), 740–755.

Lin B and Giurgiutiu V (2006), 'Modeling and testing of PZT and PVDF piezoelectric wafer active sensors', *Smart Mater Struct*, **15**(4), 1085–1093.

Lin M and Chang F (2002), 'The manufacture of composite structures with a built-in network of piezoceramics', *Compos Sci Technol,* **62**(7–8), 919–939.

Lowe M, Alleyne D and Cawley P (1998), 'Defect detection in pipes using guided waves', *Ultrasonics*, **36**(1–5), 147–154.

Luo W and Rose L (2007), 'Phased array focusing with guided waves in a viscoelastic coated hollow cylinder', *J Acoust Soc Am*, **121**(4), 1945–1955.

Lynch J and Loh K (2006), 'A summary review of wireless sensors and sensor networks for structural health monitoring', *Shock Vib Digest*, **38**(2), 91–128.

Machado J, Silva W, Xavier A and Thome Z (2000), 'An ultrasonic probe for NDT inspection of fuel assembly used in nuclear power plant reactors', *P 15th WCNDT*, **1**, 1–5.

Matsumoto E, Biwa S, Katsumi K, Omoto Y, Iguchi K and Shibata T (2004), 'Surface strain sensing with polymer piezoelectric film', *NDT&E Int*, **37**(1), 57–64

Mazille H, Roathea H and Tronel C (1995), 'An acoustic emission technique for monitoring pitting corrosion of austenitic stainless steels', *Corros Sci*, **27**(9), 1365–1375.

McLaskey G, Glaser S and Grosse C (2010), 'Beamforming array techniques for acoustic emission monitoring of large concrete structures', *J Sound Vib*, **329**(12), 2384–2394.

Measurement Specialties Inc. (2013), Available from: http://www.meas-spec.com (Accessed 11 September 2013).

Min J, Park S and Yun C (2010a), 'Impedance-based structural health monitoring using neural networks for autonomous frequency range selection', *Smart Struct Syst*, **19**(1), 125011.

Min J, Yun C, Park S and Song B (2010b), 'Development of a low-cost multifunctional wireless impedance sensor node', *Smart Struct Syst*, **6**(5–6), 689–709.

Osmont D, Dupont M, Gouyon R, Lemistre M and Balageas D (2000), 'Piezoelectric transducer network for dual-mode (active/passive) detection, localization, and evaluation of impact damages in carbon/epoxy composite plates', *P SPIE*, **4073**, 130–137.

Overly T, Park G, Farinholt H and Farrar, C (2009), 'Piezoelectric active-sensor diagnostics and validation using instantaneous baseline data', *IEEE Sens J*, **9**(11), 1414–1421.

Park C, Park J and Lee Y (2010a), 'Modeling and characterization of piezoelectric d_{33} –mode MEMS energy harvester', *J Microelectromech S*, **19**(5), 1215–1222.

Park H, Sohn H, Law K and Farrar C (2006a), 'Time reversal active sensing for health monitoring of a composite plate', *J Sound Vib*, **302**(1–2), 50–66.

Park H, Sohn H, Yun C, Chung J and Kwon I (2010b), 'A wireless guided wave excitation technique based on laser and optoeletronics', *Smart Mater Struct*, **5**(5–6), 749–765.

Park S, Ahmad S, Yun C-B and Roh Y (2006b), 'Multiple crack detection of concrete structures using impedance-based structural health monitoring techniques', *Exp Mech*, **46**(5), 609–618.

Park S, Yun C, Roh Y and Lee J (2006c), 'PZT-based active damage detection techniques for steel bridge components', *Smart Mater Struct*, **15**(4), 957–966.

Perelli A, Marchi L, Marzani A and Speciale N (2012), 'Acoustic emission localization in plates with dispersion and reverberations using sparse PZT sensors in passive mode', *Smart Mater Struct*, **21**(2), 025010.

Piezo Systems Inc. (2013), Available from: http://piezo.com (Accessed 11 September 2013).

Piezodevices Inc. (2013), Available from: http://www.piezodevices.com (Accessed 11 September 2013).

Pitchford C, Grisso B and Inman D (2007), 'Impedance-based structural health monitoring of wind turbine blades', *PSPIE*, **6532**, 1–11.

Physik PI Inc. (2013), Catalog. Available from: http://www.physikinstrumente.com/en/products (Accessed 11 September 2013).

Popovics J, Song W, Ghandehari M, Subramaniam K, Achenbach J and Shah S (2000), 'Application of wave transmission measurements for crack depth determination in concrete', *ACI Mater J*, **97**(2), 127–135.

Priya S (2007), 'Advances in energy harvesting using low profile piezoelectric transducers', *J Electroceram*, **19**(1), 167–184.

Prosser W, Gorman M and Humes D (1999), 'Acoustic emission signals in thin plates produced by impact damage', *J Acoust Emitt*, **17**(1–2), 29–36.

Qing X, Beard S, Kumar A, Ooi T and Chang F (2007), 'Built-in sensor network for structural health monitoring of composite structure', *J Intel Mat Syst Str,* **18**(1), 39–49.

Qing X, Chan H, Beard S, Ooi T and Marotta S (2006), 'Effect of adhesive on the performance of piezoelectric elements used to monitor structural health', *Int J Adhes Adhes*, **26**(8), 622–628.

Rabinovitch O and Vinson J (2002), 'Adhesive layer effects in surface-mounted piezoelectric actuators', *J Intel Mat Syst Str*, **13**(11), 689–704.

Raghavan A and Cesnik C (2007), 'Review of guided-wave structural health monitoring', *Shock Vib Dig*, **39**(2), 91–114.

Reddy S, Singh P, Raghu N and Kumar V (2002), 'Effect of type of solvent and dispersant on NANO PZT powder dispersion for tape casting slurry', *J Mat Sci*, **37**(5), 929–934.

Rose J (1999), *Ultrasonic Waves in Solid Media*, Cambridge, Cambridge University Press.

Roundy S and Wright P (2004), 'A piezoelectric vibration based generator for wireless electronics', *Smart Mater Struct*, **13**(5), 1131–1142.

Saint-Pierre N, Jayet Y, Perrissin-Fabert I and Baboux J (1996), 'The influence of bonding defects on the electric impedance of a piezoelectric embedded element', *J Phys D Appl Phys*, **29**(12), 2976–2982.

Schulz M and Sundaresan (2006), Smart sensor system for structural condition monitoring of wind turbines: Subcontract Report NREL/SR-500–40089, National Renewable Energy Laboratory, USA.

Sinha N, Wabiszewski G, Mahameed R, Felmetsger V, Tanner S, Carpick R and Piazza G (2009), 'Ultra-thin AIN piezoelectric nano-actuators', *15th Int Conf Solid-State Sensors*, **1**, 469–472.

Sirohi J and Chopra I (2000), 'Fundamental understanding of piezoelectric strain sensors', *J Intel Mat Syst Str*, **11**(4), 246–257.

Shiegeishi M, Colombo S, Broughton K, Rutiedge H, Batchelor A and Forde M (2001), 'Acoustic emission to assess and monitor the integrity of bridges', *Constr Build Mater*, **15**(1), 35–49.

Smart Materials, Corp. (2013), Available from: http://www.smart-material.com (Accessed 11 September 2013).

Soh C, Tseng K, Bhalla S and Gupta A (2000), 'Performance of smart piezoceramic patches in health monitoring of a RC bridge', *Smart Mater Struct*, **9**(4), 533–542.

Sohn H (2007) 'Effects of environmental and operational variability on structural health monitoring', *Philos T R Soc A Struct Health Monit*, **335**(1851), 539–560.

Sohn H, DeSimio M, Olson S, Brown K and Derriso M (2011a), 'Impact localization in an aircraft fuselage using laser based time reversal', *PSPIE*, 79841G, 1–11.

Sohn H, Dutta D, Yang J, Park H, DeSimio M, Olson S and Swenson E (2011b), 'Delamination detection in composites through non-contact guided wave imaging', *Compos Sci Technol*, **71**(9), 1250–1256.

Sohn H and Kim S (2010), 'Development of dual PZT transducer for reference-free crack detection in thin plate structures', *IEEE T Ultrason Ferr*, **57**(1), 229–240.

Sohn H and Lee S (2010), 'Lamb wave tuning curve calibration for surface-bonded piezoelectric transducers', *Smart Mater Struct*, **19**(1), 015007.

Sohn H, Park H, Law K and Farrar C (2007), 'Damage detection in composite plates by using an enhanced time reversal method', *J Aerospace Eng*, **20**(3), 141–151.

Song G, Gu H and Mo Y (2008), 'Smart aggregates: multi-functional sensors for concrete structures – a tutorial and a review', *Smart Mater Struct*, **17**(3), 033001.

Song G, Gu H, Mo Y, Hsu T and Dhonde H (2007a), 'Concrete structural health monitoring using embedded piezoceramic transducers', *Smart Mater Struct*, **16**(4), 959–968.

Song G, Olmi C and Gu H (2007b), 'An overheight vehicle-bridge collision monitoring system using piezoelectric transducer', *Smart Mater Struct*, **16**(2), 462–468.

Staszewski W, Boller C and Tomlinson G (2004a), *Health Monitoring of Aerospace Structures: Smart Sensor Technologies and Signal Processing*, England, John Wiley & Sons, Ltd.

Staszewski W, Lee B, Mallet L and Scarpa F (2004b), 'Structural health monitoring using scanning laser vibrometry: I. Lamb wave sensing', *Smart Mater Struct*, **13**(2), 251–260.

Stepinski T, Wu P, Gustafsson M and Ericsson L (1998), 'Ultrasonic array technique for the inspection of copper lined canisters for nuclear waste fuel', *7th Europ Conf Non-destruct Testing (Session: Nuclear Industry)*, **3**, 1–7.

Sundaresan M, Schulz M and Ghoshal A (2002), Structural health monitoring static test of a wind turbine blade: Subcontract Report, NREL/SR-500–28719, National Renewable Energy Laboratory, USA.

Takeda N, Okabe Y, Kuwahara J, Kojima S and Ogisu T (2005), 'Development of smart composite structures with small-diameter fiber Bragg grating sensors for damage detection: Quantitative evaluation of delamination length in CFRP laminates using Lamb wave sensing', *Compos Sci Technol*, **65**(15–16), 2575–2587.

Turner R, Fuierer P, Newnham R and Shrout T (1994), 'Materials for high temperature acoustic and vibration sensors: A review', *Appl Acoust*, **41**(4), 299–324.

Vautier B and Meheimani S (2005), 'Charge driven piezoelectric actuators for structural vibration control: issues and implementation', *Smart Mater Struct*, **14**(4), 575–586.

Wait J and Todd M (2007), 'Validation of macro fiber composites as strain sensors', *PIMAC-XXV*, **20533**, 1–12.

Wang Z and Xu Y (2007), 'Vibration energy harvesting device based on air-spaced piezoelectric cantilevers', *Appl Phys Lett*, **90**(26), 263512.

Weng M, Dun S, Hartt W and Brown R (1982), 'Application of acoustic emission to detection of reinforcing steel corrosion in concrete', *Corrosion*, **38**(1), 9–14.

White J, Poumeyrol B, Hale J and Stephenson R (2004), 'Piezoelectric paint: Ceramic-polymer composites for vibration sensors', *J Mater Sci*, **39**(9), 3105–3114.

Williams R, Park G, Inman D and Wilkie W (2002), 'An overview of composite actuators with piezoceramic fibers', *P IMAC*, **4753**, 421–427.

Yan W, Wang J and Chen W (2011), 'Delamination assessment of a laminated composite beam using distributed piezoelectric sensor/actuator', *Smart Mater Struct*, **20**(1), 075011.

Yi J and Liang H (2008), 'A PVDF-based deformation and motion sensor: modeling and experiments', *IEEE Sens J*, **8**(4), 384–391.

Zhang W, Ye H and Xiong R (2009), 'Metal-organic coordination compounds for potential ferroelectrics', *Coordin Chem Rev*, **253**(23–24), 2980–2997.

Zhang Y (2006), '*In situ* fatigue crack detection using piezoelectric paint sensor', *J Intel Mat Syst Str*, **17**(10), 843–852.

Zhao X, Gao H, Zhang G, Ayhan B, Yan F, Kwan C and Rose J (2007), 'Active health monitoring of an aircraft wing with embedded piezoelectric sensor/actuator network: I. Defect detection, localization and growth monitoring', *Smart Mater Struct*, **16**(4), 1208–1217.

Zhou D, Ha D and Inman D (2010), 'Ultra low-power active wireless sensor for structural health monitoring', *Smart Struct Syst*, **6**(5–6), 675–687.

5

Fiber optic sensors for assessing and monitoring civil infrastructures

K. J. PETERS, North Carolina State University, USA, and
D. INAUDI, SMARTEC S.A. Switzerland

DOI: 10.1533/9780857099136.121

Abstract: In this chapter we present a technical description of fiber optic sensors including point, multiplexed, long-base, and distributed sensors, and their advantages. In particular we highlight the sensing capabilities that have no parallel in conventional sensors. To provide a background, this chapter first presents the properties of optical fibers and internal parameters that can be exploited to sense changes in their surroundings such as strain and temperature. Practical considerations in the deployment of such sensors in structural applications are also listed. Next, the sensing mechanisms of conventional fiber optic sensors and their applications to structural monitoring are summarized. Finally, new capabilities for fiber optic sensors enabled by recent advances in optical fiber technology and instrumentation are introduced.

Key words: strain sensing, temperature sensing, sensor multiplexing, distributed sensing.

5.1 Introduction

From many points of view, fiber optic sensors (FOSs) are the ideal transducers for structural health monitoring. Being durable, stable, and insensitive to external perturbations, they are especially useful for long-term health assessments of civil structures, geostructures, and aerospace structures. Many different FOS technologies exist and offer a wide range of performances and suitability for different applications. In the last few years, FOSs have made a slow but significant entrance in the sensor panorama. After an initial euphoric phase, when FOSs seemed on the verge of becoming prevalent in the world of sensing, it now appears that this technology is mainly attractive in cases where it offers superior performance compared with the more proven conventional sensors. The additional value can include an improved quality of measurements, a better reliability, the possibility of replacing manual readings and operator judgment with automatic measurements, an easier installation and maintenance, or a lower lifetime cost.

© 2014 Woodhead Publishing Limited

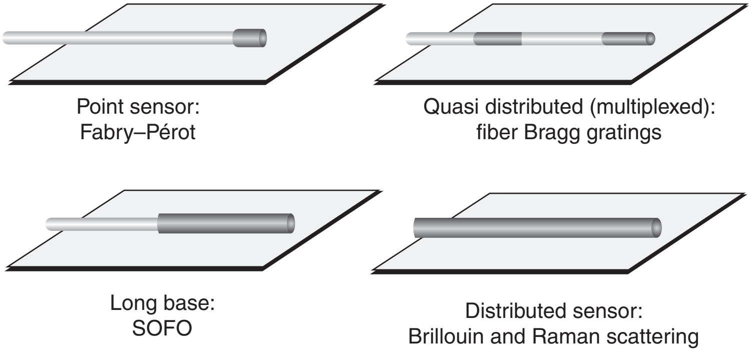

5.1 Fiber optic sensor types. (SOFO - surveillance d'ouvrages par senseurs à fibres optiques (structural monitoring by fiber optic sensors).)

Finally, distributed fiber sensors offer new exciting possibilities that have no parallel in conventional sensors.

A great variety of FOSs exist for structural and geotechnical monitoring. Figure 5.1 illustrates the four main types of FOSs:

- *Point sensors* have a single measurement point at the end of the fiber optic connection cable, similarly to most electrical sensors.
- *Multiplexed sensors* allow the measurement at multiple points along a single fiber line.
- *Long-base sensors* integrate the measurement over a long measurement base. They are also known as long-gage sensors.
- *Distributed sensors* are able to sense at any point along a single fiber line, typically every meter over many kilometers of length.

The greatest advantages of the FOSs are intrinsically linked to the optical fiber itself, that is either used as a link between the sensor and the signal conditioner, or becomes the sensor itself in the case of long-gage and distributed sensors. In almost all FOS applications, the optical fiber is a thin glass fiber that is protected mechanically by a polymer coating (or a metal coating in extreme cases) and further protected by a multi-layer cable structure designed to protect the fiber from the environment where it will be installed. Since glass is an inert material very resistant to almost all chemicals, even at extreme temperatures, it is an ideal material for use in harsh environments, such as are encountered in geotechnical applications. Chemical resistance is a great advantage for long-term reliable health monitoring of civil engineering structures, making FOSs particularly durable. Since the light confined in the core of the optical fibers used for sensing purposes does not interact with any surrounding electromagnetic field, FOSs are intrinsically immune to any electromagnetic (EM) interference.

With such unique advantage over sensors using electrical cables, FOSs are obviously the ideal sensing solution when the presence of EM, radio frequency, or microwaves cannot be avoided. For instance, FOSs will not be affected by any electromagnetic field generated by lightning hitting a monitored bridge or dam, nor from the interference produced by a subway train running near a monitored zone. FOSs are intrinsically safe and naturally explosion-proof, making them particularly suitable for monitoring applications of risky structures such as gas pipelines, coal mines, or chemical plants. But the greatest and most exclusive advantage of such sensors is their ability to offer long range distributed sensing capabilities or large networks of multiplexed sensors.

5.2 Properties of optical fibers

In this section we review basic characteristics of optical fibers and their relevance to sensing parameters. In addition, practical issues of packaging and connecting optical fiber sensors are discussed.

5.2.1 Optical fiber concepts

Optical fibers generally consist of a fused silica (SiO_2) core and cladding. During drawing of the optical fiber, dopants are added to the silica to provide an index of refraction distribution throughout the cross-section of the optical fiber,[1] with the core index normally higher than the cladding. Typical core diameters are 5–10 μm for single-mode optical fibers and greater than 50–200 μm for multi-mode optical fibers. The cladding diameter for almost all single-mode optical fibers is standardized at 125 μm to permit easy interconnection. Small diameter fibers (80 μm) have also been developed for sensing applications.[2] The small diameter makes the fiber sensor less invasive when the fiber is embedded in a host material system, and increases the sensitivity of the sensor to applied loads. It can also allow smaller bending radii.

The cross-section of a step-index optical fiber is shown in Fig. 5.2. The index of refraction distribution is only a function of the radius with

$$\begin{aligned} n(r,\theta) &= n_1 \qquad r \le a \\ n(r,\theta) &= n_2 \quad a < r \le b \end{aligned} \tag{5.1}$$

In order for propagation of guided lightwaves to occur, $n_1 > n_2$. The index of refraction difference between the core and cladding is typically less than 1%.[3]

Each component of the lightwave propagating along the fiber in the z direction has the form,

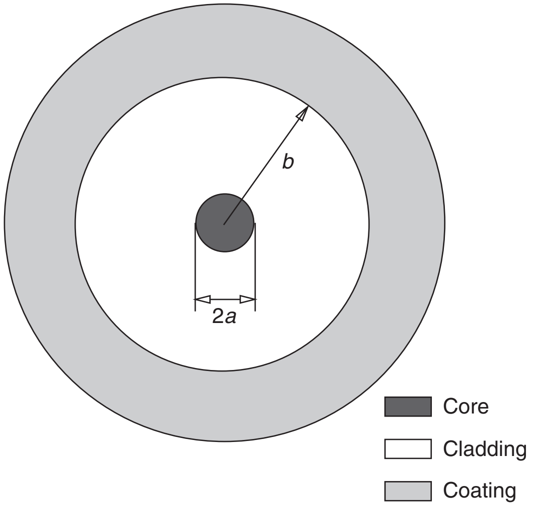

5.2 Cross-section of step-index optical fiber. Figure not to scale.

$$\psi(r,\theta,z,t)=\bar{\psi}(r,\theta)\mathrm{e}^{i(\omega t-\beta z)} \qquad [5.2]$$

where $\bar{\psi}(r,\theta)$ is the energy distribution in the plane perpendicular to the propagation direction, ω is the angular frequency ($\omega = 2\pi c/\lambda$ where c is the speed of light in a vacuum and λ is the free-space wavelength of the lightwave), t is time, and β is the propagation constant of the mode (phase shift per unit length). Each propagating mode has an effective index of refraction, $n_{\mathrm{eff}} = \beta\lambda/(2\pi)$. n_{eff} corresponds to the index of refraction of an equivalent homogeneous material for which the wave would propagate with the same propagation constant β as through the step-index fiber. For guided modes, $n_2 < n_{\mathrm{eff}} < n_1$. The effective index of refraction n_{eff}, or mode propagation constant β, will play a critical role in the response of many optical fiber sensors. Although the step-index fiber is the easiest for which to analyze mode propagation, most commercially available optical fibers have different index distributions as shown in Fig. 5.3.[1] While most optical fiber manufacturers do not provide detailed information on the index distributions, they do provide data such as the core radius, design operating wavelength, and n_{eff} at common wavelengths (see for example Reference 4). From this information, the user can calculate the response of the optical fiber sensor using the same principles as for the step-index fiber.

The number of guided modes that can propagate through the optical fiber at a particular wavelength depends upon the normalized frequency at that wavelength, V,

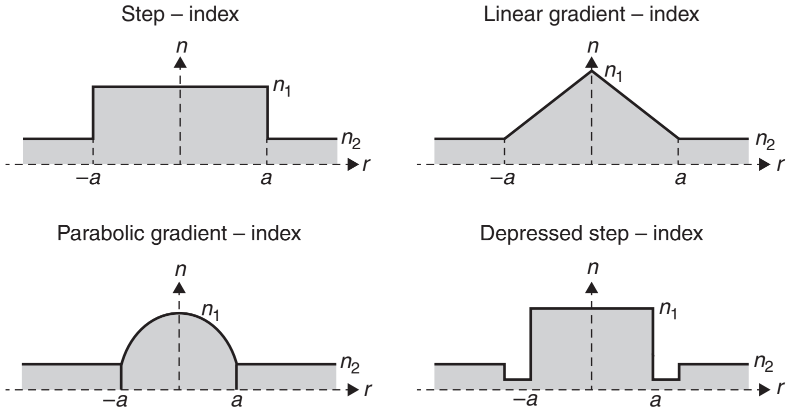

5.3 Common fiber index of refraction profiles.

$$V = \frac{2\pi}{\lambda} a \sqrt{n_1^2 - n_2^2} \qquad [5.3]$$

The first mode, also called the fundamental mode, propagates at all values of V. All other modes have a cutoff value of V below which it cannot propagate. The cutoff value for the second mode is at $V = 2.4048$. Therefore, for $V < 2.4048$ the fiber is referred to as a single-mode fiber, and for $V > 2.4048$ the fiber is referred to as a multi-mode fiber. For several sensing technologies it is important to utilize fibers that are single-mode at the wavelength to be interrogated so that the mode of propagation and coupling are well-defined. Additionally, the fundamental mode is the least affected by bending losses, as the energy is concentrated in the center of the fiber. Multi-mode sensors do exist and are generally easier to practically couple to instrumentation as the fiber core is larger and the modes are more spread out throughout the fiber cross-section.[5–10]

Finally, additional modes, called cladding modes, are possible due to the interface condition between the outer diameter of the fiber and the surrounding medium, typically polymer coating or air. The form of these modes depends upon the index of refraction of the surrounding medium, n_3, and is present in the case of $n_3 < n_2$. The cladding modes can be excited locally in long period grating (LPG) sensors and exploited for the measurement of cure monitoring, chemical, or environmental sensing.[11]

A second important class of optical fibers applied for sensing is high-birefringence fibers, also referred to as polarization maintaining (PM) fibers.[12] PM fibers present an index profile that is not rotationally symmetric and therefore propagate two separate, linearly polarized fundamental modes (LP_{01}) at two separate propagation constants, β_1 and β_2. The modes are polarized about orthogonal axes, referred to as the fast and slow axes. As the polarization axes are orthogonal, the two modes do not interfere with one another as they propagate along the optical fiber. These orthogonal modes can be used to independently measure multiple parameters. In other cases, only one of the two polarizations propagates, while the other is suppressed.

Standard fused silica fibers are linear elastic until failure for the following material properties: the elastic modulus $E = 72$ GPa, Poisson's ratio $\nu = 0.20$, and thermal expansion coefficient $a = 5.5 \times 10^{-7}/°C$.[13] Typical elongation at failure is 2–5%. A second common material class used for optical fibers is polymers. Polymer optical fibers (POF) have considerably lower stiffness than silica fibers, with $E = 2.4–3.0$ GPa and $\nu = 0.34$.[14] Their stress–strain response is also extremely sensitive to strain rate, temperature, humidity, and hysteresis effects. POF fibers can have elongations at failure of up to 100% or more.

The attenuation spectrum of a silica optical fiber can be seen in Fig. 5.4. Three primary transmission windows are therefore used in telecommunication applications: around (1) 850 nm, (2) 1300 nm, and (3) 1550 nm. The same three transmission windows are typically used for optical fiber sensors due to the relative low-cost, wide selection, and high quality of components including optical fibers, couplers, and laser sources available for telecommunications applications. POFs demonstrate considerably more attenuation at near-infrared wavelengths than fused silica fibers;[14] therefore POF sensors most often operate in the visible wavelength ranges.

5.2.2 Sensing mechanisms

External sensing parameters are generally encoded into changes within lightwaves propagating through an optical fiber in one of four manners,

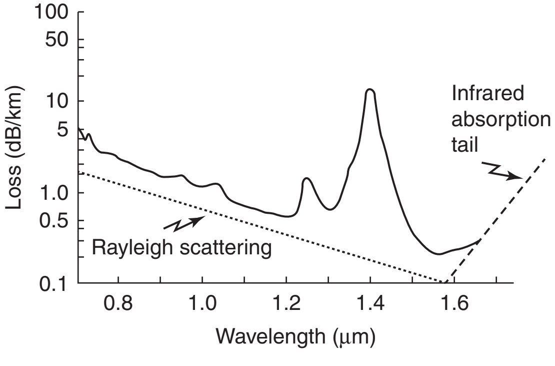

5.4 Material attenuation losses as a function of wavelength for fused silica (SiO_2).[1]

summarized in Fig. 5.5. The intensity of the lightwave propagating through an optical fiber can be modified through microbending of the optical fiber, a change in coupling from the fundamental mode to other non-guided modes, fracture of the optical fiber, or a change in power coupled into the fiber or from one fiber to another. Measuring the intensity of the propagating lightwave is relatively simple; however, light sources themselves often fluctuate in intensity. Feedback control loops can be applied to reduce these fluctuations, or the illuminating lightwave divided to create a reference intensity, as shown in Fig. 5.6a. Under these conditions, intensity-based sensors can provide absolute measurements, meaning that they are insensitive to power interruptions between data collections. One drawback to intensity-based sensors, however, is that they cannot be multiplexed for sensor networks.

The application of strain or temperature to an optical fiber changes the optical path length traversed by the lightwave as it propagates a distance L through the fiber, $n_{eff}L$. As the phase of the lightwave cannot be measured directly, the lightwave is generally re-combined with a reference lightwave from the same laser source (so that the two are coherent). When the reference lightwave is not exposed to the parameter to be measured, the relative

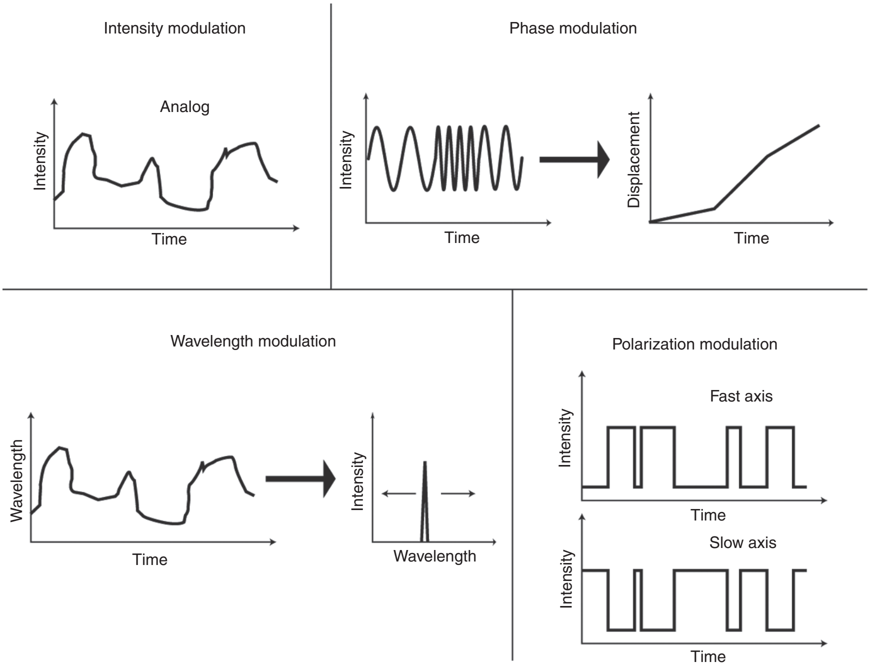
Intensity modulation
Analog
Intensity
Time
Phase modulation
Intensity
Time
Displacement
Time
Wavelength modulation
Wavelength
Time
Intensity
Wavelength
Polarization modulation
Fast axis
Intensity
Time
Slow axis
Intensity
Time

5.5 Output signals of optical fiber sensors using four primary sensing mechanisms.

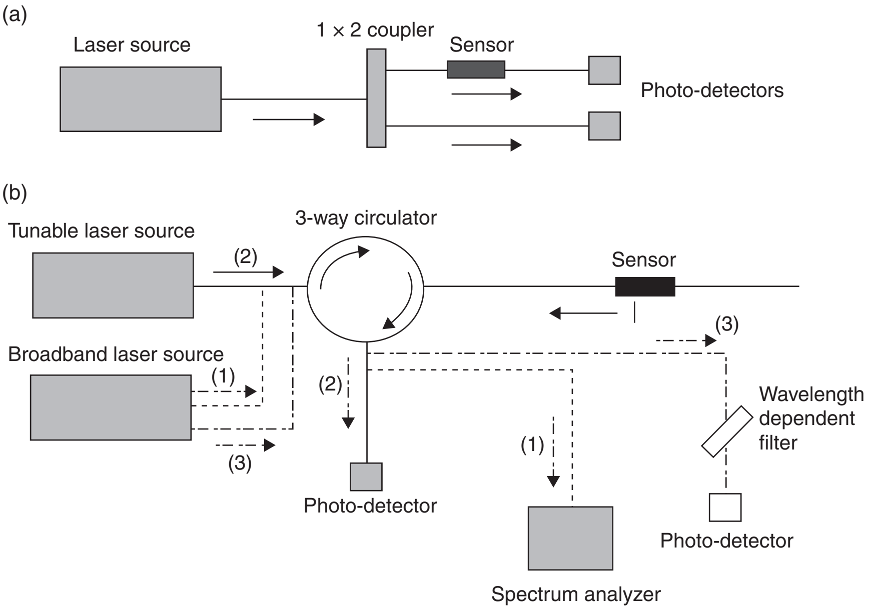
(a)
Laser source
1 × 2 coupler
Sensor
Photo-detectors
(b)
Tunable laser source
3-way circulator
Sensor
(2)
Broadband laser source
(1)
(3)
(2)
(3)
Wavelength dependent filter
(1)
Photo-detector
Photo-detector
Spectrum analyzer

5.6 Sensor interrogation schemes for (a) intensity-based sensors and (b) wavelength (frequency)-based sensors. For (b), three different possible schemes are shown. See text for details.

phase shift between the signals can be related to the applied strain or temperature. The phase modulation is extremely sensitive to strain and therefore can provide very accurate measurements;[15] however, the measurement of phase shift is not absolute due to the signal periodicity and is therefore affected by power interruptions between data collections. Techniques to alleviate these problems, such as low-coherence interferometry, are discussed later in this chapter. The reference signal can be completely sheltered from external parameters, or used for compensation of unwanted measurands such as temperature, if both fibers are exposed to them.

External sensing parameters can also be converted into spectral information of the lightwave, for example using fiber Bragg gratings (FBG) or Fabry–Pérot interferometers. Such sensors typically act as filters, transmitting certain wavelengths and radiating or reflecting others. Changes in external parameters are therefore converted into a wavelength shift of the transmitted or reflected spectrum of the sensor. A typical signal is shown in the example of Fig. 5.5, for which the reflected wavelength is changing with time. The wavelength encoded signal must then be interpreted, which is commonly performed in using one of three methods: (1) by launching a broadband of light into the fiber and applying a spectrum analyzer to select the reflected wavelength; (2) by applying a tunable laser for which the output wavelength can be scanned while the reflected intensity is measured by a photodetector; or (3) by launching a broadband of light and using a wavelength dependent filter to identify the reflected wavelength (see Fig. 5.6b).

A final method to encode sensing information for transmission through an optical fiber is through the polarization state of the propagating lightwave.[15–17] For the example shown in Fig. 5.5, the power of a lightwave propagating through a PM fiber is transferred between the mode polarized about the fast axis and the mode polarized about the slow axis. The power in each mode can be determined by applying a polarizing filter or splitter to the output signal. As mentioned above, the two modes propagating through a PM fiber do not normally transfer power as they propagate, since they are orthogonally polarized. However, external stimuli such as pressure or twisting of the optical fiber will induce transfer between the two modes.

5.2.3 Sensor packaging

Traditional fiber optic cable design aims at the best possible protection of the fiber itself from any external influence. In particular, it is necessary to shield the optical fiber from external humidity, side pressures, crushing, and longitudinal strain applied to the cable. These designs have proven very effective in guaranteeing the longevity of optical fibers used for communication and can be used as sensing elements for monitoring temperatures in the –20°C to +60°C range e.g. in conjunction with Brillouin or Raman distributed sensing systems.

However, many of the measurement techniques described in Section 5.2.2 require that the sensing part of the optical fiber is exposed to the parameter to be measured. This creates a challenge for the sensor designer, to protect the sensor from damage resulting from manipulation and exposure to the environment while at the same time allowing a faithful transfer of the measurand from the object under monitoring to the optical fiber.[18,19]

Special cable designs using non-standard coatings and buffers are required for sensing temperatures below –20°C or above +60°C, especially for Brillouin scattering systems, where it is important to guarantee that the optical fiber does not experience any strain that could be misinterpreted as a temperature change due to the cross-sensitivity between strain and temperature.

For strain and deformation sensors, the packaging must faithfully transfer the structural strain to the optical fiber, a goal contradicting all experience from telecommunication cable design where the exact opposite is required. This can be achieved by a continuous mechanical coupling between the sensor and the structure e.g., by continuously gluing the fiber to a steel beam, or by a local coupling at the ends of the sensing zone.[20]

All sensor packaging designs share common reliability goals independently from the sensing technique and application domain used:

- The optical fibers must be compatible with the selected sensing system: single-mode or multi-mode.
- The fibers must be protected from external mechanical actions during installation and while in use. In particular, the cable design must allow easy manipulation without the risk of fiber damage.
- The cable design must allow sufficient shielding of the optical fibers from chemical aggression by humidity, water, and other harmful substances.
- All optical losses must be kept as low as possible in order not to introduce degradation to the instrument's performances.
- Installation of connectors and repair of damaged sensors should be compatible with field operations.

5.2.4 Cables, connectors, and splicing

The above considerations on sensor packaging also apply to the interconnection cables, connectors, and splices. In most cases it is however possible to borrow tools and techniques widely used in the telecommunication industry. Cables with different levels of protection are to be used depending on their location: indoor, outdoor, overhead, rodent-resistant, compatible with extreme temperatures, presence of radiation, or chemically aggressive environments.

Standard telecom connectors can be used in junction boxes, but more rugged versions for direct exposure to the elements also exist. Examples include outdoor and waterproof connectors, up to extreme cases such as deep-water remotely operated underwater vehicle (ROV)-matable connectors. Splicing is considered a more reliable way to permanently interconnect optical fibers, but requires tools and expertise that are not always compatible with field conditions. Therefore, an accurate analysis of the project will lead to the appropriate choice of a connector, a splice, or a very long cable.

5.3 Common optical fiber sensors

We now present examples of the most common optical fiber sensors applied to civil infrastructure systems. The sensors are divided into categories based on the mechanism used to convert the sensing parameters into a measurement.

5.3.1 Coherent interferometers

Butter and Hocker[21] demonstrated the first in-fiber strain sensor. This 'fiber optics strain gage' was based on the measurement of the change in phase shift of a lightwave propagating through an optical fiber. The phase shift was due to applied axial strain through both the elongation of the optical fiber and the material property change of the silica with strain. The phase shift measurement replicated a conventional bulk optic coherent interferometer. Coherent, in-fiber interferometric sensors such as this present an extremely high sensitivity to external parameters. Additionally, as the optical fiber itself is used as the measurement device, such sensors are beneficial for simplicity and cost when compared to other optical fiber-based sensors.

Applying an axial tension to an optical fiber of length L, with a resulting axial strain ε, and a uniform temperature change, ΔT, along the entire optical fiber, we find the change in phase shift, $\Delta\varphi$, of a lightwave propagating through the fiber by:

$$\Delta\varphi = \frac{2\pi}{\lambda} n_{\text{eff}} L \left\{ \varepsilon - \frac{1}{2}\varepsilon n_{\text{eff}}^2 \left[p_{12} - \nu\left(p_{11} + p_{12}\right)\right] + \frac{1}{n_{\text{eff}}}\frac{dn_{\text{eff}}}{dT}\Delta T \right. \\ \left. + \frac{n_{\text{eff}}^2}{2}\left(p_{11} + 2p_{12}\right)\alpha\Delta T \right\} \qquad [5.4]$$

where λ is the wavelength of the lightwave.[22] The phase shift is therefore linearly proportional to the applied strain and the applied temperature change. Typical material property values for fused silica are $p_{11} = 0.17$, $p_{12} = 0.36$, $a = 0.5 \times 10^{-6}$ °C^{-1}, and $dn_{\text{eff}}/dT = 1.2 \times 10^{-5}$ °C^{-1}.[22]

The above equations consider a constant strain field applied along the gage length of the optical fiber. In general, the fiber can be mounted in any orientation on a surface, therefore these strain components can also vary along the length of the gage. We find the total phase shift by integrating the local phase shift along the optical fiber

$$\varphi = \int_0^L \left(\frac{d\varphi}{ds}\right) ds = \left(\frac{2\pi}{\lambda}\right) \int_0^L n_{\text{eff}}\left(1 - p_e\right)\left(1 + \varepsilon_n\right) ds \qquad [5.5]$$

where ε_n is the strain component tangent to the fiber path at each location and s is the variable along the path length.[23] The transfer of shear stress and transverse stresses are negligible for surface mounted sensors, however, these components could be significant for sensors embedded in materials.[22,24]

When using an optical fiber as strain sensor, it is not possible to measure the phase shift directly; therefore, we typically measure the interference between the sensor fiber and a second reference fiber that is not exposed to the environmental changes and therefore has a constant phase. Additionally, this second fiber can be exposed to only some of the loading, for example temperature, so as to provide compensation during the measurements. The interferometric measurement of phase shifts for in-fiber sensors parallels that for classical free-space interferometers. The two most commonly applied interferometric arrangements are the Mach-Zehnder and Michelson interferometers.[25] Figures 5.7 and 5.8 show each of these classical interferometers and their equivalent for in-fiber sensors. These are typical examples of long-base sensors.

Assuming that the light source has a high coherence length, and polarization effects are compensated between the two fibers, the average intensity of the interference pattern varies sinusoidally, as shown in Fig. 5.9. The cyclic form of the intensity measurement presents two challenges when the intensity is near one of the quadrature points i.e., where $dI/d\varphi = 0$. The first challenge is that the direction of fringe movement cannot be

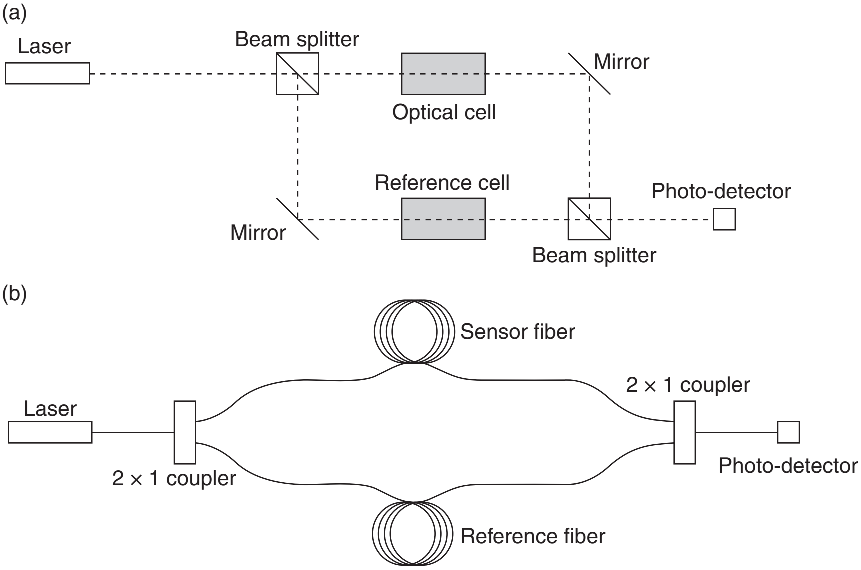

5.7 Schematic of Mach-Zehnder interferometer: (a) free-space optics version measures the difference in optical path length through the optical cell and reference cell and (b) in-fiber version measures the difference in optical path length through sensor fiber and reference fiber.

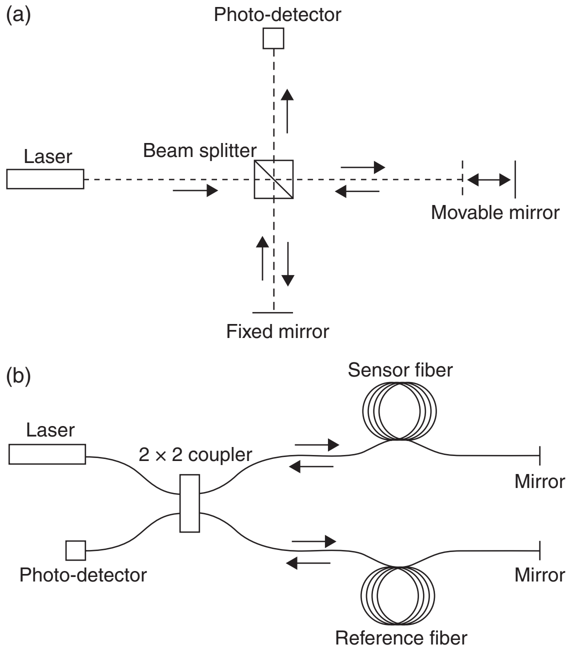

5.8 Schematic of Michelson interferometer: (a) free-space optics version and (b) in-fiber version.

determined at the quadrature point (directional ambiguity), and the second is that the measurement sensitivity goes to zero at the same point (signal fading). A variety of signal processing techniques have been applied to remove these difficulties, generally categorized into passive and active demodulation.[26–28] One example of a passive homodyne demodulation is shown in Fig. 5.9. For this example, the sensor lightwave is divided into two channels, with one phase shifted by 90°, and the other interfered with the reference lightwave. When one signal is near a quadrature point, the other is at the point of maximum sensitivity, removing both the signal fading and directional ambiguity issues.

Furthermore, the measurement of phase shift is not an absolute measurement. Specifically, in order to know the current strain level, the system must be continually operated throughout the lifetime of the structure with a sufficient data acquisition frequency to catch every shift of more than half wavelength. This presents significant challenges for continuous monitoring of structures, since power interruptions lead to a loss of the zero point calibration. One solution to this problem is through low-coherence interferometry, which will be described in the following section. Another challenge is multiplexing interferometric based sensors. Kersey[29] reviews multiplexing

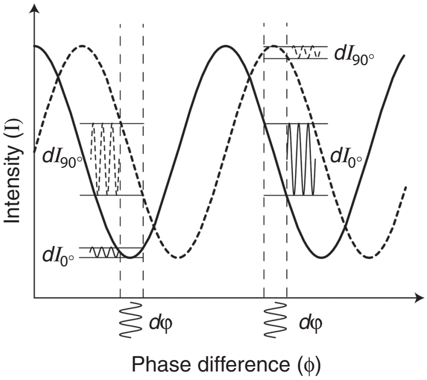

5.9 Intensity signals as a function of interferometer phase difference for two sensor signals, phase shifted by 0° and 90°. When one signal is as a quadrature point ($dI/d\varphi = 0$), the other is at the location of maximum sensitivity. (*Source*: Adapted from Reference 25.)

strategies for interferometric optical fiber sensors, including time-division multiplexing (TDM) and frequency-division multiplexing examples.

5.3.2 Low-coherence interferometers

The light source used in an interferometer sensor is never pure and always contains a spectrum of wavelength distributed around the main wavelength. This causes the sinusoidal interference pattern to fade in intensity with an increasing path difference between the two arms. This fading is faster if the spectral distribution of the source is larger. The path difference for which the interference intensity falls to $1/e$ is called the coherence length of the source. This negative effect for traditional interferometers can be used advantageously to obtain absolute measurements, while maintaining the high resolution typical of interferometric sensors. If a light source with very low coherence length (i.e. with a large spectral width) is used, the interference pattern will fade very quickly with increasing path imbalance. It is, however, possible to restore the interference if the light is passed through a second interferometer that matches the path imbalance in the sensor. If the path imbalance of the second interferometer can be controlled precisely, it becomes possible to measure the unknown path imbalance in the sensor with the same accuracy, by finding the matching condition that maximizes the fringe intensity. Examples of low-coherence sensors include the surveillance d'ouvrages par senseurs à fibres optiques (SOFO) sensors and Fizeau readout units for Fabry–Pérot Sensors (see next paragraph).

The SOFO interferometric sensors are long-base sensors, integrating the measurement over a long measurement base that can reach 10 m or more. The SOFO system[30,31] is a fiber optic displacement sensor with a resolution in the micrometer range and excellent long-term stability. The measurement set-up uses low-coherence interferometry to measure the length difference between two optical fibers installed on the structure to be monitored (Plate I in the color section between pages 294 and 295), by embedding in concrete or surface mounting (see Fig. 5.10a). The measurement fiber is pre-tensioned and mechanically coupled to the structure at two anchorage points in order to follow its deformations, while the reference fiber is free and acts as temperature reference. Both fibers are installed inside the same plastic pipe, and the gage length can be chosen between 200 mm and 10 m. The SOFO readout unit, shown in Fig. 5.10b, measures the length difference between the measurement fiber and the reference fiber, by compensating it with a matching length difference in its internal interferometer. The precision of the system is of ±2 μm independently from the measurement basis and its accuracy of 0.2% of the measured deformation even over years of operation.

The SOFO system has been used in particular to monitor civil and geotechnical structures, including bridges,[32] tunnels, piles,[33] anchored walls, dams, historical monuments,[34] and nuclear power plants, as well as laboratory models. The use of long-base SOFO sensors allows the gapless monitoring

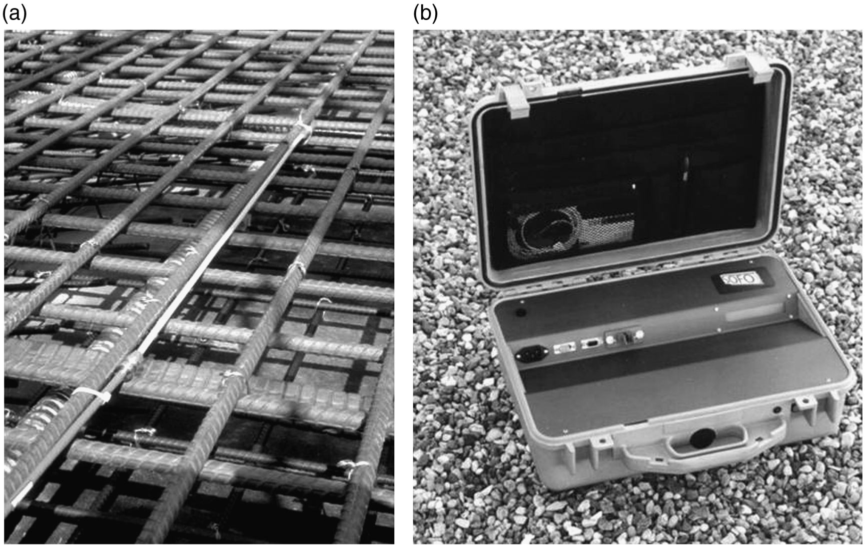

5.10 Example of SOFO sensor installed on a (a) rebar and (b) SOFO readout unit.

of the whole length of the structure, and provides average data that are not affected by local features or defects of the construction materials.

5.3.3 Fabry–Pérot interferometers

Fabry–Pérot interferometric sensors[35] are a typical example of point sensors and have a single measurement point at the end of the fiber optic connection cable. An extrinsic Fabry–Pérot interferometer (EFPI) consist of a capillary glass tube containing two partially mirrored optical fibers facing each other, but leaving an air cavity of a few microns between them, as shown in Fig. 5.11a. When light is coupled into one of the fibers, a back-reflected interference signal is obtained. This is due to the reflection of the incoming light on the two mirrors. This interference can be demodulated using coherent or low-coherence techniques to reconstruct changes in the fiber spacing. Since the two fibers are attached to the capillary tube near its two extremities (with a typical spacing of 10 mm), the gap change will correspond to the average strain variation between the two attachment points shown in Fig. 5.11a. Based on the same principle, it is possible to design pressure sensors (Fig. 5.11b) and displacement sensors (Fig. 5.11c).

Many sensors based on this principle are currently available as a one-to-one replacement of traditional sensors used in civil and geotechnical monitoring,[36] including piezometers, weldable and embedded strain gages,

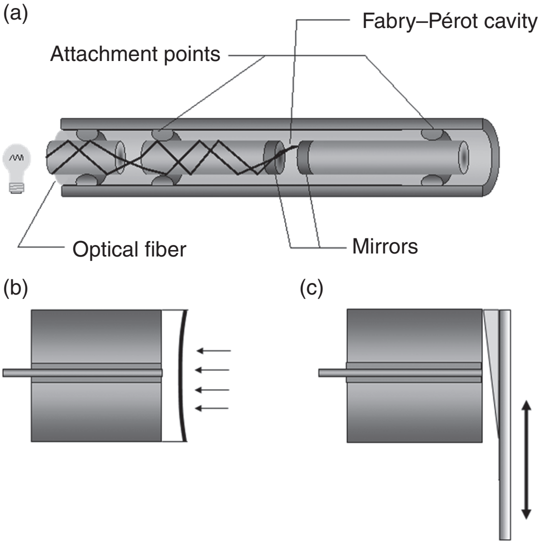

5.11 Schematic overview of Fabry–Pérot sensors for (a) strain, (b) pressure, and (c) displacement.

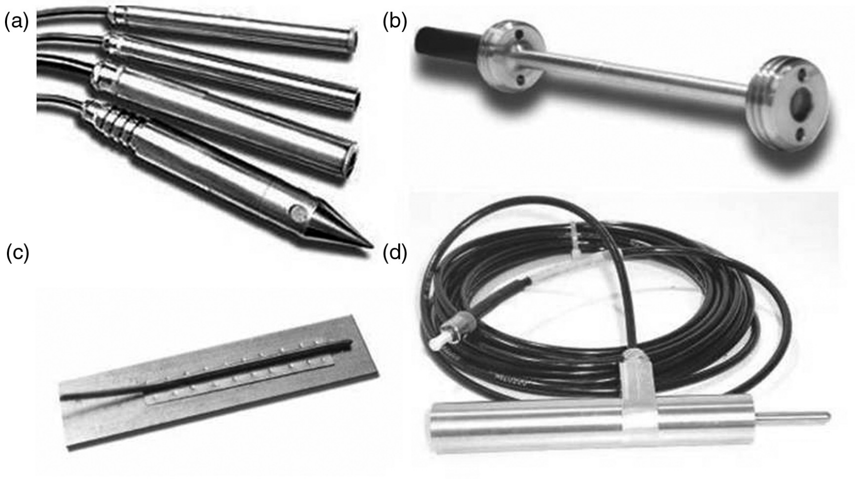

5.12 (a) Fabry–Pérot piezometers, (b) embeddable strain sensors, (c) spot-weldable strain sensor, and (d) displacement sensor.

temperature sensors, pressure sensors, and displacement sensors. Examples are shown in Fig. 5.12.

Because they are immune to electromagnetic interference, such as that found in railway applications, or the static electricity and frequent thunderstorms that are found in dams at high altitudes, fiber optic instruments offer an important advantage over the traditional vibrating wire technology for those applications. They are more rugged in such a harsh environment and allow very long cable lengths without the need for any lightning protection.

5.3.4 Fiber Bragg gratings

Fiber Bragg grating (FBG) sensors have many advantages for strain sensing in structural health monitoring applications, including the ability to measure localized strain and temperature and the potential to multiplex hundreds of sensors with a single ingress/egress fiber. They are the most commonly used type of multiplexed sensor. FBG sensors have been applied for a variety of structural health monitoring applications including spacecraft,[37,38] bonded aircraft repairs,[39–41] cryogenic composite tanks,[42,43] highway and railway bridges,[44–47] offshore platforms,[48] and nuclear reactors.[49]

The FBG, shown in Fig. 5.13, is a permanent, periodical perturbation in the index of refraction of the optical fiber core. Hill *et al.*[50] first fabricated permanent Bragg gratings in an optical fiber as a wavelength selective filter for telecommunication applications. When a broad spectrum of wavelengths

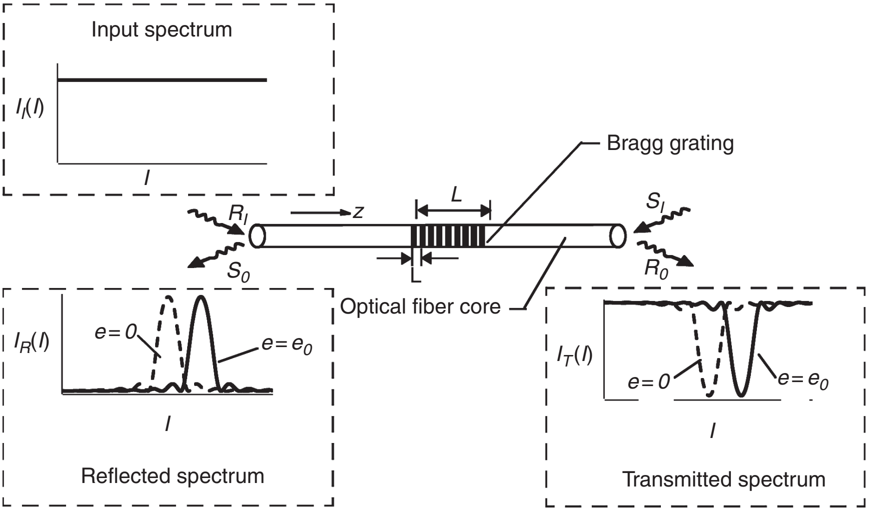
Input spectrum
$I_I(l)$
l
Bragg grating
L
z
R_I
S_0
S_I
R_0
L
Optical fiber core
$I_R(l)$
$e=0$
$e=e_0$
l
Reflected spectrum
$I_T(l)$
$e=0$
$e=e_0$
l
Transmitted spectrum

5.13 Optical FBG sensor. Reflected and transmitted spectra are shown for a broadband input spectrum. Dashed line is for unstrained FBG, solid line is for strained FBG.

is passed through the FBG, a narrow bandwidth of wavelengths is reflected, while all others are transmitted (see Fig. 5.13). The wavelength at maximum reflectivity is referred to as the Bragg wavelength, λ_B, and is determined by the condition

$$\lambda_B = 2n_{\text{eff}}\Lambda \tag{5.6}$$

where Λ is the period of the index of refraction variation.

The reflectivity coefficient is defined as the ratio of the intensity of the input lightwave to that of the reflected lightwave, as a function of wavelength, and is given by:

$$r = \frac{\sinh^2\left(L\sqrt{\kappa^2 - \hat{\sigma}^2}\right)}{\cosh^2\left(L\sqrt{\kappa^2 - \hat{\sigma}^2}\right) - \left(\hat{\sigma}^2/\kappa^2\right)} \tag{5.7}$$

where κ and $\hat{\sigma}$ are the coupling coefficients defined as:

$$\begin{aligned} \kappa &= \frac{\pi}{\lambda}\nu\overline{\delta n_{\text{eff}}} \\ \hat{\sigma} &= \frac{2\pi}{\lambda}\left(n_{\text{eff}} + \overline{\delta n_{\text{eff}}}\right) - \frac{\pi}{\Lambda} \end{aligned} \tag{5.8}$$

where L is the grating length, $\overline{\delta n_{\text{eff}}}$ is the amplitude of the index of refraction modulation, and v is the modulation fringe visibility. For sensing applications, FBGs with a narrow bandwidth and high reflectivity produce the largest signal-to-noise ratio. Procedures such as apodization are often applied to the FBG sensor during fabrication to reduce the secondary peaks and narrow the bandwidth.[51]

As axial strain, ε, is applied to the FBG, the Bragg wavelength shifts to lower wavelengths (compression) or higher wavelengths (tension). The applied strain is thus encoded in the FBG Bragg wavelength shift. For the specific case of pure axial loading we find:

$$\frac{\Delta\lambda_B}{\lambda_B} = (1 - p_e)\varepsilon \qquad [5.9]$$

where p_e is the effective photo-elastic constant for axial strain. A typical value of p_e for silica optical fibers is 0.22–0.25.[52]Thus, the shift in Bragg wavelength is linearly related to the applied axial strain.

Similarly, FBG sensors are also sensitive to temperature through

$$\frac{\Delta\lambda_B}{\lambda_B} = (\alpha + \zeta)\Delta T \qquad [5.10]$$

where α is the thermal expansion coefficient and ζ is the thermo-optic coefficient of the optical fiber material. A typical value for fused silica is $(\alpha + \zeta) = 6.67 \times 10^{-6}\ ^{\circ}\text{C}^{-1}$.[52] It is important to note that the thermal sensitivity of an FBG sensor is considerably higher than that of its electrical strain gage counterpart, increasing the need for thermal compensation for strain measurement applications.

One of the strongest advantages of FBG sensors over other available strain or temperature sensors for structural health monitoring applications is the fact that they can be multiplexed into a large sensor network. For structural health monitoring applications, having only a single or limited ingress/egress points and lead cables is a notable advantage because it can significantly reduce the weight of the lead cables and disruptions to the structure itself.[37] Several approaches to multiplexing large FBG sensor networks have been applied in which the sensors are interrogated using wavelength-division and time-division multiplexing (WDM, TDM) and combinations thereof. For WDM applications, reducing the wavelength spacing between each FBG reduces the time required to scan the network, however also increases the cross-talk losses between FBGs. For TDM

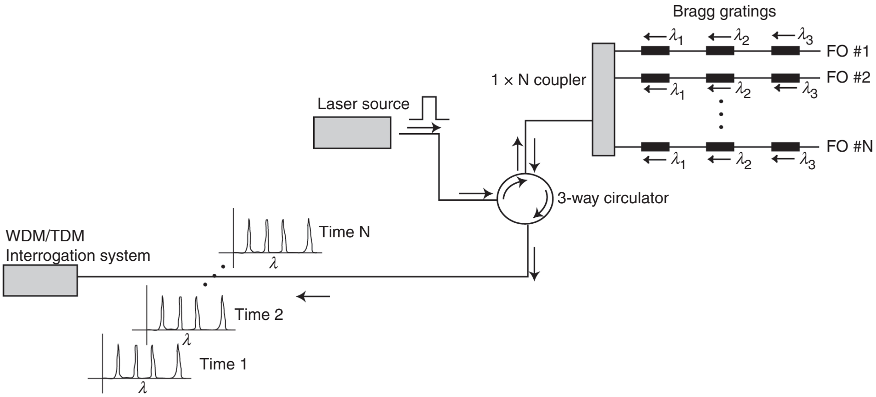

5.14 Combined WDM and TDM for FBG sensor network. (FO refers to fiber optic.)

applications low reflectivity gratings ($r_{\max} \cong 1\%$) should be used to allow for a large number of multiplexed sensors. By combining WDM with TDM, as shown in Fig. 5.14, one can reduce the power loss per FBG, as well as reducing the total wavelength range that must be scanned to interrogate the entire network.[52] Several commercial interrogators are now available for networks of FBG sensors.[53–55] Interferometric methods have also been applied for high speed interrogation of FBG sensor networks.[56–58]

FBG strain and temperature sensors can also distinguish between multiple strain components and/or temperature changes through the birefringence that occurs in the optical fiber due to applied transverse loads. Figure 5.15 shows an example of three independent loads applied to the optical fiber, along with the resulting three principal strain components at the center of the fiber core. The effect of the axial load (P_1) is to shift the reflected peak to higher or lower wavelengths; however, the effect of the transverse loads (P_2 and P_3) is to create peak-splitting due to the fast and slow axes that develop in the optical fiber. A typical example of peak-splitting behavior is also shown in Fig. 5.15. In general, FBGs written in PM optical fibers exhibit enhanced discrimination between multiple loading components.[59] The response of the FBG sensor to the multiple load components can either be predicted numerically[59–62] or experimentally calibrated.[63]

Distortion of the grating spectrum due to strain gradients has also been observed in several applications of embedded FBG sensors.[64–73] An example of experimentally measured spectral distortion due to the highly nonuniform strain field near a notch tip is shown in Fig. 5.16.[54] This sensitivity of the sensor response to the form of the strain profile is unique to the optical FBG, since other strain gages (e.g., the classical electrical strain gage) average the applied strain over the gage length. This full-spectral information

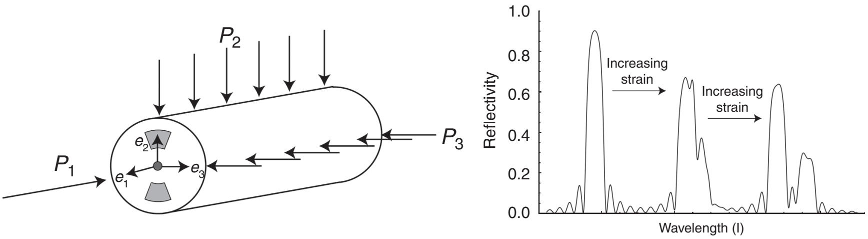

5.15 Multi-axis loading applied to FBG sensor written into bowtie PM fiber. The graph plots the effects of the multi-axis loading on a single FBG (peak on the left-hand side is the initial peak before load is applied).

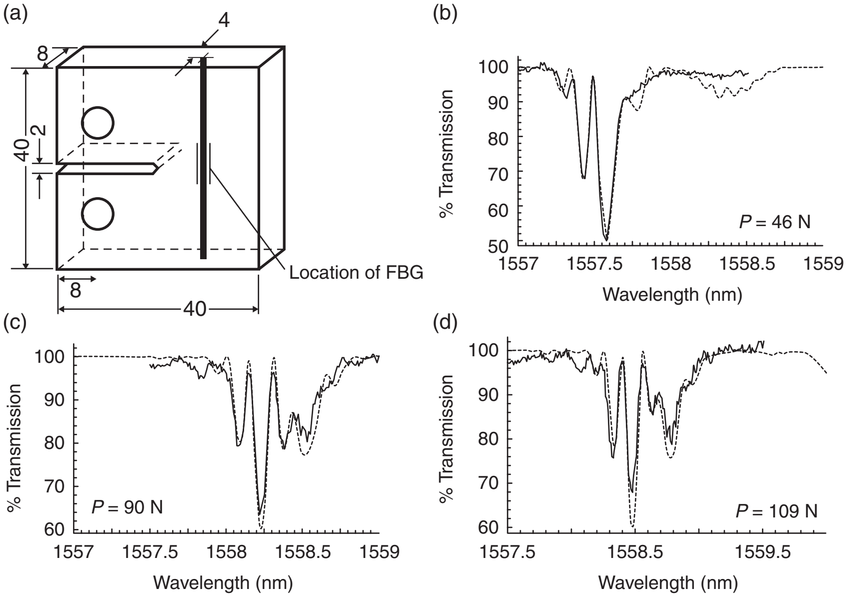

5.16 Response of FBG embedded in compact tension specimen. Location of 10 mm grating is shown in sketch of specimen. Experimental grating spectral data in transmission (solid lines) are shown for three load levels (P). The simulated spectra calculated using the transfer matrix method are also plotted (dashed lines).

has been used to measure crack bridging distributions and damage states in laminates. Recently, Vella *et al.*[74] demonstrated a full-spectral interrogator that operates up to 100 kHz for dynamic measurements.

Finally, while FBGs reflect or transmit lightwaves at certain wavelengths based on coupling between counter-propagating core modes, long period grating (LPG) sensors are based on coupling between the forward

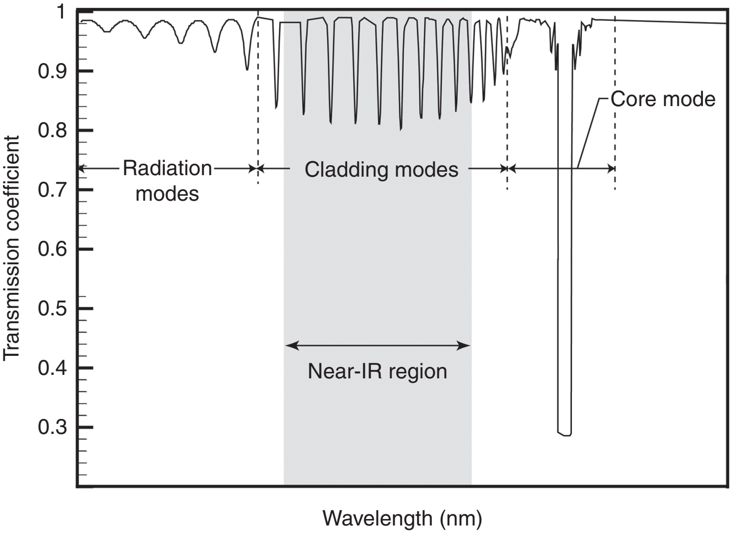

5.17 Theoretical transmission spectrum for long period FBG. Portion of spectrum in near-IR region is indicated.

propagating core mode and forward propagating cladding modes. The large period of the LPG (100 μm < Λ < 1 mm) results in cladding mode coupling at wavelengths in the near-IR range, appearing as multiple loss peaks in the transmission spectrum (see Fig. 5.17).[75] LPG sensors have primarily been applied to the measurement of environmental or chemical parameters due to their strong sensitivity to the index of refraction of the surrounding material system.

5.3.5 Brillouin and Raman scattering distributed sensors

Distributed fiber optic sensing offers the ability to measure temperatures and strains at thousands of points along a single fiber. This is particularly interesting for the monitoring of large structures such as dams, dikes, levees, tunnels, pipelines, and landslides, where it allows the detection and localization of movements and seepage zones with sensitivity and localization accuracy unattainable using conventional measurement techniques.

Unlike electrical sensors and localized FOSs, distributed sensors offer the unique characteristic of being able to measure physical parameters, in particular strain and temperature, along their whole length, allowing the measurements of thousands of points from a single readout unit. The most developed technologies of distributed FOSs are based on Raman[76] and Brillouin scattering.[77,78] Both systems make use of a nonlinear interaction between the light and the glass material of which the fiber is made. If an intense light at a

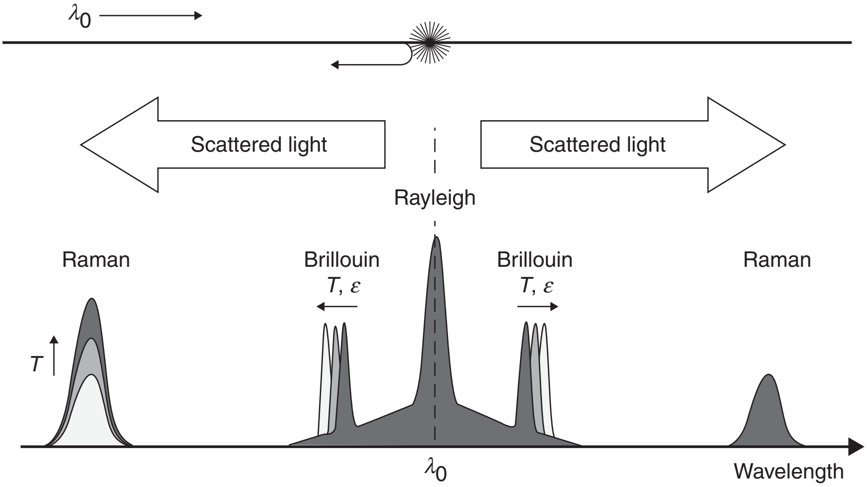

5.18 Light scattering in optical fibers and its use for strain and temperature sensing. At every section of fiber, the incoming wavelength λ_0 is scattered backward. The backscattered light contains new wavelengths that carry information about the strain and temperature conditions at the location where the scattering occurred.

known wavelength is shone into a fiber, a very small amount of it is scattered back from every location along the fiber itself. Besides the original wavelength (called the Rayleigh component), the scattered light contains components at wavelengths that are higher and lower than the original signal (called the Raman and Brillouin components). These shifted components contain information on the local properties of the fiber, in particular its strain and temperature. Figure 5.18 shows the main scattered wavelengths components for a standard optical fiber. If λ_0 is the wavelength of the original laser signal generated by the readout unit, the scattered components appear both at higher and lower wavelengths.

The two Raman peaks are located symmetrically to the original wavelength. Their position is fixed, but the intensity of the peak at lower wavelength is temperature dependent, while the intensity of the one at higher wavelength is unaffected by temperature changes. Measuring the intensity ratio between the two Raman peaks therefore yields the local temperature in the fiber section where the scattering occurred.

The two Brillouin peaks are also located symmetrically at the same distance from the original wavelength. Their position relative to λ_0 is however proportional to the local temperature and strain changes in the fiber section. Brillouin scattering is the result of the interaction between optical and ultrasound waves in optical fibers. The Brillouin wavelength shift is proportional to the acoustic velocity in the fiber that is related to its density. Since the density depends linearly on the strain and the temperature of the optical fiber, we can use the Brillouin shift to measure those parameters.

When light pulses are used to interrogate the fiber it becomes possible, using a technique similar to RADAR, to discriminate different points along the sensing fiber through the different time-of-flight of the scattered light. Combining the radar technique and the spectral analysis of the returned light, one can obtain the complete profile of strain or temperature along the fiber. Typically, it is possible to use a fiber with a length of up to 30 km and obtain strain and temperature readings every meter. In this case we would talk of a distributed sensing system with a range of 30 km and a spatial resolution of 1 m. Figure 5.19 schematically shows an example of distributed strain and temperature sensing.

Systems based on Raman scattering typically exhibit temperature accuracy of the order of ±0.1°C and a spatial resolution of 1–3 m over a measurement range up to 30 km. The best Brillouin scattering systems offer a temperature accuracy of ±0.1°C, a strain accuracy of ±20 microstrain, and a measurement range of 50 km, with a spatial resolution of 1–3 m.[79] The readout units are portable and can be used for field applications.

Since the Brillouin frequency shift depends on both the local strain and temperature of the fiber, the sensor set-up will determine the actual response of the sensor. For measuring temperatures it is necessary to use a cable designed to shield the optical fibers from an elongation of the cable. The fiber will therefore remain in its unstrained state and the frequency shifts can be unambiguously assigned to temperature variations. Measuring distributed strains also requires a specially designed sensor. A mechanical coupling between the sensor and the host structure along the whole length

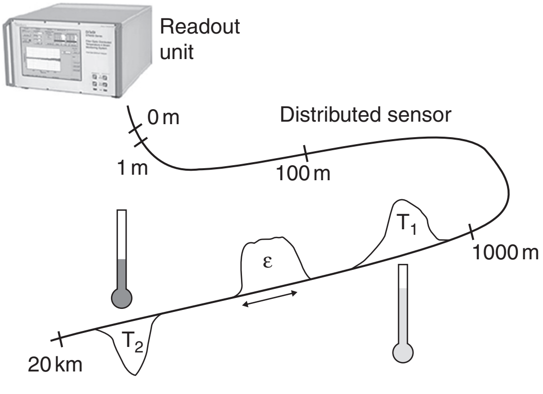

5.19 Schematic example of a distributed strain and temperature measurement.

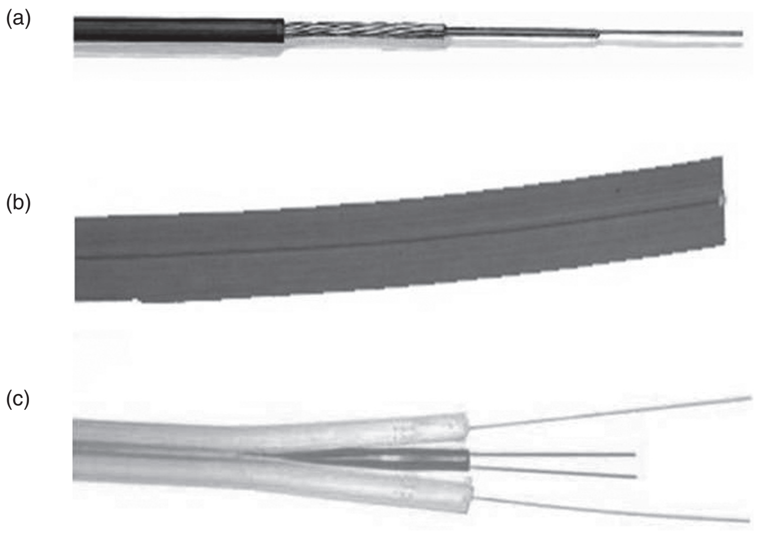

5.20 Distributed sensor cables examples: (a) temperature sensor, (b) strain sensor, and (c) combined strain and temperature sensor.

of the fiber has to be guaranteed. To resolve the cross-sensitivity to temperature variations, it is also necessary to install a reference fiber along the strain sensor. Special cables, containing both free and coupled fibers, allow a simultaneous reading of strain and temperature. Figure 5.20 shows examples of temperature, strain, and combined cables.[20]

Sensing systems based on Brillouin and Raman scattering are used to detect and localize seepage in dams and dikes, allowing the monitoring of hundreds of kilometers along a structure with a single instrument and the localization of the water path with an accuracy of 1 or 2 m. Distributed strain sensors are also used to detect landslide movements and to detect the onset of cracks in concrete dams and steel bridges.[80]

Early applications of this technology have demonstrated that the design and production of sensing cables, incorporating and protecting the optical fibers used for the measurement, as well as their optimal locating and installation in the structure under scrutiny, are critical elements for the success of any distributed sensing instrumentation project.

5.4 Future trends

In this section, we describe recent advances in optical fiber and measurement technologies, and new opportunities in optical fiber sensing enabled by these advances.

5.4.1 Multicore fiber sensors

The recent fabrication of multicore optical fibers has led to new sensing capabilities for strain and temperature measurements. An example of a multicore optical fiber is shown in Fig. 5.21. The multiple cores are introduced with spacing sufficient such that there is minimal overlap between modes propagating through each core. These independently propagating modes permit the presence of multiple sensors in the same fiber cross-section. Coupling to the different cores is typically achieved by graded index lenses or fan-outs.[81] The most common application of these multicore fiber sensors has been the measurement of curvature of different axes in the fiber cross-section by interfering the different propagating lightwaves or writing FBGs in the different cores.[82–84] As the cores are located at different locations relative to the neutral bending axes (see Fig. 5.21), the local curvature can be measured at high accuracies with inherent axial strain and temperature compensation. For example, Blanchard *et al.*[83] achieved a bend angle resolution of 100 μrad using a three-core optical fiber. By separating the multiple cores by polarization axes, the axial strain and temperature can also be measured independently.[85,86]

Multiplexing FBG sensors along the fiber (in each of the different cores) have also been applied for high resolution shape sensing by integrating the local curvatures (about multiple axes) along the optical fiber length.[82,87,88] Flockhart *et al.*[89] and Cranch *et al.*[90] wrote sets of FBG pairs in each core to act as a low-finesse Fabry–Pérot interferometer to enhance the static and dynamic resolution of the distributed shape measurements.

5.4.2 Microstructured optical fiber sensors

The recent invention of microstructured optical fibers has created great potential for both optical fiber communication systems and optical fiber sensors. Such fibers have a complex cross-sectional geometry including both silica and air holes. Confinement of the propagating lightwaves is generated either by an effective index contrast similar to that of conventional optical fibers in which the air holes significantly reduce the cladding index of refraction ('holey' fibers) or through a photonic bandgap effect (photonic crystal fibers).[91] One example of a microstructure fiber is shown in Fig. 5.22. In either case, the complex geometry of these microstructured fibers provides both new sensing possibilities and enhanced response characteristics for sensors applied to these fibers.

For sensing applications the main potential benefits of these fibers are the following: (1) the reduced amount of silica through which the fundamental mode propagates means that the temperature sensitivity of the sensors can

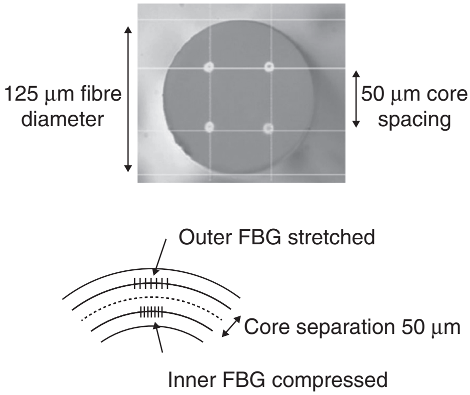
125 μm fibre diameter
50 μm core spacing
Outer FBG stretched
Core separation 50 μm
Inner FBG compressed

5.21 Cross-section of multicore fiber illuminated with white light and principle of curvature measurement from FBG pairs in different cores[67].

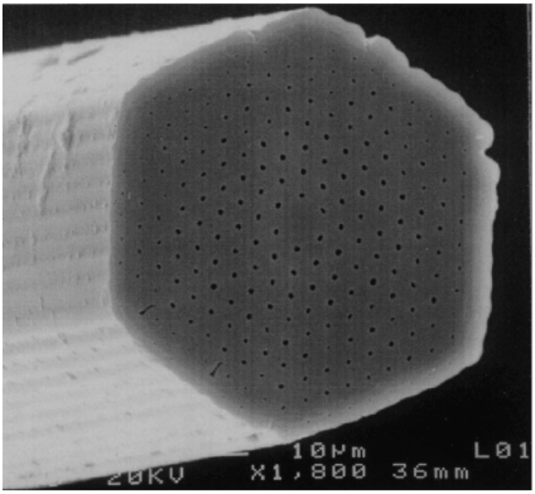
10μm L01
20KV X1,800 36mm

5.22 Scanning electron microscope image of the end of a photonic crystal fiber.[78]

be reduced to near zero;[92] (2) the fibers can act in single-mode over a wide range of wavelengths, permitting multiplexing of sensors at significantly different wavelengths;[93] (3) for chemical sensing applications, the gas to be sensed can be inserted into the air holes, permitting a long interaction surface between the propagating mode and the gas;[94] and (4) PM fibers can be fabricated through the arrangement of the air holes, without the need for induced thermal residual stresses, making the birefringence more stable to temperature variations.[95]

Nasilowski *et al.*[95] and Bock *et al.*[96] applied microstructured holey fibers for the measurement of temperature and pressure. Several researchers have also written long period FBGs into microstructured fibers through CO_2 laser or electric arc etching.[97–99] These gratings demonstrate an excellent strain sensitivity, with little or no temperature sensitivity.[97,99] Finally, researchers have also succeeded in writing FBGs into photonic crystal optical fibers for use as discrete strain sensors.[100]

5.4.3 Polymer optical fiber sensors

While the previous discussion has been limited to silica optical fibers, many of the same sensing techniques have been applied to polymer optical fibers (POFs) as well. POFs have additional advantages for sensing, such as their high elastic strain limit, high fracture toughness, high flexibility in bending, higher sensitivity to strain than silica, and negative thermo-optic coefficient.[101–104] Additionally, many polymeric materials have a high biocompatibility. More details on the properties of POFs can be found in References 14 and 105.

On the other hand, a significant challenge to applying POFs as sensors is the difficulties in fabrication of these fibers. Due to the fabrication difficulties, most POF sensors are based on multi-mode POFs.[14] Multi-mode POFs are less expensive and easier to couple than silica single-mode optical fibers; however, they are also larger in diameter. POFs also demonstrate viscoelastic behavior and are extremely sensitive to humidity.[102,104,106,107] Typical stress–strain curves for a POF at different applied strain rates are shown in Fig. 5.23. Additionally, many POF sensors operate at lower wavelengths than comparable silica fiber sensors, due to the high attenuation of polymers in the near-infrared range. Multi-mode POF sensors have been demonstrated based on many of the same measurement principles as silica optical fiber sensors, including intensity losses, back scattering, and time-of-flight.[108]

Recently, both single-mode solid POFs and single-mode microstructured POFs have been developed that present new capabilities for POF sensors.[109,110] The emergence of these optical fibers has created the potential for high precision, large deformation optical fiber sensors for a variety of applications. Kiesel *et al.*[111] recently demonstrated coherent interferometry in a single-mode POF in-fiber Mach-Zehnder interferometer up to 15.8% elongation of the POF (see Plate II in the color section between pages 294 and 295). After calibration of both the mechanical and opto-mechanical parameters of the single-mode POF,[102,103] the authors applied the sensor for strain measurements on tensile coupons.[112] Additionally strategies to couple the single-mode POF sensor to single-mode silica

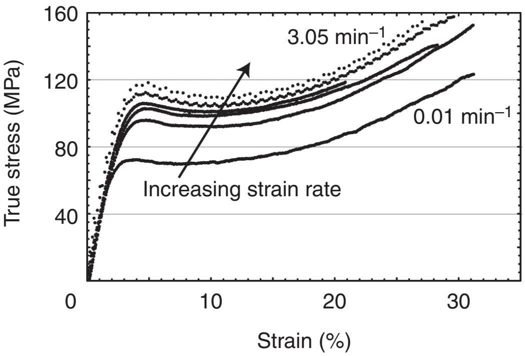

5.23 Measured true stress–strain curves for a single-mode PMMA doped core POF at different applied strain rates.[102]

optical fibers to remove the attenuation limits were developed.[113] Peng *et al.*[114] first demonstrated the writing of FBGs into single-mode POFs for localized strain sensing over large strain ranges. The POF FBG sensors demonstrate a 22% increase in strain sensitivity as compared to silica Bragg gratings[115] and have been tuned over a 18 nm wavelength shift by applying a temperature change of 50°C.[116] Finally, van Eijkelenborg *et al.*[117] fabricated microstructured POFs to overcome the high intrinsic attenuation properties of common POFs. These microstructured POFs have since been applied as sensors through inscribed LPGs and FBGs.[118–120]

5.4.4 Rayleigh scattering distributed sensors

A more recent development in distributed fiber optic sensing is the use of Rayleigh backscattering for the interrogation of strain and temperature along an optical fiber. As for the previous distributed sensors, a standard optical fiber can be applied as the sensor, providing distributed measurements over large distances, without expensive individual sensors. Gifford *et al.*[121,122] applied swept-wavelength interferometry (SWI) to measure the backscattered signal in silica and POFs. This interrogation method is fundamentally different from optical time-domain reflectometry measurements, since SWI measures phase shifts rather than amplitudes in the backscattered signal. While the spectrum of the backscattered signal is random, it is deterministic. Local changes in temperature or strain create a wavelength shift in the response, similar to the effect measured by FBG sensors. Interrogating the backscatter spectrum with SWI can provide a high spatial resolution (up to 10 s of microns) with strain resolution up to 1 $\mu\varepsilon$ and temperature resolution up to 0.1°C.[121] A similar set-up can also be used to produce a distributed acoustic sensor that can be used for intrusion detection and localization.

5.5 Sources for further information and advice

There are a wide variety of available sources of information on optical fiber sensors. For an overall survey of a variety of sensors, the books of Measures,[123] Udd,[124] Glišić and Inaudi,[125] and the Structural Health Monitoring (SHM) encyclopedia[126] are all excellent options. Méndez[127] also provides information on specialty optical fibers and their potential for sensing applications. Many articles related to the research and development of optical fiber sensors are available in archival journals. The field of optical fiber sensing is highly multi-disciplinary, which means that such articles are distributed among a large number of journals including *Smart Materials and Structures*, *Measurement Science and Technology*, *Journal of Lightwave Technology*, *Applied Optics*, *Optical Fiber Technology*, *IEEE Sensors*, and others.

The past 10 years have seen a rapid growth in the number of commercial businesses developing and installing optical fiber sensors and interrogators for civil infrastructure, aerospace, and energy applications. Their websites provide helpful descriptions of available products and applications. Examples include Roctest-Smartec,[128] Micron Optics,[53] Technobis,[54] FISO,[36] and Luna Innovations.[129] Additionally, the organization Opticalfibersensors.org[130] provides an excellent starting point to search for companies, products, upcoming events, and recent news in the field of optical fiber sensors.

5.6 Conclusions

FOSs are increasingly utilized in structural health monitoring in civil, aerospace, and energy applications. The recent surge in commercial demonstrations of these sensor systems highlights their unique capabilities that are not found in networks of conventional sensors. FOSs can be multiplexed to provide a large number of discrete sensors, or truly distributed measurements can be made using the optical fiber as a measurement device. In addition, a large variety of sensing mechanisms are available to convert the properties of lightwaves transmitted through or reflected from the optical fiber into information on the state of the structure. Their long-term durability, immunity to electromagnetic interference, and ease of integration within structural systems make FOSs ideal candidates for monitoring of full-scale structural systems. At the same time, recent research advances in optical fiber technology and instrumentation point to future capabilities and applications of FOSs that will be realized in the next few years.

5.7 References

1. Ghatak A and Thyagarajan K. (1998) Introduction to Fiber Optics; Cambridge University Press: Cambridge, UK.

2. Takeda N and Okabe Y. (2005) Durability analysis and structural health management of smart composite structures using small-diameter fiber optic sensors. *Science and Engineering of Composite Materials,* **15**: 1–12.
3. Buck J A. (2004) *Fundamentals of Optical Fibers*, John Wiley & Sons, Inc.: Hoboken, NJ.
4. Corning SMF-28: Optical Fiber Product Information, 2003.
5. Kosaka T, Takeda N and Ichiyama T. (1999) Detection of cracks in FRP by using embedded plastic optical fiber. *Materials Science Research International*, **5**: 206–209.
6. Xie G P, Keey S L and Asundi A. (1999) Optical time-domain reflectormetry for distributed sensing of the structural strain and deformation. *Optics and Lasers in Engineering,* **32**: 437–447.
7. Doyle C, Martin A, Liu T, Wu M, Hayes S, Crosby P A, Powell G R, Brooks D and Fernando G F. (1998) *In situ* process and conditioning monitoring of advanced fibre-reinforced composite materials using optical fibre sensors. *Smart Materials and Structures*, **7**: 145–158.
8. Jiang M Z and Gerhard E. (2001) A simple strain sensor using a thin film as a low-finesse fiber-optic Fabry-Perot interferometer. *Sensors and Actuators A,* **88**: 41–46.
9. Kuang K S C, Cantwell W J and Scully P J. (2002) An evaluation of a novel plastic optical fibre sensor for axial strain and bend measurements. *Measurement Science and Technology*, **13**: 1523–1534.
10. Han W and Wang A B. (2006) Mode power distribution effect in white-light multimode fiber extrinsic Fabry-Perot interferometric sensor systems. *Optics Letters,* **31**: 1202–1204.
11. James S W and Tatam R P. (2003) Optical fibre long-period grating sensors: characteristics and application. *Measurement Science and Technology*, **14**: R49–R61.
12. Emslie C. (2007) Polarization maintaining fibers. *Specialty Optical Fibers Handbook*; Méndez A and Morse T F (ed.) Academic Press: Amsterdam, NL.
13. Carmen G P and Sendeckyj G P. (1995) Review of the mechanics of embedded optical sensors. *Journal of Composites Technology & Research*, **17**: 183–193.
14. Zubia J and Arrue J. (2001) Plastic optical fibers: an introduction to their technological processes and applications. *Optical Fiber Technology*, **7**: 101–140.
15. Measures R M. (2001) *Structural Monitoring with Fiber Optic Technology*; Academic Press: San Diego, CA.
16. Murukeshan V M, Chan P Y, Seng O L and Asundi A. (1999) On-line health monitoring of smart composite structures using fiber polarimetric sensor. *Smart Materials and Structures,* **8**: 544–548.
17. Spillman W B. (2006) Multimode polarization sensors. *Fiber Optic Sensors*; Udd E (ed.) John Wiley & Sons, Inc.: Hoboken, NJ.
18. Inaudi D. (2005) Long-term reliability testing of packaged strain sensors. In *Proceedings of SPIE Smart Structures Conference 2005*, San Diego, CA.
19. Sennhausen U. (2000) Nellen Ph. Reliability of fiber optic sensors. *Trends in Nondestructive Testing and Inspection*; Elsevier: Kidlington, Oxford, UK.
20. Inaudi D and Glisic B. (2005) Development of distributed strain and temperature sensing cables. In *Proceedings of 17th International Conference on Optical Fibre Sensors 2005*, Bruges, Belgium.

21. Butter C D and Hocker G B. (1978) Fiber optics strain-gauge. *Applied Optics,* **17**: 2867–2869.
22. Van Steenkiste R J and Springer G S. (1997) *Strain and Temperature Measurement with Fiber Optic Sensors*; Technomic Publishing Inc.: Lancaster, PA.
23. Haslach H W and Sirkis J S. (1991) Surface-mounted optical fiber strain sensor design. *Applied Optics,* **30**: 4069–4080.
24. Peters K J and Washabaugh P D. (1997) Balance technique for monitoring *in situ* structural integrity of prismatic structures. *AIAA Journal,* **35**: 869–874.
25. Rogers A J. (1988) Essential optics. *Optical Fiber Sensors: Principles and Components*; Dakin J and Culshaw B (ed.) Artech House: Boston, MA.
26. Dandridge A. (2006) Fiber optic sensors based on the Mach-Zehnder and Michelson interferometers. *Fiber Optic Sensors*; Udd E (ed.) John Wiley & Sons Inc.: Hoboken, NJ.
27. Koo K P, Tveten A B and Dandridge A. (1982) Passive stabilization scheme for fiber interferometers using (3x3) fiber directional couplers. *Applied Physics Letters*, **41**: 616–618.
28. Jackson D A, Priest R, Dandridge A and Tveten A B. (1980) Elimination of drift in a single-mode optical fiber interferometer using a piezoelectrically stretched coiled fiber. *Applied Optics*, **19**: 2926–2929.
29. Kersey A D. (2006) Distributed and multiplexed fiber optic sensors. *Fiber Optic Sensors*; Udd E (ed.) John Wiley & Sons Inc.: Hoboken, NJ.
30. Inaudi D, Elamari A, Pflug L, Gisin N, Breguet J and Vurpillot S. (1994) Low-coherence deformation sensors for the monitoring of civil-engineering structures. *Sensor and Actuators A*, **44**:125–130.
31. Lloret S, Inaudi D, Glisic B, Kronenberg P and Vurpillot S. (2000) Optical set-up development for the monitoring of structural dynamic behavior using SOFO® sensors. In *Proceedings of SPIE, 7th International Symposium on Smart Structures and Materials 2000*, Newport Beach, USA, (SPIE Vol. 3986): 199–205.
32. Inaudi D, Bolster M, Deblois R, French C, Phipps A, Sebasky J and Western K. (2009) Structural health monitoring system for the new I-35W St Anthony Falls bridge. In *Proceedings of 4th International Conference on Structural Health Monitoring on Intelligent Infrastructure (SHMII-4) 2009*, Zurich, Switzerland.
33. Glisic B, Inaudi D, Vurpillot S, Bu E and Chen C J. (2003) Piles monitoring using topologies of long-gage fiber optic sensors. In *Proceedings of First International Conference on Structural Health Monitoring and Intelligent Infrastructure 2003*, Tokyo, Japan.
34. Inaudi D, Del Grosso A, Messervey T, Walder R and Fuggini C. (2010) Long-Term Structural Health Monitoring Of The Royal Villa Of Monza. In *Proceedings of CSHM-3 International Workshop on Preservation of Heritage Structures 2010*, Ottawa, Canada.
35. Pinet É, Hamel C, Glišic B, Inaudi D and Miron N. (2007) Health monitoring with optical fiber sensors: from human body to civil structures. In *Proceedings of 14th SPIE Annual Symposium on Smart Structures and Materials & Nondestructive Evaluation and Health Monitoring 2007*, (SPIE Vol. 6532) San Diego (CA), USA.
36. http://www.fiso.com.
37. Friebele E J, Askins C G, Bosse A B, Kersey A D, Patrick H J, Pogue W R, Putnam M A, Simon W R, Tasker F A, Vincent W S and Vohra S T. (1999) Optical fiber sensors for spacecraft applications. *Smart Materials and Structures*, **8**: 813–838.

38. Ecke W, Latka I, Willsch R, Reutlinger A and Graue R. (2001) Fibre optic sensor network for spacecraft health monitoring. *Measurement Science and Technology,* **12**: 974–980.
39. McKenzie I, Jones R, Marshall I H and Galea S. (2000) Optical fibre sensors for health monitoring of bonded repair systems. *Composite Structures,* **50**: 405–416.
40. Sekine H, Fujimoto S E, Okabe T, Takeda N and Yokobori T. (2006) Structural health monitoring of cracked aircraft panels repaired with bonded patches using fiber Bragg grating sensors. *Applied Composite Materials*, **13**: 87–98.
41. Li H C H, Beck F, Dupouy O, Herszberg I, Stoddart P R, Davis C E and Mouritz A P. (2006) Strain-based health assessment of bonded composite repairs. *Composite Structures,* **76**: 234–242.
42. Mizutani T, Takeda N and Takeya H. (2006) On-board strain measurement of a cryogenic composite tank mounted on a reusable rocket using FBG sensors. *Structural Health Monitoring – An International Journal,* **5**: 205–214.
43. Kang D H, Kim C U and Kim C G. (2006) The embedment of fiber Bragg grating sensors into filament wound pressure tanks considering multiplexing. *NDT&E International,* **39**: 109–116.
44. Chan T H T, Yu L, Tam H Y, Ni Y Q, Chung W H and Cheng L K. (2006) Fiber Bragg grating sensors for structural health monitoring of Tsing Ma bridge: background and experimental observation. *Engineering Structures,* **28**: 648–659.
45. Zhang W, Gao J Q, Shi B, Cui H L and Zhu H. (2006) Health monitoring of rehabilitated concrete bridges using distributed optical fiber sensing. *Computer-Aided Civil and Infrastructure Engineering,* **21**: 411–424.
46. Kister G, Winter D, Badcock R A, Gebremichael Y M, Boyle W J O, Meggitt B T, Grattan K T V and Fernando G F. (2007) Structural health monitoring of a composite bridge using Bragg grating sensors. Part 1: evaluation of adhesives and protection systems for the optical sensors. *Engineering Structures,* **29**: 440–448.
47. Lau K T, Yuan L B, Zhou L M, Wu J S and Woo C H. (2001) Strain monitoring in FRP laminates and concrete beams using FBG sensors. *Composite Structures,* **51**: 9–20.
48. Ren L, Li H N, Zhou J, Li D S and Sun L. (2006) Health monitoring system for offshore platform with fiber Bragg grating sensors. *Optical Engineering*, **48**: Art. No. 084401.
49. Bin Lin Y, Lin T K, Chen C C, Chiu J C and Chang K C. (2006) Online health monitoring and safety evaluation of the relocation of a research reactor using fiber Bragg grating sensors. *Smart Materials and Structures,* **15**: 1421–1428.
50. Hill K O, Fujii Y, Johnson D C and Kawasaki B S. (1978) Photosensitivity in optical fiber waveguides – application to reflection filter fabrication. *Applied Physics Letters,* **32**: 647–649.
51. Kashyap R. (1999) *Fiber Bragg Gratings*; Academic Press: San Diego, CA.
52. Kersey A D, Davis M A, Patrick H J, LeBlanc M, Koo K P, Askins C G, Putnam M A and Friebele E J. (1997) Fiber grating sensors. *Journal of Lightwave Technology,* **15**: 1442–1463.
53. http://www.micronoptics.com/.
54. http://www.technobis-fibre-technologies.nl/.
55. http://www.smartfibres.com/.

56. Koo K P and Kersey A D. (1995) Bragg grating-based laser sensors systems with interferometric interrogation and wavelength-division multiplexing. *Journal of Lightwave Technology*, **13**: 1243–1249.
57. Todd M D, Johnson G A and Chang C C. (1999) Passive, light intensity-independent interferometric method for fibre Bragg grating interrogation. *Electronics Letters*, **35**: 1970–1971.
58. Todd M D, Johnson G A and Althouse B L. (2001) A novel Bragg grating sensor interrogation system utilizing a scanning filter, a Mach-Zehnder interferometer and a 3 x 3 coupler. *Measurement Science and Technology*, **12**: 771–777.
59. Lawrence C M, Nelson D V, Udd E and Bennett T. (1999) A fiber optic sensor for transverse strain measurements. *Experimental Mechanics,* **39**: 202–209.
60. Bosia F, Giaccari P, Botsis J, Facchini M, Limberger H G and Salathé R. (2003) Characterization of the response of fibre Bragg grating sensors subjected to a two-dimensional strain field. *Smart Materials and Structures*, **12**: 925–934.
61. Prabhugoud M and Peters K. (2006) Finite element model for embedded fiber Bragg grating sensor. *Smart Materials and Structures*, **15**: 550–562.
62. Prabhugoud M and Peters K. (2007) Finite element analysis of multi-axis strain sensitivities of Bragg gratings in PM fibers. *Journal of Intelligent Material Systems and Structures,* **18**: 861–873.
63. Chehura E, Ye C C, Staines S E, James, S W and Tatam R P. (2004) Characterization of the response of fibre Bragg gratings fabricated in stress and geometrically induced high birefringence fibres to temperature and transverse load. Smart *Materials and Structures,* **13**: 888–895.
64. Peters K, Studer M, Botsis J, Iocco A, Limberger H and Salathé R. (2001) Embedded optical fiber Bragg grating sensor in a nonuniform strain field: measurements and simulations. *Experimental Mechanics*, **41**: 19–28.
65. Studer M, Peters K and Botsis J. (2003) Method for determination of crack bridging parameters using long optical fiber Bragg grating sensors. *Composites Part B*, **34**: 347–359.
66. Ling H Y, Lau K T, Chen L and Chow K W. (2005) Embedded fibre Bragg grating sensors for non-uniform strain sensing in composite structures. *Measurement Science and Technology*, **16**:2415–2424.
67. Ling H Y, Lau K T, Su Z and Wong E T T. (2007) Monitoring mode II fracture behavior of composite laminates using embedded fiber-optic sensors. *Composites Part B*, **38**: 488–497.
68. Kang D H, Park S O, Hong C S and Kim C G. (2005) The signal characteristics of reflected spectra of fiber Bragg grating sensors with strain gradients and grating lengths. *NDT&E International*, **38**: 712–718.
69. Kuang K S C, Kenny R, Whelan M P, Cantwell W J and Chalker P R. (2001) Embedded fibre Bragg grating sensors in advanced composite materials. *Composites Science and Technology*, **61**: 1379–1387.
70. Guemes J A and Menéndez J M. (2002) Response of Bragg grating fiber-optic sensors when embedded in composite laminates. *Composites Science and Technology*, **62**: 959–966.
71. Takeda N, Yashiro S and Okabe T. (2006) Estimation of the damage patterns in notched laminates with embedded FBG sensors. *Composites Science and Technology*, **66**: 684–693.

72. Yashiro S, Okabe T and Takeda N. (2007) Damage identification in a holed CFRP laminate using a chirped fiber Bragg grating sensor. *Composites Science and Technology*, **67**: 286–295.
73. Minakuchi S. (2007) Real-time detection of debonding between honeycomb core and facesheet using a small-diameter FBG sensor embedded in adhesive layer. *Journal of Sandwich Structures and Materials*, **9**: 9–33.
74. Vella T, Chadderdon S, Selfridge R, Schultz S, Webb S, Park C, Peters K and Zikry M. (2010) Full-spectrum interrogation of fiber Bragg gratings at 100 kHz for detection of impact loading. *Measurement Science and Technology*, **21**: 094009.
75. James S W and Tatam R P. (2003) Optical fibre long-period grating sensors: characteristics and application. *Measurement Science and Technology*, **14**: R49–R61.
76. Dakin J P, Pratt D J, Bibby G W and Ross J N. (1988) Distributed optical fiber Raman temperature sensor using a semiconductor light source and detectors. *Electronics Letters*, **21**: 569–570.
77. Horiguchi T, Kurashima T and Tateda M. (1990) Distributed temperature sensing using stimulated Brillouin scattering in optical silica fibers. *Optics Letters*, **15**:1038–1040.
78. Niklès M, Thévenaz L and Robert P. (1995) Simple distributed fiber sensor based on Brillouin gain spectrum analysis. *Optics Letters*, **21**: 758–760.
79. Niklès M, Briffod F, Burke R and Lyons G. (2005) Greatly extended distance pipeline monitoring using fibre optics, in *Proceedings of OMAE05 24th International Conference on Offshore Mechanics and Arctic Engineering*, Halkidiki, Greece.
80. Ravet F, Glisic B, Niklès M and Inaudi D. (2009) Sub-millimeter crack detection with Brillouin based fiber optic sensors. *IEEE Sensor Journal*, **9**:1391–1396.
81. MacPherson W N, Flockhart G M H, Maier R R J, Barton J S, Jones J D C, Zhao D, Zhang L and Bennion I. (2004) Pitch and roll sensing using fibre Bragg gratings in multicore fibre. *Measurement Science and Technology*, **15**: 1642–1646.
82. MacPherson W N, Silva-Lopez M, Barton J S, Moore A J, Jones J D C, Zhao D, Zhang L, Bennion I, Metje N, Chapman D N and Rogers C D F. (2006) Tunnel monitoring using multicore fibre displacement sensor. *Measurement Science and Technology*, **17**: 1180–1185.
83. Blanchard P M, Burnett J G, Erry G R G, Greenaway A H, Harrison P, Mangan B, Knight J C, Russell P St J, Gander M J, McBride R and Jones J D C. (2000) Two-dimensional bend sensing with a single, multi-core optical fibre. *Smart Materials and Structures*, **9**: 132–140.
84. MacPherson W N, Gander M J, McBride R, Jones J D C, Blanchard P M, Burnett J G, Greenaway A H, Mangan B, Birks T A, Knight J C and Russell P S. (2001) Remotely addressed optical fibre curvature sensor using multicore photonic crystal fibre. *Optics Communications*, **193**: 97–104.
85. Frazão O, Silva S F O, Viegas J, Baptista J M, Santos J L, Kobelke J and Schuster K. (2010) All fiber Mach-Zehnder interferometer based on suspended twin-core fiber. *IEEE Photonics Technology Letters*, **22**: 1300–1302.
86. Frazão O, Silva S F, Viegas J, Baptista J M, Santos J L and Roy P. (2010) A hybrid Fabry-Perot/Michelson interferometer sensor using a dual asymmetric core microstructured fiber. *Measurement Science and Technology*, **21**: 025205.

87. Duncan R G, Froggatt M E, Kreger S T, Seeley R J, Gifford D K, Sang A K and Wolfe M S. (2007) High accuracy fiber-optic shape sensing. In *Proceedings of the SPIE Smart Sensor Systems and Networks: Phenomena, Technology and Applications for NDE and Health Monitoring* (SPIE Vol. 6530), Peters K (ed). SPIE: Bellingham, WA, pp. 65301S-1–65301S-11.
88. http://www.lunainnovations.com/technologies/shape-sensing.htm.
89. Flockhart G M H, Cranch G A and Kirkendall C K. (2006) Differential phase tracking applied to Bragg gratings in multi-core fibre for high accuracy curvature-measurement. *Electronics Letters*, **42**: 390–391.
90. Cranch G A, Flockhart G M H, MacPherson W N, Barton J S and Kirkendall C K. (2006) Ultra-high sensitivity two-dimensional bend sensor. *Electronics Letters*, **42**: 520–522.
91. Zolla F, Renversez G, Nicolet A, Kuhlmey B, Guenneau S and Felbacq D. (2005) *Foundations of Photonic Crystal Fibres*; Imperial College Press: London, UK.
92. Kim H M, Kim T H, Kim B and Chung Y. (2010) Temperature-insensitive torsion sensor with enhanced sensitivity by use of a highly birefringent photonic crystal fiber. *IEEE Photonic Technology Letters*, **22**: 1539–1541.
93. Birks T A, Knight J C and Russell P S. (1997) Endlessly single-mode photonic crystal fiber. *Optics Letters*, **22**: 961–963.
94. Gayraud N, Kornaszewski L W, Stone J M, Knight J C, Reid D T, Hand D P and MacPherson W N. (2008) Mid-infrared gas sensing using a photonic bandgap fiber. *Applied Optics*, **47**: 1269–1277.
95. Nasilowski T, Martynkien T, Statkiewicz G, Olszewski J, Golojuch G, Urbanczyk W, Wojcik J, Mergo P, Makara M, Berghmans F and Thienpont H. (2005) Temperature and pressure sensitivities of the highly birefringent photonic crystal fiber with core asymmetry. *Applied Physics B*, **81**: 325–331.
96. Bock W J, Urbańczyk W and Wojcik J. (2004) Measurements of sensitivity of the single-mode photonic crystal holey fibre to temperature, elongation and hydrostatic pressure. *Measurement Science and Technology*, **15**: 1496–1500.
97. Wang Y P, Xiao L, Wang D N and Jin W. (2006) Highly sensitive long-period fiber-grating strain sensor with low temperature sensitivity. *Optics Letters*, **31**: 3414–3416.
98. He Z, Zhu Y and Du H. (2007) Effect of macro-bending on resonant wavelength and intensity of long-period gratings in photonic crystal fiber. *Optics Express*, **15**: 1804–1810.
99. Petrovic J S, Dobb H, Mezentsev V K, Kalli K, Webb D J and Bennion I. (2007) Sensitivity of LPGs in PCFs fabricated by an electric arc to temperature, strain and external refractive index. *Journal of Lightwave Technology*, **25**: 1306–1312.
100. Martelli C, Canning J, Groothoff N and Lyytikainen K. (2005) Strain and temperature characterization of photonic crystal fiber Bragg gratings. *Optics Letters*, **30**: 1785–1787.
101. Silva-López M, Fender A, MacPherson W N, Barton J S, Jones J D C, Zhao D, Dobb H, Webb D J, Zhang L and Bennion I. (2005) Strain and temperature sensitivity of a single-mode polymer optical fiber. *Optics Letters*, **30**: 3129–3131.
102. Kiesel S, Peters K, Hassan T and Kowalsky M. (2007) Behaviour of intrinsic polymer optical fibre sensor for large-strain applications. *Measurement Science and Technology*, **18**: 3144–3154.
103. Kiesel S, Peters K, Hassan T and Kowalsky M. (2009) Calibration of a single-mode polymer optical fiber large-strain sensor. *Measurement Science and Technology*, **20**: 034016.

104. Jiang C, Kuzyk M G, Ding J L, Johns W E and Welker D J. (2002) Fabrication and mechanical behavior of dye-doped polymer optical fiber. *Journal of Applied Physics*, **92**: 4–12.
105. Kuzyk M G. (2007) *Polymer Fiber Optics: Materials, Physics and Applications* Boca Raton, FL: CRC/Taylor & Francis.
106. Large M C J, Moran J and Ye L. (2009) The role of viscoelastic properties in strain testing using microstructured polymer optical fibres (mPOF). *Measurement Science and Technology*, **20**: 034014.
107. Zhang C, Zhang W, Webb D J and Peng G D. (2010) Optical fibre temperature and humidity sensor. *Electronics Letters*, **46**: 643–644.
108. Peters K. (2011) Polymer optical fiber sensors – a review. *Smart Materials and Structures*, **20**, 013002.
109. Garvey D W, Zimmerman K, Young P, Tostenrude J, Townsend J S, Zhou Z, Lobel M, Dayton M, Wittorf R, Kuzyk M G *et al.* (1996) Single-mode nonlinear-optical polymer fibers. *Journal of the Optical Society of America A*, **18**: 2017–2023.
110. Large M C J, Poladian L, Barton G W and van Eijkelenborg M A. (2007) *Microstructured Polymer Optical Fibers* Berlin: Springer-Verlag.
111. Kiesel S, Peters K, Hassan T and Kowalsky M. (2008) Large deformation in-fiber polymer optical fiber sensor. *IEEE Photonics Technology Letters*, **20**: 416–418.
112. Abdi O, Peters K, Kowalsky M and Hassan T. (2011) Validation of a single-mode polymer optical fiber sensor and interrogator for large strain measurements. *Measurement Science and Technology,* **22**: Art. No. 075207.
113. Abdi O, Wong K C, Hassan T, Peters K J and Kowalsky M J. (2009) Cleaving of single mode polymer optical fiber for strain sensor applications. *Optics Communications*, **282**: 856–861.
114. Peng G D, Xiong Z and Chu P L. (1999) Photosensitivity and gratings in dye-doped polymer optical fibers. *Optical Fiber Technology*, **5**: 242–251.
115. Liu H Y, Liu H B and Peng G D. (2005) Tensile strain characterization of polymer optical fibre Bragg gratings. *Optics Communications*, **251**: 37–43.
116. Liu H Y, Peng G D and Chu P L. (2001) Thermal tuning of polymer optical fiber Bragg gratings. *IEEE Photonics Technology Letters*, **13**: 824–826.
117. van Eijkelenborg M A, Large M C J, Argyros A, Zagari J, Manos S, Issa N A, Bassett I, Fleming S, McPhedran R C, de Sterke C M and Nicorovici N A P. (2001) Microstructured polymer optical fibre. *Optics Express*, **9**: 319–327.
118. Hiscocks M P, van Eijkelenborg M A, Argyros A and Large M C J. (2006) Stable imprinting of long-period gratings in microstructured polymer optical fibre. *Optics Express*, **14**: 4644–4647.
119. Carroll K E, Zhang C, Webb D J, Kalli K, Argyros A and Large M C J. (2007) Thermal response of Bragg gratings in PMMA microstructured optical fibers. *Optics Express*, **15**: 8844–8850.
120. Dobb H, Webb D J, Kalli K, Argyros A, Large M C J and van Eijkelenborg M A. (2005) Continuous wave ultraviolet light-induced fiber Bragg gratings in few- and single-mode microstructured polymer optical fibers. *Optics Letters*, **30**: 3296–3298.
121. Gifford D K, Kreger S T, Sang A K, Froggatt M E, Duncan R G, Wolfe M S and Soller B J. (2007) Swept-wavelength interferometric interrogation of fiber Rayleigh scatter for distributed sensing applications. *Proceedings of SPIE Fiber Optic Sensors and Applications V*, **6770**: 6770OF.

122. Kreger S, Sang A K, Gifford D K and Froggatt M E. (2009) Distributed strain and temperature sensing in plastic optical fiber using Rayleigh scatter. *Proceedings of SPIE Fiber Optic Sensors and Applications VI*, **7316**:73160A.
123. Measures R M. (2001) *Structural Monitoring with Fiber Optic Technology*; Academic Press: San Diego, CA.
124. Udd E (ed.). (2006) *Fiber Optic Sensors*; John Wiley & Sons, Inc.: Hoboken, NJ.
125. Glišić B and Inaudi D. (2007) *Fibre Optic Methods for Structural Health Monitoring*; John Wiley & Sons, Inc.: Hoboken, NJ.
126. Boller C, Chang F K and Fujino Y (eds.). (2009) *Encyclopedia of Structural Health Monitoring*; John Wiley & Sons, Inc.: Chichester, UK.
127. Méndez A and Morse T F. (2007) *Specialty Optical Fibers Handbook*; Academic Press: Amsterdam.
128. www.roctest-group.com.
129. www.lunatechnologies.com.
130. www.opticalfibersensors.org.

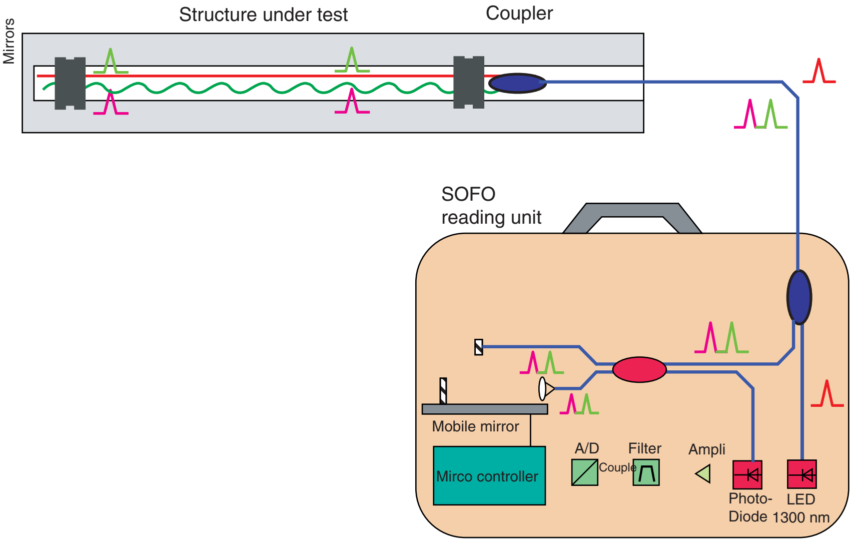
Mirrors
Structure under test
Coupler
SOFO
reading unit
Mobile mirror
Mirco controller
A/D
Couple
Filter
Ampli
Photo-
Diode
LED
1300 nm

Plate I (Chapter 5) Schematic overview of SOFO system.

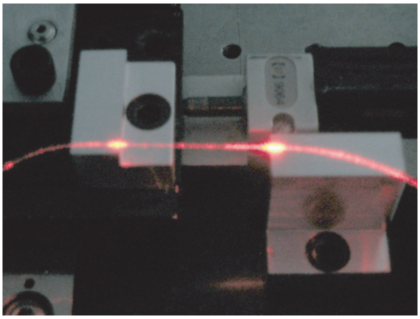

Plate II (Chapter 5) Single-mode POF during loading with uniform visible light attenuation. Bright spots are locations where POF is glued to supports (Kiesel S, Peters K, Hassan T and Kowalsky M. (2008) Large deformation in-fiber polymer optical fiber sensor. *IEEE Photonics Technology Letters*, **20**: 416–418).

6

Acoustic emission sensors for assessing and monitoring civil infrastructures

M. MEO, University of Bath, UK

DOI: 10.1533/9780857099136.159

Abstract: This chapter presents a review of recent developments in acoustic emission (AE) techniques applied to civil structures. It recapitulates the significant milestones achieved by previous researchers, including various methods and models developed in AE testing of civil structures. The aim is to provide an overview of the use of AE techniques for structural health monitoring of civil structures carried out over the years. Basic principles are introduced, followed by acoustic source localization and severity assessment methods. An overview of AE equipment technology is then presented with field application of AE. Finally, current and future challenges are discussed.

Key words: acoustic emission monitoring, acoustic detection, concrete, Kaiser effect, non-destructive evaluation.

6.1 Introduction

As the infrastructure ages, civil structures reach the end of their economic lives. Replacement costs and life extension become critical issues and reliable inspection-based maintenance protocols ensure their safe, reliable and economic operation without undue risk to public health and safety. The classical fail-safe design and maintenance approach does not tolerate any known crack or defects, and it has had major financial implications in ensuring integrity of structures. This has forced civil infrastructure operators to adopt a new approach used in the aerospace industry, whereby flaws or damage are tolerated as long as they do not compromise a structure's ability to perform its function. Significant cost savings result by detecting defective parts before the end of their design life and avoiding unnecessary replacement of sound components. Visual inspection and non-destructive testing (NDT) is the basis for the retirement-for-cause approach. NDT examines materials or components in ways that do not impair future usefulness and serviceability and is used to detect, locate, measure, and evaluate flaws/damage and to assess integrity. Various NDT technologies, such as radiographic

© 2014 Woodhead Publishing Limited

methods, ultrasonic-based methods, acoustic emission (AE) techniques, to name a few, are used to monitor civil structures. Each NDT technique has both advantages and disadvantages with regard to cost, speed, accuracy, and safety, and the choice of a technique is strictly correlated with the kind of structure to be analysed and the data to be extracted.

AE is a significant resource with a specific role to play in the spectrum of maintenance resources both in its own right and as a complement to other monitoring technologies. AE is defined as the transient stress waves generated by the rapid energy from localized sources within a structure. After originating, stress waves travel to the surface and become surface waves. The surface mechanical waves can be detected by sensors. These AE bursts can be used both to locate cracks and to evaluate their rate of growth as a function of the applied stress. One of the main advantages of AE methods is that they detect and locate cracks in one measurement. In addition to this, since acoustic waves propagate through the structure, they can provide remote monitoring of inaccessible areas and the ability to monitor with a minimum number of sensors. This is in contrast to most other NDT methods, which require point-by-point inspection and are therefore limited to accessible areas of a structure. However, AE testing does not determine the size of cracks – it allows a reduction of the area to be scanned by other non-destructive test techniques to quantify problems in the areas identified by AE testing. Further analysis by fracture mechanics can be used to determine the severity of defect from the structural integrity point of view.

6.2 Fundamentals of acoustic emission (AE) technique

AE monitoring is a passive monitoring technique aimed at detecting acoustic stress waves generated in materials that arise from the rapid release of strain energy from micro-structural changes in a material.[1] The sources of AE are initiation/growth of cracks, yielding, failure of bonds, fibre failure, delamination in composites, etc. Most of the sources of AEs are damage-related; thus, the detection and monitoring of these emissions are commonly used to predict material failure. Localized energy release travelling as elastic waves move to the surface and, if the waves are of sufficient amplitude, are detected by transducers attached to the surface of the specimen provided. Acoustic stress wave detection is a complex task, since it is strongly related to the main features of propagating stress waves, attenuation, effects of multiple paths, source location algorithm criterion, etc.[1]

In contrast to other NDT/structural health monitoring (SHM) methods, AE is usually applied during loading to verify the occurrence of AE, while most others are applied before or after loading of a structure.

Table 6.1 AE process

Step	Action
1. Structure under in-service loads	Produce stress
2. Source mechanisms	Release elastic energy
3. Wave propagation	Direct wave path from the source to the sensor and reflections
4. AE transducers	Stress waves are converted into an electrical AE signal
5. Acquisition of measurement data	Converting the electrical AE signal into data with amplification and filtering
6. Data post-processing	Convert waveforms into meaningful parameters
7. Integrity evaluation	Assess damage based on processed data

The AE technique is a procedure for monitoring and analysing of AE, whereas AE testing is a method to test the presence or absence of AE activity. The AE method analyses the evolution of cracks and estimates the released strain energy during their propagation in structural members.

The AE waves may consist of only a single transient event, or be composed of a number of discrete cracks and microcracks, each producing an AE, depending on the material and the stress regime failure.

Typical AE waves generated through sudden release of energy are usually of low amplitude. In general, AEs can be classified into primary and secondary emissions. Primary emissions are those originating from within the material of interest, while secondary emissions refer to all other emissions generated from external sources. Therefore, in AE monitoring it is vital to reduce the noise mixed up with signal parts related to the fracture process. To enhance the signal-to-noise ratio in AE analysis there is a need to employ efficient filter techniques.

The typical AE process step consists of the following steps and actions reported in Table 6.1.

Basically, the AE monitoring technique detects a crack growth process as it occurs.

6.3 Interpretation of AE signals

A typical burst AE signal and the typical parameters used for AE techniques are shown in Plate III in the colour section between pages 294 and 295.[2] In the AE method, also called ring-down counting or event-counting, when the amplitude of stress waves acquired by the AE transducer is over a certain threshold level (measured in volts), an AE event is captured. The peak of the signal defines the amplitude of the AE event, and the AE count is the number of times the wave crosses the threshold.

The amplitude is closely related to the magnitude of the source event, and it is an important parameter in determining the system's detectability.

The *duration* of an AE event is defined by the time period between the rising edge of the first count and the falling edge of the last count, and the *rise time* is the time period between the rising edge of the first count and the peak of the AE event. It must be noted that 'counts' are strongly dependent on the operating frequency and clearly the employed threshold. The area under the envelope of the AE event is the *energy*. It is usually more appropriate to analyse the energy to interpret the magnitude of source event over counts because it is sensitive to the amplitude as well as the duration, and less dependent on the operating frequencies and voltage threshold.

AE technique involves recording the stress waves by means of sensors placed on the surface of the structure and subsequent analysis of the recorded signals to locate and gather information about the nature of the source of emission.

6.4 AE localization methods

Traditional AE uses only some of the features of AE signals, due to the main limitations of available sensors as well as data-capturing and analysis capability. Recent progress has been made in transducer technology, wide-band, acquisition systems, etc. New AE sensors able to capture the whole waveform have been developed, allowing accurate localization as well as characterization of the nature of AE sources from the waveform captured.

Localization of the AE source is a complex procedure for civil structures due to the large area needed to be monitored, and the distortion of the waveforms due to presence of different materials, non-linear effects, tapered sections, etc. It is possible to solve inverse wave-propagation problems to identify the source of the AE signals detected using one or more sensors by analysing the whole waveform.

A typical conventional AE set-up consists of many sensors distributed around potential source locations to be assessed. AE source localization is an inverse problem. By measuring the arrival time differences of the elastic wave emitted by the AE sources fracture at each sensor, the source location can be calculated by assessing the AE event origin time and the AE source coordinates (x_0, y_0, z_0). The computed location corresponds to the point in space and time where the crack growth is initiated. Generally a point source is assumed.

In most of the localization methods, the onset times, the coordinates of each corresponding sensor and the velocities of the compressional and shear wave for bulk materials or group velocity (dispersion curves) for thin walled structures are needed.

While for homogeneous and isotropic material the direct ray path between source and receiver can be used for calculation of the source location, in the case of layered materials or heterogeneous and anisotropic material, directional properties of stress wave propagation must be taken into consideration for an accurate localization.

One of the most difficult tasks to estimate source location is the determination of the time of arrival (TOA) or onset picking. The simplest method for TOA estimation is to use an amplitude threshold picker. However, a pure threshold approach would not be applicable to signals with small amplitudes and/or signals with high noise levels.

Another approach used in the seismic application is to model the signal as an autoregressive process,[3] whereby a time series is divided into stationary segments modelled as an autoregressive process (Akaike Information Criterion, abbreviated as AIC). This approach developed has been transferred to the AE field by Kurz *et al.*[4]

Another common TOA estimation method is cross-correlation, whereby the correlation between two signals acquired by two sensors is defined by the following formulas:

$$C(t) = \int S_{\text{sensor}1}(\tau) \cdot S_{\text{sensor}2}(\tau + t)dt \qquad [6.1]$$

where $S_{\text{sensor }1}(\tau)$ is the time history of the acquired waveform. Then the time difference is:

$$\Delta t = t\big|_{\max\{C(t)\}} \qquad [6.2]$$

An example is reported in Fig. 6.1.

The sensor 1 in this approach is commonly termed the master sensor, which will help in calculating the time difference that will be used for the localization approach. The cross-correlation function gives a measure of the similarity of two time series shifted along each other. The maximum value of $f(t)$ indicates the maximum correlation of the two signals gained at the time shift t. A detailed comparison of these techniques for TOA estimation strategies can be found in Reference 4. Other techniques include using wavelets, which were employed for the aerospace sector and applied with success. A detailed discussion can be found in References 5 and 6.

There are a number of methods to localize the source of AEs. In 1-D, by knowing the propagation velocity V, the distance D between the two sensors, the onset time at each sensor or the time difference Δt between the arrival time at sensor 1 and 2 as explained in Fig. 6.1, the distance of the source x_{source} can be calculated by this formula, as shown in Fig. 6.2.

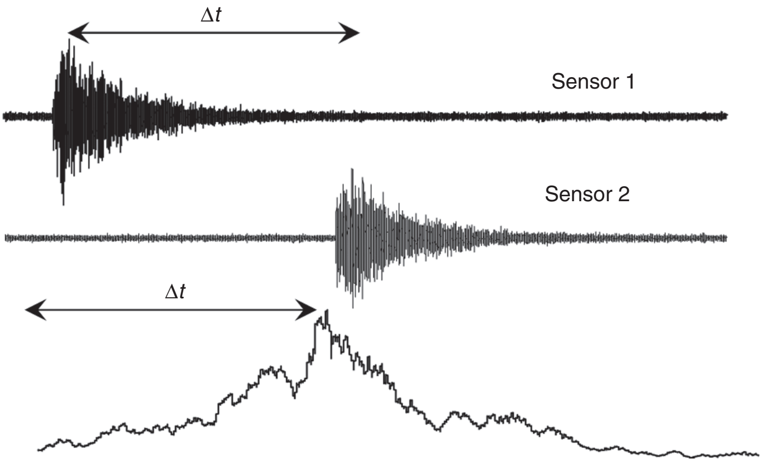

6.1 Normalized cross-correlation function.

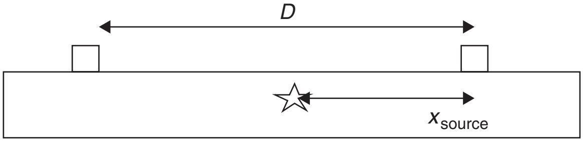

6.2 1-D source localization.

$$x_{\text{source}} = \frac{1}{2}(D - \Delta t\, V) \qquad [6.3]$$

This approach can be applied to structures such as pipes. To perform a 2-dimensional (2-D) localization there is the need to determine the coordinates x_{source} and y_{source} of the AE source. For 2-D structures, where the thickness is small compared to other geometrical entities, and for waves with wavelengths longer than the thickness of the structure, group velocities of plate or Lamb waves have to be used for localization. At least three sensors are needed for a 2-D localization. Assuming constant velocity and three measured arrival times t_1, t_2 and t_3 of the wave, at three different sensors, the AE source can be calculated by the hyperbola[7] or circle method[8] as the intersection of the three curves as shown in Fig. 6.3.

Because of measurement error, to improve localization accuracy extra sensors may be needed. This technique can be extended to 3D structures, but there is the need to have one extra sensor to detect also the z_{source}. It must

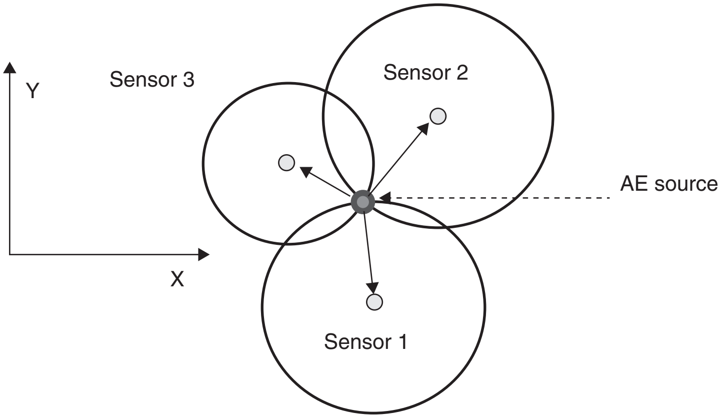

6.3 2-D source localization.

be noted that these techniques are valid under the assumption of homogenous and isotropic materials and the AE source can be assumed as a point source. Due to the presence of different sources (noise, etc.), the determination of the arrival times can lead to incorrect AE source estimation. One particularly important issue when recording AE events is background or environmental noise, and particular care is needed during the experiment. A solution is to set the frequency range of the measurement above that of the environmental noise, achieved by grounding the equipment. Then a band-pass filter can be used to reduce/eliminate spurious sources of noise. Generally, it is necessary to perform error analysis to assess the accuracy and reliability of any localization result. The bandwidth from several kHz to several 100 kHz or 1 MHz is usually used in AE measurements. For layered media the group velocity is direction dependent, and therefore complex algorithms are necessary to locate the source.

Recently Meo *et al.*[9,10] suggested a localization method to detect the source location in reverberant complex composite structures using only one passive sensor. This technique was based on the time reversal acoustic method applied to a number of waveforms stored in a database containing the impulse response (Green's function) of the structure. The proposed method allowed the optimal focalization of the AE source in the time and spatial domain overcoming the drawbacks of other ultrasonic techniques. This was mainly due to the dispersive nature of guided Lamb waves, as well as the presence of multiple scattering and mode conversion that can degrade the quality of the focusing, causing poor localization. Conversely, by using the benefits of a diffuse wave field, the imaging of the source location was obtained through a virtual time reversal procedure, which did not require any iterative algorithms and a priori knowledge of the mechanical properties and the anisotropic group speed. The efficiency of this method was experimentally demonstrated on a stiffened composite panel. The results showed that the source location was retrieved with a high level of accuracy in any position of the structure, with a maximum error of less than 3%.

6.5 Severity assessment

A material is known to produce acoustic waves only after until the previous load peak is achieved or exceeded. This phenomenon, named the 'Kaiser' effect, can be seen in the load vs AE plot (Fig. 6.4). AE is generated when load is increased (AB), but as the load lowered (BC) and raised again (CB), AE can be recorded until the previous load maximum is exceeded. As load is increased again the cumulative AE events increase (BD), and stop as the load is lowered for the second time (DE). On further increase of the load, a different emission pattern is observed: AE is observed at a lower load than the previous maximum load is attained (F). Emission continues as the load is increased (FG). The Kaiser effect can be observed if no permanent damage within the specimen has occurred.[11] In the presence of permanent damage (load D), AE activity starts to be observed even under lower stress (load D) than that of the maximum stress experienced, and this new condition is known as the Felicity effect. Basically, at point F, the applied load is high enough to cause significant emissions even though the previous maximum load (D) was not reached. The significance of this effect and its related damage is defined by a Felicity ratio, which is the load at which AE events are

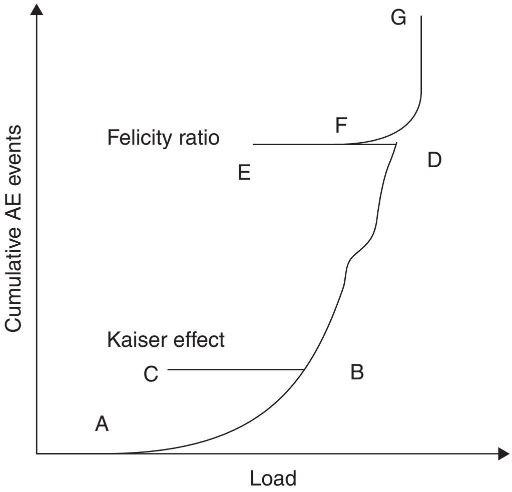

6.4 Kaiser effect.

first generated upon reloading divided by the previously applied maximum load. Insignificant flaws tend to show the Kaiser effect, while structurally significant flaws tend to show the Felicity effect. The latter has been successfully applied in monitoring damage progression in composite materials.[11]

Analysis of the above mentioned conventional AE parameters can provide qualitative results. In order to evaluate the level of deterioration, quantitative damage assessment is necessary. Golaski[12] suggested the use of statistical analysis-based parameters to measure deterioration of materials applied to concrete bridges. They proposed to describe the intensity of an emission source by calculating the historic and severity index taken during the proposed loading. The historic index (HI) compares the signal strength of the most recent hits to all the hits defined by:

$$H(t) = \frac{N}{N-K}\left(\frac{\sum_{i=K+1}^{N} S_{Oi}}{\sum_{i=1}^{N} S_{Oi}}\right) \qquad [6.4]$$

where $H(t)$ is the HI at time t, N is the number of hits up to and including time t, S_{Oi} is the signal strength of the i-th event and K is an empirically derived factor that varies with the number of hits. The values of K are dependent on materials and N.[13]

The severity index (S_r) is defined as the average signal strength for the J events having the largest numerical value of signal strength, and is defined by the following equation:

$$S_r = \frac{1}{J}\sum_{i=1}^{1=J} S_{Oi} \qquad [6.5]$$

where S_r is severity and S_{Oi} is the signal strength of the i-th event as above. This procedure was first introduced in Reference 13 for damage evaluation in composite tanks and pipelines.

To determinate the intensity, the maximum HI and severity values are collected by each sensor and plotted on a chart. An example is shown in Fig. 6.5 where the severity index and maximum value of HI are plotted and the intensity chart is divided into zones with different levels of damage.[14] The location of the sensor point in the chart will indicate the level of damage.

Depending on the type of cracks, different types of AE signals with varying frequency ranges and amplitudes are generated. Microcracks are characterized by a large number of events of small amplitude, in contrast

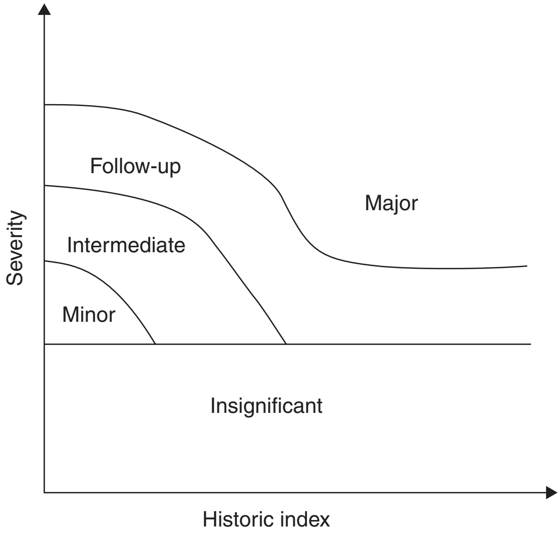

6.5 Example of intensity chart.

to macrocracks where fewer events with larger amplitude are generated. In open cracks, where most of the energy has already been released, many AE events are created with small amplitude. Furthermore, while shear cracks create smaller amplitude signals, tensile cracks spawn large amplitude AE. The b-value analysis[15] takes these factors into account and is used as an alternative way to process and interpret data recorded during a local AE monitoring. The b-value analysis derives from seismology, where the following formula relates the number of events to peak-amplitude of AE events:

$$\log_{10} N = a - bM_L \qquad [6.6]$$

where M_L is the magnitude of an event on the Richter scale, N is the number of events with magnitudes in the range $M_L \pm \Delta M/2$, and a and b are empirical constants. This formula can be adapted for AE by substituting M_L with A_{dB} that represent the peak-amplitude of the AE events in decibels. The b-value is calculated as the negative slope of log-linear plot of the frequency-magnitude distribution of AE. The b-value changes systematically with the different stages of fracture growth so it can be used to estimate the development of fracture process.[15] When microcracks occur in the early stages of damage, the b-value is high but becomes low when macrocracks begin to occur.[15] This fact makes the b-value an indicator of the presence of damage when stresses are redistributed and damage becomes more localized.[16]

6.6 AE equipment technology

The basic AE techniques consist of AE wave sources, the detection equipment used to capture AE signals, and the processing and interpretation of the collected data. An AE wave is an elastic wave, a combination of longitudinal, transverse, reflected waves, etc., with a broadband frequency range (kHz to MHz), generated by the release of energy by the formation of a microcrack. Most traditional AE sensors consist of a piezoelectric (lead zirconate titanate (PZT)) device that transforms motion produced by an elastic wave into an electrical signal.

The frequency response of the transducer is dependent on the dimension of the PZT, and the sensitivity of an AE transducer depends on its mode of operation and construction (resonant or broadband). Piezoceramic resonant transducers tend to have high sensitivity near resonance. Broadband piezoceramic transducers are sensitive to a wide range of frequencies, although they generally have lower sensitivity than resonant transducers.

In the selection of the appropriate AE transducer, the sensitivity and frequency response should be taken into consideration based on the purpose and sensitivity required for the investigation.

For thin structures, a higher frequency transducer should be used, since wavelength is determined from the velocity divided by frequency, while for materials with high attenuation, low resonance AE transducers should be used.

Typically, the signal from the transducers is preamplified, converted into electric voltage, filtered to eliminate unwanted frequencies and processed in a data acquisition system. The preamplifiers can be integrated with the sensor or connected to it.

While the frequency spectrum of the AE signal wave is mainly dependent on the transducer characteristics, materials and wave path, the AE signal waveform is affected by thickness dimension; for example, when the wavelength is greater than the thickness, Lamb wave modes propagate and the maximum amplitude is not determined by surface waves. Knowledge of wave modes and their characteristics is particularly important when the AE source needs to be localized. To minimize energy transfer loss from the surface of the material, appropriate couplant should be used.

In presence of different acoustic sources, unidirectional sensors and sensors, more sensitive to in-plane wave modes, should be used, especially for bridge monitoring.[17]

Other types of sensors include capacitive transducers, shape memory alloys and optical fibre sensors.[18,19] A capacitive AE micromachined transducer[20] was recently produced from polymer material using microstereolithography (Fig. 6.6). With this cost-effective approach, the sensor architecture could be shaped to conform to complex geometries, ideal for *in situ* inspection. An electroded vibrating membrane was placed over an

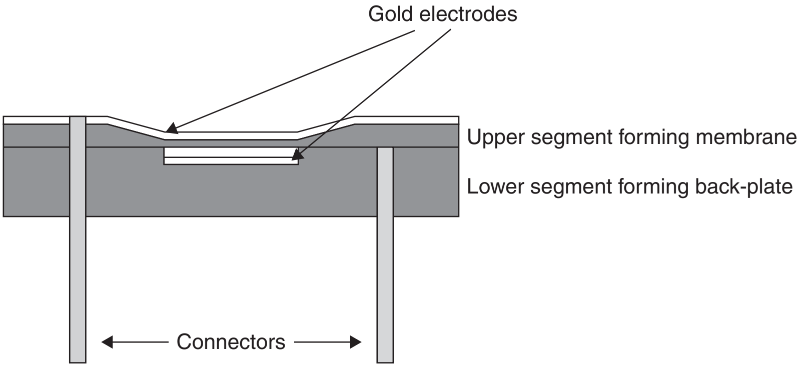
Gold electrodes
Upper segment forming membrane
Lower segment forming back-plate
Connectors

6.6 Capacitive polymer sensor constructed using micro-stereolithography techniques.[20]

air cavity, at the bottom of which a second electrode was placed. A force (acoustic generation) on the membrane was generated by applying a voltage. This showed that when introducing a DC bias, the device could also be used as a receiver, like a conventional condenser microphone.

Recently, capacitive-type AE sensors, based on multi-user micro-electro-mechanical systems (MEMS) processes (MUMPS), have attracted the attention of researchers.[21,22] MEMS technology is a collection of methods and techniques to fabricate microscale systems. The advantages of MEMS devices include miniaturization of systems, multiple systems on one chip, and reduced cost due to batch processing. MEMS devices are sometimes manufactured by a process known as surface micromachining, during which structures are built up through a process of depositing, patterning and etching different materials on the chip substrate. Typically, the substrate is silicon, and structures are formed out of polysilicon. MEMS technology makes it possible to locate multiple transducer designs on a small area, which can provide additional information about the source. In principle, MEMS technology also invites the development of sensors integrated with signal processing. However, often MEMS-based sensors have limited sensitivity and must be operated in a vacuum for practical use. In addition, most MEMS sensors and piezoceramic transducers are limited to sensing vibration normal to the surface on which the sensor is mounted (i.e., in the out-of-plane direction). Figure 6.7 shows a schematic of a resonant MEMS sensor, consisting of bottom plate fixed to the chip substrate and a top plate spring-suspended above the bottom plate.[23] When an AE source reaches the sensor, the top plate vibrates with respect to the bottom plate, resulting in a time-varying voltage. This time-varying voltage is then amplified, and captured and analysed using a data acquisition system.

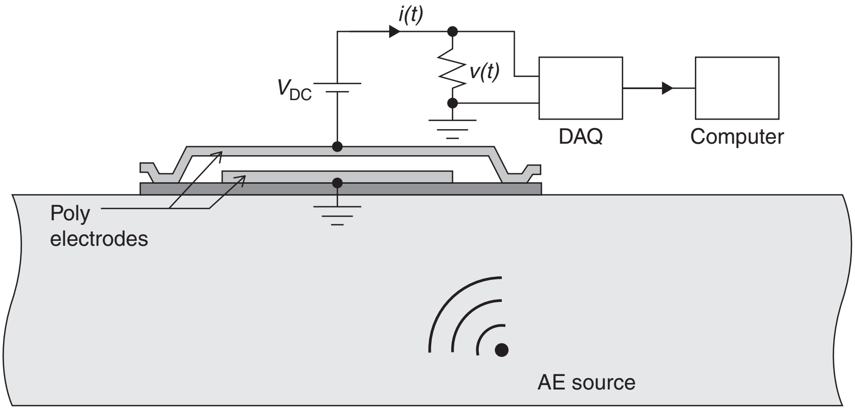

6.7 Concept of a capacitive MEMS resonator.[22]

Recently an out-of-plane and in-plane MEMS sensor was suggested by Harris *et al*.[24]

By adopting an open-grill design (Plate IV in the colour section between pages 294 and 295), the desired level of performance was achieved without requiring a vacuum. The in-plane sensor, Plate IV, a capacitive finger-type resonator, had a central stationary spine with outward projecting fingers, and a spring-suspended moving frame with inward projecting fingers. The moving frame of the in-plane device was supported by four L-shaped flexural springs.

The combination of one out-of-plane sensor and two orthogonal in-plane sensors can provide sensing in the three spatial dimensions. The potential advantages of three-dimensional sensing capabilities include improvements in characterization of structural damage by distinguishing between different wave modes and determining the direction of the source.

6.7 Field applications and structural health monitoring using AE

Current procedures for assessing the health state of civil building structures are based on visual processes. The structural integrity is evaluated by examining the surface of structures, and the interpretation and assessment relies mainly on the skills and level of experience of the engineers. Managing the sustainability of urban infrastructure requires regular health monitoring of key infrastructure. The SHM process involves measuring specific feature (displacement, acceleration, etc.) over a period of time using appropriate transducers, extraction of meaningful damage sensitive features from measurements, and analysing these data to determine the integrity of the structure. The reliability of the SHM system is obtained and enhanced by combining the information obtained at different locations and from different sensor types. Usually, deviation from the usual behaviour of the structure i.e., an outlier in a time series, is used to assess a structural change. For civil structures AE is rarely, if ever, used as the primary means of evaluation. However, AE is currently finding increased use for the structural assessment and monitoring of civil infrastructures such as bridges, buildings, etc., and the sensitivity and non-invasive nature of the method are clear advantages for many civil applications.[25]

Numerous field bridge testing applications have been conducted to demonstrate the ability of AE to detect source location and for damage intensity predictions. Corrosion of reinforcement bars and the resulting cracking is one of the main damage mechanisms that require long-term monitoring of bridges.

Yuyama and Ohtsu[26] studied AE concrete structures to analyse fracture characteristics to quantify micro-fractures and damage intensity in concrete. Beck *et al.*[27] studied the relationship between AE energy and fracture area and depth, showing that the AE energy can be used to quantify crack size, while in Reference 28 AE was used to monitor wire fracture in a prestressed concrete bridge under environmental load (regular traffic) on cables that could not otherwise be inspected. Li and Ou[29] showed AE parameters based on correlation of count, energy, duration time, amplitude and time could track the damage growth and differentiate a broken wire from an unbroken one.

Existing commercial monitoring systems use mainly wired sensor technologies that are time consuming to install and relatively expensive. In a typical civil monitoring application a large number of sensors (i.e., more than ten) connected through long cables are used. Therefore, one of the key features desirable in monitoring large civil infrastructures as bridges is remote monitoring. Replacement of these cables with wireless systems is a longstanding dream that has become a growing reality in recent years, thanks to digital communications progress. Wireless monitoring systems, along with performance enhanced sensors based on MEMS, could potentially reduce these costs significantly, and would increase the field of application. An implementation of wireless AE technique sensors was proposed by Grosse *et al.*,[30] and the basic concept is reported in Fig. 6.8. Then by using more efficient inspection methods with detailed information on the structural behaviour, maintenance costs could also be reduced.

An associated cost-cutting development is the introduction of self-powered (energy harvesting) AE systems.[31] Being wireless and self-powered, the AE system could be positioned there permanently. This is in the long term a cheaper option since if the costs, for example, of a lane closure are taken into account, it becomes clear that it is cheaper to leave the equipment in place than to close the lane in order to remove it.

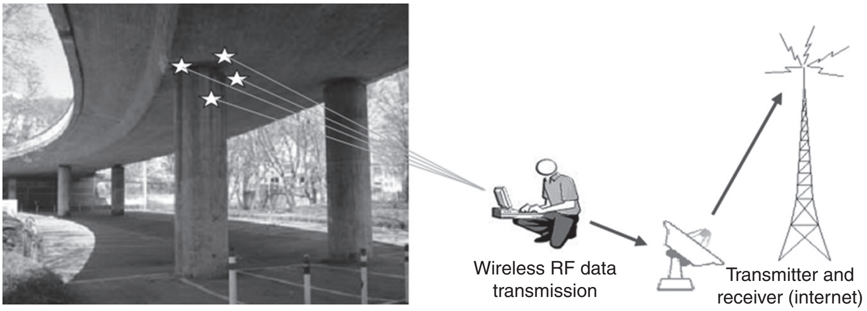
Wireless RF data transmission
Transmitter and receiver (internet)

6.8 Bridge wireless application.[2]

6.9 Crack location.[30]

For these above reasons, coupling self-powered and wireless AE systems is expected to bring about a major improvement in the practical applicability of AE technology to monitor urban infrastructures.

In 2009 a large crack was found in a fracture-critical element on the San Francisco–Oakland Bay Bridge by an on-site visual inspection (Fig. 6.9). An AE monitoring system was developed[32] and tested, validated through

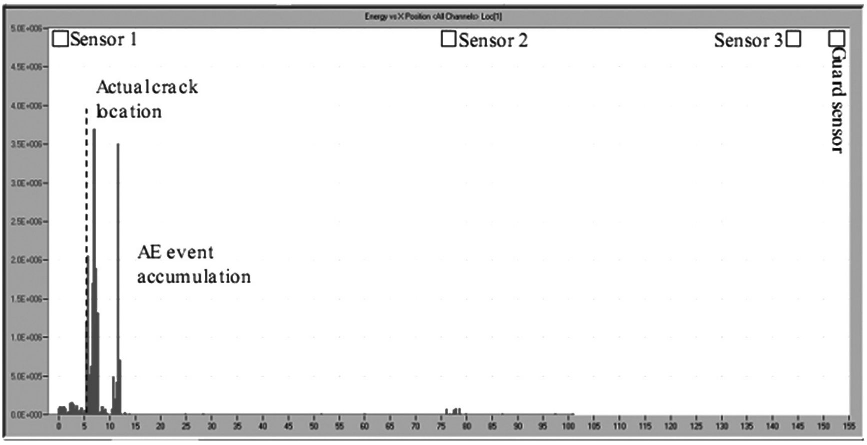

6.10 Energy vs X crack position under low cycle fatigue loading.[30]

laboratory testing for continuous monitoring to detect and localize crack initiation and growth in real time (Fig. 6.10).

A comparison of the AE results with ultrasonic, dye penetrant and visual methods in terms of the damage detection was carried out. This study showed that the initiated fatigue crack in an eyebar under fatigue loading was successfully detected, located and monitored. In addition, by using a relatively small number of AE sensors, crack nucleation was detectable and located during the early stages utilizing a relatively small number of AE sensors. Figure 6.10 shows the location histogram recorded during the fatigue cycles of the loading and the actual crack location.

As a result of this successful demonstration of the effectiveness of the AE approach, a system consisting of 640 AE sensors connected to 16 AE Workstations was installed on the San Francisco–Oakland Bay Bridge.

In Reference 1 the AE testing was evaluated on notched full-scale honeycomb sandwich composite fuselage panels as a tool for NDT method for detecting crack initiation and progression, localization of the site of damage and anticipation of ultimate fracture in using redundant arrays of AE sensors. A number of panels with different damage scenarios were studied, under a combination of quasi-static hoop and longitudinal loads. Various inspections were used to assess damage progression and location, and the AE results were correlated with photogrammetric strain fields.

The locations of the events generated by new cracks at the notch tip were identified by accounting only for the high-intensity events. Post-test signal processing was applied by filtering the AE data set according to intensities that discern emissions generated primarily by new failures from that generated by other extraneous sources.

The results showed that AE techniques could accurately detect notch-tip damage initiation and track its growth to ultimate failure.

6.8 Future challenges

In spite of being a promising tool, there are still a number of challenges to be met before the successful application of AE for civil infrastructures. The main hurdles to be overcome are:

- Handling of large amount of data during testing. Due to the high sampling rate needed for data capture, a large amount of data is usually needed for a meaningful set of AE data. This is particularly important for civil infrastructures, given their long-term usage. This will encourage the scientific community to develop and implement effective analysis, fusion and management of large collection of data minimizing human intervention and interpretation.
- Reliable and effective extraction of damage sensitive data from measurements. A number of unwanted sources can produce AEs; therefore, strategies and tools for source discriminations should be in place to identify genuine failure data from spurious data.
- The effect of environmental effect should also be carefully understood and quantified on effective damage assessment.
- Automatic onset time determination for acoustic source localization. While a number of algorithms have been developed to detect TOA, a number of challenges must still be resolved. This is particularly evident for dispersive media and/or tapered structures, where mode conversion could occur. Classical time-of-flight (TOF)-based methods assume known values of AE wave velocity; however, this is inaccurate when the wave velocity changes with the propagation direction (e.g. anisotropic composite multilayered panels etc.) or with the propagation distance (e.g. tapered sections).
- Quantification damage level and prediction of durability and remaining life time. B-values and intensity analysis using severity and historic indices are promising methods; however, understanding the condition of the structure is still an on-going issue.
- Long-term performance of monitoring systems in ‘hostile’ environments. This is a common challenge for a variety of fields, including aerospace, marine, and so on. The performance of attached/embedded systems should be carefully monitored to avoid false alarms due to transducer failure, and adhesive bonding from real material changes.
- Long-term and power storage availability. While significant progress has been made to date on developing a reliable wireless system, the availability of long-term power for permanently installed AE systems should be addressed. Clearly, for some structures a solution would be

to gather health data by employing a discrete monitoring system with limited operational life. This pushes the research community towards a unified approach whereby the energy harvesting and power storage concepts are intrinsically tied to SHM systems and should be developed and implemented simultaneously. Finally, long-term reliability of power storage and energy harvester should also be further developed.

6.9 Conclusion

In this chapter, an overview of AE for civil applications is presented. Basic principles of AE and methods for the localization of AE sources are discussed. Most of the methods discussed in this chapter assume a homogeneous and isotropic material, an assumption that is generally valid for materials used in construction. However, some examples considering non-homogeneous and non-isotropic materials are also shown. Different past and current approaches to assess the severity of flaws/cracks are reviewed. A number of applications of AE use for SHM of civil structures are described. Finally, major current and future challenges to be met for the successful application of AE for civil infrastructures are introduced.

6.10 References

1. Holford KM and Lark RJ (2005) In: Gongkang Fu, editor. *Acoustic Emission Testing of Bridges: Inspection and Monitoring Techniques for Bridges and Structures*. Cambridge (UK): Woodhead Publishing Ltd. p. 183215.
2. Nair A and Cai CS (2010) Acoustic emission monitoring of bridges: Review and case studies. *Eng. Struct.*, **32**(6): 1704–1714.
3. Akaike H (1974) Markovian representation of stochastic processes and its application to the analysis of autoregressive moving average processes. *Ann. Inst. Stat. Math.*, **26**: 363–387.
4. Kurz JH, Grosse CU and Reinhardt HW (2005) Strategies for reliable automatic onset time picking of acoustic emissions and of ultrasound signals in concrete. *Ultrasonics,* **43**(7): 538–546.
5. Ciampa F and Meo M (2010) Acoustic emission source localization and velocity determination of the fundamental mode A_0 using wavelet analysis and Newton-based optimization technique. *Smart Mater. Struct.*, **19**, 1–14.
6. Meo M, Zumpano G, Pigott M and Marengo G (2005) Impact identification on a sandwich plate from wave propagation responses. *Compos. Struct.*, **71**, 302–306.
7. Bath M (1979) *Introduction to Seismology*. 2nd Edition, Basel: Birkhäuser Verlag.
8. Pujol J (2004) Earthquake location tutorial: graphical approach and approximate epicentral location techniques. *Seismological Res. Lett.,* **75**(1): 63–74.
9. Ciampa F and Meo M (2011) Acoustic emission localization in complex dissipative anisotropic structures using a one channel reciprocal time reversal method. *J. Acoust. Soc. Am.,* **130**(1): 168–175.

10. Ciampa F and Meo M (2012) Impact detection in anisotropic materials using a time reversal approach. *Struct. Health Monitor.,* **11**(1): 43–49.
11. Gostautas RS, Ramirez G, Peterman RJ and Meggers D (2005) Acoustic emission monitoring and analysis of glass fiber reinforced composites bridge decks. *J. Bridge Eng. ASCE*, **10**(6): 71321.
12. Golaski L, Gebski P and Ono K (2002) Diagnostics of reinforced concrete bridges by acoustic emission. *J. Acoust. Emiss.,* **20**: 83–98.
13. Fowler TJ, Blessing JA and Conlisk PJ (1989) New directions in testing. *Proceedings of 3rd International Symposium on AE from Composite Materials*, Paris, France.
14. Committee on Acoustic Emission from Reinforced Plastics (CARP). (1987) Recommended practice for acoustic emission of fiberglass reinforced plastic resin (RP) tanks/vessels. New York: Composites Institute, Society of the Plastics Industry.
15. Colombo S, Main IG and Forde MC (2003). Assessing damage of reinforced concrete beam using 'b-value' analysis of acoustic emission signals. *J. Mater. Civil Eng.*, **15**(3): 280–286.
16. Carpinteri A, Lacidogna G and Puzzi S (2009). From criticality to final collapse: Evolution of the 'b-value' from 1.5 to 1.0. *Chaos, Soliton. Fract.*, **41**(2): 843–853.
17. Carter DC and Holford KM (1998) Strategic consideration for AE monitoring of bridges: A discussion and case study. *INSIGHT – J. British Inst. NDT,* **40**(2): 112–116.
18. Tan P, Tong L and Sun D (2002) Dynamic characteristics of a beam system with active piezoelectric fiber reinforced composite layers. *Compos. Part B: Eng.*, **33**: 545–555.
19. Or SW, Chan LW and Choy CL (2000) P(VDF-TrFE) copolymer acoustic emission sensors. *Sensors Actuat A*, **80**: 237–241.
20. Hutchins DA, Billson DR, Bradley RJ and Ho KS (2011) Structural health monitoring using polymer-based capacitive micromachined ultrasonic transducers (CMUTs). *Ultrasonics*, **51**(8): 870–877.
21. Jin X. Ladabaum I and Khuri-Yakub BT (1998) The microfabrication of capacitive ultrasonic transducers. *J. Microelectromech. Sys.*, **7**: 295–302.
22. Wu W, Greve DW and Oppenheim IJ (2007) Characterization and noise analysis of capacitive MEMS acoustic emission transducers. *Proceeding of IEEE Sensors Conference*, Atlanta, Georgia, USA, pp. 1152–1155.
23. Wu W, Greve DW and Oppenheim IJ (2007) Characterization and noise analysis of capacitive MEMS acoustic emission transducers. *IEEE Sensor Conf.* pp 1152–1155.
24. Harris AW *et al*, (2011) Smart Mater Struct, 20: 075018, doi:10.1088/0964-1726/20/7/075018.
25. Ziehl P, Galati N, Tumialan G and Nanni A, (2008) *In situ* evaluation of two RC slab systems – Part II: Evaluation criteria. *ASCE J. Perform. Constr Fac.*, **22(**4): 217–227.
26. Yuyama S and Ohtsu M (2000) Acoustic emission evaluation in concrete. In: Kishi T, Ohtsu M and Yuyama S, editors. *Acoustic Emission-Beyond the Millennium*. Elsevier Science Ltd. p. 187213.
27. Beck P, Bradshaw TP, Lark RJ, and Holford KM (2003) A quantitative study of the relationship between concrete crack parameters and acoustic

emission energy released during failure key engineering materials. Trans Tech Publications, Switzerland, pp. 245–246 461–466.

28. Brevet P, Robert JL and Aubaagnac A (2002) Acoustic emission monitoring of bridge cables: Application to a pre-stressed concrete bridge. *DEStech Publications, First European Workshop on Structural Health Monitoring, SHM 2002*, ENS Cachan France. p. 28793.
29. Li D and Ou J (2008) Acoustic emission monitoring and critical failure identification of bridge cable damage. In: *Nondestructive Characterization for Composite Materials, Aerospace Engineering, Civil Infrastructure, and Homeland Security* 2008, *Proceedings of SPIE – The International Society for Optical Engineering*, vol. **6934**, 1–5.
30. Grosse CU, Finck F, Kurz JH and Reinhardt HW (2004) Monitoring techniques based on wireless AE sensors for large structures in civil engineering. *Proceedings of EWGAE 2004 Symposium* in Berlin, BB90, pp. 843–856.
31. Karami M, Farmer J and Inman D (2012) Nonlinear dynamics of the bi-stable piezoelectric wind energy harvester. *SPIE Conference – Smart Structures and Materials and Nondestructive Evaluation and Health Monitoring*, San Diego, California, 11–15 March.
32. Johnson Michael B, Ozevin Didem, Washer Glenn, Ono Kanji, Gostautas Richard S, Tamutus Terry (2012) Real time steel fatigue crack detection in eyebar using acoustic emission method. *Presented at Transportation Research Board (TRB)* January 2012.

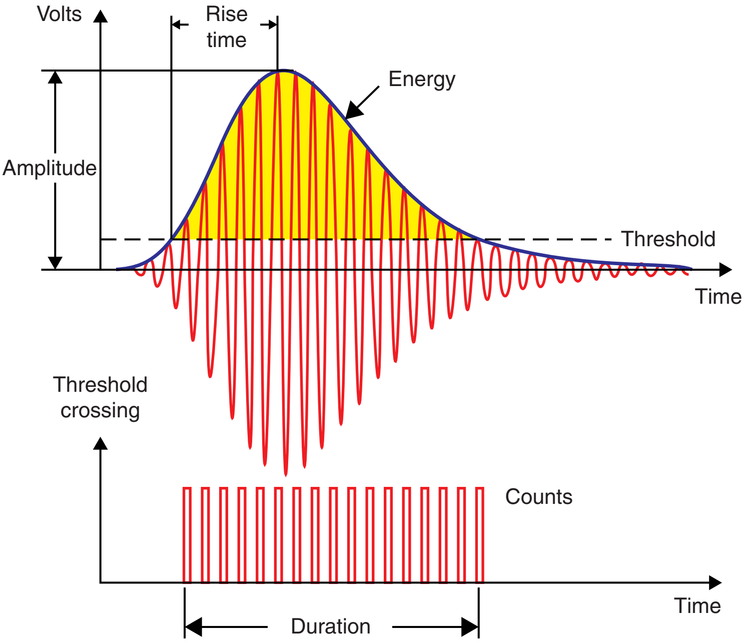

Plate III (Chapter 6) AE signal and the commonly used parameters of AE techniques (Nair A and Cai CS (2010) Acoustic emission monitoring of bridges: Review and case studies. *Eng. Struct.*, **32**(6): 1704–1714).

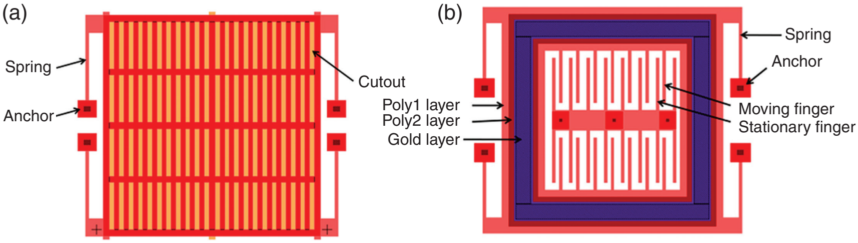
(a)
Spring
Anchor
Cutout
(b)
Poly1 layer
Poly2 layer
Gold layer
Spring
Anchor
Moving finger
Stationary finger

Plate IV (Chapter 6) Layout of (a) out-of-plane and (b) one in-plane sensor (Wu W, Greve DW and Oppenheim IJ (2007) 'Characterization and noise analysis of capacitive MEMS acoustic emission transducers', *Proceeding of IEEE Sensors Conference*, Atlanta, Georgia, USA, pp. 1152–1155).

7

Nonlinear acoustic and ultrasound methods for assessing and monitoring civil infrastructures

M. MEO, University of Bath, UK

DOI: 10.1533/9780857099136.179

Abstract: This chapter presents an overview of nonlinear acoustic and ultrasound methods and their application to civil structures. The major nonlinear ultrasonic methods are thoroughly reviewed and the underlying physics and laboratory studies are reported. In particular, phenomena such as higher harmonic generation, subharmonic generation, nonlinear resonance, and mixed frequency response are discussed and the basic physical mechanism of each phenomenon is introduced with applications for evaluation of damage in civil structures. Research results to date show higher sensitivity of these techniques than the conventional linear ultrasonic methods in detecting microdamage in commonly used material for civil structures, such as concrete and mortar. Finally, current and future challenges are discussed for the successful future implementations of these methods in a maintenance programme.

Key words: nonlinear acoustic, acoustic nonlinearity, nonlinear wave modulation, nonlinear resonance ultrasound spectroscopy, harmonics.

7.1 Introduction

With the rising concerns on the durability of concrete infrastructures, research in new maintenance tools and methods has drawn more and more attention from the research community. In addition, as a consequence of high cost of inspection,[1] the scientific community has been trying to develop reliable and effective non-destructive technique (NDT) and structural health monitoring (SHM) tools to detect the occurrence of critical failure modes, and to estimate them at an early stage so as to reduce the risk of further catastrophic failure.

Non-destructive evaluations based on linear ultrasonic waves are well-established and reliable methods to assess flaws, defects, degradation, etc. of materials. Conventionally, linear ultrasonic methods based on phase velocity and amplitude attenuation measurements are currently used for damage assessment of civil structures because of the relatively easy procedure and

© 2014 Woodhead Publishing Limited

underlying physics. They are based on the fact that when a wave propagates through the medium, the phase and amplitude of the wave changes according to material properties, discontinuities, flaws, etc. These variations are used to estimate damage in materials. The use of guided waves in ultrasonic inspection of plate structures has been applied successfully for the localization of defects (inclusions, delaminations, cracks), but is more complicated than conventional bulk wave inspection.[2–34] This is mainly due to dispersion effects and multimode propagation. Moreover, linear acoustic/ultrasonic methods can be difficult to apply to inhomogeneous materials, such as composite materials, and in particular to damaged materials where the crack size is comparable with the wavelength. Moreover, these linear non-destructive evaluation (NDE) techniques are based on the fundamental assumption that the material constitutive behaviour is linear-elastic. However, most of the materials used for civil application, such as concrete and mortar, are not linearly elastic, even before the formation of cracks. More importantly, the nonlinear elasticity of cement-based materials increases significantly in the presence of cracks. The sensitivity and reliability of linear NDE techniques are thus not as well suited to quantitatively measuring damage in such materials as concrete.

Detailed studies of dynamic nonlinearities and hysteresis in inhomogeneous media have shown that the presence of rupture, cohesive bonds, opening/closing of microcracks, etc. in the material structure give rise to strongly nonlinear dynamic phenomena accompanying the elastic wave propagation.[6] These nonlinear effects are observed in the course of the degradation process much sooner than any degradation-induced variations of linear parameters (propagation velocity, attenuation, elastic moduli, rigidity, etc.). Nonlinear parameters have proved to be very sensitive to the presence of any inhomogeneities and progressive degradation of the material structure.[7]

Based on these studies a new class of promising nonlinear NDE/SHM techniques are being developed where the integrity of structures is monitored by analysing the material nonlinear elastic behaviour caused by the presence of damage.[8–14] Laboratory tests show that these techniques appear to be more effective than linear acoustic methods since they are able to detect microcracks long before changes of linear acoustic properties.[15] In particular, research has indicated that nonlinear ultrasonic waves are quite sensitive in detecting contact-type defects, which involves clapping and rubbing of the crack surfaces.

For materials such as concrete, the acoustic properties are strongly dependent on their microstructures and presence of defects, such as grains, dislocations, cracks, etc. Due their inherent nonlinear acoustic behaviour, nonlinear ultrasonic and acoustic methods offer considerable promise in detecting damage in these materials.

This chapter presents a review of nonlinear acousto-ultrasound methods used for characterizing media and damage in materials used in civil applications, mainly concrete. The main methods covered are as follows:

- Higher harmonic and subharmonic generation
- Nonlinear wave modulation
- Nonlinear resonance frequency shift.

7.2 Fundamentals of nonlinear acousto-ultrasound techniques

The nonlinear acousto-ultrasound techniques were originally developed to estimate the nonlinear elastic properties of heterogeneous material such as rocks. It has been shown that some damaged materials have a complex compliance and exhibit a nonlinear behaviour that cannot be explained with classic nonlinear models.[17] The stress–strain curve of damaged materials may exhibit classic nonlinearity, hysteresis, and discrete memory.[18] The stress–strain in one dimension in quasi-static condition can be written as follows:

$$\sigma = \int \mathrm{K}\left(\varepsilon, \dot{\varepsilon}\right) d\varepsilon \qquad [7.1]$$

where σ is the stress, ε is the strain, $\dot{\varepsilon}$ is the time derivative strain, and K is the elastic modulus. A phenomenological description of the nonlinear nonclassic hysteretic elastic modulus based on the Preisach-Mayergoyz space representation describing both second and higher order nonlinearity is shown in Equation [7.2]:

$$K\left(\varepsilon, \dot{\varepsilon}\right) = K_0\left[1 - \beta\varepsilon - \delta\varepsilon^2 + \alpha\left(\Delta\varepsilon + \mathrm{sign}\left(\dot{\varepsilon}\right)\varepsilon + \cdots\right)\right] \qquad [7.2]$$

where K_0 is the linear modulus, β and δ are second and third order nonlinearity, respectively, $\Delta\varepsilon$ is the local strain amplitude, and α is a material hysteresis measure that takes into account also the history of stress through the terms $\mathrm{sign}\left(\dot{\varepsilon}\right)$ and equals +1 if the strain rate is positive and –1 if negative. Depending on the sign of β, δ, and α, a material may soften or harden when excited with increasing driving amplitude. Some material may exhibit a reduction/increase of the resonant frequency as a function of the driving amplitude.

The term β represents the variation of the wave's velocity resulting from the residual strain, in the case of both static and dynamic loading. This phenomenon is known as acousto-elasticity in homogeneous materials.[19,20] For strongly inhomogeneous (rocks, concrete) and/or damaged materials, the non-classic nonlinearity parameter α enables hysteresis and discrete memory phenomena to be represented.[17] Material used for civil applications is generally heterogeneous, exhibiting nonlinear behaviour even for low level of damage and, when damaged under large strain amplitude, may exhibit nonlinear hysteretical behaviour.

Traditional acoustic/ultrasonic NDT tries to detect variation of the linear Young's modulus K_0 caused by damage, by analysing wave speed changes, reflection of waves, linear attenuation, etc.). If damage increases, the modulus K decreases. In contrast with linear methods, nonlinear vibration-acousto-ultrasound techniques are vibration/acoustic/ultrasonic NDT that monitor the presence of anomalous behaviour (damage) by measuring and quantifying the first, second, etc. order deviations of elastic modulus from the Hooke's law of elasticity.

7.3 Harmonic and subharmonic generation

Nonlinear ultrasonic methods often use harmonic generation to detect damage in materials. Higher harmonic generation is the classic phenomenon, where the waveform of the incident wave is distorted by the nonlinear elastic response of the medium to that wave. When sending an ultrasonic tone burst of amplitude A_0 at frequency f_0, the detected signal passing through the damage will be distorted and the detected wave will possess a component of amplitude A_1 at the fundamental frequency f_0, a component of amplitude A_2 at the second-harmonic frequency $2f_0$, A_3 at the third harmonic frequency $3f_0$, and so on.

Cantrell[42] used the second order solution approximation of the nonlinear wave equation to obtain the following expression of the quadratic nonlinearity parameter,

$$\beta = \frac{8A_2}{A_1^2 k^2 x} \qquad [7.3]$$

where A_1 and A_2 are respectively the frequency amplitudes of first and second harmonics of the recorded time domain waveforms, k is the wavenumber, and x is the propagation distance.

Similarly the third order nonlinear elastic coefficient is expressed as[43]

$$\gamma \approx \frac{A_3}{A_1^3} \frac{48}{k^3 x} \qquad [7.4]$$

where A_3 is the amplitude of the third harmonics. Typically, as damage increases, the magnitude of the nonlinear interaction also increases and energy is converted from the fundamental frequency to higher harmonics. The material degradation can be therefore evaluated by measuring the nonlinearity of the ultrasonic wave propagating through the target material.

The highly nonlinear elastic response can also be observed when a stress wave impinges the interface of parts in contacts. This is usually called acoustic nonlinearity (CAN). The CAN is generated by the asymmetric stress–strain relation of the interface, where the stiffness in compression is higher than in tension. This results in a strong local stiffness modulation. When a sinusoidal wave impinges an imperfect contact interface, the compressional part of the waves can penetrate it, while the tensile part tends to open the crack and therefore cannot penetrate it (see Plate V in the colour section between pages 294 and 295). Thus, after penetrating the interface, the full sine wave becomes nearly half-wave rectification generating nonlinearity. This results in high harmonics allowing a closed crack or mating parts conditions to be detected by measuring these nonlinear effects.

A parametrically driven CAN can be generated under harmonic excitation and if the driving excitation locally resonates the material, a number of fractional sub-harmonics $mf/2$ are generated, where $m = 1, 2, 3, \ldots$. These instability phenomena, having a resonance nature, exhibit sharp dependence on crack surface variations and can be used to detect closed cracks, adhesive debonding, etc. (Fig. 7.1).[7]

A number of laboratory studies have been conducted using nonlinear bulk waves to detect damage in concrete structures.[25,26] Concrete material

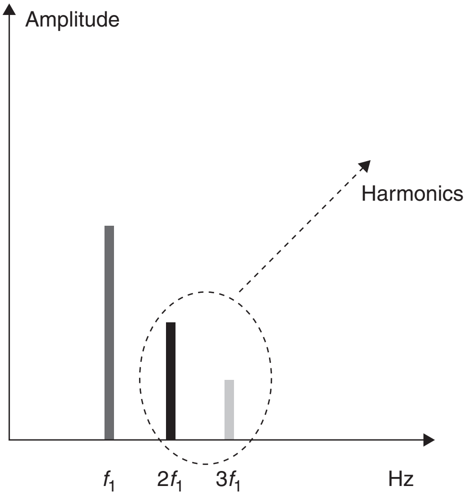

7.1 Harmonic generation.

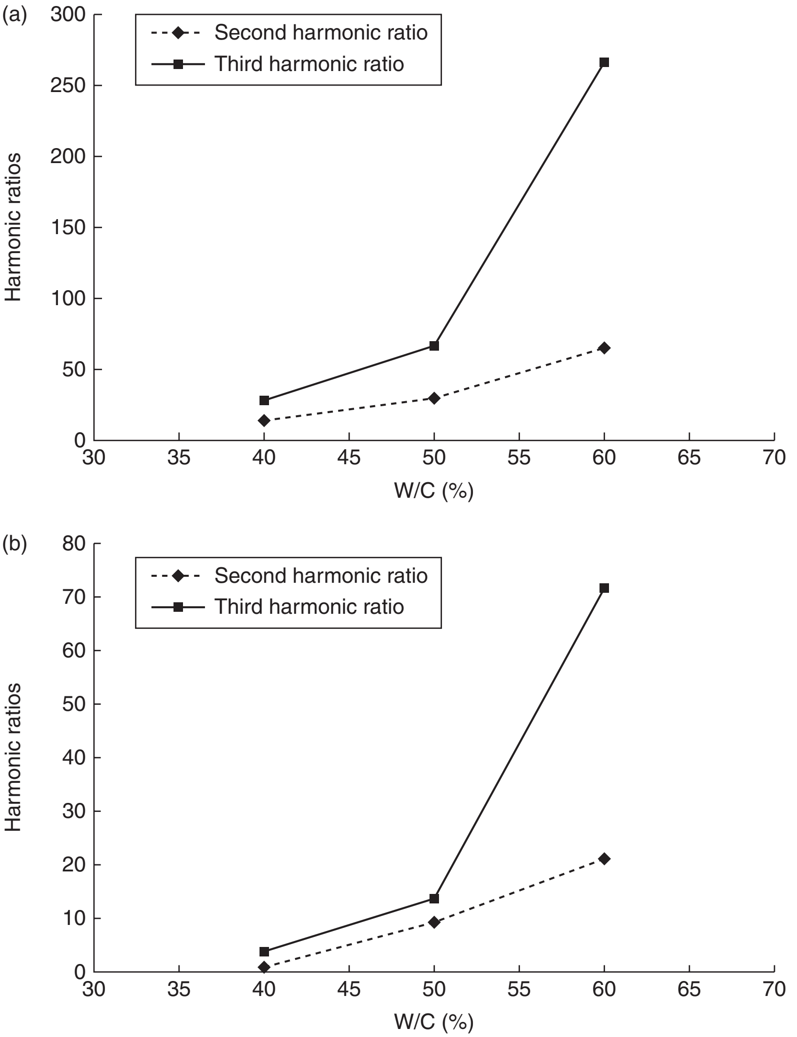

7.2 Harmonic ratio as a function of water-to-cement content for (a) 500 kHz broadband source and (b) 50 kHz narrowband source.

is complex, characterized by the presence of microcracks due to shrinkage, and stresses resulting from curing. In particular, microcracking can develop at the interface between the cement paste and aggregate, due to mismatch of properties such as modulus of elasticity, density, moisture content, etc.

Various studies have been conducted on exploring and evaluating the physical/mechanical properties of concrete using nonlinear methods. In Reference 1 curing (phase change) of concrete has been monitored by harmonic generation. Before the thermal peak, in the liquid state, harmonics were not present. Harmonics generation and a non-classic, nonlinear dependency were observed at percolation point. A direct correlation between nonlinear response and linear response that relates to a known microstructure evolution of the connection of particles in the material was measured.

In Reference 26, the nonlinear harmonic generation was used to detect the water-to-cement ratio in concrete structures. The effect of various type of source excitation, narrow and broadband transducers, was also studied on the detected nonlinear response. It was concluded that the use of a narrowband transmitter provided greater sensitivity to damage in concrete while using broadband transducer 'noise' in the time domain waveforms and numerous peaks in the frequency domain spectra were observed. Both the harmonic ratios and the nonlinear parameters were found to increase as the water-to-cement ratio increased (Fig. 7.2). The increase in third order nonlinear parameters was larger than the second order parameters. This was attributed to the hysteretic material behaviour of concrete.

7.4 Nonlinear wave modulation

Another method to evaluate the nonlinear acoustic signature of damage in material is to measure the modulation of an ultrasonic wave by low-frequency vibration. Commonly, this method is known as nonlinear wave modulation spectroscopy (NWMS). Assume the propagation of two different harmonic waves through nonlinear mesoscopic elastic (NME) material, whose frequencies are different: low-frequency f_L and high-frequency f_H, and $f_H \gg f_L$. If the two waves meet at a crack location, modulation occurs and new waves are measured in the output signal. The generated waves have the frequency characteristics related with f_H and f_L. In this case, the nonlinear coefficients β and δ can be expressed as a ratio of amplitudes given by the following equations:

$$\beta \propto \frac{A(f_H \pm f_L)}{A(f_H)A(f_L)} \qquad \delta \propto \frac{A(f_H \pm 2f_L)}{A(f_H)A(f_L)} \tag{7.5}$$

Care must be taken in measuring the amplitude terms in Equation [7.5], due to the complexity of resonant modes and the high-frequency modulation. Dislocations, rupture, cohesive bonds, porosity, opening/closing of microcracks, debonding, delaminations, etc. may give rise to classic and/or 'non-classic' nonlinearity effects generated by the material's nonlinear classic and hysteretical behaviour.[16] The output signals for a linear and a nonlinear material are shown in Fig. 7.3.

The physical explanation of this modulation is explained in Fig. 7.4. In the presence of a crack, Fig. 7.4a, when the structure is excited with a low-frequency vibration, a sinusoidal signal changes the width of the crack depending on the phase of the vibration. During the compressive phase of the signal the crack is closed, as long as there is sufficient energy, while in the tension phase the crack is opened. Then, the crack is excited with a high-frequency signal. When the crack is opened by the low-frequency signal, the impedance mismatch causes a reduction of the amplitude of the high-frequency signal passing through the crack. When the crack is closed by the low-frequency signal, no impedance mismatch is present; therefore the closed crack does not interrupt the ultrasonic signal and the amplitude of the transmitted signal amplitude increases. This amplitude fluctuation of transmitted signals results in an amplitude modulation of the ultrasonic signal as shown in Fig. 7.4. Fourier transformation of the excitation signal reveals new frequency components, indicating that a flaw or crack is present. In the frequency domain the wave spectrum acquires sidebands: new frequencies are created that are the sum and difference of the frequencies of the ultrasonic probe and vibration signals. This nonlinear process that is possible in undamaged materials (due to e.g., van der Waals forces in some

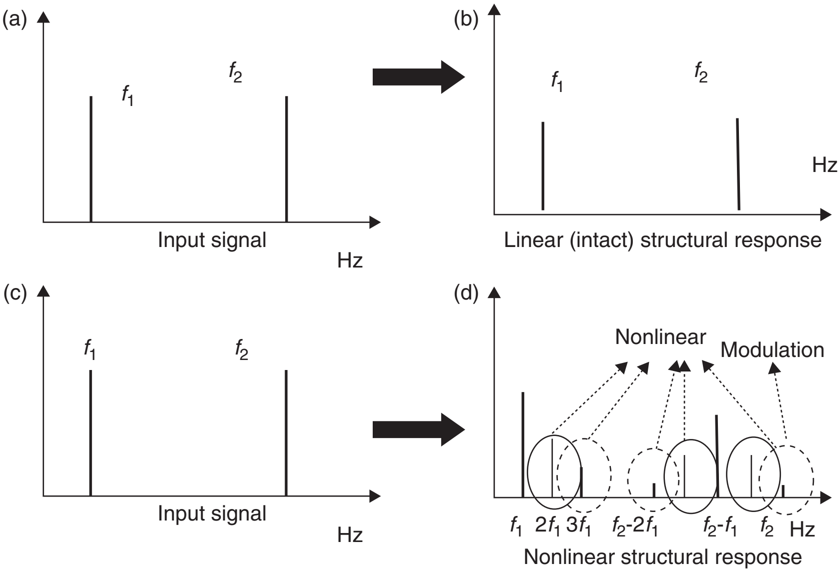

7.3 Linear and nonlinear modulation effect. (a) Excitation frequencies. (b) Response of a linear undamaged. (c) Excitation frequencies. (d) Nonlinear response of a damaged material: harmonics and sidebands.

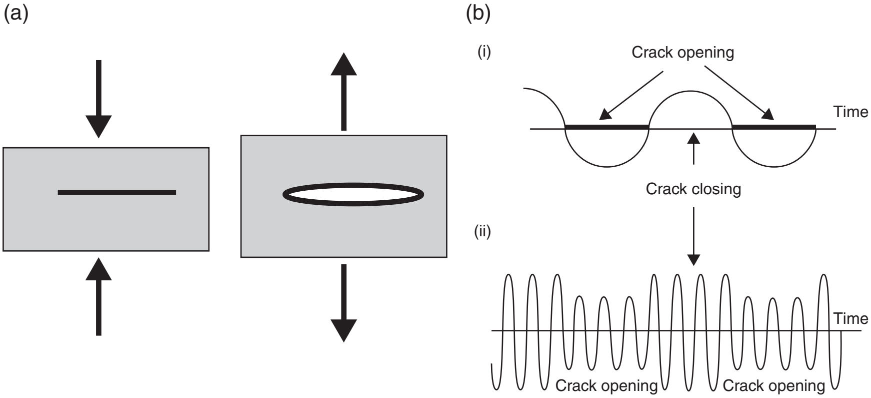

7.4 (a) Material with a crack: closed and open under vibration and (b) amplitude modulation of probe signal: (i) vibration and (ii) ultrasonic signal.[24]

materials) is strongly enhanced in the presence of damage. If the nonlinearity is strong enough, additional sidebands can appear, thus forming a complex modulational spectrum.

In the presence of cracks, defects, etc. in materials such as concrete, composite material[3] sidebands and harmonics of the excited frequencies are generated. Crack, voids, etc. act as multipliers and nonlinear mixers of the excitation frequencies. If a material shows classic nonlinear behaviour, both harmonics and sidebands can be generated. For purely hysteretical damaged material such as concrete, odd harmonics[8] are present with a much higher amplitude with a quadratic behaviour with the fundamental strain amplitude. Moreover, for damaged material, by inserting two frequencies f_1 and f_2 with amplitudes A_1 and A_2, a second order sideband $f_2 + 2f_1$ with amplitudes proportional to $\alpha A_1 A_2$ will be generated.

This behaviour is typical for rocks and material used for construction.

Nonlinear wave modulation of acoustic waves was studied in Reference 35 for the evaluation of damage in concrete structures. The results showed that both active and passive modulation (spectral analysis of regular dilatational ultrasonic signals) of probe frequencies contain nonlinear parameters; however, the active modulation was more sensitive to early concrete damage. The underlying generation phenomenon of this nonlinear behaviour was attributed to the fact that in concrete structures, stresses are not evenly distributed throughout the material due to its heterogeneous nature. This results in the formation of small cracks and stress redistribution even at low loads from the presence of processing flaws or material imperfections.

The feasibility of using nonlinear ultrasonic techniques to track the progress of damage in alkali-silica reaction (ASR) in cement-based materials was studied in Reference 34. ASR is a chemical process occurring in cement-based materials (mortars, concretes, etc.), wherein the siloxane groups (Si-O-Si) of the siliceous mineral components in the aggregates are attacked by hydroxyl ions and generate an alkali-silica gel that swells in the presence of water from the surrounding material. This reaction occurs in four stages: (1) gel formation, (2) internal pressure build-up, (3) microcrack initiation, and (4) crack growth. In presence of cracks produced by ASR, the durability of a concrete structure's service life can be drastically reduced.

A co-linear wave mixing method for assessing ASR damage was employed by sending two longitudinal waves f_1 and f_2, and a new longitudinal wave

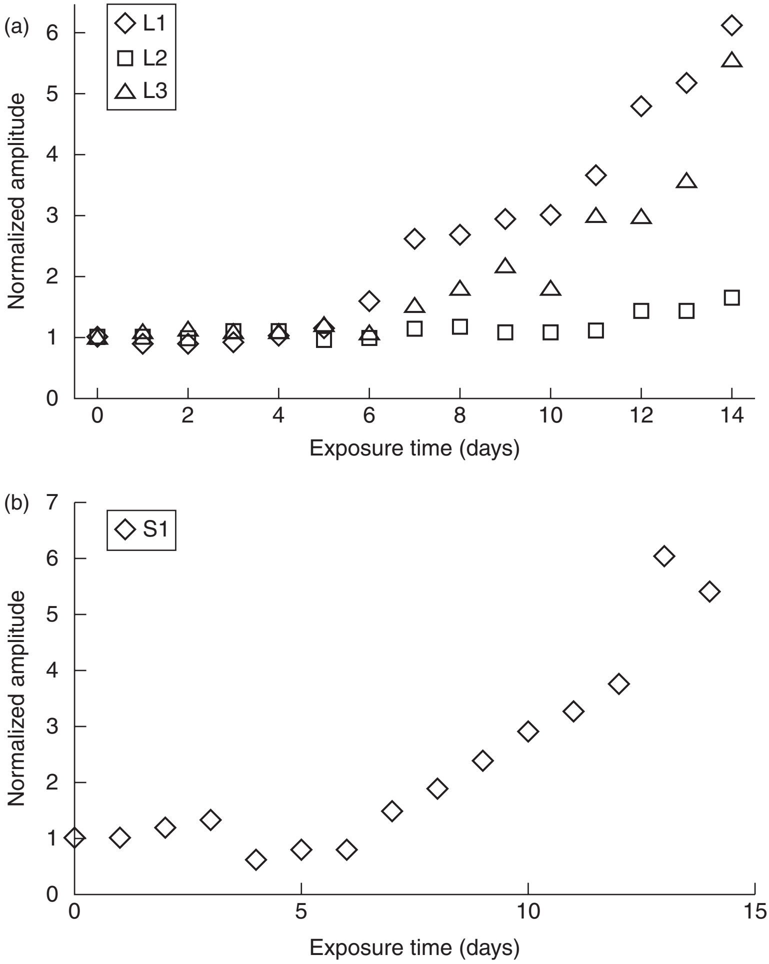

7.5 Nonlinear parameter measured (a) at three locations in a thick sample and (b) in thinner sample S1.[13]

with a lower frequency was generated f_2-f_1. The amplitude of this new wave was proportional to the acoustic nonlinear parameter β which was obtained from the frequency spectrum of the newly generated longitudinal wave. The results showed the correlation of the measured acoustic nonlinearity parameter to ASR damage in concrete, even in its early stages, provide the spatial variation, and allowed identification of the different stages of ASR damage and tracking of the intrinsic characteristics of the ASR damage (Fig. 7.5).

Unlike other expansion-based methods used to assess ASR, the nonlinear modulation method was found to be not dependent on the expansion of the concrete bar.

The degradation of mechanical properties was studied in Reference 36 using an impact-modulation technique to measure nonlinearities due to thermal damage. A comparison between nonlinear modulation with the linear ultrasonic method, phase velocity and dynamic modulus measurement was conducted (Fig. 7.6). The nonlinearity parameter and the phase velocity and dynamic modulus follow different trends as a function of the thermal damage. The phase velocity and dynamic modulus follow a linear shaped curve, while the nonlinearity parameter increases sharply for low thermal damage then reaches a plateau.

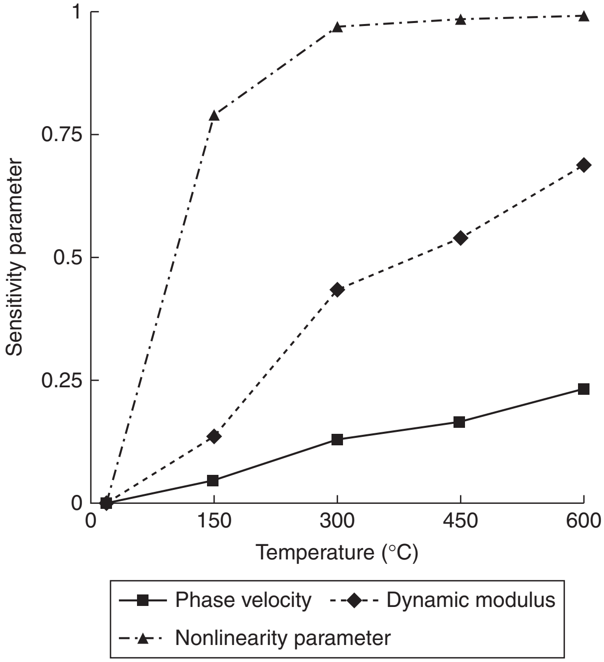

7.6 Linear and nonlinear ultrasonic methods on thermally damaged concrete.

The results showed a higher sensitivity of the impact-modulation method in detecting early stage of damage of an order or magnitude. This is justified by the fact that lower thermal damage is characterized by contact-type defects, while in increasing the temperature the opening of pores is such that contact-type defects are not activated and it behaves in a linear fashion. As a consequence, linear methods become effective.

Optical microscopy showed clearly the opening and pores due to the hygrothermal physical effects and chemical dehydration (Fig. 7.7a and 7.7b). These opening and pores at the micro-scale were classified as microcracks or contact-type defects. The level of thermal damage was characterized in terms of the permeable pore related to the occurrence of opening and pores, and the nonlinearity parameter was related to the increase of contact-type

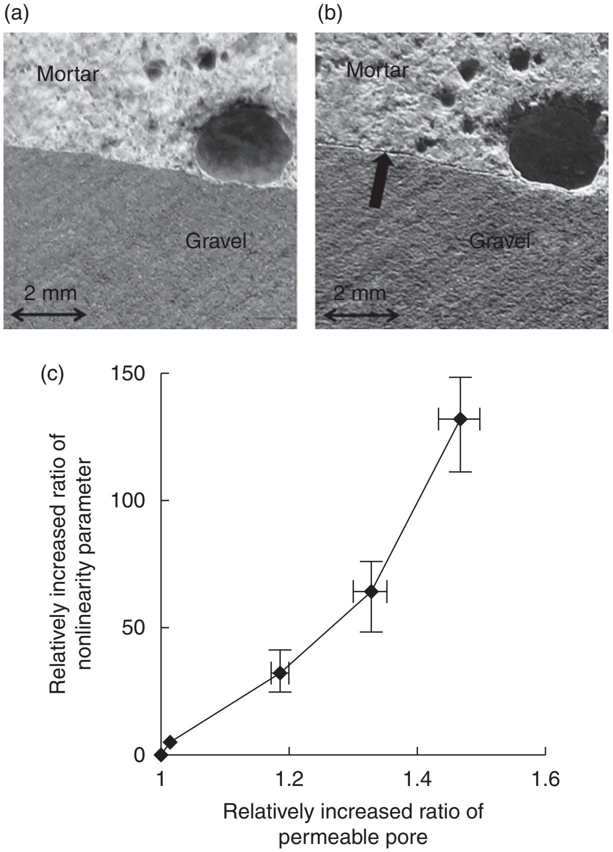

7.7 (a) A location before heating and (b) the same location after heating. (c) Increase of the permeable pore vs nonlinearity measurements.

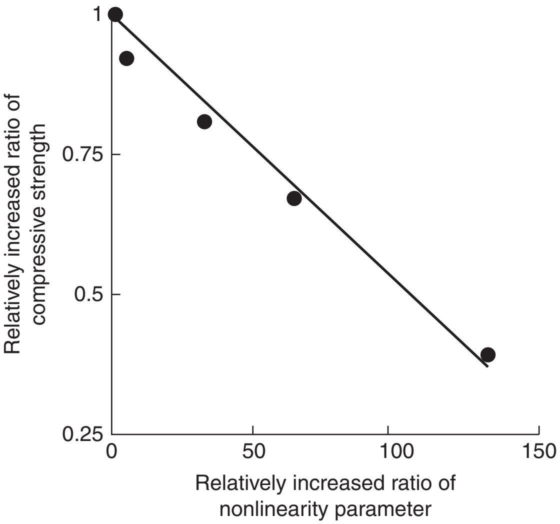

7.8 Correlation between variation of compressive strength and nonlinearity parameter.

defects. Both quantitative measurements were compared to thermal damage and showed a similar trend.

In Fig. 7.7c the relationship between the increase in pores and nonlinear parameters showed that the nonlinearity parameter was increasing with the permeable pore measurements related to the void space in thermally damaged concrete.

It was attempted to relate the thermal damage to the degradation of the compressive strength, due to generation of permanent debonding within internal components and a loss of physicochemical resistance to external stress. The correlation between the measured nonlinearity and the compressive strength of thermally damaged concrete showed a directly linear relationship (Fig. 7.8).[36] This shows that the nonlinear ultrasonic method is a promising tool to provide a reliable measure of thermally damaged concrete and its residual strength.

7.5 Nonlinear resonance ultrasound spectroscopy

While linear resonance methods analyse the frequency shift due to structural anomalies, nonlinear resonance methods analyse the dependence of the resonance frequency on the strain amplitude while exciting the sample at relatively low amplitudes. In Fig. 7.9, the acceleration vs excitation frequency are reported for an undamaged and a damaged material[23] when the sample is excited at a resonant frequency with increasing driving amplitudes. By analysing the frequency shift, the presence of damage in material can be revealed. For undamaged material no frequency shift can be observed, while in damaged material a frequency relative shift is evident. This method is usually referred to as nonlinear resonance ultrasound spectroscopy (NRUS).[23] The term ultrasound is wrongly used for this application since the resonance modes often used are the low vibration natural modes (first, second bending, etc.).

The stress–strain nonlinear model (Equation [7.2]) predicts a softening or hardening of the material with increasing driving amplitude depending on the signs of β and δ and α. In materials like concrete, the net effect is negative and the resonant frequency decreases as a function of wave amplitude. Empirical evidence suggests that the nonlinear hysteretic behaviour proportional to α dominates;[37] therefore when exciting damaged materials at increasing strain amplitude level, the nonlinear parameter α[8] can be evaluated as follows:

$$\alpha\Delta\varepsilon = \frac{f_0 - f_i}{f_0} \tag{7.6}$$

where $\Delta\varepsilon$ is the average strain amplitude, f_0 is the natural frequency of intact material or the lowest resonance mode excited and measured, and f_i is the natural mode measured for each drive amplitude, represented by the maximum value of each curve shown in Fig. 7.9. The damage is evaluated by measuring the relative frequency shift dependence (slope α) as a function of the load (strain) amplitude. This method can also be used to assess damage magnitude or growth, as long as a baseline of a previous material state is available.

Concrete is among the most used materials for civil application. The physical properties of concrete change significantly during curing,

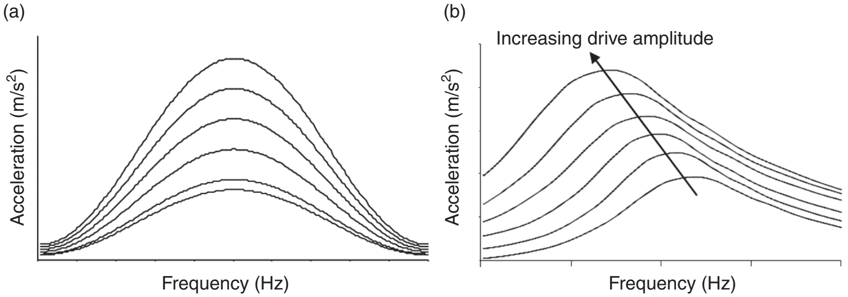

7.9 Resonance frequency vs drive amplitude: (a) intact sample and (b) damaged sample.[15]

exhibiting a phase change from the liquid to solid state. It is characterized by structural heterogeneity and, in its hardened state, caused by the reaction of hydration of the cement, concrete exhibits strong elastic nonlinearity similar to rock geomaterials in general. In addition to classical Landau and Lifschitz theory,[31] the nonlinear response may be physically explained at different scales by dislocations, opening/closing of microcracks, recovery of intergrain cohesive bonds, porosity, etc. Hysteresis in the pressure strain response, the phenomenon of slow dynamics (time-dependent recovery of elastic properties to its initial value after being softened by large strain), and exhibit end point memory were experimentally measured in Reference 29.

In Reference 37 thermal damage in concrete structures was induced and the nonlinear parameters were measured as a function of the damage. A visible shift in resonance frequency was observed and the nonlinear parameter measured as a function of the damage temperature, derived from equation (the slope of the dotted straight line), showed a dynamic range ten times greater than the variation velocity of the ultrasonic waves (Fig. 7.10).

Similar studies were conducted in Reference 38 showing the high sensitivity of the nonlinear α parameter to small variations of material behaviour at the very early stages of a damage process, therefore reducing damage detection threshold (Fig. 7.11).

A nonlinear impact resonance acoustic spectroscopy (NIRAS) technique for the characterization of progressive damage introduced through the deleterious ASR was studied in Reference 39. The microcracks and debonded

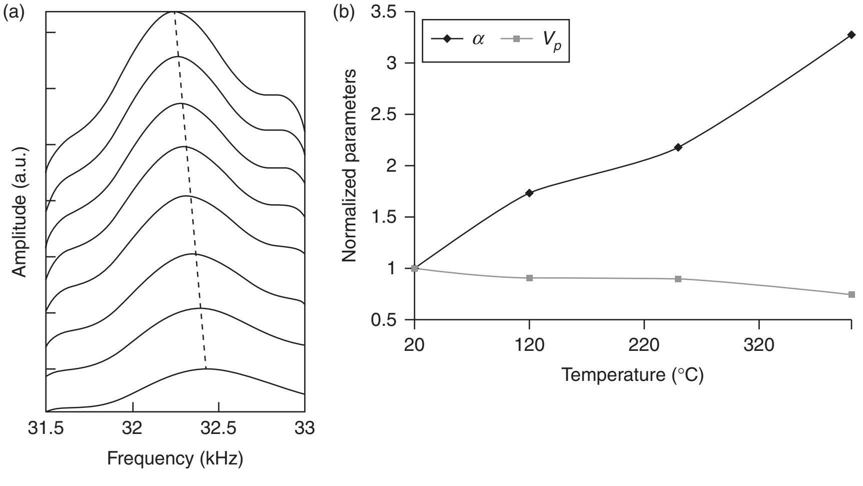

7.10 NRUS experiment for the damaged sample. (a) Relative variation of the nonlinear parameter and (b) velocity of pressure waves as a function of the damage temperature.[37]

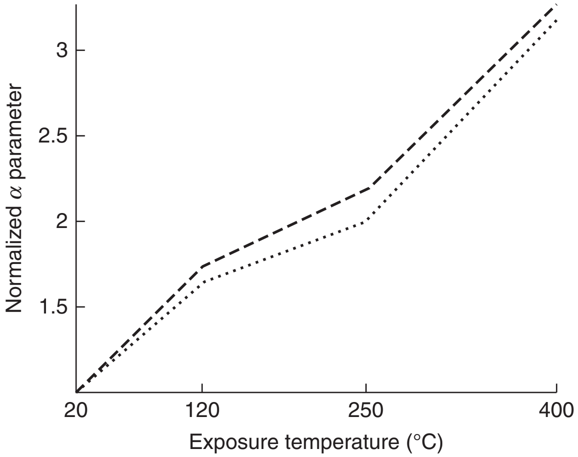

7.11 Nonlinear parameter as a function of exposure temperature for the P mode (dashed line) with the S mode (dotted line).[29]

interfaces acted to increase the nonlinearity of concrete and to measure it, and the response of the specimen to impact loading was analysed.

The ability of the NIRAS measurements to distinguish between concrete that is accumulating damage and undamaged concrete was assessed by comparing nonlinearity data for concrete cast from the same mixture but subjected to different environmental conditions. The recorded nonlinearity for the baseline samples was very low (close to zero) while the shift in the resonance frequency for damaged samples at the same age is clearly evident (Fig. 7.12).

It was concluded that for potentially reactive aggregate, the technique could offer a more definitive assessment of the damage state of the specimen and could be used to distinguish marginally reactive aggregates. The results demonstrated not only a clear distinction between nonreactive and reactive aggregates, but also the capability to quantitatively track ASR-induced damage in concrete.

The NRUS methods could be the foundation of new field assessment and monitoring systems.

However, a number of challenges need to be faced before its successful implementation into an inspection programme despite its large dynamic range. First, the role of other potential parameters affecting the nonlinear behaviour should be carefully assessed and discerned from the real nonlinear behaviour caused by flaws, cracks, etc. among which there is water content, the concrete's porosity, etc.

Then, the NRUS is based on knowledge of the resonance mode of a structure. This clearly will pose additional challenges and complexity, especially

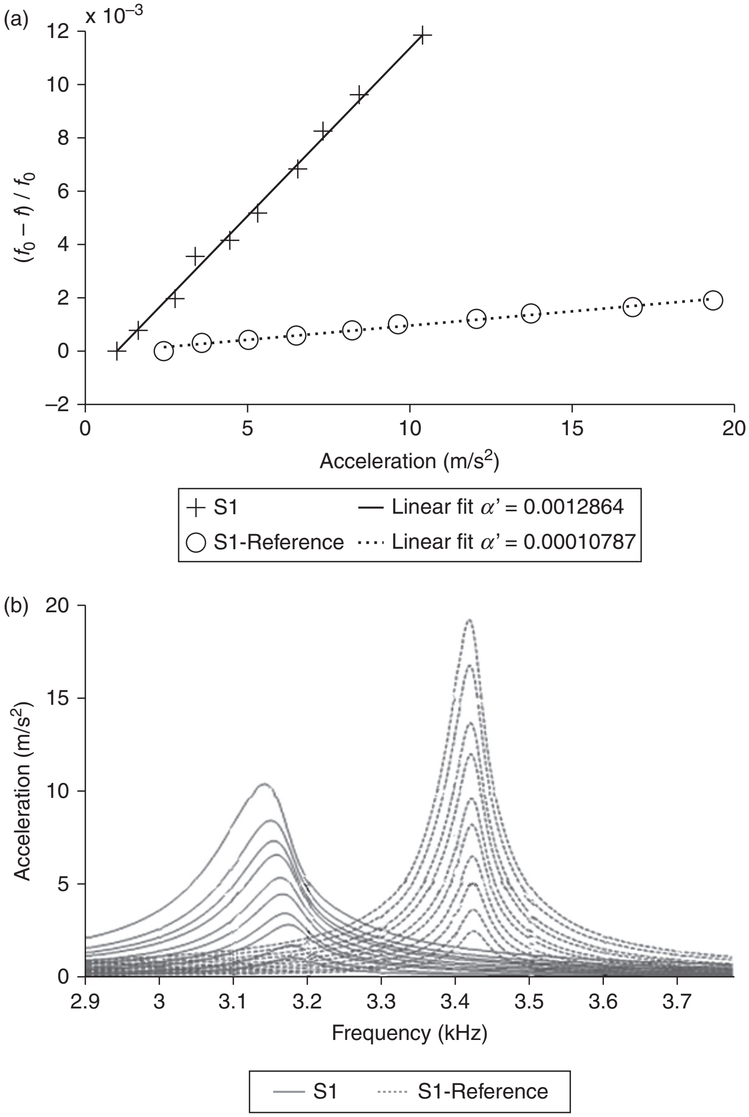

7.12 (a) Nonlinearity comparison between reference and tested samples for highly reactive S1 mixture at 55 days. (b) Comparison between reference and tested samples for highly reactive S1 mixture at 55 days in the frequency domain.

for large scale structures. Then the *in situ* generation of stress waves of sufficient amplitude to create a shift in the resonance frequency poses real challenges in terms of instrumentation and power needed, and reproducibility of results.

7.6 Future trends

Despite the growing interest in nonlinear-acousto-ultrasound methods for NDT/SHM of civil structures, a number of scientific and technical hurdles must be overcome for the widespread use of these methods. The main challenges to be met are:

- *Nonlinear effect not related to material conditions*: Presence of nonlinearities in the measured signal is often generated by a number of unwanted sources, such as instrumentation, mating parts, material inherent nonlinearities, etc. Therefore, strategies and tools for nonlinear source discrimination should be systematically adopted using rigorous measurement protocols. This will strongly help in identifying incipient material failures from spurious data.
- *Nonlinear imaging*. While the interest of the scientific community is strongly focused on developing linear imaging methods, there is still the need to further develop and implement nonlinear imaging methods in an SHM system.[52]
- *Local nature of high-frequency harmonics*. When interrogating a large structure to identify faults using harmonics, due to the large attenuation at high frequencies the harmonics may not propagate to the network of sensors. This local nature of 'harmonics' has been demonstrated in a number of studies and may limit the use of this technique for SHM applications. In the case of thin-walled structures it has been demonstrated that 'phase matching' will overcome this problem. When possible, sub-harmonics could be used to overcome this issue.
- *Non-contact technologies*. Non-contact technology could be a solution to inherent instrumentation nonlinearities. While there is an increasing development of non-contact sensors, there is still a significant deficit in non-contact excitation technologies capable of providing enough 'linear' energy for generating nonlinear mechanics e.g. opening and closing of cracks. This needs to be a major research area for years to come for a successful implementation of Nonlinear and Acoustic Ultrasound Methods (NAUM) for SHM of civil structures.
- *Lack of physical models*. Numerical models are key for the development and optimization of NAUM. Despite the effort in modelling nonlinear effects with many material models available, there is still a deficit of validated, if any, models able to predict the measured nonlinear behaviour of materials. This is due to the inherent complexity, and sometimes chaotic generation, of nonlinear features.
- *Performance of permanently installed transducers*. The performance of an attached/embedded system should be carefully monitored to avoid

false alarms due to adhesive bonding, since this will generate nonlinear behaviour and could disguise real material changes. This, however, is a challenge for linear methods as well.

- *High power needed*. Because the highlighted methods need relatively higher energy (with respect to linear ultrasound methods) to induce nonlinear material behaviour, this limits the application of these methods to wired connections, unless new high energy harvester and power storage solutions are found.

7.7 Conclusions

In this chapter, an overview of nonlinear acousto-ultrasound methods for civil applications is presented. Basic principles of harmonic generation, NRUS and nonlinear wave modulation are introduced. Most of the methods discussed in this chapter assume a homogeneous and isotropic material, an assumption that is generally valid for materials used in construction. Different past and current approaches to detect and assess the severity of flaws/cracks are reviewed. A number of applications of lab applications for monitoring civil materials were discussed. Then, challenges to be faced in the future for widespread and field use of these methods are highlighted.

7.8 References

1. K.J. Folliard, B. Fourier and M. Thomas (2000), ASR testing and evaluation protocols, Protocol A: Determining the reactivity of concrete aggregates and selecting appropriate measures for preventing deleterious expansion in concrete, Federal Highways Administration, Washington D.C.
2. S.C. Rosalie, M. Vaughan, A. Bremmer and W.K. Chiu (2004), Variation in the group velocity of Lamb waves as a tool for the detection of delamination in GLARE aluminium plate-like structures, *Compos. Struct.*, **66**, pp. 77–86.
3. K. Diamanti, C. Soutis and J.M. Hodgkinson (2005), Lamb waves for the non-destructive inspection of monolithic and sandwich composite beams, *Compos. Part A: Appl. Sci. Manuf.*, **36**(2), pp. 189–195.
4. K. Diamanti, C. Soutis and J.M. Hodgkinson (2005), Non-destructive inspection of sandwich and repaired composite laminated structures, *Compos. Sci. Technol.*, **65**(13), pp. 2059–2067.
5. S.S. Kessler, S.M. Spearing and C. Soutis (2002), Damage detection in composite materials using Lamb wave methods, *Smart Mater. Struct.*, **11**(2), pp. 269–278.
6. P. Johnson (1999), The new wave in acoustic testing, *Mater. World*, **7**(9), pp. 544–546, September 1999.
7. M. Meo and G. Zumpano (2005), Nonlinear elastic wave spectroscopy identification of impact damage on a sandwich plate, *Compos. Struct.*, **71**(3–4), pp. 469–474.

8. K. Van Den Abeele, P.A. Johnson and A. Sutin (2000), Nonlinear elastic wave spectroscopy (NEWS) techniques to discern material damage, part I: Nonlinear wave modulation spectroscopy (NWMS), *Res. Nondestruct. Eval.*, **12**(1), pp. 17–30.
9. R.A. Guyer and P.A. Johnson (April 1999), Nonlinear mesoscopic elasticity: Evidence for a new class of materials, *Phys. Today*, **52**(4), pp. 30–36.
10. K. Van Den Abeele and J. De Visscher (2000), Damage assessment in reinforced concrete using spectral and temporal nonlinear vibration techniques, *Cem. Concr. Res.*, **30**(9), pp. 1453–1464.
11. C. Campos-Pozuelo and J.A. Gallego-Juárez (2003), Experimental analysis of the nonlinear behaviour of fatigued metallic samples, WCU 2003, Paris, 7–10 September.
12. K.E.-A. Van Den Abeele, A. Sutin, J. Carmeliet and P.A. Johnson (2001), Micro-damage diagnostics using Nonlinear Elastic Wave Spectroscopy (NEWS), *NDT&E Int.*, **34**, pp. 239–248.
13. K. Van Den Abeele, K. Van de Velde and J. Carmeliet (2001), Inferring the degradation of pultruded composites from dynamic nonlinear resonance measurements, *Polym. Compos.*, **22**(4), pp. 555–567.
14. M. Meo and G. Zumpano (2008), Damage localization using transient nonlinear elastic wave spectroscopy on composite structures, *Int. J. Non-Linear Mech.*, **43**(3) pp. 217–230.
15. M. Meo, U. Polimeno and G. Zumpano (2008), Detecting damage in composite material using nonlinear elastic wave spectroscopy methods, *Appl. Compos. Mater.*, **15**(3), pp. 115–126.
16. G. Zumpano and M. Meo (2008), Damage detection in an aircraft foam sandwich panel using nonlinear elastic wave spectroscopy, *Comput. Struct.,* **86**(3–5) pp. 483–490.
17. R.A. Guyer and P.A. Johnson (1999), Nonlinear mesoscopic elasticity: Evidence for a new class of materials, *Phys. Today*, **52**, 30–35.
18. P.A. Johnson and X. Jia (2005), Nonlinear dynamics, granular media and dynamic earthquake triggering, *Nature*, **437**, 871–874.
19. F.D. Murnaghan (1951), *Finite Deformations of an Elastic Solid*, John Wiley, New York.
20. D.S. Hughes and J.L. Kelly (1953), Second-order elastic deformation of solids, *Phys. Rev*., **92**, p. 1145.
21. P.B. Nagy (1998), Fatigue damage assessment by nonlinear ultrasonic material characterization, *Ultrasonics*, **36**(1–5), pp. 375–381.
22. U. Polimeno and M. Meo (2009), Detecting barely visible impact damage detection on aircraft composites structures, *Compos. Struct.*, **91**(4), Special Issue, pp. 398–402.
23. L.A. Ostrovsky and P.A. Johnson (2001), Dynamic nonlinear elasticity in geomaterials, *Rivista Del Nuovo Cimento*, **24**(7).
24. Y. Zheng, R.G. Maev and I.Y. Solodov (1999), Non-linear acoustic applications for material characterization: A review, *Can. J. Phys.,* **77**, pp. 927–967.
25. C. Woodward, K.R. White, D.V. Jauregui and J.D. Stauffer (2004), Non-linear ultrasonic evaluation of concrete microcracking, *Rev. Prog. Quant. Non-destruct Eval.,* **23**, pp. 1022–1026.

26. A.A. Shah, Y. Ribakov and S. Hirose (2009), Non-destructive evaluation of damaged concrete using non-linear ultrasonics, *Mater. Des.,* **30**(3), pp. 775–782.
27. B.A. Korshak, I.Y. Solodov and E.M. Ballad (2002), DC effects, sub-harmonics, stochasticity and 'memory' for contact acoustic non-linearity, *Ultrasonics*, **40**(1), pp. 707–713.
28. J.C. Lacouture, P.A. Johnson and F. Cohen-Tenoudji (2003), Study of critical behavior in concrete during curing by application of dynamic linear and nonlinear means, *J. Acoust. Soc. Am.*, **113**, pp. 1325–1332.
29. C. Payan, V. Garnier, J. Moysan and P.A. Johnson (2007), Applying nonlinear resonant ultrasound spectroscopy to improving thermal damage assessment in concrete, *J. Acoust. Soc. Am.,* **121**(4), pp. EL125–EL130.
30. K. Van Den Abeele, J. Carmeliet, J. TenCate and P.A. Johnson (2000), Nonlinear elastic wave spectroscopy (NEWS) techniques to discern material damage. Part II: Single-mode nonlinear resonance acoustic spectroscopy, *Res. Nondestruct. Eval.*, **12**, pp. 31–43.
31. L.D. Landau and E.M. Lifshitz (1959), *Theory of Elasticity*, Pergamon Press, New York.
32. J.C. Lacouture, P.A. Johnson and F. Cohen-Tenoudji (2003), Study of critical behavior in concrete during curing by application of dynamic linear and nonlinear means, *J. Acoust. Soc. Am.*, **113**, pp. 1325–1332.
33. K. Warnemuende and H.C. Wu (2004), Actively modulated acoustic nondestructive evaluation of concrete, *Cem. Concr. Res.*, **34**, pp. 563–570.
34. M. Liu, G. Tang, L.J. Jacobs and J. Qu (2012), A nonlinear wave mixing method for detecting Alkali-Silica reactivity of aggregates, *AIP Conf. Proc.*, **1430**, pp. 1524–1531.
35. K. Warnemuende and H.C. Wu (2004), Actively modulated acoustic nondestructive evaluation of concrete, *Cem. Concr. Res.*, **34**, pp. 563–570.
36. H.J. Yim, J.H. Kim, S.-J. Park and H.-G. Kwak (2012), Characterization of thermally damaged concrete using a nonlinear ultrasonic method, *Cem. Concr. Res.,* **42**(11), November 2012, pp. 1438–1446.
37. C. Payan, V. Garnier and J. Moysan (2010), Potential of nonlinear ultrasonic indicators for nondestructive testing of concrete, *Adv. Civil Eng.*, **2010**, p. 8.
38. K. Van Den Abeele and J. De Visscher (2000), Damage assessment in reinforced concrete using spectral and temporal nonlinear vibration techniques, *Cem. Concr. Res.*, **30**, pp. 1453–1464.
39. K.J. Les´nicki, J.Y. Kim, K.E. Kurtis and L.J. Jacobs (2001), Characterization of ASR damage in concrete using nonlinear impact resonance acoustic spectroscopy technique, *NDT&E International,* **44**, pp. 721–727.
40. F. Ciampa and M. Meo (2012), Nonlinear elastic imaging using reciprocal time reversal and third order symmetry analysis, *J. Acoust. Soc. Am.*, **131**(6), pp. 4316–4323.
41. M. Bentahar, H. El Aqra, R. El Guerjouma, M. Griffa and M. Scalerandi (2006), Hysteretic elasticity in damaged concrete: Quantitative analysis of slow and fast dynamics, *Phys. Rev. B*, **73**, p. 014116.
42. J.H. Cantrell (2004), Fundamentals and applications of non-linear ultrasonic nondestructive evaluation. In: KunduTribikram, editor. *Ultrasonic Non-Destructive Evaluation*, vol. **6**. Woodhead Publishing Limited, Boca Raton (FL), pp. 363–434.

43. M. Amura, M. Meo and F. Amerini (2011), Baseline-free estimation of residual fatigue life using a third order acoustic nonlinear parameter, *J. Acoust. Soc, Am.*, **130** (4), pp. 1829–1837.
44. A.M. Sutin and P.A. Johnson (2005), Nonlinear elastic wave Nde II. Nonlinear wave modulation spectroscopy and nonlinear time reversed acoustics, *AIP Conf. Proc.*, **760**(1), pp. 385–392.

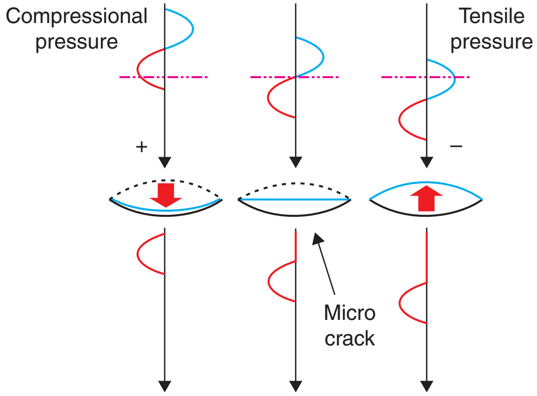
Compressional pressure
Tensile pressure
+
–
Micro crack

Plate V (Chapter 7) Physical explanation of CAN (U. Polimeno and M. Meo (2009), 'Detecting barely visible impact damage detection on aircraft composites structures', *Compos. Struct.*, **91**(4) Special Issue, pp. 398–402).

8

Radar technology: radio frequency, interferometric, millimeter wave and terahertz sensors for assessing and monitoring civil infrastructures

D. HUSTON, University of Vermont, USA and D. BUSUIOC,
DB Consulting, USA

DOI: 10.1533/9780857099136.201

Abstract: Radar and millimeter wave methods provide a means of remote and noncontacting examination of structures through controlled electromagnetic (EM) interactions. Metallic and nonmetallic structures reflect and scatter EM waves impinging at the outer surfaces. Nonmetallic, i.e., dielectric, materials allow for EM waves to penetrate the surface, and scatter or reflect off of subsurface objects and features. Actively measuring surface and subsurface reflectivity and scattering by the controlled launching and receiving of EM waves provides information that when suitably processed can indicate surface and subsurface feature geometry, material properties, and overall structural condition. These active EM technical tests are often called 'Ground Penetrating Radar' for EM wave frequencies less than about 10 GHz and 'Millimeter Wave' methods for those at higher frequencies. This chapter describes the range of uses, operating principles, signal processing, and data interpretation for these methods.

Key words: electromagnetic, ground penetrating radar, radar, millimeter wave, dielectric, concrete, corrosion.

8.1 Introduction

Radar-based sensors use radio frequency (RF) and higher electromagnetic (EM) field disturbances to identify, locate, and assess structures and materials. Civil engineering applications include probing subsurface conditions in concrete, asphalt, and masonry for cracks, delaminations, and corrosion; determining the presence of water, ice, or other contaminants on surfaces; detecting corrosion under painted surfaces; imaging objects through walls; and overall geometric structural shape assessment. An important feature of radar sensing is that the EM field disturbances act both as probes for measurement and as signal transmitters. Figure 8.1 shows a typical sensing system configuration that generates, measures, and analyzes EM fields.

© 2014 Woodhead Publishing Limited

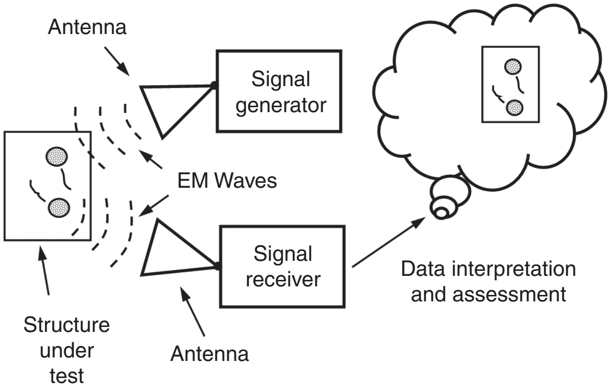

8.1 Generic EM structural sensing system.

Many of these instruments are known as ground penetrating radars (GPR). Interferometric, millimeter wave, and/or terahertz sensors are more accurate terms for some of these systems.

Radar and millimeter wave sensors have several advantages:

1. An ability to sense remote and subsurface conditions with a convenience that is difficult to match with other sensors.
2. An underlying sensing mechanism that operates at the speed of light. Measurement throughput can be quite fast.
3. The energy in the EM fields is generally small, inherently safe, and nondestructive.
4. The performance versus cost of the sensor systems continues to improve with ongoing developments in hardware, software, and testing protocols.
5. The instrument operators need only a modest level of training.

There are some disadvantages:

1. EM waves cannot penetrate all materials. Conductors reflect EM waves. Lossy dielectrics quickly absorb and attenuate waves. Nonhomogeneous materials scatter EM waves and reduce the strength of return signals.
2. Longer wavelengths and lower frequency waves generally tend to penetrate more deeply into dielectric materials, but at a cost of reduced spatial resolution.
3. Complicated signal processing techniques are often required.
4. Many data sets routinely require highly trained experts for interpretation.

5. The instruments tend to be relatively expensive and complicated.
6. Government agencies regulate the levels of radiated EM emissions. This constrains achievable penetration depths and other performance parameters.

8.2 Brief history of ground penetrating radar (GPR) systems

GPRs transmit high-frequency EM waves out through specialized antennas. The waves project onto, and often penetrate into, the surfaces of solids. A portion of the waves reflects back to a receiver antenna. The arrival time, shape, and amplitude of the return wave relates to the location, variation, and nature of dielectric properties in the material (air/asphalt or asphalt/concrete, reinforcing steel, etc.). Figure 8.2 shows how an EM wave reflects off of features inside a steel reinforced concrete bridge deck. Capturing, processing, and displaying the reflected wave signals illustrates the subsurface dielectric properties, which often correlate with underlying material properties of interest.

The roots of GPR technology lie in the development of EM field theories by some of the prominent physicists of the nineteenth century (Ampere, Heaviside, Henry, Hertz, Maxwell, Lorenz) and through the first half of the twentieth century with the development of radio transmission systems (Annan, 2002). The 1940s, with the Second World War, gave rise to the rapid development of radar systems, primarily for the location of airplanes and ships. The first noted use of radar to probe subsurface conditions was in 1956 with the detection of water table depths by El Said in 1956 (El Said, 1956). Geological and archeological applications appeared in the 1970s, especially for materials with low losses, such as coal and salt (Holser *et al.*, 1972; Cook,

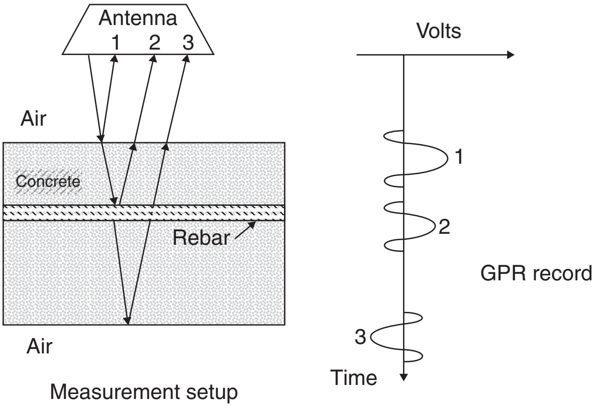

8.2 EM wave interactions with a concrete bridge deck. (*Source*: Figure derived from Maser, 1989.)

1973; Thierbach, 1974). Commercial GPR systems became available following the 1970 formation of Geophysical Survey System, Inc. in Salem, NH (GSSI) (Morey, 1974). An early civil engineering application was geological evaluations of Alaska pipeline routes by Olhoeft (Olhoeft, 1975).

The need for a convenient nondestructive tool for assessing steel reinforced concrete bridge decks motivated much of the development of GPR for structural engineering. Corrosion of steel reinforcing bars is a major maintenance problem. Many of the problems are progressive damage processes that start with the combined application of deicing salts, harsh environmental and loading conditions, and end with the disintegration of the roadway. Normally, the alkaline nature of concrete forms a passivating layer that protects embedded steel from corrosion. Chlorides, water, and oxygen can break the passivation layer and initiate a complicated multiyear process that eventually renders the deck unserviceable (Fig. 8.3). Similar processes occur in other concrete structural elements. Early detection with instruments, such as GPR, can enable early and low cost intervention.

Some of the notable structural engineering studies of GPR in the early 1980s include that of Steinway *et al.* (1981), Ulriksen (1982), Alongi *et al.* (1982), Manning and Holt (1984), Chung *et al.* (1984), and Clemena and Joyce (1984). The indication was that GPR instruments could detect layers in asphalt-overlaid concrete and bare concrete bridge decks. The presence of chlorides increased asphalt reflectivity. Good concrete exhibited a 'smoother' waveform than distressed concrete. Maser (1989) found a positive correlation between the total deterioration observed on asphalt-overlaid bridge decks and the high values of the dielectric constant of the concrete measured immediately below the asphalt layer. Based on the observation that the amplitudes of the reflections from subsurface steel reinforcing bars drop off with increased chloride content, and possibly with delaminations, an attempt to standardize resulted in the provisional specification AASHTO TP36–93 (1993). This specification was not widely adopted, but the underlying concept remains relevant today.

Starting in the late 1980s, there began a series of detailed studies of the interactions of damage to materials and measured dielectric properties. (Zoughi *et al.*, 1995). Halabe *et al.* (1990) conducted a numerical study of the sensitivity of the concrete reflectivity to moisture and chloride content. The study used EM models for predicting radar waveforms from concrete and asphalt material properties. The results were that both moisture and chloride content increase the reflectivity of the concrete, and that it was feasible to calculate the bulk physical properties of concrete directly from the radar waveform.

The 1990s saw some significant technical developments with the appearance of micropower impulse radar (MIR) and synthetic aperture radar (SAR). McEwan (1994a, b) invented MIR, which uses step recovery diodes (SRDs) to generate low power ultrawideband (UWB) pulses that synchronize tightly with a return waveform sampler. The resulting design can be low cost and versatile. The advent of modern SAR signal processing

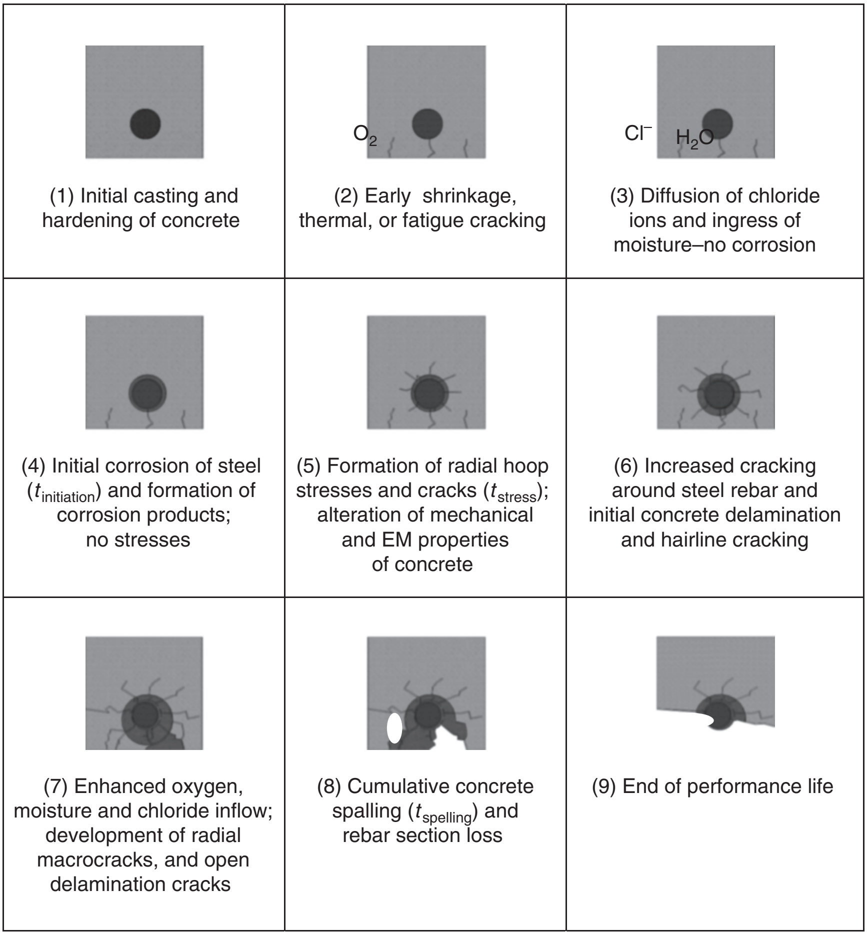

(1) Initial casting and hardening of concrete

(2) Early shrinkage, thermal, or fatigue cracking

(3) Diffusion of chloride ions and ingress of moisture–no corrosion

(4) Initial corrosion of steel ($t_{\text{initiation}}$) and formation of corrosion products; no stresses

(5) Formation of radial hoop stresses and cracks (t_{stress}); alteration of mechanical and EM properties of concrete

(6) Increased cracking around steel rebar and initial concrete delamination and hairline cracking

(7) Enhanced oxygen, moisture and chloride inflow; development of radial macrocracks, and open delamination cracks

(8) Cumulative concrete spalling (t_{spelling}) and rebar section loss

(9) End of performance life

8.3 Nine stages of progressive chloride-induced corrosion cracking damage in reinforced concrete (Jalinoos, 2009). From Materials Evaluation, Vol. 67, No. 11. Reprinted with permission of The American Society for Nondestructive Testing, Inc. This reprint contains copyrighted property of ASNT and may not be duplicated or altered in any manner.

algorithms opened up the possibility of processing return waveforms to produce images of subsurface features in reinforced concrete bridge decks (Soumehk, 1999). Some of the early demonstrations of SAR techniques on reinforced concrete were by Mast (1993), Mast and Johannson (1994), and Johannson and Mast (1994). MIR and SAR successfully converged into a single platform with the High-speed Electromagnetic Roadway Mapping and Evaluation System (HERMES) for multichannel roadway inspection (Chase, 1999).

Table 8.1 lists wavelengths that are typically encountered in the use of GPR in various media. Technical advancements continue to ease testing at

Table 8.1 EM wavelengths as a function of frequency for different media

	Wavelength (mm)			
Frequency	Air	Asphalt	Concrete	Water
(GHz)	$\varepsilon_r = 1.0$	$\varepsilon_r = 5.0$	$\varepsilon_r = 7.5$	$\varepsilon_r = 78.0$
	Vel. = 3E + 8 m/s	Vel. = 1.34E + 8 m/s	Vel. = 1.09E + 8 m/s	Vel. = 3.39E + 7 m/s
0.5	600	268	219	67.9
1	300	134	110	34.0
2	150	67	54.8	17.0
4	75	33.5	27.4	8.49
8	37.5	16.8	13.7	4.25
16	18.8	8.39	6.85	2.12
32	9.38	4.19	3.42	1.06
64	4.69	2.10	1.71	0.531

Vel.: velocity.

higher frequencies. The definition of high frequency is somewhat arbitrary, and continues to creep upward. One way of defining is to use an arbitrary cutoff frequency, such as 10 GHz. A similar, but perhaps more physically-based definition, is a specific wavelength value. Waves with lengths smaller than 10 mm have frequencies of 30 GHz and higher. It is common practice to use an inclusive factor of 10 in adjectival descriptions of wavelength and frequency. For example, millimeter waves have wavelengths of 10 mm or less, and terahertz waves have frequencies 0.1 THz (100 GHz) and higher.

Most GPR systems use UWB EM pulses with very rapid rise and fall times to probe structures for subsurface features and damage. UWB technology dates back to the earliest days of radio communication with spark gap generators. The term 'ultrawideband' appears to have originated in an OSD/DARPA workshop in 1990 (MSSI, 2000). Most GPR UWB signals consist of a series of UWB pulses. This introduces two different frequency descriptors for the signals. The first is the frequency content of a single UWB pulse. Typical GPR UWB pulse widths run from 300 to 3000 ps. The corresponding frequency domain representation of narrow time domain UWB pulses is to cover a very broad frequency band (~0.5–10 GHz). The second frequency descriptor is the pulse repetition frequency (PRF), which typically runs from tens of kHz to 1 MHz or more.

In 1990, the OSD/DARPA Radar Review Panel issued a report establishing UWB radar as any system with a fractional bandwidth (FBW) greater than 0.25 regardless of the center frequency.

$$\mathrm{FBW} = 2\frac{(f_H - f_L)}{(f_H + f_L)} \tag{8.1}$$

f_H and f_L are the upper and lower frequencies, respectively, of the –20 dB emission point (FCC, 2002). The average of the upper and lower frequencies defines the center frequency, f_c, of the transmission.

$$f_c = \frac{(f_H + f_L)}{2} \qquad [8.2]$$

Practical considerations led the Federal Communications Commission (FCC) to define UWB as signal with a FBW greater than 0.20 or a –10 dB bandwidth occupying more than 500 MHz of spectrum (FCC, 2002).

While there have been few, if any, credible reports of UWB GPR systems causing interference, the possibility of serious public safety consequences raises concerns. A NASA study demonstrated that UWB devices can interfere with commercial aviation navigation equipment (Ely, 2002). The tests found that a UWB transmitter with a 10 MHz PRF could interfere with aircraft navigation equipment using a carrier frequency approximately eleven times higher than the PRF. The exact mechanism of interference was not identified. One possibility is a high order harmonic of the PRF. This prompted the FCC to investigate and eventually to promulgate regulations for the unlicensed operation of UWB systems in the United States with the FCC 02–48 regulations (FCC, 2002; Olhoeft, 2002). The regulations established three general categories for UWB devices: imaging systems, vehicular radar systems, and communications and measurement systems. The imaging system category comprises GPR systems, wall imaging systems, through-wall imaging systems, surveillance systems, and medical systems. The regulations include the following guidelines:

- *Applications* – Imaging systems may not be used for data or voice information transfer.
- *Operating Frequency* – The operating frequency band is defined as the UWB bandwidth, i.e., the –10 dB emission bandwidth. GPRs and wall imaging systems must operate with this bandwidth contained below 10.6 GHz.
- *System Operators* – GPRs and wall imaging systems may only be used for law enforcement, firefighting, emergency rescue, scientific research, commercial mining, or construction purposes.
- *Emission Limits* – All imaging systems are required to comply with section 15.209 emission levels for frequency bands at or below 960 MHz. These emission levels are measured in terms of the field strength at a specified distance from the device. Table 8.2 lists the emission limits of 15.209 and provides a conversion of these levels to equivalent isotropically radiated power (EIRP) (NTIA, 2001). Table 8.3 shows the EIRP limits for radiation in bands above 960 MHz. Table 8.4 lists the limits for emissions measured using a resolution bandwidth of no less than 1 kHz.

Table 8.2 FCC 15.209 emission limits

Frequency (MHz)	Field strength (μV/m)	Measurement distance (m)	EIRP (dBm)
0.009–0.490	2400/F (kHz)	300	11.8–20 $\log_{10}$F (kHz)
0.490–1.705	24 000/F (kHz)	30	12.3–20 $\log_{10}$F (kHz)
1.705–30.0	30	30	–45.7
30–88	100	3	–55.3
88–216	150	3	–51.7
216–960	200	3	–49.2

Table 8.3 Maximum average emission limits for frequency bands above 960 MHz

GPR and wall imaging systems	
Frequency (MHz)	EIRP (dBm)
960–1610	–65.3
1610–1990	–53.3
1990–3100	–51.3
3100–10 600	–41.3
Above 10 600	–51.3

Table 8.4 Maximum average emission limits using a resolution bandwidth of no less than 1 kHz

GPR and wall imaging systems	
Frequency (MHz)	EIRP (dBm)
1164–1240	–75.3
1559–1610	–75.3

The limitations imposed by these regulations form a significant barrier to routine GPR operation, especially for applications that favor high PRFs and air-launched measurements, such as the sensing of subsurface roadway conditions at highway travel speeds. Nonetheless, technical workarounds are beginning to appear, e.g., full waveform digitization to reduce the PRF along with shaped UWB pulses (Xia *et al.*, 2012).

8.3 Current challenges and state of the art systems

The state of the art is that a variety of commercial systems are available at a reasonable cost. The present systems continue to improve in terms of performance, ease of use, data processing, and presentation capability.

Systems are available in a variety of frequency bands, some are over 3 GHz. Handheld units are increasingly usable and lower cost. For structural engineering applications, these systems are capable of inspecting roadways, tunnel walls, and building façades, locating buried utilities, and detecting water leaks in buried pipes.

There remain several technical challenges affecting the use of GPR for structural inspection. Automated data interpretation software has improved considerably, but much of the interpretation still requires considerable expertise. Vehicle mounted systems still use prohibitively large antennas. Penetration depth versus frequency and resolution tradeoff remains less than desirable. Source/receiver coupling is a persistent problem in impulse-type bistatic antenna systems. Measuring roadways at highway travel speeds with cm-scale spatial resolution while remaining compliant with emitted radiation level specifications, such as FCC 02–48, remains problematic. Cm-scale position registration without the prepositioning of supplemental navigational assist hardware is also a challenge.

8.4 Fundamentals of operation

EM wave propagation and interaction with materials underlies the operation of radar and millimeter wave systems, along with high-speed analog and digital signal processing. The mathematical modeling of EM fields can be highly technical. Different models with various degrees of rigor and complexity are available. Wisely choosing the physical model eases the analytical burden. Figure 8.4 shows a taxonomy of mathematical models, ranging from the relatively simple ray tracing models through scalar and vector waves to the fairly recondite quantum field models. At the moment, there are only a few situations related to GPR and millimeter wave sensing that require the power of quantum mechanics. An exception is the need for quantum techniques to design and model the solid state electronics that generate and receive EM waves (Taylor, 2001). The interactions of EM waves with materials are also quantum phenomena, but empirical models that fit within the framework of continuum-based Maxwell's equations and simpler models seem to be adequate for most cases (Feynmann, 1977). An intriguing possibility is the use of Bell's theorem in radar sensors (Allen and Karageorgis, 2008). The reader is referred to standard texts for more details on these topics (Moon and Spencer, 1960; Taflove and Hagness, 2005; Klauder and Sudarshan, 2006; Balanis, 2012).

Maxwell's equations provide an excellent representation of EM phenomena on scales ranging from macroscopic to quantum. Maxwell's equations treat the EM interactions in terms of electric and magnetic field vectors that propagate and reflect as waves. Often, scalars instead of vectors can represent the propagation of EM waves. Scalar forms simplify the mathematics at the

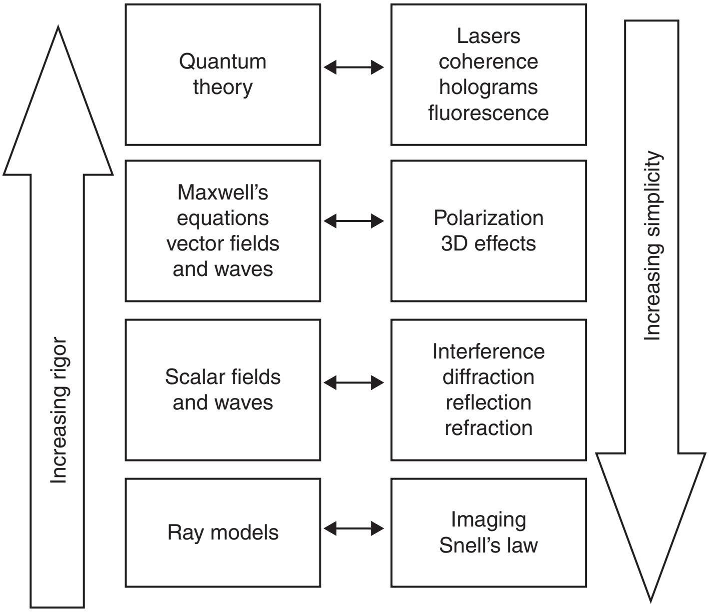
Quantum theory
Lasers coherence holograms fluorescence
Maxwell's equations vector fields and waves
Polarization 3D effects
Scalar fields and waves
Interference diffraction reflection refraction
Ray models
Imaging Snell's law
Increasing rigor
Increasing simplicity

8.4 Various models of EM wave propagation (Huston, 2010).

expense of a loss of transverse directional information and cannot treat vector-based phenomena i.e. polarization. If the wavelengths are small compared to directional changes in propagation, then a geometric ray tracing model can be used. Ray tracing replaces the differential wave equations with geometric and trigonometric relations. A further simplification occurs if the media appear as a multi-layered planar structure with the wave direction being normal to the surface of the planes. This forms a 1-D multi-layered model.

Vector field equations describe many EM phenomena. The principal EM vector fields are the electric field, $\vec{E}$; the magnetic field, $\vec{H}$; the electric displacement, $\vec{D}$; and the magnetic induction, $\vec{B}$. In the absence of material discontinuities, these vector fields are normally finite, continuous, and differentiable functions of position and time. Heaviside's version of Maxwell's equations combines the four field vectors in a concise description of the field interactions

$$\nabla \times \vec{H} = \frac{\partial \vec{D}}{\partial t} + \vec{J}_s + \vec{J}_c \qquad [8.3]$$

and

$$\nabla \times \vec{E} = -\frac{\partial \vec{B}}{\partial t} \qquad [8.4]$$

$$\nabla \cdot \vec{H} = 0 \tag{8.5}$$

$$\nabla \cdot \vec{E} = 0 \tag{8.6}$$

$\vec{J}_s$ is the source current density and $\vec{J}_c$ is the conductivity current density $\left(\vec{J}_c = \rho\vec{E}\right)$.

In addition to Maxwell's equations, EM wave descriptions also need constitutive material properties. In isotropic media, $\vec{D}$ is parallel to $\vec{E}$, and $\vec{H}$ is parallel to $\vec{B}$, i.e.

$$\vec{D} = \varepsilon\vec{E} \tag{8.7}$$

and

$$\vec{B} = \mu\vec{H} \tag{8.8}$$

ε and μ are the electrical permittivity and magnetic permeability, respectively. In a vacuum, or air at most wavelengths, $\varepsilon_0 = 8.854 \times 10^{-12}$ farad/m and $\mu_0 = 4\pi \times 10^{-7}$ N/A^2, with the relation for the wave speed, c_0, in a vacuum

$$c_0 = \frac{1}{\left(\varepsilon_0\mu_0\right)^{1/2}} = 2.998 \times 10^8\,\text{m/s} \tag{8.9}$$

Modeling the interaction of EM fields with anisotropic materials generally requires using tensor-based constitutive models.

For nonconducting and nondispersive homogeneous media, a condensation of Maxwell's equations produces vector wave equations for both the electric and magnetic fields

$$\nabla^2\vec{H} = \varepsilon\mu\frac{\partial^2\vec{H}}{\partial t^2} = \frac{1}{c^2}\frac{\partial^2\vec{H}}{\partial t^2} \tag{8.10}$$

$$\nabla^2\vec{E} = \varepsilon\mu\frac{\partial^2\vec{E}}{\partial t^2} = \frac{1}{c^2}\frac{\partial^2\vec{E}}{\partial t^2} \tag{8.11}$$

c is the wave speed. The quantity $(\varepsilon\mu_0)^{1/2}$ is known as the refractive index.

These equations permit a wide variety of solutions, including plane waves of the form

$$\varphi = \Phi_0 \exp[j(\vec{K} \cdot \vec{r} - \omega t)] \tag{8.12}$$

φ and Φ_0 are scalar components of the vector wave. $\vec{K}$ is the wave number, which points in the direction of wave propagation. $\vec{r}$ is the position in space. $f = \omega/2\pi$ is the frequency. Plane waves extend to infinity in the transverse directions. Feynman (1977) shows that for linear and homogeneous media, it is possible to represent almost any propagating EM wave via a superposition of different plane waves. Alternative formulations, such as spherical waves or Gaussian beams, are more tractable in particular situations (Verdeyen, 1989). Decomposing the propagating field disturbances with Fourier's theorem and noting the linear nature of most wave propagation produces a simplified scalar sinusoidal waveform, $d(x,t)$, that retains many of the essential features of wave propagation, where

$$d(x,t) = D\sin\left[2\frac{\pi}{\lambda}(x - ct)\right] \qquad [8.13]$$

An examination of $d(x,t)$ indicates that the instantaneous amplitude repeats when $x/\lambda = ct/\lambda = 1$. This leads to the definitions of λ as the wavelength (reciprocal of the wavenumber), and $f = c/\lambda$ as the frequency.

EM waves propagate through a vacuum with no loss of energy or dispersion. The propagation of EM waves through all other media is lossy with a conversion of EM wave energy into other forms e.g. heat. A useful macroscopic representation of wave transmission losses is a linear model with complex-valued permittivities and permeabilities, i.e., $\varepsilon^* = \varepsilon' + j\varepsilon''$ and $\mu^* = \mu' + j\mu''$ (Condon and Odishaw, 1967).

$$\nabla^2 \vec{E} = \varepsilon^* \mu^* \frac{\partial^2 \vec{E}}{\partial t^2} \qquad [8.14]$$

The propagation factor, γ, is

$$\gamma = i\omega[\varepsilon^* \mu^*]^{1/2} = \alpha + i\beta \qquad [8.15]$$

a is the attenuation factor ($a = 0$ for loss-free media). β is the phase factor, which indicates the phase velocity of the wave. For most dielectric materials, it is reasonable to absorb the loss factor into the imaginary part of the permittivity ε^*, which leaves a real expression for the magnetic permeability. A useful and relatively easy to measure version of the loss factor is the loss tangent, $\delta = \varepsilon''/\varepsilon'$. Using complex-valued loss functions is generally appropriate only in the context of oscillations with stationary frequency content, e.g. harmonic inputs and outputs. Using complex loss function models in transient analyses can cause anomalous non-causal behaviors. Purely imaginary dielectric values correspond to strong reflections and are useful for modeling metallic surfaces.

An antenna produces EM field disturbances by driving time-varying electric currents through conductive elements. The motion of the electric charges induces time-varying magnetic fields, which in turn induce time-varying electric fields. The repeated interchange of space- and time-varying electric and magnetic fields propagates the EM field. The near-field region is the space near the antenna where the initial magnetic fields form. The size of the near-field is typically in the order of one wavelength. The reactive near-field is a quarter wavelength or less. The far-field is typically two wavelengths or more away from the antenna. A transition region lies in between. The distinctions between near-field and far-field are not crisp and depend on the geometry and other details of the antenna design. The concept of reactive near-field is particularly important in ground-coupled antennas.

For GPR applications, ray tracing methods can provide insight into the interactions of EM waves with layered media and bulk conductors, especially when the transverse spatial variation of dielectric properties occurs over lengths that are larger than several wavelengths. These methods use rays (directed lines) to describe the propagation of EM field disturbances. An important application is to use rays to describe the hyperbolic nonlinearity that is characteristic of an isolated reflector in a B-scan. A GPR identifies the presence of a reflector by measuring the time, Δt, for a wave to launch, reflect, and return. Denoting r as the distance from the antenna to the reflector gives

$$r = \frac{1}{2} c_m \Delta t \qquad [8.16]$$

c_m = the speed of light in the medium. The factor of ½ appears in Equation [8.16] because the wave has to make a round trip. Equation [8.16] is particularly useful if the reflector is known to be directly down range of the antenna, or if the reflector is planar, such as a layer of material with a refractive index that is different from the one above it. If the reflector is isolated and is positioned laterally from the source antenna, then Equation [8.16] is still valid, but the travel distance, r, is the diagonal distance from the antenna to the reflector (Fig. 8.5).

$$r = [(x_r - \xi)^2 + y_r^2]^{1/2} \qquad [8.17]$$

From a single trace, it is not possible to discern simultaneously the cross-range and down-range position of an isolated reflector. If it is erroneously

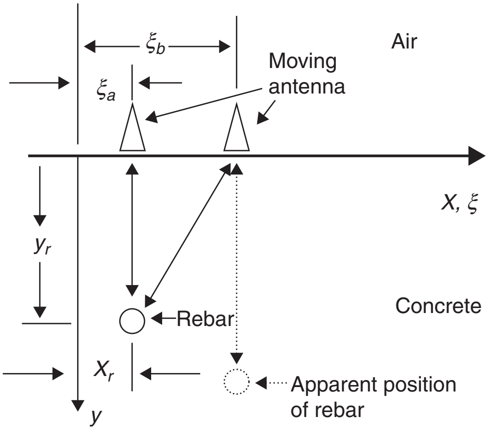

8.5 2-D geometry of moving monostatic antenna and hyperbolic nonlinear distortion (Huston *et al.*, 2000a).

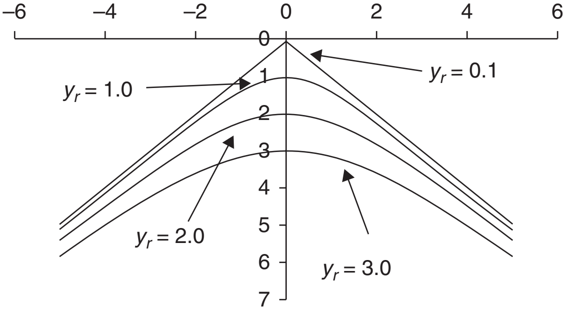

8.6 Hyperbolic nonlinearity that results from moving an antenna relative to a fixed reflector at various depths (reflector cross-range $x_r = 0$) (Huston, *et al.*, 2000b).

assumed that a reflector is immediately down range from the antenna, when its position actually has a cross-range component as well, then the apparent position of the object is directly down range at a distance equal to combined down-range and cross-range position. The time for a signal to travel round trip from the antenna to the reflector is

$$\Delta t = \frac{2}{c_m}[(x_r - \xi)^2 + y_r^2]^{1/2} \qquad [8.18]$$

Moving the antenna across the surface, collecting a series of scans, stacking the scans, and plotting the amplitude in terms of pixel brightness produces a B-scan.

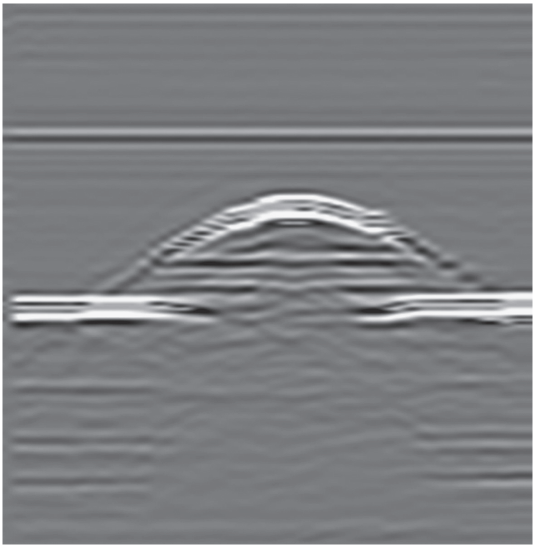

8.7 B-scan of an aluminum bar suspended in air with hyperbolic nonlinearity (Huston, *et al.*, 2000b).

For a fixed-position reflector, Equation [8.18] forms a hyperbola in ξ and Δt. Figure 8.6 shows the hyperbolae that result from having a reflector at various depths. Deeper reflectors produce a hyperbola with flatter appearance.

Figure 8.7 shows a B-scan image of the reflections from a round aluminum bar suspended in air.

A polarized EM wave with the electric field vector parallel to the x-y plane and the magnetic field parallel to the x-z plane is a transverse electric (TE) polarized wave. When the wave is polarized so the that the magnetic field vector is parallel to the x-y plane and the electric field vector lies in the x-z plane, the wave is called a transverse magnetic (TM) polarized wave. TE waves and TM waves interact differently with a boundary between materials with differing refractive indices, n_1 and n_2 (Udd, 1991). The reflection (R) and transmission (T) coefficients are

$$R_{\mathrm{TE}} = \left(\frac{E_r}{E_i}\right)_{\mathrm{TE}} = \frac{n_1 \cos\theta_i - n_2 \cos\theta_t}{n_1 \cos\theta_i + n_2 \cos\theta_t} \qquad [8.19]$$

$$T_{\mathrm{TE}} = \left(\frac{E_t}{E_i}\right)_{\mathrm{TE}} = \frac{2n_1 \cos\theta_i}{n_1 \cos\theta_i + n_2 \cos\theta_t} \qquad [8.20]$$

$$R_{\mathrm{TM}} = \left(\frac{E_r}{E_i}\right)_{\mathrm{TM}} = \frac{n_2 \cos\theta_i - n_1 \cos\theta_t}{n_1 \cos\theta_t + n_2 \cos\theta_i} \tag{8.21}$$

$$T_{\mathrm{TM}} = \left(\frac{E_t}{E_i}\right)_{\mathrm{TM}} = \frac{2n_1 \cos\theta_i}{n_1 \cos\theta_t + n_2 \cos\theta_i} \tag{8.22}$$

When the angle of incidence $\theta_I = 0$, the situation corresponds to testing in a monostatic (single antenna) mode with layered media. Equations [8.19] to [8.22] simplify to

$$R_{\mathrm{TE}} = -R_{\mathrm{TM}} = \frac{n_1 - n_2}{n_1 + n_2} \tag{8.23}$$

$$T_{\mathrm{TE}} = T_{\mathrm{TM}} = \frac{2n_1}{n_1 + n_2} \tag{8.24}$$

If the two media are dielectric and if it can be assumed that the change in wave speed is due to changes in the dielectric permittivity constants (rather than the magnetic permeabilities), the reflection and transmission coefficients for a wave traveling from medium 1 to 2 are

$$R_{12} = \frac{\sqrt{\varepsilon_1} - \sqrt{\varepsilon_2}}{\sqrt{\varepsilon_1} + \sqrt{\varepsilon_2}} \tag{8.25}$$

$$T_{12} = \frac{2\sqrt{\varepsilon_1}}{\sqrt{\varepsilon_1} + \sqrt{\varepsilon_2}} \tag{8.26}$$

If ε_1 is less than ε_2, then R_{12} has a negative value. If ε_1 is larger than ε_2, then R_{12} is positive. The magnitude of the reflection coefficient dictates the amplitude of the reflected wave, and the sign of the reflection coefficient dictates the phase shift of the returning wave. When R_{12} is negative the incident wave undergoes a 180° phase shift upon reflection. When R_{12} is positive, no shift in phase occurs (Carter *et al.*, 1986). Setting the dielectric constant ε_2 to infinity models the reflection from a metal surface. In this case $R_{12} = -1$ and $T_{12} = 0$.

The different reflectivities of a dielectric surface and a metallic surface provide a means to determine the dielectric constant of a roadway surface.

Denoting A as the amplitude of the reflection from a normal incidence wave off of the surface of the roadway and A_{PL} as the amplitude of the reflection off of a metal plate placed on the roadway surface gives the dielectric constant for the roadway as

$$\varepsilon_1 = \left[\frac{\left(1 + A / A_{pt}\right)}{\left(1 - A / A_{pt}\right)}\right]^2 \tag{8.27}$$

Many cases of EM modeling are intractable with analytic tools. Numerical methods often provide a viable alternative. The finite difference time domain (FDTD) method models transient EM waves (Yee, 1966; Taflove and Hagness, 2005). A drawback is that stable and convergent solutions often require small grid spacings and high computational loads. Many practical situations restrict FDTD solutions to 2-D.

8.5 Electromagnetic interactions with materials

Many of the interactions of EM waves with homogeneous materials depend on a combination of the atomic nature of the material along with the frequency of the waves. The mobility of the electrons at the atomic scale governs many of the constitutive properties. If the electrons are free to move, as in a metallic conductor, they will move to counter the action of EM waves. The effect is that metals reflect EM waves and do not permit much penetration of the EM fields past a skin on the surface. Alternative atomic arrangements bind most of the electrons into molecular structures. In these cases, EM waves cause the molecules to rotate and align internal charge gradients with the external fields. This effect gives rise to dielectric materials (Debye, 1960). If the molecules rotate elastically, then the input energy regenerates and the material is a lossless dielectric. If the rotations convert energy into heat, the material is a lossy dielectric. GPR models commonly use four types of EM properties:

1. *Vacuum or air*: The EM properties of air and a vacuum are virtually identical for the frequencies and transmission distances commonly encountered in GPR. EM waves propagate through air with minimal losses.
2. *Dielectric*: Dielectrics are insulating materials containing dipoles. Electric fields exert moments on dipoles, often in proportion to the strength of the field,

$$\vec{D} = \varepsilon_r \vec{E} \tag{8.28}$$

$\vec{D}$ is the electric displacement vector, ε_r is the dielectric constant for the material, and $\vec{E}$ is the applied electric field. The permittivity of air is often normalized to unity and the dielectric constant ε_r is also normalized, with a value that is always greater than or equal to one.

3. *Lossy dielectric*: Ideal dielectrics allow the propagation of EM waves without any losses. All real passive materials produce losses, which convert the EM energy into heat and attenuate the amplitude. A linear model with complex-valued permittivities and permeabilities is the usual approach to modeling the loss mechanisms.
4. *Metallic reflective:* Free electrons in metals move quickly to counter incoming EM waves. This gives metals a shiny appearance and makes them reflect light and other EM waves. It is common to use a dielectric constant of ∞ for metals.

The deterioration of concrete and asphalt often changes the EM constitutive properties. Many damage features are smaller than 1 cm, which is smaller than the spatial resolution of most GPR systems. This limitation in resolution reduces the ability of radar to detect the fine dielectric discontinuities that result from deterioration mechanisms and instead leads to bulk continuum models of dielectric properties. Halabe *et al*. (1990) developed a model to characterize the complex dielectric constant of asphalt and concrete mixtures as a function of wave frequency, sample temperature, moisture content, chloride content, and mix constituents. The model calculates the dielectric permittivity of concrete from the known permittivity of its discrete constituents (i.e., aggregate, air, water, chloride, cement paste). Although water and salt compose a relatively small percentage of a given concrete or asphalt pavement sample, the effect on the permittivity can be quite large. Unbound water molecules increase the average dielectric constant of the material. Salt and other ionic substances increase the attenuation of traveling EM waves (Al-Qadi *et al*., 1995). Several models predict the dielectric properties of a mixture from the properties and volumetric proportions of the constituents (Halabe *et al*., 1993, 1995). The components in these models include coarse and fine aggregate, cement paste, air, water, and salt. Water and salt, only when dissolved in solution, have the greatest effect on the dielectric constant. A form of the Debye expression for the relative dielectric permittivity of salt water (ε_{sw}) is

$$\varepsilon_{\text{sw}} = \varepsilon_\infty + \frac{\varepsilon_o - \varepsilon_\infty}{1 - i2\pi\tau f} + i\frac{\sigma}{2\pi\varepsilon_o^* f} \tag{8.29}$$

ε_o = static dielectric constant of the solvent, ε_∞ = high-frequency dielectric constant of solvent, τ = relaxation constant, σ = conductivity of water, and f = EM wave frequency. Water plays such a large role because the dielectric constant (≈80) is much greater than that of dry natural rock, soil, and concrete (2.5–8.0).

The complex reactive index mixture (CRIM) method assumes a volume average of the complex refractive indexes of the constituents.

$$\sqrt{\varepsilon_r} = (1-\phi)\sqrt{\varepsilon_m} + (1-S)\phi\sqrt{\varepsilon_a} + \phi S\sqrt{\varepsilon_{sw}} \qquad [8.30]$$

ϕ = porosity of concrete = (volume of voids)/(total volume of concrete), S = degree of saturation = (volume of water)/(volume of voids), ε_m= relative dielectric permittivity of concrete solids ~ 5.0 (real), ε_a = relative dielectric permittivity of air = 1.0 (real), $\varepsilon_{\mathrm{sw}}$ = relative complex permittivity of water, and ε_r = relative dielectric permittivity of resulting concrete mixture = $\varepsilon^{\mathrm{I}} + i\varepsilon^{\mathrm{II}}$.

8.6 Transmitter and receiver design

GPR systems generally fall into two main classes for the transmitter and receiver design. One is based on using short EM impulses. These are known as *impulse* radar systems. The second class uses sinusoidal waves that sweep over a range of frequencies, and are known as *step-frequency* or *continuous-wave* radar systems. Most commercial GPR systems are impulse radars. Many academic researchers favor step-frequency systems. Other transmit/receive designs are in use, such as noise-modulated radar (Reeves, 2010).

The advantages of impulse systems lie mainly in the ability of a single impulse wave to produce a return wave that is laden with information describing subsurface features. Impulse systems are fast. The high speed is a mixed blessing. It enables rapid testing, but requires high-speed electronics for measurement. Traditional methods use sub-sampling to take a single data point sample from an impulse waveform and reconstruct a complete waveform from average samples from multiple waveforms. Full waveform single-shot digitization has been demonstrated using high-speed analog to digital conversion (ADC). In order to achieve reasonable sampling speeds, most full waveform digitizing instruments use sample and hold amplifiers to multiplex the signals to a gang of slower ADCs to form a single-shot reconstruction. Figure 8.8 shows the full waveform digitization of a 1 ns impulse using a gang of ADCs with a sampling rate of 20 GHz.

The advantages of step-frequency systems are the ease of increased dynamic range and good control of the frequency content of the outgoing waves. Disadvantages include a slower signal acquisition speed, the need to convert the frequency domain data to the time domain with digital Fourier transforms, and that the instruments tend to be more expensive.

A good approximation to the shape of impulse is the Gauss bell, $G(t)$,

$$G(t) = Ae^{-\frac{t^2}{2c^2}} \tag{8.31}$$

The coefficient A determines the height of the impulse. A measure of the width is $2c$. Derivatives of the Gauss function are known as Gauss-Hermite functions, Fig. 8.9 (Wiener, 1958). The first derivative, $G'(t)$, is known as a monocycle or doublet. The second derivative $G''(t)$ is known as a Mexican hat function (upside down in Fig. 8.9).

A useful property of the Gauss function $G(t)$ is that the Fourier transform is also a Gauss function, i.e. (Papoulis, 1968):

$$\int_{-\infty}^{\infty} G(t)e^{-2\pi ift}dt = \left(c\sqrt{2\pi}\right)e^{-2(\pi cf)^2} \tag{8.32}$$

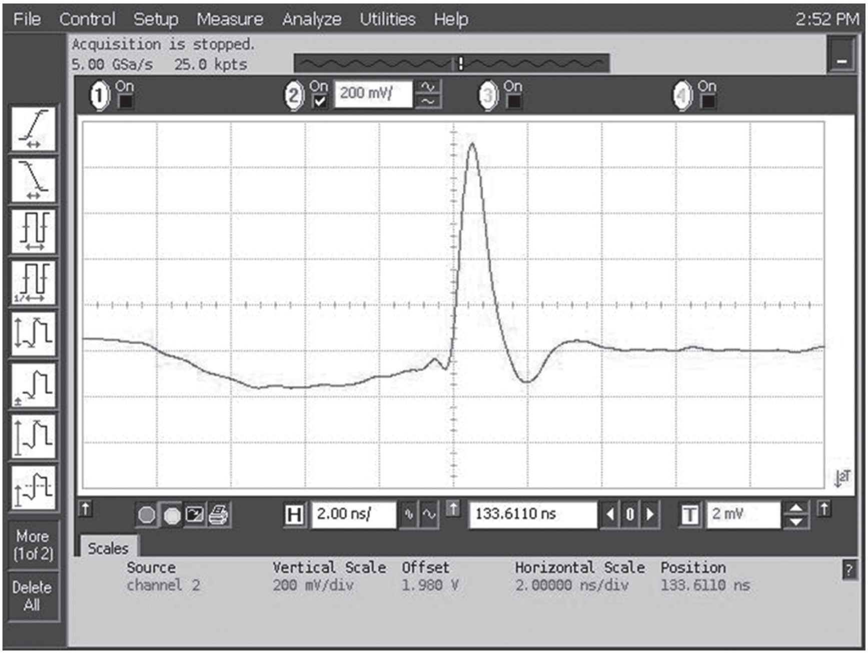

```
Acquisition is stopped.
5.00 GSa/s   25.0 kpts
```

2 On 200 mV/

H 2.00 ns/ 133.6110 ns T 2 mV

```
Source        Vertical Scale   Offset    Horizontal Scale   Position
channel 2     200 mV/div       1.980 V   2.00000 ns/div     133.6110 ns
```

8.8 Full waveform digitization of 1 ns impulse with sampling at 20 GHz by gang of ADCs.

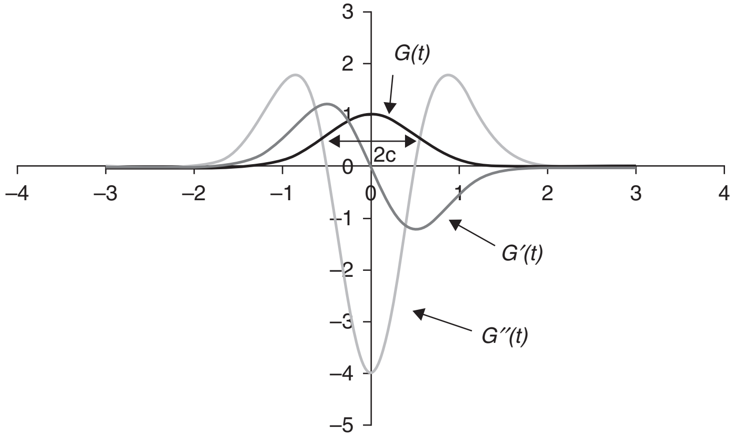

8.9 Gaussian impulses and derivatives as Gauss-Hermite functions.

This relation confirms that impulses have broadband frequency content. Narrower width impulses produce broader width frequency content. A 1 ns pulse has the bulk of its spectral energy in a region less than 1 GHz.

Creating impulses requires high-speed electronics. There are two primary methods. SRDs form the basis of one set of methods. SRDs are key components in MIR systems (McEwan, 1994b). Avalanche transistors form the basis of the second set (Morey, 1974). SRDs tend to produce low power outputs, and consume small amounts of power. Avalanche transistors can produce larger amplitude pulses, but consume more power.

Antennas launch and receive the EM waves. Collecting high quality signals depends on the ability of the antennas to direct and control the waves with minimal distortion and signal loss. Most GPR antennas operate in air-launched, ground-coupled and borehole configurations. Air-launched antennas pass EM waves through the air on both the send and receive paths, with about 50% of the signal strength being lost due to surface reflections (Smith, 1995). Most air-launched antennas have a horn geometry, Fig. 8.10. Air-launched antennas often stand 0.3–1.0 m above the ground for pavement studies. A notable exception is airborne GPR instruments, with much larger standoffs. The standoff air-launched geometry is convenient in applications that require moving the antennas across the ground surface. Ground-coupled antennas operate in close enough proximity to couple reactive near-field EM interactions directly into the ground. The typical geometry is a ground-flush mount at a gap of a few cm at most. Reactive near-field coupling enhances signal transmission and reception strength. Borehole antennas place the antenna in a hole drilled into the ground and also use near-field coupling of the EM waves. Most of the ground-coupled antennas have a bowtie geometry, which is essentially a somewhat smaller and flattened horn. Figure 8.11 shows a GPR-based roadway

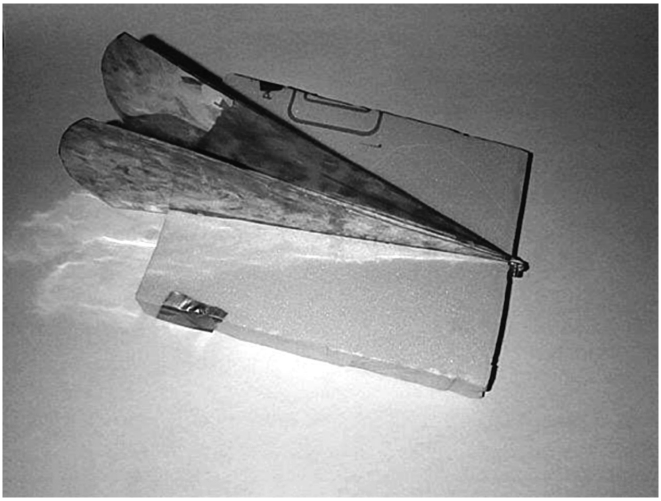

8.10 Photo of horn antenna before mounting and encasement (Huston, *et al.*, 2000b).

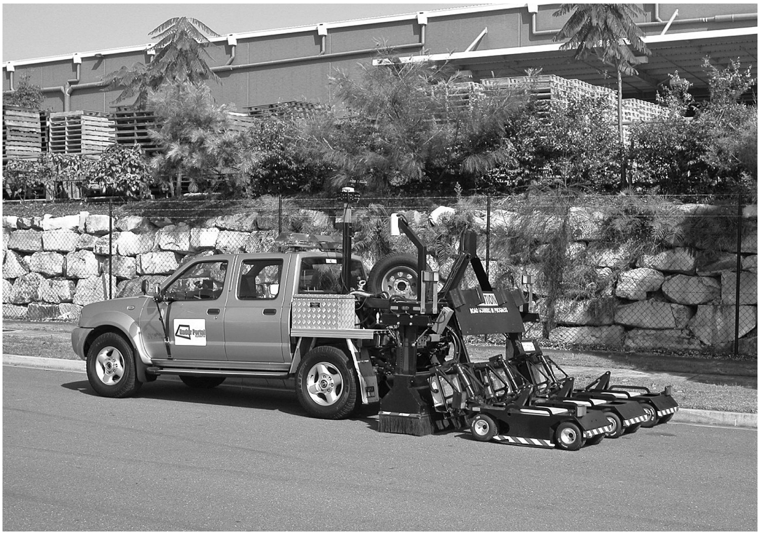

8.11 High-speed ground-coupled GPR system. (*Source*: Courtesy Radar Portal, LLC.)

inspection system that uses specialized ground-coupled antennas that can move at driving speeds. The mechanical design enables this system to combine the increased signal transmissibility of ground-coupled antennas with the mobility of an air-launched antenna to realize a 46-wide antenna array capable of producing a 3D array image, with a data density of 50 mm across the road, and 50 mm along the road, down to a depth of 1.2 m, all at 100 km/h.

Impedance matching is one of the more important concerns in the design and fabrication of radar antennas. Impedance matching has a large effect on performance, often with significant frequency-dependent effects. Impedance mismatches along a signal path causes reflections. Reflections due to impedance mismatches can contain valuable information concerning the type and geometry of subsurface features in a solid under test. When the impedance mismatches occur in the cabling and the antenna, the reflections do not contain useful information and are a source of power loss, which reduces the penetrating depth and effective resolution of the system. The voltage standard wave ratio (VSWR) quantifies the mismatch in terms of the ratio of the amplitude of the reflected voltage wave to the amplitude of the incident voltage wave, Γ.

$$\mathrm{VSWR} = \frac{\left|\widehat{V}\right|_{\max}}{\left|\widehat{V}\right|_{\min}} = \frac{1+|\Gamma|}{1-|\Gamma|} \qquad [8.33]$$

When the value of the VSWR closely approaches 1, the impedance match is satisfactory. If the impedance is totally mismatched, Γ is 1, and VSWR approaches infinity. Nominally acceptable values of the VSWR run between 1 and 2.

In an antenna, the impedance match at the apex and the impedance match at the aperture are of primary concern. The apex connects the antenna to the feed cables and then to the analyzer. A design goal for the apex is to minimize the reflections that occur with the impedance mismatch as the

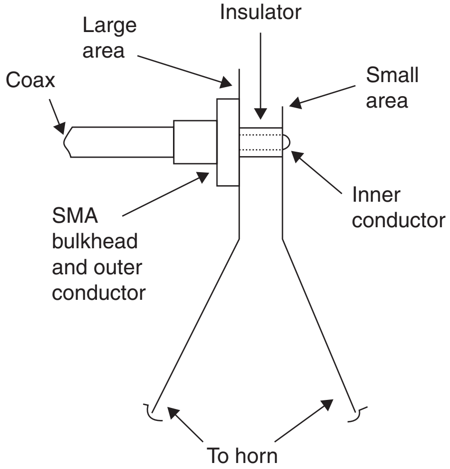

8.12 Detail of impedance-matching low-loss antenna apex connection (Huston, *et al.*, 2000b).

coaxial cable is connected into the antenna. The geometry of the coaxial cable, and the unipolar nature of the source signals, makes it difficult to create an impedance-balanced connection by directly attaching the source to the antenna. One option is to use a balun to convert from a unipolar to a bipolar format. However, total losses with baluns are typically 20 dB for a round trip signal. An alternative is to balance the connection by the inclusion of specific geometric details in a direct connection. Balanis (1997) lists several such balun direct-connect configurations. With care, an apex geometry can be found that produces a negligible impedance mismatch, such as that of Fig. 8.12. Blended geometric forms and resistive loading are standard methods of reducing impedance mismatch at the aperture (Huston *et al.*, 2000b).

8.7 Signal processing

A typical single GPR measurement collects a trace of an EM signal that reflects back from the solid under examination, Figs 8.1 and 8.2. Repeating the measurement with the antenna placed at a different point produces a measure of the reflectivity of subsurface features from a different point of perspective. The change in geometry can provide new and useful information. Taking measurements at a series of points by moving a single antenna or with a multi-antenna system gathers even more information. Condensing the data into useful information-dense formats is a primary task of GPR

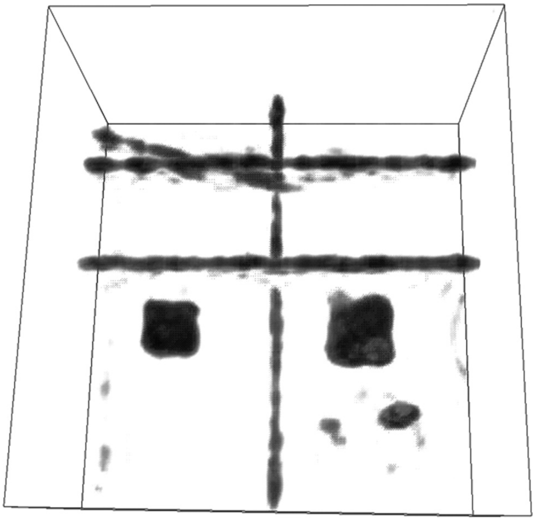

8.13 Image of rebars and defects inside a concrete slab, by Mast and Johansson (1994).

signal processing. The most common of these is a B-scan that presents a series of traces taken from a set of points along a line.

The 2-D and 3-D nature of radar signals and subsurface features often makes it difficult to discern the nature of the underlying features from a direct examination of the B-scan images. A major difficulty is the distortion due to hyperbolic nonlinearities that result from the extended distance of cross-range objects (Fig. 8.6).

The development of 2-D and 3-D imaging algorithms with applicability to GPR occurred along two independent paths – geophysical oil exploration and airborne radar. The geophysical oil exploration algorithms usually go by the name 'migration' (Stolt, 1978; Robinson, 1982). The airborne radar applications are usually called 'SAR.' Migration and SAR refer to a whole set of algorithms that attempt to deconvolve hyperbolic nonlinearities by

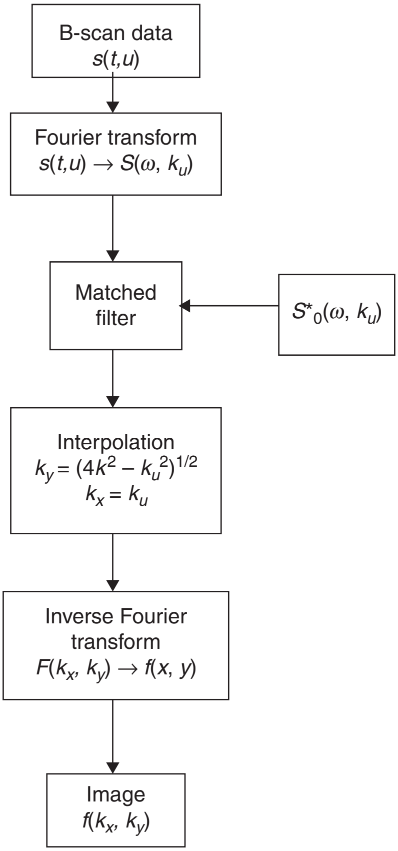
B-scan data
$s(t,u)$
Fourier transform
$s(t,u) \rightarrow S(\omega, k_u)$
Matched filter
$S^*_0(\omega, k_u)$
Interpolation
$k_y = (4k^2 - k_u^2)^{1/2}$
$k_x = k_u$
Inverse Fourier transform
$F(k_x, k_y) \rightarrow f(x, y)$
Image
$f(k_x, k_y)$

8.14 Flowchart of synthetic aperture algorithm. (*Source*: Adapted from Soumekh, 1999.)

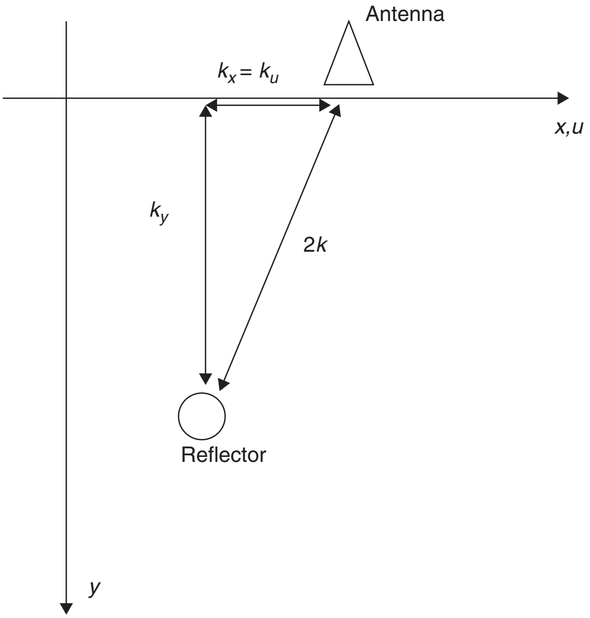

8.15 Geometry of wavenumbers associated with the synthetic aperture imaging hyperbolic nonlinearity (Huston, 2010).

various integral transforms and manipulations of entire sets of B-scan data. One of the earlier reported applications of the SAR technique to the imaging of subsurface features in concrete is by Mast (1993). Mast and Johansson (1994) further extended this work into 3-D imaging of subsurface features. Johansson and Mast (1994b) describe a related approach using multi-frequency diffraction tomography. Figure 8.13 shows the results from a test on a slab with embedded steel reinforcing bars and dielectric targets. The system is able to image the reinforcing bars and dielectric targets quite nicely. Imaging defects, such as cracks and corrosion, is more difficult.

A flowchart for the basic SAR algorithms as described by Soumekh appears in Fig. 8.14. A key feature is that combined Fourier transforms in the frequency and wave number domains algebraically remove the hyperbolic nonlinearity B-scan data (Soumekh, 1999).

The geometry of the hyperbolic nonlinearity in wave number space is shown in Fig. 8.15. The key relations are

$$k_y^2 + k_u^2 = 4k^2 \qquad [8.34]$$

or

$$k_y = (4k^2 - k_u^2)^{1/2} \qquad [8.35]$$

and

$$k_x = k_u \qquad [8.36]$$

where k_x = down-range image wavenumber, k_y = cross-range image wave number, k_u = down-range wave number, and $k = \omega/c$ = wave number. This transforms the data into a form that represents the geometry of the reflective features. Finally, the data are inverse Fourier transformed into the spatial x-y domain to form an image.

8.8 Laboratory and field studies

Water intrusion is believed to be a major factor in many progressive damage modes in roadways and structures. One method of detecting subsurface water is to note that the transmissibility at 2.4 GHz changes with phase. Liquid water absorbs EM waves at 2.4 GHz. This is the basis for microwave ovens. Frozen water is transparent at 2.4 GHz. Figure 8.16 shows the results of a test on concrete slabs with water-filled variable and uneven depth layers. Water in the form of saturated towels was placed on top of the cupcake plateaus and in some of the flat surfaces between the slabs. The relative absorption of the thawed versus frozen patterns is distinctive.

The ability of GPR to reliably detect delaminations between layers in concrete and asphalt structures remains to be established with certainty. Figure 8.17 shows the results of a laboratory study that boosts the possibility. The test used slabs of concrete with 1 mm gaps to simulate a delamination. A 1–16 GHz impulse GPR system was able to detect the 1 mm air-filled

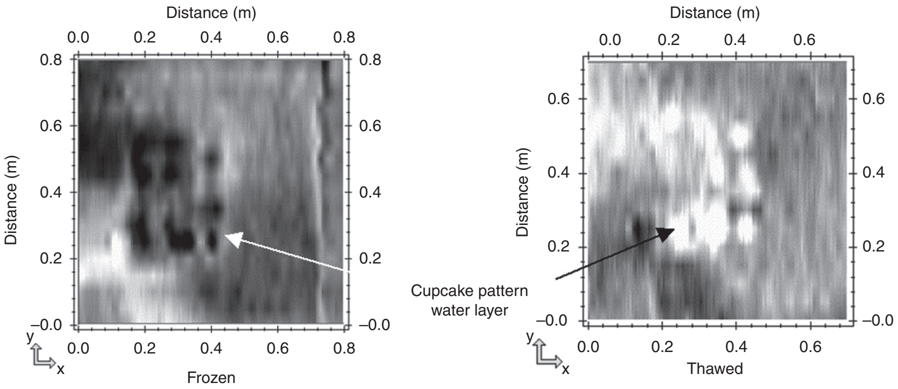

8.16 GPR measurements with 2.3 GHz handheld antenna on concrete slab specimen with frozen and thawed cupcake pattern water layer. (From Materials Evaluation, Vol. 67, No. 11. Reprinted with permission of The American Society for Nondestructive Testing, Inc. This reprint contains copyrighted property of ASNT and may not be duplicated or altered in any manner.)

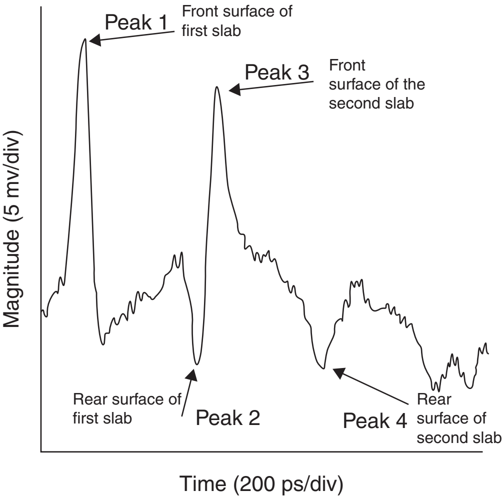

8.17 Reflected signal versus time for two 38 mm slabs stacked with a 1 mm gap using the GIMA-1 antenna and the Sandia National Labs 1–16 GHz impulse GPR system. Both surfaces of the gap are apparent (Huston *et al.*, 2000b).

gap. It should be noted that delaminations encountered in the field often have rough surfaces, and not the smooth surfaces encountered in this test. The cupcake patterns of Fig. 8.16 were part of a test regime that looked into some of these questions.

In an effort to clarify further the ability to detect corrosion damage with GPR and other sensors, a series of studies were conducted at the Federal Highway Administration (FHWA) NDE Laboratory (McLean, VA, USA) (Cui, 2012). These tests involved inducing accelerated corrosion in a reinforced concrete slab with weekly ponding, removal, and drying of saline water over the course of a year (Fig. 8.18)

A B-scan of the slab after six months of curing and before the accelerated corrosion test appears in Fig. 8.19. Hyperbolas corresponding to subsurface reinforcing bars are distinct. A B-scan of the slab after seven months of accelerated corrosion testing appears in Fig. 8.20. The hyperbolas corresponding to subsurface reinforcing bars are somewhat fuzzy. This confirms the hypothesis underlying AASHTO TP36–93 that corrosion damage causes a blurring of the reinforcing bar hyperbolas (AASHTO, 1993). However, the mechanisms that produce this blurring remain undetermined. Subsequent dissection of the slab indicated that there was minimal cracking, no delaminations, and that the amount of corrosion surrounding the reinforcing bars was approximately at Stage 4 in Fig. 8.3. Rapid chloride testing of the concrete post mortem found concentration levels of chlorides in excess of 0.5% by weight. Overall, the results of these tests indicate that

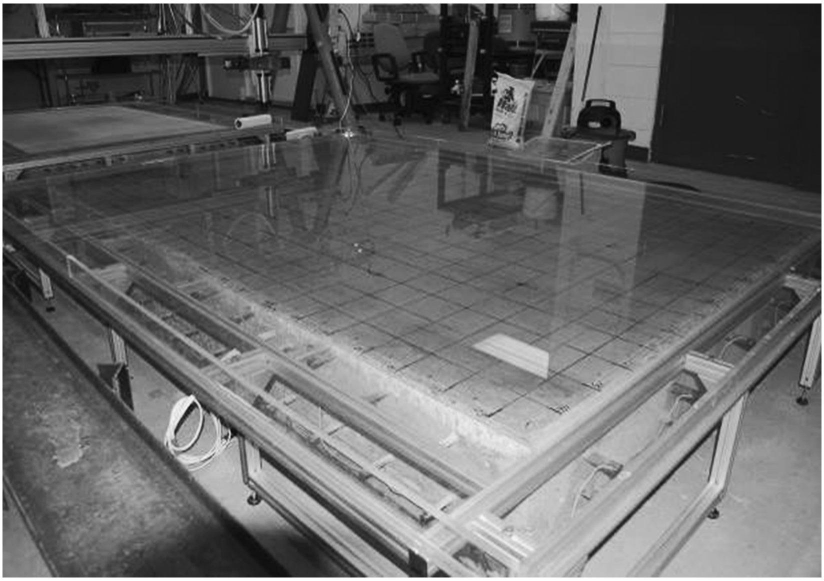

8.18 Salt water ponding as part of accelerated corrosion test on reinforced concrete slab in FHWA NDE Laboratory (McLean, VA, USA) (Cui, 2012).

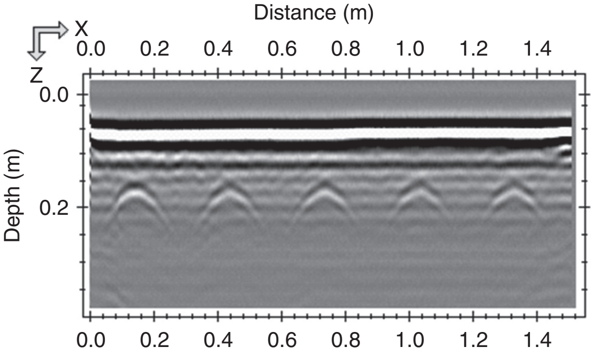

8.19 B-scan of concrete slab after six months of curing and before accelerated corrosion testing (Cui, 2012).

GPR can likely be useful in detecting early stage concrete chloride-induced corrosion damage.

A field test of a newly constructed healthy bridge deck appears in Fig. 8.21, along with a B-scan showing distinct hyperbolas from reinforcing bars in Fig. 8.22. These figures contrast with those of the Bostwick Road Bridge, Shelburne, VT, USA, Fig. 8.23. The reinforcing bar hyperbolas are barely discernible in this distressed bridge (Fig. 8.24).

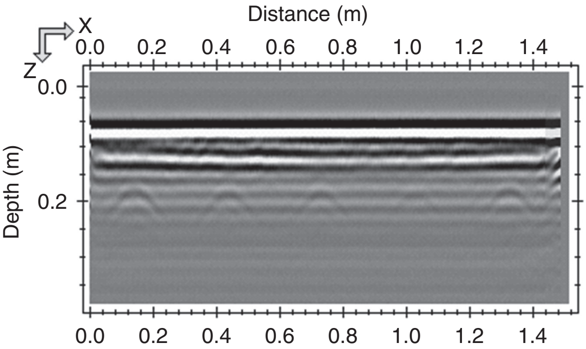

8.20 B-scan of concrete slab after seven months of accelerated corrosion testing (Cui, 2012).

8.21 Scanning the deck of the Turkey Lane Bridge, Hinesburg, VT, USA (Huston *et al.*, 2002).

The high-frequency range of EM wave NDE technology presently extends into the terahertz range. Many materials quickly attenuate terahertz EM waves, which limits their utility for subsurface probing. However, there are some applications where terahertz sensing is useful. These generally involve detecting features underneath a relatively thin outer layer that is transparent to terahertz waves. Detecting corrosion under thermal protection system (TPS) tiles or paint is a good candidate for terahertz sensing tests. Figure

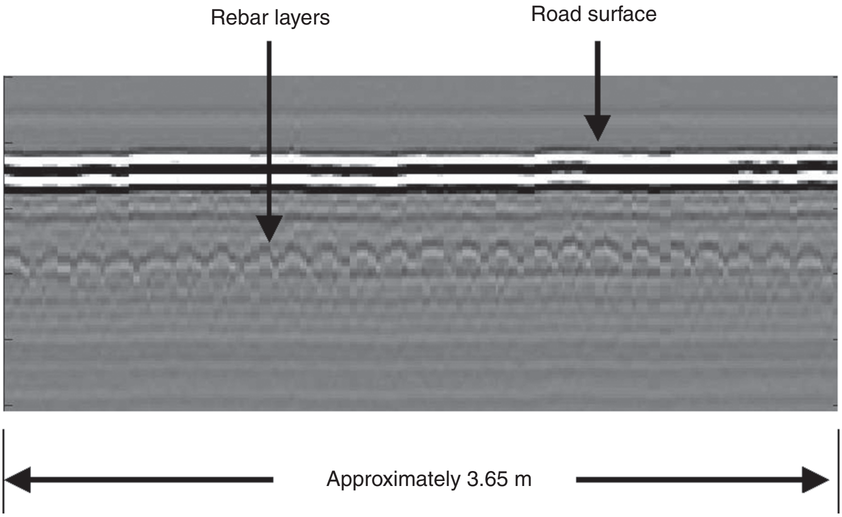

8.22 B-scan of Turkey Lane Bridge showing distinct hyperbolas of reinforcing bars (Huston *et al.*, 2002).

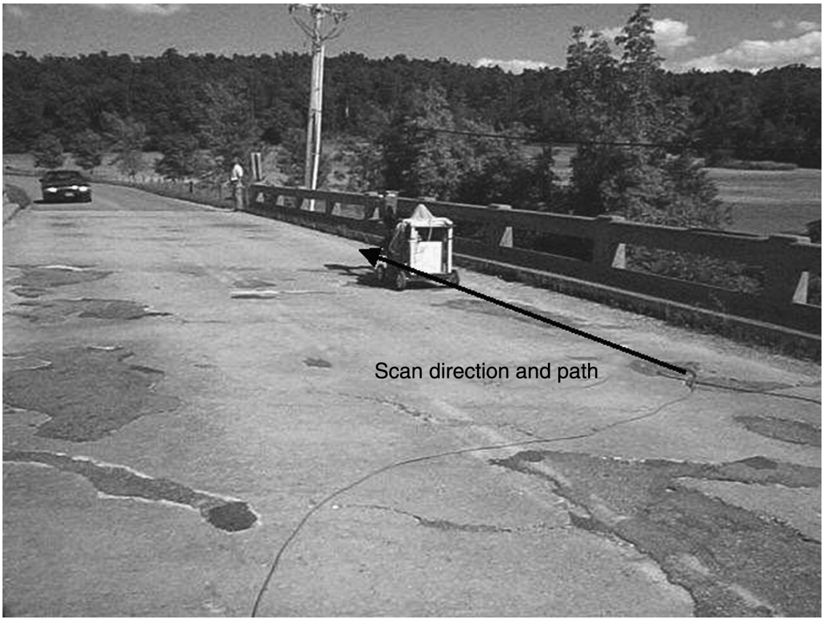
Scan direction and path

8.23 Direction and path of scan on the Bostwick Road Bridge, Shelburne, VT, USA (Huston *et al.*, 2002).

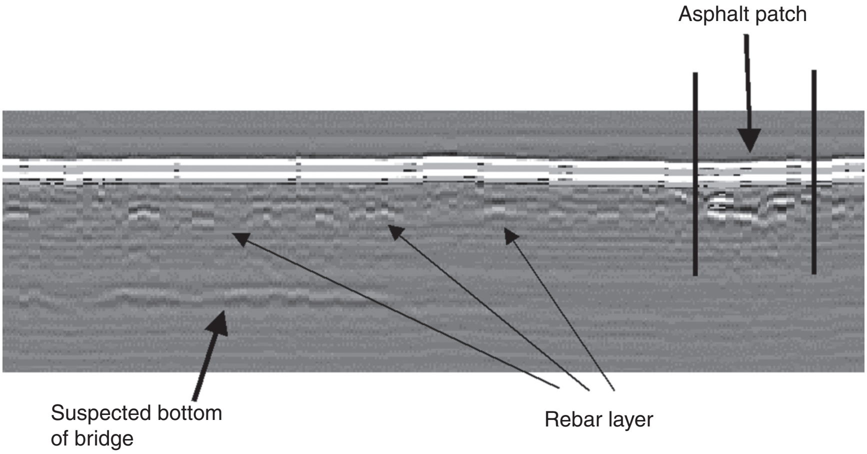

8.24 B-scan of Bostwick Road Bridge with reinforcing bar hyperbolas barely discernible (Huston *et al.*, 2002).

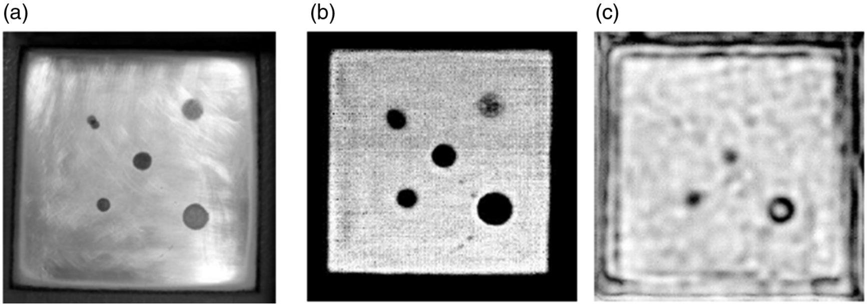

8.25 Demonstration of the ability of terahertz (75–100 GHz) imaging system to detect corrosion under Space Shuttle thermal protection tile material. (a) Photo of corrosion on metal substrate. (b) Terahertz image of metal substrate without tile. (c) Terahertz image of metal substrate with intervening 25.4 mm tile. (*Source*: Reprinted with permission from Madaras EI, Anastasi R, Smith SW, Seebo JP, Walker JL, Lomness JK, Hintze PE, Kammerer CC, Winfree WP, Russell RW. (2008) 'Application of terahertz radiation to the detection of corrosion under the shuttle's thermal protection system', Review of Quantitative Nondestructive Evaluation, 27, 421–428. Copyright 2008, AIP Publishing LLC.)

8.25 shows the ability of a 75–100 GHz system to detect corrosion under a 25.4 mm thick Space Shuttle TPS tile.

8.9 Conclusions and future trends

The ability to launch, control, and measure EM waves with increased levels of sophistication at relatively low cost opens up new opportunities and sensing modalities. Of particular note is the use of interferometric radar to monitor remotely the dynamic motions of large structures, such as bridges (Mayer *et al.*, 2010). A vibrant trend is the appearance of multichannel systems, which offer the opportunity for increased data collection rates. For example, a multichannel system can inspect a full road lane in a single pass, rather than multiple passes, as required with a single or dual-channel system. Coarse-pitch antenna arrangements essentially have the antennas operate as a set of independent single antennas. Dense-pitch arrangements, with the between-antenna spacing at less than one quarter wavelength, allow for tomographic reconstructions that avoid excessive interpolations (Grasmueck *et al.*, 2005). Another trend of note is the concept of periodic nondestructive testing (NDT), which subjects structures to repeated examinations to ascertain long-term trends and significant changes in the condition (Jalinoos, 2009). Affordable and easy-to-use instruments are an essential ingredient in periodic NDT. The increased use of digital signal processing techniques, such as high-speed ADC, may facilitate more periodic NDT approaches (Xu *et al.*, 2013).

An interesting possible future development will be the adaptation of cognitive radar system concepts to GPR systems (Haykin, 2006, 2012). A cognitive GPR system uses information gathered from real-time data analysis to provide information to the system controller for resetting the operational parameters to ensure optimal data collection performance. The technique uses the four primary actions of perception-action, memory, attention, and intelligence. A simple example would be a roadway inspection GPR that changes operating parameters based on a perception as to whether it is traveling on a road or on a bridge deck. Roadways may be best examined with low frequency waves at a fairly coarse pitch to penetrate and measure subbase conditions. Bridge decks may be best examined with a finer level of attention using high-frequency fine pitch measurements. Similarly the gains on the receiver hardware may be optimally selected by the cognitive system. A more sophisticated controller may be one that selects operational parameters based on what gives the best level of resolution and information content. The mode selection may be driven by a combination of navigational and data driven estimates of state. At the heart of the controller is an operational parameter-setting matrix that serves as a map from a discrete set of environmental (observational) condition states onto a discrete set of operational parameter states. Upon perceiving an environmental state, the controller uses the map to select the operational parameters. The process iterates as the system encounters new environmental state. A simple approach is to use an intelligent designer to preselect a static map. A more sophisticated, but possibly better, approach uses machine learning to update the map dynamically. Updating methods include greedy and reinforcement techniques that alter the map in a positive response to parameters that improve performance (Bongard *et al.*, 2006; Christensen *et al.*, 2010) and the motivational methods that attempt to reduce negative responses in a method analogous to pain avoidance (Starzyk *et al.*, 2012).

It has been proposed that corrosion of steel inside concrete produces nonlinear effects that can be measured by sub- and super-harmonic methods (Kwun, 1993). To date, however, nonlinear interactions of materials with EM waves have not been extensively studied. A primary reason is the lack of suitable test instruments and protocols. The recent appearance of nonlinear vector network analyzers and the development of algorithms based on polyharmonic distortion coefficients (X-parameters) in the frequency domain and Volterra series in the time domain may prompt future developments in this area (Verspecht and Root, 2006).

Additional areas of active and possibly fruitful research include developing multisensory data fusion methods that combine the strengths of GPR sensing with those of other sensors to produce better renditions of structural conditions (Huston *et al.*, 2011), and the development of less bulky electrically small antennas.

In conclusion, radar technologies are sufficiently mature to be able to provide useful information to users of the instruments, and technical improvements and innovations are proceeding on active paths that should lead to improved performance along with a wider range of usage.

8.10 References

AASHTO. (1993) Standard Test Method for Evaluating Asphalt-Covered Concrete Bridge Decks Using Pulsed Radar, AASHTO Designation: TP36–93, Edition 1A, September 1993.

Allen EH and Karageorgis M. (2008) 'Radar Systems and Methods using Entangled Quantum Particles' *US Patent* **7**, 375, 802.

Alongi AV, Cantor TR, Kneeter CP and Alongi, Jr A. (1982) 'Concrete Evaluation by Radar Theoretical Analysis', Transportation Research Board Record No. 853.

Al-Qadi IL, Hazim OA, Su W and Riad SM. (1995) 'Dielectric properties of portland cement concrete at low RF frequencies', *Journal of Civil Engineering Materials, ASCE*, Vol. **7**, No. 3, pp. 192–198, August 1995.

Annan AP. (2002) 'GPR-history, trends, and future developments', *Subsurface Sensing Technologies and Applications*, Vol. **3**, No. 4, pp. 253–270.

Balanis CA. (1997) *Antenna Theory*, 2nd edn., Wiley, New York.

Balanis C. (2012) *Advanced Engineering Electromagnetics*, 2nd edn., Wiley, Hoboken, NJ.

Bongard J, Zykov V and Lipson H. (2006) 'Resilient machines through continuous self-modeling', *Science*, Vol. **314**, pp. 1118–1121, 17 November.

Carter CR, Chung T, Holt FB and Manning DG. (1986) 'An automated signal processing system for the signature analysis of radar waveforms from bridge decks', *Canadian Electrical Engineering Journal*, Vol. **11**, No. 3, pp. 128–137.

Chase S. (1999) 'Tomographic imaging of bridge decks using radar', *Proceedings of ASCE Structures Congress,* New Orleans, pp. 280–283.

Chung T, Carter CR, Manning DC and Holt FB (1984) 'Signature Analysis of Radar Waveforms Taken on Asphalt Covered Bridge Decks' Canada Ministry of Transportation and Communications, Report ME-84–01.

Christensen DJ, Schultz UP and Stoy K. (2010) 'A Distributed Strategy for Gait Adaptation in Modular Robots' 2010 IEEE International Conference on Robotics and Automation Anchorage Convention District, 3–8 May 2010, Anchorage, Alaska, USA, pp. 2765–2770.

Clemena GG. (1984) 'Non-destructive Inspection of Overlaid Bridge Decks with Ground-Penetrating Radar' Transportation Research Board Record No. 899.

Condon EU and Odishaw H, eds. (1967) *Handbook of Physics*, 2nd edn., McGraw-Hill, New York.

Cook JC. (1973) 'Radar exploration through rock in advance of mining', *Trans Society Mining Engineers, AIME*, Vol. **254**, pp. 140–146.

Cui J. (2012) 'Multiple Sensor Periodic Nondestructive Evaluation on Concrete Bridge Deck Maintenance'. PhD dissertation, University of Vermont, Mechanical Engineering.

Debye JW. (1960) *Polar Molecules*, Dover Publications, New York.

El Said MAH. (1956) 'Geophysical prospection of underground water in the desert by means of electromagnetic interference fringes', *Proceedings of the I.R.E.*, Vol. **44**, pp. 24–30.

Ely JJ, Shaver TW and Fuller GL. (2002) 'Ultrawideband Electromagnetic Interference of Aircraft Radios' NASA/TM-2002–211949.

FCC (2002). 'First Report and Order FCC 02–48' Federal Communications Commission ET Docket No. 98–153, 14 February 2002.

Feynman RP. (1977) *The Feynman Lectures on Physics*, Addison Wesley Longman, Inc., Reading, MA.

Grasmueck M, Weger R and Horstmeyer H. (2005) 'Full-resolution 3-D GPR imaging', *Geophysics*, Vol. **70**, pp. K12–K10.

Halabe UB, Maser KM and Kausel E. (1990) 'Condition Assessment of Reinforced Concrete Structures Using Electromagnetic Waves', Technical Report, Contract No.DAAL 03–87-K005, MIT, Department of Civil Engineering, Cambridge, MA.

Halabe UB, Sotoodehnia A, Maser KR and Kausel EA. (1993) 'Modeling the electromagnetic properties of concrete', *ACI Materials Journal*, Vol. **90**, No. 6, November/December, pp. 552–563.

Halabe UB, Chen HL, Bhandarkar V, and Sami Z. (1997) 'Detection of sub-surface anomalies in concrete bridge decks using ground penetrating radar', *ACI Materials Journal*, Vol. **94**, 5, 396–408.

Haykin S. (2006) 'Cognitive radar: A way of the future', *IEEE Journal Signal Processing*, February pp. 30–40.

Haykin S. (2012) *Cognitive Dynamic Systems*, Cambridge University Press, Cambridge, UK.

Holser WT, Brown RJ, Roberts FA, Fredrikkson OA and Unterberger RR. (1972) 'Radar logging of a salt dome', *Geophysics*, Vol. **37**, pp. 889–906.

Huston D. (2010) *Structural Sensing Health Monitoring and Prognosis*, Taylor and Francis, Boca Raton, FL.

Huston D, Pelczarski N, Esser B, Maser K, and Weedon W. (2000a) 'Damage assessment in roadways with ground penetrating radar', *SPIE Conference on Nondestructive Evaluation and Health Monitoring of Aging Infrastructure*, 3995A-55, Newport Beach CA, A. E. Aktan and S. R. Gosselin eds.

Huston DR, Hu JQ, Maser K, Weedon W and Adam C. (2000b) 'GIMA ground penetrating radar system for infrastructure health monitoring', *Journal of Applied Geophysics*, Vol. **43**, pp. 139–146.

Huston DR, Fuhr PL, Maser K and Weedon WH. (2002) 'Nondestructive Testing Of Reinforced Concrete Bridges Using Radar Imaging Techniques' Final Research Report NETC 94–2, for New England Transportation Consortium.

Huston D, Cui J, Burns D and Hurley D. (2011) 'Concrete bridge deck condition assessment with automated multisensor techniques', *Structure and Infrastructure Engineering*, Vol. **7**: 7, 613–623, DOI: 10.1080/15732479.2010.501542, published online, September 2010.

Jalinoos F, Arndt R, Huston D and Cui J. (2009) 'Structural health monitoring by periodic NDT: NDT for bridge maintenance', *Materials Evaluation*, Vol. **67**, No. 11, pp. 1300–1307.

Johansson E and Mast JE. (1994) 'Three-dimensional ground penetrating radar imaging using synthetic aperture time-domain focusing', SPIE Proceedings Vol. 2275, Advanced Microwave and Millimeter-Wave Detectors, Satish S. Udpa, Hsiu C. Han, Editors, pp. 205–214.

Joyce RP (1984) 'Rapid Non-Destructive Delamination Detection', Federal Highway Administration FHWA RD-84/076.

Klauder JR and Sudarshan EC. (2006) *Fundamentals of Quantum Optics*, Dover Publications, Mineola, NY.

Kwun H, Burkhardt GL and Fisher JL. (1993) 'Detection of Reinforcing Steel Corrosion in Concrete Structures Using Non-Linear Harmonic and Intermodulation Wave Generation' US Patent 5,180,969.

Madaras EI, Anastasi R, Smith SW, Seebo JP, Walker JL, Lomness JK, Hintze PE, Kammerer CC, Winfree WP and Russell RW. (2008) 'Application of terahertz radiation to the detection of corrosion under the shuttle's thermal protection system', *Review of Quantitative Nondestructive Evaluation*, Vol. **27**, pp. 421–428.

Manning DG and Holt FB. (1984) 'Detecting Deterioration in Asphalt-Covered Bridge Decks', Transportation Research Board Record No. 899.

Maser KR. (1989) 'New Technology for Bridge Deck Assessment', New England Transportation Consortium Phase I Final Report, Center for Transportation Studies, MIT.

Mast J. (1993) Microwave Pulse-Echo Radar Imaging for the Nondestructive Evaluation of Civil Structures Ph.D. Dissertation, Electrical Engineering, University of Illinois at Urbana-Champaign.

Mast J and Johansson EM. (1994) 'Three-dimensional ground penetrating radar imaging using multi-frequency diffraction tomography', SPIE Proceedings Vol. 2275, Advanced Microwave and Millimeter-Wave Detectors, Satish S. Udpa, Hsiu C. Han, Editors, pp. 196–203.

Mayer L, Yanev B, Olson LD and Smyth AW. (2010) 'Monitoring of Manhattan Bridge for Vertical and Torsional Performance with GPS and Interferometric Radar Systems' Transportation Research Board 89th Annual Meeting, Washington, DC.

McEwan TE. (1994a) 'Ultra-Wideband Receiver' *US Patent* **5**, 345, 471.

McEwan TE. (1994b) 'Ultra-Wideband Radar Motion Sensor' *US Patent* **5**, 361, 070.

Morey RM. (1974) 'Geophysical Surveying System Employing Electromagnetic Impulses' *US Patent* **3**, 806, 795.

Moon P and Spencer DE (1960) *Foundations of Electrodynamics*, van Nostrand, Princeton, NJ.

MSSI. (2000) 'Response to FCC Notice of Inquiry ET Docket No. 98–153' Multispectral Solutions, Inc. Gaithersburg, MD. 1 March 2000.

NTIA. (2001) 'Assessment of Compatibility Between Ultrawideband Devices and Selected Federal Systems' National Telecommunications and Information Administration, Publication 01–43.

Olhoeft GR. (1975) 'The Electrical Properties of Permafrost', Ph.D. dissertation, University of Toronto.

Olhoeft GR. (2002) 'The New Ground Penetrating Radar Regulatory Environment' *Proceedings of the Ninth International Conference on Ground Penetrating Radar*. Santa Barbara, CA.

Papoulis A (1968) *Systems and Transforms with Applications in Optics*, McGraw-Hill, New York.

Reeves BA. (2010) 'Noise Augmented Radar System' *US Patent* **7**, 656, 341.

Robinson E. (1982) 'Spectral Approach to Geophysical Inversion by Lorentz, Fourier and Radon Transforms' *Proceedings of the IEEE*, Vol. **70**, No. 9, September 1982, pp. 1039–1054.

Smith SS. (1995) 'Detecting pavement deterioration with subsurface interface radar', *Sensors*, Vol. **12**(9), pp. 29–40, September 1995.

Soumekh M. (1999) *Synthetic Aperture Radar Signal Processing*, Wiley-Interscience, New York.

Starzyk JA, Graham JT, Raif P and Tan AH. (2012) 'Motivated learning for the development of autonomous systems', *Cognitive Systems Research,* Vol. **14**, pp. 10–25.

Steinway WJ, Echard JD and Luke CM. (1981) 'Locating Voids Beneath Pavement Using Pulsed Electromagnetic Waves', National Research Council.

Stolt R. (1978) 'Migration by Fourier transform', *Geophysics*, Vol. **43**, No. 1, February 1978, pp. 23–48.

Taflove A and Hagness S. (2005) *Computational Electrodynamics The Finite Difference Time Domain Method*, Arctech House, Norwood, MA.

Taylor JD. (2001) *Ultrawideband Radar Technology*, Woodhead Publishing Limited, Boca Raton.

Thierbach R. (1974) 'Electromagnetic reflections in salt deposits', *Journal of Geophysics*, Vol. **40**, pp. 633–637.

Udd E. (1991) *Fiber Optic Sensors*, Wiley, New York.

Ulricksen CP. (1982) 'Application of Impulse Radar to Civil Engineering' Doctoral Thesis, Lund University, Department of Engineering Geology, Sweden.

Verdeyen JT. (1989) *Laser Electronics*, 2nd edn., Prentice-Hall, Englewood Cliffs.

Verspecht J and Root DE. (2006) 'Polyharmonic distortion modeling', *IEEE Microwave Magazine*, June, Vol. **7**, No. 3, pp. 44–57.

Wiener N. (1958) *The Fourier Integral and Certain of Its Applications*, Dover Publications, New York.

Xu X, Xia T, Venkatachalam A and Huston D. (2013) 'The development of a high speed ultrawideband ground penetrating radar for rebar detection' *Journal of Engineering Mechanics*, Vol. **139**, No. 3, pp. 272–285, DOI:10.1061/(ASCE) EM.1943-7889.0000458.

Yee KS. (1966) 'Numerical solution of initial boundary value problems involving Maxwell's equations in isotropic media', *IEEE Trans. on Antennas and Propagation*, Vol. **AP-14**, No. 3, pp. 302–307.

Zoughi R, Gray SD and Nowak PS. (1995). 'Microwave nondestructive estimation of cement paste compressive strength', *ACI Materials Journal*, Vol. **92**, No. 1, pp. 64–70.

9

Electromagnetic sensors for assessing and monitoring civil infrastructures

M. L. WANG, Northeastern University, USA and G. WANG,
Chicago Bridge and Iron, USA

DOI: 10.1533/9780857099136.238

Abstract: Electromagnetic sensors are non-destructive evaluation technologies and they are widely used in health monitoring and damage detection for infrastructures. In this chapter several existing technologies with various functional theories are briefly reviewed. The application of elastomagnetic (EM) (or magnetoelastic) stress sensor technology in stress monitoring for steel cables is described. The roles of microstructure and temperature in magnetization and magnetoelasticity are discussed. The design and configuration of an EM sensor are illustrated. In addition, the design of an appropriate energizing circuit to counteract eddy currents is introduced. Field application examples with EM sensors used in existing and new constructions are provided. A removable stress measurement design is also presented as a promising monitoring tool for steel structural components.

Key words: steel tendon stress monitoring, elasto-magnetic stress sensor, cable force monitoring, cable-stayed bridge, prestressed force monitoring, structural health monitoring, electromagnetic theory, non-destructive evaluation (NDE).

9.1 Introduction to magnetics and magnetic materials

Magnetic materials were initially utilized in compasses, as recorded in Chinese literature in the first century BC. In human civilization history, magnetic materials have contributed tremendously to navigation and geographic exploration. However, modern magnetic theory was established several centuries ago by the scintillating work of Gilbert, Ampere, Oersted, and others.

In this chapter, the magnetic properties of ferromagnetic materials are the main concern. In order to understand ferromagnetism, we first review the materials' classification in accordance with their magnetic properties. The distinction between the materials in terms of magnetism lies in the interaction of the micromagnetic moment of the electron orbital motion and electron spinning, and the rearrangement of the moments caused by the applied magnetic field.

© 2014 Woodhead Publishing Limited

One can categorize inorganic materials into five groups: diamagnetic materials, paramagnetic materials, antiferromagnetic materials, ferromagnetic materials, and ferrimagnetic materials.[1] In diamagnetic materials, such as copper, silver, gold, and beryllium, the magnetic moments introduced from electron spins and orbital motions counteract each other, which leads to a negligible magnetization even when exposed to an external field. While for paramagnetic materials such as aluminum, platinum, and manganese, the overall magnetization effect is an increase in the magnetization but weak within the materials. In super-paramagnetic materials, fine ferromagnetic particles are distributed in the non-ferromagnetic matrix; as a result, no magnetic memory remains due to thermal fluctuation.

In antiferromagnetic materials such as chromium, below the Neel temperature of 37°C, under the applied magnetic field the neighboring atomic moments are antiparallel to each other, which leads to a zero net magnetization; therefore, such kind of materials are insensitive to a magnetic field. If the antiparallel moments sum up to a non-zero net magnetic moment, the material is called ferrimagnetic material, like Fe_3O_4, and can be considered as imperfectly antiferromagnetic.

Ferromagnetism occurs spontaneously in elements such as iron, nickel, and cobalt. In these elements, the magnetic moments are aligned in the same direction and are parallel to each other to produce strong magnets. The ferromagnetic materials can be either crystalline or amorphous, in which the atomic moments are aligned so as to achieve an intense magnetization higher than the applied field. At room temperature, the only ferromagnetic metals are iron, nickel, cobalt, and some alloys.

Experimental and theoretical analysis indicates that the basic functional unit in the ferromagnetic material is magnetic domain, which is a collection of atomic moments aligned in a parallel manner to minimize the exchange energy. The net magnetic moment within a domain is the summation of the atomic moments. The neighboring domains are separated by domain walls with a thickness of $10^{-8} \sim 10^{-6}$ m. The competition of the wall energy, crystal anisotropic energy, exchange energy, and magnetostatic energy determines the domain sizes, which however vary over a wide range.

Ferrimagnetic materials resemble ferromagnetic materials in such aspects as the structure of the magnetic domains and the phenomenon of hysteresis. In the ferrimagnetic materials, the magnetic moments within the neighboring sub-lattices compete with each other, and the net magnetization may demonstrate an unusual dependence on temperature, while the magnetization in ferromagnetic materials arises from the parallel alignment of the identical magnetic moments in one lattice. Otherwise, the net magnetization within all domains in ferromagnetic or ferrimagnetic specimen is zero, as indicated in Fig. 9.1.

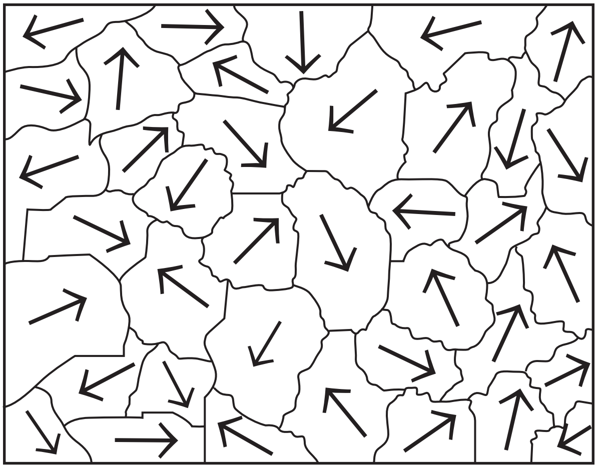

9.1 Magnetic domain in a non-magnetized ferromagnetic sample.

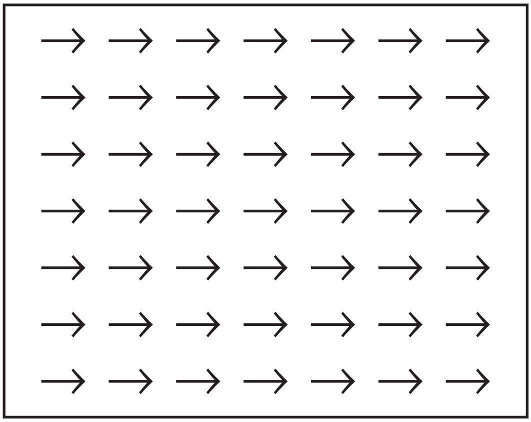

9.2 Magnetic domains in a magnetically saturated ferromagnetic sample.

If a ferromagnetic specimen is exposed to a magnetic field strong enough to magnetically saturate it, the magnetic domains will rotate until all are aligned unanimously, as shown in Fig. 9.2.

In ferromagnetic materials, the magnetizing process typically demonstrates the phenomenon of hysteresis, as shown in Fig. 9.3. There are three types of magnetic hysteresis curves. The first one is the major hysteresis curve, which depicts the variation in magnetic induction in the sample magnetized by the applied alternating field with a magnitude no lower than the technical magnetic saturation. Technical magnetic saturation means that the

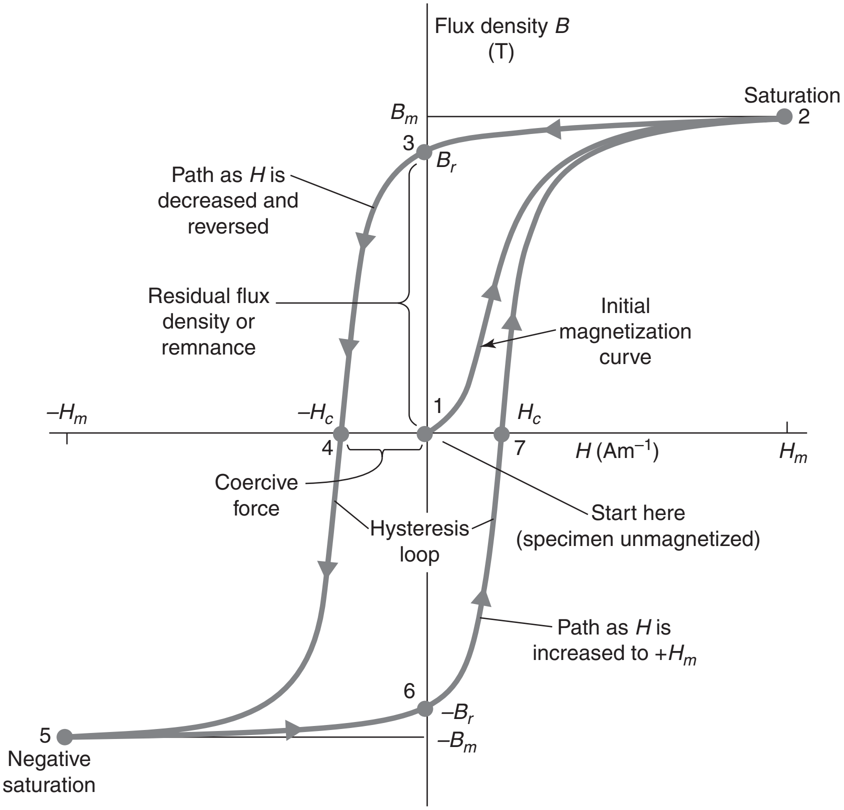
Flux density B (T)
Saturation
2
B_m
3
B_r
Path as H is decreased and reversed
Residual flux density or remnance
Initial magnetization curve
$-H_m$
$-H_c$
1
H_c
4
7
H (Am^{-1})
H_m
Coercive force
Hysteresis loop
Start here (specimen unmagnetized)
Path as H is increased to $+H_m$
6
$-B_r$
$-B_m$
5
Negative saturation

9.3 Magnetic hysteresis curves for typical ferromagnetic materials.

higher level of magnetization does not change the shape of the hysteresis. Magnetic parameters, such as remanence, coercivity, and saturated magnetization can be measured from major hysteresis curve. Owing to its high repeatability and straightforward measurability, major hysteresis is widely applied in physics and engineering.

The second type is the anhysteresis curve, which is plotted by applying a constant field superimposed with an oscillating field with descending magnitude escalating from positive saturation to zero. Each point on such curve is history-independent, and thus mainly dependent on material properties. Because of that, anhysteresis is valuable in material characterization. However, it takes a long time to complete the anhysteresis measurement, and the heat produced from the oscillating field can easily lead to a temperature rise.

The third type is the minor hysteresis curve, which is different from major hysteresis in that the magnitude of the alternating field is below technical saturation. The magnetic parameters can be defined in a similar way to major hysteresis, such as pseudo coercivity, pseudo remanence, pseudo hysteresis loss, and pseudo susceptibility, etc. Some parameters were reported to be more sensitive to a field than those derived from the major hysteresis loops.[2] Confined in the major loop, the positions of the congruent minor loops depend on magnetization history; therefore, the minor loops are usually measured when the specimens are completely demagnetized.

The magnetic properties of the materials depend heavily on temperature. The ferromagnetic and ferrimagnetic materials will turn to be paramagnetic or antiferromagnetic (for some rare earth elements) when the temperature is raised above a threshold value such as Curie's point. Antiferromagnetic materials will be paramagnetic above Neel's point.

As materials technology evolves, specific magnetic phenomena and innovative magnetic materials are continually being brought forward. Various magnetic effects have already been industrialized, such as giant magnetoresistance (GMR) – the magnetization dependence of the electrical conductivity, magnetocaloric effect – the magnetization dependence of the entropy, magnetorheological effect – the rheological properties of the magnetic powders suspended in viscous fluids, and magnetoelasticity. The magnetorheological effect has been used in magnetic dampers in infrastructures.[3] Due to the proliferation in nano-technology, nano-magnetic materials have been intensively researched for their diverse applications in ferrofluids, drug delivery, radioactive tracer, and power conversion and conditioning.[4] Magnetic shape memory, or ferromagnetic shape memory alloy, has also been studied.[5]

9.2 Introduction to magnetoelasticity

For most ferromagnetic materials, the magnetic performances are correlated with mechanical stress,[6–12] which can be described in terms such as magnetoelasticity and magnetostriction. With a theoretical basis in magnetoelasticity, elastomagnetic (EM) stress sensors have been used successfully in health monitoring for infrastructures.[13–16] Magnetoelasticity in ferromagnetic material is rooted in magnetic stress anisotropy. Several intrinsic and extrinsic factors lead to magnetic anisotropy, including crystal anisotropy, shape anisotropy, and anisotropy introduced by specific heat and mechanical treatment. Crystal anisotropy means that easy axis and plane magnetization requires relatively less amount of work; therefore, it is also called magnetocrystalline anisotropy. In non-cubic crystals, the magnetostatic interaction of atomic pairs and certain geometric arrangement of atoms generate crystal anisotropy.[6] The shape anisotropy is indeed an extrinsic property induced by the direction-dependent demagnetization. Besides, magnetic annealing, stress annealing, plastic deformation, and magnetic irradiation can also induce magnetic anisotropy, owing to the preferential diffusion or sliding of the interstitial and substitutional atoms in favor of energetic equilibrium.[7]

As to magnetic stress anisotropy, applied or residual mechanical stress affects magnetization in respect to three mechanisms – first, magnetoelastic energy rotates magnetic moments and rearranges domain structures; second, stress introduces pressure on domain walls; third, stress changes the opposite terms that are balanced for domain wall equilibrium.[9]

The summation of magnetoelastic, magnetostatic, and magnetic anisotropic energy can be expressed as:[10]

$$E=\frac{3}{2}\lambda_s\sigma\sin^2\theta_\sigma - H\ B_s\cos\theta_H + \frac{1}{2}\mu_0 DM_s\cos^2\theta_D \qquad [9.1]$$

H is the applied magnetic field, λ_S is magnetostrictive coefficient, B is flux density, and σ is tension. M_s is saturated magnetization, where θ_σ is the angle between stress axis and local magnetization, θ_H is the angle between applied field and local magnetization, and θ_D is the angle between shape anisotropy and local magnetization.

Thermodynamically, under equilibrium of magnetostatic and magnetoelastic energy, magnetoelasticity can be expressed as:[11]

$$\frac{1}{l}\frac{\partial l}{\partial H}=\frac{1}{4\pi}\frac{\partial B}{\partial\sigma} \qquad [9.2]$$

where l is the length of the sample, H is the applied magnetic field, B is flux density, and σ is tension.

Equation [9.2] can be rewritten as

$$\frac{1}{l}\frac{\partial l}{\partial B}=\frac{1}{4\pi\mu_r}\frac{\partial B}{\partial\sigma} \qquad [9.3]$$

where μ_r is relative permeability.

In order to present the effect of stress on magnetization, the following equation can be drawn:[11]

$$\left(\frac{dB}{d\sigma}\right)_H=\left(\frac{d\lambda}{dH}\right)_\sigma=\frac{d\lambda}{dM}\frac{dM}{dH}=\frac{2\mu_0 M_S}{N}\left(\frac{\lambda_S}{K}\right) \qquad [9.4]$$

where K is magnetic anisotropy constant, and N is a constant with a value of three for steel.[11] It can be seen that if $\lambda_S\, d\sigma > 0$, the magnetization increases with tension.

Alternatively, the magnetization M under applied tension σ_a and magnetic field H is expressed in Reference 8

$$M = \frac{M_S^2 H}{3\lambda_s \sigma} \qquad [9.5]$$

Equations [9.1] through [9.4] are derived with the assumption that no magnetic anisotropy is present except stress anisotropy. However, in a real situation, crystal anisotropy is usually more dominant than stress anisotropy in steels.[7] In steels magnetoelastic behaviors can be demonstrated in the measurement of magnetizing curves under different stress levels, as indicated in Fig. 9.4.

The magnetization behavior of the steel is largely determined by its metallographic characteristics, which have been exploited extensively by researchers. Byeon and Kwan have studied the magnetic properties of specific metallurgical phases in plain steels, and revealed that the coercivity and remanence decrease in the order of martensite, pearlite, and ferrite phase.[12] The aforementioned parameters are also susceptible to microscopic variation in the same type of microstructure. For example, the coercivity and remanence drop as the interlamellar spacing in pearlite increases, due to the reduction in both residual stress and pinning energy against domain wall movements.[12–18]

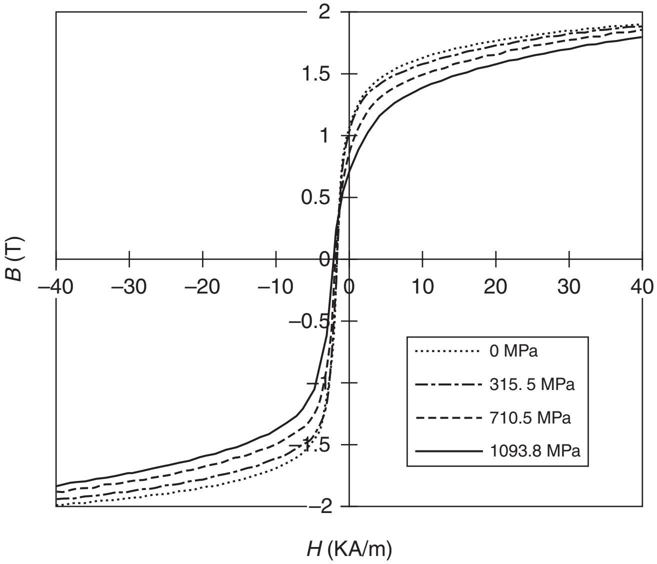

9.4 Hysteresis curves at descending stages for piano steel cable under various stress levels.

Besides, magnetization is sensitive to the formation of magnetic phases from nonmagnetic matrix.[7] Therefore, coercivity, remanence, and hysteresis loss can be employed to monitor the material degradation and microstructure evolvement,[19] such as fatigue and creep. Chemicals also play an important role in magnetic behavior of steels. The alloy elements affect magnetization significantly, since they raise the inner stress level owing to crystal distortion and interphase particles, which nail down the domain walls.

Magnetization and magnetoelasticity have been used in non-destructive evaluation (NDE) for steel or metallic components or structures. In magnetoelastic stress sensor, relative permeability is used to monitor the tensile stress.[13–15] In the ensuing sections, key factors regarding the application of this technology will be addressed.

9.3 Magnetic sensory technologies

In pre-stressed concrete structures and cable-stayed bridges, knowing the static stress in critical steel structures is extremely important for safety and reliability of structures. Catering to this requirement, magnetoelastic stress sensory technology has been developed. Prior to proceeding in this topic, some representative developments and practices in NDE using magnetic technologies are reviewed.

As of today, a series of monitoring technologies have been conceptualized and developed in order to inspect or characterize steel or metallic structures or components, and their health and degrading conditions. Below are some typical magnetic NDE approaches for metallic materials and structures:

1. *Microstructural characterizing using magnetic method*: Several magnetic parameters including magnetic coercivity and permeability are exterior characteristics of ferromagnetic materials. The microstructure characteristics, such as the content of non-ferromagnetic phases, the relative amounts of different phases, and the characteristics of precipitations, affect one or several readings of the magnetic parameters. For example, creep-induced microstructure degradation was tentatively characterized via magnetic measurement.[19,20] The magnetic phase constitution gage is a promising tool in monitoring phase transformation. A type of superconducting quantum interference device (SQUID) unit was developed in order to evaluate the transformation of d-ferrite to nonmagnetic phases during fatigue in welded steels.[21] The precondition in favor of the feasibility of this technology is that the adverse influence of microstructure or geometric anisotropy must be calibrated.
2. *Geometric/structural discontinuity (for example, cracks) inspection using magnetic method*: Conventionally, heat treatment and welding cracks are to be detected by the method of magnetic powder inspection. In

this method, the discontinuity of magnetic loops can identify structural anomalies. In a magnetic loop composed of magnetic flux emitter and steel component to be monitored, the magnetic flux constitutes a closed loop. If a structural discontinuity exists on the component to be monitored, the magnetic flux will be detected, from which the structural deformation, cracks, and other types of anomalies can be mapped. For example, the portable U-shape sensory system[16] shown in Fig. 9.5 can be used for crack inspection in steel ropes.

3. *Anomaly inspection through dynamic magnetic signal (eddy current and Barkhansen noise, and so on)*: Geometric discontinuity and materials/microstructure variation can be monitored through eddy current and the induced magnetic field, and the jump of magnetic domains. This approach has been used in detecting metallurgical failure in components such as fractures caused by stress corrosion and hydrogen embitterment; the proactive prognostic inspection of the latter can prevent catastrophic component failures.
4. *Corrosion monitoring using magnetic method*: Based on the theory of magneto-hydrodynamics, a magnetic field affects the mass transport rates and electro-transferring process in galvanic reactions;[22] on the other hand, the latter also generates certain kinds of magnetic field. It was found that with catholic protection current, a corrosion-related magnetic (CMR) field is introduced,[23] as shown in Fig. 9.6. Most metals and alloys tend to be corroded in the environment into which they were exposed, for instance the corrosion of pre-stressed tendons with exposure to liquid solution or condensates. Galvanic reaction can be used to describe the progress of this kind of corrosion.

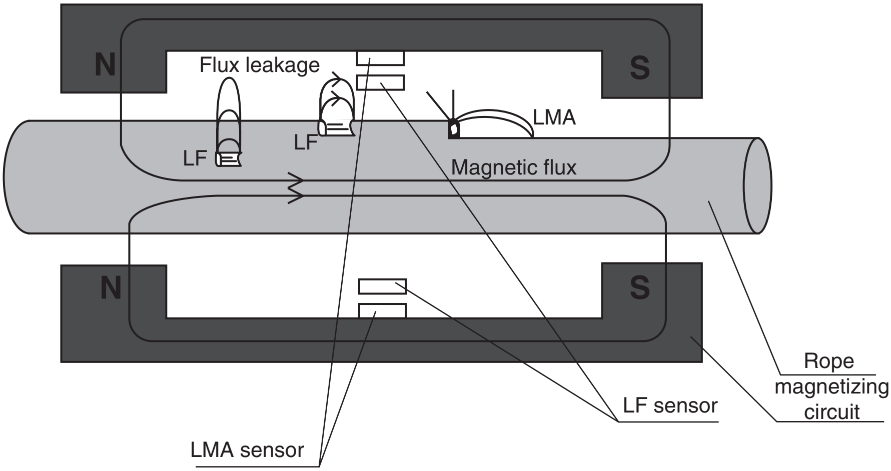

9.5 Magnetic sensors to indicate various classes of defects in steel rope.[16]

Through anodic reaction metallic atom, M, gives up one or more electrons to become a cation:

$$M \rightarrow M^{n+} + ne^- \qquad [9.6]$$

The cathodic reaction can be either

$$2\text{H}^+ + 2e^- \rightarrow \text{H}_2 \qquad [9.7]$$

or

$$\frac{1}{2}\text{O}_2 + \text{H}_2\text{O} + 2e- \rightarrow 2(\text{OH})^- \qquad [9.8]$$

In galvanic corrosion, transportation of anions and electrons is involved, therefore an electric current exist in reaction.

According to Maxwell Equations:[23]

$$\nabla^2 \vec{A} = -\mu \vec{J} \qquad [9.9]$$

where $\vec{A}$ is vector potential and $\vec{J}$ is vector of current density.

The magnetic field thus introduced can be expressed as:

$$\vec{B} = curl\vec{A} \qquad [9.10]$$

Through the inspection of this field, the galvanic corrosion can be estimated.

A magnetic sensor for corrosion monitoring based on loss and degradation of magnetic characteristics of corroded article is also a promising approach to evaluate the conditions of corrosion. For example, Yashiro *et al.* developed a method to detect the environmental deterioration of the structure by measuring the decrease in residual magnetization on probes embedded in mortar.[24] Analogous to crack inspection using magnetic methods, metallic loss or other irregularities caused by corrosion can be inspected via magnetic leakage methods.[25] More work needs to be carried out to industrialize corrosion monitoring technology through measuring and mapping of magnetic fields.

5. *Mapping and characterizing residual stress in steel structures using magnetic method*: For some steel structures like railway rails, knowing the amplitude, direction, and sign of residual stress is useful for proper maintenance and failure prevention.[26] Due to stress magnetic anisotropy, the existence of local residual stress in steel changes its magnetic properties of the related steel section. The magnetic measurement equipment is

able to deliver the required measurement resolution and can specify and map the distribution of the residual stress. The magnetic anisotropy and permeability system (MAPS) indicated in Reference 26 is a promising tool for this purpose. Depending on the interaction of residual stress and magnetization in multiple mini-scaled regions, the residual stress on a rail can be mapped, as seen in Fig. 9.7.

A magnetic anisotropy sensory approach for similar purposes was reported in Reference 27, with the configuration shown in Fig. 9.8.

6. *Magnetostrictive sensors*: In magnetostrictive materials, the magnetic properties vary as a function of applied stress; this phenomenon is called the inverse magnetostrictive effect, or the magnetomechanical effect and the same operating principle was used for the accelerometer.[28] Made primarily

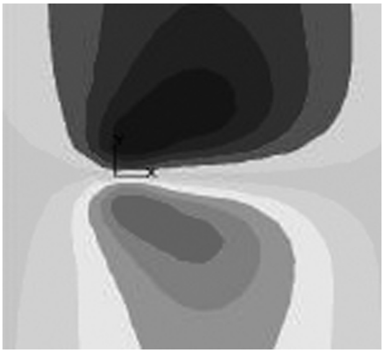

9.6 Indicative corrosion-related magnetic field on a ship.[23]

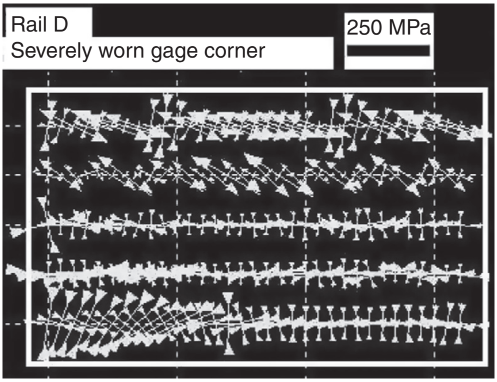

9.7 Distribution of residual principal stresses (measured by the tool of MAPS) on the longitudinal top surfaces of a rail used for 14 years.[26]

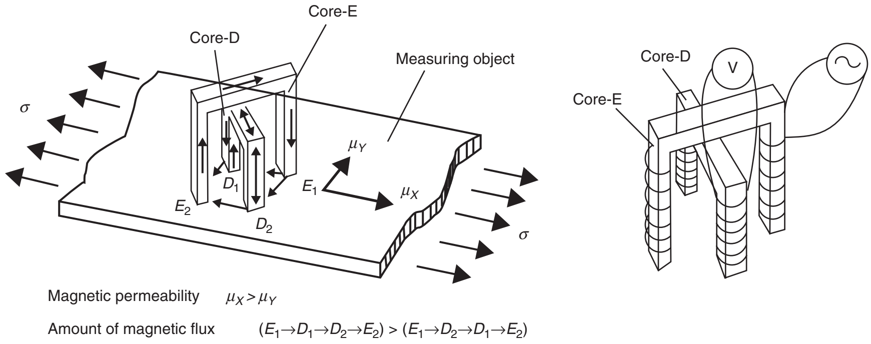
Core-E
Core-D
Measuring object
σ
μ_Y
μ_X
D_1
D_2
E_1
E_2
σ
Core-D
Core-E
V
Magnetic permeability $\mu_X > \mu_Y$
Amount of magnetic flux $(E_1 \rightarrow D_1 \rightarrow D_2 \rightarrow E_2) > (E_1 \rightarrow D_2 \rightarrow D_1 \rightarrow E_2)$

9.8 An indicative drawing of a magnetic anisotropy sensor (stress anisotropy along stress induced an output from windings on Core-D).[27]

of amorphous ferromagnetic ribbons or wires, magnetostrictive elastic sensors have been used in measuring a wide range of environmental parameters, including pressure, humidity, temperature, liquid viscosity and density, thin-film elasticity, chemicals such as carbon dioxide and ammonia, and pH value. One example is the application of the resonant frequency in a magnetostrictive material. Excited by a wave induced by AC magnetic field, the resonant frequency of the magnetostrictive wire or strip depends on density, Young's modulus, and Poisson ratio of the sensor. The characteristic resonant frequency is also dependent upon the magnitude of the DC biasing field, the ambient medium, and the sensor surface condition including surface roughness and wetting, and also the surface stress. Therefore, physical or environmental variation in the magnetostrictive agent will change the resonant frequency.[29,30] Innovative materials with large magnetostrictive coefficients are key to yielding high sensitivity in these kinds of magnetostrictive sensors; gallium alloy is a good example.[5]

7. *Application of magnetoelasticity in tensile stress monitoring*: This topic is the main subject and is covered in the following sections in detail. The method is used to monitor new steel cables during construction, as well as existing cables in service. Emphasis is on continuing monitoring for a period of time to effectively assess the overall structural health as well as to determine tension forces in cables, an important parameter for maintenance of cabling systems.

9.4 Role of microstructure in magnetization and magnetoelasticity

In magnetoelastic stress sensors, magnetic relative permeability is used to reflect stress level in steel structures. Zero-stress saturated permeability (permeability at technical magnetic saturation with no stress applied on the steel rod) defines the stress-free status of the steel to be monitored.[12–16]

Magnetic permeability implies the realigning tendency of magnetic domains in response to an exterior magnetic field. Metallurgical characteristics strongly influence magnetic permeability. The hardness represents the mechanical stiffness of the material and depends on multiple metallurgical characteristics, including composition, phase constitutes and morphology, residual stress, and grain size, etc. Those factors also play roles in pinning effects against magnetic domain reorientation. The correlation of hardness with permeability is demonstrated in Fig. 9.9 and Table 9.1. It can be seen that the harder the ferromagnetic steel, the lower the initiative permeability. There are several causes for this observation – (I) the amount of the ferrite phase decreases as carbon content increases, and ferrite is magnetically the softest microstructure in steel; (II) the carbides or other precipitates function as pinning particles against domain reorientation; (III) cold work, lattice defect, and even heat treatment and welding can introduce intrinsic (residual) stress, which decreases the initiative permeability due to the pinning effect; (IV) besides, specific intrinsic stresses lead to a certain level of magnetic anisotropy – one example is that in cold extruded steel rod, the longitudinal residual compressive stress introduces a magnetic anisotropy and a fictitious field;[21] as another example, in material with non-zero magnetostriction, magnetization can be introduced on the cutting edge of the sample,[31] owing to the influence of residual stress on magnetic moments and domains. This phenomenon can be used in NDE for geometric noncontinuity in steels. Similar effects can be observed in welding.[32]

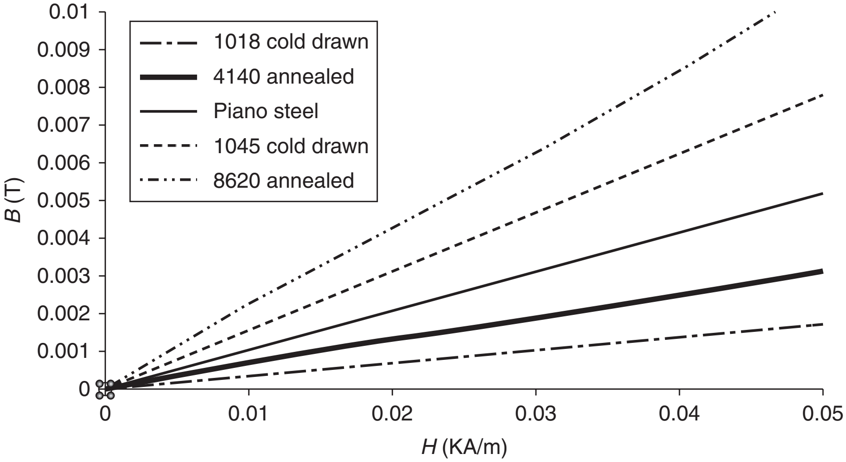

9.9 The initiative magnetization curves of various steels.

Table 9.1 Hardness of various carbon/alloy steels tested in Fig. 9.4

Steel	Microhardness (HV at 500 g)
1018 cold drawn	217
8620 annealed	230
4140 annealed	240
1045 cold drawn	331
Piano steel wire	467

HV refers to hardness in Vikers.

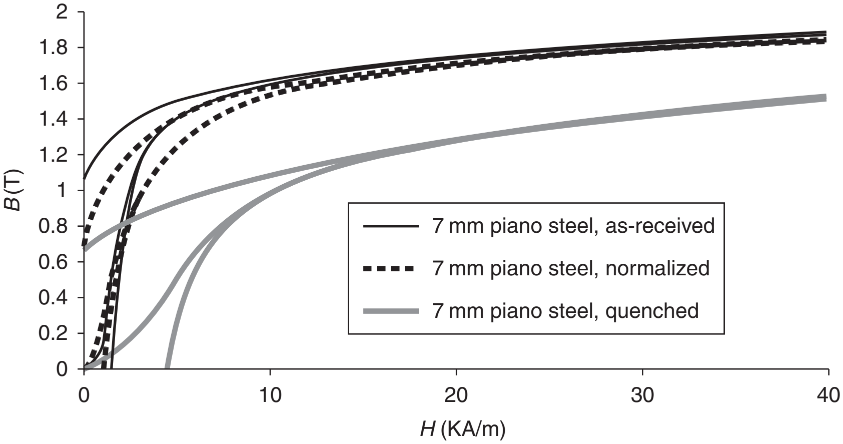

9.10 Hysteresis of piano steel having undergone different heat treatments; the hardness of the quenched, as-received, and normalized samples are respectively 740, 387, and 310 in HV.

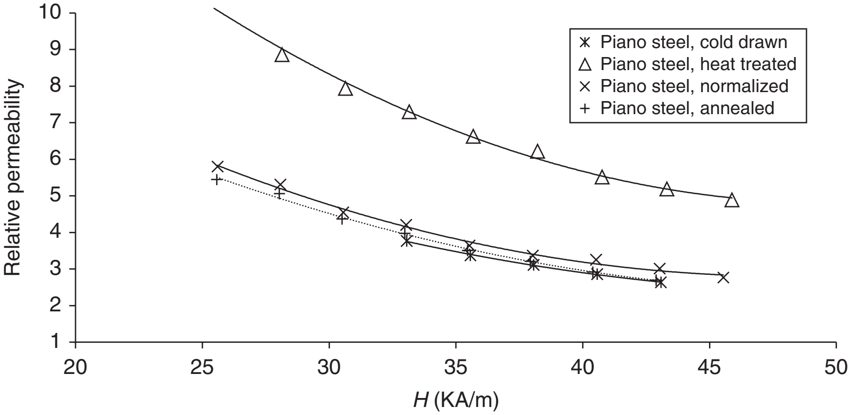

9.11 Relative permeability of piano steels having undergone different heat treatments, measured in the descending stages of hysteresis. The hardness of the heat treated, as-received (cold drawn), normalized, and annealed samples are respectively 740, 387, 310, and 210 in HV.

As indicated in Figs 9.10 and 9.11, the magnetic hysteresis and saturated permeability in steels depend on their relative heat treatments. The saturated permeability increases as hardness drops, with the exception of the as-received cold-drawn steel rod because of magnetic anisotropy caused by residual stress generated by cold drawing process.

For the EM stress sensor, relative incremental permeability under technical magnetic saturation is the parameter used for stress monitoring, as shown in Figs 9.12 and 9.13.

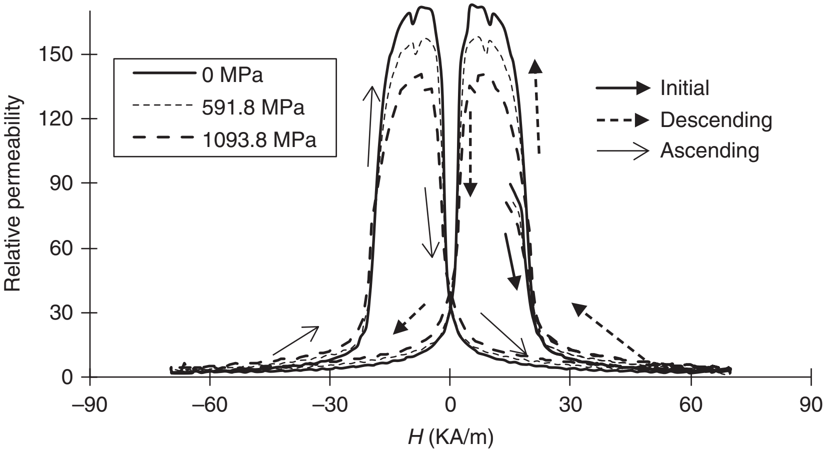

9.12 Relative permeability measurements for piano steel during initial magnetization and magnetic hysteresis at various stress levels.

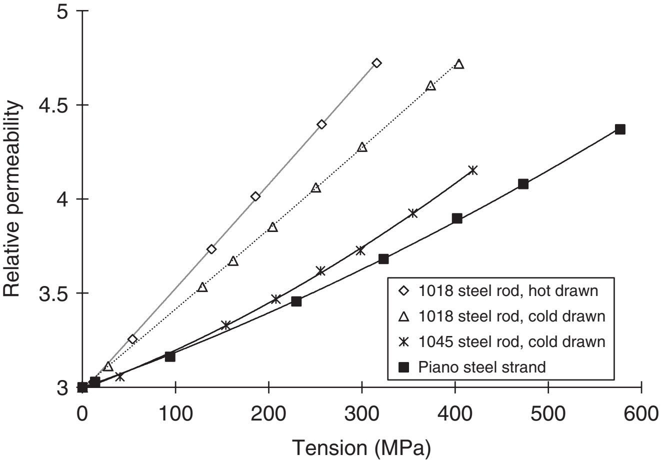

9.13 Relative permeability under technical saturation vs tension of different steel rods, tested under room temperature, permeability $\mu = \Delta B / (\mu_0 \Delta H)$; μ_0 : relative permeability of the air.

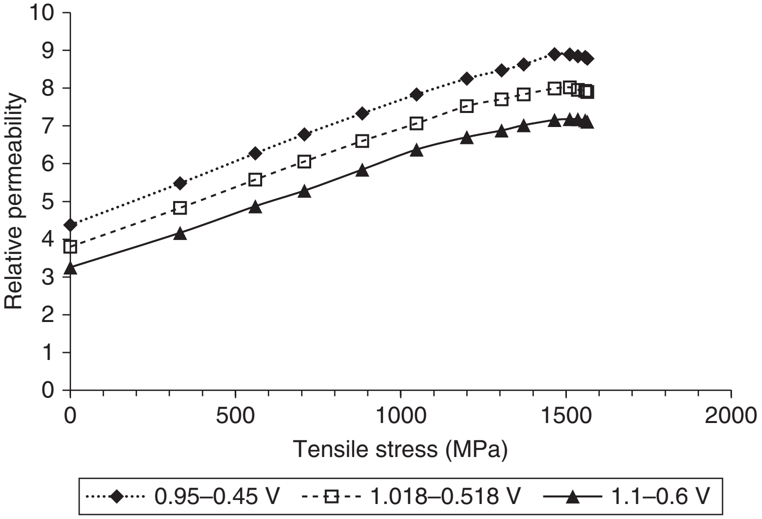

9.14 Permeability vs stress up to yield point for piano steel rod (yielding point: 1410 MPa) tested at different working points (in lieu of magnetic field).[33]

With load well below elastic limit, magnetic permeability varies monotonically with tensile stress. When the tension increases beyond yielding point, the permeability first reaches its summit and then drops, as indicated in Fig. 9.14, due to the collaborative effects of magnetoelasticity and metallurgical dislocation multiplication. Although the tensile stress tends to raise the relative permeability, the latter declines once the influence of multiplying dislocations takes the control.

9.5 Magnetoelastic stress sensors for tension monitoring of steel cables

As shown in Fig. 9.12, magnetic permeability demonstrates strong sensitivity to load at all magnetization levels, especially at low magnetization level; however, due to the drawback of minor hysteresis with magnetic offset superseded, permeability under low magnetization level is not recommended for stress monitoring. In EM tensile stress sensors presently being actively commercialized, the relative permeability is calculated from the integration of the output of the secondary coil. The sensor configuration is indicated in Fig. 9.15.

The magnetic field provided by the primary coil depends on its current amplitude *i,* which is the solution of the following equation:

$$L\frac{d^2i}{dt^2}+R\frac{di}{dt}+\frac{1}{C}i=0, \qquad [9.11]$$

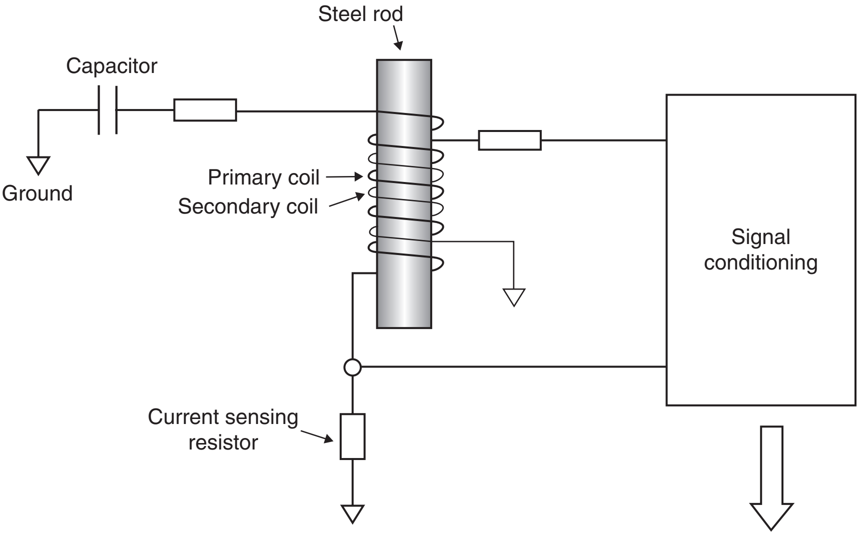
Steel rod
Capacitor
Ground
Primary coil
Secondary coil
Signal conditioning
Current sensing resistor

9.15 Indicative magnetoelastic stress sensor configuration.

where L is inductance of the primary coil, R is resistance of the circuit, C is capacitance, and t is the discharging time of the capacitor; inductance L is $n^2\mu A/(l^2+d^2)^{1/2}$, where n is the number of turns of the coil, μ is the permeability, A and d are cross-area and diameter of the coil, respectively, and l is the coil length.

The boundary conditions are given below

$$i = 0, \quad \text{when } t = 0 \qquad [9.12]$$

and

$$\int_0^\infty i\,dt = VC \qquad [9.13]$$

where V is the maximum charging voltage of the capacitor.

The solution is given below:

1. when $4L > R^2C$,

$$i = D\sin\left(\frac{1}{2}\sqrt{\frac{4L-R^2C}{L^2C}}t\right)\exp\left(-\frac{R}{2L}t\right) \qquad [9.14]$$

To determine the value of D, we need to solve Equation [9.14] and get

$$D = \frac{2VC}{\sqrt{4LC - R^2C^2}} \qquad [9.15]$$

However, when $R^2C \geq 4L$, we have other solutions.

2. When $R^2C > 4L$,

$$\begin{aligned} i = \frac{VC}{\sqrt{R^2C^2 - 4LC}} \Bigg\{ & \exp\left[\left(-\frac{R}{2L} + \frac{1}{2}\sqrt{\frac{R^2C - 4L}{L^2C}}\right)t\right] \\ & - \exp\left[\left(-\frac{R}{2L} - \frac{1}{2}\sqrt{\frac{R^2C - 4L}{L^2C}}\right)t\right]\Bigg\} \end{aligned} \qquad [9.16]$$

3. When $R^2C = 4L$, which rarely occurs,

$$i = Mt\left[\exp\left(-\frac{R}{2L}t\right)\right] \qquad [9.17]$$

where

$$M = \frac{VCR^2}{4L^2} \qquad [9.18]$$

Through delicate design of L-C circuit, the steel cable can be uniformly magnetized.

Once the data acquisition unit collects the primary current and secondary current, the magnetic permeability can then be calculated via embedded program in the CPU.

Measurement of magnetic permeability is free of influence from humidity, dust, lubricants, and non-metallic sheath. Temperature is the primary influencing factor. Researches reveal that the zero-stress saturated permeability varies linearly with ambient temperature and the permeability-stress curves are parallel over a certain temperature range;[14] we use differential permeability as a parameter to monitor stress:

$$\Delta\mu = \mu(\sigma, T) - \mu(0, T) \qquad [9.19]$$

If the saturated permeability is measured under temperature T_0, $\mu(0, T)$ can be calculated from the temperature coefficient A_T, which is the slope in Fig. 9.16.

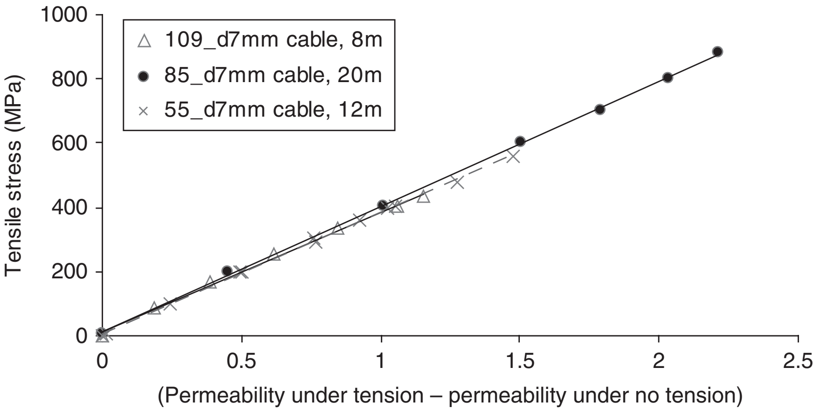

9.16 Magnetoelastic characteristics of piano steel cables with different sizes derived with EM stress sensors, permeability under no tension needs to be 4~5 for technical magnetic saturation.

Temperature coefficient A_T is dependent on the type of the material. It shifts the value of the permeability as follows (test results to be shown in Section 9.6):

$$\mu(0,T) - \mu(0,T_0) = A_T(T - T_0) \qquad [9.20]$$

Therefore,

$$\begin{aligned}\Delta\mu &= \mu(\sigma,T) - \mu(0,T) = \mu(\sigma,T) - (\mu(0,T_0) + A_T(T - T_0)) \\ &= \mu(\sigma,T) - \mu(0,T_0) - A_T(T - T_0)\end{aligned} \qquad [9.21]$$

Magnetoelastic stress sensors were used to monitor the tension (below yielding point) of the steel hanger cables on a bridge via the measurement of the relative permeability. As an example, the calibration curves are shown in Fig. 9.16 and on-site monitoring of a post-tensioning procedure is shown in Fig. 9.17a and 9.17b. The accuracy is within 5% as compared to load cell during the post-tensioning process.

9.6 Temperature effects

Temperature exerts an obvious influence on magnetization in steels. Research has revealed that in low magnetic field the increase in temperature raises the magnetization level, and vice versa in elevated magnetic field, as indicated in Fig. 9.18. With low exterior magnetic field, the thermal

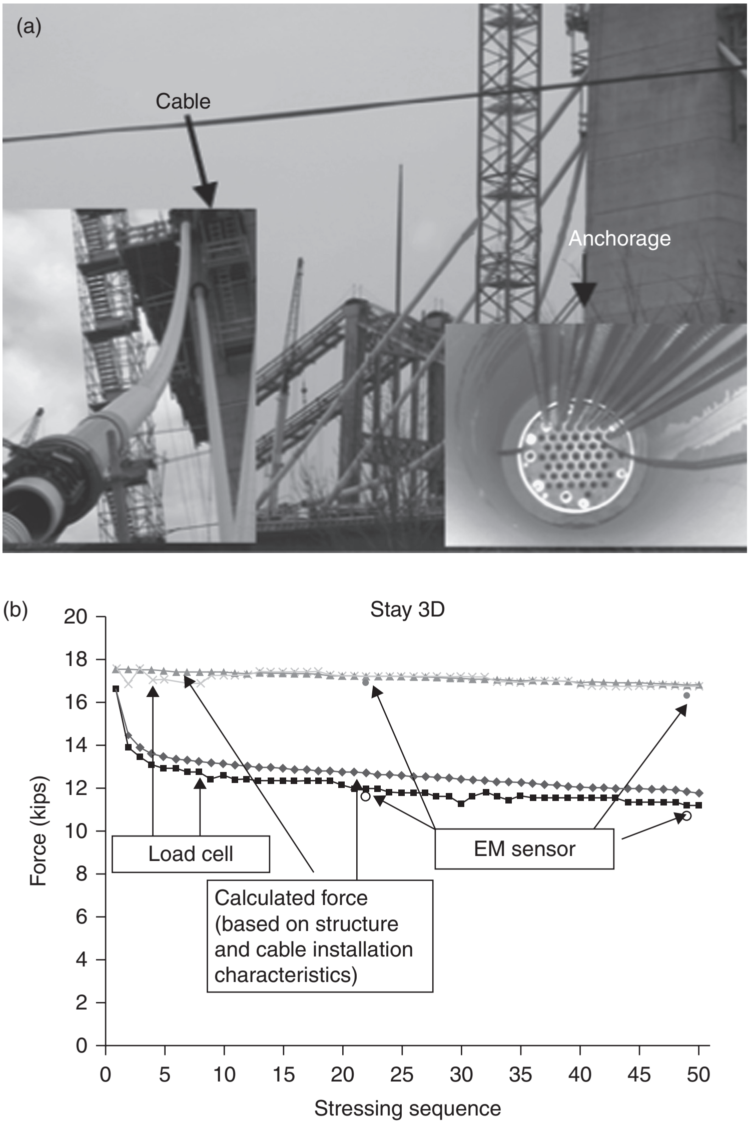

9.17 Comparison of EM sensor and load cell measurements for 0.6 inch steel strand used on a bridge in Maine, USA (a) strands in the cable on bridge and (b) tension monitoring results.

agitation at elevated temperature can relax the pinning effect (against domain reorientation), thus increasing the magnetization level. At higher magnetic field, the thermal fluctuation of the magnetic moments takes control, and therefore rise in temperature reduces the magnetization level. The

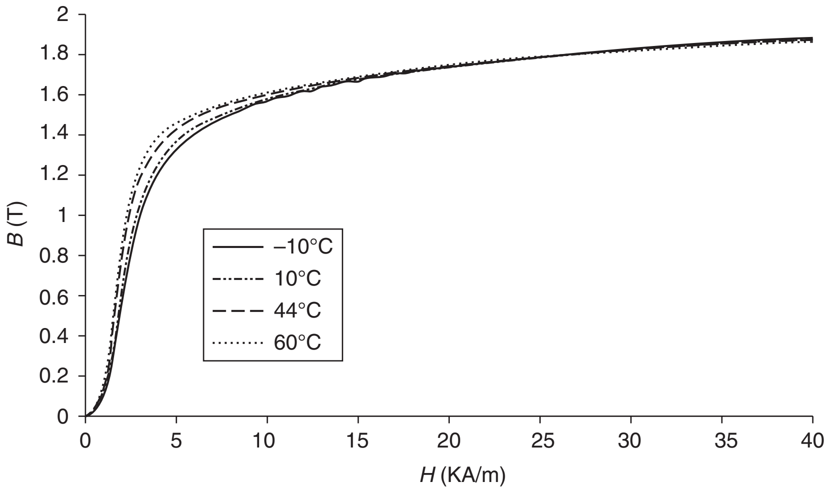

9.18 Dependence of initial magnetization curve on temperature variation, KA/m – kilo Amphere per metre.

relative permeability is defined as the tangential slope of the magnetizing curve; therefore, as temperature rises, the relative permeability drops, as shown in Fig. 9.19.

Previous research has revealed that temperature shifts the stress monitoring calibration curve in roughly a parallel manner.[14] According to the experiments illustrated in Fig. 9.15, the influence of temperature on saturated relative permeability bears insignificant dependence on the diameter of the steel cables, provided they have the same composition and microstructure. On-site measurements on the hanger cables and multistrand post-tensioned cables (both made of piano steel) yielded similar results.[14] It is to be noted that the thermo-flux in the steel cable, plastic sheath, and the ambient air easily leads to some non-uniformity in temperature.[34]

9.7 Eddy current

In the EM stress sensor application, if the gradient of the electric current through the primary coil over time is high, the steel cable cannot be uniformly magnetized due to the eddy current, as shown in Fig. 9.20. Through proper design of L-C energizing circuit, the skinning effect can be minimized due to reduced gradient of varying field over time. This effect is simulated by the authors, as indicated in Figs 9.20 and 9.21 in which magnetic flux density in steel cable drops inward axially because of eddy current. More theoretical review and explanation is provided in Reference 35.

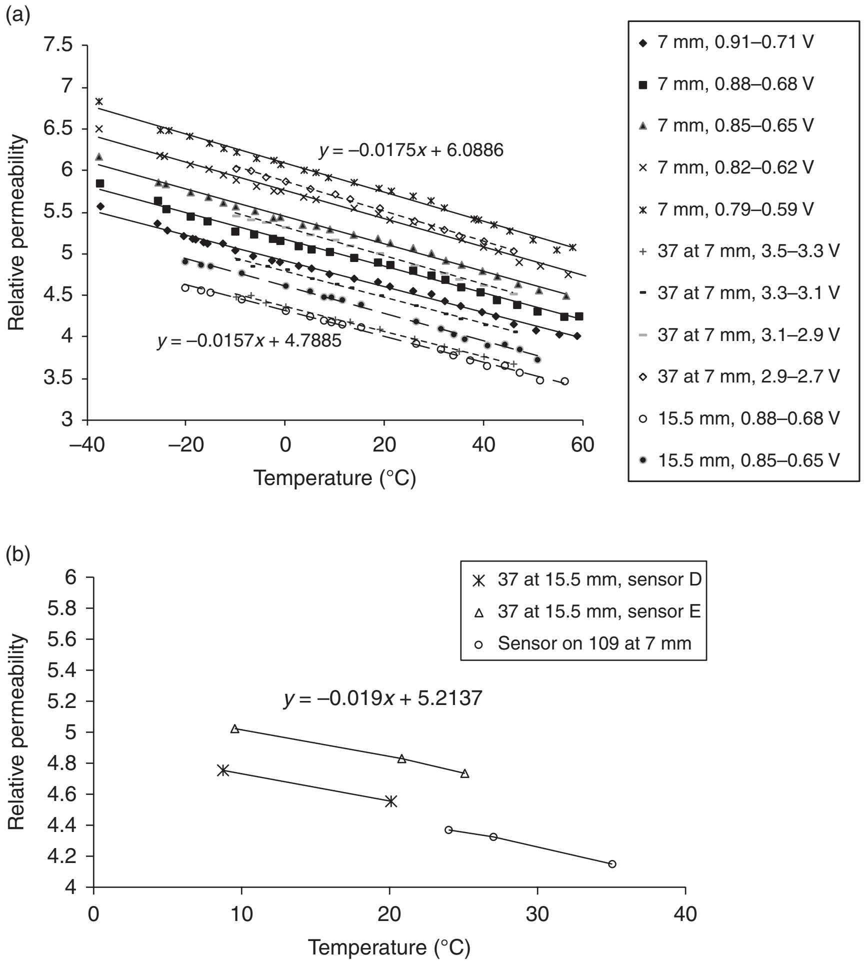

9.19 Temperature dependence of permeability – (a) $\mu(0, T)$ vs T for 7 mm steel wire, 0.6 in. twisted steel strand and Japan 37 mm × 7 mm strand, all made of piano steel, (b) test in field – $\mu(0, T)$ vs T for post-tensioned cables and hanger cable.

9.8 Removable (portable) elastomagnetic stress sensor

Several limitations exist for solenoid-type EM stress sensors. First of all, the solenoid-type sensor is usually designed to be used for ready-to-be-built structures and needs to be installed before the cable is anchored. Although the solenoid sensor can be wound on some existing structures, the calibration procedure is time-consuming. Secondly, the solenoid-type EM sensor is a permanent sensing device, and is not usable once it has been taken down

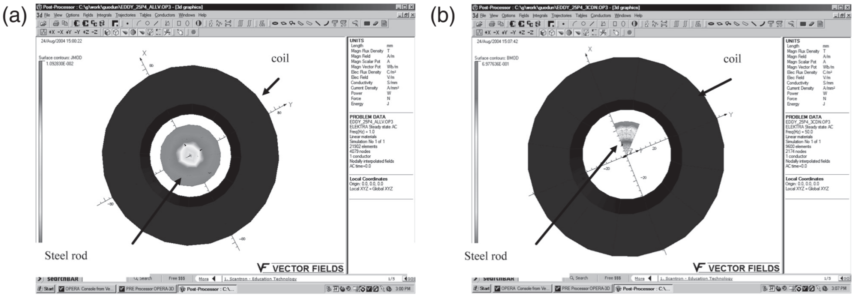

9.20 Simulation of (a) classical eddy current and (b) magnetic induction in a steel rod magnetized by solenoid.

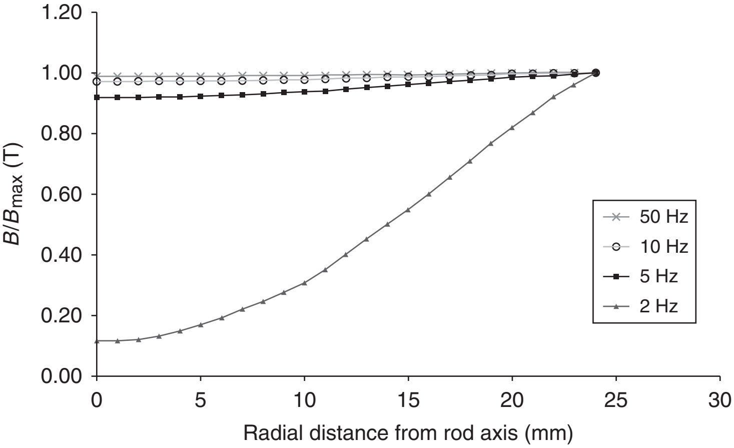

9.21 Simulation of average longitudinal induction intensity (B/B_{max}, B_{max} is the maximum value of induction) in the stress-proofed 1018 steel rods (diameter = 50.8 mm) magnetized by energizing current with different frequencies.

for any reason. Therefore, it is highly desirable to develop a portable and reusable sensor for direct load measurement in steel cable. U-shaped EM sensing technology has been developed and tested in the field. This represents an impressive breakthrough in EM sensing technology.

The U-shaped EM sensor is a magnetic circuit composed of a ferrite yoke and steel rod. It can be used in short and long-term force monitoring. Simulation of magnetic flux is given in Fig. 9.22. More test results are discussed in the References 35 and 36.

The U-shaped yoke, made of grain-oriented silicon steel laminate, can magnetically saturate the cable for stress monitoring of existing cables. The

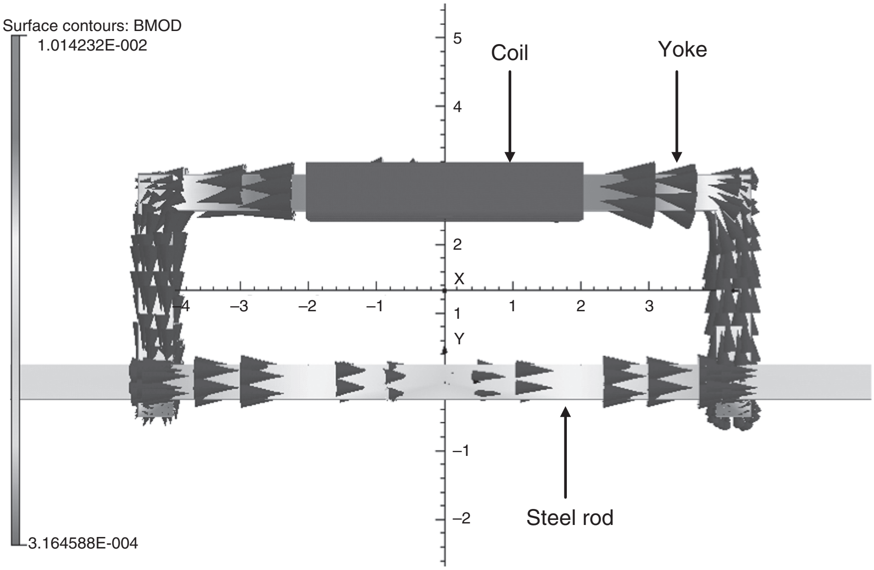
Surface contours: BMOD
1.014232E-002
3.164588E-004
Coil
Yoke
Steel rod
X
Y
5
4
2
1
–1
–2
–4
–3
–2
–1
1
2
3

9.22 Magnetostatic simulation of the induction in magnetic circuit composed of yoke and steel rod (BMOD: magnetic flux density (B) model.).

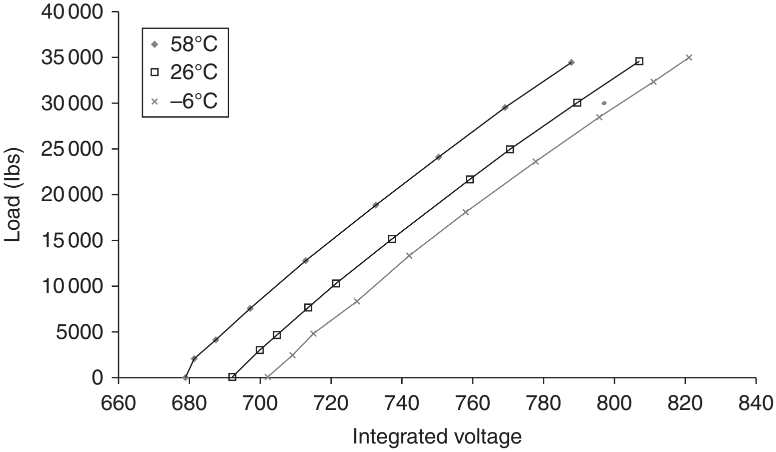

9.23 The calibration curves of U-shape stress sensor at different temperatures.

dimensions of the yoke were analyzed for a better magnetization effect. Either the permeability of the steel cable or the flux variation along the circuit reflects the steel stress level. The latter is preferable, due to its total detachability. The load calibration results are shown in Fig. 9.23.

9.9 Conclusion and future trends

Magnetism and magnetoelasticity have been applied in infrastructure health monitoring and inspection. A series of state-of-the-art magnetic and magnetoelastic NDE methods have been reviewed. Recently, EM technology has been used extensively to determine tensile forces of steel cables. The configuration and application of this technology has been described in detail. For future convenient use of EM technology, an innovative removable tensile stress monitoring unit was also developed. This technology will allow widespread use of EM technology in health monitoring of existing structures with various cable systems. Several on-going accomplishments in engineering application of magnetism were described. New and revolutionary magnetic techniques will certainly emerge continually. For example, real-time inspection of transient load in structures through the magnetic method is possible in the very near future. Likewise, *in situ* corrosion monitoring of steel cables is under extensive study. The final adaptation and field application lie on the development of a product with an integrated and user-friendly package that uses smart algorithm to exclude adverse effects of unrelated noises and interfering factors.

9.10 References

1. W. H. Hayt, Jr. and J. A. Buck (2001), *Engineering Electromagnetics*, 6th edition, McGraw-Hill Companies, Inc., New York.
2. M. A. Willard, L. K. Kurihara, E. E. Carpenter, S. Calvin and V. G. Harris (2004), Chemically prepared magnetic nanoparticles, *International Materials*, Vol. **49**, No. 3–4, pp. 125–168.
3. B. F. Spencer, S. J. Dyke, M. K. Sain and J. D. Carlson (1997), Phenomenological model of a magnetorheological damper, *Journal of Engineering Mechanics, ASCE*, Vol. **123**, No. 3, pp. 230–238.
4. Y. Shen, F. Golnaraghi and G. R. Heppler (2004), Experimental research and modeling of magnetorheological elastomers, *Journal of Intelligent Materials Systems and Structures*, Vol. **15,** January, pp. 27–34.
5. K. Ullakko, J. K. Huang, C. Kantner, R. C. O'Handley and V. V. Kokorin (1996), Large magnetic-field-induced strains in Ni_2MnGa single crystals, *Applied Physics Letters*, Vol. **69**, pp. 1966–1968.
6. E. P. Wohlfarth (1982), *Ferromagnetic Materials*, Vol. **3**, North-Holland Publishing Company, New York.
7. B. D. Cullity (1972), *Introduction to Magnetic Materials*, Addison-Wesley Publishing Company, Reading, MA.
8. L. Li and D. C. Jiles (2003), Modeling of magnetomechanical effect: application of the Rayleigh law to the stress domain, *Journal of Applied Phys*ics, Vol. **93,** No. 10, pp. 8480–8482.
9. R. Birss (1971), Magnetomechanical effects in the Rayleigh region, *IEEE Transactions on Magnetics*, Vol. **MAG-7**, pp. 113–133.

10. C. S. Schneider, P. Y. Cannell and K. T. Watts (1992), Magnetoelasticity for large stresses, *IEEE Transactions on Magnetics*, Vol. **28**, No. 5, September, pp. 2626–2631.
11. R. M. Bozorth (1951), *Ferromagnetism*, D. Van Nostrand Company, Inc., Toronto, Canada.
12. J. W. Byeon and S. I. Kwun (2003), Magnetic evaluation of microstructures and strength of eutectoid steel, *Materials Transactions*, Vol. **44**. No. 10, pp. 2184–2190.
13. L. M. Wang, G. Wang and J. Yim (2006), Smart Cables for Cable-stayed Bridge. Smart Structures Technology for Steel Structures, 16–18 November 2006, Seoul, Korea.
14. G. Wang and M. L. Wang (2006), Application of EM stress sensors in large steel cables, *International Journal of Smart Structures and Systems*, Vol. **2**, No. 2, pp. 155–168.
15. M. L. Wang, Z. Chen, S. Koontz and G. D. Lloyd (2000), Magneto-elastic permeability measurement for stress monitoring, In *Proceeding of the SPIE 7th Annual Symposium on Smart Structures and Materials, Health Monitoring of the Highway Transportation Infrastructure*, 6–9 March, CA, Vol. **3995**, pp. 492–500.
16. D. C. Jiles and C. C. H. Lo (2003), The role of new materials in the development of magnetic sensors and actuators, *Sensors and Actuators A*, Vol. **106**, pp. 3–7.
17. C. C. H. Lo, J. P. Jakubovics and C. B. Scuby (1997), Monitoring the microstructure of pearlitic steels by magnet acoustic emission, *Journal of Applied Physics*, Vol. **81**, No.8, 15 April, pp. 4069–4071.
18. H. Kwun and G. L. Burkhardt (1987), Effects of grain size, hardness, and stress on the magnetic hysteresis loops of ferromagnetic steels, *Journal of Applied Physics*, Vol. **61**, No. 40, 15 February, pp. 1576–1579.
19. A. Polar, J. E. Indacochea and M. L. Wang (2004), Application of a magnetoelastic sensor for detecting creep in power plant components. *ASME Journal of Engineering Materials and Technology*, Vol. **126**, October, pp. 392–397.
20. A. Polar, J. E. Indacochea and M. L. Wang (2010), Sensing creep evolution in 410 stainless steel by magnetic measurement, *Journal of Engineering Materials and Technology*, Vol. **132**, October, pp. 041004–1–7.
21. R. Nagendran, M. P. Janawadkar, M. Pattabiraman, D. K. Baisnab, R. Baskaran, L. S. Vaidhyanathan, Y. Hariharan, Baldev Raj, A. Nagesha, M. Valsan and K. Bhanu Sankara Rao (2007), Development of SQUID-based non-destructive evaluation system for detecting fatigue induced transformation of d-ferrite to non-magnetic phases, *NDT&E International*, Vol. **40**, pp. 215–219.
22. Z. Lu and W. Yang (2008), *In situ* monitoring the effects of a magnetic field on the open-circuit corrosion states of iron in acidic and neutral solutions, *Corrosion Science*, Vol. **50**, pp. 510–522.
23. R. Adey and J. Baynham (2000), Prediction of corrosion related electrical and magnetic fields using BEM, Computational Mechanics BEASY Ltd, Ashurst Lodge, Ashurst, Southampton, Hampshire, UK (http://www.beasy.com/images/pdf/publications/papers/UDT2000.pdf).
24. H. Yashiro, Y. Kawamata, T. Kageyama, S. Ishikawa, Y. Tsujimura, T. Oyamada and T. Fujiwara (2008), Development of Magnetic corrosion probe for non-destructive evaluation of concrete against corrosion of reinforcing bar, *Corrosion Science*, Vol. **50**, pp. 1005–1010.

25. N. B. S. Gloria, M. C. L. Areiza, I. V. J. Miranda and J. M. A. Rebello (2009), Development of a magnetic sensor for detection and sizing of internal pipeline corrosion defects, *NDT&E International*, Vol. **42**, pp. 669–677.
26. K. H. Lo, P. Mummery and D. J. Buttle (2010), Characterization of residual stresses and implications on failed railway rails, *Engineering Failure Analysis*, Vol. **17**, pp. 1273–1284.
27. L. Li, S. Huang and X. Wang (2003), Magnetic field abnormality caused by the weld residual stress, *Journal of Magnetism and Magnetic Materials*, Vol. **261**, pp. 385–391.
28. T. Meydan and P. Choudhary (2002), Magnetostrictive accelerometer using amorphous metallic alloys, *Journal of Optoelectronics and Advanced Materials,* Vol. **4**, No. 2, June, pp. 261–266.
29. C. A Grimes, K. G. Ong, K. Loiselle, P. G. Stoyanov, D. Kouzoudis, Y. Liu, C. Tong and F. Tefiku (1999), Magnetoelastic sensors for remote query environmental monitoring, *Smart Materials and Structures*, Vol. **8**, No. 5, pp. 639–646.
30. C. A. Grimes, C. S. Mungle, K. Zeng, M. K. Jain, W. R. Dreschel, M. Paulose and K. G. Ong (2002), Wireless magnetoelastic resonance sensors: A critical review, *Sensors*, Vol. **2**, pp. 294–313.
31. J. Hur, D. S. Hyun, S. S. Kim, G. H. Kang and J. P. Hong (2002), Three dimensional eddy current calculation using magnetic scalar potential in conducting regions, *Journal of Applied Physics*, Vol. **91**, No. 10, pp. 8314–8316.
32. L. Li, S. Huang and X. Wang (2003), Magnetic field abnormality caused by the weld residual stress, *Journal of Magnetism and Magnetic Materials*, Vol. **261**, pp. 385–391.
33. Z. L. Chen (2000), Characterization and constitutive modeling of ferromagnetic materials for measurement of stress, PhD thesis, the University of Illinois at Chicago.
34. G. M. Lloyd, V. Singh and M. L. Wang (2002), Experimental evaluation of differential thermal errors in magnetostatic stress sensors for Re<180, IEEE Sensors, Magnetic Sensing III, Paper No. 6.54.
35. G. Wang (2005), The application of magnetoelasticity in stress monitoring, PD thesis, the University of Illinois at Chicago, PhD thesis, the University of Illinois at Chicago.
36. G. Wang and M. L. Wang (2004), The utilities of U shape EM sensors in stress monitoring, *Structural Engineering and Mechanics*, Vol. **17**, No. 3–4, pp. 291–302.

10

Micro-electro-mechanical-systems (MEMS) for assessing and monitoring civil infrastructures

D. OZEVIN, University of Illinois at Chicago, USA

DOI: 10.1533/9780857099136.265

Abstract: This chapter discusses the current state-of-the-art micro-electro-mechanical-system (MEMS) sensors specifically designed and implemented for structural health monitoring (SHM) of civil structures. The MEMS sensors have significant potential for advancing SHM methods because of diverse manufacturing capabilities, which allow integrating multiple sensing elements on the same device and on-chip electronics. The sensor types, which are commonly manufactured using micromachining methods, include accelerometer, acoustic emission sensor, strain, and corrosion sensor. The chapter first reviews the sensor materials, micromachining methods, and sensor characteristics. The chapter then discusses typical MEMS sensor designs used for SHM, application examples, and future trends. Further reading and references are provided at the end of the chapter.

Key words: miniature sensors, micromachining, silicon, piezoresistivity, capacitance, sensor fusion.

10.1 Introduction

Micro-electro-mechanical-systems (MEMS) are combinations of mechanical and electrical structures with μm size elements for sensing or actuating, integrated with signal processing electronics on the same device or with external wires for hybrid design. MEMS have enabled the design of novel sensors and systems using vast micromachining techniques at low cost. The advantages of MEMS sensors, as compared to conventional electromechanical systems, are (a) miniaturization, (b) integration of sensors and electronics on the same device, and (c) mass fabrication at low cost.

The structure of this chapter is as follows: Section 10.2 discusses the electrical and mechanical properties of sensor materials and the micromachining techniques, including surface micromachining, bulk micromachining, and lithography, galvanoformung (electroforming) and abformung (molding) (LIGA). Section 10.3 presents the sensor

© 2014 Woodhead Publishing Limited

characteristics specific to microstructures. Section 10.4 presents the MEMS sensors for SHM including accelerometer, strain gage, acoustic emission (AE), corrosion, and ultrasonic sensor. The other common sensor types, such as temperature and pressure, will not be discussed; however, the related references are given in Section 10.8. Typical examples of the MEMS sensors for SHM are discussed in Section 10.5. As the sensors used in SHM require surviving in harsh environment, durability for long term usage is a key factor. Technical challenges of the MEMS sensors for long term implementation are discussed in Section 10.6. Section 10.7 includes future trends. Section 10.8 provides further resources to learn more specific details of MEMS sensors. Section 10.9 is dedicated to the references used in this chapter.

10.2 Sensor materials and micromachining techniques

The fabrication of MEMS sensors for SHM at varying environmental and measurement conditions requires in-depth understanding of the materials used in the MEMS manufacturing. A wide range of materials and geometries within the limits of micromachining methods can be utilized in MEMS to design unique mechanical and electrical structures. As the length scale of MEMS devices reaches down to 1 μm, mechanics-related properties become size dependent. For example, as the film thickness decreases, dislocation formation is restricted, which results in high strength material in small scale (Spearing, 2000). Therefore, the proper selection of material properties requires the identification of process limitations and property changes with size. While the micromachining processes allow a variety of material selections, in this section the properties of the materials typically used for structural monitoring applications are presented in comparison with conventional civil engineering materials. After introducing the materials, three micromachining methods, including bulk micromachining, surface micromachining, and LIGA, are presented. The micromachining processes are similar to integrated circuits (IC) technology such as lithography, deposition, and etching.

10.2.1 Sensor materials

Table 10.1 shows five typical sensor materials, namely silicon, silicon carbide, polysilicon, silicon oxide, and nickel, used in sensor development for SHM, their typical usage in the sensor system and micromachining methods being used to etch or grow on the substrate. Table 10.2 presents their typical mechanical and electrical properties in comparison to structural steel obtained from several resources. Detailed properties and functions of these materials are discussed in this section.

Table 10.1 Typical sensor materials and purposes

Material	Purpose	Micromachining methods
Silicon	Substrate, mechanical sensor such as piezoresistive pressure sensor	Bulk micromachining, surface micromachining
SiC	High temperature sensor application	Bulk and surface micromachining
Polysilicon	Microstructure design	Surface micromachining
SiO_2	Sacrificial layer to release polysilicon	Surface micromachining
Nickel	Structural layer and conductive path	Electroplating

Table 10.2 Mechanical and electrical properties of MEMS microstructure materials in comparison to structural steel

Property	Steel	Silicon	3C-SiC	Polysilicon	SiO_2	Nickel
Yield strength (GPa)	0.5–2.1	2.8–7	3.44	1.21	8.4	14–35
Young's modulus (GPa)	200	62–202	302.8–450	120–203	46–92	200
Density (kg/m^3)	7900	2320–2330	3166	2320	2200–2500	8910
Thermal expansion coefficient ($10^{-6}/K$)	17.3	2.3–2.6	2.5–3.8	2–2.8	0.4–0.55	13
Electrical resistivity (Ω*m)	5.5e-7	Depending on doping level	4.7e-4 at room temperature	Depending on doping level	1e+16	6.84e-8

a. Silicon

Single crystal silicon is the most widely used semiconductor material as a substrate material due to its excellent machinability, mechanical stability, and the potential to combine sensing elements and electronics on the same substrate. Circular wafers made of silicon are used as substrate in most MEMS sensors. The crystal orientation should be known before manufacturing, since silicon has orientation-dependent properties such as piezoresistivity coefficients and etching rates. The common orientation is (100) where the numbers represent Miller indices (Madou, 2002). As an example, Fig. 10.1 shows a (100) wafer that has a primary flat side as an indication of <110> direction. When a piezoresistive element is placed on a (100) wafer,

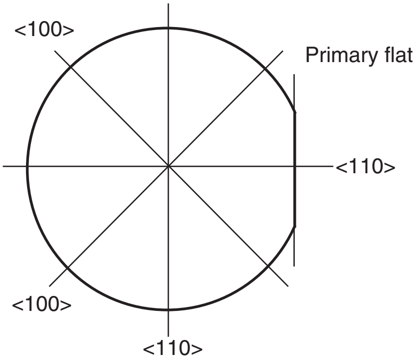

10.1 (100) wafer indicating the primary flat side and <110> and <100> directions.

the orientation should be parallel to <110> direction if the piezoresistivity coefficients in that direction are intended to be utilized.

Since Smith (1954) demonstrated the piezoresistance properties of silicon, silicon has been used extensively in the sensor design. The fractional change in resistivity can be approximated in linear proportion to stress, as follows (Nathan and Baltes, 1999):

$$\frac{\Delta\rho_{ij}}{\rho} = \sum_{k,l} \pi_{ijkl} T_{kl} \quad \text{with } i, j, k, l = 1,2,3 \qquad [10.1]$$

where π is the piezoresistivity coefficient and T is stress. The piezoresistivity coefficient depends on the crystal orientation of the silicon and the impurity concentration (i.e., dopant level and type). The piezoresistivity coefficients in the longitudinal and transverse directions are identified by the transformation of π from crystal orientation to the Cartesian coordinates (Kanda, 1982) as:

$$\pi_L = \pi_{11} - 2\left(\pi_{11} - \pi_{12} - \pi_{44}\right)\left(l_1^2 m_1^2 + m_1^2 n_1^2 + n_1^2 l_1^2\right) \qquad [10.2]$$

$$\pi_T = \pi_{12} + \left(\pi_{11} - \pi_{12} - \pi_{44}\right)\left(l_1^2 l_1^2 + m_1^2 m_1^2 + n_1^2 n_1^2\right) \qquad [10.3]$$

where $l, m,$ and n are direction cosines and $\pi_{11}, \pi_{12},$ and π_{44} are the piezoresistivity coefficients depending on the silicon crystal orientation. Kanda (1982) shows the piezoresistivity coefficients of longitudinal and transverse directions graphically for p-type and n-type doped silicon substrates. The highest coefficients in longitudinal and transverse directions for (100) plane n-type wafer are achieved in the crystallography direction of <100>.

The impurities, n-type or p-type, can be introduced into single crystal silicon using diffusion or ion implantation techniques. While ion implantation controls the amount of impurities more accurately, it is an expensive process as compared to the diffusion technique. If the impurity concentration is increased, the piezoresistivity coefficients decrease; however, their temperature dependence decreases as well. Kanda (1982) demonstrated the piezoresistance factor as a function of impurity concentration and temperature. During the design of piezoresistive sensors, the dependence of temperature should be taken into consideration. A trade-off between sensitivity and temperature dependence should be considered for a specific application. Silicon, from a mechanical perspective, is a high strength, brittle material with low toughness, and its mechanical properties are given in Table 10.2.

b. Polycrystalline silicon (polysilicon)

Polysilicon is the most common material for designing surface-micromachined devices. Polysilicon has material properties similar to single crystal silicon and can be doped via introducing impurities. Thin polysilicon layer to form microstructure can be deposited using low pressure chemical vapor deposition (LPCVP) technique. Polysilicon is made of grains that tend to increase in size with an increase in film thickness during the high temperature manufacturing steps (Zorman *et al.*, 2006). Recrystallization of polysilicon increases the surface roughness, and affects mechanical and electrical properties. The manufacturing of polysilicon thick film may require chemical polishing to obtain smooth surfaces. Because of grain boundary effect and the limitations of deposition techniques, the thickness of structures made of polysilicon is typically limited to 2–5 μm.

c. Silicon carbide

SiC is a semiconductor material with a band gap in the range of 2.3–3.4 eV, and excellent physical stability and mechanical properties with high melting point >3000°C. Therefore, it is an ideal material for high temperature applications and harsh environments (Mehregany and Zorman, 1999). SiC exhibits a one-dimensional polymorphism in various forms. Main SiC polytypes for device development are 4H-, 6H- and 3C-SiC. Micromachining SiC is more challenging than silicon. Plasma-based dry etching for SiC surface micromachining and laser ablation etching technique for SiC bulk micromachining have been typically selected. 3C-SiC is the only polytype that can be deposited on silicon substrate, which makes it the dominant polytype for MEMS sensor applications (Jiang and Cheung, 2009). Various micromachined structures can be designed using deposited polycrystalline 3C-SiC layers, such as lateral resonators and cantilevers (Fu *et al.*, 2011; Wright and Horsfall, 2007).

d. Metals

Metals are implemented as the principal conductors for power and signal transmission (e.g., aluminum) as well as structural elements (e.g., nickel). Metals are manufactured as thin films using deposition methods such as sputtering, or bulk materials using the electroplating method. To obtain a thick metal layer, a mold is applied in order to pattern an electroplated layer on the surface, as discussed under the LIGA method.

e. Sacrificial layers

Sacrificial layers are required between substrate or insulator layer and the microstructure layer in order to release the deposited microstructure layer functioning as moving element. Silicon oxide (SiO_2) is the most typical layer used in the surface micromachining method because it can be easily dissolved without affecting other layers such as polysilicon and silicon nitride. Good thermal matching of SiO_2 makes it a good candidate as compared to aluminum.

f. Insulators

Typical insulating layers include silicon dioxide, silicon nitride, and titanium nitride (Spearing, 2000). Silicon nitride has 10^{16} Ω-cm resistivity, high dielectric strength, and field breakdown limit of 10^7 V/m (Madou, 2002).

10.2.2 Micromachining methods

There are three main micromachining methods used to design and manufacture MEMS sensors for SHM including bulk micromachining, surface micromachining, and LIGA. Most of the processing steps are adapted from IC technology. Three main processes are deposition, lithography, and etching. Deposition can be achieved using oxidation, chemical vapor deposition, epitaxy, physical vapor deposition, diffusion, and ion implantation. Lithography methods to pattern the shapes are optical and electron diffusion. Etching methods are wet or dry etching. Figure 10.2 shows the process steps of three micromachining methods in order to create a freely moving microstructure layer. Each process step is explained below.

a. Bulk Micromachining: the microstructure geometry is featured by dry or wet etching of bulk three dimensional materials. Etching masks are used in order to remove selected areas for creating the design geometry. Increasing dopant concentration increases the etching rate due to the mobile carriers. Wet etching processes may increase the residual stress at films. Dry etching techniques include reactive ion etching (RIE) sputtering, ion milling, and plasma etching. Figure 10.2a shows a simple geometry design using bulk micromachining method. It is assumed that the process is started with a doped silicon substrate. Back-side etching (step 2) removes a section of substrate. Oxidation (step 3) creates an insulator layer to electrically disconnect the substrate and microstructure layer. Doped polysilicon can be deposited on the oxidized layer to be used as strain sensor.

b. Surface Micromachining: surface micromachined MEMS sensors are designed by the deposition, patterning, and etching of layers on the surface of a substrate, typically used in the complementary metal oxide semiconductor (CMOS) manufacturing. The processes can be used to

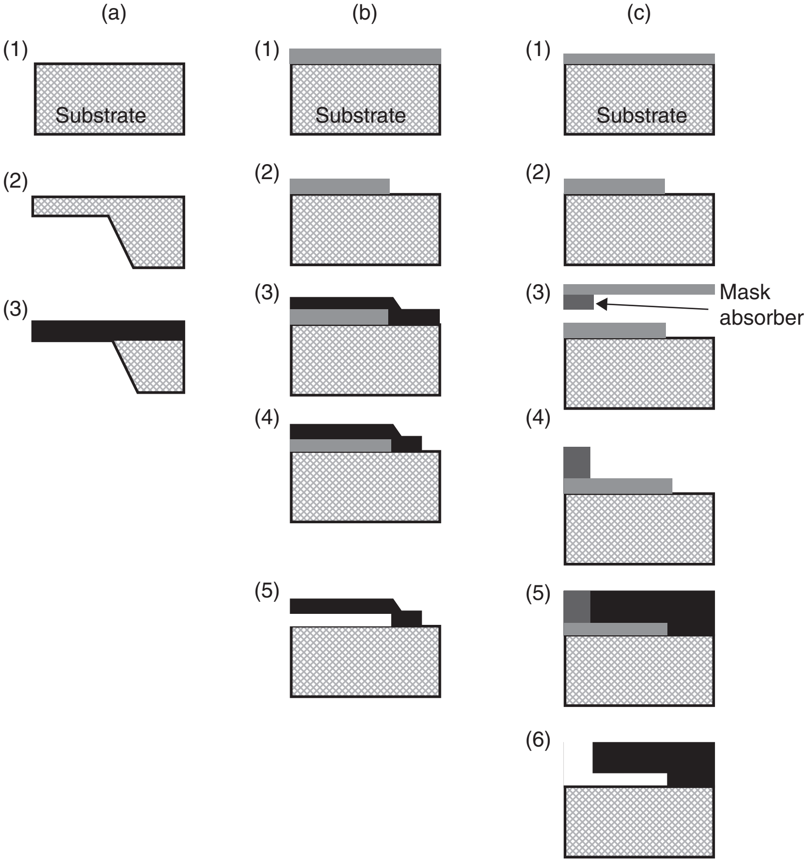

10.2 Process flows of three micromachining methods to create a freely moving microstructure layer (a) bulk micromachining, (b) surface micromachining, (c) LIGA.

fabricate standing and freely moving microstructure layers in a large two-dimensional design space. Figure 10.2b shows a simple geometric design using surface micromachining method. After depositing sacrificial layer (step 1), the layer is patterned and then etched (step 2) depending on the design geometry. The next step (step 3) is to deposit the microstructure layer and then pattern and etch it (step 4). Finally, the sacrificial layer is selectively removed (step 5) using wet etching technique in order to create a freely moving microstructure layer.

Thin film properties play an important role for the sensor characteristics. Due to the limitations of depositing techniques, the thickness of microstructure is limited to 2–5 μm. The drawbacks of the surface micromachining method include the property and thickness variability due to deposition, stiction of layers during release process (the contact of two parallel layers after the release of the freely moving microstructure layer), and thickness limitation. However, polysilicon has superior material properties and the process can be combined with the CMOS processes for on-chip electronics (e.g., pre-amplifiers, filters).

The release process may cause thin film residual stress after the sacrificial layer is removed to release the microstructure layer, which may modify the microstructure geometry (Romig *et al.*, 2003). The residual stress can be controlled to some level by annealing the microstructure layer and designing it in a form that reduces the amount of residual stress. Plate VI (in the color section between pages 294 and 295) shows the elevation measurements taken from two different capacitive sensor geometries designed by Ozevin (2005). A non-contact optical profilometer can provide the dimensions of microstructures. Anchors for the diaphragm unit in a hexagonal shape were around the periphery of the polysilicon layer, while those for the piston unit in a square shape were inside. Anchor locations of the piston transducers reduced the deformation of polysilicon layer caused by the etching step.

c. LIGA: The LIGA process uses polymer mold created by lithography and electroplating metal into the mold cavities in order to create high aspect ratio structures. Structures with vertical side walls and aspect ratio of 100:1 can be manufactured using a highly collimated X-ray source (Beeby *et al.*, 2004).

Figure 10.2c shows a simple geometry design with high aspect ratio design using LIGA. After depositing (step 1), patterning and etching (step 2) sacrificial layer, the layer is exposed to thick X-ray resist (step 3) with a mask and absorbers depending on the design pattern. X-ray resist is developed on the sacrificial layer (step 4); afterwards, a thick metal layer is electroplated (step 5). Finally, sacrificial layer is selectively etched and X-ray resist is stripped (step 6) in order to create a freely moving microstructure with high aspect ratio.

10.3 Sensor characteristics

The MEMS sensors for SHM can be built using the transduction principles of piezoresistivity, piezoelectricity, and capacitance. The size and manufacturing methods introduce several characteristics (i.e., stiction, squeeze film damping, and residual film stress) intrinsic to the MEMS sensors. This section describes the transduction principles and the MEMS sensor characteristics affected by the manufacturing methods.

10.3.1 Transduction principles

There are three main transduction principles used in the design of MEMS sensors for SHM: piezoresistivity, piezoelectricity, and capacitance. The piezoresistivity is based on the piezoresistive property of silicon demonstrated by Smith in 1954. The resistance Equation [10.4] and the relationship between resistance change (ΔR) and strain (Equation [10.5]) are:

$$R = \frac{\rho L}{A} \tag{10.4}$$

$$\frac{\Delta R}{R} = \varepsilon(1+2\upsilon) + \frac{\Delta\rho}{\rho} \tag{10.5}$$

where R is resistance, ρ is resistivity, L is length, A is cross-sectional area, ε is strain, and υ is Poisson ratio. The gage factor is defined as

$$GF = \frac{\Delta R / R}{\varepsilon} = (1+2\upsilon) + \frac{\Delta\rho}{\rho} \tag{10.6}$$

For metals, the term $\Delta\rho/\rho$ is small; therefore, the gage factor is limited by Poisson's ratio. A typical gage factor for metals is in the range of 1.4–2.0 (Barlian *et al.*, 2009). In Section 10.2, the piezoresistivity coefficients with respect to resistivity change are provided. If the sensor is sensitive to longitudinal stress, Equation [10.6] can be simplified as

$$GF = (1+2\upsilon) + \pi_L E \tag{10.7}$$

where E is Young's Modulus and approximately equals 160 GPa for silicon. The piezoresistivity coefficient of n-doped silicon in the longitudinal direction and (100) plane of 11.7 ohm-cm resistivity is –102.2E-11 Pa^{-1} (Smith, 1954). The gage factor for n-doped silicon is theoretically about 165, which is significantly higher than metal foil gages. Polysilicon also exhibits piezoresistivity; however, the piezoresistivity coefficients are the average of all the directions.

The temperature dependence of piezoresistivity coefficients is significantly reduced with increasing impurity concentration N (i.e., reducing the resistivity), while the sensitivity of the sensor or its gage factor reduces simultaneously. The design requires an optimized point for the temperature dependence and the sensitivity. With unique microstructure geometry design, the sensor response can be amplified at the sensor level without need of an amplifier (Saboonchi and Ozevin, 2012). With the piezoresistivity transduction, strain, acceleration, and pressure can be measured.

The piezoelectric thin films can be deposited on silicon substrate with an insulator layer using various deposition techniques. Tadigadapa and Mateti (2009) summarize the challenges of piezoelectric property in MEMS sensors as high temperature need for piezoelectric deposition, incompatibility with CMOS, and morphology dependent piezoelectric properties. These challenges can be overcome with deposition techniques such as sputtering of aluminum nitride, chemical solution deposition of ferroelectric lead zirconate titanate (PZT) films, and patterning with plasma processes.

The piezoelectric equations for MEMS piezoelectric materials are similar to bulk type materials (Giurgiutiu, 2008):

$$S_{ij} = S^{D}_{ijkl} T_{kl} + g_{kij} D_k \tag{10.8}$$

$$E_i = g_{ikl} T_{kl} + \beta^{T}_{ik} D_k \tag{10.9}$$

where S_{ij} and T_{kl} are the strain and stress, E_i and D_k are the electric field and electric displacement, the coefficient S_{ijkl} represents stress per unit strain (compliance), and the coefficient g_{ikl} is the piezoelectric voltage coefficients. Piezoelectric coefficients vary depending on the thin film deposition technique. Tonisch *et al.* (2006) demonstrated the d_{33} coefficient of aluminum nitride (AlN) thin film as 5.1 pm/V. While piezoelectrics have a stable behavior for a wide temperature range, the applications of the piezoelectric MEMS sensors are so far limited (Muralt, 2008). Muralt *et al.* (2005) designed and manufactured 2 μm thick PZT film based MEMS ultrasonic sensor using sol-gel technique. The piezoelectric MEMS sensors can be designed as resonant or broadband. The resonant design requires dynamic factors (e.g., dynamic coupling factor) instead of static factors (Gaucher, 2002).

A capacitance is formed by two parallel conductors that can hold opposite charges. The capacitance of two parallel layers separated by air equals

$$C_o = \frac{\varepsilon A}{g} \qquad [10.10]$$

where ε is the dielectric permittivity of material between plates, A is the overlap area between the top and bottom capacitive layers, and g is the gap between two capacitive layers. The capacitance change can occur due to the time variation of any of the variables, given in Equation [10.11] as:

$$\frac{\mathrm{d}C}{C} = \frac{\mathrm{d}E}{E} + \frac{\mathrm{d}A}{A} - \frac{\mathrm{d}g}{g} \qquad [10.11]$$

If a parallel plate capacitor is designed, the gap change is the conversion of mechanical signal to electrical signal. Figure 10.3a shows a group of parallel plate capacitors forming an AE sensor operating in out-of-plane direction manufactured using electroplating technique. If interdigital finger (i.e., comb drive) capacitors are designed, the area change or the gap change, Fig. 10.3b, is the cause of capacitance change. Major advantages of electrostatic sensing include fast response, which allows direct current (DC) level acceleration detection and simplicity. However, high power may be needed and parasitic capacitances may decrease signal-to-noise ratio.

10.3.2 Stiction and collapse voltage

The stiction is the contact of two parallel conductive layers as illustrated in Fig. 10.4 on a capacitive sensor design constructed by two polysilicon layers on an insulator layer. Figure 10.4a shows the intended microstructure layer, and Fig. 10.4b shows the microstructure layer with the stiction. The stiction can occur either during the microfabrication or during the application of an electrostatic load. When removing the sacrificial layer with wet etching, the

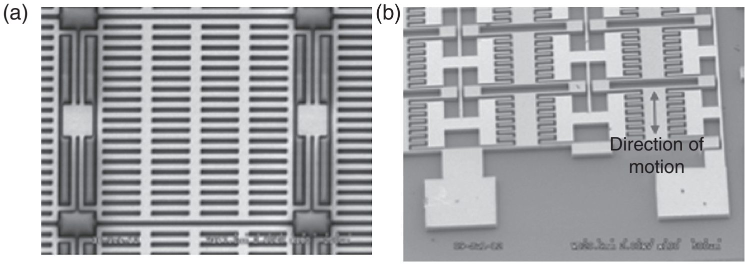

10.3 Scanning electron microscope (SEM) images of capacitive gap change design for (a) out-of-plane motion and (b) in-plane motion.

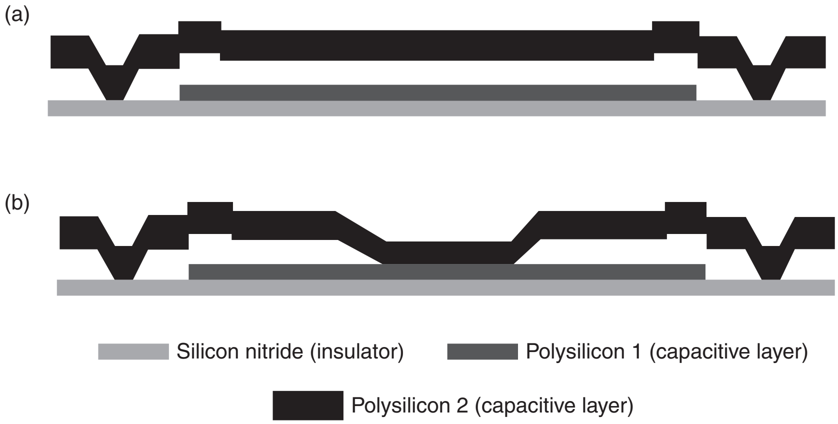
(a)
(b)
Silicon nitride (insulator)
Polysilicon 1 (capacitive layer)
Polysilicon 2 (capacitive layer)

10.4 Stiction phenomenon (a) intended microstructure and (b) consequence of stiction.

freely moving microstructure layer may come in contact with the substrate and remain there because of the surface tension created by wet etching. The stiction problem can be solved by several methods, such as designing a sufficiently rigid microstructure layer and immersing the microstructure into distilled water and alcohol immediately after the etching process (Madou, 2002). A dielectric layer deposited on the top surface of the bottom electrode can also prevent complete electrical contact and stiction while still allowing current flow due to low impedance path (Song *et al.*, 2007).

Another cause of the stiction is the excessive application of electrostatic load. The freely moving microstructure layer has anchors on the substrate, which provide the mechanical stiffness. When an electrostatic load is applied across two microstructure layers, two layers pull toward each other. If the electrostatic load is applied excessively, the pulling force brings two layers into contact and leads to the stiction of two layers. For electrostatic designs, the maximum bias voltage V_{bias} that can be applied in the stable range and prevents stiction of the capacitive layers is referred to as the collapse voltage (Labadaum *et al.*, 1998) and equals

$$V_{\text{collapse}} = \sqrt{\frac{8kg^3}{27\varepsilon_o A}} \qquad [10.12]$$

10.3.3 Squeeze film damping

Squeeze film damping occurs in microstructures separated with a narrow band, and is caused by the air resistance under vibration of a freely moving microstructure layer due to air viscosity. The damping due to the fluid squeezing between two plates is modeled using Reynolds lubrication theory (Oppenheim *et al.*, 2003a). Marrero *et al.* (2010) discuss the discrepancy between the actual measurement ($c \sim 1/h$ where h is plate thickness) and the lubrication theory ($c \sim 1/h^3$). The authors propose that the nonlinearity associated with Reynolds number is the explanation for this discrepancy. The squeeze film damping can be mitigated by increasing the gap between two capacitance layers, reducing the horizontal size of the freely moving microstructure layer, making holes in the freely moving microstructure layer to allow air to pass more readily, or by reducing the atmospheric pressure (Vinokur, 2003). Dienel *et al.* (2012) studied analytically and numerically the impact of vacuum pressure levels on the performance of MEMS sensors used in SHM to reduce the damping in resonant structures.

10.3.4 Thin film residual stress

Residual stress is induced on the microstructure layers due to mismatch in the thermal expansion coefficients of the deposited layers (e.g., polysilicon and silicon oxide), non-uniform plastic deformation, interstitial impurities, and the deposition process (Madou, 2002). The most significant effect of residual stress is gross deformation, such as curling of a cantilever, which can cause significant change in resonant frequency and buckling under compression. Plate VIa (see colour section between pages 294 and 295) shows an example of hexagon geometry and the thickness distribution along its length measured using a profilometer. The residual stress on thin film can alter stiffness, and consecutively the resonant frequency of the microstructure layer. Buckling is another consequence of thin film residual stress. Buckling is a frequent phenomenon in MEMS devices. Gaucher (2002) shows that if the dimensions of MEMS microstructure (width, thickness, and length) are decreased by a factor of 100, the Euler buckling load decreases by a factor of 10^4. The residual stress can be controlled to some level by annealing the microstructure layer. A second approach to control the residual stress is to design the microstructure layer in a form that reduces the amount of residual stress (Plate VIb).

10.3.5 Packaging

MEMS packaging is one of the critical barriers of MEMS progress in SHM for long term reliable usage, and it is still an active research field to design an effective and reliable packaging for MEMS sensors. The sensors need to be protected as well as exposed to environment for the transduction purpose, especially for corrosion sensing. For acceleration sensing, the sensing element and electronics can be sealed in a package while it still functions for inertia sensing. Li *et al.* (2013) showed that the sensitivity of a MEMS accelerometer depends on the thickness of the die adhesive and the die attachment process, and the density of the potting material. For AE sensing, the sensor surface should be in contact with the surface of the structure under health monitoring, in order to reduce the signal loss due to reflection in the layers. For a strain sensor, static strain requires complete removal of the sensor from the wafer for direct contact and the wiring should be on the mounted surface. Dynamic strain can be encapsulated in a sealed package. For a corrosion sensor, the sensing element may require direct contact with the environment, causing a reliability issue for long term implementation.

For any packaging, the die that carries the device (i.e., sensing elements and electronics) should be attached to the package as the first step, the connection pads on the device should be electrically connected to the pads in the package (metal, plastic, or ceramic as shown in Fig. 10.5) using the wire bonding method or flip-chip method as the second step, and then the package should be sealed with maximum protection that the sensing element will allow as the third step. The packaging steps can be done after or during (wafer level) the die manufacturing. The adhesive die attachment introduces stress on the sensing element, which affects the sensor behavior. Walwadkar and Cho (2006) showed that polyimide adhesive introduces less stress on the silicon die. Three failure mechanisms of protecting the MEMS device using capping are cavity deflection, cap fracture under impact, or drop and moisture penetration from sealant location, which detrimentally affect the hermetic bonding (Van Driel *et al.*, 2007). Vacuum packaging usually fails due to leakage and outgassing (Chao, 2005). Mohammed *et al.* (2011) proposed a packaging scheme for the MEMS strain sensor, utilizing flip-chip technology; however, the packaging stiffens the strain response, which decreases the sensitivity. All the failure modes for the selected package method should be investigated deeply before implementing the sensor for long term SHM.

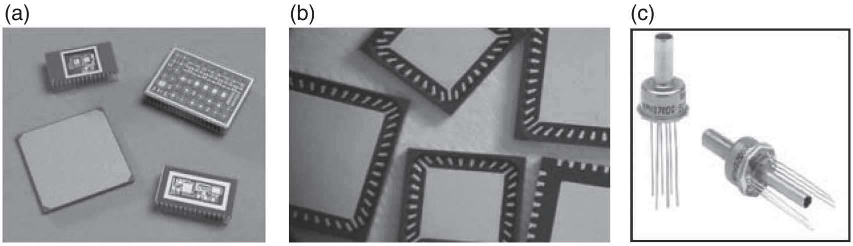

10.5 Examples of MEMS packaging (a) ceramic package (www.ntktech.com), (b) plastic molded package (www.icproto.com) and (c) metal package (www.ge-mcs.com).

10.4 MEMS sensors for SHM

This section presents the prevailing sensors and sensing methods implemented for the SHM methods. The sensors include accelerometer, AE, strain, corrosion, and ultrasonic sensors. The sensors can be designed using a variety of transduction principles such as piezoresistivity, piezoelectricity, and capacitance. The MEMS sensors are described based on their transduction principles, and their advantages and challenges for the SHM applications are presented.

10.4.1 Accelerometer

MEMS-based accelerometers can be designed using the transduction principles of piezoresistivity, piezoelectricity, and capacitance. The sensing elements can be designed for measuring multi-axis accelerations in linear and angular directions (i.e., gyroscopes). The frequency spectrum and bandwidth are controlled by mass and spring geometries. Figure 10.6 shows the schematic model of a cantilever accelerometer design, where the geometry for piezoelectric and piezoresistive types is similar. For capacitive transduction, a stationary layer is needed to form the capacitance and the gap or area change of the capacitance can be the transduction principle.

Two main challenges of MEMS accelerometers are to design a sensor operating below 1 Hz, which is a typical vibration frequency of long span bridges, and to sense low-level ambient vibrations (Jo *et al.*, 2012). Piezoresistive sensors have DC response; however, n- or p-doped silicon used as piezoresistive material has a piezoresistive coefficient depending on temperature, as discussed in Section 10.3.1. Piezoelectric sensors have fast response and are difficult to design below 1 Hz. Capacitive sensors have DC response; however, due to parasitic capacitances, as discussed in Section 10.3.1, their sensitivity is low. The selection of transduction principle for MEMS accelerometer design depends on the specifications of an SHM application. There are numerous applications that integrate MEMS accelerometers with wireless units for monitoring damage in structures (Lynch and Loh, 2006), which are discussed under Section 10.5. Another challenge is the control of damping. For thin films, squeeze film damping controls the signal decay and varies with the deflected geometry and frequency. Therefore, damping is not constant for MEMS sensors unless they operate in vacuum.

The piezoresistive accelerometers are made of proof mass and spring elements, and the piezoresistive elements are deposited on spring elements, where they convert the acceleration induced strain into voltage when they are connected to a strain gage bridge. As discussed in Section 10.3.1, the orientations of piezoresistive elements control the sensitivity value and direction.

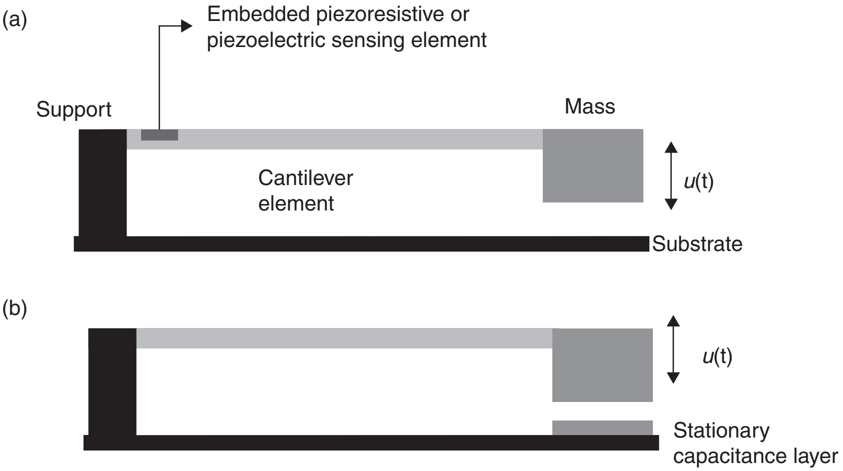
(a)
Embedded piezoresistive or piezoelectric sensing element
Support
Mass
Cantilever element
u(t)
Substrate
(b)
u(t)
Stationary capacitance layer

10.6 Cantilever accelerometer design using (a) piezoresistive or piezoelectric transduction and (b) capacitive gap change transduction.

Roylance and Angell (1979) developed the first silicon-based accelerometer operating in out-of-plane direction with a mass structure and a cantilever beam that has piezoresistive elements. The weight of the MEMS accelerometer is less than 0.02 g, which has a large bandwidth and sensitivity. The sensitivity direction can be controlled using spring stiffness values (Chen *et al.*, 1997; Partridge *et al.*, 2000). Table 10.3 shows examples of piezoresistive MEMS accelerometers in the literature with their geometries, micromachining methods, and specifications. With unique microstructure geometry and flexibility of micromachining methods, novel, high sensitivity, wide bandwidth MEMS accelerometers can be designed and manufactured in a small package.

The steady-state stress on a piezoelectric material decreases rapidly due to loss mechanisms in piezoelectric elements, which cause charge leakage. Therefore, piezoelectric sensors are designed for transient-response sensors (Tadigadapa and Mateti, 2009). Typical applications are in machine monitoring and the automobile industry. Similar to piezoresistive accelerometer sensor design is made of spring and mass. The sensing element, as piezoelectric film, is deposited on the spring to detect the acceleration induced strain (Hindriches *et al.*, 2010). The common sensing direction for piezoelectric elements is d_{31} (Hindriches *et al.*, 2010; Wang *et al.*, 2002). Yu *et al.* (2003) designed an accelerometer using interdigitated electrodes, which utilizes d_{31} and d_{33} piezoelectric coefficients for better sensitivity. The MEMS piezoelectric accelerometers can be combined with commercially available wireless electronics (Kok and Furlong, 2005).

Table 10.3 Examples of piezoresistive MEMS accelerometers in the literature

Geometry	Micromachining method	Specification	Reference
Cantilevered beam and mass	Photolithography, diffusion, and etching	Res. Freq: 2330 Hz Sensitivity: 0.5 mV/g/V supply Range: 50 g Number of axes: 1	Lynch *et al.*, 2003; Roylance and Angell 1979
Planar cantilevered proof mass and sidewall piezoresistors	Silicon on insulator (SOI) and dry reactor ion etching (DRIE) for side wall implantation	Res. Freq: 700 Hz Sensitivity: 0.6 mV/g/V supply Range: 50 g Number of axes: 1	Partridge *et al.*, 2000
Combination of bending and axial elements with a proof mass	Bulk silicon micromachining	Res. Freq: 2900 Hz Sensitivity: 24 mV/g/V supply Range: not reported Number of axes: 1	Lim *et al.*, 1999
Symmetric quad-beam structure with 20 piezoresistors	Bulk silicon micromachining on SOI and DRIE	Min Res. Freq: 2087 Hz Sensitivity: varying in each direction Range: 10 g Bandwidth: 300 Hz Number of axes: 3 or 6	Amarashinghe *et al.*, 2005, 2006

10.4.2 Acoustic emission sensor

AE are transient stress waves released within a material due to sudden stress–strain change caused by newly formed damage surfaces. The passive nature of the AE method requires sensors with high sensitivity and low noise level. The other sensor requirement is that the sensor surface area should be smaller than the smallest wavelength of the excitation signal to prevent the aperture effect. Typical frequency range used in civil structures is 60–400 kHz.

The AE sensors can be resonant or broadband types. The design of a broadband AE sensor is achieved by keeping the damping of the sensor high, which provides the fast damped response of the sensor causing a reduction in the amplitude of the output signal. Typical AE sensors are made of piezoelectric ceramics. However, it is not possible to design low frequency miniature AE sensors using conventional piezoelectric bulk ceramics.

There are three types of MEMS AE sensors designed in the literature: capacitive, piezoelectric, and optical. Ozevin *et al*. (2006) designed and characterized the first capacitive AE sensors in the literature fabricated in the commercial three-layer polysilicon surface micromachining process

(Multi-User-MEMS-Processes (MUMPs)). Each transducer is a parallel plate capacitor with one plate free to vibrate, thereby causing capacitance change which creates an output signal in the form of a current under bias voltage. While the sensors could detect the AE events due to crack development in weld metal, their sensitivities are about fifty times less than conventional piezoelectric AE sensors (Ozevin *et al.*, 2006). The current output *i(t)* in a capacitive transducer for a solid coupled system excited by *x(t)* is (Ozevin, 2005):

$$i(t) = V_{DC} \frac{\varepsilon_o A}{g^2} \frac{dx(t)}{dt} \qquad [10.13]$$

The squeeze film damping of thin films influenced the dynamic response *x(t)* of the microstructure. Harris *et al.* (2011) designed an improved capacitive AE sensor for out-of-plane sensing using the open-grill approach to reduce squeeze film damping. They also designed a comb drive sensor for in-plane sensing; however, the design limitations of the micromachining process used in this research causes coupling of in-plane and out-of-plane sensing for comb drive design. Saboonchi and Ozevin (2013a) designed and manufactured capacitive type MEMS AE sensors using an electroplating technique. The sensors are manufactured by MetalMUMPs process, which allows higher aspect ratio geometry than surface micromachined sensors. The MEMS AE sensors in this study operate at atmospheric pressure, and have signal-to-noise ratio comparable to bulk type piezoelectric sensors at their resonant frequencies.

Feng and Tsai (2010) designed a piezoelectric AE sensor made of multilayer polyvinylidene fluoride (PVDF) using a micro-embossing fabrication technique. The sensor has an operational frequency range of 10 kHz–1.4 MHz. Schoess and Zook (1998) implemented a resonant micro-beam as an AE sensor. Under an excitation signal caused by propagating elastic waves, a micro-beam made from polysilicon vibrates, which is converted to mechanical signal using a focused laser system. The MEMS design approach developed in this study can be combined with fiber optic systems for a compact AE sensor design.

10.4.3 Strain sensor

There are several recent strain sensor designs in the literature using MEMS. However, the performance of MEMS strain sensors is currently limited to laboratory scale experiments. Mohammed *et al.* (2011) designed the MEMS strain sensor with lower dopant concentration while the geometry amplifies the strain value. Direct measurement of strain requires robust bonding of the strain gage directly on the measurement surface. Kim *et al.* (2010)

designed a thin polysilicon gage that can be separated from the wafer for direct attachment to the surface. However, fragility can be an important issue for this process. Bahreyni *et al.* (2006) fabricated piezoresistive sensors using the standard MUMPs (Multi-User Polysilicon) process. The geometry is a twin-beam structure separated by air so that the total strain in the polysilicon layer is non-zero. Waterfall *et al.* (2008) demonstrated that the relationship between the bending strain and piezoresistivity of the polysilicon layer is nonlinear. The temperature dependence of the piezoresistivity coefficients of the silicon and decoupling the sensor from wafer, are two challenges that need to be addressed for the use of MEMS strain sensors to replace conventional foil gages.

Adhesive bonding degradation of strain sensors with time and environmental factors limits the lifetime of the sensors for long term monitoring. Sosnowchik *et al.* (2012) developed an alternative bonding method based on the eutectic bonding of MEMS strain sensor to steel using an induction heating system.

10.4.4 Corrosion sensor

Corrosion can be monitored indirectly using parameters such as humidity, temperature or directly using corrosion sensor. Humidity can be measured using various transduction principles of MEMS such as the capacitance change (i.e., dielectric constant change in direct proportion to humidity) and resistivity change due to humidity. MEMS temperature sensors are commercially available analog devices. Norris *et al.* (2006) demonstrated the embedded MEMS temperature and moisture sensors into concrete. The sensors were made of silicon cantilever with embedded strain gages for piezoresistivity transduction in proportion to temperature and moisture.

For direct measurement of corrosion, the sensor material should be the same as the material being monitored for corrosion. Hautefeuille *et al.* (2009) designed a MEMS corrosion sensor as part of a wireless sensor network mote using a 0.5 μm thick metal layer made of aluminum and 1% silicon as the active layer of corrosion sensor. Electrical resistance change of metal layer, due to corrosion development, is the transduction principle for corrosion monitoring. There are not many design examples for the MEMS corrosion sensor in the literature.

10.4.5 Ultrasonic sensor

The application of MEMS technology to ultrasonic transducers has been studied since 1998. Khuri-Yakub *et al.* (1998) and Jin *et al.* (1998) presented a capacitive transducer fabricated using a silicon micromachining method. The sensor sensitivity was comparable to the piezoelectric sensor, and the sensor was evaluated in air-coupled and immersion applications. The advantage of the silicon micromachined capacitive transducer, as compared to the piezoelectric transducer, is that the silicon has no acoustic mismatch problem for the ultrasonic testing at air-coupled applications. The acoustic mismatch between air and piezoelectric material results in the ultrasonic sensor having either narrow bandwidth or poor efficiency, along with the difficulty of creating the proper impedance matching layers. In addition, the capacitive MEMS sensor can be used in high temperatures, whereas the behavior of the piezoelectric sensor is modified above the Curie temperature. The researchers reported several innovative processes in the capacitive MEMS sensor fabrication to optimize sensor performance (Jin *et al.*, 1999). Bashford *et al.* (1998) also showed the superiority of water-coupled micromachined ultrasonic capacitive sensors over piezoelectric sensors.

Oppenheim *et al.* (2003a, 2003b) studied a solid coupled capacitive diaphragm MEMS sensor fabricated using the MUMPs. The geometry is similar to Plate VIa (see colour section between pages 294 and 295). The capacitance of a single diaphragm unit is insufficient to function as a sensor; therefore, 180 diaphragm units are placed in parallel to form a single sensor (Jain, 2002). An electromechanical model of capacitive MEMS sensors is described by Oppenheim *et al.* (2003a) and Ladabaum *et al.* (1998).

10.5 Application examples

MEMS sensors are continuously implemented in certain applications, such as in the automobile industry. However, in the field of civil structures, they are not sufficiently established to be implemented for continuous monitoring because of the challenges of power source and durability. The long term technical challenges of MEMS are discussed in Section 10.6. Additionally, packaging and integration with electronics are another two barriers to the extensive use of MEMS sensors in SHM (Glaser *et al.*, 2007).

Table 10.4 shows some application examples of MEMS sensors in the literature. The applications range from system identifications of buildings and bridges to concrete monitoring for corrosion. Some of these applications are limited to laboratory scale demonstrations. The most mature MEMS sensor used in civil structures is the MEMS accelerometer for system identification. Various design options are described in Section 10.3. Ramos *et al.* (2010) summarize the evolution of wireless accelerometer designs, including the MEMS accelerometer, in the field of SHM. However, there are limited numbers of field validations demonstrating the long term

Table 10.4 Examples of MEMS sensors in monitoring civil structures

Structural application	Sensor type	Manufacturing method	Transduction principle	Reference
Railroad fatigue type	Strain	BiAST, Sarcos Research Inc		Obadat *et al.*, 2003
Highway bridge system identification	Accelerometer	Surface micromachining (3801D1FB3G by PCB Piezotronics)	Capacitance	Lynch *et al.*, 2006
Offshore platform inclination	Inclination sensor	Surface micromachining	Capacitive accelerometer	Yu *et al.*, 2009
Building system identification	Accelerometer	Surface micromachining (ADXL103 from Analog Devices)	Capacitance	Kim *et al.*, 2008
Concrete moisture and temperature monitoring	Cantilever with vapor sensitive polymer and strain gages	Combination of CMOS processing steps	Piezoresistivity	Norris *et al.*, 2006
Tension identification in cable bridges	Accelerometer	CXL02LF1 from Crossbow Tech. Ing.		Cho *et al.*, 2010
Load monitoring of aerospace structures	Accelerometer, gyroscope, and magnetometer	Combined sensing elements from GLI Interactive LLC		Martinez *et al.*, 2012
Composite monitoring	Accelerometer	LIS3LV02DQ three-axis accelerometer		Mariani *et al.*, 2013
Building monitoring	Strain and accelerometers	Surface micromachining	Capacitance	Torfs *et al.*, 2013

durability of the sensors. Chung *et al.* (2004) demonstrated the integration of MEMS accelerometers manufactured by Analog Devices (ADXL 202E) and Silicon Design (SD1221) with a wireless system for monitoring a pedestrian bridge. While the MEMS sensors have lower signal-to-noise ratio, they detected the fundamental frequencies of the bridge as compared to conventional cabled sensor. However, the pedestrian bridge was a short term demonstration.

10.6 Long term technical challenges

There has been a remarkable progress in MEMS sensors since the 1980s. However, the challenges of long term durability and processing effects are still present for the implementation of the MEMS sensors in civil structures for continuous monitoring. Understanding the failure mechanisms of MEMS sensors packaged using sealant or caps is a difficult task, as removing the protective layer nondestructively is not possible (Walraven, 2005). Huang *et al*. (2012) lists typical failure modes for MEMS sensors, such as mechanical fracture, stiction, charge accumulation, wear, creep, fatigue, electrical degradation, and environmental contamination. Tanner (2009) discusses the reliability of MEMS components based on the groups as (1) no moving parts, (2) moving parts, no rubbing or impacting surfaces, (3) moving parts with impacting surfaces, and (4) moving parts with impacting and rubbing surfaces. The groups 3 and 4 include mirrors and switches where impacting and rubbing cause surface wear. The MEMS sensors used in SHM have components in groups 1 and 2. Moving parts can have fatigue, fracture, and creep depending on environmental and loading conditions, and stiction depending on the level of deformation or the applied voltage. Humidity and temperature can damage the sealant of the protective package causing outgassing for vacuum packaged sensors. The MEMS package and sensing element can also be damaged due to unintentional drop or shock vibration caused by thunder struck in highway bridges. The long term durability of the sensor should be evaluated based on the conditions of the specific application.

Repetitive cycling of silicon thin films, especially at their resonant frequencies (typically used to design an AE sensor) can cause fatigue. Silicon is a brittle material with low damage tolerance and fracture toughness (~1 MPa$\sqrt{m}$ as reported at Muhlstein *et al*., 2004). Bagdahn and Sharpe (2003) showed that the tensile strength of thin polycrystalline silicon film decreases about 35% after 10^9 cycles. Such decrease in strength and stiffness change may not be acceptable for sensor designs for long term usage. Swadener and Nastasi (2003) showed that the Ne implantation to boron-doped silicon increases the fracture toughness of silicon. Such an increase can be beneficial for long term durability of resonating parts of MEMS sensors.

As discussed earlier, the reliability of packaging influences the long term usage of MEMS sensors in civil structures. Wafer level packaging increases the durability of the sensor as compared to component level packaging, especially for the sensors, which require a vacuum environment such as inertia sensors (Gooch *et al*., 1999). Packaging influences the damage level for accidental drops (Ghisi *et al*., 2009).

10.7 Conclusion and future trends

MEMS provide diverse micromachining processes, including bulk, surface, and LIGA, which allow designing unique microstructures for sensing and actuating. There are a wide variety of sensor materials and manufacturing options that can be modified for sensing need and environmental conditions. The most common microstructure material used in SHM is silicon. The transduction mechanism can be piezoresistive, capacitive, or piezoelectric. As compared to macro-scale sensors, residual film stress and squeeze film damping are two issues related to MEMS that should be considered in the design process. The sensor design and the final packaging should be designed in order to prevent failure. While there has been a remarkable progress in MEMS sensors in laboratory scale demonstrations, packaging is still a barrier for long term implementation of MEMS sensors in civil structures.

The future trends of MEMS for SHM are grouped as novel sensor designs to increase the localized information about the structural condition, durability demonstration, electronics integration on the wafer level, and intelligent data acquisition.

a. Novel sensor design: the uncertainties in the SHM methods require data fusion in order to develop reliable prognostic models. The diversity of materials and manufacturing methods available in the MEMS field allow designing novel sensor fusion opportunities to be manufactured on the same wafer. Discrete sensor elements (e.g., AE, accelerometer) on the same device can open tremendous opportunities in SHM of civil structures (e.g., Martinez *et al.*, 2012; Saboonchi and Ozevin, 2013b). Additionally, accelerometers with six degrees of freedom can be allocated in a miniaturized package. The additional localized information increases the interpretation of system behavior and change due to deterioration.
b. Durability demonstrations: MEMS implementation in the field is affected by unknown durability conditions for long term monitoring. The MEMS sensors need to be tested in the laboratory using accelerated test models, and their durability should be validated in the field using long term data acquisition (>1 year).
c. Electronics integration: the electronics for signal conditioning and computing systems should be incorporated into the same package of sensing element in order to reduce the noise level and increase long term durability. Wireless integration of MEMS sensors with energy harvesting devices opens new opportunities for the applications that require mass, space, and power constraints. MEMS sensors should be integrated with CMOS digital circuit technology to reduce the power consumption and cost, and to increase efficiency (Tan *et al.*, 2011).
d. Intelligent data acquisition: for intelligent data acquisition, RF MEMS switches can be integrated into the design as a trigger source in order to prevent the energy consumption and the record of unwanted information.

10.8 Sources of further information and advice

The further resources are divided into three parts: (1) books for in-depth understanding of MEMS materials, manufacturing methods and applications in SHM field, (2) commercial manufacturers and foundries that allow prototype designs, and (3) journal resources related to MEMS.

MEMS related books:
An Introduction to Microelectromechanical Systems Engineering by Nadim Maluf and Kirt Williams, Artech House, 2nd Edition
Advanced MEMS Packaging by John Lau and Cheng Lee
Foundations of MEMS by Chang Liu, Pearson Education Inc, 2nd Edition
Fundamentals of Microfabrication by Mark Madou, CRC, 2nd Edition
Introduction to MEMS: Fabrication and Application by T.M. Adams
MEMS and Microsystems by T.R. Hsu
MEMS and Nanotechnology Based Sensors by A.R. Jhan
MEMS Design and Fabrication, Edited by Mohamed Gad-el-Hak
MEMS Mechanical Sensors by Stephen Beeby, Graham Ensell, Michael Kraft and Neil White
Smart MEMS and Sensor Systems by Elena Gaura

Commercial manufacturers and foundries:
Analog Devices
Advanced MicroSensors
Colibrys
Coventor
Cronos
Standard MEMS
MEMS Exchange
MEMSIC
MEMSCAP (prototype foundry)

Journal resources:
Experimental Mechanics
IEEE Transactions on Ultrasonics, Ferroelectrics and Frequency Control
International Journal of Smart Structures and Systems
Journal of Aerospace Engineering
Journal of Bridge Engineering
Journal of Infrastructure Systems
Journal of Intelligent Materials and Systems
Journal of Structural Engineering
Journal of Structural Health Monitoring
Measurement Science and Technology
Sensors and Actuators A
Smart Materials and Structures

Structural Control and Health Monitoring
Structural Engineering and Mechanics
Ultrasonics

10.9 References

Amarashinghe, R., Dao, D.V., Toriyama, T. and Sugiyama, S. (2005) ‘Design and fabrication of a miniaturized six-degree-of-freedom piezoresistive accelerometer’, *Journal of Micromechanics and Microengineering*, Vol. **15**, pp. 1745–1753.

Amarashinghe, R., Dao, D.V., Toriyama, T. and Sugiyama, S. (2006) ‘Simulation, fabrication and characterization of a three-axis piezoresistive accelerometer’, *Smart Materials and Structures*, Vol. **15**, pp. 1691–1699.

Bagdahn, J. and Sharpe, W.N. (2003). ‘Fatigue of polycrystalline silicon under long-term cyclic loading’, *Sensors and Actuators A*, Vol. **103**, pp. 9–15.

Bahreyni, B., Najafi, F. and Shafai, C. (2006). ‘Piezoresistive sensing with twin-beam structures in standard MEMS foundry processes’, *Sensors and Actuators A*, Vol. **127**, pp. 325–331.

Barlian, A.A., Park, W.T, Mallon, J.R., Rastegar, A.J. and Pruitt, B.L. (2009). ‘Review: Semiconductor piezoresistance for microsystems’, *Proceedings of the IEEE*, Vol. **97**, No. 3, pp. 513–552.

Bashford, A.G., Schindel, D.W. and Hutchins, D.A. (1998). ‘Micromachined ultrasonic capacitance transducers for ımmersion applications’, *IEEE Transactions on Ultrasonics, Ferroelectrics, and Frequency Control*, Vol. **45**, No. 2, March, pp. 367–375.

Beeby, S., Ensell, G., Kraft, M. and White, N. (2004) *MEMS Mechanical Sensors*, Artech House Inc.

Chen, H., Bao, M. and Shen S. (1997). ‘A Piezoresistive accelerometer with a novel vertical beam structure’, *Sensors and Actuators A*, Vol. **63**, pp. 19–25.

Cho, S., Lynch, J.P., Lee, J.J. and Yun, C.B. (2010). ‘Development of an automated wireless tension force estimation system for cable-stayed bridges’, *Journal of Intelligent Material Systems and Structures*, Vol. **21**, pp. 361–376.

Choa, S.H. (2005). ‘Reliability of MEMS packaging: Vacuum maintenance and packaging induced stress’, *Microsystem Technology*, Vol. **11**, pp. 1187–1196.

Chung, H.C., Enomoto, T., Shunozuka, M., Chou, P., Park, C., Yokoi, I. and Morishita, S. (2004). ‘Real time visualization of structural response with wireless MEMS sensors’, *13th World Conference on Earthquake Engineering*, Vancouver, BC, Canada, 1–6 August, paper no 121.

Dienel, M., Naumann, M., Sorger, A., Tenholte, D., Voigt, S. and Mehner, J. (2012). ‘On the influence of vacuum on the design and characterization of MEMS’, *Vacuum*, Vol. **85**, pp. 535–545.

Elwenspoek, M. and Wiegerink, R.J. (2001). *Mechanical Microsensors*, 1st edition, Springer-Verlag, Berlin, Germany.

Feng, G.H. and Tsai, M.Y. (2010). ‘Acoustic emission sensor with structure-enhanced sensing mechanism based on micro-embossed piezoelectric polymer’, *Sensors and Actuators A: Physical*, Vol. **162**, pp. 100–105.

Fu, X.A., Dunning, J.L., Mehregany, M. and Zorman, C.A. (2011)‘Low stress polycrystalline sic thin films suitable for MEMS applications’, *Journal of the Electrochemistry Society*, Vol. **158**, No. 6, pp. 675–680.

Gaucher, P. (2002). 'Piezoelectric micro-electro-mechanical systems for acoustic application', Workshop 'Piezoelectric for the End User', *Interlaken*, 25–27 February.

Ghisi, A., Fachin, F., Mariani, S. and Zerbini, S. (2009). 'Multi-scale analysis if polysilicon MEMS sensors subjected to accidental drops: Effect of packaging', *Microelectronics Reliability*, Vol. **49**, pp. 340–349.

Giurgiutiu, V. (2008). *Structural Health Monitoring with Piezoelectric Wafer Active Sensors*. Academic Press.

Glaser, S.D., Li, H., Wang, M.L., Qu, J. and Lynch, J. (2007).'Sensor technology innovation for the advancement of structural health monitoring: A strategic program of US-China research for the next decade', *Smart Structures and Systems*, Vol. **3**, No. 2, pp. 221–244.

Gooch, R., Schimert, T., McCardel, W., Ritchey, B., Gilmour, D. and Koziarz, W. (1999). 'Wafer-level vacuum packaging for MEMS', *Journal of Vacuum Science and Technology*, Vol. **17**, No. 4, pp. 2295–2299.

Harris, A.W., Oppenheim, I.J. and Greve, D.W. (2011). 'MEMS-based high-frequency vibration sensors', *Smart Materials and Structures*, Vol. **20**, pp. 1–9.

Hautefeuille, M., O'Flynn, B., Peters, F. and O'Mahony, C. (2009).'Miniaturised multi-MEMS sensor development', *Microelectronics Reliability*, Vol. **49**, pp. 621–626.

Hindriches, C.C., Almind, N.S., Brodersen, S.H., Lou-Møller, R., Hansen, K. and Thomsen, E.V. (2010). 'Triaxial MEMS accelerometer with screen printed PZT thick film', *Journal of Electroceramics*, Vol. **25**, No. 2–4, pp. 108–115.

Huang, Y., Vasan, A.S.S., Doraiswami, R., Osterman, M. and Pecht, M. (2012). 'MEMS reliability review', *IEEE Transactions on Device and Materials Reliability*, Vol. **12**, No. 2, pp. 482–493.

Jain, A. (2002).*In Situ Ultrasonic MEMS Transducer for Detecting Flaws in Structural Materials*, M.S. Thesis, Carnegie Mellon University.

Jiang, L. and Cheung, R. (2009). 'A review of silicon carbide development in MEMS applications', *International Journal of Computational Materials Science and Surface Engineering*, Vol. **2**, No. 3–4, pp. 227–242.

Jin, X., Ladabaum, I. and Khuri-Yakub, B.T. (1998). 'The microfabrication of capacitive ultrasonic transducers', *IEEE Journal of Microelectromechanical Systems*, Vol. **7**, No. 3, September, pp. 295–302.

Jin, X., Ladabaum, I., Degertekin, F.L., Calmes, S. and Khuri-Yakub, B.T. (1999). 'Fabrication and characterization of surface micromachined capacitive ultrasonic ımmersion transducers', *IEEE Journal of Microelectromechanical Systems*, Vol. **8**, No. 1, March, pp. 100–114.

Jo, H., Sim, S.H., Nagayama, T. and Spencer, B.F. (2012). 'Development and application of high-sensitivity wireless smart sensors for decentralized stochastic modal identification', *ASCE Journal of Engineering Mechanics*, Vol. **138**, No. 6, pp. 683–694.

Kanda, Y. (1982). 'A graphical representation of the piezoresistance coefficients in silicon', *IEEE Transactions on Electron Devices*, Vol. **ED-29**, No. 1, January, pp. 64–70.

Khuri-Yakub, B.T., Degertekin, F.L., Jin, X.-C., Calmes, S., Ladabaum, I., Hansen, S. and Zhang, X.J. (1998). 'Silicon micromachined ultrasonic transducers', *IEEE Ultrasonics Symposium*, Vol. **2**, pp. 985–991.

Kim, H., Kim, W., Kim, B.Y. and Hwang, J.S. (2008). 'System identification of a building structure using wireless MEMS and PZT sensors', *Structural Engineering and Mechanics*, Vol. **30**, No. 2, pp. 191–209.

Kim, Y., Kim, Y., Lee, C. and Kwon, S. (2010). 'Thin polysilicon gauge for strain measurement of structural elements', *IEEE Sensors Journal*, Vol. **10**, No. 8, pp. 1320–1327.

Kok, R. and Furlong, C. (2005). 'Development and characterization of a wireless MEMS inertial system for health monitoring of structures Part I: Description of sensor and data acquisition system', *Experimental Techniques*, Vol. **29**, No. 6, November, pp. 46–49.

Ladabaum, I., Jin, X., Soh, H.T., Atalar, A. and Khuri-Yakub, B.T. (1998).'Surface micromachined capacitive ultrasonic transducer', *IEEE Transactions on Ultrasonics, Ferroelectrics, and Frequency Control*, Vol. **45**, No. 3, May, pp. 678–689.

Li, P., Gao, S., Liu, H., Liu, J. and Shi, Y. (2013). 'Effects of package on the performance of MEMS piezoresistive accelerometers', *Microsystem Technologies,* Vol. **19**, pp. 1137–1144.

Lim, M.K., Du, H., Su, C. and Lin, W.L. (1999). 'A micromachined piezoresistive accelerometer with high sensitivity: Design and modelling', *Microelectronic Engineering*, Vol. **49**, pp. 263–272.

Lynch, J.P. and Loh, K.J. (2006). 'A summary review of wireless sensors and sensor networks for structural health monitoring', *The Shock and Vibration Digest*, Vol. **38**, pp. 91–128.

Lynch, J.P., Partridge, A., Law, K.H., Kenny, T.W., Kiremidjian, A.S. and Carryer, E. (2003). 'Design of piezoresistive MEMS-based accelerometer for integration with wireless sensing unit for structural monitoring', *Journal of Aerospace Engineering*, July, pp. 108–114.

Lynch, J.P., Wang, Y., Loh, K.J., Yi, J.H. and Yun, C.B. (2006). 'Performance monitoring of the geumdang bridge using a dense network of high-resolution wireless sensors', *Smart Materials and Structures*, Vol. **15**, pp. 1561–1575.

Madou, M.J. (2002). *Fundamentals of Micromachining*, 2nd Edition, CRC Press, Boca Raton, FL, USA.

Mariani, S., Corigliano, A., Caimmi, F., Bruggi, M., Bendiscioli, P. and Fazio, M.D. (2013). 'MEMS-based surface mounted health monitoring system for composite laminates', *Journal of Microlectronics,* Vol. **44**, pp. 598–605.

Marrero, V., Borca-Tasciuc, D.A. and Ticky, J. (2010). 'On squeeze film damping in microsystems', *Journal of Tribology*, Vol. **132**, pp. 1–6.

Martinez, M., Rocha, B., Li, M., Shi, G., Beltempo, A., Rutledge, R. and Yanishevsky, M. (2012). 'Load monitoring of aerospace structures utilizing micro-electro-mechanical-systems for static and quasi-static loading conditions', *Smart Materials and Structures*, Vol. **21**, No. 11, pp. 1–11.

Mehregany, M. and Zorman, C.A. (1999) 'SiC MEMS: Opportunities and challenges for applications in harsh environments', *Thin Solid Films*, Vol. **355–356**, pp. 518–524.

Mohammed, A.A.S., Moussa, W.A. and Lou, E. (2011). 'Development and experimental evaluation of a novel piezoresistive MEMS strain sensor', *IEEE Sensor Journal*, Vol. **11**, No. 10, pp. 2220–2232.

Muhlstein, C.L., Howe, R.T. and Ritchie, R.O. (2004). 'Fatigue of polycrystalline silicon for microelectromechanical system applications: Crack growth and stability under resonant loading conditions', *Mechanics of Materials*, Vol. **36**, pp. 13–33.

Muralt, P. (2008). 'Recent progress in materials issues for piezoelectric MEMS', *Journal of the American Ceramic Society*, Vol. **91**, No. 5, pp. 1385–1396.

Muralt, P., Ledermann, N., Baborowski, J., Barzegar, A., Gentil, S., Belgacem, B., Petitgrand, S., Bosseboeuf, A. and Setter, N. (2005). 'Piezoelectric micromachined ultrasonic transducers based on PZT thin films', *IEEE Transductions on Ultrasonics, Ferroelectrics, and Frequency Control*, Vol. **52**, No. 12, December, pp. 2276–2288.

Nathan, A. and Baltes, H. (1999). *Microtransducer CAD: Physical and Computational Aspects*. Springer, Wien New York.

Norris, A., Saafi, M. and Romine, R. (2006). 'Temperature and moisture monitoring in concrete structures using embedded nanotechnology/microelectromechanical systems (MEMS) sensors', *Construction and Building Materials*, Vol. **22**, pp. 111–120.

Obadat, M., Lee, H.D., Bhatti, M.A. and Maclean, B. (2003). 'Full-scale field evaluation of microelectromechanical system-based biaxial strain transducer and its application in fatigue analysis', *Journal of Aerospace Engineering*, Vol. **16**, No.3, July, pp. 100–107.

Oppenheim, I.J., Jain, A. and Greve, D.W. (2003a). 'Electrical characterization of coupled and uncoupled MEMS ultrasonic transducers', *IEEE Transactions on Ultrasonics, Ferroelectrics, and Frequency Control*, Vol. **50**, No. 3, March, pp. 297–304.

Oppenheim, I.J., Jain, A. and Greve, D.W. (2003b). 'MEMS ultrasonic transducers for the testing of solids', *IEEE Transactions on Ultrasonics, Ferroelectrics, and Frequency Control*, Vol. **50**, No. 3, March, pp. 305–311.

Ozevin, D. (2005). *Capacitive MEMS Transducers for Acoustic Emission Testing of Materials and Structures*. Ph.D. Dissertation, Lehigh University.

Ozevin, D., Greve, D.W., Oppenheim, I.J. and Pessiki, S.P. (2006). 'Resonant capacitive MEMS acoustic emission transducers', *Smart Materials and Structures*, Vol. **15**, 2006, pp. 1863–1871.

Partridge, A., Reynolds, J.K., Chui, B.W., Chow, E.M., Fitzgerald, A.M., Zhang, L., Maluf, N.I. and Kenny, T.W. (2000). 'A high-performance planar piezoresistive acceleration', *Journal of Micromechanical Systems*, Vol. **9**, No. 1, pp. 58–66.

Ramos, L.F., Aguilar, R. and Lourenco, P.B. (2010). 'Operational modal analysis of historical constructions using commercial wireless platforms', *International Journal of Structural Health Monitoring*, Vol. **10**, No. 5, pp. 511–521.

Romig, Jr A.D., Dugger, M.T. and McWhorter, P.J. (2003). 'Materials issues in microelectromechanical devices: Science, engineering, manufacturability and reliability', *Acta Materialia*, Vol. **51**, pp. 5837–5866.

Roylance, L.M. and Angell, J.B. (1979). 'A batch-fabricated silicon accelerometer', *IEEE Transactions on Electron Devices*, Vol. **26**, No. 12, pp. 1911–1917.

Saboonchi, H. and Ozevin, D. (2012). 'Numerical demonstration of MEMS strain sensor', *Proceedings of SPIE Smart Materials and Structures*, Vol. **8345**, pp. 83451H.

Saboonchi, H. and Ozevin, D. (2013a). 'MEMS acoustic emission transducers designed with high aspect ratio geometry', *Smart Materials and Structures*, Vol. **22**, No. 9, pp. 1–14.

Saboonchi, H. and Ozevin, D. (2013b). 'Combined MEMS acoustic emission and strain sensors for on chip data fusion', *9th International Workshop on Structural Health Monitoring*, 10–12 September, Stanford CA.

Schoess, J.N. and Zook, J.D. (1998). 'Test results of resonant integrated microbeam sensor (RIMS) for acoustic emission monitoring', *Journal of Intelligent Material Systems and Structures*, Vol. **9**, November, pp. 947–951.

Smith, C.S. (1954). 'Piezoresistance effect in germanium and silicon', *Physical Review*, Vol. **94**, No. 1, pp. 42–49.

Song, Y.T., Lee, H.Y. and Esashi, M. (2007). 'A corrugated bridge of low residual stress for RF-MEMS switch', *Sensors and Actuators A*, Vol. **135**, pp. 818–826.

Sosnowchik, B.D., Azevedo, R.G., Myers, D.R., Chan, M.W., Pisano, A.P. and Lin, L. (2012). 'Rapid silicon-to-steel bonding by induction heating for MEMS strain sensors', *Journal of Microelectromechanical Systems*, Vol. **21**, No. 2, pp. 497–506.

Spearing, S.M. (2000). 'Materials issues in microelectromechanical systems (MEMS)', *Acta Materialia*, Vol. **48**, 179–176.

Swadener, J.G. and Nastasi, M. (2003). 'Increasing the fracture toughness of silicon by ion implantation', *Nuclear Instruments and Methods in Physics Research B*, Vol. **206**, pp. 937–940.

Tadigadapa, S. and Mateti, K. (2009). 'Piezoelectric MEMS sensors: State of the art and perspectives', *Measurement Science and Technology*, Vol. **20**, No. 9, pp. 1–30.

Tan, S.S., Liu, C.Y., Yeh, L.K., Chiu, Y.H. and Hsu, K.Y.J. (2011). 'A new process for CMOS MEMS capacitive sensors with high sensitivity and thermal stability', *Journal of Micromechanical and Microengineering*, Vol. **21**, pp. 1–10.

Tanner, D.M. (2009). 'MEMS reliability: Where are we now?', *Microelectronics Reliability*, Vol. **49**, pp. 937–940.

Tonisch, K., Cimalla, V., Foerster, Ch., Romanus, H., Ambacher, O. and Dontsov, D. (2006). 'Piezoelectric properties of polycrystalline AlN thin films for MEMS application', *Sensors and Actuators A*, Vol. **132**, pp. 658–663.

Torfs, T., Sterken, T., Brebels, S., Santana, J., Hoven, R.V.D., Spiering, V., Bertsch, N., Trapani, D. and Zonta, D. (2013). 'Low power wireless sensor network for building monitoring', *IEEE Sensors*, Vol. **13**, No. 3, pp. 909–915.

Van Driel, W.D., Yang, D.G., Yuan, C.A., Van Kleef, M. and Zhang, G.Q. (2007). 'Mechanical reliability challenges for MEMS packages: Capping', *Microelectronics Reliability*, Vol. **47**, pp. 1823–1826.

Vinokur, R., (2003). 'Vibroacoustic effects in MEMS', *Sound and Vibration*, September, pp. 22–26.

Walraven, J.A. (2005). 'Failure analysis in microelectromechanical systems (MEMS)', *Microelectronics Reliability*, Vol. **45**, pp. 1750–1757.

Walwadkar, S.S. and Cho, J. (2006). 'Evaluation of die stress in MEMS packaging: Experimental and theoretical approaches', *IEEE Transactions on Components and Packaging Technologies*, Vol. **29**, No. 4, pp. 735–742.

Wang, L.-P., Deng, K., Zou, L., Wolf, R., Davis, R.J. and Trolier-McKinstry, S. (2002). 'Microelectromechanical systems (MEMS) accelerometers using lead zirconate titanate thick films', *IEEE Electron Device Letters*, Vol. **23**, No. 4, pp. 182–184.

Waterfall, T.L., Johns, G.K., Messenger, R.K., Jensen, B.D., McLain, T.W. and Howell, L.L. (2008). 'Observations of piezoresistivity for polysilicon in bending that are unexplained by linear models', *Sensors and Actuators A*, Vol. **141**, pp. 610–618.

Wright, N.G. and Horsfall, A.B. (2007). 'SiC sensors: A review', *Journal of Physics D: Applied Physics*, Vol. **40**, pp. 6345–6354.

Yu, H.G., Zou, L., Deng, K., Wolf, R., Tadigadapa, S. and Trolier-McKinstry, S. (2003). 'Lead zirconate titanate MEMS accelerometer using interdigitated electrodes', *Sensors and Actuators A*, Vol. **107**, pp. 26–35.

Yu, Y., Qu, J., Zhang, C. and Li, L. (2009). 'Development of wireless MEMS inclination sensor system for swing monitoring of large scale hook structures', *IEEE Transactions on Industrial Electronics*, Vol. **56**, No. 4, pp. 1072–1078.

Zorman, C.A. and Mehregany, M. (2006). *Materials for Microelectromechanical Systems*. Chapter 2 of MEMS design and fabrication edited by Mohamed Gad-el-Hak.

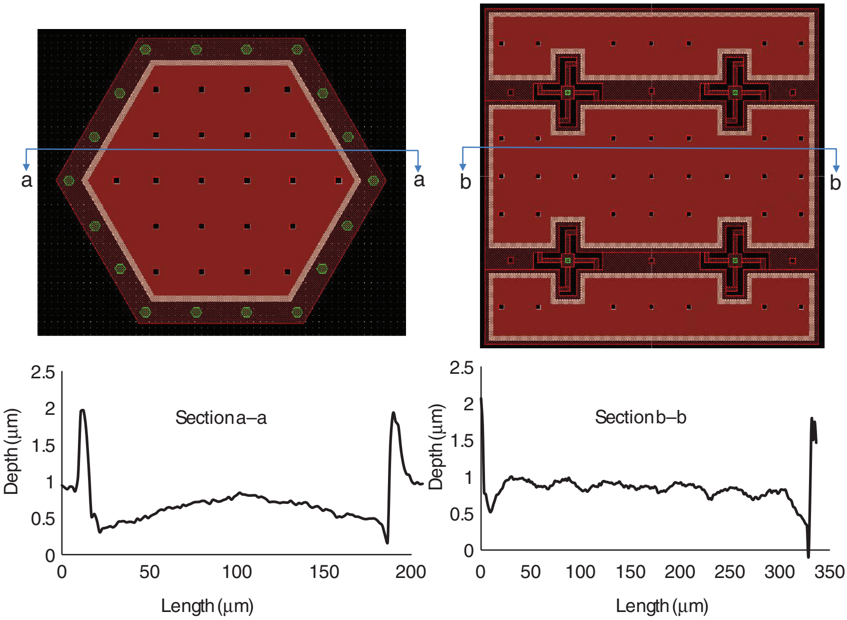

Plate VI (Chapter 10) Profilometer measurements of two capacitive sensor designs by Ozevin (2005) (Ozevin, D. (2005). *Capacitive MEMS Transducers for Acoustic Emission Testing of Materials and Structures*. Ph.D. Dissertation, Lehigh University).

11

Multifunctional materials and nanotechnology for assessing and monitoring civil infrastructures

K. J. LOH and D. RYU, University of California-Davis, USA

DOI: 10.1533/9780857099136.295

Abstract: Multifunctional materials, or material systems intentionally encoded with a multitude of engineering functionalities, are revolutionizing civil engineering practice by offering new materials that can resist loads and self-sense for damage. These new developments have been made possible by technological breakthroughs in the nanotechnology domain. New nanomaterials with impressive properties and scalable manufacturing methods have enabled the design of these multifunctional materials or composite structures. The objective of this chapter is to showcase three types of nanotechnology-enabled multifunctional materials that have impacted, and will continue to impact, the civil engineering community. Particular attention will be paid to materials assembled using two unique nanomaterials, namely carbon black and carbon nanotubes.

Key words: carbon nanomaterials, fiber-reinforced polymer composite, multifunctional, nanocomposite, smart concrete, sensing.

11.1 Introduction

Multifunctional materials, or material systems intentionally encoded with a multitude of engineering functionalities, have been regarded as potential candidates for revolutionizing the current state-of-practice in structural health monitoring (SHM). Unlike traditional technologies that only perform a specific task, multifunctional systems are tailored to simultaneously perform combinations of sensing, actuation, energy harvesting, mechanical reinforcement, thermal exchange, and energy dissipation, among many others.[1] For instance, conventional coatings seek to achieve multifunctionality by stacking individual functional layers to obtain a multilayered architecture.[2] An example is using separate coatings for thermal insulation, resisting wear, and corrosion protection of aircraft components.[3–5] On the other hand, functionally graded materials are being considered as alternatives to address issues of compatibility and adhesion between disparate layers,[6–8] although

© 2014 Woodhead Publishing Limited

it remains challenging to incorporate drastically different functionalities in one material. In contrast, the new domain of multifunctional materials seeks to encode diverse performance attributes in what is often a homogeneous structure.[9–12]

Technological breakthroughs over the last few decades in the nanotechnology domain have brought forth a plethora of new materials, tools, and methods that have enabled the assembly of revolutionary multifunctional materials.[11,13] Nanomaterials such as quantum dots, nanoparticles, fullerenes, nanotubes, and nanowires offer drastically unique material properties as compared to their bulk counterparts. On another front, the atomic force microscope, scanning tunneling microscope, and focused ion beam lithography, to name a few, have permitted imaging and manipulation of individual atoms and molecules. In essence, nanotechnology offers new ways for isolating, controlling, and assembling nanostructured morphologies for attaining high-performance functional systems.[14] 'Bottom-up' assembly by building materials starting at molecular length scales to achieve precise properties in bulk-scale systems is now possible.

The remainder of this chapter is organized into five sections. Section 11.2 begins with the introduction of two types of nanomaterials that will be the focus of this chapter, namely carbon black (CB) and carbon nanotubes (CNT). The next three sections discuss how these carbon-based nanomaterials can be integrated in different composite architectures to improve structural performance and to encode strain sensitivity or piezoresistivity. Strain sensing is of focus here, because these measurements are critical for SHM. Localized large strain measurements point to the possibility of excessive deformation or cracks, or measured strains can be directly correlated to stress fields in structural components. Section 11.3 showcases how carbon nanomaterials can be incorporated to form *smart* concrete or cementitious composites (e.g., mortar, cement mixtures, and reinforced concrete) as next-generation civil infrastructure materials. Section 11.4 is on fiber-reinforced polymer (FRP) composites, which are used primarily for aerospace, naval, and specialized civil structures (e.g., column retrofits, wind turbine blades, etc.). Section 11.5 focuses on nanocomposite coatings or thin films that can be applied onto structural surfaces. Finally, the chapter concludes with a brief summary and discussion of future trends in Section 11.6.

11.2 Properties of carbon nanomaterials

Among the diverse selection of nanomaterials, CB and CNT have attracted considerable attention in academic research and commercial developmental realms. First, CB is produced by the partial combustion of hydrocarbons.[15] While they are similar to soot, the main difference is that CB exhibits greater order, often characterized by a spherical shape with diameters ranging between 100 nm and 1 μm. Its physical morphology represents that of randomly oriented graphitic layers aggregated to form a spherical structure. It is this unique microstructure that also provides CB with interesting material properties that have motivated their use for various applications. For instance, CB density ranges from 2.05 to 2.11 g-cm^{-3}, and electrically, they are also semiconducting.[15,16] Their unique properties, wide availability, and relative low costs have promoted their use in applications such as improving the tear resistance in automobile tires, printer/copier toner pigments, and UV protection for plastics, among others.[15,16]

Second, CNTs are specific examples within a new class of nanomaterials characterized by nanometer dimensions with superior intrinsic electronic, mechanical, chemical, thermal, and optical properties that greatly differ from bulk carbon.[17,18] It is their spectacular properties that have motivated many to take advantage of single-walled carbon nanotubes (SWNT) and multi-walled carbon nanotubes (MWNT) for various applications.[19] In short, SWNTs physically comprise a single rolled sheet of graphite (or graphene) to form a cylindrical structure, and MWNTs are typically characterized by SWNTs stacked together concentrically.[19] An illustration of an SWNT is shown in Fig. 11.1. The diameter of a typical SWNT ranges between 0.4 and 2.0 nm, and they also possess high aspect ratios (greater than 10^4) that are ideal for surface functionalization.[19] Mechanically, SWNTs' Young's modulus (E) and their ultimate tensile strength (σ_f) have been estimated to be $E \approx 1.1$ TPa and $\sigma_f \approx 75$ GPa, respectively; for MWNTs, they are $E \approx 1.2$ TPa and $\sigma_f \approx 150$ GPa.[20] The electrical properties of SWNTs can be either metallic or semiconducting depending on chirality (i.e., the direction of rolling the graphene sheet).[21] Khare and Bose[22] and Kang *et al.*[23] have compiled comprehensive reviews of CNT synthesis methodologies and their impressive material properties. Despite the fact that CNTs have only been recently discovered (in 1991 by Iijima[18]), they are readily available and can be

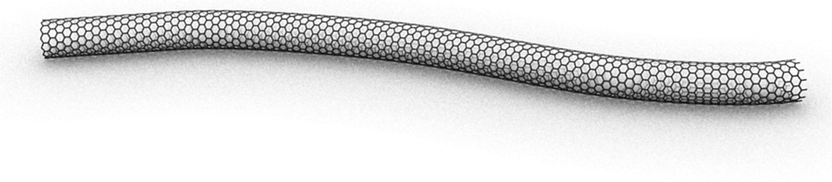

11.1 An illustration of a single-walled carbon nanotube shows that it physically represents a single sheet of graphene rolled to form its cylindrical structure. (*Source*: Image provided courtesy of Dr James Hedberg.)

Table 11.1 The properties of various types of carbon nanotubes sold by different companies

Company	Helix Material Solutions (TX, USA)			Nanocyl (Belgium; MA, USA)		Cheap tubes (VT, USA)		Unidym (CA, USA; Japan)		Nanostructured and Amorphous Materials (TX, USA)		SouthWest NanoTechnologies (OK, USA)	
CNT type	SWNT	SWNT	MWNT	SWNT	MWNT	SWNT	MWNT	SWNT	SWNT	SWNT	MWNT	SWNT	MWNT
Product # or grade	[1]HP	[2]ARC	–	NC1100	NC3100	SKU-0101	SKU-030102	[3]R	[4]P	1283YJ	1204YJ	SG65i	SMW100
Synthesis technique	[5]CVD	ARC	CVD	[6]CCVD		CCVD		[7]HiPCO		CCVD		[8]CoMoCAT®	
Outer diameter (nm)	≤1.3	1.2 ~1.5	10 ~30	2	9.5	1 ~2	8 ~15	0.8 ~1.2	0.8 ~1.2	1 ~2	8 ~15	0.76 ~0.78	6 ~9
Length (μm)	0.5 40	0.5 ~3	0.5 ~40	Several	1.5	5 ~30	10 ~50	0.1 ~1	0.1 ~1	5 ~30	10 ~50	–	1~13
Specific surface area (m^2-g^{-1})	300 ~600	300 ~600	40 ~300	1000	N/A	407	233	1000	1000	360 ~400	180 ~240	–	–
CNT purity ((%))	90	50 ~70	95	70	90	90	95	65	85	90	95	95	98
Price (US$ /10 g)	1600	700	190	–	–	975	75	5500	7700	350	170	4500	50

[1]HP: High purity; [2]ARC: Arc discharge growth; [3]R: Regular; [4]P: Purified; [5]CVD: Chemical vapor deposition; [6]CCVD: Catalytic chemical deposition; [7]HiPCO: High pressure carbon monoxide conversion; [8]CoMoCAT®: CO catalytic disproportionation with Mo.

Note: The information contained in this table is obtained from each company's website or by contacting a sales representative. The data is accurate as of November 2012.

purchased from companies around the world. Table 11.1 summarizes some of the different types of nanotubes (as well as their properties) offered by select companies (note that this is only a small subset of all companies that sell CNTs).

In order to harness the impressive material properties offered by nanomaterials such as CBs and CNTs at macro-length scales, these materials have been incorporated in devices such as nanoelectronics,[24] ultra-strong nanocomposites,[25,26] and various sensors,[27,28] among others.[21] However, incorporation of nanomaterials is met by two primary challenges, namely the dispersion of them into solution and the assembly of homogeneous percolated nanocomposites. Dispersion of nanomaterials is difficult due to their hydrophobic nature and strong van der Waals force interactions that promote aggregation and clumping.[29] Many studies have demonstrated success with dispersing nanotubes via covalent surface modification (e.g., oxidation and functionalization)[30] and steric stabilization (i.e., using surfactants, DNA, or organic solvents).[31] Even with CNTs dispersed in solution, the second challenge is to incorporate them effectively in composite architectures for its intended application. The remainder of this chapter illustrates how CBs and CNTs have been used for various composite architectures, namely cementitious-based composites in Section 11.3, fiber-reinforced polymer (FRP) composites in Section 11.4, and thin film coatings in Section 11.5.

11.3 Cementitious-based composites

To date, one of the most widely adopted construction materials for bridges, buildings, dams, and roadways, among others, is concrete.[32] In general, concrete exhibits excellent compressive strength but cannot withstand substantial tensile loads and deformation, which can result in sudden catastrophic failure due to its brittle nature.[33] Although steel reinforcement bars provide enhanced tensile load carrying capacity for this composite structure, the cementitious matrix still undergoes large cracks during applied tensile loads. By embedding fibers that can bridge these large cracks, fiber-reinforced concrete (FRC) benefits from enhanced ductility and strain capacity.[34] Further improvements to this technology have been achieved by the development of high-performance fiber-reinforced cementitious composites (HPFRCC) or engineered cementitious composites (ECC).[35,36] Similar to concrete, the material is fabricated from a mixture of cement, silica, sand, and water but with the addition of small amounts of steel, glass, carbon, or polymeric fibers.[37] Designed from a theoretical micromechanics principle,[38] these HPFRCC and ECC materials can undergo significant strain hardening via the formation of multiple and distributed micro-cracks due to fiber internal friction, deformation, and pull-out mechanisms.[39] The end result is improved mechanical and life-cycle properties.

Cementitious materials are inherently multifunctional. Not only are they used for carrying load, they are also piezoresistive by nature (i.e., their electrical properties change in response to applied strain).[12,40,41] However, their inherent piezoresistive strain sensitivity (or gage factor) is fairly low; their electrical properties do not change significantly in response to even large applied strains. Thus, by embedding conductive fillers such as fibers or particles within cement-based materials, experimental research by Chung[42] and theoretical calculations by Garas and Vipulanandan[43] have shown that cementitious composites such as FRC possess enhanced piezoresistivity. Hou and Lynch[44] have also validated the self-sensing performance of ECC composed of short poly(vinyl alcohol) (PVA) fibers. In general, Garas and Vipulanandan[43] report that the FRC's gage factor can double when the conductive filler weight concentration is increased from 3% to 6%. A study conducted by Chung[42] also explores how different concentrations and types (i.e., steel or carbon) of short and continuous fibers modify the material's inherent piezoresistivity. Most of these aforementioned studies have focused on using macro-sized fillers/fibers. It has been envisioned that nanomaterials embedded in cementitious composites can further enhance mechanical and sensing properties to achieve next-generation *smart* concrete structures.

11.3.1 Smart concrete fabrication and nanomaterial dispersion

The fabrication of *smart* concrete (i.e., ones with embedded nanomaterials) is similar to conventional concrete manufacturing procedures and will be described in this section. The main ingredients are cement, water, sand/silica, and the nanomaterial of choice. First, Portland cement and sand/silica are mixed in a rotary mixer. Second, the appropriate amount of water is measured in a separate container; typical water-to-cement ratios used range from 0.22 to 0.60.[45–48] Then, CB, or CNTs can be dispersed in water, or they can be added in their dry state to the cement–sand/silica mixture. Regardless, cement, sand/silica, water, and nanomaterials are then mixed thoroughly in a mixer for several minutes. The mixture is then poured into oiled molds and left to cure for 24 h. Finally, the specimens are demolded and cured in a humid environment, typically for 28 days. These specimens are often dried in an oven if *smart* concrete specimens are to be tested in the laboratory.

Three different methods can be used to disperse CBs or CNTs in water. First, Manzur and Yazdani[46] have mixed MWNTs in water by hand, followed by subjecting the mixture to 30 min of bath ultrasonication to disperse the nanotubes. A second alternative is to dissolve a water-reducing or superplasticizer agent in water, adding the nanomaterial, followed by the manual mixing or sonication of the solution to achieve dispersion.[48–50] The third technique is to disperse nanomaterials in dilute aqueous surfactant solutions, again via ultrasonication. For example, Han *et al.*[45] have used sodium dodecylbenzene sulfonate (NaDDBS), Yu and Kwon[51] have used sodium dodecyl sulfate (SDS) and Wille and Loh[48] have employed poly(sodium 4-styrenesulfonate) (PSS) as dispersing agents. It should be mentioned that this technique often also requires the addition of a defoamer or superplasticizer. However, the dispersion or the separation of carbon nanomaterials into its individual units is extremely difficult to accomplish.[52] They tend to aggregate and agglomerate due to their high surface energies and strong van der Waals forces.[29] Issues with regards to dispersing CNTs in cement matrices have been reported by Wansom *et al.*[53]

11.3.2 Strain sensing

To date, several works have been accomplished to enhance the inherent piezoresistivity of cement-based materials by the addition of CBs[49,54] and CNTs.[41,53] In fact, Li *et al.*[49] have shown that the inherent electrical resistivity of cementitious composites can decrease by two orders of magnitude when the volume fraction of CB is increased from 3% to 14%. In addition, the percolation threshold has been estimated to be between 7% and 11%, and tunneling is suspected to be the primary mechanism that enhances the composite's electrical conductivity and piezoresistivity. Similar enhancements in electrical conductivity and strain/pressure sensing performance have been obtained by Li *et al.*;[41] instead of using CB, 0.5 wt.% of untreated and treated CNTs (i.e., chemically oxidized) have been incorporated within the cementitious matrix. It has been determined that the high strain sensitivity of the composite is due to: nanotube's inherent piezoresistive behavior,[55] number of nanotube-to-nanotube junctions, and the effect of field emission during mechanical load testing.[41] Han *et al.*[45] have proposed the use of *smart* concrete modified with 0.1 wt.% MWNT for traffic monitoring applications such as vehicle detection, weigh-in-motion, and speed measurements (Plate VII in the color section between pages 294 and 295). The technology has been implemented in a test roadway, and sensor readouts are noticeably different depending on the size of the vehicle driven over the self-sensing concrete (i.e., passenger vehicle versus mini-van). Figure 11.2 shows two resistance time histories as measured from the self-sensing concrete, and it is clear that the size and number of vehicles can be differentiated based on these measurements. Saafi[56] has shown that strain measured by *smart* concrete can also be interrogated wirelessly using a commercial off-the-shelf system. These studies show that this technology is at the cusp of field and commercial adoption, provided that larger-scale and long-term studies are conducted to assess their viability over time.

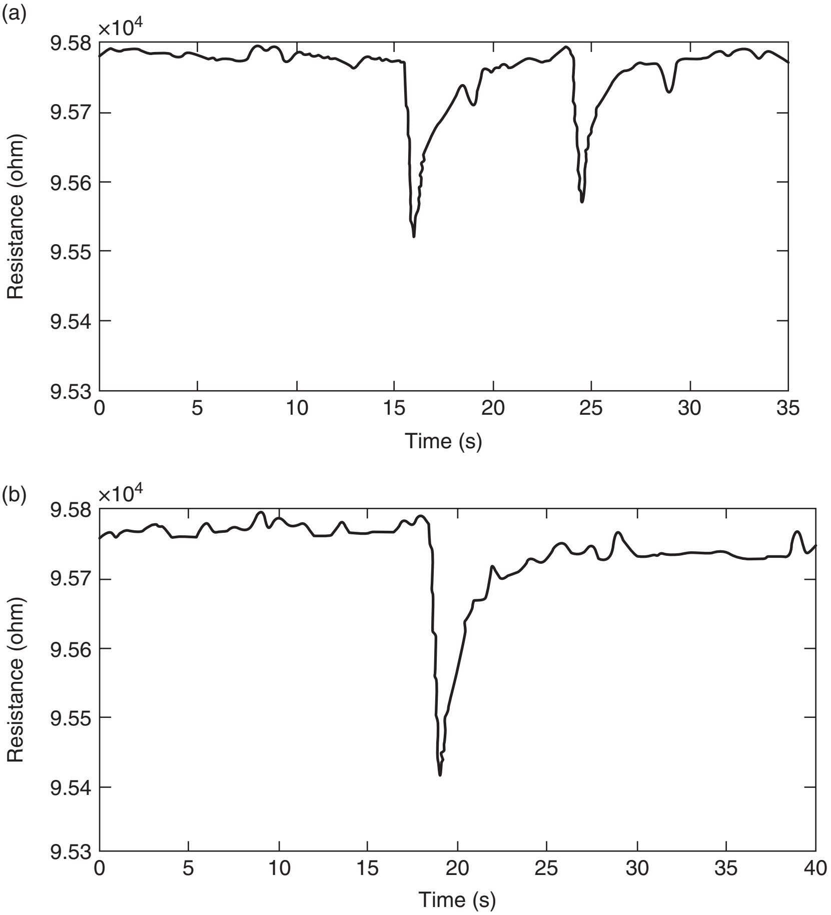

11.2 Han *et al.*[45] have measured the resistance time history of a self-sensing CNT/cement composite embedded in a test roadway. The sensor has successfully detected the (a) passing of two mid-sized passenger vehicles and (b) a mini-van. (*Source*: Image provided courtesy of IOP.)

11.3.3 Mechanical reinforcement

In addition to the enhancement of electronic properties, carbon nanomaterials have also been studied with the goal of improving the mechanical response of cementitious composites. Early investigations have suggested that significant improvements in the mechanical properties (i.e., compressive strength and failure strain) of MWNT-reinforced cement may be difficult to achieve.[57] However, this is likely due to poor dispersion of nanotubes. Musso *et al.*[50] have studied how different types of MWNTs (i.e., as-grown, annealed, and functionalized) in a concentration of 0.5 wt.% in plain cement can influence the composite's bulk compressive properties. It has been found that the modulus-of-rupture and compressive resistance decreased significantly when functionalized nanotubes have been used, which is primarily due to their strong hydrophilic nature and thus limited cement hydration. On the other hand, annealed and pristine MWNTs show enhancements in mechanical properties.[50] Similar conclusions have also been reached by Manzur and Yazdani,[46] where higher water-to-cement ratios are needed for proper hydration and strength enhancement. It has also been observed that 0.3 wt.% MWNTs and smaller-sized MWNTs provide greatest compressive strengths based on the results obtained from a parametric study.

11.4 Fiber-reinforced polymer composites

FRP composites fabricated from epoxy-bonded carbon-, aramid-, or glass-fiber laminates are widely adopted for various engineering applications, particularly for aerospace/naval vessels and civil infrastructure repair, upgrade, retrofit, or new construction.[58–60] Their low density, high strength-to-weight ratio, corrosion resistance, cost effectiveness, and conformability make them ideally suited for these applications.[60–62] For example, FRP-retrofitted concrete beams exhibit a 46–90% strength increase (as well as stiffness enhancements) as confirmed by laboratory validation studies.[63] Examples of real-world implementations of FRP jacketing and new constructions are witnessed worldwide, including the Palazzo Elmi-Pandolfi historical building (Foligno, Italy),[58] the Interstate-80 State Street Bridge (Salt Lake City, UT),[64] and the Kings Stormwater Channel Composite Bridge's FRP-based bridge deck (Riverside County, CA),[59] and others.[65] In addition, the American Composites Manufacturers Association (ACMA) reports that 256 FRP composite civilian bridges (i.e., 121 pedestrian and 135 vehicular bridges) are in service as of 2003.[66] Besides civil structures, recent aerospace vessels (e.g., Airbus A350, Boeing 787, and F-35) and wind turbines blades have up to half of their structural weight fabricated from carbon- or glass-FRP composites.[67]

Despite the performance improvements offered by FRPs, these materials are susceptible to damage such as matrix cracking, interlaminar fracture, delamination, and debonding that have the potential to cause catastrophic failure.[68,69] Similarly, FRP-retrofitted structures have experienced premature failure prior to attaining their theoretical strength.[61] In fact, numerous sources are responsible for FRP damage, including excessive loading (e.g., wind and earthquakes), fatigue, environmentally induced deterioration, material defects, and improper construction.[70,71]

One approach to using carbon fiber-reinforced polymer (CFRP) composites as a multifunctional material for SHM is to monitor its changes in electrical properties due to damage formation. In fact, in addition to being a structural material, CFRPs have been shown to be piezoresistive.[72–76] Change in resistance in response to applied strain is usually linear, although it has been shown by Ogi[73] that transverse cracking can cause deviations to this linear response. Delamination between layers can also cause changes in CFRPs' electrical resistance.[77,78] Many studies have also been conducted for detecting fatigue damage.[79–81] Measurements of electrical resistance or conductivity can be obtained in-plane or through-the-thickness of the composite, and the orientation of measurements can be used as a way to distinguish between the different possibilities of damage occurring in the CFRP structure.

11.4.1 FRP manufacturing

FRP composites are most commonly manufactured using two techniques: namely wet layup and vacuum-assisted resin-transfer molding (VARTM). In short, wet layup begins by putting an initial layer of peel ply on a mold. A first layer of fabric is then placed in the mold, and an adhesive is spread evenly until the fabric is fully wetted. The adhesive used usually consists of an epoxy resin mixed with a hardener (at an appropriate volume ratio). Then, the procedure of laying the fabric and applying epoxy/adhesive is repeated until the desired number of layers has been reached. On the other hand, VARTM FRP manufacturing follows a slightly different procedure. Here, the fabric is layered based on the desired orientations, order, and number of layers. The layered fabric is then transferred and sealed into a vacuum bag, and resin infiltration takes place. The flow of adhesive throughout the panel and bag is assisted by the use of a vacuum, for example, based on the procedure by Govignon *et al.*[82] In general, VARTM permits greater control and less variability from sample to sample, but wet layup is predominantly used for civil structures. Both manufacturing techniques are illustrated in Fig. 11.3.

Carbon nanomaterials, primarily CNTs, are introduced in FRP composites via two techniques: either as an additive to the epoxy/polymer matrix or as a thin film within or coated on the surface of the composite. This section will focus on the former case, and thin films will be discussed in Section 11.5. A popular method for dispersing nanotubes in the epoxy resin is by the manual mixing of CNTs with the resin. Then, the mixture is subjected to intense shear mixing using a three-roll mill, as has been used by Gojny *et al.*[83] and Thostenson and Chou.[84] The gap between the rolls can be adjusted from a larger spacing to a smaller gap during processing to facilitate nanomaterial dispersion. Once adequate suspension has been achieved, the nanomaterial-enhanced resin is then combined with the curing agent, heat-treated, and degassed in a vacuum oven.[84]

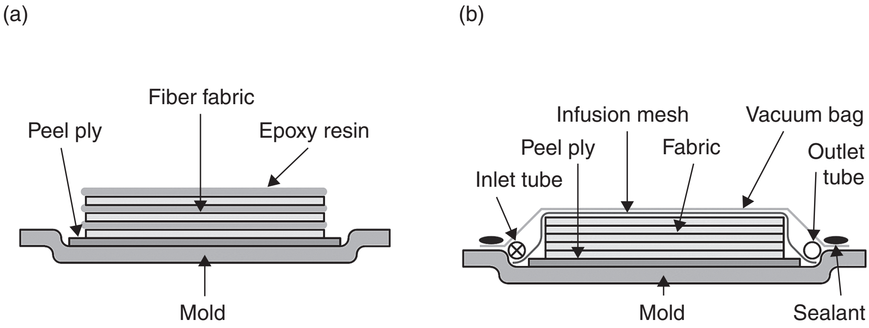

11.3 The (a) wet layup and (b) VARTM FRP composite manufacturing techniques are illustrated.

11.4.2 Improving FRP electromechanical properties

To date, several studies have attempted to enhance the electromechanical performance of FRPs, mainly by employing nanomaterials as conductive fillers in the epoxy matrix. A state-of-the-art overview of nanomaterial-modified FRP composites can be found in Loh and Azhari.[85] An earlier study conducted by Gojny *et al.*[83] and Wichmann *et al.*[86] have successfully showed that a 0.3 wt.% amino-functionalized double-walled CNT-modified epoxy resin-based glass fiber reinforced polymer (GFRP) possessed improved ultimate strength ($\sigma_f \approx 67$ MPa), Young's modulus ($E \approx 2.94$ GPa), and fracture toughness ($K_{IC} \approx 0.92$ MPa-m$^{1/2}$); anisotropic electrical conductivity has also been verified, but its piezoresistivity has not been explored. An extension to these studies by Böger *et al.*[69] has explored strain sensing by VARTM-manufactured CFRPs, where their epoxy matrices have been modified with CBs and CNTs. The results are promising and have illustrated that CFRPs' electrical resistance changes in tandem with applied incremental tensile strains, but an irreversible non-linear electrical drift exists. Figure 11.4 shows a set of representative strain sensing results obtained by Thostenson and Chou.[84] On the other hand, Anand and Mahapatra[87] have used models and experiments to show that CNT/epoxy composites that also incorporate CBs are characterized by non-linear piezoresistive properties under quasi-static loading.

Besides sensing, Rajoria and Jalili[88] have shown that CNT/epoxy composites also possess improved energy dissipation, where MWNT/epoxy composites are characterized by damping ratios up to 700% higher than their pristine epoxy-based counterparts. CNT/epoxy composites have also been demonstrated for actuation applications, as has been discussed by Yun *et al.*[89] Instead of using dispersed CNTs, Abot *et al.*[90] have proposed the use of CNT-wound thread sensors for strain monitoring. These CNT

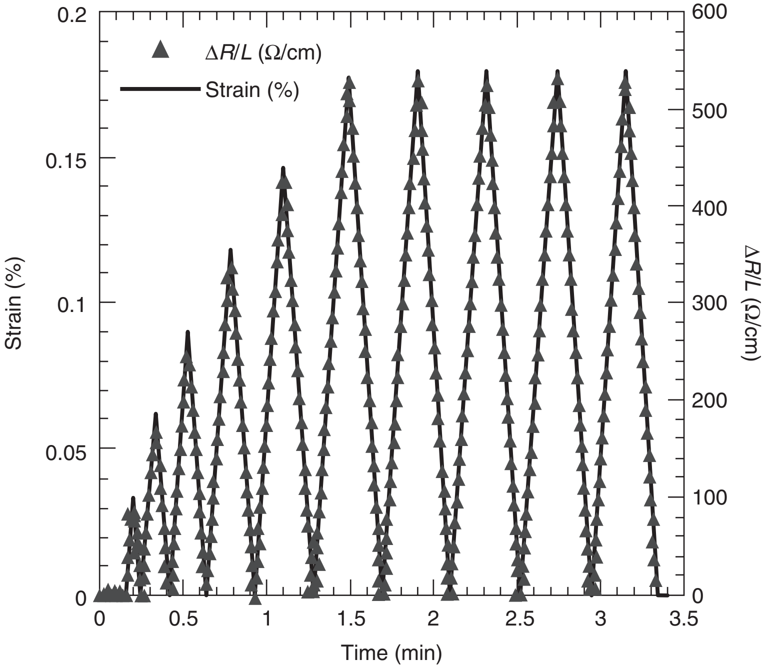

11.4 Thostenson and Chou[84] have reported that FRPs modified with CNTs exhibit great promise for strain sensing and SHM. The overlay of the resistance and applied strain time histories validate the FRPs piezoresistive performance. (*Source*: Image provided courtesy of IOP.)

threads are wound from as-grown CNT forests to form 15–30 μm-thick threads, which are also coated with a dielectric insulation layer. The CNT threads exhibit linear piezoresistivity after the application of 0.3% pre-strains. They have been stitched into CFRP composites and have been validated for delamination and crack detection.[90]

11.5 Polymer-based thin films

Unlike *smart* concrete or FRPs where CBs and CNTs can be incorporated within structural materials, these nanomaterials have also been investigated for creating advanced structural coatings or thin films. In many cases, nanomaterials are embedded in polymer matrices to form conformable coatings that can be applied onto structural surfaces, whether it is for concrete, steel, FRPs, or other types. The thin film's properties can be controlled by judiciously selecting the type of nanomaterial, polymer matrix, nanomaterial–matrix interaction, and fabrication procedure.[91] In particular, this section will present an overview of how electromechanical sensing capabilities can be encoded in these polymer-based thin films for civil infrastructure monitoring.[92] Specific attention will be on CNTs, simply due to the extensive amount of research and applications in this area.

11.5.1 Thin film fabrication

Numerous thin film fabrication techniques exist and have been employed for assembling CNT-enhanced structures. For example, extensive work has been conducted on using dispersed CNT solutions for vacuum filtration and then dried to form films called 'buckypaper.' The electrical and mechanical properties of selected works have been summarized in Tables 11.2 and 11.3, respectively. It should be mentioned that Tables 11.2 and 11.3 are not meant to be an exhaustive literature review, but rather just an overview of the wide variety of published work. In addition, buckypapers have been tested for

Table 11.2 The electrical properties of CNT buckypapers

References	[1]F-CNT-P	Fabrication technique	Addition	Further treatment	CNT concentration	Conductivity (S·m^{-1})
122	[2]EBA-[3]FWNT	Filtration	–	–	–	29 400
123	[4]O-SWNT-[5]A	Filtration	–	–	0.1 wt./vol%	30 000
		Filtration	–	10M HNO$_3$	0.1 wt./vol%	12 000
124	SWNT-[6]p	Filtration	[9]SDS	–	–	70 000
				Chemical treatment in SOCl$_2$	–	350 000
124	O-SWNT-A/[7]H	Filtration	[9]SDS	–	–	24 000
		Filtration		Chemical treatment in SOCl$_2$	–	96 000
125	[8]C-MWNT-A	Filtration	–	–	0.086 wt./vol%	10 000
		Filtration	[10]PEO	Soaking		2630
		Filtration	[11]PVA	Vacuum filtration for 24 h	0.086 wt./vol%	826
126	SWNT-p	Filtration	[12]PS	–	22% [16] M_f	100
		Filtration	PS	–	100% M_f	9000
127	MWNT	Filtration	[13]IC	–	6% [17] V_f	2880
	SWNT	Filtration	IC	–	17.9% V_f	11 700
128	SWNT	Filtration	Triton X-100	–	0.05 wt./vol%	24 700
		Filtration	[14]DNA	–	0.05 wt./vol%	30 600
		Filtration	Chitosan	–	0.05 wt./vol%	29 000
129	SWNT-p	Filtration	SOCl$_2$	Soaking	–	300 000
		Filtration	Aniline	[15]DI rinsing	–	2400

[1]F-CNT-P: functionalization-type of CNT-purification; [2]EBA-: 4-ethoxybenzoic acid; [3]FWNT: few-walled carbon nanotube; [4]O-: oxidized; [5]-A: acid-treated; [6]-p: purified; [7]-H: heat-treated; [8]C-: carboxylated; [9]SDS: sodium dodecyl sulfate; [10]PEO: polyethylene oxide; [11]PVA: poly(vinyl alcohol); [12]PS: polystyrene; [13]IC: biopolymer t-carrageenan; [14]DNA: deoxyribonucleic acid; [15]DI: deionized water; [16]M_f: mass fraction in composite; [17]V_f: volume fraction in composite.

Table 11.3 The mechanical properties of CNT buckypapers

References	[1]F-CNT-P	Fabrication technique	Addition	Further treatment	CNT concentration	Tensile strength (MPa)	Young's modulus (GPa)	Extensibility (%)
122	[2]EBA-[3]FWNT	Filtration	–	–	–	80	15	–
123	[4]O-SWNT-[5]A	Filtration	–	–	0.1 wt./vol%	10	0.8	5.6
		Filtration	–	10M H_2NO_3	0.1 wt./vol%	74	5	3
124	SWNT-[6]p	Filtration	[10]SDS	–	–	11	0.66	1.7
		Filtration	$SOCl_2$	–	–	37	0.95	4.3
130	O-SWNT-A	Filtration	–	–	–	10.5	1.5	–
		Filtration	–	E-beam	–	80	3.5	–
131	SWNT	Filtration	SDS	–	0.01 wt./vol%	15	–	1.15
	[7]C-SWNT-A	Filtration	SDS	–	0.01 wt./vol%	24	–	1.16
125	C-MWNT-A	Filtration	[11]PEO	Soaking	0.086 wt./vol%	3.5	0.323	–
		Filtration	[12]PVA	Vacuum filtration for 10 h	0.086 wt./vol%	96.1	6.23	–
132	C-SWNT-A	Filtration	–	–	–	10	1.2	2
133	SWNT-[8]H	Filtration	–	–	–	6.29	2.3	–
		Filtration	PVA	Soaking	–	57	6.9	–
127	MWNT	Filtration	[13]IC	–	6% [16]V_f	7.2	1.415	1.2
		Filtration		–	12% V_f	23.9	2.665	3.4
128	SWNT	Filtration	Triton X-100	–	0.05 wt./vol%	16	4	–
		Filtration	[14]DNA	–	0.05 wt./vol%	76	3.3	–
		Filtration	Chitosan	–	0.05 wt./vol%	149	3.4	–
134	SWNT	Filtration	Water	Soaking	0.1 wt.%	15.1	1.32	–
		Filtration	[15]BMI.Bf4	Soaking	0.1 wt.%	1.9	0.28	–
135	[9]VA CNT	Shear pressing	Epoxy	Soaking	27% V_f	300	15	–
				Soaking /5% stretched	27% V_f	402	22.3	–

[1]F-CNT-P: functionalization-type of CNT-purification; [2]EBA-: 4-ethoxybenzoic acid; [3]FWNT: few-walled carbon nanotube; [4]O-: oxidized; [5]-A: acid-treated; [6]-p: purified; [7]C-: carboxylated; [8]-H: heat-treated; [9]VA: vertically aligned; [10]SDS: sodium dodecyl sulfate; [11]PEO: polyethylene oxide; [12]PVA: poly(vinyl alcohol); [13]IC: biopolymer t-carrageenan; [14]DNA: deoxyribonucleic acid; [15]BMI.Bf4: 1-butyl-3-methyl-imidazolium tetrafluoroborate; [16]V_f: volume fraction in composite.

strain sensing, and Dharap *et al.*[93] and Kang *et al.*[94] have reported their linear piezoresistivity up to 500 με.

Besides buckypapers, examples of other fabrication methods include polymer casting,[95] epoxy molding,[26] spin coating,[96] layer-by-layer (LbL),[97] evaporation,[98] and spraying,[99] among many others.[100] For instance, Kang *et al.*[94] have assembled SWNT/polymethyl methacrylate (PMMA)-casted films. Quasi-static and dynamic cantilevered beam tests have been conducted, and the results show that these films are capable of monitoring strains while possessing high gage factors up to ~5. This study has also been extended for crack detection and corrosion monitoring using a sprayed-on CNT-neuron thin film.[99] Even higher strain sensitivities (up to ~15) have been achieved by Pham *et al.*[95] Tables 11.4 and 11.5 summarize the electrical and mechanical properties of CNT/polymer-based nanocomposites. Many of these studies also describe strain sensing using these thin films. More detailed reviews of CNT-based nanocomposite sensors can be found in Sinha *et al.,*[101] Mahar *et al.,*[102] and Li *et al.*[103]

In general, most of these film fabrication methods assemble nanocomposites characterized by a random percolated morphology of CNTs. Exceeding the percolation threshold is critical since CNTs enable electrical conductivity while also reinforcing bulk film mechanical properties, as will be shown later in this section. Two representative scanning electron microscope images of LbL-based films are shown in Fig. 11.5. Both these images show that only individual or at least small bundles of nanotubes are deposited during nanocomposite assembly.[97,104] Due to the diversity of research in this area, the remainder of this section will focus on CNT-based films fabricated using LbL.

11.5.2 Layer-by-layer (LbL) fabrication

A schematic illustrating the LbL self-assembly process is shown in Fig. 11.6, and the fabrication procedure is described in this section.[97,105] First, a cleaned charged substrate such as glass, silicon, metal, or polymer is immersed in a positively charged solution such as PVA. Electrostatic and van der Waals force interactions drive the adsorption of PVA onto the substrate surface. After several minutes, the substrate and its adsorbed PVA layer is removed from the solution and then rinsed with deionized water and dried with air, thereby completing the assembly of the first monolayer. Next, the substrate is immersed in a negatively charged solution, such as CNTs dispersed in PSS solution. As mentioned in Loh *et al.,*[97,106] SWNT-PSS dispersions are achieved by subjecting the mixture to bath sonication and high-energy tip sonication.[97,106] Adsorption of CNTs and PSS onto the previous monolayer is again based on electrostatic and van der Waals forces. The film is then rinsed and dried, and this procedure completes the

Table 11.4 The electrical properties of carbon nanotube-polymer nanocomposites

References	[1]F-CNT-P	Fabrication	Polymer	CNT concentration	Electrical conductivity $(S\cdot m^{-1})$
136	[2]O-SWNT-[3]A	Coagulation	[4]PMMA	0% [10]W_f	1E-13
				2% W_f	0.01
137	MWNT	Epoxy infusion	Epoxy 3266	0% W_f	1E-12
				10% W_f	3527
				10% W_f	7715
				17% W_f	13 084
138	MWNT	Hot pressing/mold casting	[5]NR	0 [11] phr	4E+14 (Ω·cm)
				10 phr	1000 (Ω·cm)
			[6]SBR	0 phr	3E+13 (Ω·cm)
				10 phr	1000 (Ω·cm)
			[7]EPDM	0 phr	2E+13 (Ω·cm)
				10 phr	1E+5 (Ω·cm)
139	MWNT	Solvent evaporation	[8]PS	0% [12]V_f	1E+12 (Ω/□)
				2.49% V_f	1000 (Ω/□)
127	MWNT	Solvent evaporation	[9]IC	2.29% V_f	36
				4.66% V_f	82
				7.75% V_f	558
				6.65% V_f	420
				5.79% V_f	260
	SWNT	Solvent evaporation		3.18% V_f	0.057
				6.45% V_f	25
				10.5% V_f	118
				8.94% V_f	82
				7.90% V_f	6
139	MWNT	Spin casting	PS	0% V_f	1E+12 (Ω/□)
				2.49% V_f	1000 (Ω/□)

[1]F-CNT-P: functionalization-type of CNT-purification; [2]O-: oxidized; [3]-A: acid-treated; [4]PMMA: poly(methylmethacrylate); [5]NR: natural rubber; [6]SBR: styrene-butadiene rubber; [7]EPDM: ethylene propylene diene monomer; [8]PS: polystyrene; [9]IC: biopolymer t-carrageenan; [10]W_f: weight fraction in composite; [11]phr: parts per hundred parts of rubber; [12]V_f: volume fraction in composite.

fabrication of one bilayer. The procedure is repeated multiple cycles for fabricating homogeneous nanocomposites. Films can be left on the substrate, or chemical etching using hydrofluoric acid can be performed to obtain freestanding nanocomposites. These films are denoted as $(A/B)_n$, where A and B are the film constituents (e.g., SWNT-PSS and PVA), and n is the number of bilayers.

11.5.3 Mechanical properties of LbL nanocomposites

Stress–strain testing has revealed that the average modulus of elasticity, ultimate tensile strength, and ultimate failure strain for LbL $(SWNT\text{-}PSS/PVA)_{200}$

Table 11.5 The mechanical properties of carbon nanotube-polymer nanocomposites

References	[1]F-CNT-P	Fabrication	Polymer	CNT Concentration	Tensile strength (MPa)	Young's modulus (GPa)	Extensibility (%)
137	MWNT	Epoxy infusion	Epoxy 3266	0% W_f	89	2.5	5.2
				17% W_f	231	20.4	1.2
140	CNT	Epoxy infusion	[15]BMI	–	2082	169	–
	[4]E-CNT			–	3081	350	–
138	MWNT	Hot pressing/Mold casting	[16]SBR	0 [26]phr	1.08	0.0005	326
				10 phr	6.3	0.00494	149
141	[5]B-MWNT	[13]LbL	[17]PEI/[18]PAA	–	150	4.5	0.0375
	[6]H-MWNT			–	110	2	0.045
142	[7]C-SWNT-A	[13]LbL	[19]PSS/[20]PDDA	70% [27] V_f	–	460	–
143	SWNT	[13]LbL	PSS/PVA	0.50 mg-mL^{-1}	180	10.4	2.12
144	[8]f-MWNT-A	Mold casting	PMMA	0% W_f	29.65	–	1.13
				1.5% W_f	52	–	0.9
145	[9]F-SWNT-[10]HO	Roll casting	[21]PEO	0% W_f	3.5	0.0595	–
				1% W_f	10	0.147	–
146	[11]n-MWNT-[12]p	Solvent evaporation	[22]CPP	0% V_f	13	0.22	–
				0.6% V_f	49	0.68	–
139	MWNT	Solvent evaporation	[23]PS	0% V_f	19.5	1.53	–
				2.49% V_f	30.6	3.4	–
127	MWNT	Solvent evaporation	[24]IC	2.29% V_f	15	0.859	4
				5.79% V_f	39.5	2.602	6.5
147	MWNT	Solvent evaporation	Morthane	0% V_f	2.1	0.013	1.19
				10.2% V_f	5.2	0.09	1.08
139	MWNT	Spin casting	PS	0% V_f	19.5	1.53	–
				2.49% V_f	26	3.37	–

[1]F-CNT-P: functionalization-type of CNT-purification; [2]O-: oxidized; [3]-A: acid-treated; [4]E-: epoxide; [5]B-: bamboo; [6]H-: hollow; [7]C-: carboxylated; [8]f-: functionalized; [9]F-: fluorinated; [10]-HO: H_2O_2; [11]n-: *n*-butyl lithium; [12]-p: purified; [13]LbL: layer-by-layer; [14]PMMA: poly(methylmethacrylate); [15]BMI: bismaleimide resin solution; [16]SBR: styrene-butadiene rubber; [17]PEI: poly(ethyleneimine); [18]PAA: poly(acrylic acid); [19]PSS: poly(sodium 4-styrenesulfonate).

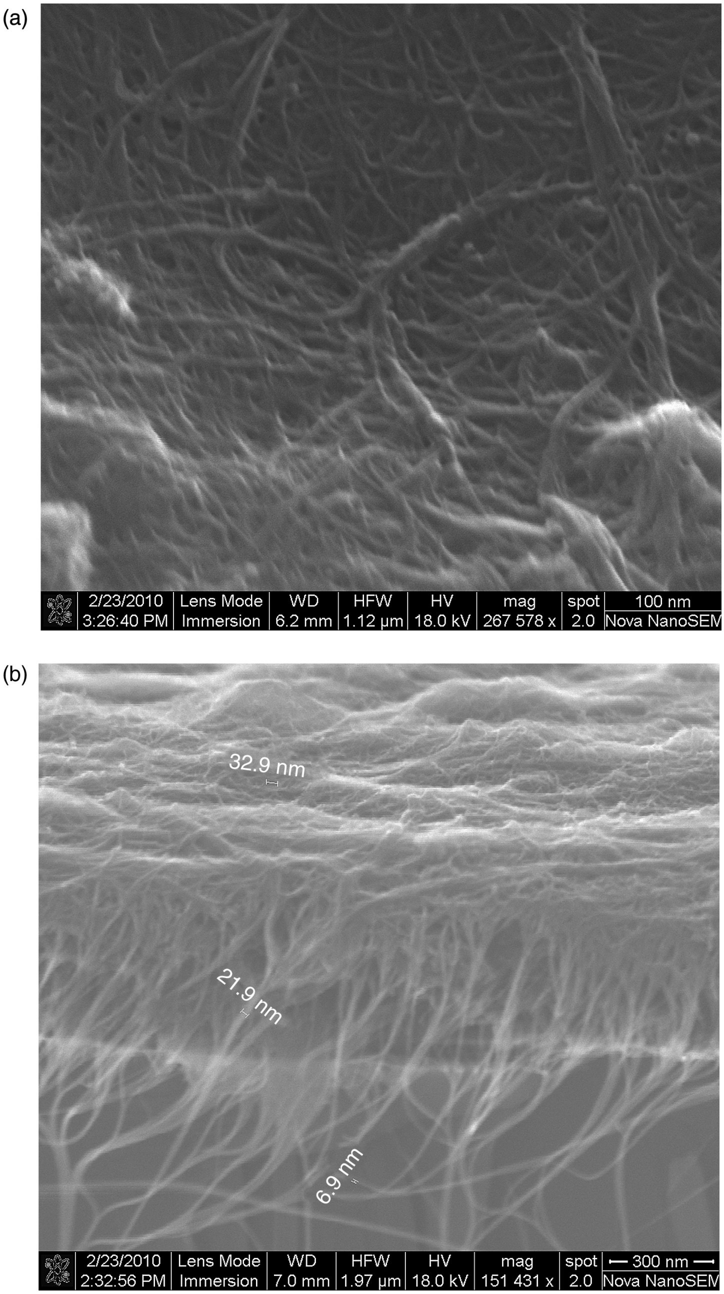
(a)
2/23/2010
3:26:40 PM
Lens Mode
Immersion
WD
6.2 mm
HFW
1.12 µm
HV
18.0 kV
mag
267 578 x
spot
2.0
100 nm
Nova NanoSEM
(b)
32.9 nm
21.9 nm
6.9 nm
2/23/2010
2:32:56 PM
Lens Mode
Immersion
WD
7.0 mm
HFW
1.97 µm
HV
18.0 kV
mag
151 431 x
spot
2.0
300 nm
Nova NanoSEM

11.5 Scanning electron microscope images of the (a) surface and (b) cross-section of a LbL SWNT-based thin film are shown.

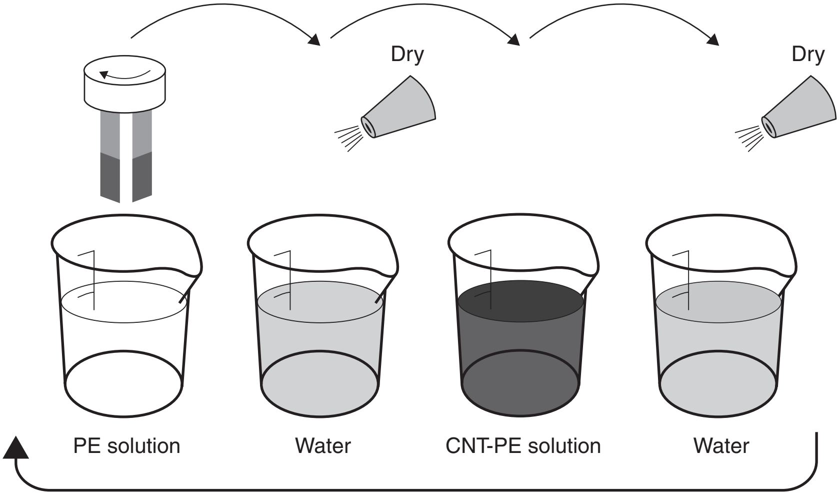

11.6 A schematic of the LbL fabrication method for assembling CNT-PE thin films is presented.

thin films are approximately 10.4 GPa, 180 MPa, and 21 200 με, respectively. As compared to the stress–strain performance of films without the addition of CNTs, these SWNT-based nanocomposites exhibit an order of magnitude improvement in bulk Young's modulus and ultimate tensile strength.[9] Although the ultimate failure strain is significantly lower than its pure polymeric counterpart, they remain fairly flexible. Zhao and Loh[107] have also shown that additional mechanical property enhancements can be achieved by adjusting post-fabrication parameters, such as by performing thermal annealing.

11.5.4 Strain sensing

Characterization of thin film piezoresistivity has been performed by applying tensile-compressive cyclic loads to $(\text{SWNT-PSS/PVA})_n$ specimens while simultaneously measuring their electrical resistance (or resistivity) using a two-point probe method. The resistance time history response of a representative thin film strain sensor subjected to multiple cycles of tensile-compressive loading to ±5000 με is shown in Fig. 11.7. It can be clearly seen that the nanocomposite exhibits piezoresistive behavior. In addition, film resistance increases in tandem with increasingly applied strain, and the opposite is true when the films are subjected to compression. Similar results are also obtained for films fabricated with different CNT and polyelectrolyte (PE) concentrations and number of bilayers.[97,106] However, closer inspection of these results show that their electromechanical responses are distorted and show rounded peaks, despite the fact that a saw-tooth cyclic load pattern

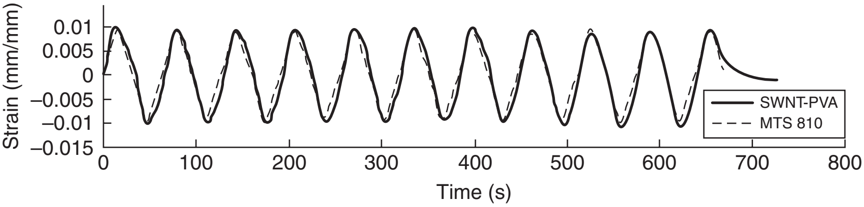

11.7 The resistance time history response of an SWNT-PE LbL thin film subjected to a 10-cycle tensile-compressive load pattern to ±5000 με is overlaid with the applied load pattern.

has been applied. The resistance time history shown in Fig. 11.7 actually approaches that of a sinusoidal signal. It is possible that measurement of bulk film time-domain resistance is insufficient since the films also possess inherent capacitance to cause such distortions. Their capacitive nature has been identified through electrical impedance spectroscopic studies conducted by Loh *et al.*[106] A parallel resistor–capacitor equivalent circuit model has been derived for modeling these thin films' electromechanical properties.

11.5.5 'Sensing skins' for spatial damage detection

Structural damage such as cracks, impact, and delamination are inherently localized phenomena that are difficult to detect and monitor using global-based techniques such as modal analysis. Conventional sensors (such as strain gages and accelerometers) only measure structural response parameters at discrete and instrumented locations. Detecting the presence, magnitude, and location of damage thus requires instrumenting a dense network of these discrete transducers and combining them with methods of interpolating between sensor nodes. Often, a dense sensor network may be cost prohibitive, and the estimation of structural response over large spatial domains may be inaccurate.

In this section, the LbL CNT-PE thin films described in Section 11.5.2 are used as the platform for assembling multifunctional *sensing skins* capable of direct spatial damage detection and strain mapping. While other types of skin-like sensors have been developed and have been summarized by Loh and Azhari,[85] this section will showcase one particular technology. Here, spatial sensing is enabled by employing the SWNT-PE thin films, instrumenting them with a set of boundary electrodes, and then applying a technique known as electrical impedance tomography (EIT).[108] The EIT algorithm utilizes boundary current input and voltage output measurements for reconstructing the spatial conductivity distribution of the film (or any conductive or semi-conductive body).[108,109] Due to the impracticality of obtaining a continuum spatial conductivity distribution and an applied boundary potential function, solving the EIT inverse problem relies on using a finite element model (FEM) of the film.[110] The FEM model utilizes discrete elements for describing the film's spatial conductivity distribution, and each element possesses constant properties (i.e., in this case, electrical conductivity). The true spatial conductivity of the *sensing skin* is determined by solving this inverse problem in an iterative fashion. During each iteration, the electrical conductivity of each FEM element is updated, and the model's boundary voltage estimations are compared to experimental ones. The inverse problem continues until the differences between the numerical and experimental results are within a predefined error threshold. The entire EIT procedure is illustrated in Fig. 11.8.[111]

EIT is advantageous, as compared to a dense sensor instrumentation strategy, because *sensing skin* measurements are only obtained along the film boundaries. This eliminates the need to physically probe every location on the film surface, or the need for instrumenting a dense network of transducers. Instead, the only requirement is that the film can be coated or painted onto the structural surface of interest (or embedded within structural materials like FRP). Since thin film conductivity (or resistivity) is calibrated to strain or damage other phenomena,[9,97,106] the spatial conductivity maps are directly related to spatial damage in the structure. The end result

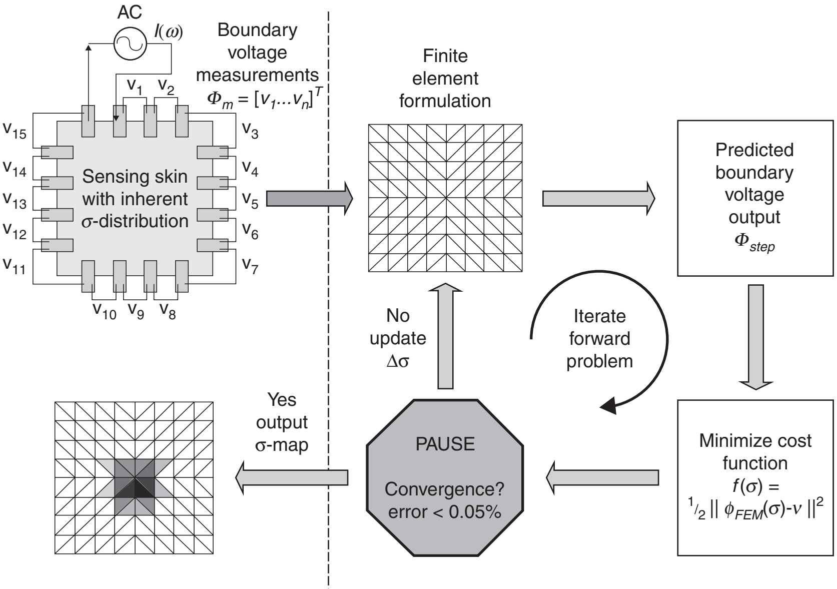
AC
$I(\omega)$
Boundary voltage measurements
$\Phi_m = [v_1 \ldots v_n]^T$
v_1 v_2 v_3 v_4 v_5 v_6 v_7 v_8 v_9 v_{10} v_{11} v_{12} v_{13} v_{14} v_{15}
Sensing skin with inherent σ-distribution
Finite element formulation
Predicted boundary voltage output Φ_{step}
No update $\Delta\sigma$
Iterate forward problem
Minimize cost function $f(\sigma) = \frac{1}{2} \| \phi_{FEM}(\sigma) - v \|^2$
PAUSE
Convergence? error < 0.05%
Yes output σ-map

11.8 A schematic illustrating the procedure for solving the EIT inverse problem for spatial conductivity mapping is shown.[111] (*Source*: Image provided courtesy of Springer.)

is a 2D strain map (or stress map) of the structure. It has been shown that the EIT-estimated spatial conductivities are within 2% error, as compared to two-point probe experimental measurements of the same film and spatial region.[112]

Loh *et al.*[111] have assessed the performance of *sensing skins* for identifying the severity and location of impact damage on metallic structures. LbL $(\text{SWNT-PSS/PVA})_{50}$ thin films have been coated onto aluminum plates. An impact apparatus has been used to impart different degrees of damage (i.e., permanent deformation) at various locations on the *skin*-coated plate (Plate VIIIa in the color section between pages 294 and 295). Using EIT, the *sensing skin* conductivity maps have been obtained and are shown as a 2D strain map in Plate VIIIb or as a 3D contour plot in Plate VIIIc. These results clearly show dramatic changes in film electrical conductivity at their points of impact. The relative change in conductivity (as compared to its baseline undamaged case) also decreases in tandem with the severity of impact. Based on these results, it is clear that this technology is viable for detecting the location and severity of structural damage. Other work has also been conducted for using this technique for crack damage detection in cementitious composites,[113] corrosion formation on steel specimens,[114] and for sensing pH changes on film surfaces.[112] Based on these results, this *sensing skin* technology has the potential for field and commercial adoption.[115]

11.6 Conclusion and future trends

It is evident from the discussions in this chapter that nanotechnology-enabled multifunctional materials are entering the commercial and field implementation domains. Since the discovery of CNTs in 1991, multiple industries have developed and advanced technology to manufacture these nanomaterials at high throughput and low costs. Decades of intensive basic research have allowed this field of study to mature in a relatively short amount of time. In fact, one can find a plethora of issued patents related to nanotechnology and multifunctional systems. Agencies such as the US Department of Defense has active projects investigating the use of nanomaterials for enhancing warfighter capabilities, and these projects are often conducted by joint partnerships between academia and industry. Another example is that sprayed CNT/polymer-based thin films are being integrated with GFRPs for *in situ* sensing and damage detection;[116,117] they will be integrated with wind turbine blades and validated as a next-generation multifunctional composite material through a study sponsored by the US National Science Foundation.[118]

There is no doubt that as some of these existing multifunctional nanocomposite systems make their way into practice, more advanced systems will continue to be developed. An area with tremendous room for technological innovation is in the domain of biologically inspired sensing systems. Such bio-inspired technologies extend beyond mimicking biological sensing functionalities, but the focus is to learn how nature assembles and organizes to form those sensory features that outperform the manmade counterparts. A review by Bar-Cohen[119] has highlighted advancements in sensor technologies inspired by the various biological senses. Another example is the development of photosynthesis-inspired structural coatings by Ryu and Loh.[120] Unlike conventional sensors that require a constant power supply for operations, the coating is photoactive and can generate electrical energy in response to broadband light illumination (Plate IXa in the color section between pages 294 and 295). The magnitude of current also changes in tandem with applied strains (Plate IXb), thereby making them ideally suited for remote monitoring of civil structures (i.e., for applications where a constant energy supply may be difficult to achieve). All in all, these different bio-inspired sensors that are currently still in their research phases have the potential to revolutionize and find applications for civil SHM/damage detection in the very near future,[121]

11.7 References

1. Mukhopadhyay, S., ed. (2012), *Nanoscale Multifunctional Materials: Science and Applications*, John Wiley & Sons: Hoboken, NJ.
2. Zunino Iii, J.L. (2007), 'Development of materials and sensors for the U.S. army's active coatings technology program', *Sensors & Transducers*, **84**(10), 51–59.
3. Miller, R.A. (1997), 'Thermal barrier coatings for aircraft engines: History and directions', *Journal of Thermal Spray Technology*, **6**(1), 35–42.
4. Twite, R.L. and Bierwagen, G.P. (1998), 'Review of alternatives to chromate for corrosion protection of aluminum aerospace alloys', *Progress in Organic Coatings*, **33**(2), 91–100.
5. Hegedus, C.R., Pulley, D.F., Spadafora, S.J., Eng, A.T. and Hirst, D.J. (1989), 'A review of organic coating technology for U.S. naval aircraft', *Journal of Coatings Technology*, **61**(778), 31–44.
6. Miyamoto, Y., Kaysser, W.A., Rabin, R.H., Kawasaki, A. and Ford, R.G. (1999), *Functionally Graded Materials: Design, Processing and Applications*, Kluwer Academic: Dordrecht, The Netherlands.
7. Shukla, A., Jain, N. and Chona, R. (2007), 'A review of dynamic fracture studies in functionally graded materials', *Strain*, **43**, 76–95.
8. Kim, J.-H. and Paulino, G.H. (2002), 'Finite element evaluation of mixed mode stress intensity factors in functionally graded materials', *International Journal for Numerical Methods in Engineering*, **53**, 1903–1935.
9. Loh, K.J. (2008), 'Development of Multifunctional Carbon Nanotube Nanocomposite Sensors for Structural Health Monitoring', Ph.D. Thesis, University of Michigan, Department of Civil & Environmental Engineering, Ann Arbor, MI.
10. Dai, L. (2008), 'Aligned carbon nanotubes for multifunctional nanocomposites and nanodevices: From plastic optoelectronics to bioceramics', *Advances in Applied Ceramics*, **104**(4), 177–189.

11. Baur, J. and Silverman, E. (2007), 'Challenges and opportunities in multifunctional nanocomposite structures for aerospace applications', *MRS Bulletin*, **32**(4), 328–334.
12. Chung, D.D.L. (2003), *Multifunctional Cement-Based Materials*, Marcel Dekker: Brazil.
13. Rentrop, C.H.A., Batenburg, L.F., Dam, R.A.V., Hogerheide, M.P., Meinema, H.A., Gielgens, L.H. and Fischer, H.R. (2000), 'Multifunctional nanocomposite coatings', *Proceedings of Materials Research Society Symposium*, **628**, CC4.8.1–CC4.8.6.
14. Bhushan, B., ed. (2003), *Springer Handbook of Nanotechnology*, Springer: Berlin, Germany.
15. Donnet, J.-B., Bansal, R.C. and Wang, M.-J., ed. (1993), *Carbon Black*, Marcel Dekker: New York, NY.
16. Aminabhavi, T.M., Cassidy, P.E. and Thompson, C.M. (1990), 'Electrical resistivity of carbon-black-loaded rubbers', *Rubber Chemistry and Technology*, **63**(3), 451–471.
17. Gogotsi, Y., ed. (2006), *Nanomaterials Handbook*, Taylor & Francis: Boca Raton, FL.
18. Iijima, S. (1991), 'Helical microtubules of graphitic carbon', *Nature*, **354**(6348), 56–58.
19. Saito, R., Dresselhaus, G. and Dresselhaus, M.S. (1998), *Physical Properties of Carbon Nanotubes*, Imperial College Press: London.
20. Meyyappan, M., ed. (2005), *Carbon Nanotubes: Science and Applications*, CRC Press: Boca Raton, FL.
21. Baughman, R.H., Zakhidov, A.A. and De Heer, W.A. (2002), 'Carbon Nanotubes – the route toward applications', *Science*, **297**(5582), 787–792.
22. Khare, R. and Bose, S. (2005), 'Carbon nanotube based composites – a review', *Journal of Minerals & Materials Characterization & Engineering*, **4**(1), 31–46.
23. Kang, I., Heung, Y.Y., Kim, J.H., Lee, J.W., Gollapudi, R., Subramaniam, S., Narasimhadevara, S., Hurd, D., Kirikera, G.R., Shanov, V., Schulz, M.J., Shi, D., Boerio, J., Mall, S. and Ruggles-Wren, M. (2006), 'Introduction to carbon nanotubes and nanofiber smart materials', *Composites: Part B*, **37**(6), 382–394 .
24. Tsukagoshi, K., Yoneya, N., Uryu, S., Aoyagi, Y., Kanda, A., Ootuka, Y. and Alphenaar, B.W. (2002), 'Carbon nanotube devices for nanoelectronics', *Physica B*, **323**(1–4), 107–114 .
25. Andrews, R., Jacques, D., Rao, A.M., Rantell, T., Derbyshire, F., Chen, Y., Chen, J. and Haddon, R.C. (1999), 'Nanotube composite carbon fibers', *Applied Physics Letters*, **75**(9), 1329–1331.
26. Thostenson, E.T. and Chou, T.-W. (2002), 'Aligned multi-walled carbon nanotube-reinforced composites: Processing and mechanical characterization', *Journal of Physics D*, **35**(16), L77–L80.
27. Kong, J., Franklin, N.R., Zhou, C., Chapline, M.G., Peng, S., Cho, K. and Dai, H. (2000), 'Nanotube molecular wires as chemical sensors', *Science*, **287**(5453), 622–625.
28. Loh, K.J., Kim, J., Lynch, J.P., Kam, N.W.S. and Kotov, N.A. (2007), 'Multifunctional layer-by-layer carbon nanotube-polyelectrolyte thin films for strain and corrosion sensing', *Smart Materials and Structures*, **16**(2), 429–438.

29. Dekker, C. (1999), ‘Carbon nanotubes as molecular quantum wires’, *Physics Today*, **52**(5), 22–28.
30. Chen, Y.K., Green, M.L.H., Griffin, J.L., Hammer, J., Lago, R.M. and Tsang, S.C. (1996), ‘Purification and opening of carbon nanotubes via bromination’, *Advanced Materials*, **8**(12), 1012–1015.
31. Tan, Y. and Resasco, D.E. (2005), ‘Dispersion of single-walled carbon nanotubes of narrow diameter distribution’, *Journal of Physical Chemistry B*, **109**(30), 14454–14460.
32. Bentur, A. (2002), ‘Cementitious materials-nine millennia and a new century: Past, present, and future’, *Journal of Materials in Civil Engineering*, **14**(1), 2–22.
33. Wight, J.K. and Macgregor, J.G. (2008), *Reinforced Concrete: Mechanics and Design*, 5th edn., Prentice Hall: Upper Saddle River, NJ.
34. Fischer, G. and Li, V.C. (2007), ‘Effect of fiber reinforcement on the response of structural members’, *Engineering Fracture Mechanics*, **74**(1–2), 258–272.
35. Kunieda, M. and Rokugo, K. (2006), ‘Recent progress on Hpfrcc in Japan’, *Journal of Advanced Concrete Technology*, **4**(1), 19–33.
36. Li, V.C. (2003), ‘On engineered cementitious composites (Ecc) – a review of the material and its applications’, *Journal of Advanced Concrete Technology*, **1**(3), 215–230.
37. Zhang, J., Leung, C.K.Y. and Cheung, Y.N. (2006), ‘Flexural performance of layered Ecc-concrete composite beam’, *Composites Science and Technology*, **66**(11–12), 1501–1512.
38. Perumalsamy, N.B. and Surendra, P.S. (1992), *Fiber-Reinforced Cement Composites*, McGraw-Hill: New York, NY.
39. Li, V.C. and Stang, H. (1997), ‘Interface property characterization and strengthening mechanisms in fiber reinforced cement based composites’, *Journal of Advanced Cement Based Materials*, **6**(1), 1–20.
40. Hammond, E. and Robson, T.D. (1955), ‘Comparison of electrical properties of various cements and concretes’, *Engineer*, **199**(5166), 114–115.
41. Li, G.Y., Wang, P.M. and Zhao, X. (2007), ‘Pressure-sensitive properties and microstructure of carbon nanotube reinforced cement composites’, *Cement & Concrete Composites*, **29**(5), 377–382.
42. Chung, D.D.L. (2002), ‘Piezoresistive cement-based materials for strain sensing’, *Journal of Intelligent Material Systems and Structures*, **13**(9), 599–609.
43. Garas, V.Y. and Vipulanandan, C. (2006), ‘Behavior of piezoresistive cement-based materials’, *Proceedings of Earth and Space* 2006, 1–8.
44. Hou, T.-C. and Lynch, J.P. (2005), ‘Conductivity-based strain monitoring and damage characterization of fiber reinforced cementitious structural components’, *Proceedings of SPIE – Smart Structures and Materials*, **5765**, 419–429.
45. Han, B., Yu, X. and Kwon, E. (2009), ‘A self-sensing carbon nanotube/cement composite for traffic monitoring’, *Nanotechnology*, **20**(445501), 1–5.
46. Manzur, T. and Yazdani, N. (2010), ‘Strength enhancement of cement mortar with carbon nanotubes’, *Journal of the Transportation Research Board*, **2142**, 102–108.
47. Yazdanbakhsh, A., Grasley, Z., Tyson, B. and Abu Al-Rub, R.K. (2010), ‘Distribution of carbon nanofibers and nanotubes in cementitious composites’, *Journal of the Transportation Research Board*, **2142**, 89–95.

48. Wille, K. and Loh, K.J. (2010), 'Nano-engineering ultra-high performance concrete with multi-walled carbon nanotubes', *Journal of the Transportation Research Board*, **2142**, 119–126.
49. Li, H., Xiao, H.-G. and Ou, J.-P. (2006), 'Effect of compressive strain on electrical resistivity of carbon black-filled cement-based composites', *Cement & Concrete Composites*, **28**(9), 824–828.
50. Musso, S., Tulliani, J.-M., Ferro, G. and Tagliaferro, A. (2009), 'Influence of carbon nanotubes structure on the mechanical behavior of cement composites', *Composites Science and Technology*, **69**(11–12), 1985–1990.
51. Yu, X. and Kwon, E. (2009), 'A carbon nanotube/cement composite with piezoresistive properties', *Smart Materials and Structures*, **18**(5), 055010 .
52. Martin, C.A., Sandler, J.K.W., Shaffer, M.S.P., Schwarz, M.K., Bauhofer, W., Schulte, K. and Windle, A.H. (2004), 'Formation of percolating networks in multi-wall carbon-nanotube-epoxy composites', *Composites Science and Technology*, **64**(15), 2309–2316.
53. Wansom, S., Kidner, N.J., Woo, L.Y. and Mason, T.O. (2006), 'Ac-impedance response of multi-walled carbon nanotube/cement composites', *Cement & Concrete Composites*, **28**(6), 509–519.
54. Ou, J. and Han, B. (2008), 'Piezoresistive cement-based strain sensors and self-sensing concrete components', *Journal of Intelligent Material Systems and Structures*, **20**(3), 329–336.
55. Tombler, T.W., Zhou, C., Alexseyev, L., Kong, J., Dai, H., Liu, L., Jayanthi, C.S., Tang, M. and Wu, S.-Y. (2000), 'Reversible electromechanical characteristics of carbon nanotubes under local-probe manipulation', *Nature*, **405**(6788), 769–772.
56. Saafi, M. (2009), 'Wireless and embedded carbon nanotube networks for damage detection in concrete structures', *Nanotechnology*, **20**(39), 395502.
57. Li, G.Y., Wang, P.M. and Zhao, X. (2005), 'Mechanical behavior and microstructure of cement composites incorporating surface-treated multi-walled carbon nanotubes', *Carbon*, **43**(6), 1239–1245.
58. Bastianini, F., Corradi, M., Borri, A. and Tommaso, A.D. (2005), 'Retrofit and monitoring of an historical building using 'smart' CFRP with embedded fibre optic brillouin sensors', *Construction and Building Materials*, **19**(7), 525–535.
59. Guan, H., Karbhari, V.M. and Sikorsky, C.S. (2007), 'Long-term structural health monitoring system for a FRP composite highway bridge structure', *Journal of Intelligent Material Systems and Structures*, **18**(8), 809–823.
60. Lau, K.-T., Zhou, L.-M., Tse, P.-C. and Yuan, L.-B. (2002), 'Applications of composites, optical fibre sensors and smart composites for concrete rehabilitation: An overview', *Applied Composite Materials*, **9**(4), 221–247.
61. Buyukozturk, O. and Hearing, B. (1998), 'Failure behavior of precracked concrete beams retrofitted with FRP', *Journal of Composites for Construction*, **2**(3), 138–144.
62. Einde, L.V.D., Zhao, L. and Seible, F. (2003), 'Use of FRP composites in civil structural applications', *Construction and Building Materials*, **17**(6–7), 389–403.
63. Zhao, M., Dong, Y., Zhao, Y., Tennant, A. and Ansari, F. (2007), 'Monitoring of bond in FRP retrofitted concrete structures', *Journal of Intelligent Material Systems and Structures*, **18**(8), 853–860.
64. Pantelides, C.P., Alameddine, F., Sardo, T. and Imbsen, R. (2004), 'Seismic retrofit of state street bridge on interstate 80', *Journal of Bridge Engineering*, **9**(4), 333–342.

65. Xiao, Y. (2004), 'Applications of FRP composites in concrete columns', *Advances in Structural Engineering*, **7**(4), 335–343.
66. 'Global FRP Use in Bridge Applications', *American Composites Manufacturers Association (ACMA)*, (2003).
67. Black, S. (2004), 'Composite Rib Structure for Airbus A380 Vertical Tail', High Performance Composites, March.
68. Todo, M., Nakamura, T., Mada, T. and Takahashi, K. (1998), 'Measurement of dynamic interlaminar fracture toughness of FRP laminates using dynamic displacement measuring apparatus', *Advanced Composite Materials*, **7**(3), 285–297.
69. Böger, L., Wichmann, M.H.G., Meyer, L.O. and Schulte, K. (2008), 'Load and health monitoring in glass fibre reinforced composites with an electrically conductive nanocomposite epoxy matrix', *Composites Science and Technology*, **68**(7–8), 1886–1894.
70. Erbay, O.O. and Sharff, P.A. (2008), 'Crack propagation evaluation of polymer composite FRP panels subjected to static and cyclic loading', *Proceedings of 2008 Structures Congress: Crossing the Borders*, **314**, 1–10.
71. Saafi, M. and Sayyah, T. (2001), 'Health monitoring of concrete structures strengthened with advanced composite materials using piezoelectric transducers', *Composites Part B*, **32**(4), 332–342.
72. Inoue, H. and Ogi, K. (2007), 'Piezoresistance behaviour of CFRP cross-ply laminates with transverse cracking', *Key Engineering Materials*, **334**(2), 961.
73. Ogi, K. (2007), 'A model for piezoresistance behavior in a cfrp cross-ply laminate with transverse cracking', *Journal of Solid Mechanics and Materials Engineering*, **1**(8), 975–985.
74. Taya, M., Kim, W. and Ono, K. (1998), 'Piezoresistivity of a short fiber/elastomer matrix composite', *Mechanics of materials*, **28**(1–4), 53–59.
75. Todoroki, A. and Yoshida, J. (2004), 'Electrical resistance change of unidirectional CFRP due to applied load', *JSME International Journal Series A Solid Mechanics and Material Engineering*, **47**(3), 357–364.
76. Wang, S. and Chung, D. (2000), 'Piezoresistivity in continuous carbon fiber polymer-matrix composite', *Polymer Composites*, **21**(1), 13–19.
77. Todoroki, A. (2008), 'Delamination monitoring analysis of CFRP structures using multi-probe electrical method', *Journal of Intelligent Material Systems and Structures*, **19**(3), 291–298.
78. Todoroki, A., Kobayashi, H. and Matuura, K. (1995), 'Application of electric potential method to smart composite structures for detecting delamination', *JSME International Journal, Series A: Mechanics and Material Engineering*, **38**(4), 524–530.
79. Abry, J., Bochard, S., Chateauminois, A., Salvia, M. and Giraud, G. (1999), '*In situ* detection of damage in CFRP laminates by electrical resistance measurements', *Composites Science and Technology*, **59**(6), 925–935.
80. Seo, D.-C. and Lee, J.-J. (1999), 'Damage detection of CFRP laminates using electrical resistance measurement and neural network', *Composite Structures*, **47**(1–4), 525–530.
81. Irving, P. and Thiagarajan, C. (1998), 'Fatigue damage characterization in carbon fibre composite materials using an electrical potential technique', *Smart Materials and Structures*, **7**(4), 456–466.

82. Govignon, Q., Bickerton, S., Morris, J. and Kelly, P.A. (2008), 'Full field monitoring of the resin flow and laminate properties during the resin infusion process', *Composites Part A*, **39**(9), 1412–1426.
83. Gojny, F.H., Wichmann, M.H.G., Fieldler, B., Bauhofer, W. and Schulte, K. (2005), 'Influence of nano-modification on the mechanical and electrical properties of conventional fibre-reinforced composites', *Composites: Part A*, **36**(11), 1525–1535.
84. Thostenson, E.T. and Chou, T.-W. (2008), 'Real-time *in situ* sensing of damage evolution in advanced fiber composites using carbon nanotube networks', *Nanotechnology*, **19**(21), 215713/215711–215716.
85. Loh, K.J. and Azhari, F. (2012), 'Recent advances in skin-inspired sensors enabled by nanotechnology', *Journal of Materials*, **64**(7), 793–801.
86. Wichmann, M.H.G., Sumfleth, J., Gojny, F.H., Quaresimin, M., Fieldler, B. and Schulte, K. (2006), 'Glass-fibre reinforced composites with enhanced mechanical and electrical properties – benefits and limitations of a nanoparticle modified matrix', *Engineering Fracture Mechanics*, **73**(16), 2346–2359.
87. Anand, S.V. and Mahapatra, D.R. (2009), 'Quasi-static and dynamic strain sensing using carbon nanotube/epoxy nanocomposite thin films', *Smart Materials and Structures*, **18**(4), 045013/045011–045013.
88. Rajoria, H. and Jalili, N. (2005), 'Passive vibration damping enhancement using carbon nanotube-epoxy reinforced composites', *Composites Science and Technology*, **65**(14), 2079–2093.
89. Yun, Y.-H., Shanov, V., Schulz, M.J., Narasimhadevara, S., Subramaniam, S., Hurd, D. and Boerio, F.J. (2005), 'Development of novel single-wall carbon nanotube–epoxy composite ply actuators', *Smart Materials and Structures*, **14**(6), 1526–1532.
90. Abot, J.L., Schulz, M.J., Song, Y., Medikonda, S. and Rooy, N. (2010), 'Novel distributed strain sensing in polymeric materials', *Smart Materials and Structures*, **19**(8), 085007.
91. Coleman, J.N., Khan, U. and Gun'ko, Y.K. (2006), 'Mechanical reinforcement of polymers using carbon nanotubes', *Advanced Materials*, **18**(6), 689–706.
92. Winey, K.I., Kashiwagi, T. and Mu, M. (2007), 'Improving electrical conductivity and thermal properties of polymers by the addition of carbon nanotubes as fillers', *MRS Bulletin*, **32**(4), 348–353.
93. Dharap, P., Li, Z., Nagarajaiah, S. and Barrera, E.V. (2004), 'Nanotube film based on single-wall carbon nanotubes for strain sensing', *Nanotechnology*, **15**(3), 379–382.
94. Kang, I., Schulz, M.J., Kim, J.H., Shanov, V. and Shi, D. (2006), 'A carbon nanotube strain sensor for structural health monitoring', *Smart Materials and Structures*, **15**(3), 734–748.
95. Pham, G.T., Park, Y.-B., Liang, Z., Zhang, C. and Wang, B. (2008), 'Processing and modeling of conductive thermoplastic/carbon nanotube films for strain sensing', *Composites Part B*, **39**, 209–216.
96. Yim, J.H., Kim, Y.S., Koh, K.H. and Lee, S. (2008), 'Fabrication of transparent single wall carbon nanotube films with low sheet resistance', *Journal of Vacuum Science & Technology B*, **26**(2), 851–855.
97. Loh, K.J., Kim, J.H., Lynch, J.P., Kam, N.W.S. and Kotov, N.A. (2007), 'Multifunctional layer-by-layer carbon nanotube-polyelectrolyte thin films for strain and corrosion sensing', *Smart Materials and Structures*, **16**(2), 429–438.

98. Dinh-Trong, N., Steitz, J., Lei, B. and Kanoun, O. (2009), 'Influence of the composition of mwcnts layers on the properties of strain gauges', *Proceedings of 9th IEEE Conference on Nanotechnology*, Genoa, Italy, 477–480.
99. Kang, I., Lee, J.W., Choi, G.R., Jung, J.Y., Hwang, S.-H., Choi, Y.-S., Yoon, K.J. and Schulz, M.J. (2006), 'Structural health monitoring based on electrical impedance of a carbon nanotube neuron', *Key Engineering Materials*, **321–323**, 140–145.
100. Breuer, O. and Sundararaj, U. (2004), 'Big returns from small fibers: A review of polymer/carbon nanotube composites', *Polymer Composites*, **5**(6), 630–645.
101. Sinha, N., Ma, J. and Yeow, J.T.W. (2006), 'Carbon nanotube-based sensors', *Journal of Nanoscience and Nanotechnology*, **6**(3), 573–590.
102. Mahar, B., Laslau, C., Yip, R. and Sun, Y. (2007), 'Development of carbon nanotube-based sensors—a review', *IEEE Sensors Journal*, **7**(2), 266–284.
103. Li, C., Thostenson, E.T. and Chou, T.-W. (2008), 'Sensors and actuators based on carbon nanotubes and their composites: A review', *Composites Science and Technology*, **68**(6), 1227–1249.
104. Zhao, Y., Loyola, B.R. and Loh, K.J. (2011), 'Characterizing the viscoelastic properties of layer-by-layer carbon nanotube-polyelectrolyte thin films', *Smart Materials and Structures*, **20**, 075020.
105. Decher, G. (1997), 'Fuzzy nanoassemblies: Toward layered polymeric multicomposites', *Science*, **277**(29), 1232–1237.
106. Loh, K.J., Lynch, J.P., Shim, B.S. and Kotov, N.A. (2008), 'Tailoring piezoresistive sensitivity of multilayer carbon nanotube composite strain sensors', *Journal of Intelligent Material Systems and Structures*, **19**(7), 747–764.
107. Zhao, Y. and Loh, K.J. (2010), 'Tuning the mechanical performance of carbon nanotube sensing skins via post-film fabrication thermal annealing', *Proceedings of 5th World Conference on Structual Control and Monitoring*, Tokyo, Japan, 1–9.
108. Brown, B.H. (2003), 'Electrical impedance tomography (EIT): A review', *Journal of Medical Engineering & Technology*, **27**(3), 97–108.
109. Borcea, L. (2002), 'Electrical impedance tomography', *Inverse Problems*, **18**(6), R99–R136.
110. Vauhkonen, M. (1997), 'Electrical Impedance Tomography and Prior Information,' Ph.D. Thesis, Kuopio University, Natural and Environmental Sciences, Kuopio, Finland.
111. Loh, K.J., Hou, T.-C., Lynch, J.P. and Kotov, N.A. (2009), 'Carbon nanotube sensing skins for spatial strain and impact damage identification', *Journal of Nondestructive Evaluation*, **28**(1), 9–25.
112. Hou, T.C., Loh, K.J. and Lynch, J.P. (2007), 'Spatial conductivity mapping of carbon nanotube composite thin films by electrical impedance tomography for sensing applications,' *Nanotechnology*, **18**(31), 315501/315501–315509.
113. Loh, K.J., Hou, T.-C., Lynch, J.P. and Kotov, N.A. (2007), 'Nanotube-based sensing skins for crack detection and impact monitoring of structures', *Proceedings of 6th International Workshop on Structural Health Monitoring*, Stanford, CA, 1–8.
114. Pyo, S., Loh, K.J., Hou, T.-C., Jarva, E. and Lynch, J.P. (2011), 'A wireless impedance analzyer for automated tomographic mapping of a nanoengineered sensing skin', *Smart Structures and Systems*, **8**(1), 137–153.
115. Lynch, J.P., Hou, T.-C., Kotov, N.A., Kam, N.W.S. and Loh, K.J. (2012), Electrical Impedance Tomography of Nanoengineered Thin Films. Patent, U.S. US 8,159,235 B2, April 17.

116. Loyola, B.R., La Saponara, V. and Loh, K.J. (2010), '*In situ* strain monitoring of fiber-reinforced polymers using embedded piezoresistive nanocomposites', *Journal of Materials Science*, **45**(24), 6786–6798.
117. Loyola, B.R., Zhao, Y., Loh, K.J. and Saponara, V.L. (2012), 'The electrical response of carbon nanotube-based thin films subjected to mechanical and environmental effects', *Smart Materials and Structures*, **22**(02500), 1–11.
118. Loh, K.J. and La Saponara, V. (2012), 'Collaborative Research: Integrated Wind Turbine Blade and Tower Health Monitoring and Failure Prognosis', National Science Foundation (NSF), Division of Civil, Mechanical, and Manufacturing Innovation (CMMI), http://nsf.gov/awardsearch/showAward?AWD_ID=1200521&HistoricalAwards=false.
119. Bar-Cohen, Y. (2011), 'Biological senses as inspiring model for biomimetic sensors', *IEEE Sensors Journal*, **11**(12), 3194–3201.
120. Ryu, D. and Loh, K.J. (2012), 'Strain sensing using photocurrent generated by photoactive P3ht-based nanocomposites', *Smart Materials and Structures*, **21**(065017), 1–9.
121. Ou, J. and Li, H. (2010), 'Structural health monitoring in Mainland China: Review and future trends', *Structural Health Monitoring*, **9**(3), 219–231.
122. Kumar, N.A., Jeon, I.-Y., Sohn, G.-J., Jain, R., Kumar, S. and Baek, J.-B. (2011), 'Highly conducting and flexible few-walled carbon nanotube thin film', *ACS Nano*, **5**(3), 2324–2331.
123. Zhang, X., Sreekumar, T.V., Liu, T. and Kumar, S. (2004), 'Properties and structure of nitric acid oxidized single wall carbon nanotube films', *Journal of Physical Chemistry B*, **108**(42), 16435–16440.
124. Dettlaff-Weglikowska, U., Skakalova, V., Graupner, R., Jhang, S.H., Kim, B.H., Lee, H.J., Ley, L., Park, Y.W., Berber, S., Tomanek, D. and Roth, S. (2005), 'Effect of $SOCl_2$ treatment on electrical and mechanical properties of single-wall carbon nanotube networks', *Journal of the American Chemical Society*, **127**(14), 5125–5131.
125. Xu, G., Zhang, Q., Zhou, W., Huang, J. and Wei, F. (2008), 'The feasibility of producing MWCNT paper and strong MWCNT film from vacnt array', *Applied Physics A (Materials Science Processing)*, **92**(3), 531–539.
126. Blighe, F.M., Hernandez, Y.R., Blau, W.J. and Coleman, J.N. (2007), 'Observation of percolation-like scaling-far from the percolation threshold-in high volume fraction, high conductivity polymer-nanotube composite films', *Advanced Materials*, **19**(24), 4443–4447.
127. Aldalbahi, A. and In Het Panhuis, M. (2012), 'Electrical and mechanical characteristics of buckypapers and evaporative cast films prepared using single and multi-walled carbon nanotubes and the biopolymer carrageenan', *Carbon*, **50**(3), 1197–1208.
128. Whitten, P.G., Gestos, A.A., Spinks, G.M., Gilmore, K.J. and Wallace, G.G. (2006), 'Free standing carbon nanotube composite bio-electrodes', *Journal of Biomedical Materials Research Part B: Applied Biomaterials*, **82B**(1), 37–43.
129. Skakalova, V., Kaiser, A.B., Dettlaff-Weglikowska, U., Hrncarikova, K. and Roth, S. (2005), 'Effect of chemical treatment on electrical conductivity, infrared absorption, and Raman spectra of single-walled carbon nanotubes', *Journal of Physical Chemistry B*, **109**(15), 7174–7181.

130. Wang, S., Liang, Z., Wang, B. and Zhang, C. (2007), 'High-strength and multifunctional macroscopic fabric of single-walled carbon nanotubes', *Advanced Materials*, **19**(9), 1257–1261.
131. Malik, S., Rosner, H., Hennrich, F., Bottcher, A., Kappes, M.M., Beck, T. and Auhorn, M. (2004), 'Failure mechanism of free standing single-walled carbon nanotube thin films under tensile load', *Physical Chemistry Chemical Physics*, **6**(13), 3540–3544.
132. Baughman, R.H., Cui, C., Zakhidov, A.A., Iqbal, Z., Barisci, J.N., Spinks, G.M., Wallace, G.G., Mazzoldi, A., De Rossi, D., Rinzler, A.G., Jaschinski, O., Roth, S. and Kertesz, M. (1999), 'Carbon nanotube actuators', *Science*, **284**(5418), 1340–1344.
133. Coleman, J.N., Blau, W.J., Dalton, A.B., Munoz, E., Collins, S., Kim, B.G., Razal, J., Selvidge, M., Vieiro, G. and Baughman, R.H. (2003), 'Improving the mechanical properties of single-walled carbon nanotube sheets by intercalation of polymeric adhesives', *Applied Physics Letters*, **82**(11), 1682–1684.
134. Whitten, P.G., Spinks, G.M. and Wallace, G.G. (2005), 'Mechanical properties of carbon nanotube paper in ionic liquid and aqueous electrolytes', *Carbon*, **43**(9), 1891–1896.
135. Bradford, P.D., Wang, X., Zhao, H., Maria, J.-P., Jia, Q. and Zhu, Y.T. (2010), 'A novel approach to fabricate high volume fraction nanocomposites with long aligned carbon nanotubes', *Composites Science and Technology*, **70**(13), 1980–1985.
136. Du, F., Fischer, J.E. and Winey, K.I. (2003), 'coagulation method for preparing single-walled carbon nanotube/poly(methyl methacrylate) composites and their modulus, electrical conductivity, and thermal stability', *Journal of Polymer Science, Part B: Polymer Physics*, **41**(24), 3333–3338.
137. Cheng, Q.F., Wang, J.P., Wen, J.J., Liu, C.H., Jiang, K.L., Li, Q.Q. and Fan, S.S. (2010), 'Carbon nanotube/epoxy composites fabricated by resin transfer molding', *Carbon*, **48**(1), 260–266.
138. Bokobza, L. (2012), 'Enhanced electrical and mechanical properties of multiwall carbon nanotube rubber composites', *Polymers for Advanced Technologies*, **23**(12), 1543–1549.
139. Safadi, B., Andrews, R. and Grulke, E.A. (2001), 'Multiwalled carbon nanotube polymer composites: Synthesis and characterization of thin films', *Journal of Applied Polymer Science*, **84**(14), 2660–2669.
140. Cheng, Q., Wang, B., Zhang, C. and Liang, Z. (2010), 'Functionalized carbon-nanotube sheet/bismaleimide nanocomposites: Mechanical and electrical performance beyond carbon-fiber composites', *Small*, **6**(6), 763–767.
141. Olek, M., Ostrander, J., Jurga, S., Mohwald, H., Kotov, N., Kempa, K. and Giersig, M. (2004), 'Layer-by-layer assembled composites from multiwall carbon nanotubes with different morphologies', *Nano Letters*, **4**(10), 1889–1895.
142. Zhang, D. and Cui, T. (2012), 'Tunable mechanical properties of layer-by-layer self-assembled carbon nanotube/polymer nanocomposite membranes for M/Nems', *Sensors and Actuators A*, **185**, 101–108.
143. Zhao, Y. (2011), 'Mechancial Characterization of Multifunctional Layer-by-Layer Carbon Nanotube-Polyelectrolyte Thin Films', M.S. Project Report, University of California, Davis, Department of Civil & Environmental Engineering, Davis, CA.

144. Velasco-Santos, C., Martinez-Hernandez, A.L., Fisher, F.T., Ruoff, R. and Castano, V.M. (2003), 'Improvement of thermal and mechanical properties of carbon nanotube composites through chemical functionalization', *Chemistry of Materials*, **15**(23), 4470–4475.
145. Geng, H., Rosen, R., Zheng, B., Shimoda, H., Fleming, L., Liu, J. and Zhou, O. (2002), 'Fabrication and properties of composites of poly(ethylene oxide) and functionalized carbon nanotubes', *Advanced Materials*, **14**(19), 1387–1390.
146. Blake, R., Gun'ko, Y.K., Coleman, J., Cadek, M., Fonseca, A., Nagy, J.B. and Blau, W.J. (2004), 'A generic organometallic approach toward ultra-strong carbon nanotube polymer composites', *Journal of the American Chemical Society*, **126**(33), 10226–10227.
147. Koerner, H., Liu, W., Alexander, M., Mirau, P., Dowty, H. and Vaia, R.A. (2005), 'Deformation–morphology correlations in electrically conductive carbon nanotube-thermoplastic polyurethane nanocomposites', *Polymer*, **46**(12), 4405–4420.

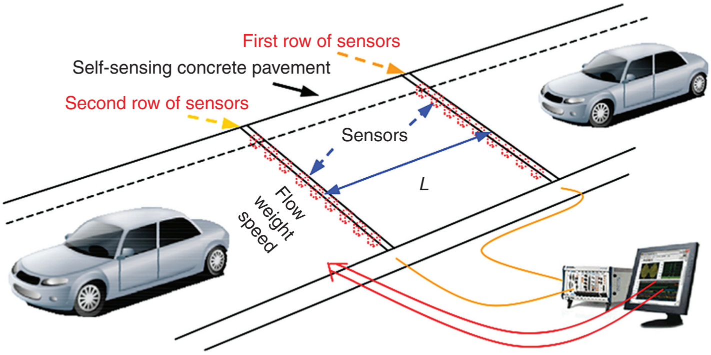
First row of sensors
Self-sensing concrete pavement
Second row of sensors
Sensors
L
Flow
weight
speed

Plate VII (Chapter 11) This schematic shows how *smart* concrete can be embedded in pavements for traffic monitoring applications (Han, B., Yu, X. and Kwon, E. (2009), 'A self-sensing carbon nanotube/cement composite for traffic monitoring', *Nanotechnology*, **20**(445501), 1–5). (*Source*: Image provided courtesy of IOP.)

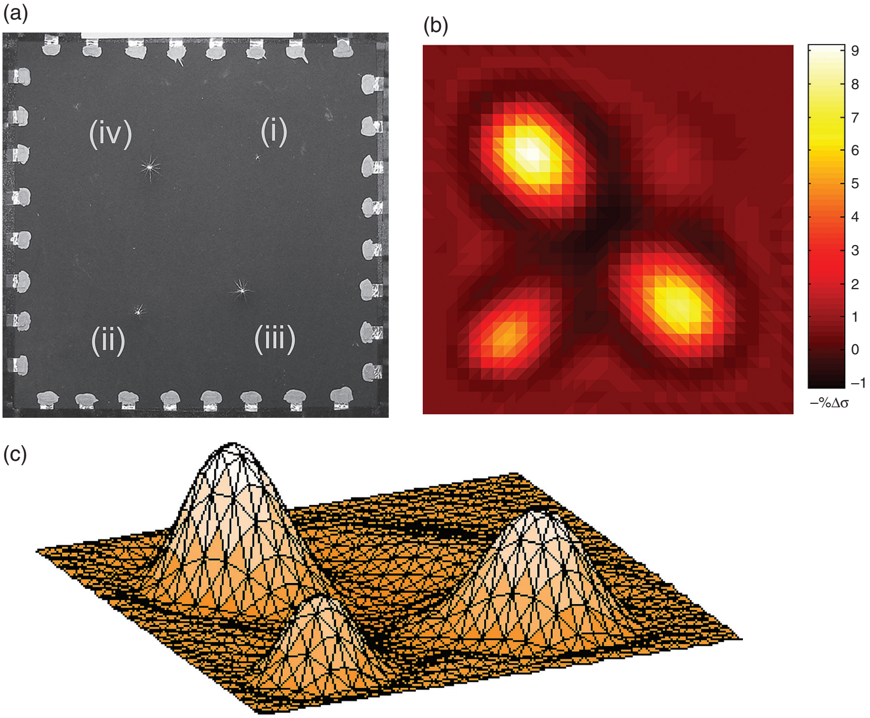

Plate VIII (Chapter 11) (a) The carbon nanotube *sensing skin* has been coated onto an aluminum plate. Upon impact testing, the relative (b) 2D and (c) 3D view of the conductivity maps of the *sensing skin* identify the location and severity of impact damage (Loh, K.J., Hou, T.-C., Lynch, J.P. and Kotov, N.A. (2009), 'Carbon nanotube sensing skins for spatial strain and impact damage identification', *Journal of Nondestructive Evaluation*, **28**(1), 9–25). (*Source*: Images provided courtesy of Springer.)

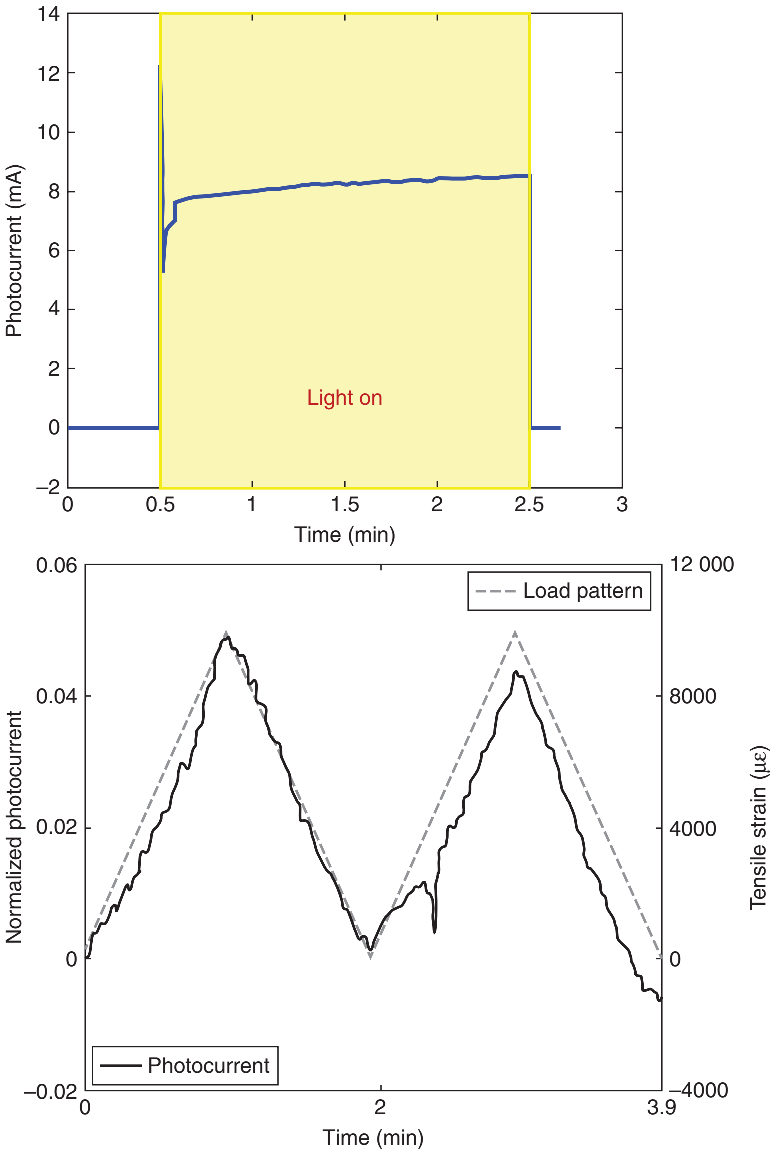

Plate IX (Chapter 11) Photosynthesis-inspired CNT-based multifunctional thin films have been shown (a) to be able to generate photocurrent in response to light, and (b) the amount of generated photocurrent scales with applied strains.

12

Laser-based sensing for assessing and monitoring civil infrastructures

T-Y. YU, University of Massachusetts Lowell, USA

DOI: 10.1533/9780857099136.327

Abstract: This chapter provides an overview of current laser-based sensing techniques and their applications in science and engineering. The chapter first introduces the principles of lasers, followed by a technical description of several laser-based sensing techniques including laser interferometry or electronic speckle pattern interferometry (ESPI), digital shearography, scanning photogrammetry, laser Doppler vibrometry (LDV), and laser-ultrasound. Other laser-related techniques are also discussed, with an emphasis on civil infrastructure applications. The chapter then addresses the safety issue associated with the use of lasers.

Key words: laser, electronic speckle pattern interferometry (ESPI), digital shearography, scanning photogrammetry, laser Doppler vibrometry (LDV), laser-ultrasound, safety.

12.1 Introduction

Since the debut of light amplification by stimulated emission of radiation (LASER) in the 1960s, laser-based sensing techniques have found expanding application and growing influence in science and engineering, as well as in academia and industry. The noncontact nature of using coherent electromagnetic waves (monochromatic radiation) in detecting the characteristics of a remote target in a laser-based sensing is enabled by the high energy levels at which laser beams are generated. This high energy level characteristic of laser-based sensing improves the signal-to-noise ratio (SNR) in many engineering inspection problems, still creating new applications for laser in the twenty-first century.

Laser-based sensing can be destructive (e.g., electric speckle pattern interferometry (ESPI)) or nondestructive (e.g., laser Doppler vibrometry (LDV)), depending on the purpose of investigation. It is one of the noncontact inspection/evaluation/testing (NDI/E/T) methods applied to assess and monitor the performance/condition of engineering materials and structures. While the theoretical foundation of laser-based sensing was laid down by A. Einstein in 1917 (Einstein, 1917), its practical use and

© 2014 Woodhead Publishing Limited

wide application were not possible until W.E. Lamb and R.C. Retherford demonstrated the mechanism of stimulated emission in hydrogen spectra in 1947, the principle of microwave amplification by stimulated emission of radiation (MASER) developed by J.R. Gordon, H.J. Zeiger, and C.H. Townes in 1955, the method of optical pumping theoretically by A. Kastler in 1950 and experimentally by J. Brossel, A. Kastler, and J. Winter in 1952 (Brossel *et al.*, 1952; Kastler, 1957), the experimental work on the use of ruby for lasers, and the MASER principle for the amplification of light proposed by A.L. Schawlow and C.H. Townes in 1958. G. Gould coined the acronym LASER in 1959, while Schawlow and Townes proposed 'optical maser' for the same concept in 1957.

Early developments of lasers include the first solid-state laser (made of synthetic ruby crystal) built by T.H. Maiman at the Hughes Research Labs in 1960, and the first gas laser (made of helium–neon) built by D.R. Herriott, A.M. Javan, and W.R. Bennett at the Bell Telephone Labs in 1960. A.M. Prokorov and N. Basov also made major contributions in the theoretical development of lasers.

While widely used in precision manufacturing at the present time, lasers have been applied in the sensing, inspection, and measurement applications in science and engineering. Since lasers can range in power from the harmless level (>1 mW) (e.g., laser pointer) to the dangerous level (1.3 PW or 1.3×10^{15} W) (e.g., the laser developed by the Lawrence Livermore National Laboratory (LLNL)), they are suitable for the distant inspection and remote sensing of physical parameters such as displacement/deformation and velocity in hostile environments (e.g., high temperature) for a wide variety of applications. Furthermore, lasers have also been used to ignite and/or drive a nuclear fusion reaction. The US National Ignition Facility at the LLNL is a representative example.

When choosing laser-based sensing techniques for a particular application, energy level (watts or W for continuous wave (CW) laser and millejoules or mJ for pulsed laser), laser carrier wavelength (nm), laser resolution (e.g., spot size = μm, angular resolution), laser pulse length (ns) (for pulsed lasers), and pulse interval (ns) (for pulsed lasers) of a selected laser system are usually evaluated. CW or pulsed lasers can be selected, depending on the required sampling resolution for time-dependent parameters such as velocity and dynamic strain. In general, the advantages of laser techniques include (i) noncontact nature of measurement, (ii) flexible range of measurement, (iii) multi-dimensional measurement, and (iv) real-time assessment. On the other hand, the disadvantages of laser techniques include safety considerations and data interpretation.

In this chapter, the principles of lasers are first introduced in a concise manner. Current laser-based sensing techniques including laser interferometry or ESPI, laser digital shearography, laser scanning photogrammetry, LDV, and laser-ultrasound, and other techniques are also described. Safety measures and standards in the use of laser-based sensing techniques are also provided. Finally, research issues associated with laser-based sensing are discussed in Section 12.11.

12.2 Laser principles

A laser is a device that generates an intense light beam of highly monochromatic radiation (coherent electromagnetic waves in space and time) through externally amplifying a light source inside an optical resonator/cavity. In other words, it is an optical oscillator, consisting of an amplifying medium placed inside an optical resonator. Standing waves are excited within the medium to amplify the input light beam in order to produce an intense, highly monochromatic output beam. Theoretically, this is achieved by stimulated or induced emission of radiation by atomic systems. In the following, key principles in the formation of laser are addressed.

12.2.1 Stimulated emission and thermal radiation

As A. Einstein first introduced in 1917, radiation of atomic systems can be generated by the concept of stimulated (induced) emission. When an active, amplifying medium is subject to an intense burst of broadband (incoherent) light, some of the input light energy is absorbed by the atoms of the medium (or the atoms in the medium are excited) such that the energy level of these atoms is increased to a higher level. After achieving the desired energy level, these atoms are released to return to their unexcited state (ground state, lower energy level), accompanied by the emission of light waves (photons).

Selection of a laser amplifying medium is made based upon the requirement that the excited (stimulated) atoms in the amplifying medium can pause or stay in an energy level (metastable state) before returning to their ground state. Light emission of the same input light wavelength in the medium can occur during this process. In other words, stimulated atoms start emitting single wavelength (coherent) light. Figure 12.1 shows three energy states in laser.

Consider a quantized atomic system in two different energy states: E_1 and E_2 with the numbers of atoms N_1 and N_2, respectively. Assuming that E_2 is higher than E_1 and the system is in equilibrium with thermal radiation at a given temperature T, the relationship between N_1 and N_2 can be determined by Boltzmann's equation:

$$\frac{N_2}{N_1} = \frac{\exp(-E_2/kT)}{\exp(-E_1/kT)} \qquad [12.1]$$

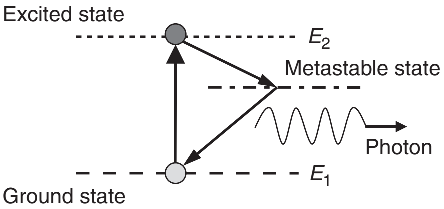

12.1 Three energy states in laser.

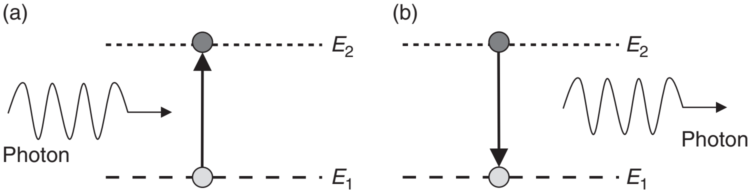

12.2 Energy absorption (a) and emission (b).

where $k = R/N_A$ is the Boltzmann constant ($k = 1.380648 \times 10^{-23}$ J/K), R the gas constant (= 8.314462 J/mol/K), N_A the Avogadro constant (= 6.022141×10^{23} mol^{-1}), and T the absolute temperature (K).

Emission of a photon occurs when an atom in E_2 decays to E_1. Figure 12.2 conceptually describes the energy absorption and emission of atoms. The frequency of emitted/radiated photons (light wave), f, is determined by:

$$v = \frac{(E_2 - E_1)}{h} \qquad [12.2]$$

where h is the Planck constant (= $6.6260069 \times 10^{-34}$ J-s). Since the emission of photons by an atom can be created spontaneously or by stimulation, the energy equilibrium between emission and absorption is:

$$N_2 A_{21} + N_2 B_{21} u_v = N_1 B_{12} u_v \qquad [12.3]$$

where A_{21} is the probability per unit time for spontaneous emission, B_{21} the proportional constant for stimulated emission, B_{12} the proportional constant for stimulated absorption, and u_v the energy density of the radiation frequency v. By applying the Planck radiation formula, the energy density of the radiation frequency can be found by:

$$u_v = \left(\frac{A_{21}}{B_{21}}\right)\frac{1}{\left(\exp(hv/KT)-1\right)} \tag{12.4}$$

The ratio of stimulated emission rate to spontaneous emission rate, R_{ss}, is determined by:

$$R_{ss} = \frac{(B_{21}u_v)}{A_{21}} = \frac{1}{\left(\exp(hv/KT)-1\right)} \tag{12.5}$$

When the value of kT becomes much greater than that of hv, R_{ss} is significantly increased, as shown in Fig. 12.3.

12.2.2 Optical amplification of lights in a medium

The Planck radiation condition requires $B_{21} = B_{12}$, suggesting that $N_2 > N_1$, which means the number (population) of atoms in E_2 is greater that in E_1 (called population inversion). When population inversion occurs, a light

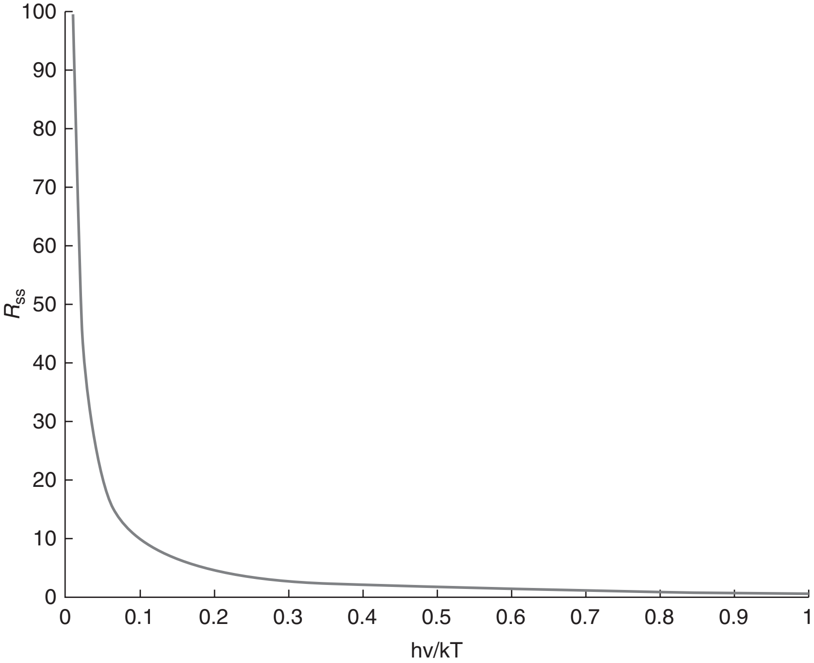

12.3 The ratio of stimulated emission rate to spontaneous emission rate, R_{ss}.

beam will increase in intensity (or be amplified) as it passes through the amplifying medium. In other words, optical amplification happens when the gain due to stimulated emission exceeds the loss due to absorption.

There are several approaches to achieving optical amplification, including (i) optical pumping (photon excitation), (ii) electron excitation, (iii) inelastic atom–atom collisions, and (iv) chemical reactions. In the optical pumping approach, an external light source is applied to produce a high population of energy levels in the amplifying medium by selective optical absorption. Solid-state lasers and the ruby laser are based on this principle. In the electron excitation approach, direct electron excitation is employed in a gaseous discharge process to produce population inversion. Examples include the gaseous ion lasers and the argon laser. In the inelastic atom–atom collision approach, two different types of gas atoms are used, whose excited energy states coincide or are very close. If one excited state of a gas atom is metastable, then the other gas atom will decay by radiation and emit photons. For example, in the helium–neon laser, the energy level of a neon atom is first increased by an excited helium atom, and the laser transition occurs in the neon atom. In the chemical reaction approach, an excited state of molecules or atoms is achieved by the chemical change in these molecules or atoms. In the example of the hydrogen fluoride chemical laser, excited hydrogen fluoride molecules are generated from a chemical reaction. Other theoretical topics on the principle of lasers can be found in the literature (Kock, 1969; Fowles, 1975; Svelto, 1982; Weber, 2001; Csele, 2004; Chang, 2005; Stenholm, 2005; Chu 2007).

Examples of laser include gas lasers (e.g., helium–neon or He–Ne, argon or Ar, krypton, carbon dioxide or CO_2), solid-state lasers (e.g., ruby, neodymium, calcium fluoride, calcium tungstate, and neodymium-doped yttrium aluminum garnet (Nd:YAG)), dye lasers (e.g., sodium fluorescein, rhodamine, cresyl violet, and coumarin), semiconductor diode lasers (e.g., light-emitting-diode (LED)), and fiber lasers (e.g., erbium, neodymium, dysprosium, praseodymium, thulium, and ytterbium). These lasers are developed for various purposes and different materials. For example, the Nd:YAG laser typically works with metals and composite materials, while the CO_2 laser is best for glasses and ceramics. Table 12.1 lists the properties of selected lasers.

Table 12.1 Properties of selected lasers

	Color	Wavelength (nm)
Ruby laser	Red	693
Helium–neon laser	Orange-red	632.8
Argon laser	Blue-green	488
Nitrogen laser	Ultraviolet	337.1
Carbon dioxide	Infrared	1060

12.3 Laser interferometry or electronic speckle pattern interferometry

Laser interferometry or ESPI, also known as computer-aided speckle pattern interferometry (CASPI), television holography, and video holography, is the electronic processing of speckle patterns produced by a laser interferometer consisting of two laser beams (using a beam splitter) generated from the same laser source. Interferometers can be categorized into amplitude-splitting (e.g., Michelson, Mach-Zehner (Zipser and Franke, 2004), Fabry–Pérot, Fizeau) and wavefront-splitting (e.g., Fresnel bi-prism, Rayleigh, Lloyd's mirror).

When a target with a perfectly-smooth surface is illuminated by laser, no speckles will be generated and an amplitude-splitting interferometer such as Michelson interferometer can be used. However, when a rough surface is encountered, a speckle pattern (irregular fringe pattern) will be revealed by the use of a coherent light source such as a laser. In ESPI, the laser interferometer generates a primary beam split into two beams: one is the object beam, which passes through a beam expander and is used to illuminate the target, and the other is the reference beam, which is directed to the image recording device or sensor, typically a charge-coupled device (CCD). The returned beam reflected from the target surface is also recorded by the CCD. When the beam path difference between the object beam and the reference beam is within the coherent length of the primary laser beam, the two beams will interfere and produce a speckle pattern. The purpose of a frame grabber is to capture and store these speckle images for post-processing and data interpretation. Further information on speckle interferometry can be found at Jones and Wykes (1989).

Measurement schemes for in-plane and out-of-plane deformation and velocity are shown in Figs 12.4 and 12.5, respectively.

12.3.1 Laser holographic interferometry

Laser holographic interferometry is a technique combining laser interferometry and holography. The principle of holography is based on the fact that, via simultaneously recording a reference light (laser) beam (split by a beam splitter) and a returned, scattered light beam from the surface of a target on a holographic plate, reconstruction of an exact replica of the target can be achieved. The image recorded on the holographic plate is called a hologram of the target, which carries both the amplitude and phase of the returned, scattered beam from the target. The first exposure of the holographic plate by the reference beam results in a reference hologram, while the second exposure by the returned beam imposes all changes of the target to the reference hologram. The result is a fringe pattern of the target,

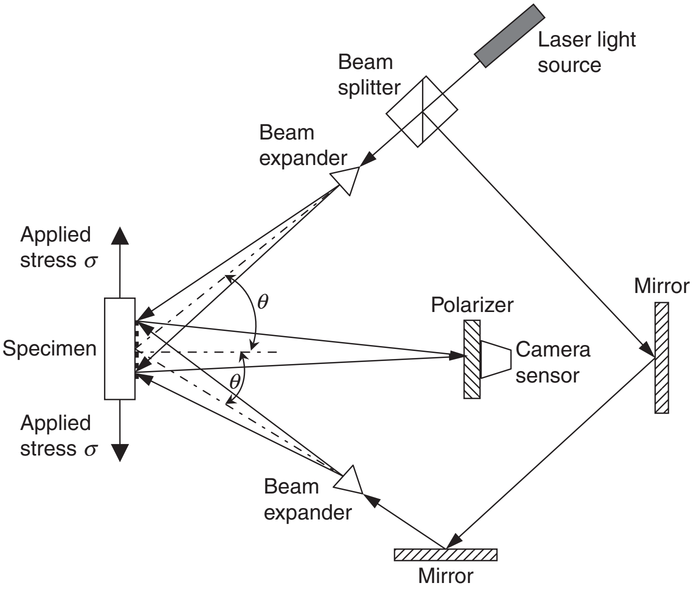
Laser light source
Beam splitter
Beam expander
Applied stress σ
θ
Polarizer
Mirror
Specimen
Camera sensor
θ
Applied stress σ
Beam expander
Mirror

12.4 Laser interferometry or ESPI for in-plane measurement.

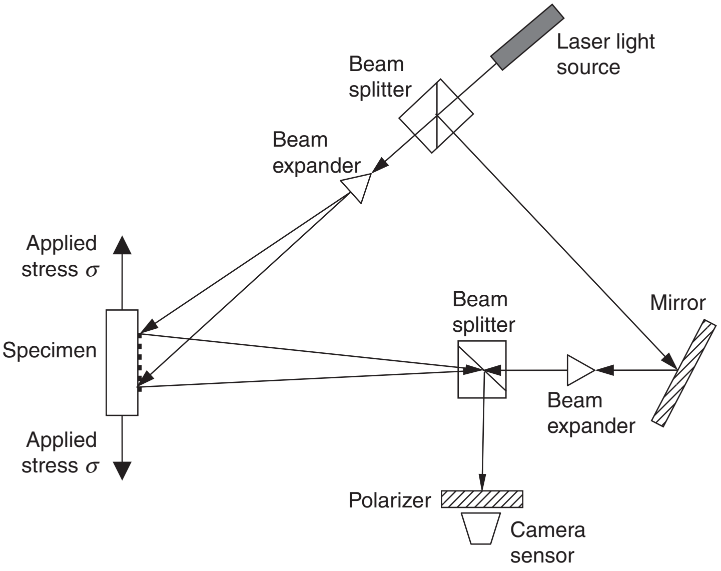
Laser light source
Beam splitter
Beam expander
Applied stress σ
Beam splitter
Mirror
Specimen
Beam expander
Applied stress σ
Polarizer
Camera sensor

12.5 Laser interferometry or ESPI for out-of-plane measurement.

containing all information about the change that occurred between the first and the second exposures. In laser holographic interferometry, both a reference beam and a returned beam (scattered from the target) are required. Additional information on holographic imaging can be found at Erf (1974)

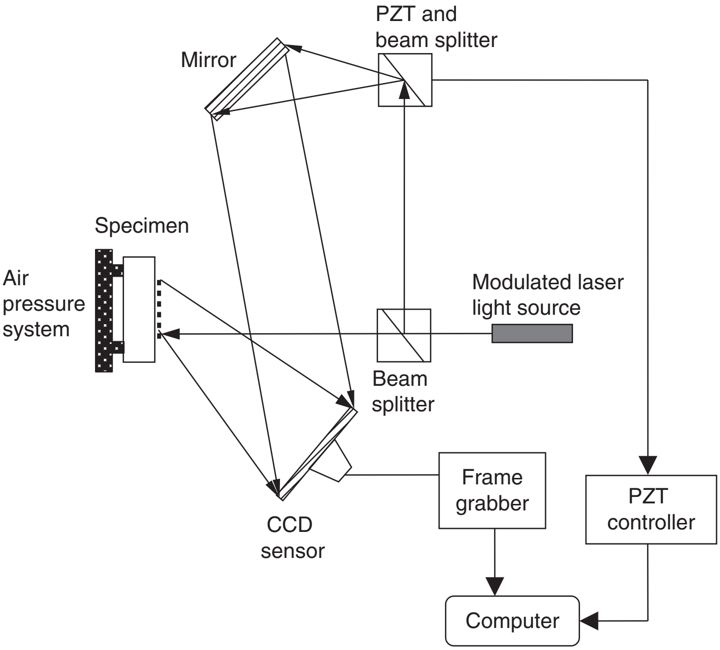

12.6 Laser phase shifting holographic interferometry. (*Source*: Modified after Twitto *et al.*, 1996.)

and Vest (1979). Further information on laser interferometry can be found at Chu (2007) and Hariharan (2007).

Twitto *et al.* (1996) used an He–Ne laser to illuminate loaded brass plate specimens and a piezoelectric (PZT) crystal controlled mirror for the holographic imaging of the specimen. The reflected laser beam from the specimen was measured by a CCD sensor and the PZT mirror. Phase shifting was included in the development of their work. Figure 12.6 illustrates the experimental set-up of a holographic interferometry utilizing phase shift.

12.4 Laser digital shearography

Laser digital shearography is an interferometric technique developed to overcome the limitations of holography, due to the advantages including (i) removing requirement for a reference light beam, (ii) reduced coherence length, and (iii) direct measurement of surface strain (Hung *et al.*, 2007). The principle of image shearing is based on a light beam passing through a doubly refractive prism and splitting into two angularly separated beams. Figure 12.7 shows the principle of laser digital shearography. Through the image-shearing device, two nonparallel light beams scattered from two different object points become nearly collinear, and the resulting low spatial

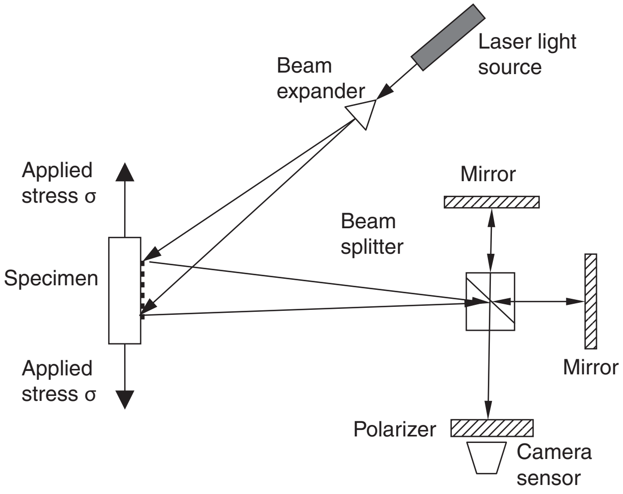

12.7 Laser digital shearography.

frequency of the interference fringes can be resolved with a low resolution image sensor such as a CCD. The two sheared wavefronts transmitted by the two axes of the image's hearing device, however, are orthogonally polarized. Therefore, they will not interfere with each other. To enable interference, a polarizer with its polarization axis oriented at an azimuth of 45° is required, as shown in Fig. 12.7. Since the illuminated object surface is generally optically rough, interference of the two sheared wavefronts will result in a speckle pattern embedded in the shearographic image. This speckle pattern image of the specimen before loading can be represented by Hung and Ho (2005):

$$I - I_0(1+\mu\cos\phi) \qquad [12.6]$$

where I is the speckle image intensity at the image plane of the CCD sensor before loading, I_0 the intensity of the laterally sheared image, μ the amplitude of modulation of the speckle pattern, and ϕ the random phase angle. The speckle pattern image of the specimens after loading can be expressed by:

$$I' = I_0\left[1+\mu\cos(\phi+\Delta)\right] \qquad [12.7]$$

where I' is the speckle image intensity at the image plane of the CCD sensor after loading and Δ the phase angle change due to surface deformation. To remove the random phase angle change, the difference between I and I' is used:

$$I_d = 2I_0\,[\mu \sin]\left(\phi + \frac{\Delta}{2}\right)\sin\frac{\Delta}{2} \qquad [12.8]$$

where I_d is evaluated at the pixel level and used for relating the level of loading and surface deformation. Digital shearography using multiple wavelengths has also been proposed by Kastle *et al*. (1999). A comparison between digital shearography and ESPI can be found at Findeis and Gryzagoridis (2004).

12.5 Laser scanning photogrammetry

Laser scanning is a remote inspection/sensing method in which laser beams are steered/directed along a line (2D) (Fig. 12.8) or within an area (3D) for distance measurement. Laser scanners operate in either (i) stationary mode or (ii) mobile mode. In stationary mode, laser scanners are typically installed on a tripod, while in mobile mode, laser scanners can be handheld, vehicle-mounted, robot-mounted, or aircraft-mounted. Laser scanning photogrammetry is an integrated technique combining laser scanning and digital photogrammetry. Digital photogrammetry is based on the processing of images and produces digital terrain models (DTM), digital surface models (DSM), orthoimages, and 2D/3D reconstruction and classification of objects for mapping and visualization purposes (Baltsavias, 1999). The main differences between laser scanning and digital photogrammetry are summarized in Table 12.2.

Key components of laser scanning photogrammetry include: (i) a laser scanner, (ii) a digital camera, (iii) global positioning system (GPS) (when the position of the laser scanner is changed), (iv) a total station (optional), (v) a portable computer, and (vi) data processing software for 3D modeling and data registration.

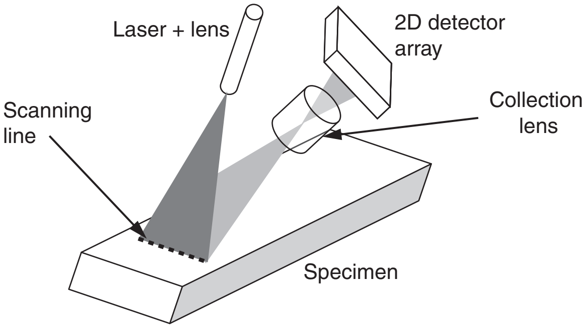

12.8 Principle of 2D laser scanning.

Table 12.2 Comparison between laser scanning and photogrammetry

	Laser scanning	Digital photogrammetry
Sensing scheme	Active	Passive
Power level	High	Low
Sensor type	Point sensors with polar geometry	Frame/linear sensors with perspective geometry
Sampling area	Full area	Point wise sampling
Acquisition of 3D coordinates	Direct	Indirect
Image type	Monochromatic (low quality, single spectral)	Geometrical/radiometrical (high quality, multi-spectral)

El-Omari and Moselhi (2007, 2008) applied a 3D laser scanning system (Riegl LPM 100 VHS LADAR) and photogrammetry (including software, computer, and a digital camera) to generate point cloud data of a construction site and several boxes for image reconstruction and 3D modeling. Scanning angular resolution varied from 0.015° to 0.75°, and the inspection distance ranged from 1 to 50 m. Image resolution (or the distance between any two points in the point cloud image) depended on (i) the distance between the target and the laser scanner, and (ii) the angular resolution of the laser scanner. Inspection time depended on the required image resolution and the spatial range of inspection (size of the target). For example, with a distance of 4.3 m, horizontal angular range of 21°, vertical angular range of 18°, and an angular resolution of 0.015°, the total inspection time was 58 min, while the total inspection time could be reduced to 15 s in the case of 0.75° angular resolution (El-Omari and Moselhi, 2008).

Rodriguez *et al.* (2008) developed a portable laser photogrammetric sensor by combining a laser distance meter (ranger) (Leica Zinder Distro Plus) and a digital camera. The laser distance meter could measure distance ranging from 0.2 to 200 m at a resolution of 1.5 mm. Sturzenegger and Stead (2009) adopted laser scanning photogrammetry in a photogrammetric rock cut survey and used a 3D laser scanner (Optech ILRIS-3D), a digital camera, and data processing software. They scanned few terrestrial targets at distances ranging from 29 to 163 m. Armesto *et al.* (2009) applied an analog semi-metric camera, a laser total station, and a monoscopic digital photogrammetric station for the close-range (<100 m) evaluation of timber roof construction. 3D finite element modeling was also adopted to perform static and dynamic analyses of the timber roof structure. In other damage detection problems such as surface potholes in asphalt pavement structures, 3D laser scanning technology was applied in literature (Koch and Brilakis, 2011).

12.6 Laser Doppler vibrometry

A laser Doppler vibrometer is a passive, nondestructive, dynamic interferometer in which the beam emerging from the laser is divided into two: one of which is used as a transmitting beam and the other as a reference beam for coherent detection.

The transmitting beam illuminates the surface of a target (which can be a solid structure, or a particle in air or in fluid), while the reference beam is combined with the returned beam from the target at the detector for coherent detection. The frequency shift between the returned beam and the reference beam is related to the instantaneous velocity of target, due to the Doppler effect. This frequency shift is the Doppler frequency shift. The basic laser Doppler vibrometer is a single point vibrometer. With the addition of a video camera and two orthogonal mirrors, scanning LDV systems can be made to allow large surface measurement with high spatial resolution. LDV is a mature technique for the nondestructive measurement of velocities of macroscopic objects (e.g., engineering structures), fluids (e.g., fluid flow structure), and vibration noise.

Depending on the type of velocity to be measured, LDV can be categorized into translational, rotational, and torsional LDV (Fig. 12.9). In translational LDV, the direction of measured motion is in parallel to the laser beam direction, while in rotational and torsional LDV, the direction of measured motion is perpendicular to the laser beam direction. LDV has been applied

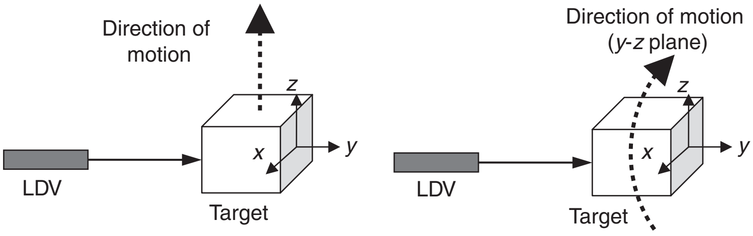

Translational LDV

Rotational LDV

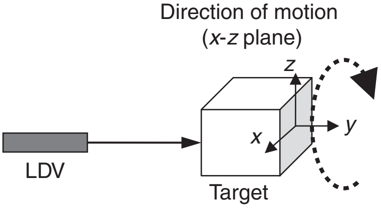

Torsional LDV

12.9 Types of LDV.

in the measurements of translational, rotational (Bell and Rothberg, 2000), and torsional (Halliwell, 1996; Drew and Stone, 1997; Oberholster *et al.*, 2012) velocities in literature.

The principle of LDV is briefly described as follows. Consider the rotational velocity measurement problem using LDV, in which the laser beam is configured on the plane perpendicular to the axis of rotation. The target position x can be assumed to be:

$$x = x_0 \cos(\omega_t t) \tag{12.9}$$

where x_0 is the maximum amplitude of x, ω_t the angular velocity of rotation, and t the time variable. The rotational velocity υ is found by:

$$\upsilon = \frac{dx}{dt} = -x_0 \omega_t \sin(\omega_t t) \tag{12.10}$$

When measuring the laser beam returned from a moving target, the optical frequency is shifted due to the Doppler effect. This Doppler frequency shift f_d is given by:

$$f_d = 2\upsilon \cos \frac{\alpha}{\lambda} \tag{12.11}$$

where α is the intersection angle between the laser beam and the target velocity direction, and λ the optical wavelength. Substituting Equation [12.10] into Equation [12.11] leads to:

$$f_d = -2x_0 \omega_t \sin(\omega_t t) \cos \frac{\alpha}{\lambda} \tag{12.12}$$

The intensity of measured returned laser beam I_V can be expressed as:

$$I_V = I_{V0} \cos[2\pi f + \phi] = I_{V0} \cos\left[2\upsilon \cos \frac{\alpha}{\lambda} + f_0\right] + \phi \tag{12.13}$$

where I_{V0} is the maximum intensity of the returned beam, $f = f_d + f_0$ the total frequency shift, f_0 a fixed frequency shift used to improve SNR, and ϕ the random phase angle. In this result, the rotational velocity υ is related to the measured intensity of the returned laser beam I_V.

For basic LDV systems, the lead time for changing one point position to another can be less than 10^{-3} s. Typical velocity range for LDV is up to 11 000 rpm or 1000 rad/s. The frequency range in rotational velocity measurement problems is from 1 Hz to 10 kHz, at a calibration accuracy of approximately 0.5% (Castellini *et al.*, 2006). For out-of-plane translational velocity measurements, the frequency range is from 0 Hz to 1 MHz (Olson *et al.*, 2010).

Further information on the theory of rotational vibration measurements using LDV can be found at Bell and Rothberg (2000) and Rothberg and Tirabassi (2012).

LDV has been applied in various fields including modal vibrational analysis, rotating structures, on-line quality control, structural damage detection, assessment of microelectromechanical systems (MEMS) (DeCoster *et al.*, 2008), micro-optical-electromechanical systems (MOEMS), and nanoelectromechanical systems (NEMS),material characterization (Huang *et al.* 2007), biomedical applications, and condition assessment in civil engineering (Castellini *et al.*, 2006).

Pascal *et al.* (1993) applied a laser Doppler vibrometer (Polytec OFV 1000) to the characterization of vibrating plates.

Castellini and Santolini (1998) applied a laser Doppler vibrometer (Polytec OFV 3000) to measure the vibration of a naval propeller in water. Mallet *et al.* (2004) used LDV and Lamb waves on two rectangular plates for crack detection. Vanlanduit *et al.* (2004) investigated the microphony problem of a mask of a picture tube in a television using LDV. Damljanovic and Weaver (2005) applied a laser Doppler vibrometer (Polytec PDV 100) of 50 μm spot size and 0.05 μm/s resolution to the vibration measurement problem of rail specimens. Hong *et al.* (2007) applied an scanning laser Doppler vibrometer (SLDV) (Polytec LSV PSV 3000) to determine the piezoelectric coefficients and elastic constant of a piezoelectric thin film on silicon substrate cantilevers. The SLDV was used to measure the displacement and first/fundamental resonant frequency of thin film specimens. Prazenica *et al.* (2007) used LDV in the surface inspection of artwork and frescoes. Hapsara and Iliescu (2008) applied LDV to biomedical sensing by inspecting a bovine cortical tibia *in vitro* using a Polytec PSV 400 system. Olson *et al.* (2010) used LDV (Polytec PSV 400 3D-M) and Lamb waves to inspect 7075-T6 aluminum sheets. Oberholster and Heyns (2011) applied LDV (Polytec PSV 300) to characterize a multi-blade test rotor in operation.

Limitations of LDV include (i) measurement resolution (e.g., range-dependent and frequency-dependent resolution of analog and digital velocity decoders), (ii) measurement uncertainty (e.g., in the optical components of LDV and in the analog signal processor), (iii) direction uncertainty (e.g., misalignment of laser beam path with respect to the out-of-plane velocity direction), (iv) LDV standoff distance (e.g., surface reflection-dependent performance of LDV), (v) SLDV spatial resolution (e.g., minimum spot size of the laser beam), (vi) SNR (e.g., poor SNR on measuring low diffusive surfaces due to speckle effects), and (vii) environmental measurement conditions (e.g., dust, temperature, and pressure)

(Castellini *et al.*, 2006). Signal denoising and filtering to improve SNR of LDV can be achieved by hardware design or by software processing. Both frequency-domain (e.g., Fourier analysis) and time-domain (e.g., wavelets and multiresolution analysis (Prazenica *et al.*, 2007)) filtering techniques can be applied.

Also, data compression and evaluation are needed when dealing with large amounts of data. Techniques such as principal component analysis (PCA) and singular value decomposition (SVD) can be used to evaluate the quality of data and to reduce the data size for interpretation (Vanlanduit *et al.*, 2004). In addition, the use of auxiliary computational models in LDV, 3D modeling tools such as SolidWork® can be used for data visualization. Finite element (FE) models can also be used to complement the experimentally obtained LDV data (Olson *et al.*, 2010).

12.7 Laser-ultrasound

Laser-ultrasound (also known as laser-ultrasonics, laser-based ultrasound) is an active, nondestructive, dynamic, interferometric, sensing method capable of revealing the subsurface condition of a target. Different from LDV, in laser-ultrasound, surface/subsurface ultrasonic vibration of a target is generated by one laser and the response is measured either by another laser (Amziane *et al.*, 2012), or by other sensors (Park *et al.*, 2009). In the case of using laser for both excitation and measurement, an interferometer is required to couple the two lasers. In laser-ultrasound the material surface serves as the emitting ultrasonic transducer. The ultrasonic source is produced either by a thermoelastic mechanism or material ablation. Detection is based on the Doppler effect that produces a frequency or phase modulation in the returned laser beam. Demodulation of laser signals is performed by the interferometer that is insensitive to speckle (confocal Fabry–Pérot, or photorefractive or Michelson interferometer). Laser-ultrasound is particularly useful for detecting flaws in targets with complex geometry and measurements on hot surfaces.

In laser-ultrasound techniques, ultrasonic waves or mechanical waves including body waves and surface waves are used to characterize a target. The governing equation of mechanical wave propagation in media is the Navier equation of motion. For homogeneous and isotropic materials (Malvern, 1969),

$$(\lambda_L + \mu_L)\nabla(\nabla \cdot u) + \mu_L \nabla^2 x + \rho F = \rho \frac{\partial^2 u}{\partial t^2} \qquad [12.14]$$

where $\lambda_L = Ev/(1+v)(1-2v)$ and $\mu_L = E/2(1+v)$ are the Lamé constants, ∇ the Laplace operator or Laplacian, $u = u(x_{i;}\, i = 1, 2, 3)$ the displacement (position) field of a unit cell, ρ the density of the unit cell, and F the body force of the unit cell per unit mass. The traction boundary condition is needed for solving the observable displacement field at the boundary.

$$\lambda_L(\nabla \cdot u)\hat{n} + \mu_L\left(\frac{\partial u_i}{\partial x_j} + \frac{\partial u_j}{\partial x_i}\right) \cdot \hat{n} = F_{BC} \qquad [12.15]$$

where $\hat{n}$ is the normal vector at the boundary and F_{BC} the prescribed force function acting on the boundary. Displacement fields at the boundary in different conditions (e.g., different mechanical properties: λ_L, μ_L) are measured in order to retrieve the variation in the mechanical properties of materials. Velocity fields $\partial u/\partial t$ and acceleration fields $\partial^2 u/\partial t^2$ can be determined either analytically when displacement fields u are obtained by evaluating the Navier equation, or numerically when displacement fields are measured over a period of time. The Navier equation is also the general form of the governing equation of mechanical waves.

Depending on the boundary condition of the medium, different modes of mechanical waves can be accommodated by the medium. Body waves including compressional waves (or dilational waves, pressure waves or P-waves) and distortional waves (or equivoluminal waves, rotational waves, or shear or S-waves) can occur in an infinite medium or in a medium without finite boundaries. Surface waves including Rayleigh waves and Love waves can occur in a semi-infinite medium or in a medium with one finite boundary. Lamb waves can occur in thin plate and shells (special finite media). Table 12.3 lists the properties of selected mechanical waves. In Table 12.3, the direction of particle movement is determined with respect to the direction of wave propagation. It is obvious that changes in the mechanical properties (E, ν, ρ) of a target are reflected in the variation of these wave velocities. The presence of anomalies on/inside a target, on the other hand, can also be reflected in the change of wave velocity, owing to the scattering of waves when encountering the anomalies. The phase and group velocities of Love waves (Jardetzky *et al.*, 1957) can be numerically evaluated, while the phase and group velocities of Lamb waves can be obtained by solving the Rayleigh-Lamb equation (Viktorov, 1967). Further information about laser-ultrasound can be found at Scruby and Drain (1990).

Pedrini *et al.* (2002) combined 3D digital holography with LDV (a pulsed Q-switched ruby laser) and a high-resolution CCD (Pulnix TM-1001) camera to reconstruct the dynamic profile of specimens with curved surfaces. Markov *et al.* (2003) proposed a whole field laser Doppler vibrometer, and demonstrated the performance of the system on a clamped, circular thin plate. The thin plate was remotely excited by a pulsed acoustical exciter, which generates

Table 12.3 Types of mechanical waves

Class	Particle movement	Wave velocity	Name
Body wave	Parallel	$v=\sqrt{\dfrac{E(1-\upsilon)}{\rho(1+\upsilon)(1-2\upsilon)}}$	P-wave
	Orthogonal	$v=\sqrt{\dfrac{E}{2\rho(1+\upsilon)}}$	S-wave
Surface wave	Elliptical orbit, symmetrical mode	$v\cong\dfrac{0.87+1.2\upsilon}{1+\upsilon}\sqrt{\dfrac{E}{2\rho(1+\upsilon)}}$	Rayleigh wave
	Horizontally polarized, shear mode		Love wave
	Orthogonally symmetric and asymmetric	$v_p=\dfrac{v_g}{\sin\varphi}$ where v_p = phase velocity, v_g = group velocity, φ = angle of incidence of the incident longitudinal wave	Lamb wave

a brief, broadband shock wave that stimulates the vibration of the plate. Huber *et al.* (2005) developed laser-acoustic microscopy using an Nd:YAG laser to generate 800 MHz (and higher) longitudinal mode ultrasound in several polymer films. Longo *et al.* (2006) used a Panametrics 10 MHz transducer to generate surface acoustic waves (SAW) on a steel beam and a laser vibrometer (Polytec PSV 300) for measuring the SAW response of the specimen. Kim *et al.* (2006) used a pulsed Nd:YAG laser to generate focused ultrasonic (Lamb) waves on an aluminum plate and a Michelson interferometer (Fiberpro MI7000) for measuring the response. Zhang *et al.* (2006) applied a pulsed Nd:YAG laser to generate Lamb waves on paper samples and a CW photorefractive laser interferometer for measurement. The ultrasonic wave response was used to determine the Young's modulus, shear rigidity, and thickness of paper samples. In the aerospace industry, Kalms *et al.* (2008) applied a pulsed CO_2 laser to generate ultrasounds in semicrystalline polyphenylene sulfide thermoplastic composites (a material used in modern aircrafts such as Airbus A380) and a macropulse YAG laser for detection. In the nuclear industry, Liu and Yang (2008) applied a pulsed Nd:YAG laser, an interferometer (Polytec OFV 511), and an oscilloscope to characterize the cladding condition on hydrogen-charged Zircaloy tubes that are used in nuclear reactors. Material properties such as Young's modulus and Poisson's ratio were identified from the experiment.

Yu and Haupt (2010) proposed a distant acoustic-laser nondestructive evaluation (NDE) technique utilizing a high powered standoff parametric acoustic array (PAA) and LDV for the detection of debonding and delamination in multi-layer fiber reinforced polymer (FRP) wrapped-concrete systems. In their development, a focused sound beam is generated by the PAA such that the beam diameter can be controlled to directly and locally excite the surface area (where damages/defects are embedded) in the FRP-concrete systems, from a distance exceeding 30 m. Flaws and structural damage embedded underneath the externally bonded FRP plates or wrapped FRP sheets will be detected through the acoustically excited vibration launched by the system (Fig. 12.10). Surface dynamic signatures (Rayleigh waves) of damaged and intact regions are collected by laser Doppler vibrometer and analyzed for damage detection. The laser vibrometer beam size provides us the opportunity to obtain spatial resolution on the order of a millimeter. In this development, the PAA has two sources of sound: one source is high frequency, which is generated directly from one or more high-frequency transducers (2–7 kHz) and the other is low frequency, which is generated from nonlinear effects in the volume of air in front of the transducer (500 Hz–2 kHz). The PAA source can provide a practical means to deliver the necessary level of acoustic power in air to the void underneath the FRP sheet while minimizing system size and weight, reducing the sound level imposed on personnel close to the source. To be able to detect voids of small size between FRP and concrete, the use of PAA source exhibits potential advantages on this particular application.

Amziane *et al.* (2012) investigated the crack detection problem in a composite spherical particle consisting of four spherical layers, using a laser

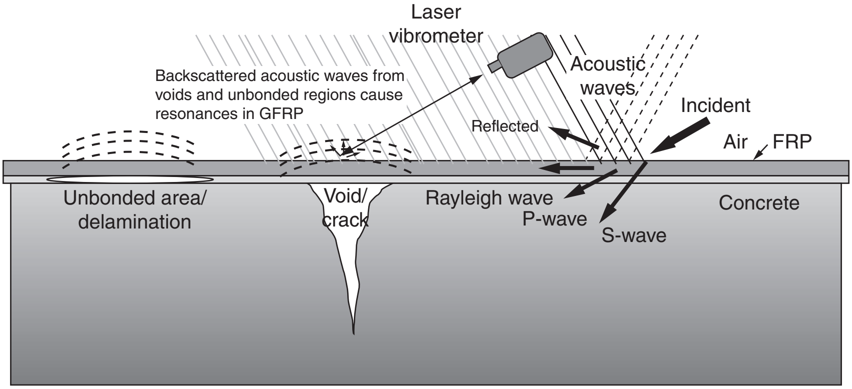
Laser vibrometer
Backscattered acoustic waves from voids and unbonded regions cause resonances in GFRP
Acoustic waves
Incident
Reflected
Air
FRP
Unbonded area/ delamination
Void/ crack
Rayleigh wave
P-wave
S-wave
Concrete

12.10 Laser-acoustic technique for detecting subsurface debonding and cracking. GFRP, Glass fiber reinforced polymer. (Yu and Haupt, 2010).

homodyne interferometer with 532 nm wavelength, 8 mm focal length, 0.5 numerical aperture, and 1 μm spot resolution.

Advantages of laser-ultrasound techniques include (i) noncontact and remote nature, (ii) applicability in hostile environments, (iii) rapid scanning capability, (iv) applicability on geometrically complex targets, (v) ability to generate ultrasonic point source both temporally and spatially, (vi) broadband inspection (in pulsed laser), (vii) high resolution, (viii) ability to generate both surface and bulk acoustic waves, and (ix) ability to generate various ultrasonic surface wavefronts.

Disadvantages of laser-ultrasound techniques include (i) being relatively expensive, (ii) lower sensitivity (iii) material-dependent ultrasound generation efficiency (e.g., material's optical absorption properties), and (iv) laser safety requirements.

12.8 Other laser-based techniques

Laser diffraction grating: Kurita and Ma (1998) used an He–Ne (helium–neon) laser beam (wavelength = 0.6328 μm) to illuminate the surface of a structural steel specimen in order to determine surface strain (ε_x) using a laser diffraction grating method. The intensity distribution of the diffracted laser beam was measured with a plasma-coupled device (PCD) sensor. The strain was calculated from the shift of the locations of the first-order laser beam spots measured with the PCD sensor. They found that neither the incident angle of laser nor the deformation of the grating affect the measured surface strain. Figure 12.11 schematically shows the experimental set-up of the method.

Laser-acoustic-emission (laser-AE) technique: Enoki and Nishinoiri (2005) proposed an He–Ne laser-AE system to measure high-temperature (~773 K) AE signals during sintering of alumina ceramics and thermal

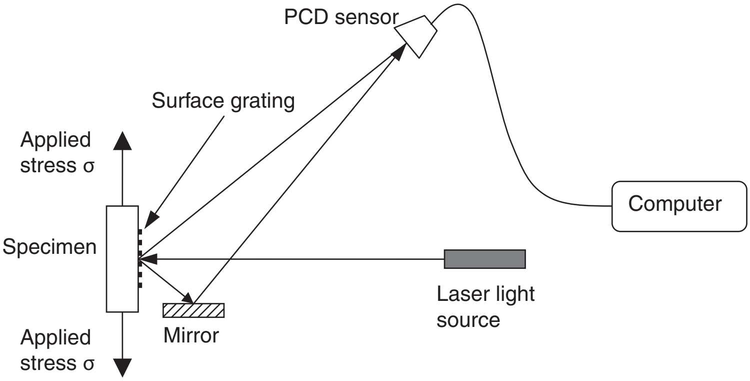

12.11 Laser diffraction grating.

spying of alumina powder on steel substrate to overcome the difficulties associated with conventional AE sensors, which typically do not perform well above 600 K.

Laser infrared photothermal radiometry (laser IR-PTR): Mandelis (2001) developed a laser IR-PTR using an argon-ion laser modulated by an acousto-optic modulator to direct the laser beam onto the specimen surface. The laser beam is broadened with a diffuser to attain a larger spot size for 1D analysis. The emitted IR radiation from the specimen surface is collected and focused onto the detector using two off-axis paraboloidal mirrors. Collected signals (amplitude and phase) are pre-amplified, sent to a lock-in amplifier, and recorded over a range of laser modulation frequencies for data analysis. Experimental work was reported on the surface roughness measurement of thermally processed carbon steels, thermal-barrier coatings, and industrial silicon wafers. Figure 12.12 shows the inspection scheme of laser IR-PTR.

Laser photoacoustic spectroscopy: van Neste *et al.* (2008) used a pulsed quantum cascade laser (QCL) to illuminate the surface of stainless steel specimens coated with varying amounts of chemical residue and a quartz crystal tuning fork (QCTF) to detect the scattered laser beam in developing a laser photoacoustic spectroscopy system.

Wireless power transmission using laser: Park *et al.* (2012) inspected aluminum plates using an Nd:YAG laser as power source to remotely excite

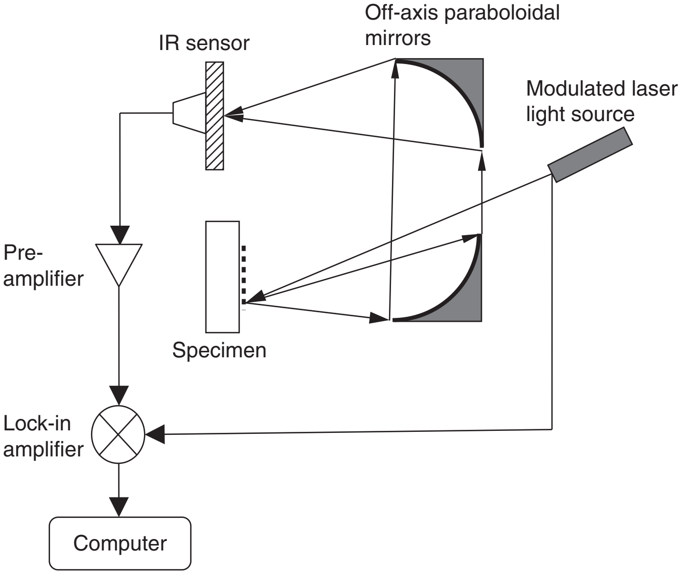

12.12 Laser infrared (IR) photothermal radiometry (PTR). (*Source*: Modified after Mandelis, 2001.)

ultrasonic transducers used for sensing, achieved by converting modulated optical power into electrical power.

12.9 Civil infrastructure applications

In civil engineering, laser-based sensing has shown its potential and practical value in a number of inspection and monitoring problems in bridges, buildings, tunnels, railways, roadways, and material characterization, due to its advantages in terms of (i) capability to access difficult to reach locations, (ii) non-invasive nature of interrogation, (iii) remote inspection, and (iv) relatively quick configuration. Selected applications are summarized as follows.

- *Bridge cable tension measurements* – in the condition assessment of cable-stayed bridges, tension levels in cables are of primary importance in ensuring the safety and preserving the integrity of the cable-stayed bridge. Laser-based sensing techniques such as LDV can be applied to extract the dynamic characteristic of stay cables under temperature variation and ambient vibration for condition assessment. Chen and Petro (1999) applied an LDV (Ometron VPI 4000) to a highway bridge to measure the frequency and tension in cables under ambient conditions.
- *Construction monitoring* – during construction, kinematic information on the ground and the surface of a temporary supporting system indicates the on-site soil condition and the structural integrity of the supporting system. Laser scanners can be applied to such engineering geodesy applications to monitor the movement and deflection of targets in the field during construction for safety assurance and quality control. Zogg and Grimm (2008) applied a profile laser scanner (SICK LMS200–30106) to monitor field deflections in airport construction. A 200-ton crane simulated airplane loading. The size of the bow wave, which occurs on the first wheel when driving into the ground, was measured and studied.
- *Tunnel liner inspection* – in the condition assessment of railway, subway, and roadway tunnels, surface characteristics and internal check of concrete liners are important to the structural integrity of tunnels. Physical damage including concrete cracking, concrete spalling, steel corrosion, and material deterioration indicates excessive earth pressure, abnormal change in geological conditions, and other causes, which can lead to structural failure. By measuring the surface profile and calculating the histogram of laser return intensity, geometric and physical characteristics of tunnels can be identified and used for damage detection. Yoon *et al.* (2009) combined LDV (Optech ILRIS-3D) and a line scanner (Acuity

AR-4000) in a locomotive laser scanning system for the inspection of a railway tunnel.

- *Rail track evaluation* – laser-based sensing techniques can be applied to the inspection of rail tracks by (i) surface profiling of railways and (ii) laser-induced thermal vibration in rail tracks. Surface profiling is capable of providing the texture characteristics of rail tracks, ties, and ballast, while laser-induced thermal vibration can reveal the subsurface condition of rail tracks. Mandelis *et al.* (1999) applied laser IR-PTR and tomographic imaging for the subsurface defect detection in steel rail tracks. Depth-dependent thermal diffusivity of steel rail tracks was used to reveal the presence of a subsurface defect in a steel sample. Kenderian *et al.* (2006) developed a laser-ultrasound technique for the detection of vertical split head cracks, rail base cracks, shattered rim cracks, thermal fatigue cracks in wheel tread in rails, using time-domain analysis and waveform analysis of acoustic wave.
- *Image segmentation for stone aggregates* – with the accuracy and efficiency laser scanners can provide, 3D image analysis of stone aggregates becomes available and can be used to determine the volume and size of the minimum square opening through which it can pass in an aggregate sample. Kim *et al.* (2003) proposed a particle segmentation method in the development of the laser-based aggregate scanning system (LASS).
- *Dynamic/modal analysis* – by measuring the dynamic response of structures using LDV to generate the cross-correlation functions and applying the eigenvalue realization algorithm (ERA) to identify modal parameters of structures, operational modal analysis can be conducted using laser-based sensing techniques. Identification of modal parameters can be performed by time-domain methods (e.g., covariance-driven, data-driven), frequency-domain methods, or crosstime-frequency-domain methods (e.g., Hilbert-Huang transform, wavelet transform). Bourgard and Ellis (1998) conducted extensive measurement of building vibration, including an eight-story steel frame building, a six-story timber frame building, and a concrete building. Siringoringo and Fujino (2009) used a scanning LDV (using He–Ne laser) to determine the modal parameters of a steel plate clamped by bolts, using several threshold criteria and extended modal amplitude coherence to identify vibration modes.
- *Structural health monitoring* – compared to other structural health monitoring techniques including strain sensors (e.g., linear variable displacement transducers, fiber optics), accelerometers (e.g., piezoelectric sensors, MEMS), and vision-based sensors (e.g., CCD and LED), laser-based sensing techniques do not require the deployment of a large number of sensors for large civil infrastructure systems (hence, no wiring cost

for wired sensors and no maintenance cost for wireless sensors), neither do they require the direct access to reach structures and the need to illuminate the structure. Laser-based sensing techniques are capable of measuring maximum deflections/displacements and vibration level and are independent of natural light sources as compared with other passive digital camera sensors. Park *et al.* (2007) demonstrated the use of a scanning LDV system (Optech ILRIS-3D) to measure the displacement and deformation shape of a steel beam specimen in their development of a terrestrial laser scanning (TLS) system. Vertical deflections and maximum stress were measured by their TLS and compared with linear variable differential transformer (LVDT), strain gage, and fibre optic sensor (FOS) sensors. Nassif *et al.* (2005) used an LDV system (Polytec OFV-3001) on a four-span bridge under a dynamic live load test to verify the displacement measurement collected by LVDT sensors and the velocity measurement collected by geophone sensors.

- *Pavement texture characterization* – in the mix design of bituminous/asphalt pavements, the adopted compaction condition of bituminous mixtures can affect the physical, mechanical, and volumetric properties of the mixture. Laser profilers can be used in determining the geometry of the pavement surface by measuring the texture depth, mean profile depth, and average asperity density. Gabriele *et al.* (2009) proposed a testing protocol to evaluate a Superpave gyratory compactor's ability to produce bituminous mixtures able to effectively represent both the density and the surface properties of the mixture in site. Vilaca *et al.* (2010) developed a laboratory prototype equipment to characterize the texture of asphalt pavement road surfaces by using a laser range finder (LRF). Wang *et al.* (2011) also used an LRF in the development of a portable device to measure the macrotexture of roadway pavement.
- *Street mapping* – when combined with GPS, laser scanners can be turned into a field mapping system for landscapes and street views. Such applications usually require a mobile carrier and a 3D platform to enable the laser scanner to maneuver within the angular range of inspection. Barber *et al.* (2008) developed a street mapping system using a van and studied the elevation accuracy and planimetric accuracy of scanned data.
- *Limit analysis of historical structures* – in the survey and documentation of historical structures, shape and mechanical condition of historical structures can be used as an indication of the collapse load value and position which are obtained in the limit analysis. Geometric survey and documentation of historical structures using laser scanners can accelerate this process without jeopardizing the structures. Riveiro *et al.* (2011) demonstrated the use of a time-of-flight (TOF) laser scanner (Riegl LMS Z-390i 3D), a digital camera (Nikon D200), and a CCD sensor in the limit analysis of a medieval masonry arch bridge.

12.10 Laser safety

In laser-based sensing, potential hazard to the eye and skin from laser radiation are possible, depending on the laser wavelength, exposure duration, and viewing conditions. Specific safety measures must be obeyed, and safety procedures must be followed to avoid potential hazards, including:

- American National Standards Institute (ANSI) Z136.1 'Safe Use of Lasers,' and Z136.3 'Safe Use of Lasers in Health Care Facilities' (ANSI, 2012)
- Laser Institute of America (LIA) 'Laser Safety Guide' (LIA, 2012)
- US Department of Labor, Occupational Safety and Health Administration (OSHA) Technical Manual Section III: Chapter 6 'Laser Hazards' (OSHA, 2012)

Laser systems are categorized into five classes:

- Class 1: Very low power, eye-safe, output beam below maximum permissible exposure; safe to view.
- Class 2: Low-power visible lasers only; safe for brief (<0.25 s) viewing; intentional extended viewing is considered hazardous.
- Class 3A: Medium power; safe for brief (<0.25 s) viewing; direct beam should not be viewed with magnifying optics such as a microscope, binoculars, or telescope.
- Class 3B: Medium power; not safe for brief viewing of direct beam or specular reflections; control measures should eliminate this possibility.
- Class 4: High power; not safe for momentary viewing; potential for skin, fire, or diffuse reflection hazard.

Exposure times or exposure limits (EL) are used to quantitatively evaluate the level of potential hazards imposed to human inspectors, from one nanosecond (ns) to 8 h and for wavelengths between 180 nm in the ultraviolet (UV) spectrum (at the end of the ultraviolet C band; 100–280 nm) to 1 mm in the extreme end of IR spectrum (at the edge of microwave spectrum).

For example, the maximum permissible exposure (MPE) for a CO_2 laser with wavelength 10.6 mm is 100 mW/cm^2 for 10 s to 8 h for limited area exposure and 10 mW/cm^2 for >10 s for whole-body exposure. The MPE for a He–Ne laser with wavelength 632.8 nm is 3.2 mW/cm^2 for 0.1 s and 1.0 mW/cm^2 for 10 s. Other MPEs for various lasers can be found in ANSI Z136.1.

When using Class 3B and Class 4 lasers, eye protection is required wherever the exposure above the MPE of the laser occurs. ANSI Z136.1 provides general guidance for the use of eye protection devices.

12.11 Conclusion

Laser-based sensing has been a promising technology since its debut in 1960s and has been widely adopted in a variety of material characterization, damage/defect detection, and condition assessment applications in science and engineering. Owing to the flexibility of its energy level, the laser can be used as a tool for passive sensing or a source for active sensing, as well as either a nondestructive technique or a destructive technique. The integration of laser measurement with other imaging methodologies such as holography and tomography further enables laser-based sensing to be applied to the inspection problems that were previously considered difficult or impossible using laser and other sensing methods. This improvement on data visualization for laser-based sensing has fundamentally changed the face of laser-based sensing from a frequency-domain technique (spectroscopy) to a space domain technique. Although laser-based sensing basically measures the surface response of a target, it can be used to interrogate the subsurface region of a target when the optical energy carried by laser beams is converted to the mechanical energy to enable acoustic/ultrasonic waves propagating inward towards the target. When the surface response of a target can be successfully correlated to the subsurface condition of the target with the aid of theoretical and computational modeling, laser-based sensing can be used as an effective approach in some applications.

When applied in civil engineering applications, laser-based sensing is capable of accessing difficult to reach locations, non-invasive, remote, and relatively quick to set up in the field configuration. With all the promising technical capabilities possessed by the laser-based sensing techniques, laser safety remains a necessary concern in laboratory and in practice. Care must be taken when using high-power laser systems on large-size engineering structures (e.g., bridges, buildings, tunnels, railroads) for long inspection. Trade-offs between the safety and SNR (performance) of selected laser systems need to be assessed in the planning stage.

12.12 References

Amziane A, Amari M, Mounier D, Breteau J-M, Joly N, Banchet J, Tisseur D and Gusev V (2012), 'Laser ultrasonics detection of an embedded crack in a composite spherical particle', *Ultrasonics*, **52**, 39–46.

ANSI (2012), American National Standards Institute, website: http://www.ansi.org/.

Armesto J, Lubowiecka, Ordonez C and Rial FI (2009), 'FEM modelling of structures based on close range digital photogrammetry', *Auto Constr*, **18**, 559–569.

Baltsavias EP (1999), 'A comparison between photogrammetry and laser scanning', *ISPRS J Photogram Remote Sens*, **54**, 83–94.

Barber D, Mills J and Smith-Voysey S (2008), 'Geometric validation of a ground-based mobile laser scanning system', *Photogram Remote Sens*, **63**, 128–141.

Bell JR and Rothberg SJ (2000), 'Rotational vibration measurements using laser Doppler vibrometry: comprehensive theory and practical application', *J Sound Vibration*, **238**, 4, 673–690.

Brossel J, Kastler A and Winter JM (1952), 'Creation of an inquality in ground-state magnetic sublevels', *J de Physique et le Radium*, **13**, 668.

Bourgard AJ and Ellis BR (1998), 'Laser measurement of building vibration and displacement', *Proc SPIE*, **3411**, 3411–3436.

Castellini P, Martarelli M and Tomasini EP (2006), 'Laser Doppler vibrometry: development of advanced solutions answering to technology's needs', *Mech Sys Signal Process*, **20**, 1265–1285.

Castellini P and Santolini C (1998), 'Vibration measurements on blades of naval propeller rotating in water with tracking laser vibrometer', *Measurement*, **24**, 43–54.

Chang, WSC (2005), *Principles of Lasers and Optics*, Cambridge, Cambridge University Press.

Chen S-E and Petro S (1999), 'Laser vibrometer application on bridge cable tension measurements', *Proc SPIE*, **3897**, 511–519.

Chu B (2007), *Laser Light Scattering – Basic Principles and Practice*, 3rd edn, New York, Dover.

Csele M (2004), *Fundamentals of Light Sources and Lasers*, New Jersey, John Wiley & Sons.

Damljanovic V and Weaver RL (2005), 'Laser vibrometry technique for measurement of contained stress in railroad rail', *J Sound Vibration*, **282**, 341–366.

DeCoster J, Haspeslagh L, Witvrouw A and DeWolf I (2008), 'Long-term reliability measurements on MEMS using a laser-Doppler vibrometer', *Proc SPIE*, **7155**, 71550G-1–9.

Drew SJ and Stone BJ (1997), 'Removal of speckle harmonics in laser torsional vibrometry', *Mech Sys Signal Process*, **11** (5), 773–776.

Einstein A (1917), 'Zur Quantentheorie der Strahlung (on the quantum mechanics of radiation)', *Physikalische Zeitschrift*, **18**, 121–128.

El-Omari S and Moselhi O (2007), 'Hybrid methodology for automated collection of data from construction sites', In: *Proc 24th Intl Symp Auto & Robotics Constr (ISARC)*, IIT Madras (Ed.), 93–97.

El-Omari S and Moselhi O (2008), 'Integrating 3D laser scanning and photogrammetry for progress measurement of construction work', *Auto Constr*, **18**, 1–9.

Enoki M and Nishnoiri S (2005), 'Non-contact damage monitoring by laser AE technique', *Proc SPIE*, **5852**, 214–219.

Erf RK (1974), *Holographic Nondestructive Testing*, New York, Academic Press.

Findeis D and Gryzagoridis J (2004), 'A comparison of the capabilities of portable shearography and portable electronic speckle pattern interferometry', *Proc SPIE*, **5393**, 41–49.

Fowles GR (1975), *Introduction to Modern Optics*, 2nd edn, New York, Dover.

Gabriele B, Bernardo C, Clara C and Antonio A (2009), 'Evaluation of the laboratory prediction of surface properties of bituminous mixtures', *Constr Bldg Mater*, **23**, 943–952.

Halliwell NA (1996), 'The laser torsional vibrometer: a step forward in rotating machinery diagnostics', *J Sound Vibration*, **190**, 3, 399–418.

Hapsara M and Iliescu DD (2008), 'Lamb wave detection in a bovine cortical tibia using scanning laser vibrometry', *Proc SPIE*, **6920**, 69200N-1–12.

Hariharan P (2007), *Basics of Interferometry*, New York, Elsevier.

Huang Z, Leighton G, Wringht R, Duval F, Chung HC, Kirby P and Whatmore RW (2007), 'Determination of piezoelectric coefficients and elastic constant of thin films by laser scanning vibrometry techniques', *Sensors Actuat A*, **135**, 660–665.

Huber RD, Chinn DJ, Balogun OO and Murray TW (2005), 'High frequency laser-based ultrasound', *Proc QNDE Conf*, 31 July–5 Aug, Brunswick, ME.

Hung YY and Ho HP (2005), 'Shearography: an optical measurement technique and applications', *Mater Sci Eng R*, **49**, 61–87.

Hung YY, Chen YS, Ng SP, Shepard SM, Hou Y and Lhota JR (2007), 'Review and comparison of shearography and pulsed thermography for adhesive bond evaluation', *Opt Eng*, **46**, 5, 051007–1~16.

Jardetzky WS, Ewing WM and Press F (1957), *Elastic Waves in Layered Media*, New York, McGraw-Hill.

Jones R and Wykes C (1989), *Holographic and Speckle Interferometry*, 2nd edn, Cambridge Press, Cambridge, 1989.

Kalms M, Focke O and Kopylow C (2008), 'Applications of laser ultrasound NDT methods on composite structures in aerospace industry', *Proc SPIE*, **7155**, 71550E-1–11.

Kastle R, Hack E and Sennhauser U (1999), 'Multiwavelength shearography for quantitative measurements of two-dimensional strain distributions', *Appl Opt*, **38**, 1, 96–100.

Kastler A (1957), 'Optical methods of atomic orientation and of magnetic resonance, *J Opt Soc Am*, **47**(6), 460–465.

Kenderian S, Djordjevic BB, Cernigia D and Garcia G (2006), 'Dynamic railroad inspection using the laser-air hybrid ultrasonic technique', *Insight*, **48**(6), 336–341.

Kim H, Haas CT and Rauch AF (2003), '3D image segmentation of aggregates from laser profiling', *Comp Aid Civil Infrastruct Eng*, **18**, 254–263.

Kim H, Jhang K, Shin M and Kim J (2006), 'A noncontact NDE method using a laser generated focused-Lamb wave with enhanced defect-detection ability and spatial resolution', *NDT&E Int*, **39**, 312–319.

Koch C and Brilakis I (2011), 'Pothole detection in asphalt pavement images', *Adv Eng Infomatics*, **25**, 507–515.

Kock WE (1969), *Lasers and Holography – An Introduction to Coherent Optics*, 2nd edn, New York, Dover.

Kurita M and Ma Y (1998), 'Strain measurement by a diffraction grating method', *NDT&E Int*, **31**(2), 77–83.

LIA (2012), Laser Institute of America, website: http://www.lia.org/.

Liu I-H and Yang C-H (2008), 'Laser ultrasound technique for nondestructive characterization of material properties in hydrogen-charged Zircaloy tubes', *Proc 1st Intl Symp Laser Ultrasonics Sci Tech Appl*, 16–18 July, Montreal, Canada.

Longo R, Vanlanduit S and Guillaume P (2006), 'Laser vibrometer measurements of SAWs for non-destructive testing', *Proc SPIE*, **6345**, 63450X-1–8.

Malvern LE (1969), *Introduction to the Mechanics of a Continuous Medium*, New Jersey, Prentice-Hall.

Mandelis A, Munidasa M and Nicolaides L (1999), 'Laser infrared photothermal radiometric depth profilometry of steels and its potential in rail track evaluation', *NDT/E Int*, **32**, 437–443.

Mandelis A (2001), 'Diffusion-wave laser radiometric diagnostic quality-control technologies for materials NDE/NDT', *NDT/E Int*, **34**, 277–287.

Markov V, Trolinger J, Webster J and Pardoen G (2003), 'Optioacoustical sensor to examine the structural integrity of transportation systems', *Opt Eng*, **42**(5), 1277–1287.

Mallet L, Staezewski WJ, Lee BC and Scarpa F (2004), 'Structural health monitoring using scanning laser vibrometry: II. Lamb wave for damage detection', *Smart Mater Struct*, **13**, 261–269.

Nassif HH, Gindy M and Davis J (2005), 'Comparison of laser Doppler vibrometer with contact sensors for monitoring bridge deflection vibration', *NDT&E Int*, **38**, 213–218.

Oberholster AJ and Heyns PS (2011), 'Eulerian laser Doppler vibrometry: online blade damage identification on a multi-blade test rotor', *Mech Sys Signal Process*, **25**, 344–359.

Oberholster AJ, Heyns PS and Newby M (2012), 'The removal of speckle noise from torsional laser Doppler vibrometer signals in machine health monitoring', *Proc 18th World Conf NDT*, 16–10 April, Durban, South Africa.

Olson SE, DeSimio MP, Davies MJ, Swenson ED and Sohn H (2010), 'Computational Lamb wave model validation using 1D and 3D laser vibrometer measurements', *Proc SPIE*, **7650**, 7650M-1–12.

OSHA (2012), Occupational Safety and Health Administration, website: http://www.osha.gov/.

Park HS, Lee HM, Adeli H and Lee I (2007), 'A new approach for health monitoring of structures: terrestrial laser scanning', *Comp Aid Civil Infrastruct Eng*, **22**, 19–30.

Park H-J, Sohn H, Kwon I-B and Yun C-B (2009), 'Development of an optic-based wave excitation technique', *Proc SPIE*, **7295**, 72950Y-1–9.

Park W, Lee C and Park S (2012), 'Nd-YAG pulsed laser based flaw imaging techniques for noncontact NDE of an aluminium plate', *Proc SPIE*, **8346**, 835461H-1–7.

Pascal J-C, Loyau T and Carniel X (1993), 'Complete determination of structural intensity in plates using laser vibrometers', *J Sound Vibration*, **161**, 3, 527–531.

Pedrini G, Schedin S and Tiziani HJ (2002), 'Pulsed digital holography combined with laser vibrometry for 3D measurements of vibrating objects', *Opt Lasers Eng*, **38**, 117–129.

Prazenica RJ, Kurdila AJ and Vigola JF (2007), 'Spatial filtering and proper orthogonal decomposition of scanning laser Doppler vibrometry data for the nondestructive evaluation of frescoes', *J Sound Vibration*, **304**, 735–751.

Riveiro B, Morer P, Arias P and de Arteaga I (2011), 'Terrestrial laser scanning and limit analysis of masonry arch bridges', *Constr Bldg Mater*, **25**, 1726–1735.

Rodriguez J, Martin MT, Arias P, Ordonez C and Herraez J (2008), 'Flat elements on buildings using close-range photogrammetry and laser distance measurement', *Opt Lasers Eng*, **46**, 541–545.

Rothberg S and Tirabassi M (2012), 'A universal framework for modelling measured velocity in laser vibrometry with applications', *Mech Sys Signal Process*, **26**, 141–166.

Scruby CB and Drain LE (1990), *Laser Ultrasonics: Techniques and Applications*, New York, Taylor & Francis.

Siringoringo DM and Fujino Y (2009), 'Noncontact operational modal analysis of structural members by laser Doppler vibrometer', *Comp Aid Civil Infrastruct Eng*, **24**, 249–265.

Stenholm S (2005), *Foundations of Laser Spectroscopy*, 2nd edn, New York, Dover.

Sturzenegger M and Stead D (2009), 'Close-range terrestrial digital photogrammetry and terrestrial laser scanning for discontinuity characterization on rock cuts', *Eng Geol*, **106**, 163–182.

Svelto O (1982), *Principles of Lasers*, New York, Plenum.

Twitto A, Shamir J, Bekker A and Notea A (1996), 'Detection of internal defects using phase shifting holographic interferometry', *NDT&E Int*, **29**, 3, 163–173.

Vanlanduit S, Verboven P, Cauberghe B, Huysmans L and Guillaume P (2004), 'On the use of a laser Doppler vibrometer for quality control of picture tubes', *Proc SPIE*, **5503**, 380–390.

Van Neste CW, Senesac LR and Thundat T (2008), 'Standoff photoacoustic spectroscopy', *Appl Phys Lett*, **92**, 234102–1-3.

Vest CM (1979), *Holographic Interferometry*, New York, John Wiley.

Viktorov IA (1967), *Rayleigh and Lamb Waves: Physical Theory and Applications*, New York, Plenum Press.

Vilaca JL, Fonseca JC, Pinho ACM and Freitas E (2010), '3D surface profile equipment for the characterization of the pavement texture – TexScan', *Mechatronics*, **20**, 674–685.

Wang W, Yan X, Huang H, Chu X and Abdel-Aty M (2011), 'Design and verification of a laser based device for pavement macrotexture measurement', *Transport Res C*, **19**, 682–694.

Weber MJ (2001), *Handbook of Lasers*, CRC Press, Boca Raton, FL.

Yoon J-S, Sagong M, Lee JS and Lee K (2009), 'Feature extraction of a concrete tunnel liner from 3D laser scanning data', *NDT&E Int*, **42**, 97–105.

Yu TY and Haupt R (2010), 'Damage detection of fiber reinforced polymer-concrete systems using a distant acoustic-laser NDE technique', *Proc SPIE*, **7649**, 76491J-1–8.

Zhang X, Jackson T and Lafond E (2006), 'Stiffness properties and stiffness orientation distributions for various paper grades by non-contact laser ultrasonics', *NDT&E Int*, **39**, 594–601.

Zipser L and Franke H (2004), 'Laser-scanning vibrometry for ultrasonic transducer development', *Sensors Actuat A*, **110**, 264–268.

Zogg H-M and Grimm D (2008), 'Kinematic surface analysis by terrestrial laser scanning', *Proc 1st Intl Conf Machine Control Guidance*, 24–26 June, 1–8.

13

Corrosion sensing for assessing and monitoring civil infrastructures

A. POURSAEE, Clemson University, USA

DOI: 10.1533/9780857099136.357

Abstract: Concrete structures with steel-reinforced rebar are in a continuous and losing battle with corrosive elements that naturally occur from long-term exposure to an aggressive environment. Additionally, because such structures are now required to perform longer than mandated by their original design, many are now woefully obsolete. Clear understanding of the condition of such structures is crucial, from the points of view of both economy and safety. Prediction of the deterioration of steel-reinforced concrete structures due to corrosion and adapting the accurate maintenance protocol are difficult tasks, which would be enhanced by using different corrosion measurement techniques and corrosion sensors. This chapter describes some corrosion measurement methods and their applications in corrosion sensors.

Key words: corrosion measurement, corrosion sensors, concrete deterioration, service life.

13.1 Introduction

The low cost of steel-reinforced concrete, and the ready availability of raw materials with which it is formed, make it the most widely used structural material available. The durability of structures made from steel-reinforced concrete is related to its ability to impede, or greatly reduce, the rate of moisture transport or the ingress of aggressive ions. However, because many existing concrete structures are under constant degradation from hostile environments, they suffer from durability issues, particularly the corrosion of the steel bars within such structures. This corrosion, in turn, has created a multi-billion-dollar infrastructure deficit, the annual direct cost of which, in the US, is estimated at $22.6 billion a year (Koch *et al.*, 2001) and growing. The corrosion of the reinforcing steel in concrete is a serious problem, from the perspectives of both safety and economy, which directly can affect the sustainability of the infrastructure. Indeed, the Federal Highway Administration (FHWA) report on corrosion protection of concrete bridges estimated the average annual cost through

© 2014 Woodhead Publishing Limited

the year of 2011 for just maintaining the US bridge infrastructure to be \$5.2 billion (Yunovich *et al.*, 2001)

13.2 Principles of corrosion

Concrete provides physical corrosion resistance to the steel reinforcement by acting as a barrier, and chemical corrosion resistance due to its high pH. Concrete that is not exposed to any external influences usually exhibits a pH between 12.5 and 13.5 (Hansson, 1984). As shown in the Pourbaix diagram (Fig. 13.1) that defines the range of electrochemical potential and pH for Fe-H_2O system in the alkaline environment, at potentials and pH normal within the concrete a protective passive layer forms on the surface of steel. It is believed that this layer is an ultra-thin (<10 nm), protective oxide or hydroxide film that decreases the anodic dissolution rate to negligible levels (Zakroczymski *et al.*, 1985; Montemor *et al.*, 1998; Carnot *et al.*, 2002). However, reinforcing steel does corrode. The partial or complete loss of the passive layer, known as depassivation, leads to corrosion of the steel bars.

As can be seen in Fig. 13.2, the corrosive products of iron are expansive, and their formation can cause cracking and further deterioration in the concrete, which ultimately reduces the service life and causes safety problems in the infrastructure.

Formation of passive film on iron begins with dissolution of the metal, which produces electrons and the reduction of oxygen that uses those electrons. The ferrous ions from the anodic dissolution of iron are attracted to the cathodic part of the steel and combined with hydroxide ions from the cathodic reaction of oxygen to form the ferrous hydroxide. If this film is

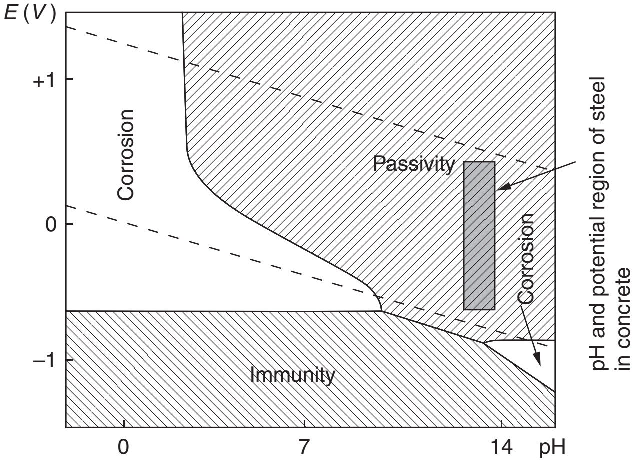

13.1 Pourbaix diagram for Fe-H_2O at 25°C (Pourbaix, 1974).

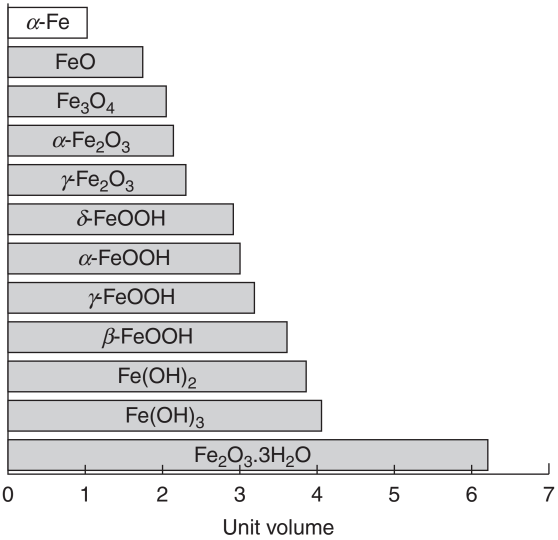

13.2 Corrosion products of iron (Lide, 1999).

exposed to the oxygen, other passive oxide layers, such as Fe_3O_4 or Fe_2O_3, may form on the outer surface of the film. The protective nature of this layer can be reduced, and the result would be active corrosion of steel in concrete. Chloride ions, mostly from de-icing salts or seawater, and carbon dioxide, from the atmosphere, are two major factors that can break the passive film on the surface of steel and initiate corrosion, and the mechanism will be discussed in the following sections. Insufficient oxygen to preserve the passive film, galvanic cell formation from the contact of different metals, and stray currents are the other factors that may also cause active corrosion in reinforcing steel structures.

13.2.1 Chloride induced corrosion

Chloride ions can be present in the concrete due to the use of chloride-contaminated components or the use of $CaCl_2$ as an accelerator when mixing the concrete, or by diffusion into the concrete from the outside environment (Thuresson, 1996). A localized breakdown of the passive layer occurs when sufficient amounts of chlorides reach reinforcing bars, and the corrosion process is then initiated. Chlorides in concrete can be either dissolved in the pore solution (free chlorides) or chemically and physically bound to the cement hydrates and their surfaces (bound chlorides). Only the free chlorides dissolved in the pore solution are responsible for initiating the process of corrosion (Martin-Perez *et al.*, 2000).

There are three theories about the chloride attack (ACI Committee 222, 1996):

1. Chloride ions penetrate to the oxide film on steel through pores or defects in the film is easier than the penetration of other ions.
2. Chloride ions are adsorbed on the metal surface in competition with dissolved O_2 or hydroxyl ions.
3. Chloride ions compete with hydroxyl ions for the ferrous ions produced by corrosion, and a soluble complex of iron chloride forms, which can diffuse away from the anode, destroying the protective layer of $Fe(OH)_2$ and permitting corrosion to continue.

13.2.2 Carbonation induced corrosion

When concrete is exposed to air, the calcium hydroxide reacts with water and carbon dioxide in the air:

$$Ca(OH)_2 + CO_2 \rightarrow CaCO_3 + H_2O \qquad [13.1]$$

The effect of carbonation is to reduce the pH value of the surface layer of the concrete to less than 8.3. This pH is sufficient to make the passive layer on the reinforcement rebar unstable (Allen and Forrester, 1983). The process of carbonation can be summarized in the following steps:

1. CO_2 diffuses into concrete.
2. In the presence of moisture, it reacts with CH (calcium hydroxide).
3. The pH decreases from about 12.6 to 8.3.
4. At this pH, steel is not passive.

13.2.3 Mechanism of corrosion in reinforced concrete

Corrosion is an electrochemical reaction that consists of anodic and cathodic half-cell reactions. Micro-cell corrosion is the term given to the situation where active dissolution and the corresponding cathodic half-cell reaction take place at adjacent parts of the same metal part. For a steel reinforcing bar (rebar) in concrete, this process always occurs in practice. The surface of the corroding steel can act as a mixed electrode containing both anode and cathode regions that are connected by the bulk steel. Macro-cell corrosion can also form on a single bar exposed to different environments within the concrete, or where part of the bar extends outside the concrete. In both cases, concrete pore solution functions as an electrolyte.

For steel embedded in concrete, based on the pH of the concrete (electrolyte) and the presence of aggressive ions, the following would be the possible anodic reactions (Hansson, 1984; Ahmed, 2003):

$$3Fe + 4H_2O \rightarrow Fe_3O_4 + 8H^+ + 8e^- \tag{13.2}$$

$$2Fe + 3H_2O \rightarrow Fe_3O_3 + 6H^+ + 6e^- \tag{13.3}$$

$$Fe + 2H_2O \rightarrow HFeO_2^- + 3H^+ + 2e^- \tag{13.4}$$

$$Fe \rightarrow Fe^{2+} + 2e^- \tag{13.5}$$

The possible cathodic reactions depend on the availability of O_2 and on the pH near the steel surface. The most likely reactions are as follows (Hansson, 1984; Ahmed, 2003):

$$2H_2O + O_2 + 4e^- \rightarrow 4OH^- \tag{13.6}$$

$$2H_2O + 2e^- \rightarrow H_2 + 2OH^- \tag{13.7}$$

13.3 Corrosion evaluation techniques

Corrosion consists of electrochemical reactions at the interface between the metal and an electrolyte solution. During the anodic reaction, a metal is oxidized and releases electrons. These electrons are consumed by the cathodic reaction in which the reduction occurs. By equating these two reactions, a corrosion current, I_{corr}, which is the absolute value of the corrosion rate, and half-cell potential (also called corrosion potential or open circuit potential), E_{corr}, which is the probability of corrosion, can be found.

E_{corr} is equivalent to the voltage of a cell or battery versus a reference electrode under no-load conditions, and can be measured with a high impedance voltmeter or potentiometer (Elsener *et al.*, 2003; Corrosion Doctors, 2005). I_{corr} cannot be measured directly, but it can be estimated using electrochemical techniques, while E_{corr} must be determined as the potential difference between the metal surface and a reference electrode.

As mentioned, corrosion of steel in concrete occurs via electrochemical reactions. Therefore, electrochemical techniques are ideal for the study of the corrosion processes. Usually, in electrochemical measurements, a cell consists of a working electrode (the corroding metal), a counter electrode, a reference electrode, and electrolyte. All of the electrodes are connected to a potentiostat, which allows the potential of the metal to be changed in a controlled manner and the resultant current flow to be measured as a function of potential. This changing of the potential is called ‘polarization.’ When the polarization is done potentiostatically (controlled by potential), the current is measured, and when it is done galvanostatically (controlled by current), the potential is measured (Fontana, 1987; Jones, 1992; Gamry Instruments, 2005).

13.3.1 Half-cell potential technique

The half-cell potential technique is the most widely used technique to evaluate the corrosion of the steel rebars in concrete. It was introduced in the 1970s by Richard F. Stratfull in North America and by the Danish Corrosion Center in Europe (Stratfull 1968,1972; FORCE Technology, 2004). In 1980, the test was approved as a standard by the ASTM (ASTM, 2009). This technique is based on measuring the electrochemical potential of the steel rebar with respect to a standard reference electrode (copper/copper sulfate electrode (CSE) is suggested by the ASTM-C876) placed on the surface of the concrete, and can provide an indication of the corrosion risk of the steel. Figure 13.3 shows the basics of half-cell potential measurement.

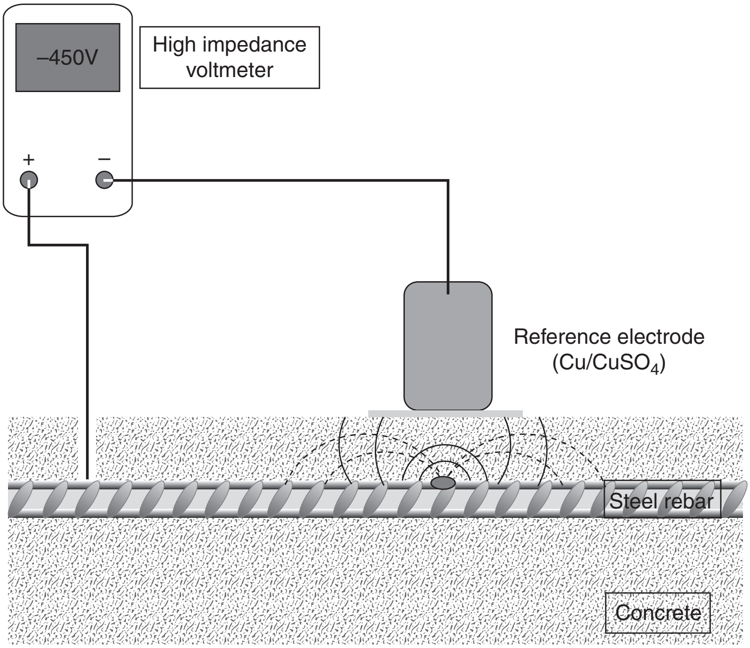

13.3 Apparatus for half-cell potential method described in ASTM C876 to measure surface potential associated with corrosion current.

According to the ASTM Standard recommended guidelines for interpretation of the results, if the measured potential is more negative than −350 mV versus CSE, the probability of active corrosion is more than 90%. If the measured potential is more positive than −200 mV versus the CSE, the probability of not having active corrosion is 90%, and between −200 and −350 mV is the uncertainty region. The most common way of presenting the half-cell potential data is plotting the potential distribution or potential mapping contour. It should be emphasized that, since half-cell potential value is defined as the thermodynamic measure of the ease of removing electrons from the metal in steady state condition, it cannot be used as direct measurement of corrosion rate. It should be noted that half-cell potential is the probability of corrosion activity, while I_{corr} is the direct measurement of corrosion rate. A simple comparison of the half-cell potential data with the ASTM guidelines on steel reinforcement corrosion probability could cause mistakes in the evaluation of the structure. It has been accepted by those who work in the field that a more negative reading of potential means a higher probability of corrosion. However, this general rule may not always be correct. Some precautions are necessary in interpreting the data from half-cell potential measurements, because there are many factors that may affect the magnitude of the potentials. Details about difficulties with the half-cell potential method are discussed in Poursaee and Hansson (2009).

13.3.2 Linear polarization resistance (LPR)

Figure 13.4 shows a schematic plot of the relationship between potential and current in the region of the open circuit potential. The curve plots the applied potential versus measured current, and vice versa. As shown in Fig. 13.4, there is an approximately linear region around the open circuit potential. The LPR measurements are performed by applying a potential in the range of ±10 mV about the E_{corr}, either as a constant pulse (potentiostatic) or a potential sweep (potentiodynamic) and measuring the current response. Alternatively, a current pulse (galvanostatic) or a current sweep (galvanodynamic) can be applied, and potential response is measured. Polarization resistance (R_p) is the resistance of the specimen to oxidation while an external potential is applied, and the corrosion rate, which is inversely related to the R_p, can be calculated from it.

R_p is determined by calculating the slope of this linear region:

$$R_p = \frac{\Delta E}{\Delta I} \qquad [13.8]$$

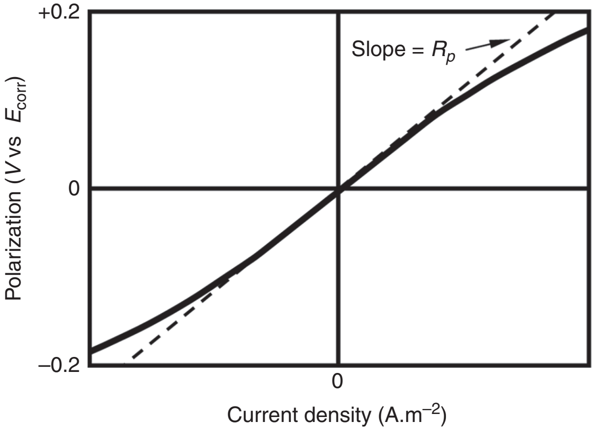

13.4 Schematic illustration of the linear polarization curve.

where ΔE = change in potential and ΔI = change in current. The Stern-Geary equation relates corrosion current to R_p (Stern and Geary, 1957):

$$I_{corr} = \frac{B}{R_p} \quad [13.9]$$

$$B = \frac{\beta_a \beta_c}{2.3(\beta_a + \beta_c)} \quad [13.10]$$

The corrosion current density, i_{corr}, can be calculated by dividing the corrosion current (I_{corr}) by the surface area of the polarized area (A):

$$i_{corr} = \frac{B}{R_p A} \quad [13.11]$$

B is the Stern-Geary constant, and β_a and β_c are anodic and cathodic Tafel constants, respectively. The value of B should be determined empirically. However, for most cases, it can be assumed to be 0.026 V for active and 0.052 V for passive corrosion of steel in concrete (Andrade and González, 1978; Andrade *et al.*, 1990).

The resistance measured by the LPR is actually the sum of the polarization resistance, R_p, and the electrolyte resistance, R_Ω. If $R_p >> R_\Omega$, the resistance that is measured by the LPR is close enough to the polarization resistance, which can be used as the actual value. However, in some environments with low conductivity, and/or high corrosion rates, the R_Ω is significant and should be considered (Jones, 1992).

According to some researchers, corrosion current densities over ~1 μA/cm^2 have been identified as the level of high corrosion risk, and corrosion current density below 0.1 μA/cm^2 are characterized as passive corrosion in the system (Gonzalez *et al.*, 1995; Alonso *et al.*, 2000; Polder and Peelen, 2002). However, it seems that the equipment used by these researchers generally gives lower values than does other commercial equipment (Gepraegs, 2002). Therefore, applying such definitions may over- or under-estimate the corrosion rate and cause errors in evaluation and life prediction. Interpreting the corrosion current density values of embedded steel bars in concrete, obtained from the LPR technique, is difficult in large part because determining the actual corroding area of steel is almost impossible and usually causes underestimation of the actual corrosion current density in the areas of active corrosion. The LPR has some advantages over the other measurement techniques, which makes it popular in the evaluation of the corrosion rate in reinforced concrete: it is a non-destructive technique; it is a simple method and it usually needs only a few minutes for corrosion rate determination. Because of its rapidity, it can be effectively used in kinetic studies of corrosion monitoring (Jones, 1992).

13.3.3 Potentiostatic LPR

In the potentiostatic LPR technique, a constant potential signal (usually ±10 mV) is applied for a certain period of time, which is determined by the time for the current to reach steady state, in the form of square wave between the working electrode (steel bar in concrete) and reference electrode, and the response current is measured. By using Equation [13.8], the $R_{P,}$ and consequently the corrosion current density and corrosion rate, can be calculated.

13.3.4 Galvanostatic pulse technique

The galvanostatic pulse technique was introduced for field application in 1988 (Newton and Sykes, 1988). This method is a rapid non-destructive polarization technique. A short-time anodic current pulse is applied galvanostatically between a counter electrode placed on the concrete surface and the rebar. The applied current is usually in the range of 10–100 μA, and the typical pulse duration is between 5 and 30 s. The reinforcement is anodically polarized and the resulting change of the electrochemical potential of the reinforcement is measured with a reference electrode, which is usually in the center of the counter electrode and recorded as a function of polarization time (Klinghoffer, 1995; Elsener *et al.*, 1997). A typical potential response for a corroding reinforcement is shown in the Fig. 13.5.

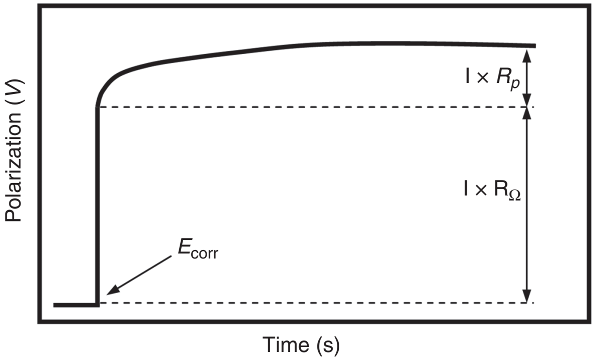

13.5 Schematic illustration of galvanostatic pulse results.

When the constant current, $I_{\text{app},}$ is applied to the rebar, the polarization of the rebar, η_t, at given time t can be expressed as (Jones and Greene, 1966):

$$\eta_t = I_{\text{app}} \times \left[R_p \times \left[1 - e^{\left(\frac{-t}{R_p C_{dl}}\right)} \right] + R_\Omega \right] \qquad [13.12]$$

where R_p = polarization resistance, C_{dl} = double-layer capacitance, and R_Ω = ohmic resistance of the concrete cover.

By transferring Equation [13.12] to logarithmic form, the values of R_p and C_{dl}, can be calculated as following (Newton and Sykes, 1988):

$$\ln(\eta_{\max} - \eta_t) - \ln(I_{\text{app}} \times R_p) - \left(\frac{t}{R_p C_{dl}} \right) \qquad [13.13]$$

where $\eta_{\max}$ is the final steady state potential value. Figure 13.6 plots Equation [13.13].

If this straight line is extrapolated to $t = 0$, it will give an intercept of $I_{\text{app}} \times R_{\text{p}}$ and the slope of the line in $1/R_p C_{dl}$. The remaining over-potential corresponds to $I_{\text{app}} \times R_\Omega$, which is the ohmic voltage drop across the concrete cover. After determining the polarization resistance (R_p) by the above method, the corrosion current I_{corr} can be calculated from the Stern-Geary equation (Stern and Geary, 1957; Newton and Sykes, 1988).

13.3.5 Equipment with the guard ring

An auxiliary counter electrode, referred to as a guard ring electrode, can be used to confine the polarization to a known length of reinforcing bar. The counter electrode and the guard ring are typically arranged as annular

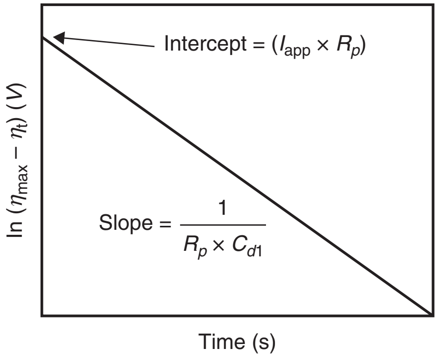

13.6 Schematic illustration of Equation [13.13] (Newton and Sykes, 1988).

metal rings with a reference electrode in the center. The potential or current applied from the guard ring tends to repel the signals from the central counter electrode, confining them to an area of the structure located approximately under the counter electrode, as schematically shown in Plate X in the color section between pages 294 and 295.

There are two well-known equipment works based on the galvanostatic pulse technique:

1. The GECOR is considered a galvanostatic pulse technique instrument although it is often referred to as an LPR device (Broomfield, 1996; Feliu *et al.*, 1996; Newhouse and Weyers, 1996). The electrode assembly has a total of three reference electrodes, one located in the center and two located between the counter electrode and guard ring, and they are used to adjust the guard electrode current to maintain the potential difference between the two reference electrodes constant during the polarization procedure.
2. The GalvaPulse is a galvanostatic pulse instrument developed by the FORCE Institute in Denmark. Signal confinement is over a 70 mm length of bar, and measurements can be made with or without the guard ring electrode. The measuring cell has an Ag/AgCl reference electrode at the center with a zinc counter electrode and a zinc guard ring. Based on the suggestion of the manufacturer, 10–20 μA for 5–10 s, in passive areas, should give a reasonable polarization of the reinforcement. The recommended applied current pulse in active areas is 80–100 μA for 5–10 s.

13.3.6 Electrochemical impedance spectroscopy (EIS)

The EIS studies the system response to the application of a small amplitude alternating potential or current signal at different frequencies. The popularity of the EIS methods for reinforced concrete has increased remarkably in recent years, because analysis of the system response provides information about the double-layer capacitance, interface, structure, reactions which are taking place, corrosion rate, and electrolyte (environment) resistance (Silverman, 1990; Jones, 1992; Lasia, 1999). An electrochemical process can be considered as an electrical circuit with basic elements such as resistors, capacitors, and inductors. Therefore, in interpreting the response to an alternating current (AC), the AC circuit theory can be used successfully to demonstrate a corrosion process, and it may also be used to understand the behavior of the corrosion process and predict the corrosion rates.

In direct current, Ohm's law is as follows:

$$V = IR \tag{13.14}$$

(V = Potential, I = Direct current, R = Actual resistor)

In the AC, Ohm's law becomes:

$$V = IZ \tag{13.15}$$

(V = Potential, I = Alternative current, Z = Impedance)

Direct current can be viewed as alternating current at zero frequency. In this case, the resistance is composed of only one or more actual resistors. When the frequency is not zero, all circuit elements that can affect the flow of current, e.g., resistors, capacitors, and inductors, cause the resistance. The resistance created by capacitors and inductors depends on the frequency, while that created by a resistor is not dependent on frequency (Silverman, 1986). A sinusoidal current or voltage can be represented as a rotating vector, as shown in Fig. 13.7. In this figure, the x-component shows the observed current so it becomes the real component of the rotating vector, while the contribution of the y-component is not observed; therefore, it is called the imaginary component of the rotating vector.

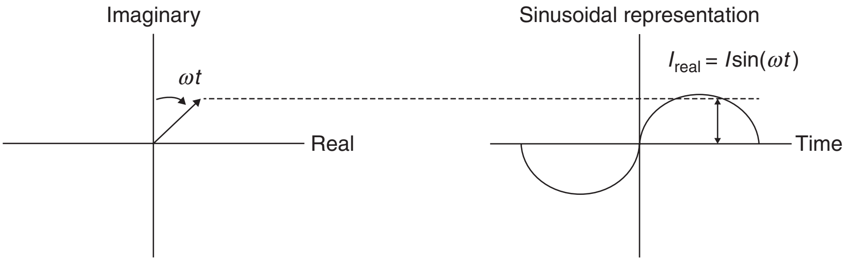

13.7 Relationship between sinusoidal AC current and rotating vector representation.

The mathematical descriptions of the two components are as follows:

$$\text{Real current} = I_x = |I|\cos(\omega t) \tag{13.16}$$

$$\text{Imaginary current} = I_y = |I|\sin(\omega t) \tag{13.17}$$

where t = time and ω = frequency in radians per second = $2\pi f$ (f = frequency in Hertz).

To separate the real (x) and imaginary (y) components, the magnitude of the imaginary part should be multiplied by $j = \sqrt{-1}$[1] and then the real and imaginary values can be reported separately. The equations for AC impedance become:

$$E_{\text{total}} = E_{\text{real}} + E_{\text{imaginary}} = E' + jE'' \tag{13.18}$$

$$I_{\text{total}} = I_{\text{real}} + I_{\text{imaginary}} = I' + jI'' \tag{13.19}$$

$$Z_{\text{total}} = Z' + Z'' = \frac{E' + jE''}{I' + jI''} \tag{13.20}$$

The absolute amplitude of the impedance (that is the length of the vector) and the phase angle are defined by (Princeton Applied Research, 2006):

$$|Z| = \sqrt{Z' + Z''^2} \tag{13.21}$$

$$\tan\theta = \frac{Z''}{Z'} \tag{13.22}$$

The goal of AC impedance is to measure the impedance Z as Z' and Z'', and then model the response by using an equivalent simple circuit (Silverman, 1986).

Data presentation

There are different ways to illustrate the response of an electrochemical system to an applied AC potential or current. The most common plots are the Nyquist plot and Bode plot. If, at each excitation frequency, the real part is plotted on

---

[1] Mathematicians use i to stand for $\sqrt{-1}$, but electrochemists use j to avoid confusion with i, the symbol for current.

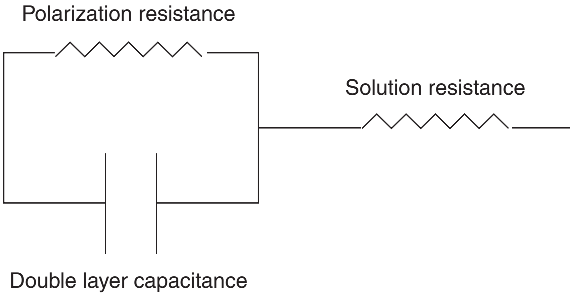

13.8 Equivalent circuit for a simple electrochemical system.

the *x*-axis and the imaginary part is plotted on the *y*-axis of a chart, a 'Nyquist plot' is formed. A simple corroding system can be assumed as: solution resistance, in series with a combination of a resistor and a capacitor, which represent the polarization resistance and double-layer capacitance, respectively. This simple representation is called a Randles cell and is shown in Fig. 13.8.

Figure 13.9 schematically illustrates the Nyquist plot for a simple electrochemical system corresponding to the analog circuit in Fig. 13.8. It should be noted that each point on the Nyquist plot is the impedance at one frequency. On the Nyquist plot, the impedance can be represented as a vector of length $|Z|$, and the angle between this vector and the *x*-axis is the phase angle 'θ' (Gamry Instruments, 2006; Princeton Applied Research, 2006). At high frequencies, at the leftmost end of the semicircle, where the semicircle touches the *x*-axis, the impedance of the Randles cell is entirely produced by the ohmic resistance, R_Ω. The frequency reaches its lower limit at the rightmost end of the semicircle. At this frequency, the Randles cell also approximates a pure resistance, but now the value is $(R_\Omega + R_p)$ (Princeton Applied Research).

The Nyquist plot has some limitations (Princeton Applied Research):

1. The frequency is not clearly shown on the plot and it is not possible to determine, for a specific point, the frequency used to record that point;
2. The ohmic and polarization resistances can be directly determined from the plot but the electrode capacitance can be only calculated if the frequency information is known, using Equation [13.23]:

$$C = \frac{1}{\omega_{\max} \times R_p} \qquad [13.23]$$

3. If there are high and low impedance components in the circuit, the larger impedance controls plot scaling, and distinguishing the low impedance semicircle would probably be impossible.

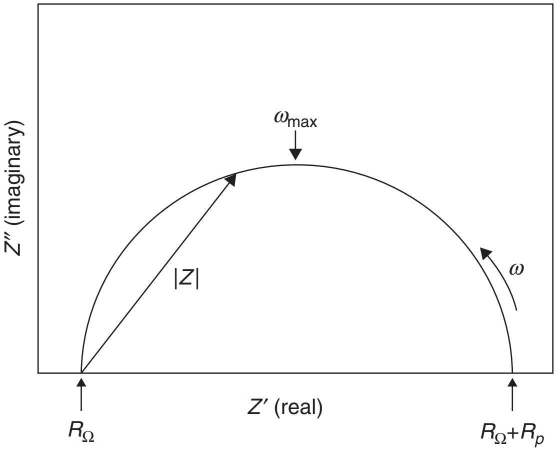

13.9 Nyquist plot for a simple electrochemical system.

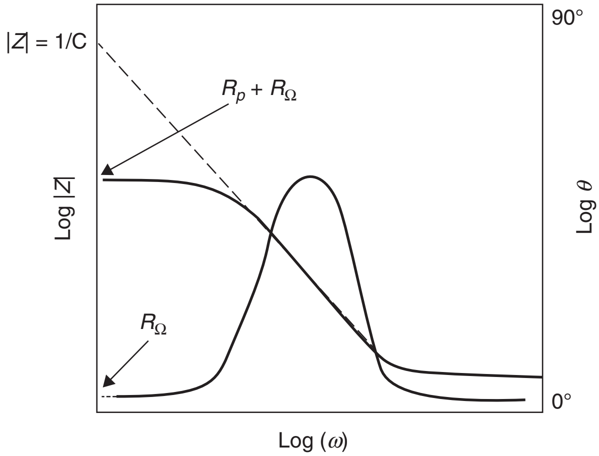

13.10 Bode plot for the same system shown in Fig. 13.9.

A Bode plot is another popular presentation method for the impedance data. In the Bode plot, the data are plotted with log of frequency on the abscissa and both the log of absolute value of the impedance ($|Z|$) and phase-shift (θ) on the ordinate (Gamry Instruments, 2005). Figure 13.10 schematically shows a Bode plot for the same system shown in Fig. 13.8. Since the frequency appears as one of the axes in the Bode plot, it is easy to understand the dependence of impedance on the frequency from the plot. The log $|Z|$ versus log ω curve can be used to determine the values of R_p and R_Ω. At very high and very low frequencies, $|Z|$ becomes independent of frequency. At the highest frequencies the ohmic resistance controls the impedance and log (R_Ω) can be read from the high frequency horizontal level. On the other hand, at the lowest frequencies, polarization resistance contributes, and log ($R_p + R_\Omega$) can be read from the low frequency horizontal portion.

The Bode format is advantageous when data scatter prevents satisfactory fitting of the Nyquist semicircle. In general, the Bode plot provides a more understandable description of the frequency-dependent behavior of the electrochemical system than does the Nyquist plot, in which frequency values are not clear (Princeton Applied Research, 2006).

13.3.7 Cyclic polarization

Cyclic potentiodynamic polarization technique is a relatively non-destructive measurement that can provide information about the corrosion rate, corrosion potential, susceptibility to pitting corrosion of the metal, and concentration limitation of the electrolyte in the system. The technique is built on the idea that prediction of the behavior of a metal in an environment can be made by forcing the material from its steady state condition and monitoring how it responds to the force as the force is removed at a constant rate and the system is reversed to its steady state condition. Applied potential is the force and is raised at a continuous, often slow, rate by using a potentiostat (Silverman, 1998). This rate is called the polarization scan rate, and is an experimental parameter. The potential of the specimen is changed continuously while the resulting current is monitored, and then the applied potential is plotted versus the logarithm of the resulting current density. The conductivity of the electrolyte (environment) is a very important factor that should be considered in all electrochemical experiments, especially in the cyclic polarization technique. The electrolyte resistance causes a potential drop between the working electrode and reference electrode and can cause errors. This effect has important impacts on the interpretation, and should be compensated.

13.4 Corrosion sensors for field monitoring

Application of sensors to monitor the corrosion activity of steel in concrete and to measure the corrosion rate of steel has been of great attraction. The embeddable corrosion sensors can provide early warning of conditions that damage steel reinforcement, leading to cracking and deterioration of concrete structures. In addition, lost cost, and no or minimal need for trained personnel and maintenance, make the application of sensors even more attractive.

13.4.1 Electrochemical sensors

The sensor most used for this purpose is basically an embeddable inert and stable reference electrode in high alkaline environment in concrete such as: Mn/MnO_2 or Ti/TiO_2 (Muralidharan *et al.*, 2007; Duffó and Farina, 2009; Dong *et al.*, 2011), to perform half-cell potential measurement. The other type of sensor is designed to measure the half-cell potential and the corrosion current density, and consequently corrosion rate. These sensors are based on utilizing three electrodes (reference, counter or auxiliary, and working electrodes), which are usually used in conventional electrochemical measuring systems. Most of the sensors in this category use the metal–metal oxide (MMO) as reference electrodes, such as Mn/MnO_2 and Ti/TiO_2, stainless steel as counter electrode, and the reinforcing bar as the working electrode (Anderade and Martinez, 2009; Duffó and Farina, 2009; Dong *et al.*, 2011). In the sensor developed by Poursaee, graphite rods were used as both reference and counter electrodes. The stability of graphite in high pH was evaluated, and it was concluded that the potential of the graphite is stable enough during the period of measurement, and the potentiostatic LPR can be performed successfully, using this configuration (Poursaee, 2009). However, graphite cannot be used as the permanent reference electrode, unless it undergoes special treatment (Swette *et al.*, 1999). The sensors with the three electrochemical components can be used to perform all the techniques, such as the LPR, galvanostatic pulse, cyclic polarization, and the EIS.

Electrochemical sensors: some examples

The embedded corrosion instrument (ECI)

ECI – designed and manufactured by the Virginia Technologies (Virginia Technologies Inc, 2012), monitors five key factors in corrosion of the reinforcing steel: LPR, open circuit potential, resistivity, chloride ion concentration, and temperature. The ECI is designed to monitor bridges, buildings, dams, erosion control structures, flood control channels, parking garages, piers, pylons, roadways, and spillways. The ECI consists of a stainless steel conductivity sensor, a stainless steel counter electrode, a mild steel working electrode, a Mn/MnO_2 reference electrode, and an Ag/AgCl chloride sensor. The ECI corrosion monitor is combined with a NetCon-10 interface module. The NetCon-10 is a connection module that helps in organizing large networks of corrosion monitors and guarding them against voltage spikes.

900 concrete multi-depth sensor

The multi-depth sensors, designed by the Rohrback Cosasco Systems (Rohrback Cosasco Systems, 2012) may be used to assess the depth of chloride or carbonation ingress, and the instantaneous corrosion rate. The multi-depth sensor has four galvanic couples of mild steel and stainless steel. These couples are located at four depths from the concrete surface. The couple furthest from the surface should be placed above the rebar. A zero resistance ammeter (ZRA) is used to measure the current flow between the two electrodes. An increase in current flow indicates the ingress of chloride contamination and increased corrosivity at that electrode level. The multi-depth sensor can also measure the instantaneous corrosion rate of steel in concrete by using the LPR method. The electrodes of the sensor use adjacent carbon steel elements for the LPR measurement. It seems that the couple of mild steel and stainless steel can be used as the counter and reference electrodes, respectively. The sensors can be monitored frequently or continuously to track changes in corrosion rate. It is suggested by the manufacturer that the multi-depth sensors be positioned at the most susceptible locations for corrosion, adjacent to the rebar but on the side that will see chloride or moisture ingress first. This will allow precautionary measures to be taken before the onset of corrosion.

CorrWatch multi-sensor

The CorrWatch multi-sensor, which is developed by FORCE Technology (FORCE Technology, 2012) can be embedded in new concrete structures. This probe can measure most parameters necessary for assessment of the corrosion state. The CorrWatch consists of four mild steel (anode) probes and the measuring electrodes in variable positions but with a known distance to the reinforcement and a measuring electrode of noble metal (cathode). Anode heights are flexible and can be adjusted to fit the concrete covering thickness. In order to predict when the reinforcement starts corroding, the current between the individual anodes and the cathode is measured, either by a specially designed handheld ZRA or a specially developed data logger.

SensCore corrosion sensor

The SensCore corrosion sensor, designed by the The Roctest Group (The Roctest Group, 2012) measures both corrosion initiation and corrosion rate. Those two measurements are performed at four different depths, between the concrete surface and the reinforcement bars depth, which allows the evaluation of the corrosion front progression. Humidify sensor is also combined with the SensCore to provide a complete picture of the corrosion initiation and progression in a reinforced concrete structure. The SensCore corrosion sensor is composed of four mild steel rebars that are secured to a stainless steel support. The probe is then placed in the concrete and the SensCore data logger measures the corrosion current for each bar separately. A zero current indicates that corrosion is inhibited at that depth. A non-zero current indicates that the conditions for rebar corrosion are present at that depth, while the corrosion current gives an indication of the corrosion rate.

Intertek-CAPCIS probes

Intertek-CAPCIS (Oliver *et al.*, 2009) equipment provides sensors for measuring and monitoring the corrosion condition of steel reinforcement in concrete structures. For this purpose, three sensors were developed by the Intertek-CAPCIS: M3 probe, C4 probe, and M9 probe.

M3 probe – this sensor is a multi-element sensor developed for monitoring the corrosion rate of the reinforcing bars in concrete structures. This probe is designed to be installed during concrete construction. A standard M3 probe consists of a carbon steel working electrode, a silver/silver chloride/potassium chloride (Ag/AgCl/KCl) reference electrode, an AISI316 stainless steel auxiliary electrode, and a thermistor to measure the temperature.

C4 probe – this probe is also a multi-element sensor for monitoring the corrosion rate and condition of reinforced concrete. It is mainly designed for use with tunnel elements. However, the C4 probe can also be installed into any reinforced concrete structure. The following information can be obtained, using C4 probe: corrosion potential, corrosion rate (using LPR), concrete resistivity, concrete temperature, and concrete humidity.

M9 probe – this is a multi-layered variation of the standard M3 probe. The design provides long-term service life, which makes M9 probe ideal for use in aggressive environments or where the ability to make measurements at various cover depths yielding early warning of deterioration is crucial, such as in nuclear waste storage plants.

13.4.2 Other sensors

The onset of corrosion in steel-reinforced concrete can also be detected by different methods. The inductively coupled magnetic fields, with the core typically made of a simple LC resonator, have been used by researchers to sense the initiation of corrosion (Carkhuff and Cain, 2003; Andringa *et al.*, 2005; Bhadra *et al.*, 2010). Change of the inductance or the capacitance of the LC circuit will change the resonant frequency that is the basis of such sensors. The resonant frequency of the whole LC circuit, schematically shown in Fig. 13.11, is given by the Thompson formula:

$$f = \frac{1}{2\pi\sqrt{LC}} \qquad [13.24]$$

where L is the total inductance of the circuit and C is the total capacitance of the circuit.

According to the Equation [13.24], the change of the inductance or the capacitance of the circuit will change the resonant frequency. As can

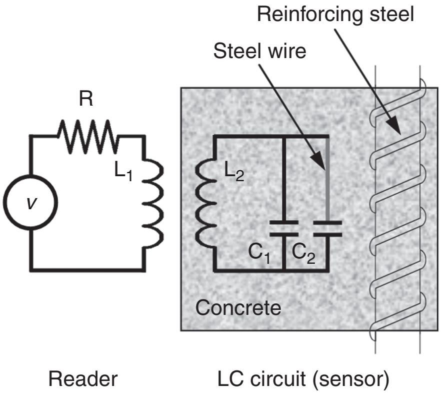

13.11 Circuit diagram for a corrosion sensor, based on inductance.

be seen in Fig. 13.11, the resonant frequency of the circuit depends on the state of the steel wire. When the steel wire is not broken, the total capacitance of the circuit is equal to the summation of the two capacitances (C = C1 + C2). However, when the steel wire is broken due to corrosion, the total capacitance of the circuit becomes C1. The diameter of the steel wire is usually much smaller than that for the reinforcing steel, and the steel wire will corrode before considerable corrosion damage has occurred in the reinforcement.

Eddy currents have also been used to detect the corrosion on the embedded steel bars in concrete (Gaydecki and Burdekin, 1994; Miller *et al.*, 2003; Kumar *et al.*, 2006). Eddy currents are generated in a conductive material by a changing magnetic field. In the eddy current technique, the magnetic field in a coil induces eddy currents in the rebar. This eddy current generates a magnetic field of its own that interferes with the main magnetic field. The change in inductance of the coil is then measured using the meter.

Sensors based on the application of fiber optics to detect corrosion have also been developed. An optical fiber consists of a glass core surrounded by a glass cladding that differs in index of refraction. The glass fiber is then coated during the manufacturing process with a protective polymer layer (Merzbachery *et al.*, 1996). The direct spectroscopy of corroded versus uncorroded materials is the basis of this method. Spectrally broadband light is coupled into an optical fiber and then illuminates the region under measurement. The presence of corrosion is determined using color modulation of the broadband input signal (Fuhr and Huston, 1998).

The principle of light reflection has also been used to develop fiber optic sensors to detect corrosion of steel in concrete. The sensor consists of an optical fiber reflection sensor, a sacrificial metallic film, joined to a steel tube. One side of the film is finely polished and is isolated from the environment, while the other side is exposed to the corrosive environment. The corrosion pits initiated at the exposed film surface slowly penetrate the sacrificial film as the exposure time increases. The corrosion pits that reach the polished surface reduce the surface reflectivity of the polished surface. This decrease in reflectivity can be detected by the optical fiber reflectivity sensor (Wang and Huang, 2011).

The fiber Bragg grating (FBG) is used for the corrosion detection purpose as well (Lo and Xiao, 1998; Yang *et al.*, 2006; Gaon *et al.*, 2011). Normal optical fibers are uniform along their lengths. In a simple FBG, the refractive index of the fiber core varies periodically along the length of the fiber. The FBG reflects particular wavelengths of light and transmits all others, and therefore can be used as an inline optical filter to block certain wavelengths, or as a wavelength-specific reflector. The difference between the reflection of corrosion products and that of the steel rebar can be used to detect the corrosion activity on the surface of the rebar.

Acoustic emission (AE) monitoring of concrete is the other technique that has been used to detect rebar corrosion (Zdunek *et al.*, 1995; Yoon *et al.*, 2000; Golaski *et al.*, 2002; Idrissia and Limam, 2003; Reis *et al.*, 2003; Assouli *et al.*, 2005; Fariduddin *et al.*, 2007). AE energy is released when a crack propagates. Since corrosion products are expansive (Lide, 1999), they cause multiple micro-fractures, which ultimately lead to macro-cracks. This activity can be detected by AE sensors. As a result, the initiation of corrosion, location of the zone containing intense corrosion products, crack formation mechanism, and the loss of bond strength due to corrosion between reinforcing steel and the surrounding concrete, can be investigated using this method. However, at this time, expensive equipment and the need for highly trained personnel limit the application of AE technique mainly to laboratory investigations.

13.5 Conclusion and future trends

Different corrosion devices and sensors have been developed to measure the corrosion activity of reinforcing steel bars in concrete. The calculations for the measurements make certain assumptions during the test. As a result, different devices may give different corrosion rates, even when the tests were performed at the same point. However, because the components of sensors are close together, and usually different sensors such as temperature are combined with corrosion sensors, such sensors are generally able to differentiate between regions of high and low corrosion rates more efficiently and provide more accurate results. It is important to recognize that a corrosion rate measurement represents the conditions at the time of the test. Changes in the factors that may affect corrosion rate, such as temperature, concrete resistivity, and oxygen availability, will change the corrosion rate.

Therefore, it is difficult to extrapolate service life based on one measurement. Measurements need to be continuous and repeated under different seasons and conditions to have a clear understanding of the corrosion activity of the steel rebars. This task is only possible by using sensors. Prediction of the deterioration of steel-reinforced concrete structures due to corrosion and adapting the accurate maintenance protocol is a difficult task, which will be enhanced by using corrosion sensors.

A typical concrete structure is not equipped with sensors, especially corrosion sensors. However, it is obvious that in the future this will change, and the management of concrete structures will use sensors to monitor such structures. Application of corrosion sensors as a tool for health monitoring of civil engineering structures is a relatively new development with enormous potential. Rising concerns for safety, convenience, efficiency factors, and sustainability tied with government mandates, will increase sensor usage to an unprecedented level, including corrosion sensors, in infrastructures and research on these concepts will continue in the near future.

13.6 References

ACI Committee 222 (1996). 222R-96: Corrosion of Metals in Concrete.

Ahmed, S. (2003). 'Reinforcement corrosion in concrete structure, its monitoring and service life prediction-a review'. *Cement and Concrete Composite* **30**(4–5): 459–471.

Allen, R. T. L. and Forrester, J. A. (1983). The investigation and repair of damaged reinforced concrete structures. A. P. Crane. London, Society of Chemical Industry: 193–222.

Alonso, C., Andrade, C., Castellote, M. and Castro, P. (2000). 'Chloride threshold values to depassivated reinforcing bars embedded in a standardised OPC mortar.' *Cement and Concrete Research* **30**: 1047–1055.

Anderade, C. and Martinez, I. (2009). Embedded sensors for the monitoring of corrosion parameters in concrete structures. NDTCE'09, Non-Destructive Testing in Civil Engineering. Nantes, France.

Andrade, C. and González, J. A. (1978). 'Quantitative measurements of corrosion rate of reinforcing steels embedded in concrete using polarization resistance measurements'. *Werkstoffe und Korrosion* **29**: 515–519.

Andrade, C., Marcias, A., Feliu, S., Escudero, M. L. and Gonzalez, J. A. (1990). Quantitative measurement of the corrosion rate using a small counter electrode in the boundary of passive and corroded zones of a long concrete beam. Corrosion Rates of Steel in Concrete, ASTM STP 1065. N. S. Berke, V. Chaker and D. Whiting. Philadelphia, PA, ASTM.

Andringa, M. M., Neikirk, D. P., Dickerson, N. P. and Wood, S. L. (2005). Unpowered wireless corrosion sensor for steel reinforced concrete. *4th IEEE Conferemce on Sensors, Irvine*, California, USA.

Assouli, B., Simescu, F., Debicki, G. and Idrissi, H. (2005). 'Detection and identification of concrete cracking during corrosion of reinforced concrete by acoustic emission coupled to the electrochemical techniques.' *NDT & E International* **38**: 682–689.

ASTM (2009). C876–09: Standard Test Method for Half-cell Potentials of Uncoated Reinforcing Steel in Concrete. 03.02: 446–451.

Bhadra, S., Bridges, G. E. and Thomson, D. J. (2010). Coupled Coil Sensor for Detecting Surface Corrosion on Steel Reinforcement. *14th International Symposium on Antenna Technology and Applied Electromagnetics [ANTEM] and the American Electromagnetics Conference [AMEREM]*, Fairmont Chateau Laurier, Ontario, Canada.

Broomfield, J. P. (1996). Field measurement of the corrosion rate of steel in concrete using a microprocessor controlled unit with a monitored guard ring for signal confinement. N. S. Berke, E. Escalante, C. K. Nmai and D. Whiting, ASTM International.

Carkhuff, B. and Cain, R. (2003). 'Corrosion sensors for concrete bridges'. *IEEE Instrumentation & Measurement Magazine* **6**(2): 19–24.

Carnot, A., Frateur, I., Marcus, P. and Tribollet, B. (2002). 'Corrosion mechanisms of steel concrete moulds in the presence of a demoulding agent'. *Journal of Applied Electrochemistry* **32**: 865–869.

Corrosion Doctors (2005). http://www.corrosion-doctors.org.

Dong, S., Lin, C., Hu, R., Li, L. and Du, R. (2011). 'Effective monitoring of corrosion in reinforcing steel in concrete constructions by a multifunctional sensor'. *Electrochimica Acta* **56**: 1881–1888.

Duffó, G. S. and Farina, S. B. (2009). 'Development of an embeddable sensor to monitor the corrosion process of new and existing reinforced concrete structures'. *Construction and Building Materials* **23**: 2746–2751.

Elsener, B., Gulikers, J., Polder, R. and Raupach, M. (2003). 'Half-cell potential measurements – Potential mapping on reinforced concrete structures.' *Materials and Structures* **36**: 461–471.

Elsener, B., Klinghoffer, O., Frolund, T., Rislund, E., Schiegg, Y. and Böhni, H. (1997). Assessment of reinforcement corrosion by means of galvanostatic pulse technique. Repair of Concrete Structures. A. Blankvoll. Svolvær, Norway: 391–400.

Fariduddin, A. K. M., Ohtsu, M., Hossain, K. M. A. and Lachemi, M. (2007). 'Simulation of reinforcement-corrosion-induced crack propagation in concrete by acoustic emission technique and boundry element method analysis'. *Canadian Journal of Civil Engineering* **34**: 1197–1207.

Feliu, S., Gonzalez, J. A. and Andrade, C. (1996). Electrochemical methods for on-site determination of corrosion rates of rebars. Techniques to assess corrosion activity of steel reinforced concrete structures, ASTM STP 1276. N. S. Berke, E. Escalante, C. Nmai and D. Whiting, ASTM 107–118.

Fontana, M. G. (1987). *Corrosion Engineering*, McGraw-Hill, Singapore.

FORCE Technology (2004). Evolution of corrosion in reinforced concrete structures, www.force.dk/NR/rdonlyres/7A1681DB-71A2–4424-B948-D44EEDC-38C35/204/17861en3.pdf.

Force Technology (2012). CorroWatch Multisensor. http://www.forcetechnology.com/en/Menu/Products/Concrete-monitoring/Concrete-monitoring-probes/corrowatchmultisensor.htm.

Fuhr, P. L. and Huston, D. R. (1998). 'Corrosion detection in reinforced concrete roadways and bridges via embedded fiber optic sensors'. *Smart Materials and Structures* **7**: 217–228.

Gamry Instruments (2005). DC corrosion techniques. Application Notes, http://www.gamry.com/App_Notes/DC_Corrosion/GettingStartedWithEchem-CorrMeasurements.htm.

Gamry Instruments (2005). Electrochemical Impedance Spectroscopy Primer. Application Notes, http://www.gamry.com/App_Notes/EIS_Primer/EIS_Primer.htm.

Gamry Instruments (2006). Basics of Electrochemical Impedance Spectroscopy. http://www.gamry.com/App_Notes/EIS_Primer/EIS%20Primer%202006.pdf, Gamry Instruments.

Gaon, J., Wu, J., Li, J. and Zhao, X. (2011). 'Monitoring of corrosion in reinforced concrete structure using Bragg grating sensing'. *NDT & E International* **44**: 202–205.

Gaydecki, P. A. and Burdekin, F. M. (1994). 'An inductive scanning system for two-dimensional imaging of reinforcing components in concrete structures'. *Measurement Science and Technology* **5**: 1272–1280.

Gepraegs, O. K. (2002). Comparison and Evaluation of Electrochemical Techniques and Monitoring Instruments to determine the Corrosion Rate of Steel in Concrete, University of Waterloo. MA.Sc.

Golaski, L., Gebski, P. and Ono, K. (2002). 'Diagnostic of reinforced concrete bridges by acoustic emission'. *Journal of Acoustic Emission* **20**: 83–98.

Gonzalez, J. A., Andrade, C., Alonso, C. and Feliu, S. (1995). 'Comparison of rates of general corrosion and maximum pitting penetration on concrete embedded steel reinforcement'. *Cement and Concrete Research* **25**: 257–264.

Hansson, C. M. (1984). 'Comments on electrochemical measurements of the rate of corrosion of steel in concrete'. *Cement and Concrete Research* **14**: 574–584.

Idrissia, H. and Limam, A. (2003). 'Study and characterization by acoustic emission and electrochemical measurements of concrete deterioration caused by reinforcement steel corrosion'. *NDT & E International* **36**: 563–569.

Jones, D. A. (1992). *Principles and Prevention of Corrosion*, Macmillan Publishing Company, Prentice Hall, Upper Saddle River, NJ.

Jones, D. A. and Greene, N. D. (1966). 'Electrochemical measurement of low corrosion rates'. *Corrosion* **22**: 198–204.

Klinghoffer, O. (1995). *In Situ Monitoring of the Reinforcement Corrosion by Means of Electrochemical Methods*. Published in Nordic Concrete Research. 16.

Koch, G. H., Brongers, P. H., Thompson, N. G., Virmani, Y. P. and Payer, J. H. (2001). Corrosion Costs and Preventive Strategies in the United States. Washington DC, Federal Highway Administration (FHWA), Office of Infrastructure Research and Development.

Kumar, K., Muralidharan, S., Manjula, T., Karthikeyan, M. S. and Palaniswamy, N. (2006). 'Sensor systems for corrosion monitoring in concrete structures'. *Sensors & Transducers Magazine* **67**(5): 553–560.

Lasia, A. (1999). Electrochemical impedance spectroscopy and its applications. *Modern Aspects of Electrochemistry*, B. E. Conway, J. Bockris and R. E. White. Kluwer Academic/Plenum Publishers, New York. **32:** 143–248.

Lide, D. R. (1999). *CRC Handbook of Chemistry and Physics*. New York, NY, CRC Press.

Lo, Y. and Xiao, F. (1998). 'Measurement of corrosion and temperature using a single-pitch Bragg grating fiber sensor.' *Journal of Intelligent Material Systems and Structures* **9**(10): 800–807.

Martin-Perez, B., Zibara, H., Hooton, R. D. and Thomas, M. D. A. (2000). 'A study of the effect of chloride binding on service life predictions'. *Cement and Concrete Research* **30**(8): 1215–1223.

Merzbachery, C. I.,Kersey, A. D. and Friebele, E. J. (1996). 'Fiber optic sensors in concrete structures: a review'. *Smart Materials and Structures* **5**: 196–208.

Miller, G., Gaydecki, P., Quek, S., Fernandes, B. T. and Zaid, M. (2003). 'Detection and imaging of surface corrosion on steel reinforcing bars using a phase-sensitive inductive sensor intended for use with concrete'. *NDT&E International* **36**(1): 19–26.

Montemor, M. F., Simoes, A. M. P. and Ferreira, M. G. S. (1998). 'Analytical characterization of the passive film formed on steel in solutions simulating the concrete interstitial electrolyte'. *Corrosion* **54**(5): 347–353.

Muralidharan, S., Ha, T. H., Bae, J. H., Ha, Y. C., Lee, H. G. and Kim, D. K. (2007). 'A promising potential embeddable sensor for corrosion monitoring application in concrete structures.' *Measurement* **40**(6): 600–606.

Newhouse, C. D. and Weyers, R. E. (1996). Modeling the measured time to corrosion cracking. STP 1276 – Techniques to assess the corrosion activity of steel reinforced concrete structures. N. S. Berke, E. Escalante, C. K. Nmai and D. Whiting. West Conshohocken, PA, ASTM International.

Newton, C. J. and Sykes, J. M. (1988). 'A galvanostatic pulse technique for investigation of steel corrosion in concrete'. *Corrosion Science* **28**(11): 1051–1074.

Oliver, K. E.,Gooderham, T. and Newton, C. J. (2009). Corrosion monitoring systems and sensors to track material durability in concrete structures and down-hole applications, Intertek-CAPCIS.

Polder, R. B. and Peelen, W. H. A. (2002). 'Characterisation of chloride transport and reinforcement corrosion in concrete under cyclic wetting and drying electrical resistivity'. *Cement & Concrete Composites* **24**: 427–435.

Pourbaix, M. (1974). *Atlas of Electrochemical Equilibria in Aqueous Solutions*, Houston, Texas, National Association of Corrosion Engineers.

Poursaee, A. (2009). 'Automatic system for monitoring corrosion of steel in concrete'. *Advances in Engineering Software* **40**(11): 1179–1182.

Poursaee, A. and Hansson, C. M. (2009). 'Potential pitfalls in assessing chloride-induced corrosion of steel in concrete'. *Cement and Concrete Research* **39** (5): 391–400.

Princeton Applied Research (2006). 'Basics of Electrochemical Impedance Spectroscopy, Application Note AC-1.', http://new.ametek.com/content-manager/files/PAR/078.pdf.

Reis, H. L. M. D.,Ervin, B.,Kuchma, D. A. and Bemhard, J. T. (2003). Evaluation of corrosion damage in steel reinforced concrete. International Workshop on Structural Health Monitoring Stanford, CA, USA.

Rohrback Cosasco Systems (2012). 900 Concrete Multi-Depth Sensor. http://www.cosasco.com/multi-depth-corrosion.html.

Silverman, D. C. (1998). 'Tutorial on Cyclic Potentiodynamic Polarization Technique', CORROSION-98, NACE International, San Diego, CA, paper No. 299.

Silverman, D. C. (1986). Primer on the AC impedance technique. Electrochemical techniques for corrosion engineering. R. Baboian, NACE.

Silverman, D. C. (1990). Simple Models/Practical Answers Using the Electrochemical Impedance Technique. Corrosion Testing and Evaluation. R. Baboian and W. Dean, Silver Anniversary Volume, ASTM.

Stern, M. and Geary, A. L. (1957). 'Electrochemical polarisation: I. A theoretical analysis of the shape of polarisation curves'. *Journal of The Electrochemical Society* **104**(1): 56–63.

Stratfull, R. F. (1968). *Laboratory Corrosion Test of Steel in Concrete*. Sacramento, California, California division of highways, State of California.

Stratfull, R. F. (1972). *Half-Cell Potential and the Corrosion of Steel in Concrete*. Sacramento, California, California division of highways, State of California.

Swette, L. L., Manoukian, M., Hamdan, M., LaConti, A., Sohanghpurwala, A. and Scannell, W. T. (1999). Reference electrode for monitoring steel-in-concrete potential. U. S. Patent. USA. 5964992.

The Roctest Group (2012). SensCore Corrosion Sensor. http://www.roctest-group.com/sites/default/files/datasheets/products/16.1010ENDS_SensCore%20Corrosion%20Current%20Sensor.pdf.

Thuresson, T. I. (1996). Electrochemical monitoring of the influence of concrete quality on the reinforcing steel corrosion in industrial effluent, Queen's University. MA. Sc. .

Virginia Technologies Inc (2012). The Embedded Corrosion Instrument – ECI. http://www.vatechnologies.com/eciIndex.htm.

Wang, Y. and Huang, H. (2011). 'Optical fiber corrosion sensor based on laser light reflection'. *Smart Materials and Structures* **20**: 1–7.

Yang, S., Cai, H. W. and Geng, J. X. (2006). Advanced fiber grating corrosion sensors for structural health monitoring. *The Second International Conference on Structural Health Monitoring of Intelligent Infrastructure*. J. P. Ou, H. Li and Z. D. Duan. Shenzhen, China: 441–443.

Yoon, D., Weiss, W. J. and Shah, S. P. (2000). 'Assessing damage in corroded reinforced concrete using acoustic emission'. *Journal of Engineering Mechanics* **126**(3): 1–11.

Yunovich, M.,Thompson, N. G.,Balvanyos, T. and Lave, L. (2001). Corrosion Costs and Preventive Strategies in the United States, Appendix D: Highway Bridges. Washington DC, Federal Highway Administration (FHWA), Office of Infrastructure Research and Development.

Zakroczymski, T., Fan, C.-J. and Szklarska-Smialowska, Z. (1985). 'Kinetics and mechanism of passive film formation on iron in 0.05M NaOH'. *Journal of Electrochemical Society* **132**(12): 2862–2867.

Zdunek, A. D., Prine, D., Li, Z., Landis, E. and Shah, S. P. (1995). Early detection of steel rebar corrosion by acoustic emission monitoring. *Corrosion 95*. Baltimore, Maryland, USA, The NACE International.

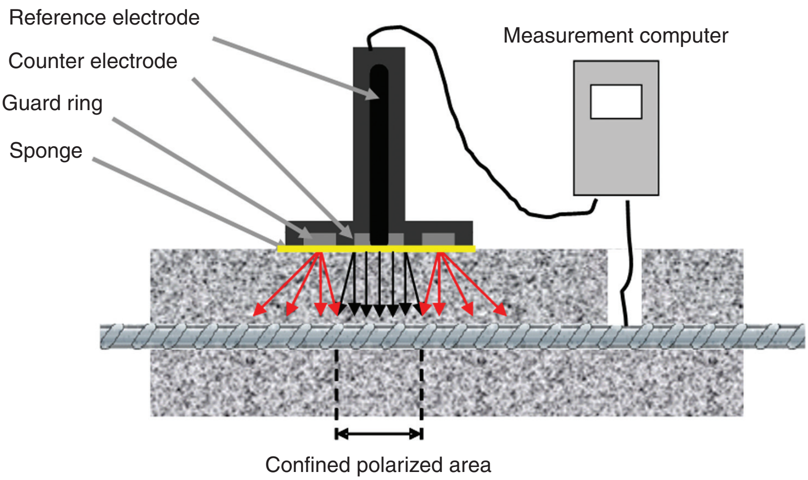
Reference electrode
Counter electrode
Guard ring
Sponge
Measurement computer
Confined polarized area

Plate X (Chapter 13) Schematic plan of an equipment with guarding to limit the polarized area while performing the corrosion measurement.

14

Vision-based sensing for assessing and monitoring civil infrastructures

Y. F. JI, Tongji University, China and C. C. CHANG, Hong Kong
University of Science and Technology, Hong Kong

DOI: 10.1533/9780857099136.383

Abstract: Recently, vision-based measurement techniques have emerged as an important non-destructive evaluation (NDE) method, due to the availability of low cost but high image resolution commercial digital cameras and effective image processing algorithms. In this chapter, some important issues that might affect the accuracy of the vision-based measurement techniques are presented and discussed. Results from laboratory tests and field tests are obtained to illustrate the accuracy and applicability of some vision-based measurement techniques.

Key words: displacement measurement, photogrammetry, videogrammetry, computer vision.

14.1 Introduction

A growing number of research efforts have been devoted to the area of structural health monitoring (SHM) over the past two decades to assess the safety and integrity of civil infrastructures. One SHM approach, global vibration-based technique, relies on the analysis of structural dynamic responses for assessment. Generally, these dynamic responses are in terms of acceleration, as they can be easily measured by accelerometers. Structural displacement response remains difficult to measure directly, although it is important for structural model updating and damage detection (Doebling *et al.*, 1996; Sohn *et al.*, 2004). Currently available displacement measurement techniques can be roughly classified into two categories: indirect measurement and direct measurement. Indirect measurement techniques include double integration of recorded acceleration time history and inferring from mathematical models using measured quantities such as strains (Kim and Cho, 2004). The accuracy of indirect measurement techniques, however, has always been a concern. Hudson (1979) commented that the double integration of acceleration is not readily automated and requires selection of filters and baseline correction and the use of judgment when anomalies exist in

© 2014 Woodhead Publishing Limited

the records. Applicable direct measurement techniques include the global positioning system (GPS) and the laser Doppler vibrometers. GPS can provide real-time displacement measurement with millimeter-level accuracy at a frequency up to 20 Hz. Xu *et al.* (2002) showed that a real-time kinematic GPS system installed on a suspension bridge achieved 5 and 10 mm resolution along the horizontal and the vertical direction, respectively. The laser Doppler vibrometer can provide accurate displacement measurement at multiple locations within its applicable distance (Nassif *et al.*, 2005). These direct measurement instruments, however, are quite costly. When displacements at a large number of locations are desired, measuring them using these sensors can be prohibitively expensive, if not impossible (Fu and Moosa, 2002).

With the advent of inexpensive and high-performance cameras and associated image processing techniques, a measurement technique based on images acquired from these cameras has attracted significant interest for its potential application in various engineering disciplines. Compared with the other measurement sensors, this vision-based measurement technique has several advantages: (1) it is a non-contact three-dimensional (3D) measurement technique; (2) it is economical in terms of both installation and cost; and (3) it can measure simultaneously a large number of points, or even a continuous spatial displacement profile on a structure.

The development of vision-based measurement technique can be traced to classical photogrammetry, which uses photographs to establish the geometrical relationship between a 3D object and its two-dimensional (2D) photographic images. Developments in photogrammetry have followed four development cycles (Konecny, 1985): plan table photogrammetry (1850–1900); analog photogrammetry (1900–1960); analytical photogrammetry (1960 to present); and digital photogrammetry (1990–present). The photogrammetric technique can usually be classified into aerial or terrestrial, depending on the types of images used in the analysis (Mikhail *et al.*, 2001). The aerial photogrammetric technique uses images acquired overhead from aircrafts, satellites, or hot air balloons. On the other hand, the terrestrial photogrammetric technique uses images from ground-based cameras. When the camera-to-object distance is within the range of 100 mm ~ 100 m, terrestrial photogrammetry is further defined as close-range photogrammetry (Atkinson, 2003; Luhmann *et al.*, 2007). Note that most civil engineering applications fall under this category.

In the earlier development of the photogrammetric technique, researchers used high-precision industrial grade metric cameras for the image acquisition. These metric cameras have precisely known internal geometries and very low lens distortion, but are quite expensive and require factory calibration. Also, the principal distance of these metric cameras needs to be fixed during application, which limits their distance range during application. While it is possible that image measurement accuracy using these metric cameras can exceed 1:200 000 of the cameras' field of view, using non-metric, even 'amateur' cameras is not excluded for some special measurement cases with a lower demand of accuracy, say, 1:1000 to 1:20 000. Along with the advancements in electronics, optics, and computer technologies in recent years, close-range photogrammetry has undergone a remarkable evolution and has been transformed to digital close-range photogrammetry (also called videogrammetry) using non-metric video components such as digital charge coupled device (CCD) cameras, video recorders, and frame grabbers for image acquisition. The evolution of videogrammetry has involved many special skills, such as geometric modeling of sensor imaging process, digital image analysis, feature extraction, and object reconstruction.

Computer vision, the study of enabling computers to understand and interpret visual information from static images and video sequences, emerged in the late 1950s and early 1960s and is expanding rapidly throughout the world. It belongs to the broader field of image-related computation, and relates to areas such as image processing, robot vision, machine vision, medical imaging, image databases, pattern recognition, computer graphics, artificial intelligence, psychophysics, and virtual reality (Bebis *et al.*, 2003). Computer vision produces measurements or abstractions from geometrical properties recorded in images. The goal of computer vision is then completed by interpreting the obtained measurements or abstractions. Computer vision is becoming a mainstream subject of study in computer science and engineering with the rapid explosion of multimedia and the extensive use of video- and image-based communications over the World Wide Web.

While the photogrammetrists developed accurate instruments as well as solid fundamental theories on camera calibration and camera-object geometry, the computer vision researchers further contributed theories on multiview geometry, image flow, ego-motion, etc. from the image-understanding viewpoint. These two areas of research, although not intensively interactive in the past, have started to become synergized and intertwined. Generally, a videogrammetric task can be fulfilled through the following steps: (1) control target layout and camera network setting; (2) target survey and camera calibration with lens distortion; (3) image acquisition and processing; and (4) point or object coordinates reconstruction using images. These steps center on a precise understanding of the camera models and their intrinsic and extrinsic parameters, as well as the geometrical relationship between the acquired images and the 3D object. The introduction of computer vision theories further makes possible the elimination of target requirement as well as the compensation for camera movement. These developments add flexibility to videogrammetric measurement techniques and create ample of opportunities for application to various engineering disciplines, including civil engineering.

14.2 Vision-based measurement techniques for civil engineering applications

In the past 20 years, there have been a few applications involving using photogrammetric or videogrammetric technique for various measurement purposes in civil engineering. Bales (1985) measured the deflection of a continuous three span steel bridge under dead load using close-range photogrammetric technique. Though the reported results were revealed to match very well with those of conventional methods in the average difference of 3.2 mm, the whole process was labor-intensive, time-consuming, and not cost-effective due to the need for a metric camera, special processing equipment, and well-trained workers. Li and Yuan (1988) developed a 3D photogrammetric vision system consisting of TV cameras and 3D control points to identify the bridge deformation. The Direct Linear Transform method was employed for camera calibration using 3D control-point information, which produced an accuracy of 0.32 mm. Aw and Koo (1993) used three standard CCD cameras to determine 3D coordinates of pre-marked targets. An averaged accuracy of 2.24 mm was obtained by a bundle adjustment method. Whiteman *et al*. (2002) developed a two-camera videogrammetric system with a precision of 0.25 mm to measure the vertical deflection of a concrete beam during a destructive test. It is to be noted in respect of the above three studies, the measurement systems were neither flexible nor cost-effective, as the coordinates of the control points were obtained by other surveying equipment. Some similar metrology applications employing videogrammetry have been realized successfully, such as concrete deformation measurement during dehydration process (Niederöst and Maas, 1997), thermal deformation of steel beams (Fraser and Riedel, 2000), vertical deflection measurement of existing bridges of different types (Jáuregui *et al*., 2003), and development of the Image Based Integrated Measurement (IBIM) system based on a low-cost stereo-vision-based sensing system for structural 3D modeling (Ohdake and Chikatsu, 2004). An image-based deformation measurement technique has been developed by Take *et al*. (2005) for real-time monitoring of construction settlements. The technique combined the technologies of remote digital photography, automated file transfer, the image processing technique of Particle Image Velocimetry, and a web-based reporting system. Alba *et al*. (2010) presented the development and results of a vision-based method for displacement measurement that allowed rapid deformation analysis along the cross-sections of a tunnel.

There have also been a few research activities involving structure dynamic measurement and system identification using the videogrammetric principle. Olaszek (1999) developed a videogrammetric method to investigate the dynamic characteristics of bridges. The application was performed for real-time displacement measurement of chosen points at bridge structure using CCD cameras with a telephoto-lens. The motive for adopting the videogrammetric technique was to resolve the difficulty of measuring some hard-to-access points at structure. Patsias and Staszewski (2002) used a videogrammetric technique to measure mode shapes of a cantilever beam. The wavelet edge detection technique was adopted to detect the presence of damage in the beam. A Kodak high-speed professional camera system with a maximum sampling rate of 600 frames per second (fps) was used to capture the beam vibration. The system, however, was limited to 2D planar vibration measurement since only one camera was used. Yoshida *et al.* (2003) used a videogrammetric technique to capture the 3D dynamic behavior of a membrane. Their measurement system consisted of three progressive CCD cameras with 1.3 million pixels and 30 fps. The cameras were calibrated using a calibration plate anchored on a linear guide system with accurate positioning capability.

Chung *et al.* (2004) used digital image techniques for identifying nonlinear characteristics in systems. Applications showed that digital image processing could identify the coulomb friction coefficient of a pendulum as well as nonlinear behavior of a base-isolated model structure. Poudel *et al.* (2005) proposed a video imaging technique for damage detection of a prismatic steel beam. A high-speed complementary-metal-oxide-semiconductor (CMOS) camera was employed to capture the dynamic response of the beam. Mode shapes of the beam were extracted by wavelet transform and were used for damage localization. A monocular-vision-based measurement system was developed by Lee *et al.* (2007) for health monitoring of bridges. A specially designed plane pattern was used for simple camera calibration as well as target tracking. As the system used only one camera, it could only measure the in-plan 2D displacement of a specially designed target. Chang and Ji (2007) developed a binocular-vision system to measure 3D structural vibration response. A two-step plane-based calibration process, including individual and stereo calibration, was proposed to effectively obtain the camera parameters. Caetano *et al.* (2007) reported the application of a monocular-vision-based technique for a target-camera distance of 850 m and a field of view of 300 m. A detailed review of vision-based sensing in bridge measurement was conducted by Jiang *et al.* (2008). Based on a monocular-vision theorem, Chang and Xiao (2010) developed a novel measurement technique to capture structural 3D displacement. Results of a field test showed that the method could measure quite accurately the 3D translation and rotation of a planar target attached to a bridge. Ozbek *et al.* (2010) discussed the pros and cons of using photogrammetric technique for health monitoring of wind turbines. The 3D dynamic response of the rotor was captured at 33 different locations simultaneously using 4 CCD cameras. Jeon *et al*. (2011) proposed a paired vision-based system comprising lasers, a camera, and a screen to measure displacement of large structures. Kim and Kim (2011) proposed a digital image correlation technique to measure multi-point displacement response for civil infrastructures. Recently, an image-based technique was used to measure minimum vertical under-clearance for bridges during routine inspection (Riveiro *et al*., 2012).

Note that the development of vision-based measurement techniques is not limited to the academic community; some commercial systems have been developed in the last two decades for various applications. PhotoModeler (Eos, 2012) is a software system that performs image-based modeling and close-range photogrammetry for tasks such as performing accurate measurement, creating CAD-like models, and modeling man-made, organic, or natural shapes. The Australis software suite (Photometrix, 2012) is designed to perform automated image-based 3D coordinate measurements from recorded digital images. The software can provide fully automatic measurement of targeted objects to high accuracy or low-to-moderate accuracy semi-automatic or manual measurements in photogrammetric networks comprising natural feature points and images from off-the-shelf cameras. The iWitness photogrammetry software systems (DCS, 2012) produce 3D measurements and models from digital camera images and scanned analog photographs using coded target technology. The systems have been used in engineering measurement, architectural, and archaeological measurement, and biomedical measurement, as well as 3D documentation in support of virtual reality modeling. Vic-3D 2010 (Correlated, 2012) is a turnkey system for measuring the shape, displacement, and strain of surfaces in three dimensions. It uses the digital image correlation principle and can measure displacements and strains from 50 micro-strains to 2000% strain for specimen sizes ranging from 1 mm to 10 m. The Bersoft Image Measurement (BIM) (Bersoft, 2012) is Windows-based software that acquires, measures, stores, compares, and analyzes digital images. BIM performs image analysis functions that include gray scale and 24-bit color measurements: angle, distance, perimeter, area, point, line, pixel profile, object counting, histogram, and statistics.

14.3 Important issues for vision-based measurement techniques

In this section, several important core issues that affect the accuracy of vision-based measurement techniques are discussed.

14.3.1 Camera calibration

Camera calibration is the recovery of the intrinsic parameters of a camera. Traditionally, cameras, especially metric cameras, are calibrated in laboratories in a well-controlled environment. Laboratory calibration can be done using either a goniometer or a multicollimator (Mikhail *et al.*, 2001). Although the camera parameters can be obtained with high precision, the calibration is rather intensive and costly. In addition, the principal distance of the calibrated cameras needs to be fixed during application, which limits the flexibility of these laboratory-calibrated cameras. More and more uses of non-metric cameras have demanded more flexible, and preferably on-site, calibration.

A general projective camera, such as the one equipped with CCD sensors, can be described using a pinhole model as (see Fig. 14.1):

$$\lambda m = PM \tag{14.1}$$

where $m = (u, v, 1)^T$ is a 2D homogenous image coordinate defined by pixels, a 3D real point is denoted by a homogenous vector $M = (X, Y, Z, 1)^T$, λ is a scale factor, and P is a 3×4 matrix called camera projective matrix, and can be described by the following relationship:

$$P = KR[I \mid t] \tag{14.2}$$

$$K = \begin{bmatrix} \alpha_x & s & u_0 \\ 0 & \alpha_y & v_0 \\ 0 & 0 & 1 \end{bmatrix} \tag{14.3}$$

Note that α_x and α_y are the focal lengths of the camera in terms of pixel dimensions in the u and v directions, respectively, s is the skew parameter,

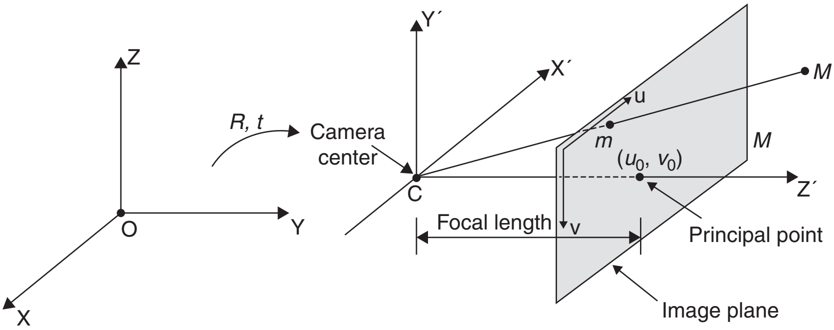

14.1 Pinhole camera model.

and u_0 and v_0 are the coordinates of the principal point in terms of pixel dimensions, R is a 3×3 rotation matrix representing the orientation of camera coordinate frame, I is a 3×3 unity matrix, and t is a 3×1 translation vector relating image and object coordinate system. There are a total of 11 parameters to be calibrated for a single camera, which means at least six control points have to be pre-measured (i.e., known XYZ coordinates relative to one another in an arbitrary Cartesian reference system). These camera parameters can be found by the least squares solution of Equation [14.1]. In addition, camera lens might suffer from a distortion problem that could affect the accuracy when used for videogrammetric applications. Assume an ideal image point $(u, v, 1)$ is distorted by an unknown amount; its corresponding distorted and observed image coordinates $(\hat{u}, \hat{v}, 1)$ can be expressed as:

$$\begin{cases} \hat{u} = u + \overline{u}\left(k_1 r^2 + k_2 r^4\right) + k_3\left(r^2 + 2\overline{u}\right) + 2k_4\overline{uv} \\ \hat{v} = v + \overline{v}\left(k_1 r^2 + k_2 r^4\right) + k_4\left(r^2 + 2\overline{v}\right) + 2k_4\overline{uv} \end{cases} \tag{14.4a}$$

$$\begin{cases} \overline{u} = u - u_0 \\ \overline{v} = v - v_0 \end{cases}, \quad r^2 = \overline{u}^2 + \overline{v}^2 \tag{14.4b, c}$$

where k_1 and k_2 are coefficients of radial lens distortion, and k_3 and k_4 are coefficients of decentering lens distortion. With the selection of these additional distortion parameters, the minimum requirement for one camera calibration should increase to eight control points.

The calibration can be performed based on control targets that are spatially distributed in 3D space and not coplanar as shown in Fig. 14.2. The problem with this kind of calibration method exists in appropriate settings of cameras and targets, and tedious geometric survey of those control points. Therefore, when the measurement object or motion is not much larger, a plane-based method is considered as a more suitable way for camera calibration due to its reliability and flexibility. The plane-based camera calibration is a method between photogrammetric calibration and self-calibration that utilizes various relationships between different real plane information and corresponding image coordinates to verify all the parameters in camera projective matrices for all the views. Figure 14.3 shows one typical plane pattern for camera calibration. The corner points of black and white squares are used as control targets for the calibration.

There are several important issues related to the calibration (Kwon, 1998): (i) the calibration frame must be large enough to fully include the space of motion; (ii) the camera setting must not be altered once calibration is done;

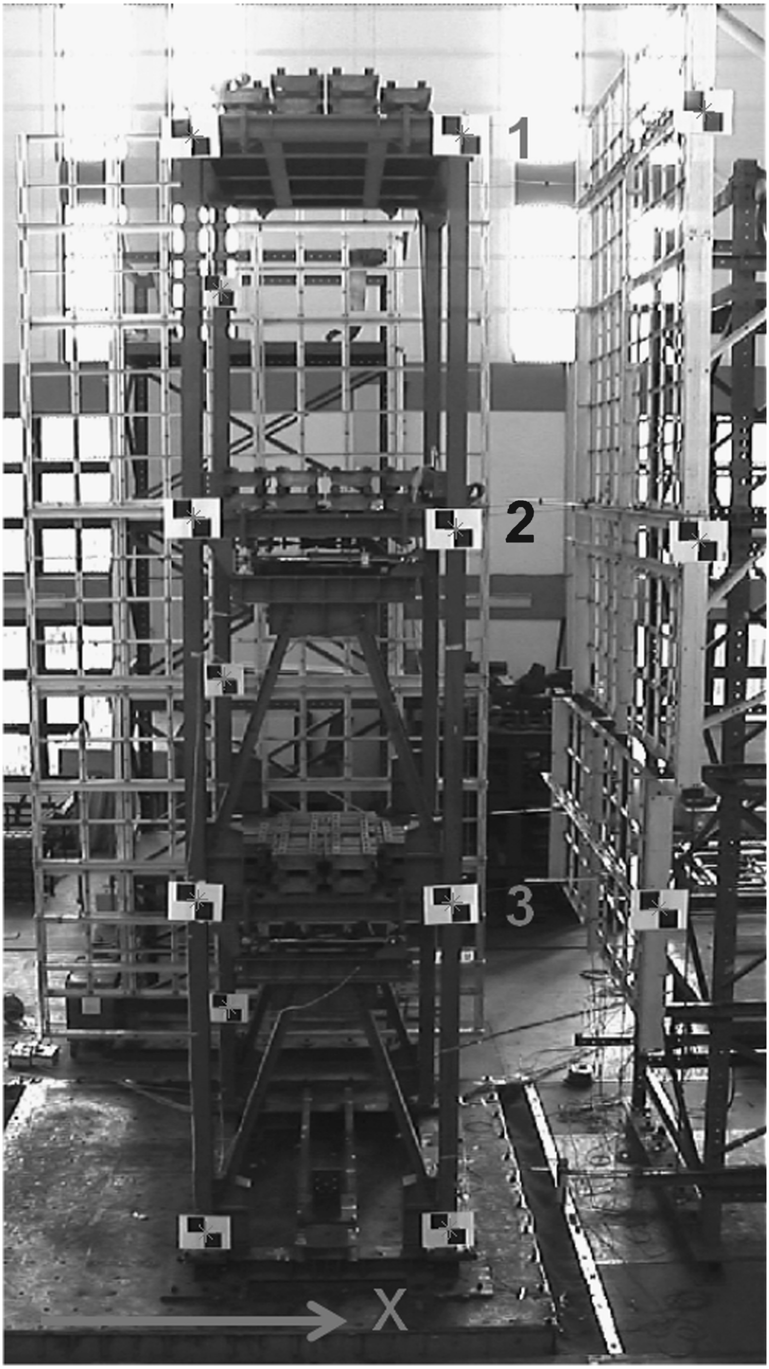

14.2 A steel building frame with targets for camera calibration and tracking.

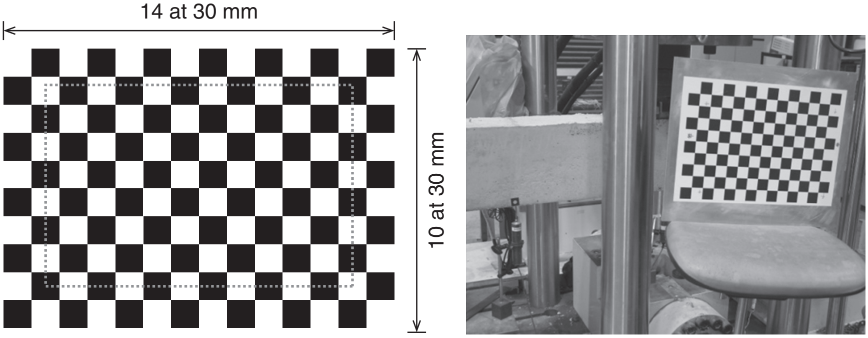

14.3 Plane-based camera calibration.

(iii) as many control points as possible should be included and spread uniformly throughout the control volume; and (iv) the calibration frame should be set properly to align the axes well in relation to the direction of motion. The camera calibration methods currently being developed in the computer vision have been moving toward more flexibility with less use of artificial control points. For example, Deutscher *et al*. (2000) proposed an automatic method for obtaining the approximate calibration of a camera from a single image of an unknown scene that contains three orthogonal directions (the so-called Manhattan World image).

14.3.2 Target and correspondence

Vision-based sensing is often concerned with identifying and locating predefined targets. These targets are used for two purposes: to provide coordinates for the point of interest, and to establish correspondence for the point of interest in an image sequence. A number of techniques can be used to locate a predefined target. These techniques depend on the type and shape of the target, whether its image is affected by perspective effects, and how much its average gray level differs from the background.

Figure 14.4 shows the identification of one common target. The algorithm includes the following tasks: (i) convert images to binary form; (ii) obtain intersections of image skeleton using image morphology techniques; (iii) filter out the outliers and determine the most-likely corner point; and (iv) use the detected point in Step (ii) as an initial guess to find the exact corner point using corner detection techniques such as the Harris corner detection method. After a target point has been identified from one image frame, it is necessary to track this target point from the subsequent images. A point matching criterion can be introduced to solve this correspondence problem. Assume that the target point is the center pixel of a square mask with *r* rows

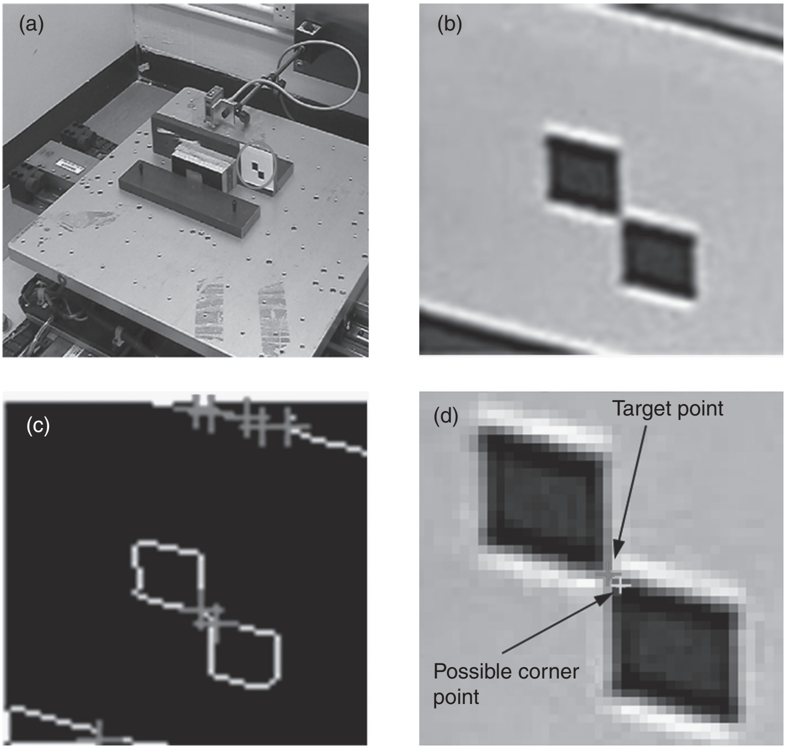

14.4 Target point extraction. (a) Target pattern, (b) zoom-in of target pattern, (c) intersection of image skeleton, (d) detected target point.

and c columns as shown in Fig. 14.5. A cross correlation coefficient between square mask a in Image I and square mask b in Image II can be calculated as follows:

$$k_{a,b} = \frac{\sum_{i}^{r}\sum_{j}^{c}\left(f_a(i,j)-\overline{f_a}\right)*\left(f_b(i,j)-\overline{f_b}\right)}{\sqrt{\sum_{i}^{r}\sum_{j}^{c}\left(f_a(i,j)-\overline{f_a}\right)^2*\sum_{i}^{r}\sum_{j}^{c}\left(f_b(i,j)-\overline{f_b}\right)^2}} \qquad [14.5]$$

where f is the pixel gray level, $\overline{f}$ denotes the mean gray level of square mask, and $k_{a,b}$ is the correlation coefficient that satisfies $k_{a,b} \leq 1$. Among those candidate points, the point that gives the maximum $k_{a,b}$ value is the one matching with the reference. A triangular method can be used to determine the 3D coordinates of the target point from two image points recorded by a calibrated camera.

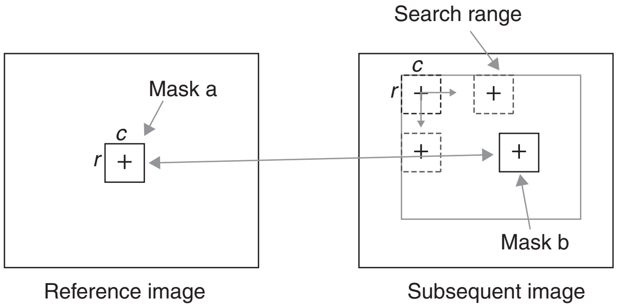

14.5 Target point tracking by a correlation-based method.

When no target is available, an approach developed in the computer vision, the optical flow technique, can be used (Jain *et al.*, 1995). Optical flow is the velocity field resulting from an intensity change on the image plane. Figure 14.6 shows a schematic illustration of the optical flow technique. Two segments of cable images, one from time $t = t_1$ and the other from time $t = t_1 + dt$, are overlaid in the figure, where dt is a time increment. Without a specific target, it is impossible to know precisely where a point, say point k, would move to in the next time instant. Assume that the intensity of a point $j(u, v, t_1)$ at $t = t_1$ is expressed as $I(u, v, t_1)$ where u and v are the coordinates on the image plane. At $t = t_1 + dt$, this point moves to $j(u + du, v + dv, t_1 + dt)$ with an intensity of $I(u + du, v + dv, t_1 + dt)$ where du and dv are the displacement increments along u and v, respectively. These two intensities can be approximately related through Taylor series expansion as:

$$I\left(u+du, v+dv, t_1+dt\right) \approx I\left(u, v, t_1\right) + I_u du + I_v dv + I_t dt \qquad [14.6]$$

where I_u, I_v, and I_t denote the partial derivatives of the intensity with regard to u, v, and t, respectively. Assuming the lighting on the cable segment is the same on the two images, the two intensity values can then be assumed to be the same. And we can easily derive the governing equation of pixel movement as follows:

$$I_u \dot{u} + I_v \dot{v} = I_t \qquad [14.7]$$

where $\dot{u}$ and $\dot{v}$ are the velocity components of the image point $j(u, v, t_1)$, and $\left(\dot{u}\,\dot{v}\right)^T$ is termed as the optical flow vector. Furthermore, on the assumption that there is a region of interest (ROI) R in which all points have the same constant optical flow vector, this optical flow vector should satisfy the following equation:

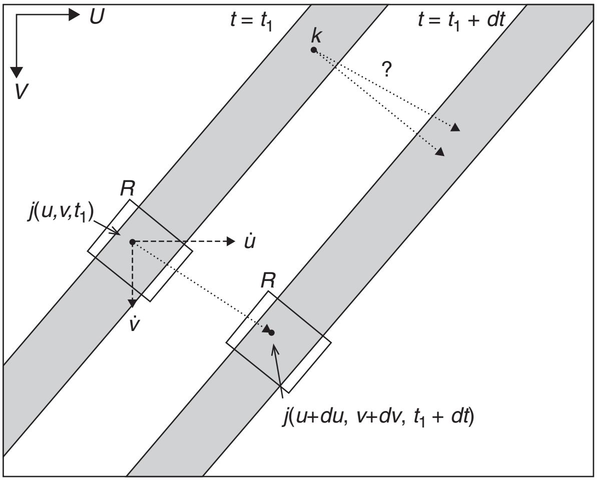

14.6 A schematic illustration of the optical flow method.

$$\begin{bmatrix} \sum_R I_u I_u & \sum_R I_u I_v \\ \sum_R I_u I_v & \sum_R I_v I_v \end{bmatrix} \begin{Bmatrix} \dot{u} \\ \dot{v} \end{Bmatrix} = - \begin{Bmatrix} \sum_R I_u I_t \\ \sum_R I_u I_t \end{Bmatrix} \tag{14.8}$$

This equation can be used to compute the optical flow vector. The direction and the magnitude of the optical flow vector then indicate the direction and the magnitude of motion for the ROI in the image plane.

For the case of an object moving in the 3D domain, the optical flow technique can still be adopted using two or more cameras. For a two-camera image acquisition system, the epipolar geometry condition requires that two optical centers of the cameras C^1 and C^2, the point M, and its image projection points m^1 and m^2 should lie on the so-called epipolar plane as shown in Fig. 14.7. The two image points should satisfy the following equation (Hartley and Zisserman, 2003):

$$(m^1)^T Fm^2 = 0 \tag{14.9}$$

where F is defined as the fundamental matrix. This equation essentially defines a line on the second image if the image coordinates on the first image are given and vice versa. It is then possible to establish a point correspondence from the two images without the use of any target.

14.3.3 Camera movement

Most vision-based sensing techniques were developed based on the assumption that the camera was fixed on the ground. On the other hand, more and

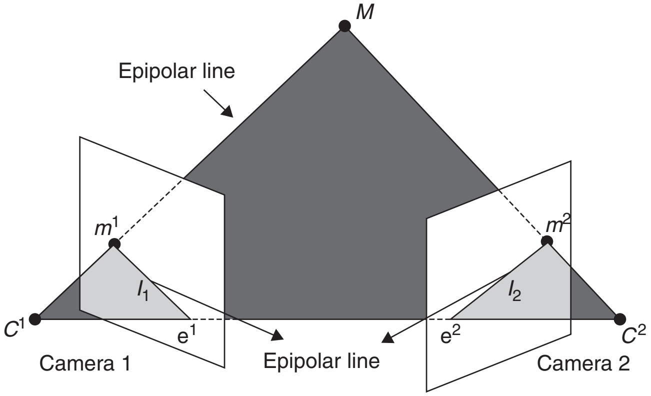

14.7 Epipolar geometry for a two-camera image acquisition system.

more applications in the computer vision community have demanded an investigation into the effect of camera motion, termed the ego-motion, on image understanding. The object motion recorded on an image sequence is a combined result of the actual object motion and the ego-motion. The effect of ego-motion becomes an issue of great concern for civil engineering applications. Civil infrastructures are normally large, and mounting cameras on fixed supports becomes a challenge. Several algorithms have been developed to extract the motion of a camera moving with respect to a fixed scene. These methods can be categorized either as discrete-time methods or as instantaneous-time methods (Tian *et al.*, 1996). Simultaneous recovery of object motion and ego-motion has also been studied (Georgescu and Meer, 2002).

14.4 Applications for vision-based sensing techniques

To illustrate the applicability of vision-based measurement techniques, some measurement examples are presented in this section. These examples used only commercial grade non-metric cameras equipped with 1.18 million-pixel progressive CCD and could record high-definition (HD) images with a pixel resolution of 1280 × 720 at 29.97 fps.

14.4.1 Small-scale building model test

In this example, the plane-based method introduced above was used to calibrate two non-metric cameras. The small-scale three-story building model was made out of aluminum with a uniform story height of 0.38 m and a total height of 1.21 m as shown in Figure 14.8. Four targets, A, B, C, and D were

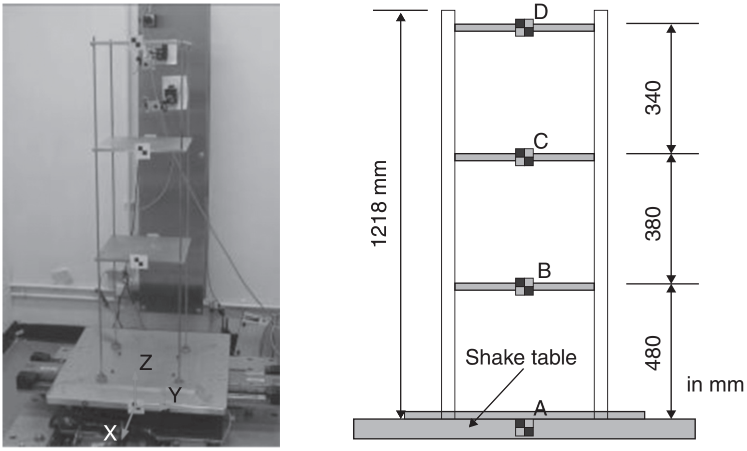

14.8 Experiment set-up of three-story building model.

attached to the base and the three stories. The model was excited by the NS component (i.e. the earthquake component in the 'North-South' direction) of the 1940 El Centro earthquake ground displacement record and the 1995 Kobe earthquake 2D ground displacement record, respectively. Four laser linear variable differential transformers (LVDTs) were set up to measure the displacement time histories for the shake table and the three stories. Figures 14.9 and 14.10 show the two sets of results. These results indicate that image-based measurement can achieve good agreement with the LVDT measurement.

14.4.2 Large-scale steel building frame test

As shown in Fig. 14.2, a three-story steel building frame was mounted on a shake table in the National Center for Research on Earthquake Engineering of Taiwan. This frame was excited by the 1940 El Centro earthquake 2D ground displacement record. The frame model had dimensions of 3 m × 4 m × 12 m with three stories evenly distributed in height. Fourteen control targets were attached on and around the frame for calibrating the two cameras. Some of these targets were used as target points for the displacement measurement. All control points were carefully surveyed by a total station. The camera calibration results showed that the mean reconstruction error of all targets was around 0.5–0.8 mm, which provided an indication on the measurement error for the set-up. Figure 14.11 shows the comparison of measurement results between the image-based technique and the LVDT. It can be seen that the proposed videogrammetric technique is able to track the dynamic displacement quite accurately.

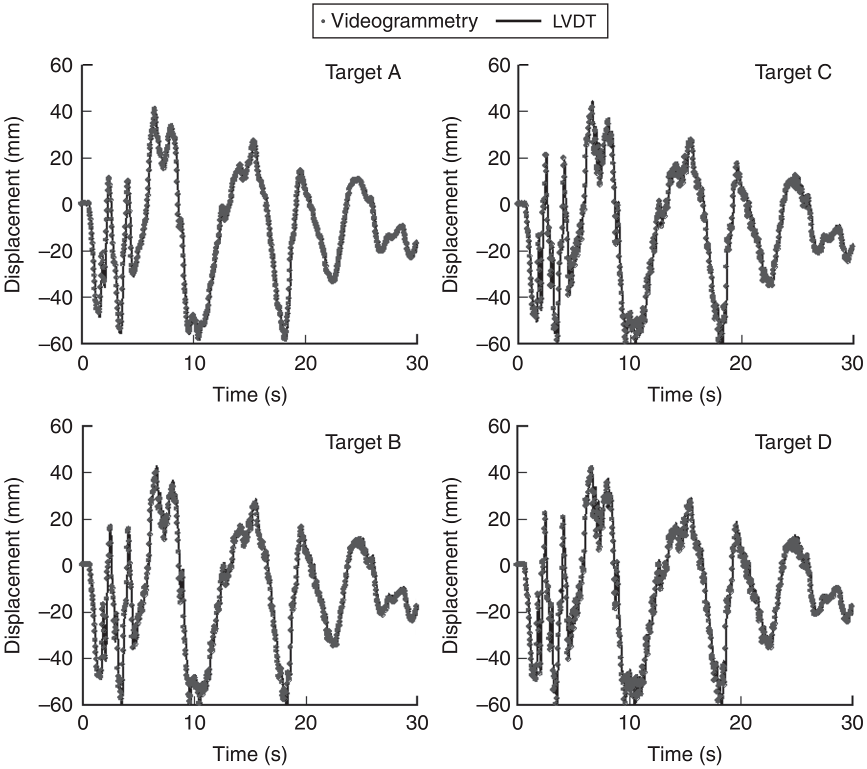

14.9 Displacement responses of the three-story building model under the 1940 El Centro earthquake.

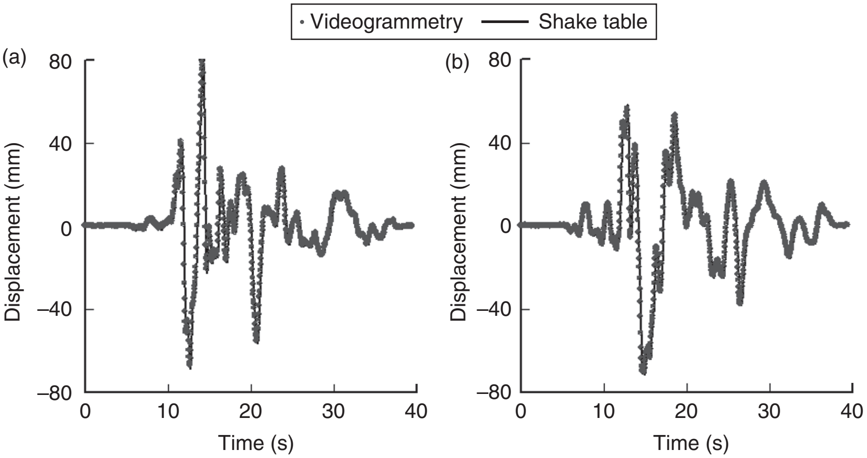

14.10 Comparative results of videogrammetric measurement and shake table input at Target A under the 1995 Kobe earthquake. (a) X direction, (b) Y direction.

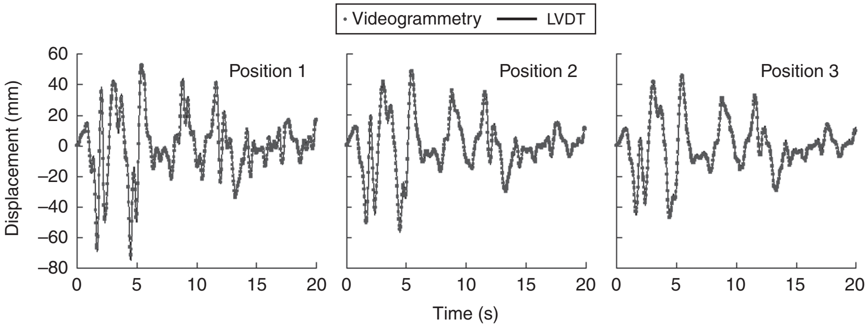

14.11 Displacement responses (along X) at Position 1, 2 and 3 of the building frame in Fig. 14.2.

14.4.3 Wind tunnel bridge sectional model test

Figure 14.12 shows a wind tunnel set-up for a bridge sectional model test. The sectional model consisted of two wooden box girders connected by crossbars. The model was rigidly connected to circular rotatable shafts. The shafts were then attached to rigid rectangular bars, which were supported by four linear springs to provide the necessary stiffness for the section model. Two laser LVDTs were positioned at locations as shown in Fig. 14.12 to measure the displacement time histories during the test. Two targets were placed at locations as shown to validate the applicability of the vision-based sensing technique for such a test. The cameras were placed at about 1.2 m from the targets and the angle between the two cameras was about 30°. The focal lengths of the two cameras were both set at 15.6 mm. The model was pulled by a string and released to vibrate under a mild and steady wind condition. As the supporting rectangular bars were rigid, the readings from the laser LVDTs could be linearly scaled to the deformations at the two target locations for comparison. Figure 14.13 shows the measurement results at the two target locations. The close match between the two measured results indicates that the vision-based sensing technique is able to track the two targets quite accurately.

14.4.4 Bridge cable test

In this example, the use of the optical flow approach for measuring bridge cable vibration (in-plane motion) by monocular-vision-based sensing technique is demonstrated. Only one camera is used for the image acquisition. Assume that a bridge cable vibrates predominately along the in-plane perpendicular to chord direction as shown in Fig. 14.14. Any point

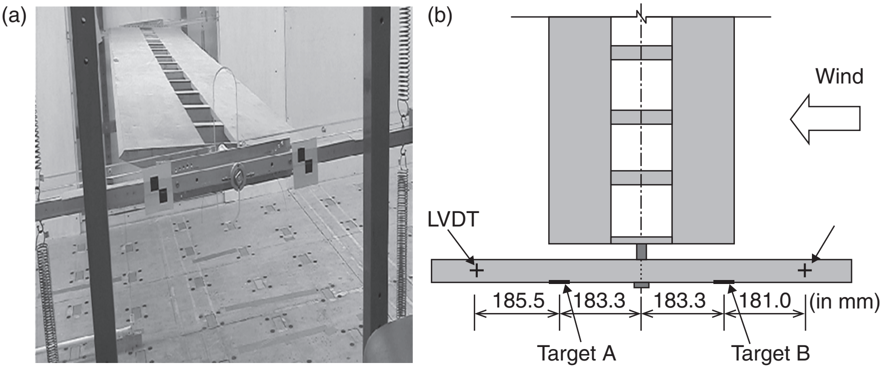
(a)
(b)
Wind
LVDT
185.5
183.3
183.3
181.0
(in mm)
Target A
Target B

14.12 Wind tunnel test for a bridge sectional model. (a) Photo of the section model in the wind tunnel test; (b) the general plan of the model including some dimensions and explanations.

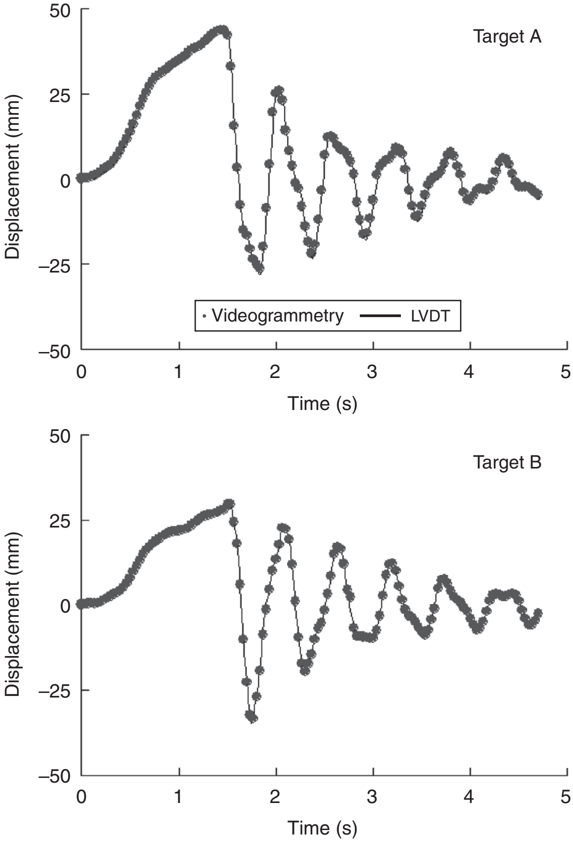

14.13 Measured responses at Target A and Target B.

on the cable can be regarded as making a 1D motion. Define the line trajectory of this point in the 3D object space and in the 2D image plane as $N(t)$ and $n(t)$, respectively, where t is time. For a projective camera, the mapping between the 1D motion in the 3D object space and the corresponding 1D motion in the 2D image plane can be obtained via a pinhole camera model. For a line-to-line projection, the camera matrix **P** becomes a 2 × 2 matrix:

$$\mathbf{P} = \begin{bmatrix} p_1 & p_2 \\ p_3 & p_4 \end{bmatrix} \qquad [14.10]$$

where p_i, $i = 1$–4 are the camera projection coefficients. Eliminating λ in Equation [14.1] gives:

$$n(t) = \left(p_1 N(t) + p_2\right) / \left(p_3 N(t) + p_4\right) \qquad [14.11]$$

It can be seen that the line $N(t)$ in 3D space and the line $n(t)$ on 2D image plane are nonlinearly correlated. Under the affine camera assumption, p_3 in the camera matrix is equal to 0. Hence, Equation [14.11] becomes:

$$n(t) = p_1' N(t) + p_2' \qquad [14.12]$$

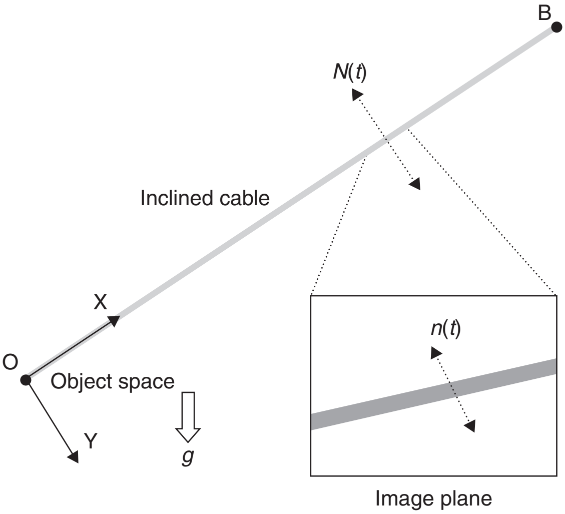

14.14 A schematic diagram of an inclined cable.

where the scaling factor $p_1' = p_1 / p_4$ and the initial factor $p_1' = p_1 / p_4$.

It can be seen that the 1D motion in the 3D object space $N(t)$ and its corresponding 1D motion in the 2D image plane $n(t)$ are linearly correlated and their frequency contents would be the same. Under such conditions, it is possible to obtain the natural frequencies of stay cables from the cable image motion recorded from a single camera. The object motion $N(t)$ can be obtained from the image motion $n(t)$ if the scaling factor p_1' can be determined. Setting the initial factor $p_2' = 0$, the 1D motion in the object space $N(t)$ can be obtained from the 1D motion on the image plane $n(t)$ as:

$$N(t) = \frac{n(t)}{p_1'} \tag{14.13}$$

It should be noted that the estimation of cable displacement presented above is applicable to those cables without a noticeable sag effect.

To illustrate, one cable of a small cable-stayed pedestrian bridge (see Fig. 14.15) was selected for measurement. The diameter of the cable was measured to be 40 mm. This cable was subjected to an initial deformation in the vertical plane and underwent free vibration. Two camcorders, placed at 2 and 3 m distance, respectively, were employed to measure the vibration of the cable separately. The focal lengths for both camcorders were set at 52 mm, and the ratios of the field of view to the cable-camera distance were both around 0.07 to meet the assumption of an affine camera. The two camcorders recorded the motion of the same segment on the cable so that comparison could be made. A total station was used to measure the coordinates

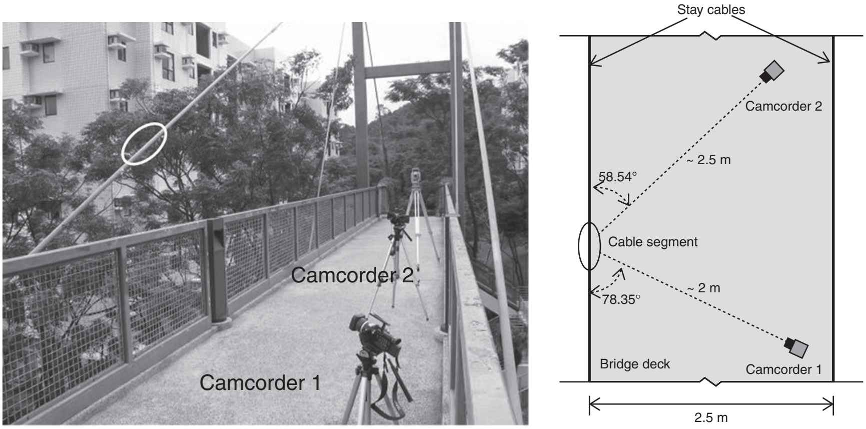

14.15 Field measurement of cable vibration.

of the two camcorders as well as the two anchorage locations of the cable. An accelerometer was also attached to the cable to obtain the cable frequencies for comparison.

Figures 14.16a and 14.16b show one of the images captured by Camcorders 1 and 2, respectively. From the optical flow technique, the directions of the optical flow vector for the ROIs from Camcorder 1 and Camcorder 2 are shown in Figs 14.16c and 14.16d. Plate XIa (in the color section between pages 294 and 295) shows the displacement time histories of the cable segment obtained from both camcorders. It can be seen that the cable segment oscillates between –30 and 30 mm. Plate XIb shows the power spectral densities of the two displacement time histories shown in Plate XIa. It can be seen that in the frequency range of 0 to 8 Hz, the current image-based technique can obtain three frequencies: 2.05, 3.81, and 5.84 Hz. Three frequencies can also be obtained from the accelerometer: 2.05, 3.81, and 5.76 Hz. These results indicate that the vision-based sensing technique is capable of measuring the natural frequencies of this bridge cable quite accurately.

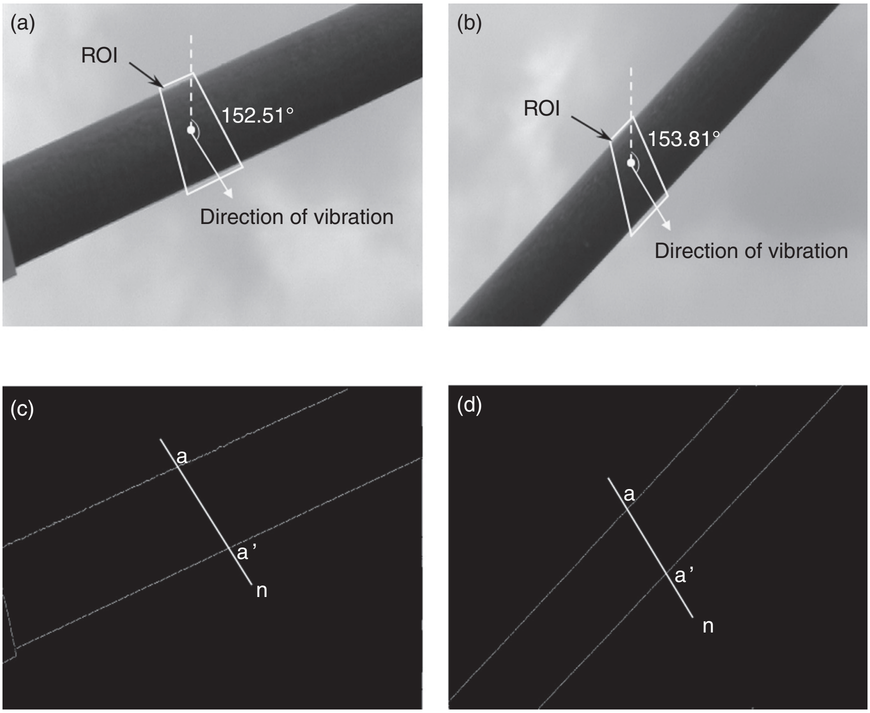

14.16 Images of cable segment recorded by the two camcorders. (a) An image of cable segment (Camcorder 1), (b) an image of cable segment (Camcorder 2), (c) binary image of (a), (d) binary image of (b).

14.4.5 Pedestrian bridge test

This test was conducted on a small-scale single-pylon pedestrian bridge. The 3D dynamic displacement of the bridge deck was measured using monocular-vision sensing technique. The planar target used for the camera calibration and the target tracking was placed at one side of the bridge deck (see Fig. 14.17). The camera was placed at about 5.2 m away from the target at about the same height, and the extrinsic parameter of the camera from the first frame indicated that the inclination angle between the Z and $-Z_c$ axes was about 59.5°. The bridge was excited by two persons jumping on the bridge deck. A 20s image sequence was recorded for measuring the three-dimensional motion of the target. Based on the predefined world coordinate system, the displacement of the bridge deck was predominately along the X direction.

Figure 14.18a shows the measured displacement time histories along X, Y, and Z axes, respectively. It can be seen that the displacements along the X direction are larger than those along the other two directions. The first 9 s of the X displacements corresponds to the period of time when the bridge vibration was building up by the two persons continuously jumping on the deck. Beyond that the jumping was stopped and the bridge went through a free decay vibration, as shown in Fig. 14.18a. The maximum displacement amplitude along the X direction is about 6 mm. The measured displacements along the Y and the Z directions, however, do not show the built-up and the free decay behavior as seen along the X direction. These Y and Z displacements can be regarded as due more to the measurement noise than to the actual displacement of the bridge deck. The standard deviations of the displacements along the Y and the Z directions are found to be 0.76 and 1.09 mm, respectively. Figure 14.18b also shows the measured rotation angles about the three axes, which were all found to be less than 0.1°.

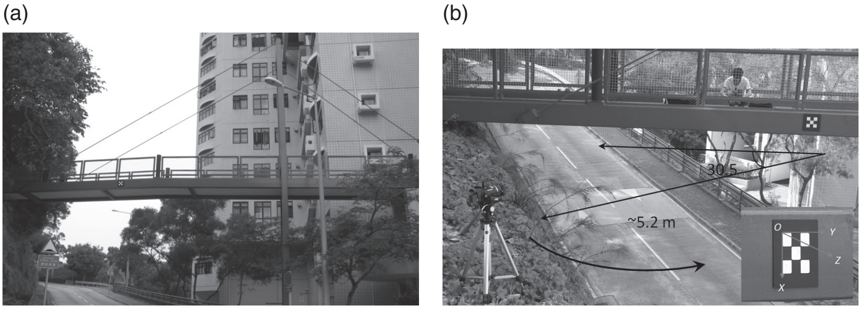

14.17 (a) The pedestrian bridge, (b) set-up of the test.

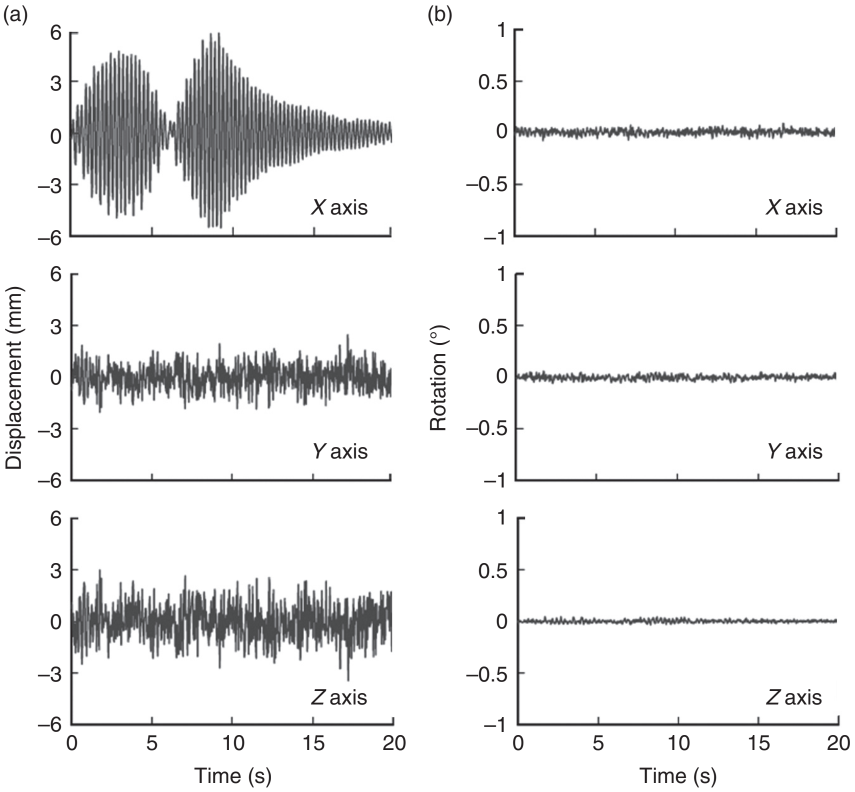

14.18 (a) Displacements along X, Y and Z axes, (b) rotations about X, Y and Z axes.

14.5 Conclusions

Measuring static and dynamic displacement of in-service structures is an important issue for the purpose of design validation, performance monitoring, or safety assessment. Currently, the available measurement techniques either cannot provide sufficient accuracy or are quite expensive when a large number of measurement locations are desired. Recently, vision-based measurement techniques have emerged as an important non-destructive evaluation (NDE) method, due to the availability of low cost but high image resolution commercial digital cameras and effective image processing algorithms. These vision-based measurement techniques synergize research developments from the photogrammetry and the computer vision discipline and offer a direct displacement measurement in both temporal and spatial domains for civil engineering structures. Furthermore, the cameras used in these techniques can be calibrated on-site, which offers great flexibility and significantly simplifies the installation process. In this chapter, some important issues that might affect the accuracy of the vision-based measurement techniques are presented and discussed. Results from laboratory tests and field tests show that the vision-based measurement techniques can remotely capture displacement response of structures with accuracy comparable to that of the GPS. With the rapid development in the digital image acquisition and processing, it is expected that the vision-based measurement techniques will continue to improve in accuracy and offer a viable cost-effective solution for obtaining three-dimensional displacement responses for civil engineering structures. It should be mentioned that, despite their advantages and potential, the current vision-based techniques that use commercial digital cameras nonetheless suffer from a few limitations including low sampling frequency, high measurement noise, and weather/light constraints, which might restrict their field applications. Further research efforts are needed to circumvent some of these limitations, perhaps by integrating these vision-based measurement techniques with other sensors available to the civil engineering community.

14.6 Acknowledgment

This study is supported by the Hong Kong Research Grants Council Competitive Earmarked Research Grant 611409.

14.7 References

Alba M, Barazzetti L, Giussani A, Roncoroni F and Scaioni M (2010), 'Development and testing of a method for tunnel monitoring via vision metrology', *International Archives of Photogrammetry, Remote Sensing and Spatial Information Sciences*, Vol. **XXXVIII**, Part 5, Commission V Symposium, Newcastle upon Tyne, UK. Commission V Symposium, Newcastle upon Tyne, UK. 2010, 17–22.

Atkinson K B (2003), *Close Range Photogrammetry and Machine Vision*, Whittles Publishing, Caithness, Scotland, UK.

Aw Y B and Koo T K (1993), 'Phototriangulation using CCD camera in close-range environment', *Journal of Surveying Engineering*, **119**(2), 52–58.

Bales F B (1985), 'Close-range photogrammetry for bridge measurement', *Transportation Research Record*, 950, Transportation Research Board, Washington DC, 39–44.

Bebis G, Egberg D and Shah M (2003), 'Review of computer vision education', *IEEE Transactions on Education.*, **46**(1), 2–21.

Bersoft Software & Technology (2012), *Bersoft Image Measurement*, http://bersoft.com/index.htm (Accessed 31 October 2012).

Caetano E, Silva S and Bateira J (2007), 'Application of a vision system to the monitoring of cable structures', *Seventh International Symposium on Cable Dynamics*, Vienna, 225–236.

Chang C C and Ji Y F (2007), 'Flexible videogrammetric technique for three-dimensional structural vibration measurement', *Journal of Engineering Mechanics, ASCE*, **133**(6), 656–664.

Chang C C and Xiao X H (2010), 'Three-dimensional structural translation and rotation measurement using monocular videogrammetry', *Journal of Engineering Mechanics, ASCE*, **136**(7), 840–848.

Chung H, Liang J, Kushiyama S and Shinozuka M (2004), 'Digital image processing for non-linear system identification', *International Journal of Non-linear Mechanics*, **39**(5), 691–707.

Correlated Solutions Inc. (2012), *Vic-3D 2010*, http://www.correlatedsolutions.com / index.php/home (Accessed 31 October 2012).

DCS Inc. (2012), *iWitness*, http://www.iwitnessphoto.com/index.html (Accessed 31 October 2012).

Deutscher J, Isard M and MacCormick J (2002), 'Automatic camera calibration from a single Manhattan image', *Proceedings of ECCV*, Compenhagen, 175–188.

Doebling S W, Farrar C R, Prime M B and Shevitz D W (1996), 'Damage identification and health monitoring of structural and mechanical systems from changes in their vibration characteristics: a literature review', *Research Report LA-13070-MS*, ESA-EA Los Alamos National Laboratory, Los Alamos, NM, USA.

Eos System Inc. (2012), *PhotoModeler*, http://www.photomodeler.com/index.htm (Accessed 31 October 2012).

Fraser C S and Riedel B (2000), 'Monitoring the thermal deformation of steel beams via vision metrology', *ISPRS Journal of Photogrammetry & Remote Sensing*, **55**(4), 268–276.

Fu G and Moosa A G (2002), 'An optical approach to structural displacement measurement and its application', *Journal of Engineering Mechanics, ASCE*, **128**(5), 511–520.

Georgescu B and Meer P (2002), 'Balanced recovery of 3D structure and camera motion from uncalibrated image sequences', *Proceedings of ECCV*, Compenhagen, 294–308.

Hartley R and Zisserman A (2003), *Multiple View Geometry in Computer Vision*, 2nd Edn, Cambridge University Press, UK.

Hudson D E (1979), 'Reading and interpreting strong motion accelerograms', *EERI Engineering Monographs on Earthquake Criteria, Structural Design, and Strong Motion Records*, Vol. **1**, Earthquake Engineering Research Institute, Berkeley, Calif.

Jain R, Kasturi R and Schunck B G (1995), *Machine Vision*, McGraw-Hill Co. Inc.

Jáuregui D V, White K R, Woodward C B and Leitch K R (2003), 'Non-contact photogrammetric measurement of vertical bridge deflection', *Journal of Bridge Engineering, ASCE*, **8**(4), 212–222.

Jeon H, Bang Y and Myung H (2011), 'A paired visual serving system for 6-DOF displacement measurement of structures', *Smart Materials and Structures,* **4**(20), 1–16.

Jiang R, Jáuregui D V and White K R (2008), 'Close range photogrammetry applications in bridge measurement: literature review', *Measurement*, **41**, 823–834.

Kim N S and Cho N S (2004), 'Estimating deflection of a simple beam model using fiber optic Bragg-Grating sensors', *Experimental Mechanics*, **44**, 433–439.

Kim S W and Kim N S (2011), 'Multi-point displacement response measurement of civil infrastructures using digital image processing', *Procedia Engineering*, **14**, 195–203.

Konecny G (1985), 'The international society for photogrammetry and remote sensing – 75 years old, or 75 years young', *Photogrammetric Engineering and Remote Sensing*, **51**(7), 919–933.

Kwon Y H (1998), *DLT Method*. Available from: http://www.kwon3d.com/theory/dlt/dlt.html (Accessed 1 January 2012).

Lee J J, Fukuda Y, Shinozuka M, Cho S and Yun C B (2007), 'Development and application of a vision-based displacement measurement system for structural health monitoring of civil structures', *Smart Structures and Systems* **3**(3), 373–384.

Li J C and Yuan B Z (1988), 'Using vision technique for bridge deformation detection', *Proceedings of the International Conference on Acoustic, Speech and Signal Processing*, New York, 912–915.

Luhmann, T, Robson S, Kyle S and Harley I (2007), *Close Range Photogrammetry: Principles, Techniques and Applications,* Whittles Publishing, Caithness, Scotland, UK.

Mikhail E M, Bethel J S and McGlone J C (2001), *Introduction to Modern Photogrammetry*, John Wiley & Sons Inc, New York.

Nassif H H, Gindy M and Davis J (2005), 'Comparison of laser Doppler vibrometer with contact sensors for monitoring bridge deflection and vibration', *NDT&E Int*, **38**, 213–218.

Niederöst M and Maas H G (1997), 'Automatic deformation measurement with a digital still video camera', *Optical 3-D Measurement Techniques IV*, Zurich, Wichmann Verlag, Karlsruhe, 266–271.

Ohdake T and Chikatsu H (2004), 'Development of image based integrated measurement system and performance evaluation for close-range photogrammetry', *International Archives of Photogrammetry and Remote Sensing*, Vol. **XXXV**, Part 5, 296–301.

Olaszek P (1999), 'Investigation of the dynamic characteristic of bridge structures using a computer vision method', *Measurement*, **25**, 227–236.

Ozbek, M, Rixen D J, Erne O and Sanow G (2010), 'Feasibility of monitoring large wind turbines using photogrammetry', *Energy*, **35**, 4802–4811.

Patsias S and Staszewski W J (2002), 'Damage detection using optical measurements and wavelets', *Structural Health Monitoring*, **1**(1), 7–22.

Photometrix (2012), *Australis*, http://www.photometrix.com.au/products.html (Accessed 31 October 2012).

Poudel U P, Fu G and Ye J (2005), 'Structural damage detection using digital video imaging technique and wavelet transformation', *Journal of Sound & Vibration,* **286**(4–5), 869–895.

Riveiro B, Jauregui D V, Arias P, Armesto J and Jiang R (2012), 'An innovative method for remote measurement of minimum vertical underclearance in routine bridge inspection.' *Automation in Construction*, **25**, 34–40.

Sohn H, Farrar C R, Hemez F M, Shunk D D, Stinemates D W, Nadler B R and Czarnecki J J (2004), 'A review of structural health monitoring literature: 1996–2001', *Research Report LA-13976-MS*, ESA-EA Los Alamos National Laboratory, Los Alamos, NM, USA.

Take W A, White D J, Bowers K H and Moss N A (2005), 'Remote real-time monitoring of tunnelling-induced settlement using image analysis', *Proceedings of the 5th International Symposium TC28 on Geotechnical Aspects of Underground Construction in Soft Ground*, Amsterdam, the Netherlands, 15–17 June 2005, edited by E. A. Kwast, K. J. Bakker, W. Broere, and A. Bezuijen, Taylor & Francis 2006.

Tian T Y, Tomasi C and Heeger D J (1996), 'Comparison of approaches to ego motion computation', *Proceedings of Computer Vision and Pattern Recognition (CVPR '96)*, IEEE, 315–320.

Whiteman T, Lichti D D and Chandler I (2002), 'Measurement of deflections in concrete beams by close-range digital photogrammetry', *Proceedings of the Joint International Symposium on Geospatial Theory, Processing and Applications,* Ottawa, Canada.

Xu L, Guo J J and Jiang J J (2002), 'Time-frequency analysis of a suspension bridge based on GPS', *Journal of Sound & Vibration*, **254**(1), 105–116.

Yoshida J, Abe M, Kumano S and Fujino Y (2003), 'Construction of a measurement system for the dynamic behaviors of membrane by using image processing', *Structural Membrane 2003 – International Conference on Textile Composites and Inflatable Structures,* Barcelona, Spain.

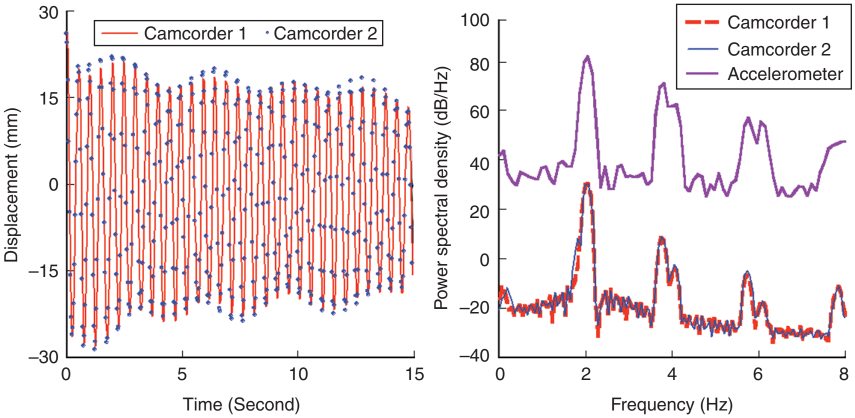

(a) Displacement of the cable segment

(b) Comparison of cable frequencies

Plate XI (Chapter 14) Displacement time histories of the cable segment and the cable's natural frequencies.

15

Robotic sensing for assessing and monitoring civil infrastructures

H. MYUNG, H. JEON and Y-S. BANG, Korea Advanced Institute
of Science and Technology (KAIST), Republic of Korea and
Y. WANG, Georgia Institute of Technology, USA

DOI: 10.1533/9780857099136.410

Abstract: This chapter discusses robotic sensing technologies for assessing and monitoring civil infrastructures. The chapter first reviews the use of robotic sensing techniques to monitor civil structures. Vision-based robotic sensing techniques that are used for structural crack detection and structural displacement monitoring are discussed in detail. Remote robotic sensing techniques for structural health monitoring (SHM) are discussed, including wireless sensing for SHM, wireless power transmission, and wireless sensor nodes based on microwave and lasers. Finally, vibration-based mobile wireless sensors including climbing robots for structural damage detection are overviewed. A case study for mobile sensor networks using climbing robots is introduced.

Key words: robotics, structured light (SL), remote sensing, mobile wireless sensors.

15.1 Introduction

For several decades, various sensors and sensing systems have been developed to monitor the safety condition of structures. This chapter describes structural health monitoring (SHM) or inspection systems using robotic technologies. The field of robotics had been widely explored long before SHM technologies attracted significant attention. However, only in recent years have robotic prototypes developed to a level of maturity that makes them suitable for realistic application in SHM. This survey will include robotic systems equipped with various sensing technologies, such as optical sensors, laser sensors, mobile wireless sensors, etc. Details of some example systems are also provided in subsequent sections.

Thus far, robotic development for SHM has concentrated primarily on the inspection of structures rather than the continuous monitoring of structures. These robots have unique locomotion systems to provide mobility in the structures to be inspected, and are equipped with various sensors, such

© 2014 Woodhead Publishing Limited

as vision cameras, lasers, radio frequency (RF), optical fibers, etc., to monitor and assess structural condition. Robots specialized for SHM application have only recently been developed, but their use is expected to largely increase in the near future.

Based on the literature, the locomotion mechanisms of SHM/inspection robots can be classified as follows:

1. *Wheeled robots moving on horizontal surfaces*: these include most common types of robots that use wheels for locomotion on relatively flat horizontal surfaces or guided rails. For example, Yu *et al.* (2007) proposed a mobile robot system for inspecting and measuring cracks in concrete structures. The safety of a subway inner wall is evaluated in this study. The mobile robot system was controlled to maintain a constant distance from walls while acquiring image data with a camera. There have not been many examples of wheeled locomotion, since this mechanism is not adequate for inspecting various structural elements other than the planar ground.
2. *Wall-climbing/crawling robots*: certain climbing and crawling mechanisms, some of which are bio-mimetic, have been developed for movement on vertical walls or uneven surfaces. Examples include gecko-like locomotion that can climb on smooth surfaces using directional adhesion, a vacuum-creating suction adhesion, and a climbing mechanism using adhesive materials. An article by M. Siegel deals with the status and prospects of remote and automated inspection methods for aircraft inspection (Siegel, 1997). Most of the methods use climbing and crawling devices. A climbing service robot for duct inspection and maintenance application in a nuclear reactor is another good example (Luk *et al.,* 2001). Recently, a miniature crawler robot for structural inspection was introduced (Sheng *et al.,* 2008). Their study dealt with the navigation of a miniature crawler robot performing an aircraft rivet inspection task. The authors used a vision-based localization algorithm and developed an efficient coverage path planning method. Teleoperated climbing inspection robots are often used, since they do not need complex navigation algorithms (Balaguer *et al.,* 2000). Another type of robot for aerospace structures also used crawlers (Bar-Cohen and Backes, 2000). In addition, a bio-inspired miniature wall-climbing caterpillar robot has been developed by Zhang *et al.* (2010). A portable climbing robot used two legs that could adhere to a surface by suction cups (Bahr and Wu, 1994). As well as designing a wall-climbing robot, a control architecture based on fuzzy logic has been developed (Xiao, 2002; Xiao *et al.*, 2004).
3. *Snake-like robots*: this type of robot is suitable for inspecting confined spaces and rough terrains that are hard to navigate, such as air ducts, pipes, and tubes too small for humans to enter. For example, Tokyo

Tech's Hirose-Fukushima Lab has developed some of the world's most amazing mechanical snakes (Mori and Hirose, 2006; Guizzo, 2010).

4. *Modular robots*: by cascading multiple small modular robots, it is possible to build a robot capable of going through rough terrain and uneven surfaces. Self-reconfiguring modular robots have been developed, whereby multiple modules can automatically morph the configuration in arbitrary ways using small hooks for reconfigurable connection (Murata and Kurokawa, 2007). Recently, mobile sensor nodes have been developed by connecting two magnet-wheeled modules by a flexible beam (Lee *et al.*, 2009; Zhu *et al.*, 2010). This mobile sensing node can also attach an accelerometer to, or detach it from, the structural surface. Another example is a pair of wall-climbing robots with magnetic wheels (Fischer *et al.*, 2007).
5. *Aerial vehicles*: robots in the form of quadrotors, helicopters, and airships can freely fly through and inspect structures. Quadrotors and miniature helicopters have been extensively tested. Most of the current prototypes have limited payload capacity and thus cannot carry many sensors (Pratt *et al.*, 2008).
6. *Underwater vehicles*: submersible robots have been developed to inspect underwater structures. Several prototypes have been designed for inspecting oil storage tanks (Abdulla *et al.,* 2010) and pipelines (Conte *et al.,* 1996; Bodenmann *et al.,* 2009).

Using a robot platform with an appropriate locomotion mechanism, different sensors can be incorporated for structural inspection purposes. Examples of these sensors, which can also be used in combination, are listed as follows:

1. *Cameras*: a camera is a useful sensor that can capture a lot of information, yet at the same time camera data are sensitive to illumination conditions (Lee and Shinozuka, 2006; Sheng *et al.,* 2006). In order to achieve proper operation, it is important to calibrate the camera before use and compensate for noise and variations in illumination.
2. *Optical scanners*: the three-dimensional shape or motion of structures can be remotely reconstructed using optical scanners, although the cost of such scanners is usually high. Some low-cost solutions have recently been proposed and are still under development (Sergiyenko *et al.*, 2009).
3. *Fiber optics*: fiber Bragg grating (FBG) sensors have been used for SHM. Some researchers have tried to use a PZT (lead zirconate titanate) transducer as a transmitter and an FBG as a receiver to detect impact and/or measure strain (Wild and Hinckley, 2007).
4. *Combinations*: a combination of different sensors carried by robots can provide more complete information about the structure. For example, a

modular paired structured light (SL) system, which consists of lasers and a camera, was proposed to measure the 6-degrees of freedom (DOF) motion of large structures (Jeon *et al.*, 2011a; Myung *et al.*, 2011).

Besides using robots as sensor carriers, some research has also exploited robots for wirelessly delivering electrical power to SHM sensor nodes in close proximity. Inductive power transmission with RF signals (Huston *et al.,* 2001), or optical delivery using power lasers can be used for this purpose (Park *et al.,* 2010; Bang *et al.,* 2011).

Robotic technologies have been utilized for inspecting/monitoring a large variety of structures. The following list provides a brief summary of different target structures for SHM or inspection robots.

1. *Aircraft*: since the aircraft surfaces to be inspected are not planar, several crawling or wall-climbing robots have been developed for aircraft inspection (Bar-Cohen and Backes, 2000). The researchers developed a multifunction automated crawling system (MACS) that offers an open architecture robotic platform for non-destructive evaluation (NDE) boards and sensors. MACS was designed to perform complex scanning tasks, taking advantage of its ability to easily turn or move forward and backward while attaching to a curved surface through suction cups.
2. *Bridges and bridge cables*: some robotic systems have been developed for bridge and bridge cable inspection. For steel bridge inspection, magnet-based locomotion has been explored (Mazumdar and Asada, 2010; Romero, 2010; Zhu, 2010). For cable inspection, wheel-based (Xu *et al.*, 2008) or reconfigurable robots (Yuan *et al.*, 2010) have been developed.
3. *Power lines*: power transmission lines have been inspected using cable climbing robots (Nayyerloo *et al.*, 2009). The Hydro-Québec Research Institute in Canada unveiled their LineScout robot, which climbed on high-voltage power lines for inspection (Bouchard, 2010). Equipped with cameras, a thermo-infrared imager, and a smart navigation system, the LineScout robot can inspect line condition and determine locations in need of attention. In addition, a Tokyo-based company HiBot is working with the Kansai Electric Power Co. in Japan to deploy a new robot prototype in the field. Named Expliner, the robot can inspect several power cables simultaneously (Corley, 2009).
4. *Pipelines, ducts, tubes, and sewages*: narrow spaces that are not easily accessible for human beings can be inspected by a special robot with crawling mechanism. Robots for sewage inspection (Kirchner and Hertzberg, 1997; Adria *et al.,* 2004), pipe cleaning and inspection (Li *et al.,* 2009), and tube inspection (Kostin *et al.*, 1999) have been developed.

15.2 Vision-based robotic sensing for structural health monitoring (SHM)

Due to the great advances in vision-based information processing technology, vision-based sensors or systems have been widely studied. Vision-based sensing is a highly important technique, particularly in robotics, and it is used for obstacle avoidance, mapping, and localization (Siegwart and Nourbakhsh, 2004). Also, in the field of civil engineering, much attention has been given to vision-based SHM, such as vision-based crack detection or vision-based structural displacement monitoring. In the following, various vision-based SHM systems and methods are introduced and their advantages and limitations are discussed.

15.2.1 Vision-based structural crack detection

Currently, to monitor structural conditions, inspectors periodically check visually for cracks on the structure, and the crack location is manually measured (Lim *et al.*, 2011). Afterwards, structural safety is evaluated based on the number of cracks, their lengths and widths (Oh *et al.*, 2009). As a result, the accuracy of the inspection may be lacking, and highly dependent on environmental conditions during the inspection and knowledge of the inspectors. Several research efforts related to a vision-based automated crack detection system using a mobile robot or a specially designed car (Tung *et al.*, 2002; Yu *et al.*, 2007; Oh *et al.*, 2009; Lim *et al.*, 2011) have been undertaken to address these problems. In most vision-based crack detection systems, a camera installed on the mobile robot or car captures images of the structure. Then various image processing techniques such as feature extraction and object recognition are used to detect cracks from the raw image. Since the size of the image is known from the geometry between the camera and the imaged object, the width and length of the crack can be calculated. Also, the location of the crack can be estimated using a localization system on the mobile robot.

One example of vision-based crack detection systems applied to bridges is shown in Fig. 15.1. As shown in the figure, a specially designed car with a multi-linkage manipulator is used to monitor the condition of the bridge deck. By moving the multi-linkage manipulator, the entire structure can be monitored from a camera, which is mounted at the end of the manipulator. Although this system can detect cracks reliably, it is problematic when there is traffic, due to its large mass and low speed, or when the shape of the bridge is complex. Therefore, vision-based crack inspection systems with relatively small mobile robots have also been studied (Yu *et al.*, 2007; Lim *et al.*, 2011).

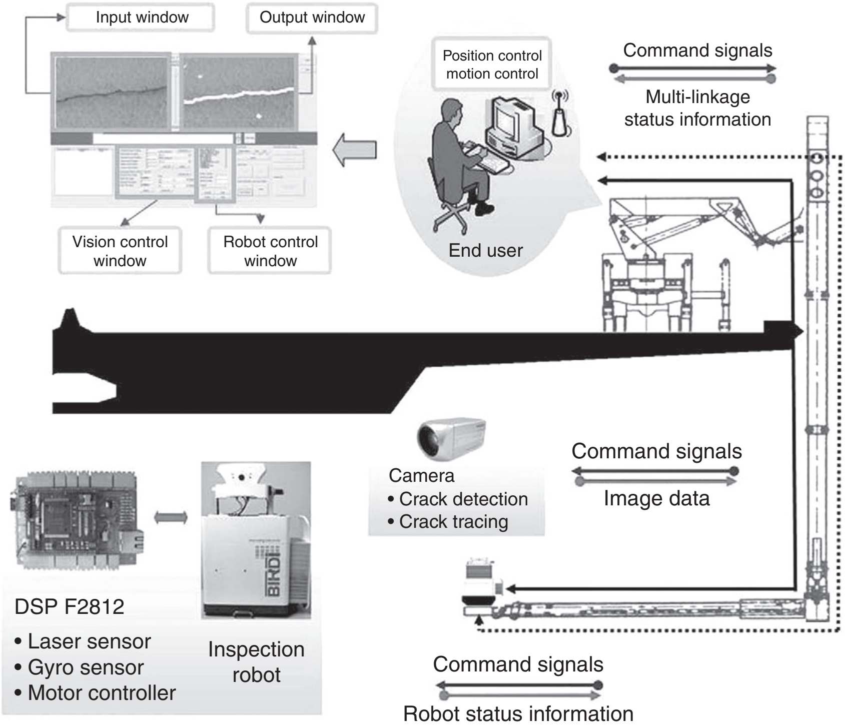
Input window
Output window
Position control motion control
Command signals
Multi-linkage status information
Vision control window
Robot control window
End user
Command signals
Image data
Camera
• Crack detection
• Crack tracing
DSP F2812
• Laser sensor
• Gyro sensor
• Motor controller
Inspection robot
BIRDI
Command signals
Robot status information

15.1 Schematic diagram of Bridge Inspection Robot Development Interface (BIRDI) (Oh *et al.*, 2009). DSP, Digital Signal Processor. (*Source*: Courtesy of Oh and Elsevier.)

15.2.2 Vision-based structural displacement monitoring

Since most civil structures are subject to external loads such as traffic, earthquakes, and wind loads, it is important to monitor the structural behavior, especially the displacement, continuously. A number of studies have been performed on structural displacement monitoring methods or systems, and various sensors have been developed. Among the displacement measurement sensors or systems, vision-based displacement monitoring systems have gained great attention due to their low cost. Vision-based displacement monitoring systems most often use a high quality camera and artificial targets, or an SL, or laser range finder.

Since the 1960s, researchers have tried to use vision systems to directly measure structural displacement. Some approaches include the use of infrared lamp tracking systems (Marecos *et al.*, 1969), laser beam pointing tracking systems (Isyumov *et al.*, 1984), and transputer-based feature tracking systems (Stephen *et al.*, 1993). Laser beams have been used at the Foyle Bridge (Leitch *et al.*, 1989), where their images on target screens were tracked by a fixed camera. More recent examples have used specially manufactured optical devices to concurrently measure reference and target points using one image capturing device (Olaszek, 1999) or a high resolution camera system (Wahbeh *et al.*, 2003), which required an expensive special purpose camera. Other researchers used a camera system with 30 × optical zooming capability installed far from the observation points at which artificial landmarks using light-emitting diodes (LEDs) are attached (Lee and Shinozuka, 2006). The problem with this approach is that it requires fixed observation points and precisely located landmarks. One current SHM system with vision sensors is installed on the Guangzhou New TV Tower, China, with a height of 610 m (Ni and Wong, 2009; Ni, 2009a). This system uses a high resolution camera with a telescopic lens having optical zooming capability observing markers at the target position. This system has some advantages, as it can directly measure displacement and its cost is relatively low. However, it can only measure 2D translational displacement and it is easily affected by external environmental conditions such as weather or illumination changes, due to the long distance between the target and the camera. For example, it cannot measure displacement in case of fog or obstructions in the line of sight (LoS). Another paper proposed a Kalman filtering scheme to fuse accelerometer signals with vision data for extracting 3D translation and rotation of a cubic target (Ni, 2009b). Others utilized a high resolution camera with a telescopic lens observing a cubic marker installed at the target position, which has the same limitations as before (Ni and Wong, 2009; Ni, 2009a).

To mitigate those limitations, a novel vision-based displacement monitoring method has been introduced (Myung *et al.,* 2011; Jeon *et al.,* 2011a; Park *et al.*, 2011b). To measure the three-dimensional translational and rotational displacements, and to make it robust to external environmental changes, Myung *et al.* developed a paired SL system. In a conventional SL approach, a simple pattern of beams is projected onto the target, and then depth and surface geometry are calculated from the image captured by a camera, as shown in Fig. 15.2 (Siegwart and Nourbakhsh, 2004). To precisely estimate long distance observations, a visually servoed paired (ViSP) SL system has been recently designed, as shown in Fig. 15.3 (Jeon *et al.*, 2011a, b).The system is composed of two sides facing each other, each with a camera, one or two lasers, a screen, and a manipulator. Each laser projects its beams to the distant screen on the opposite side, and the camera near the screen captures the image of the screen. Due to the short distance between the screen and the camera, typically less than 20 cm, it is highly robust to environmental changes such as weather or illumination changes. A 2-DOF manipulator, which holds the lasers, controls the positions of the projected laser beams on the opposite side to be on the screen before it gets off the screen boundary.

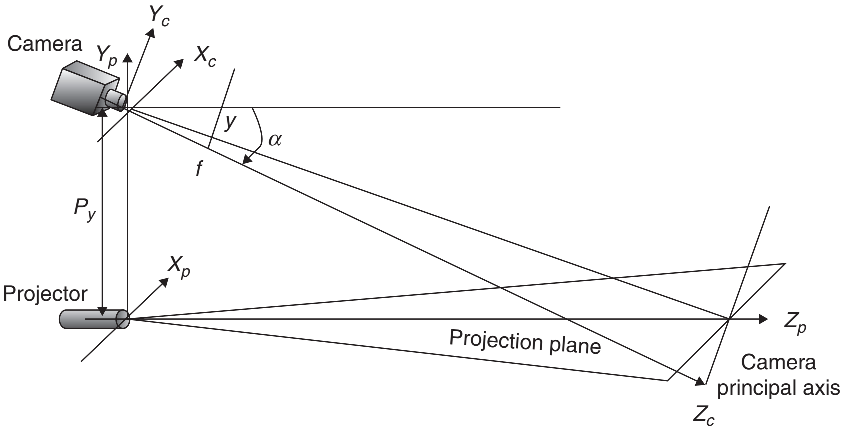
Camera
Y_c
Y_p
X_c
y
α
f
P_y
X_p
Projector
Projection plane
Z_p
Camera principal axis
Z_c

15.2 Configuration of conventional SL.

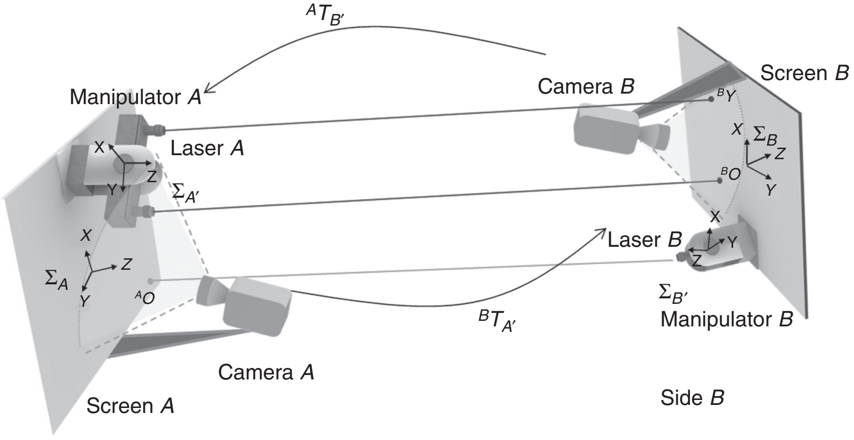
${}^{A}T_{B'}$
Manipulator A
Laser A
$\Sigma_{A'}$
Σ_A
${}^{A}O$
Camera A
Screen A
Side A
Camera B
Screen B
${}^{B}Y$
Σ_B
${}^{B}O$
Laser B
$\Sigma_{B'}$
Manipulator B
${}^{B}T_{A'}$
Side B
X
Y
Z
${}^{A}T_{B'}\ {}^{B}T_{A'}$: Transformation matrix

15.3 Schematic diagram of the visually servoed paired structured light system (ViSP) (Jeon *et al.*, 2011a). (*Source*: Courtesy of IOP Publication.)

In this system, the relative 6-DOF displacement between the two sides can be calculated by using the positions of the three projected laser beams and the rotated angles of the manipulators.

The entire process of the system operation is shown in Fig. 15.4. As shown in the figure, the camera on each side captures the image of the screen. Then, lens distortion is corrected. The boundary and the homography of the image are calculated from the undistorted image. After finding the boundary, the positions of the laser beams can be calculated from the known boundary size. The rotation angles of the 2-DOF manipulator

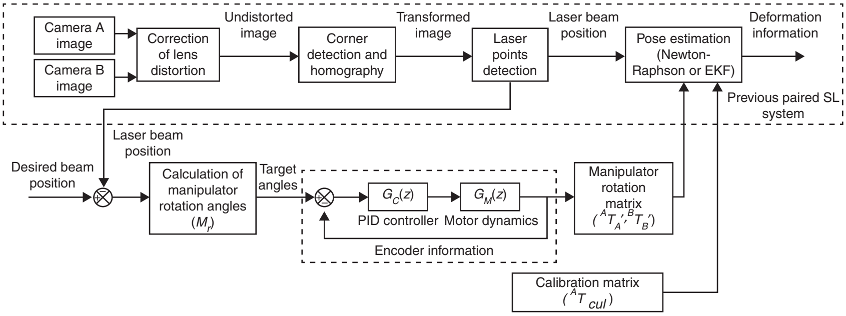
Camera A image
Camera B image
Correction of lens distortion
Undistorted image
Corner detection and homography
Transformed image
Laser points detection
Laser beam position
Pose estimation (Newton-Raphson or EKF)
Deformation information
Previous paired SL system
Laser beam position
Desired beam position
Calculation of manipulator rotation angles (M_r)
Target angles
$G_C(z)$
$G_M(z)$
PID controller
Motor dynamics
Encoder information
Manipulator rotation matrix ($^AT_{A'}$, $^BT_{B'}$)
Calibration matrix ($^AT_{cul}$)

15.4 Process of the visually servoed paired structured light system (ViSP) (Jeon *et al.*, 2011a). (*Source*: Courtesy of IOP Publication.)

are calculated from the current and desired positions of the laser beams. Afterwards, the manipulator rotation matrix is formed from encoder information taken from the motors for the proportional-integral-derivative (PID) controller. In this way, the 6-DOF displacement between two sides can be calculated by using the positions of the three laser beams and the manipulator rotation matrices.

The kinematics of the 6-DOF displacement defines the geometric relationship between the observed data $m = [{}^AO, {}^BO, {}^AY]^T$, rotated angles of the manipulators, and estimated displacement $p = [x, y, z, \theta, \varphi, \psi]^T$. Here ${}^AO$ is the projected laser beam on the screen A and ${}^BO$ and ${}^BY$ are the projected laser beams on the screen B. The observed data can be calculated as follows:

$$\begin{aligned} {}^AO &= {}^AT_B \cdot {}^BT_{B'} \begin{bmatrix} 0 & L & Z_{AB} & 1 \end{bmatrix}^T \\ {}^BO &= {}^BT_A \cdot {}^AT_{A'} \begin{bmatrix} 0 & -L & Z_{AB} & 1 \end{bmatrix}^T \\ {}^BY &= {}^BT_A \cdot {}^AT_{A'} \begin{bmatrix} 0 & L & Z_{AB} & 1 \end{bmatrix}^T \end{aligned} \qquad [15.1]$$

where, ${}^AT_B$ and ${}^BT_A$ are transformation matrices that transform the screen coordinates A and B, ${}^AT_A$, and ${}^BT_B$, are manipulator rotation matrices on sides A and B, respectively, L is the offset of a laser point from the center of a screen in the Y direction, and Z_{AB} is the distance from screen A to screen B. The ${}^AT_A$ can be represented as:

$$R_x(-\theta_{Aene}) \bullet R_y(-\psi_{Aene})$$

where θ_{Aene} and ψ_{Aene} are the rotated angles of the manipulator on side A about the X and Z axes, respectively. Since the laser beam is projected on the 2-DOF screen, the z component of the projected laser beams should be zero. By putting these three constraints together, the kinematic equation M_{vs} containing 6-DOF displacement p can be derived as follows (Jeon *et al.,* 2011a):

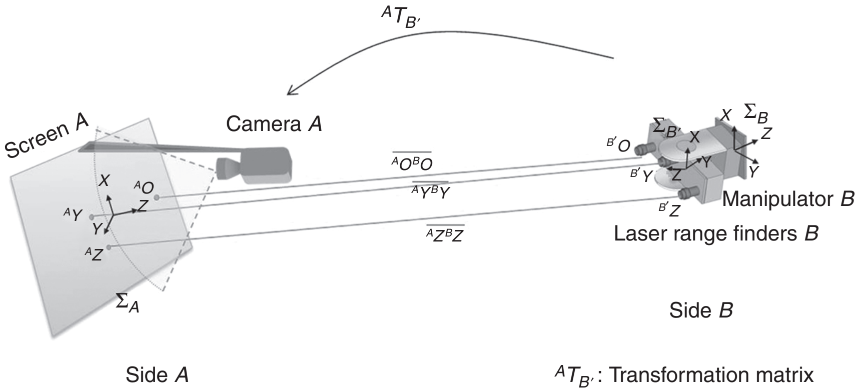
$^AT_{B'}$
Screen A
Camera A
$\overline{^AO^BO}$
$\overline{^AY^BY}$
$\overline{^AZ^BZ}$
X
^AO
^AY
Y
Z
^AZ
Σ_A
$^{B'}O$
$^{B'}Y$
$^{B'}Z$
$\Sigma_{B'}$
X
Y
Z
Σ_B
X
Z
Y
Manipulator B
Laser range finders B
Side B
Side A
$^AT_{B'}$: Transformation matrix

15.5 Schematic diagram of the 6-DOF displacement estimation method using three laser range finders.

$$M_{vs} = \begin{bmatrix} {}^AO_x & {}^AO_y & {}^BO_x & {}^BO_y & {}^BY_x & {}^BY_y \end{bmatrix}^T \qquad [15.2]$$

The 6-DOF displacement p can be estimated by using the Newton-Raphson or EKF (extended Kalman filter) method (Moon and Stirling, 2000; Welch and Bishop, 2006; Jeon *et al.*, 2011a).

Another approach to measuring the structural displacement in 6-DOF is to use 1-D laser range finders, as shown in Fig. 15.5. As the figure shows, at least three 1-D laser range finders project parallel beams onto the screen from the opposite side, and a camera near the screen captures the image of the screen. Unlike the previous SL-based system, not only the positions of the projected laser beams but also the distance measured from each laser range finder are used to calculate a relative 6-DOF displacement between the two sides. Since the laser range finders are installed only on one side and a single camera captures the image of the screen, the entire system is simpler than the previous system. However, the cost of the entire system is higher than SL systems, since the laser range finder with the data transmission function is more than five times more expensive on average than a 1-D laser projector.

15.3 Remote robotic sensing for SHM

15.3.1 Introduction to wireless sensing and wireless power transmission (WPT)

The RF or laser-based wireless sensing system is often used for remote monitoring of structural conditions. Wireless sensing nodes (WSN) can form a sensor network that assesses the condition of a structure. Eliminating the expensive cable installation, wireless sensing is considered to be a valuable method for the SHM of large structures. Nevertheless, large-scale field application of wireless sensing still faces many challenges. Even though designed to consume minimum energy, most WSNs operate with batteries that have limited life span. Therefore, the batteries should be monitored, replaced, or recharged regularly, requiring a significant amount of cost and labor for maintenance. To overcome these problems, WPT technology has been investigated to transmit energy to a remote receiver node for SHM. Power transmission is mainly achieved by either microwave or laser.

15.3.2 Wireless structural health monitoring

Since SHM of large civil infrastructures has gained great attention from recent collapses of bridges and buildings, wireless sensing technology is considered an important future sensing paradigm. Wireless sensors can constitute a network to share and gather measured data and to facilitate information aggregation for maintenance of a large structure.

Performance of wireless sensors should be considered according to the purpose of SHM. Lynch (2005) introduced a wireless active sensing unit for SHM. As shown in Fig. 15.6, the wireless sensor system sends the measured data to the host after converting an analog sensor output to digital data via analog to digital converter (ADC). Some sensors, such as PZT, require an additional subsystem to excite the sensor. An impedance-based wireless sensor node was used to obtain the response of the PZT sensor (Mascarenas *et al.,* 2007). A later version of the system was incorporated into a mobile robot system to expand the monitoring area using the robot's mobility (Taylor *et al.,* 2009). These wireless sensors used RF communication to send the response data to a base system. On the other hand, Park

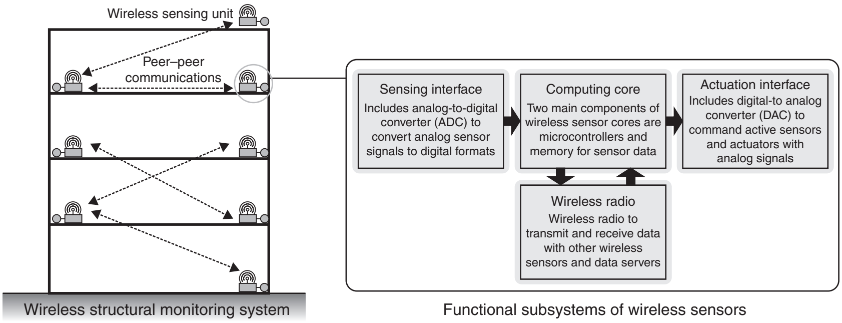
Wireless sensing unit
Peer–peer communications
Sensing interface
Includes analog-to-digital converter (ADC) to convert analog sensor signals to digital formats
Computing core
Two main components of wireless sensor cores are microcontrollers and memory for sensor data
Actuation interface
Includes digital-to analog converter (DAC) to command active sensors and actuators with analog signals
Wireless radio
Wireless radio to transmit and receive data with other wireless sensors and data servers

Wireless structural monitoring system

Functional subsystems of wireless sensors

15.6 Functional elements of a wireless sensor for structural monitoring applications (Lynch and Loh, 2006). (*Source*: Courtesy of Lynch.)

et al.(2011a) developed an optics-based wireless impedance measurement system, which transmits the response of the sensor through laser in continuous wave form, reducing computational load due to encoding sensor measurements.

15.3.3 Microwave-based WPT

Researchers have tried to develop a WPT system using microwave, because it has distinct advantages for distributing power through atmosphere and space, like broadcasting, toward multiple nodes. Several articles discuss the history of WPT using microwave (William, 1996; Matsumoto, 2002). Microwave-based WPT has been widely applied to operate many sensors installed around a site for SHM. Mascarenas *et al.*(2007) introduced a WPT system using 10 GHz X-band signals to supply power to the impedance sensing node. The performance of WPT at long distance was demonstrated with high power levels (Choi *et al.,* 2004; Kim *et al.,* 2006). However, doing so requires a large transmitter and receiver system. In the case of using WPT for SHM, the system size should be small and easy to install on a structure.

Autonomous robots can be used to access deployed sensors, transmit power, and collect the sensor information from a large WPT system. Todd *et al.* describes a sensor network paradigm using unmanned aerial vehicles (UAV) flown remotely or autonomously by a global positioning system (GPS)-based autopilot with RF communication system (Todd *et al.,* 2007). The vehicle has onboard processing and storage systems to interrogate sensors, and gather and store data. The mobile robot system introduced above is also used as a WPT system for SHM that transmits energy to sensor nodes (Taylor *et al.,* 2009). The WPT system as installed on the mobile robot communicates over 5.8 GHz to avoid interference with communication over the commonly used 2.4~2.5 GHz frequency. Experiments on sensing the acceleration of a bridge girder have been performed using WSNs operated by the WPT system. After approaching the wireless sensor node, the mobile robot begins to transmit power via the transmitter antenna. Received energy from the rectenna (receiver antenna) array installed on the mobile robot is stored in a capacitor for 40 s and used to operate a piezoelectric sensor for several seconds. Measured information is sent back to the mobile robot via RF.

In general, even though the transmitter antenna on the mobile robot is manually controlled to face the rectenna, the microwave-based WPT system needs careful design of the antennas and placement of the receiver sensors along with distributed beam forming of the microwave signal to increase efficiency.

15.3.4 Laser-based WPT

Compared to microwave, laser-based WPT has some advantages, such as reduced system size, collimated propagation, and no radio-frequency interference. The size of a given WPT system varies with the beam wavelength and its propagation characteristics. Laser wavelengths are significantly shorter than microwave, and the laser beam stays narrow over long distances. This means that the laser-based system can be more compact in size and lower in cost. In addition, interference with existing radio communication signals such as WiFi and cellular networks is avoided with the laser-based system. However, a significant limitation in laser-based WPT is that the laser and the receiver node should be at LoS to transmit power. In other words, the laser has to be directly aimed at the position of the receiver node.

With the assumption that laser can be pointed to the desired position in advance, Park *et al.* (2010) developed a wireless sensing system for SHM that can provide a laser-based guided waveform to excite a PZT transducer. At the receiver node, the guided waveform can be measured with efficiency of 12.87% at up to 5 m distance. To obtain a higher efficiency, Ugur and Herbert (2006) developed a photovoltaic cavity converter system using Nd:YAG radiation for WPT, resulting in about 40% conversion efficiency. Laser flight testing with manual tracking of the laser indoors was demonstrated by Blackwell (2005). Laser-based WPT systems are restricted to motionless environments and manual operation. Although laser targeting can be done by a human operator over a short distance, it is difficult to control precisely. To resolve this problem, the laser targeting needs to be autonomously controlled by a robot system. Bang *et al.* (2011) introduced a mobile robot system that controls the robot's manipulator for laser targeting using an image-based visual servoing (IBVS) technique, as shown in Fig. 15.7. They describe a robot system that can control the robot's manipulator to project a laser to the receiver node position using visual information. The robot system consists of a camera, a laser, a 2-DOF manipulator, and a mobile platform. The camera is used to track positions of the projected laser points and the target object on a structure. Captured images are used to calculate the distance between the camera and the target. Laser targeting is done by controlling the manipulator. The velocity of the manipulator, $\dot{q}$, is related to the velocity of the image feature, $\dot{s}$, by a total Jacobian, J_{tot}, as follows:

$$\dot{s} = J_{\text{tot}}\dot{q} \tag{15.3}$$

The total Jacobian is composed of the image Jacobian, J_{img}, the transformation matrix, ${}^{c}T_{w}$, and the robot Jacobian, ${}^{w}J_{r}$, as follows:

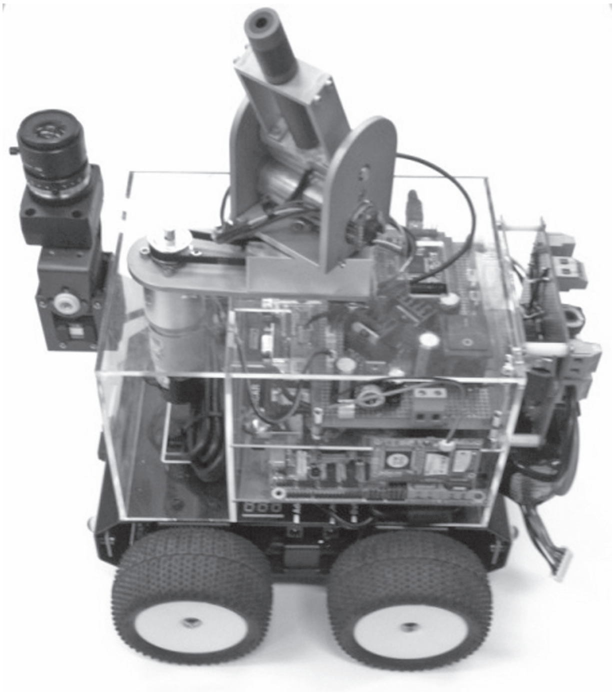

15.7 Prototype of laser targeting mobile robot system.

$$J_{\text{tot}} = J_{\text{img}} \cdot {}^{c}T_{w} \cdot {}^{w}J_{R} \qquad [15.4]$$

The image Jacobian describes the relationship between the gradient of an image feature and the behavior of the corresponding object in a Cartesian space. The transformation matrix transforms the reference frame from the world frame to the camera frame. The robot Jacobian represents the kinematics of the robot's manipulator. By defining an error function, containing the difference in the positions of the laser and the target, the desired velocity of the manipulator can be calculated using the pseudo inverse of the total Jacobian. A proportional control law is used to control the desired angles of the manipulator:

$$\dot{q} = -K_{p}J_{\text{tot}}^{+}e(s) \qquad [15.5]$$

where K_p is the proportional gain of the controller.

Relative position error will be continually reduced as the laser point approaches within the defined boundary around the target position. Figure 15.8 shows the result on a plane where the target is installed on the ceiling and in Fig. 15.9 with the ceiling tilted. Subfigure (a) in each

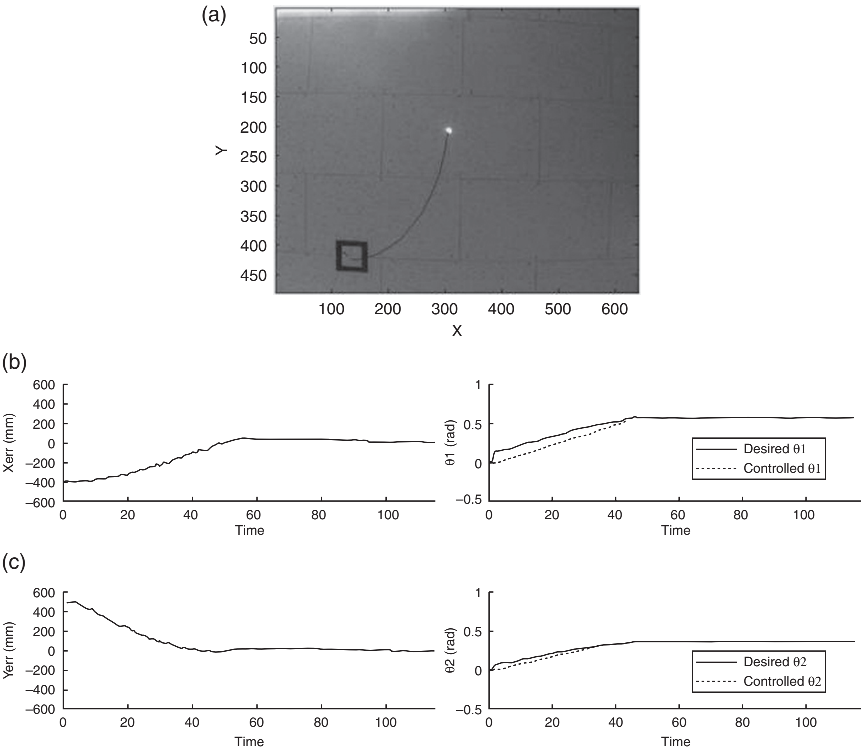

15.8 Laser targeting on the orthogonal ceiling: (a) laser spot trajectory, (b) joint angle (solid: desired angle, dotted: control angle), (c) position error to the target in Cartesian space.

figure shows the trajectory of the laser beam as controlled by the robot. Compared with the orthogonal ceiling, the performance on the tilted ceiling shows a bigger error near the target due to the error of the image Jacobian. However, the visual control law gives feedback information to the manipulator in order to eliminate position errors between the laser point and the target node. The experimental results validate that the proposed system has potential application to the laser-based WPT system.

15.4 Vibration-based mobile wireless sensors

Another recent advance in robotic sensing is to employ miniature robots as wireless sensor carriers that can autonomously navigate on a large structure. These robotic sensor carriers constitute a mobile sensor network. Each mobile sensing node can explore its surroundings and exchange

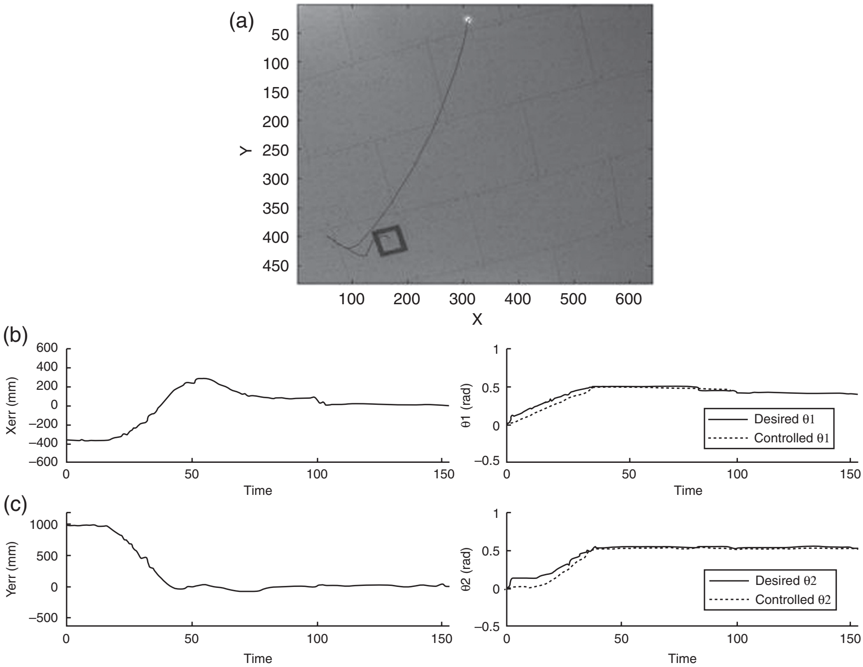

15.9 Laser targeting on the inclined ceiling: (a) laser spot trajectory, (b) joint angle (solid: desired angle, dotted: control angle), (c) position error to the target in Cartesian space.

information with its peers through wireless communication. The mobility of a sensing node has the potential to resolve some of the most critical challenges faced by static wireless sensor networks. For example, in order to provide enough information for updating the finite element model of a large-scale structure, measurement locations need to be as dense as possible. However, the cost of current high-precision wireless accelerometers is still prohibitive for dense deployment in practice. To resolve this difficulty, as illustrated in Fig. 15.10, a mobile sensor network offers flexible architectures. A relatively small number of mobile sensing nodes can provide adaptive and high spatial resolutions, while autonomously navigating through a large structure.

In addition, limited power supply is one of the largest constraints for wireless sensor networks (Churchill *et al.,* 2003; Roundy, 2003; Sodano *et al.,* 2004). This constraint can be alleviated by mobile sensor networks, if the mobile sensing nodes can periodically return to a base station for automatic recharging. Last but not least, for structural damage detection, mobile robots can be incorporated with functionality to excite a

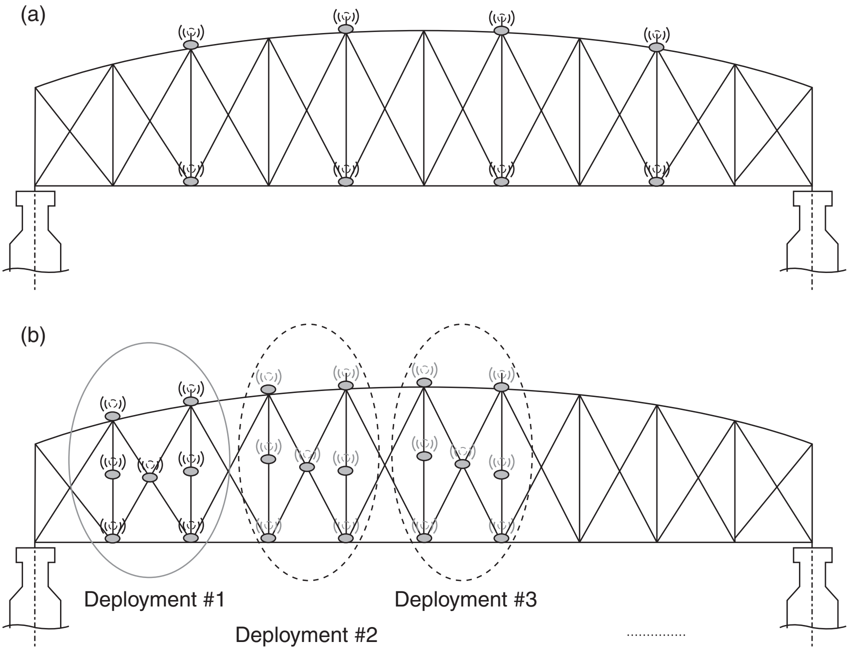

15.10 Comparison between static sensor networks and mobile sensor networks. (a) A static sensor network with fixed deployment scheme and low spatial resolution. (b) A mobile sensor network with flexible deployment scheme and high spatial resolution.

small section of the structure at a time, so that vibration signals can be obtained at a high signal-to-noise ratio. Compared with low-amplitude ambient vibrations that characterize structural global response, vibration signals caused by local excitation can provide more abundant information for component-level structural diagnosis. In the following, Section 15.4.1 provides a brief literature review on previous climbing robots and mobile sensor prototypes for civil structures. Section 15.4.2 showcases the performance of a recently developed magnet-wheeled mobile sensor for SHM.

15.4.1 Literature review on climbing robots and mobile sensors

Recent development in robotics has generated many prototypes that are capable of climbing in 3D environment. For example, the Robug IV prototype has eight legs and weighs 40 kg (Urwin-Wright *et al.,* 2002). It uses pneumatic suction cups for adhesion and transports 5 kg of payload. Another prototype, Roma2, has two legs and also uses vacuum cups for 3D climbing (Balaguer *et al.,* 2005). The Roma2 model has reduced kinematics and lighter weight (25 kg); it moves at a maximum speed of 2.5 cm/s during linear motion. Nevertheless, these robot prototypes are large and clumsy as mobile sensor carriers that need to move, for example, on a truss bridge.

Smaller robot prototypes have also been developed. Latest bio-mimetic research has led to the design of StickyBot, a wall-climbing robot prototype that was named by Time Magazine as one of the 'Best Inventions in 2006' (Kim *et al.,* 2007). The StickyBot mimics gecko movement and can climb on smooth surfaces using directional adhesion. It weighs only 370 g and moves at a maximum speed of 4.0 cm/s. Waalbot, which uses elastomer adhesion, is another recent robot prototype that climbs on walls (Murphy and Sitti, 2007). Although these robot prototypes function well in controlled laboratory experiments, significant development is needed for tetherless operation in a tough outdoor environment. As robotic technologies continue to progress, small, agile, and tetherless 3D climbing robots are expected to become available in the near future.

Besides development in robotics, a number of mobile sensor network platforms have been investigated by researchers in computer science. These mobile sensor nodes are normally carried by wheeled vehicles and move on 2D floors, which therefore cannot fulfill the requirement of climbing on 3D civil structures in the field (Kahn *et al.,* 1999; Dantu *et al.,* 2005; O'Hara *et al.,* 2005). Motivated by the interest in incorporating mobility into traditional sensors, a few robotic prototypes have been developed for SHM and damage detection. For example, a robot able to crawl on a 2D surface was developed for visually inspecting aircraft exteriors; the robot used ultrasonic motors for mobility and suction cups for adherence (Backes *et al.,* 1997). A beam-crawler has been developed for wirelessly powering and interrogating battery-less peak-strain sensors; the crawler moves along the flange of an I-beam by wheels (Huston *et al.,* 2001). In addition, based upon magnetic on-off robotic attachment devices, a magnetic walker has been developed for maneuvering on a 2D surface (Brian *et al.,* 2004). Overall, although individual robots have been developed for structural inspection, mobile sensor networks with dynamic reconfiguration have rarely been explored by researchers.

15.4.2 Case study: development and validation of a mobile sensor network

This subsection describes in detail the development and validation of a prototype mobile sensor network for SHM. The mobile nodes are equipped with wireless accelerometers for high-fidelity vibration measurement with adaptive and dense spatial resolutions. The subsection begins with the mechatronic hardware and software implementation of the mobile sensing nodes. Laboratory validation experiments, including three damage scenarios, for the mobile sensing nodes are then presented. The subsection finally describes the field validation experiments of the mobile sensor nodes on a space frame steel bridge.

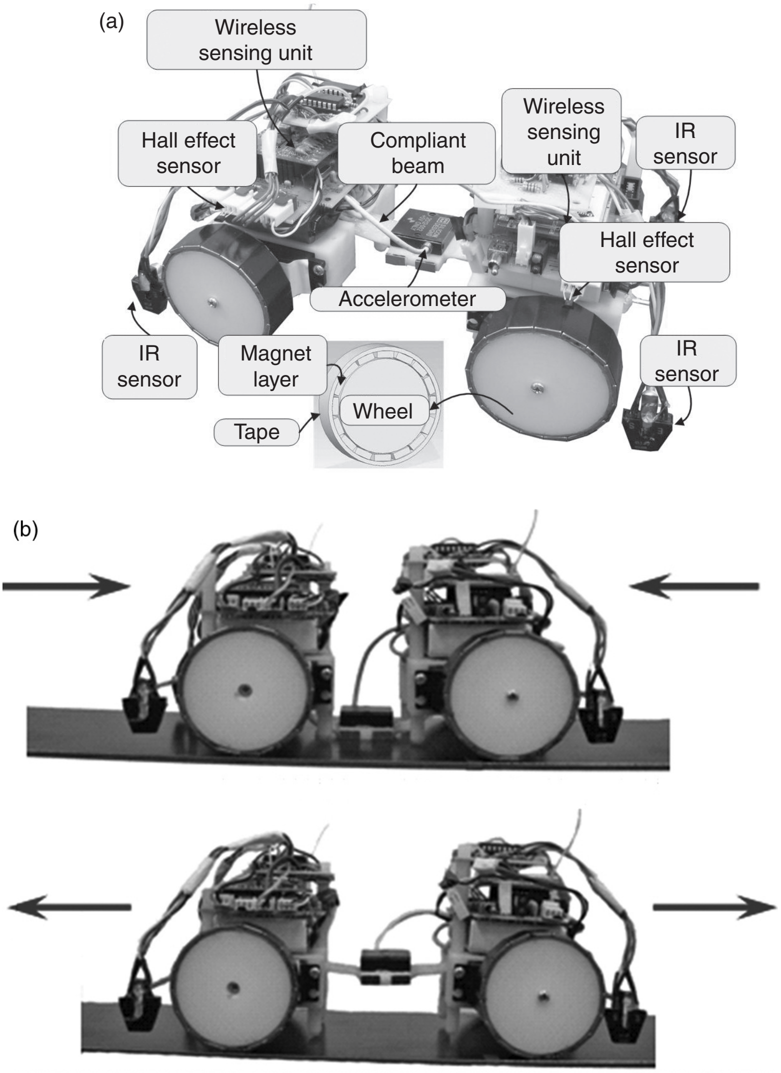
(a)
Wireless sensing unit
Hall effect sensor
Compliant beam
Wireless sensing unit
IR sensor
Hall effect sensor
Accelerometer
IR sensor
Magnet layer
IR sensor
Wheel
Tape
(b)

15.11 Magnet-wheeled mobile sensing node: (a) mobile sensor components, (b) accelerometer attachment/detachment, (c) corner negotiation.

(c)

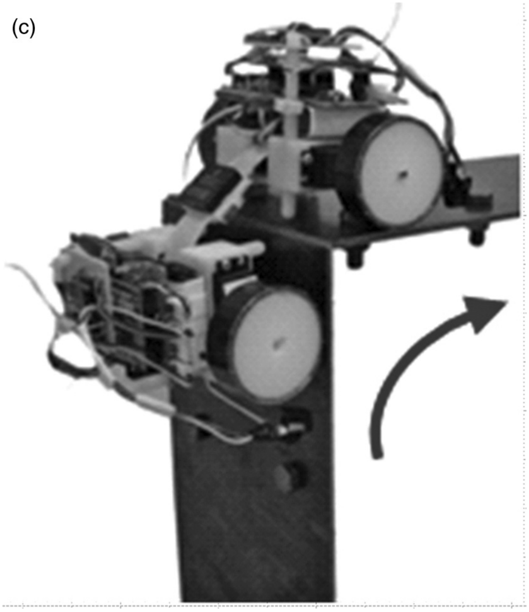

15.11 Continued

Design of a magnet-wheeled mobile sensing node

Figure 15.11a shows the picture of a magnet-wheeled mobile sensing node (Lee *et al.,* 2009; Zhu *et al.,* 2010). The width of the mobile sensing node is 0.152 m (6 in.), the height is 0.091 m (3.6 in.), and the length is 0.229 m (9 in.). The overall weight of the mobile sensing node is about 1 kg (2.2 lbs). The mobile sensing node consists of three substructures: a pair of two-wheel cars and a compliant connection beam. Each two-wheel car contains a body frame, two motorized wheels, batteries, a wireless sensing unit, as well as a number of sensors for motion control. The compliant connection beam is made of spring steel. An accelerometer (manufactured by Silicon Designs, Inc.) is mounted at the middle of the compliant beam between the two cars. The acceleration data are collected and processed by a wireless sensing unit. Each wireless sensing unit contains three basic modules: sensor signal digitization, a computational core, and wireless communication (Wang *et al.,* 2007).

As shown in Fig. 15.11a, the wheels of the mobile sensing node are surrounded by thin magnets for providing sufficient attractive force to climb on ferromagnetic structures. Hall-effect sensors, which are capable of measuring the flux of a magnetic field, are fixed above the magnet wheels. As the wheel rotates, the north and south poles of the small magnets sequentially pass underneath the Hall-effect sensor. Therefore, the magnetic flux density measured by the Hall-effect sensor changes periodically, and the angular velocity of the wheel can be derived and then controlled in real time. In order to move the mobile sensing node (both forward and backward) safely on the underlying structural surface, infrared (IR) sensors are placed at both left and right sides of the front and rear two-wheel cars for surface boundary detection. When an IR sensor moves outside the surface boundary, changes can be captured from the strength of the reflected IR signal, so that the movement direction can be immediately corrected. Real-time feedback control of the motors is performed by the wireless sensing units.

The other feature of the mobile sensing node is the ability to offer accurate acceleration measurement by firmly attaching the accelerometer onto the structural surface (Fig. 15.11b). The attaching procedure is achieved by commanding the two cars to move towards each other to bend the center of the compliant beam towards the structural surface. In addition, small-size magnet pieces are arranged around the center of the beam to further firmly attach the accelerometer onto the steel structural surface. After measurement, the two cars move in opposite directions to straighten the beam and lift the accelerometer away from the steel surface. After the accelerometer is lifted, the mobile sensing node resumes its mobility and moves to next location for another measurement. In addition, the compliant beam facilitates corner negotiation by the mobile sensing node (Fig. 15.11c). When the mobile sensing node climbs over a sharp corner, the front car and back car assist each other through the compliant connection beam. Thus, additional safety is achieved for corner negotiation, when comparing the compliant mechanism to a rigid body design. Detailed mechanical analysis for the compliant mechanism can be found in Guo *et al*. (2012).

Laboratory validation experiments for structural damage detection

A laboratory steel portal frame is constructed (Fig. 15.12). The span of the portal frame is 1.524 m (5 ft.) and the height is 0.914 m (3 ft.). The beam and two columns have the same rectangular section area of 0.152 m (6 in.) × 0.005 m (3/16 in.). Hinge connection is adopted at the base of each column. Each column is connected with the beam through a bolted angle plate, with four bolts on the beam and four bolts on the column. The torque of every bolt is initially set at 13.56 Nm (120 lbs-in.) for the undamaged structure.

As shown in Fig. 15.12, two mobile sensing nodes are used to sequentially take measurements at every pair of locations (A1–A2, A2–A3,…, A10–A11). In the experiments, when the two mobile sensing nodes arrive at one pair of measurement locations, the accelerometers carried by both mobile nodes are attached onto the structural surface. A hammer impact is then applied at the middle of these two adjacent measurement locations. Impact responses at these two locations are recorded by the mobile sensing nodes. The mobile

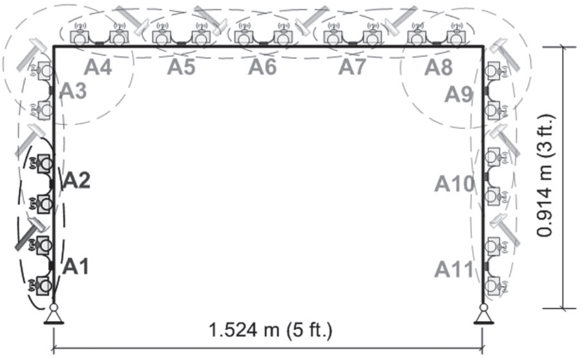

15.12 The laboratory steel portal frame for damage detection using two mobile sensing nodes.

sensing nodes can either transmit the measurement data to the server, or conduct onboard analysis. After finishing the task at one location pair, the two mobile sensing nodes detach accelerometers from the structural surface, and move to the next pair of locations for next set of measurements. The sampling rate for acceleration measurement is assigned to be 2500 Hz.

Transmissibility function analysis, which can identify damage with output data only, is used to process the mobile sensor data for damage detection, (Zhang *et al.,* 1999; Johnson *et al.,* 2004; Kess and Adams, 2007; Devriendt and Guillaume, 2008). If external excitation is only applied at the k-th DOF, the transmissibility function $T_{ij}(\omega)$ between the DOF i and reference-DOF j is defined as the ratio between the frequency spectra of the acceleration at DOF i and DOF j, $A_i(\omega)$ and $A_j(\omega)$:

$$T_{ij}(\omega) = \frac{A_i(\omega)}{A_j(\omega)} \qquad [15.6]$$

It can be derived that for single excitation (at the k-th DOF), the transmissibility function is equivalent to the ratio between two entries of the frequency response function (FRF) matrix, $H_{ik}(\omega)$ and $H_{jk}(\omega)$:

$$T_{ij}(\omega) = \frac{H_{ik}(\omega)}{H_{jk}(\omega)} \qquad [15.7]$$

Equation [15.7] illustrates that transmissibility functions corresponding to inherent dynamic properties of the structure, and is independent of the excitation amplitude. In addition, Equation [15.6] shows that during experiments, the determination of transmissibility functions does not require measuring the excitation force. In order to reduce the effect of experimental uncertainties, the vibration experiments are repeated for N times ($N = 20$ in this study). Then the average transmissibility function $\tilde{T}_{ij}$ is calculated:

$$\tilde{T}_{ij} = \frac{1}{N}\sum_{l=1}^{N}(T_{ij})_l \qquad [15.8]$$

where $(T_{ij})_l$ represents the transmissibility function T_{ij} calculated from the l-th repeated test at DOFs i and j. The damage indicator (DI) between DOFs i and j is defined as following:

$$\mathrm{DI}_{ij} = \int_{\omega_1}^{\omega_2} \frac{\left|\ln\left|\tilde{T}_{ij}^{U}\right| - \ln\left|\tilde{T}_{ij}^{D}\right|\right|}{\left|\ln\left|\tilde{T}_{ij}^{U}\right|\right|} d\omega \qquad [15.9]$$

where ω_1 and ω_2 are the lower and upper boundaries of the interested frequency span; $\tilde{T}_{ij}^{U}$ represents the average transmissibility function of the undamaged structure; $\tilde{T}_{ij}^{D}$ represents the average transmissibility function of the damaged structure; 'ln' means natural logarithm. In this experimental study, ω_1 and ω_2 are set to 100 and 1000 Hz, respectively.

Three damage scenarios are studied. In Damage Scenario I (Fig. 15.13a), a steel mass block of 0.575 kg (1.27 lbs) is bonded at the left column between locations A1 and A2 (as marked in Fig. 15.12) for simulating a reversible damage. In contrast, the mass of the left column is 4.985 kg (10.99 lbs). In Damage Scenario II, four bolts at the upper left corner of the structure, which connect the beam and the angle plate, are loosened (Fig. 15.13b). The torque of each of the four bolts is reduced from 13.56 Nm (120 lbs-in.) to 0.565 Nm (5 lbs-in.). In Damage Scenario III, reduction in section area is introduced to the left column (Fig. 15.13c). The width of the section reduction is 0.006 m (0.25 in.), and the total length of the reduction is 0.0075 + 0.0075 = 0.015 m (0.6 in.). The location of the section reduction is at 0.533 m (21 in.) above the column base, which is between locations A2 and A3 marked in Fig. 15.12.

During the experiment for both the undamaged and damaged structures, the two mobile sensing nodes take measurement at every pair of locations (A1–A2, A2–A3, …, A10–A11) in sequence, and measurement at each location pair is repeatedly taken for 20 times. With all the experimental data sets, the average transmissibility functions for both the undamaged and damaged structures are computed for all ten location pairs using Equations [15.6] and [15.8]. The DIs are then obtained by Equation [15.9], and shown in Fig. 15.14.

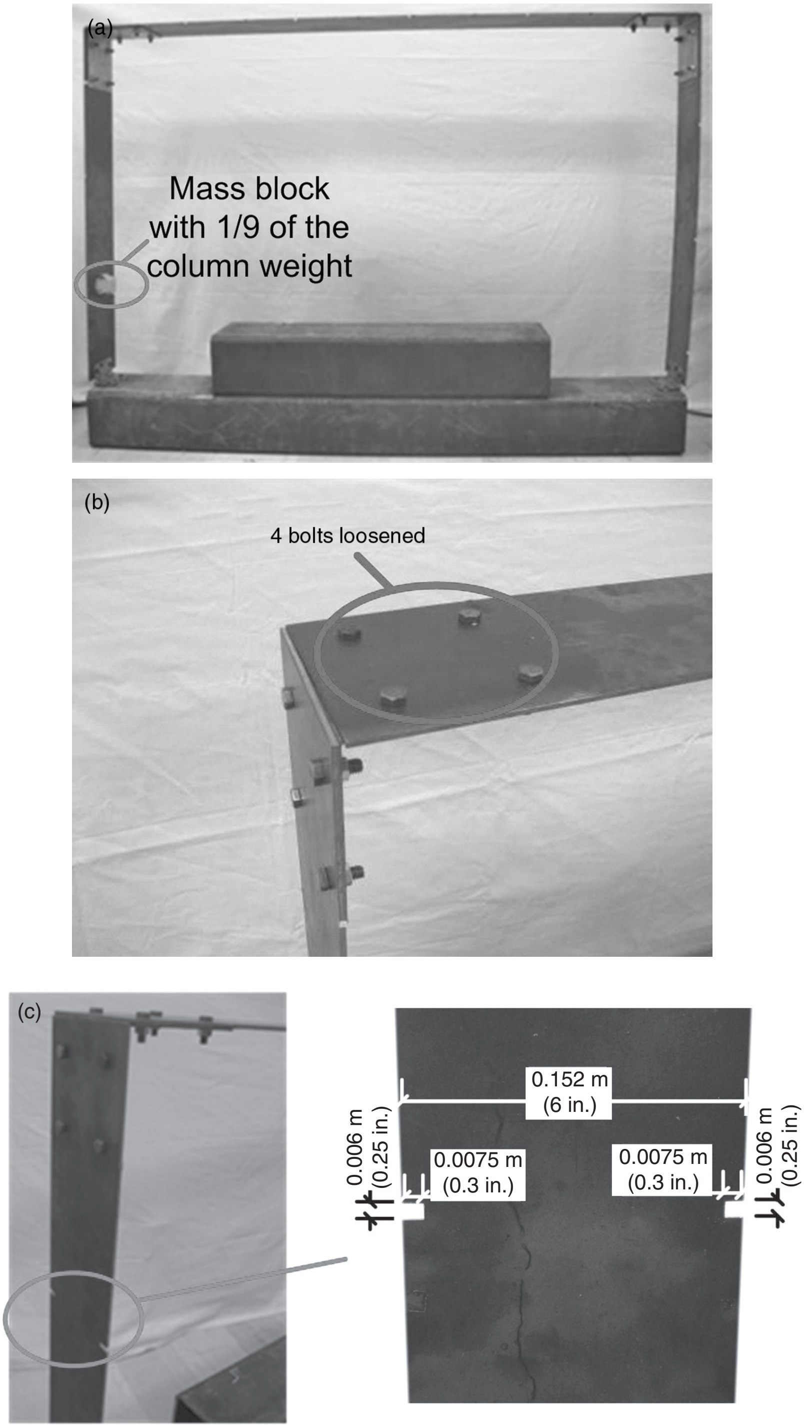
(a)
Mass block with 1/9 of the column weight
(b)
4 bolts loosened
(c)
0.152 m (6 in.)
0.006 m (0.25 in.)
0.0075 m (0.3 in.)
0.0075 m (0.3 in.)
0.006 m (0.25 in.)

15.13 Three damage scenarios on the laboratory frame structure: (a) Damage Scenario I, (b) Damage Scenario II, (c) Damage Scenario III.

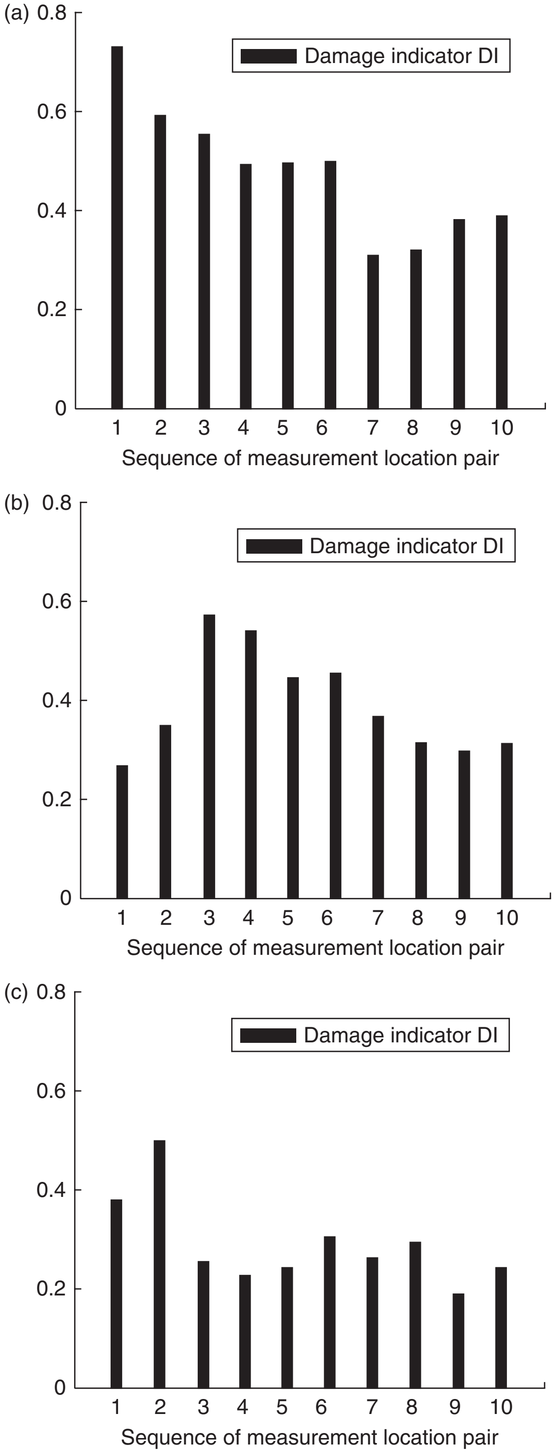

15.14 DIs for three damage scenarios: (a) Damage Scenario I, (b) Damage Scenario II, (c) Damage Scenario III.

For each damage scenario, the sequence number of the location pair with the largest DI agrees with the correct damage location. For example, the largest DI in Damage Scenario II occurs at the third location pair i.e. locations A3–A4. This corresponds to the upper left corner of the frame where the bolts are loosened. It is demonstrated that using the high resolution data collected by a small number of mobile sensors, accurate damage detection has been achieved.

Field validation experiments for vibration modal analysis

Field deployment of the flexure-based mobile sensing nodes is carried out on a steel pedestrian bridge (Zhu *et al.,* 2011). The bridge consists of eleven chord units, each unit 9 ft. long. The length, width, and height of the bridge are 99, 7, and 9 ft., respectively (Fig. 15.15). The frame members are made of square tubes with cross section dimension of 6 in. × 6 in. Diagonal bracing members are allocated in vertical side planes and horizontal planes of the frame for enhancing structural stiffness.

15.15 Picture of the space frame bridge on Georgia Tech campus.

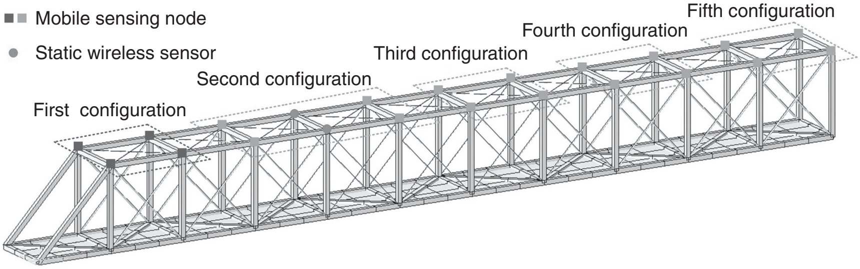
■■ Mobile sensing node
● Static wireless sensor
First configuration
Second configuration
Third configuration
Fourth configuration
Fifth configuration

15.16 3D illustration of five measurement configurations for the mobile sensing nodes.

Four mobile sensing nodes are deployed in this experiment for navigating on the top plane of the frame. A total of five measurement configurations are adopted for the mobile sensing nodes. As shown in Fig. 15.16, each mobile configuration consists of four measurement locations. Two static wireless sensors are mounted as reference nodes for assembling the mode shapes of the bridge. At each measurement configuration, the mobile sensing nodes attach accelerometers onto the structural surface, and measure structural vibrations in the vertical direction.

During testing, the mobile sensing nodes start from the inclined members at one side of the bridge (Fig. 15.17a), climb up over the corner, and then move to the first measurement configuration (Fig. 15.17b). Figure 15.17c shows a mobile sensing node that has attached an accelerometer onto the structural surface for vibration measurement. A vertical hammer impact is applied around the center of the bridge span. Acceleration data are collected by the mobile sensors at 200 Hz sampling rate, and wirelessly transmitted to a laptop server located at one side of the bridge. After finishing the measurement at the first configuration, the four mobile sensing nodes move to the second configuration and so on, till they cover the entire bridge span. At each configuration, the hammer impact and data collection procedures are repeatedly performed.

Upon data collection, the eigensystem realization algorithm (ERA) is applied to the mobile sensor data for extracting modal characteristics at each configuration (Juang and Pappa, 1985). The mode shapes of the entire bridge are assembled through the reference nodes with static wireless sensors. Figure 15.18 shows the first three mode shapes of the bridge that have significant vertical components. The first vertical mode shape shows all nodes moving along one direction, which is expected for such a simply supported bridge. With increasing complexities, other modes also agree with typical behavior of this type of structures. The field study again validated the performance of the mobile sensor network in collecting high spatial-resolution data, with a limited number of sensing nodes and consuming little human effort.

15.5 Conclusions and future trends

Technological advances are providing unprecedented opportunities for adopting miniature robots for SHM applications. Carrying a variety of small-size sensors, SHM robots with unique locomotion systems can provide autonomous mobility while inspecting structures. Examples of different locomotion mechanisms include wheeled robots moving on horizontal surfaces, wall-climbing and crawling robots, snake-like robots, modular robots, aerial vehicles, underwater vehicles, etc. Various sensors, such as cameras, optical scanners, and their combinations have been incorporated for structural

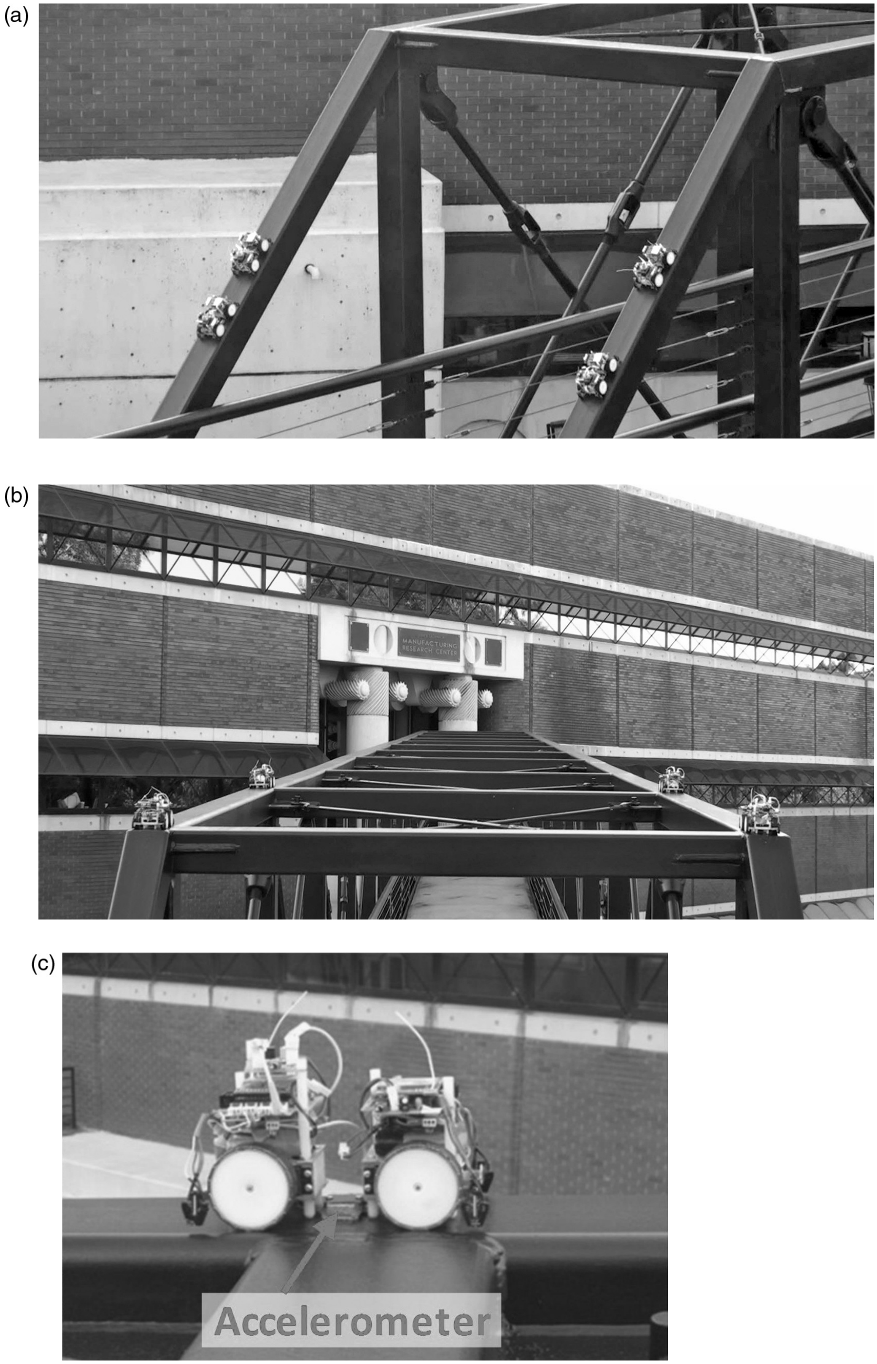
(a)
(b)
MANUFACTURING RESEARCH CENTER
(c)
Accelerometer

15.17 Pictures of the mobile sensing nodes during field testing. (a) Mobile sensing nodes start from the incline frame members. (b) Mobile sensing nodes arrive at the 1st measurement configuration. (c) An accelerometer attached onto the structural surface.

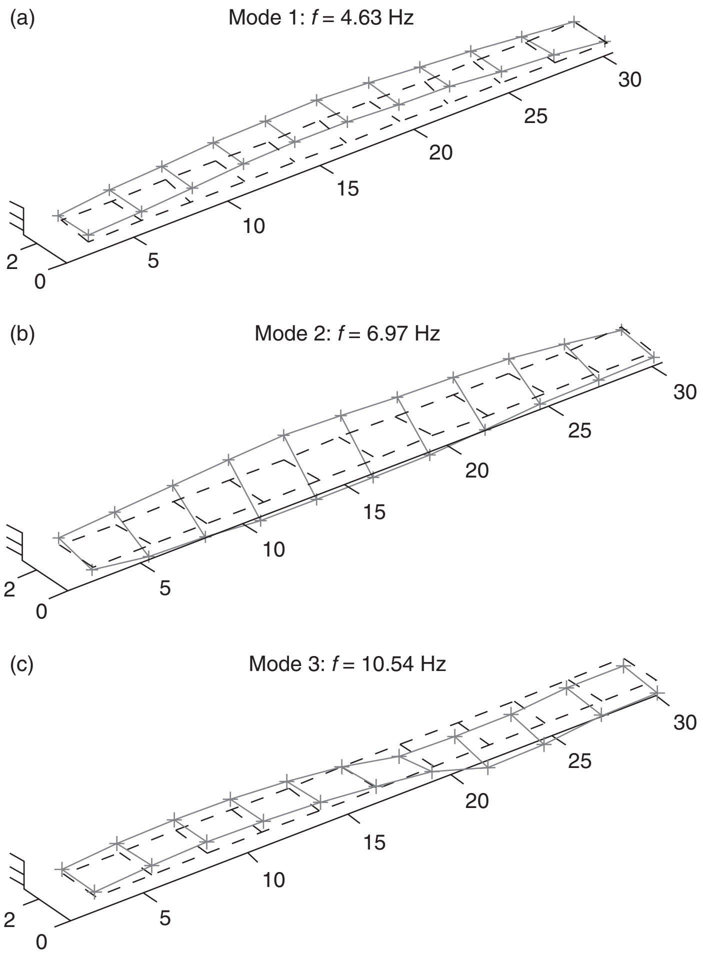

15.18 First three mode shapes with significant vertical components.

inspection purposes. SHM or inspection robots have been applied to different target structures, such as aircrafts, bridges and bridge cables, power lines, pipelines, ducts, tubes, sewage, etc.

In this chapter, vision-based robotic sensing for SHM was surveyed in depth as one of the emerging research field due to the recent advancement of the vision-based technology. The recent break-through in depth-image (RGB-depth) sensor technology is expected to boost up the related research. Remote robotic sensing might be another interesting research topic, thanks to the progress in wireless sensing and WPT technologies.

This chapter also presented exploratory work harnessing mobile sensor networks for SHM. Two mobile sensor nodes are demonstrated to first navigate on a laboratory portal frame. Cross-correlation function analysis is applied to mobile sensor data for damage detection and location. During field testing, a four-node mobile sensor network is used to navigate autonomously to different sections of a steel bridge, for measuring vibrations due to hammer impact and ambient excitation at high spatial resolution. Modal analysis is successfully conducted using the mobile sensor data.

Although robots specialized for SHM application have only recently been developed, their use is expected to largely increase in the near future. New SHM markets will be opened by equipping agile robot systems with advanced sensor technologies. In general, future work can be devoted to both implementation and analysis. With respect to implementation, more agile mobile sensors are needed for navigating on complicated real-world structures. In addition, a mobile excitation node can be developed for applying small-magnitude impact forces to one local area of a structure. With respect to analysis, efficient damage detection or condition evaluation algorithms are needed in order to best utilize high-density measurements provided by a group of mobile sensors. For example, substructure-based finite element model updating algorithms can be developed for efficiently analyzing dense mobile sensor data collected from one section of a large structure.

15.6 References

Abdulla A S A, Khalil A M A, Shehhi A, Karki H and Fok S C (2010), ‘Localization of a submersible mobile inspection platform in an oil storage tank’, *Proceedinds of 7th International Symposium on Mechatronics and its Applications (ISMA)*, 1–6.

Adria O, Steich H and Hertzberg J (2004), ‘Dynamic replanning in uncertain environments for a sewer inspection robot’, *International Journal of Advanced Robot Systems*, **1**, 33.

Backes P G, Bar-Cohen Y and Joffe B (1997), ‘The multifunction automated crawling system (MACS)’ in Bar-Cohen, Y. (Ed.) *Proceedings of the 1997 IEEE International Conference on Robotics and Automation*, Albuquerque, NM, 20–25, April 1997.

Bahr B and Wu F (1994), ‘Design and safety analysis of a portable climbing robot’, *International Journal of Robot Automation*, **9**, 160.

Balaguer C, Gimenez A, Pastor J M, Padron V M and Abderrahim M (2000), ‘A climbing autonomous robot for inspection applications in 3-D complex environments’, *Robotica*, **18**, 287–297.

Balaguer C, Gimenez, A and Jardon A (2005), ‘Climbing Robots’ Mobility for inspection and maintenance of 3D complex environments’, *Autonomous Robots*, **18**, 157–169.

Bang Y, Park J and Myung H (2011), ‘Mobile robot-based visual targeting for wireless power transmission to WSN (2011)’, *Proceedings of Advanced Structural Engineering and Mechanics (ASEM’ 11),* Seoul.

Bar-Cohen Y and Backes P (2000), ‘Scanning large aerospace structures using open-architecture crawlers’, *Proceedings of National Space Missile Materials Symposium*, San Diego, CA.

Blackwell T (2005), ‘Recent demonstrations of Laser power beaming at DFRC and MSFC’, *AIP Conference Proceedings*, **766**, 73–85.

Bodenmann A, Thornton B, Ura T and Painumgal U V (2009), ‘Visual mapping of internal pipe walls using sparse features for application on board autonomous underwater vehicles’, *Proceedings of OCEANS 2009 – EUROPE*, 1–8.

Bouchard S (2010), ‘LineScout robot climbs on live power lines to inspect them’, *IEEE Spectrum online*, Available from: http://spectrum.ieee.org/automaton/robotics/industrial-robots/linescout-robot-climbs-on-live-power-lines-to-inspect-them.

Brian E, Jon M, Dryver R H and Phil B (2004), ‘Robotic systems for homeland security’, in Steven, R. D., Yoseph, B.-C., Aktan, A. E. and Wu, H. F. (Eds.) *Proceedings of SPIE, Nondestructive Detection and Measurement for Homeland Security II*, 16 March 2004.

Choi S H, Song K D, Golembiewskii W, Chu S-H and King G C (2004), ‘Microwave power for smart material actuators’, *Smart Materials and Structures*, **13**, 38.

Churchill D L, Hamel M J, Townsend C P and Arms S W (2003), ‘Strain energy harvesting for wireless sensor networks’, *Proceedings of SPIE, Smart Structures and Materials 2003: Smart Electronics, MEMS, BioMEMS, and Nanotechnology*, 3 March.

Conte G, Zanoli S, Perdon A M, Tascini G and Zingaretti P (1996), ‘Automatic analysis of visual data in submarine pipeline inspection’, *Proceedings of MTS/IEEE.OCEANS ‘96*, **3**, 1213–1219.

Corley A-M (2009), ‘Robotic tightrope walkers for high-voltage lines’, *IEEE Spectrum online*, Available from: http://spectrum.ieee.org/robotics/industrial-robots/robotic-tightrope-walkers-for-highvoltage-lines/0.

Dantu K, Rahimi M, Shah H, Babel S, Dhariwal A and Sukhatme G (2005), ‘Robomote: enabling mobility in sensor networks’, in Rahimi M. (Ed.) *Proceedings of the 4th International Symposium on Information Processing in Sensor Networks (IPSN)*, 25–27 April.

Devriendt C and Guillaume P (2008) ‘Identification of modal parameters from transmissibility measurements’, *Journal of Sound and Vibration*, **314**, 343–356.

Fischer W, Tache F and Siegwart R (2007), ‘Inspection system for very thin and fragile surfaces, based on a pair of wall climbing robots with magnetic wheels’, *Proceedings of IEEE/RSJ International Conference on Intelligent Robots and Systems (IROS 2007)*, 1216–1221.

Guizzo E (2010), ‘Japanese snake robot goes where humans can’t’, *IEEE Spectrum online*, Available from: http://spectrum.ieee.org/automaton/robotics/industrial-robots/japanese-snake-robot-goes-where-humans-cant.

Guo J, Lee K M, Zhu D, Yi X and Wang Y (2012) ‘Large-deformation analysis and experimental validation of a flexure-based mobile sensor node’, *IEEE/ASME Transactions on Mechatronics*, **17**, 606–616.

Huston D R, Esser B, Gaida G, Arms S W and Townsend C P (2001), ‘Wireless inspection of structures aided by robots’, *Proceedings of SPIE, Health Monitoring and Management of Civil Infrastructure Systems*, Newport Beach, CA, 6 March.

Isyumov J, Davenport A G and Monbaliu J (1984), 'CN tower: model and full-scale response to wind', In: *IABSE 12th Congress*, Vancouver.

Jeon H, Bang Y and Myung H (2011a), 'A paired visual servoing system for 6-DOF displacement measurement of structures', *Smart Materials and Structures*, **20**, 045019.

Jeon H, Bang Y and Myung H (2011b), 'Structural displacement monitoring using visual servoeing of paired structured light system', *Proceedings of Advanced Structural Engineering and Mechanics (ASEM' 11)*, Seoul.

Johnson T J, Brown R L, Adams D E and Schiefer M (2004), 'Distributed structural health monitoring with a smart sensor array', *Mechanical Systems and Signal Processing*, **18**, 555–572.

Juang J N and Pappa R S (1985), 'An eigensystem realization algorithm for modal parameter identification and modal reduction', *Journal of Guidance Control and Dynamics*, **8**, 620–627.

Kahn J M, Katz R H and Pister K S J (1999), 'Next century challenges: mobile networking for 'Smart Dust', *Proceedings of the 5th Annual ACM/IEEE International Conference on Mobile Computing and Networking*, 17–19 August.

Kess H R and Adams D E (2007), 'Investigation of operational and environmental variability effects on damage detection algorithms in a woven composite plate', *Mechanical Systems and Signal Processing*, **21**, 2394–2405.

Kim J, Yang S Y, Song K D, Jones S, Elliott J R and Choi S H (2006), 'Microwave power transmission using a flexible rectenna for microwave-powered aerial vehicles', *Smart Materials and Structures*, **15**, 1243–1248.

Kim S, Spenko M, Trujillo S, Heyneman B, Mattoli V and Cutkosky M R (2007), 'Whole body adhesion: hierarchical, directional and distributed control of adhesive forces for a climbing robot', *Proceedings of the IEEE International Conference on Robotics and Automation*, 10–14 April.

Kirchner F and Hertzberg J (1997), 'A prototype study of an autonomous robot platform for sewerage system maintenance, autonomous robots', *Autonomous Robots*, **4**, 319.

Kostin G V, Chernousko F L, Bolotnik N N and Pfeiffer F (1999), 'Regular motions of a tube-crawling robot: simulation and optimization', *Proceedings of the First Workshop on Robot Motion and Control* (*RoMoCo*).

Lee J J and Shinozuka M (2006), 'Real-time displacement measurement of a flexible bridge using digital image processing techniques', *ExpMech*, **46**, 105–114.

Lee K M, Wang Y, Zhu D, Guo J and Yi X (2009), 'Flexure-based mechatronic mobile sensors for structure damage detection', *Proceedings of the 7th International Workshop on Structural Health Monitoring*, 9–11 September.

Leitch J G, Thompson A and Sloan T D (1989), 'A novel dynamic deflection measurement system for large structure', *Proceedings of 4th International Conference on Civil and Structural Engineering Computing* (London),ed BHV Topping (Edinburgh: Civil-CompPress), **2**, 301–306.

Li Z, Zhu J, He C and Wang W (2009), 'A new pipe cleaning and inspection robot with active pipe-diameter adaptability based on ATmega64', *Proceedings of 9th International Conference on Electronic Measurement & Instruments (ICEMI)*, Beijing, China.

Lim R S, La H M, Shan Z and Sheng W (2011), 'Developing a crack inspection robot for bridge maintenance', *Proceedings of IEEE International Conference on Robotics and Automation,* Shanghai.

Luk B L, White T S, Cooke D S, Hewer N D, Hazel G and Chen S (2001), 'Climbing service robots for duct inspection and maintenance applications in a nuclear reactor', *Proceedings 32nd International Symposium on Robotics*, Seoul, South Korea, 41.

Lynch J P (2005), 'Design of a wireless active sensing unit for localized structural health monitoring', *Structural Control and Health Monitoring*, **12**, 405–423.

Lynch J P and Loh K J (2006), 'A summary review of wireless sensors and sensor networks for structural health monitoring', *The Shock and Vibration Digest*, **38**, 91–128.

Marecos J, Castanheta M and Trigo J T (1969), 'Field observation of targus river suspension bridge', *Journal of Structural Division-ASCE*, **95**, 555–583.

Mascarenas D L, Todd M D, Park G and Farrar C R (2007), 'Development of an impedance-based wireless sensor node for structural health monitoring'', *Smart Materials and Structures*, **16**, 2137.

Matsumoto H (2002), '5.2 Wireless power transmission', *Advanced Materials and Technologies, • Energy Technologies, • Fossil Energy*, **3A**, 187–197.

Mazumdar A and Asada H (2010), 'An under-actuated, magnetic-foot robot for steel bridge inspection', *ASME Journal of Mechanisms Robotics*, **2**, 031007.

Moon T K and Stirling W C (2000), *Mathematical Methods and Algorithms for Signal Processing*, New Jersey, US: Prentice Hall.

Mori M and Hirose S (2006), 'Locomotion of 3D snake-like robots; shifting and rolling control of active cord mechanism ACM-R3', *Journal of Robotics and Mechatronics*, **18**, 521–528.

Murata S and Kurokawa H (2007), 'Self-reconfigurable robots', *IEEE Robotics & Automation Magazine*, **14**, 71–78.

Murphy M P and Sitti M (2007), 'Waalbot: an agile small-scale wall-climbing robot utilizing dry elastomer adhesives', *Mechatronics, IEEE/ASME Transactions on*, **12**, 330–338.

Myung H, Lee S and Lee B J (2011), 'Paired structured light for structural health monitoring robot system', *Structural Health Monitoring*, **10**, 49–64.

Nayyerloo M, Chen X, Wang W and Chase J G (2009), 'Cable-climbing robots for power transmission lines inspection', in *Mobile Robots – State of the Art in Land, Sea, Air, and Collaborative Missions*, InTech, 63–84.

Ni Y Q (2009a), 'Structural health monitoring of the Gguangzhou new TV tower', *In: Mini Symposium on Structural Health Monitoring Test Bed,* Boston.

Ni Y Q (2009b), 'Fusion of vision-based displacement and acceleration using Kalman filter', *Proceedings of Fifth International Workshop on Advanced Smart Materials and Smart Structures Technology (ANCRiSST 2009),* Boston, 118.

Ni Y Q and Wong K Y (2009), 'Health checks through landmark bridges to sky-high structures', *In Proceedings of Fifth International Workshop on Advanced Smart Materials and Smart Structures Technology(ANCRiSST 2009),* Boston.

O'Hara K J, Walker D B and Balch T R (2005), 'The Gnats – low-cost embedded networks for supporting mobile robots', in Parker, L. E., Schneider, F. E. and

Schultz, A. C. (Eds.) Multi-Robot Systems. *From Swarms to Intelligent Automata Volume **III***, Dordrecht, The Netherlands, Springer, The Netherlands.

Oh J K, Jang G, Lee J H, Yi B J, Moon Y S, Lee J S and Choi Y (2009), 'Bridge inspection robot system with machine vision', *Automation in Construction*, **18**, 929–941.

Olaszek P (1999), 'Investigation of the dynamic characteristic of bridge structures using a computer vision method', *Measurement*, **25**, 227–236.

Park H J, Sohn H, Yun C B, Chung J and Lee M (2011a), 'Application of a laser-based wireless active sensing system to structural health monitoring', *Proceedings of Advanced Structural Engineering and Mechanics (ASEM' 11),* Seoul, 3600–3611.

Park H J, Sohn H, Yun C B, Chung J and Kwon I B (2010), 'A wireless guided wave excitation technique based on laser and optoelectronics', *Smart Structures and Systems*, **6**, 749–765.

Park J W, Lee J J, Jung H J and Myung H (2011b), 'Vision-based displacement measurement method for high-rise building structures using partitioning approach', *NDT & E Int*, **43**, 642–647.

Pratt K S, Murphy R R, Burke J L, Craighead J, Griffin C and Stover S (2008), 'Use of tethered small unmanned aerial system at Berkman plaza II collapse', *Proceedings of IEEE International Workshop on Safety, Security and Rescue Robotics (SSRR 2008)*, Sendai, Japan, 134–139.

Romero J, 'Bridge Robot Moonwalks on Magnets' (2010), *IEEE Spectrum online*, Available from: http://spectrum.ieee.org/video/robotics/industrial-robots/bridge-robot-moonwalks-on-magnets.

Roundy S J (2003), 'Energy Scavenging for Wireless Sensor Nodes with a Focus on Vibration to Electricity Conversion'. PhD Dissertation, Department of Mechanical Engineering, the University of California, Berkeley. Berkeley, CA.

Sergiyenko O, Hernandez W, Tyrsa V, Cruz L F D, Starostenko O and Peña-Cabrera M (2009), 'Remote sensor for spatial measurements by using optical scanning', *Sensors*, **9**, 5477–5492.

Sheng W, Chen H and Xi N (2008), 'Navigating a miniature crawler robot for engineered structure inspection', *IEEE Transactions on Automation Science and Engineering*, **5**, 368–373.

Sheng W, Shen Y and Xi N (2006), 'Mobile sensor navigation with miniature active camera for structure inspection', *Proceedings of IEEE/RSJ International Conference on Intelligent Robots and Systems IROS 2006*, 1177–1182.

Siegel M (1997), 'Remote and automated inspection: status and prospects', *Proceedings 1st Joint DOD/FAA/NASA Conference Aging Aircraft*.

Siegwart R and Nourbakhsh I R (2004), *Introduction to Autonomous Mobile Robots* Cambridge, MA, MIT Press.

Sodano H A, Inman D J and Park G (2004), 'A review of power harvesting from vibration using piezoelectric materials', *The Shock and Vibration Digest*, **36**, 197–205.

Stephen G A, Brownjohn J M W and Taylor C A (1993), 'Visual monitoring of the Humber bridge', *Engineering Structures*, **15**, 197–208.

Taylor S G, Farinholt K M, Flynn E B, Figueiredo E, Mascarenas D L, Moro E a, Park G, Todd M D and Farrar C R (2009), 'A mobile-agent-based wireless sensing network for structural monitoring applications', *Measurement Science and Technology*, **20**, 045201.

Todd A M, Mascarenas D, Flynn E, Rosing T, Lee B, Musiani D, Dasgupta S, Kpotufe S, Hsu D and Gupta R (2007), 'A different approach to sensor networking for SHM: remote powering and interrogation with unmanned aerial vehicle', *Proceedings 6th International Workshop on Structural Health Monitoring*, Stanford, CA.

Tung P C, Hwang Y R and Wu M C (2002), 'The development of a mobile manipulator imaging system for bridge crack inspection', *Automation in Construction*, **11**, 717–729.

Ugur O and Herbert F (2006), 'Powersphere: A Photovoltaic Cavity Converter for Wireless Power Transmission using High Power Lasers', *Conference on Photovoltaic Energy Conversion*, 126–129.

Urwin-Wright S, Sanders D and Chen S (2002), 'Terrain prediction for an eight-legged robot', *Journal of Robotic Systems*, **19**, 91–98.

Wahbeh A M, Caffrey J P and Masri S F (2003), 'A vision-based approach for the direct measurement of displacements in vibrating systems', *Smart Materials and Structures*, **12**, 785–794.

Wang Y, Lynch J P and Law K H (2007), 'A wireless structural health monitoring system with multithreaded sensing devices: design and validation', *Structure and Infrastructure Engineering*, **3**, 103–120.

Welch G. and Bishop G. (2006), *An introduction to the Kalman filter, TR95–041. Department of Computer Science*, University of North Carolina, Chapel Hill.

Wild G and Hinckley S (2007), 'Fiber Bragg grating sensors for acoustic emission and transmission detection applied to robotic NDE in structural health monitoring', *Proceedings of IEEE Sensors Applications Symposium (SAS '07)*, 1–6.

William C B (1996), 'The history of wireless power transmission', *Solar Energy*, **56**, 3–21.

Xiao J (2002), *Development of Miniature Climbing Robots – Modeling, Control And Motion Planning*, Doctoral Dissertation, Michigan State University.

Xiao J, Xi N, LalTummala R and Mukherjee R (2004), 'Fuzzy controller for wall-climbing microrobots', *IEEE Transactions on Fuzzy Systems*, **12**, 466.

Xu F, Wang X and Xie Q (2008), 'Obstacle crossing ability of a new wheel-based cable climbing robot', *Proceedings of 15th International Conference on Mechatronics and Machine Vision in Practice (M2VIP)*, Auckland, New Zealand.

Yu S M, Jang J H and Han C S (2007), 'Auto inspection system using a mobile robot for detecting concrete cracks in a tunnel', *Automation in Construction*, **16**, 255–261.

Yuan J, Wu X, Kang Y and Ben A (2010), 'Research on reconfigurable robot technology for cable maintenance of cable-stayed bridges in-service', *Proceedings of 2010 International Conference on Mechanic Automation and Control Engineering (MACE)*, Wuhan, China, 1019–1022.

Zhang H, Schulz M J, Ferguson F and Pai P F (1999), 'Structural health monitoring using transmittance functions', *Mechanical Systems and Signal Processing*, **13**, 765–787.

Zhang H, Wang W, Gonzalez-Gomez J and Zhang J (2010), ‘A bio-inspired small-sized wall-climbing caterpillar robot’, in *Mechatronic Systems Applications*, Paola A. M. D. D. and Cicirelli G (eds), InTech.

Zhu D, Guo J, Wang Y and Lee K M (2011), ‘Field validation of flexure-based mobile sensing nodes on a space frame bridge’, *Proceedings of the 8th International Workshop on Structural Health Monitoring*, 13–15 September.

Zhu D, Yi X, Wang Y, Lee K M and Guo J (2010), ‘A mobile sensing system for structural health monitoring: design and validation’, *Smart Materials and Structures,* **19**, 055011.

16

Design and selection of wireless structural monitoring systems for civil infrastructures

M. B. KANE, C. PECKENS and J. P. LYNCH, University of Michigan, USA

DOI: 10.1533/9780857099136.446

Abstract: A dichotomy exists in structural monitoring installations: those with sensors tethered to the data repository with wires, and those which use wireless communication to create a distributed network of sensors. This chapter discusses the impact of the paradigm shift from the wired monitoring systems traditionally used, to the wireless systems recently developed. This new technology is capable of achieving effective measurements on par with its predecessor, and introduces new possibilities of large-scale networks of hundreds of sensors made possible by low installation costs and scalable in-network data processing. Design and selection considerations covered in this chapter include network architecture, wireless node hardware, and distributed embedded software. Although rapidly maturing and reaching commercialization, research opportunities still exist in the fields of data and power management, which are discussed as the chapter culminates.

Key words: wireless sensors, ZigBee, sensor network, multi-hop communications, time synchronization.

16.1 Introduction

Monitoring systems transfer measurement data between sensors and a data aggregator (i.e., data acquisition system) via three possible modes: conductive wires, optical fibers, and wireless radio waves. This chapter is aimed at readers familiar with traditional wired and optical monitoring systems but wishing to learn more about the design and deployment of state-of-the-art wireless sensor networks (WSNs) for structural monitoring applications. Throughout the chapter, recommendations are given that take advantage of the two key features available in wireless monitoring systems: low costs and embedded data processing. Low installation costs are made possible by wireless communication, and in-network distributed data processing is made possible by the embedded computing capabilities integrated into the hardware design of the wireless sensors.

© 2014 Woodhead Publishing Limited

The potential to reduce the cost of sensor installations in large, complex structures is a major driver of the growing interest in wireless sensing. An associated benefit of lower cost sensors is the possibility of deploying increasing numbers of sensors in a structure. The ability to process raw sensor data at the wireless sensor node reduces volumes of measurement data into more compressed information. This improves the system scalability, reduces power requirements, and ensures that the system communication is reliable.

This chapter will proceed as follows: the remainder of this section will summarize the motivation for the paradigm shift to wireless telemetry. Section 16.2 then provides the reader with elementary knowledge of wireless communications, including the hierarchical design model. Section 16.3 contains an overview of WSN hardware and peripherals. A selection of commercially available wireless sensors and academic prototypes is presented, but this is by no means an exclusive list and is meant only to provide the reader with the advantages and disadvantages of broad families of wireless sensors. Section 16.4 describes the firmware that is embedded in the wireless sensors and the selection criterion for key features. The chapter concludes with Section 16.5, which lays out the future commercial opportunities and research needs for the wireless monitoring field.

16.1.1 State of the practice

The advances made by the structural health monitoring (SHM) community over the past two decades will only benefit society if the value of the information provided by these systems is able to offset the costs of installation and operation of the SHM systems themselves. Presently, monitoring systems are considered cost-effective for only a select set of scenarios:[1]

- prior to, or during, structural retrofits,[2]
- following a possible overloading (e.g., after a bridge–ship impact[3]),
- during demolition or retrofit,[4]
- continuously, when long-term degradation is suspected (e.g., corrosion[5]),
- as needed for the performance assessment of building codes,[6]
- continuously, when there are concerns about the fatigue life of the structure,[7] and
- during the construction of novel structural systems.[8]

The common attribute among all of these motivations for monitoring is that the structure's owner or other major stakeholders can see a low-risk, short-term return-on-investment for the monitoring system. That return can be realized as reduced liability, more cost-effective maintenance decisions, or reduced construction costs.[9]

For example, the 2011 Los Angles Amendment Building Code §91.1613.10[10] requires the installation of a limited number of accelerometers to measure strong ground motions and structural responses in areas of high seismicity. The information collected by these relatively inexpensive systems has been used for post-disaster condition assessment and improvement of seismicity models.[11] In one case, inspection of accelerometer data showed that damage had occurred to a building during an earthquake. However, the location of the damage could not be identified and manual inspections of the structural connections were still necessary, costing a few hundred to a few thousand dollars for each connection.[12] A reduction in per-sensor installation costs, and the introduction of in-network data processing, both made possible with a WSN, may bring about automated condition assessment with higher spatial resolution, thereby reducing the need for costly manual inspections.

Moss and Matthews[1] categorize the sensors used for SHM into three groups: those sensors that measure the application of loads to the structure (e.g., wind pressure sensors, anemometers, thermometers, and load cells); those that measure structural responses to applied load (e.g., linear variable differential transformers (LVDT), inclinometers, fiber optics, accelerometers, and strain gages); and those that directly measure structural degradation such as scour and corrosion. Transducers in these categories can vary greatly in price, from less than a dollar to over ten thousand dollars per sensor. The quintessential trade-off with cost is performance; a more expensive device will generally have a lower noise floor, better resistance to extreme environments, higher sensitivity, and a broader frequency response. Variations in these performance measures all affect the capabilities of the SHM system as a whole. The actual cost of monitoring systems has been noted to be up to $4000 per channel for strong ground motion accelerometers in buildings.[6] At these prices, the broad application of SHM systems is in doubt, especially when higher sensor densities are required for improved spatial resolution of damage detection. Clearly, lower cost sensors are direly needed.

Toward achieving this goal, academia and industry alike have focused effort on reducing the cost of SHM by exploiting recent wireless communication breakthroughs. The main challenges associated with the design and deployment of a successful structural monitoring program are cost-effective data transmission, data management, and system identification (ID).[9] Each of these challenges is lessened when switching to a wireless monitoring system, but new surmountable challenges arise (e.g., supplying wireless nodes with power and maintaining data quality on par with wired systems[13]). The development of a cost-effective, high-performance SHM architecture with wireless telemetry has applicability beyond civil structures (e.g., aircraft[14] and naval vessels[15,16]).

16.1.2 State of the art

The idea of structural monitoring using wireless data transmission was first proposed by Straser and Kiremidgjian[17] in the mid 1990s as a method to reduce the costs associated with using cables. Since then, researchers have developed a wide variety of wireless sensor prototypes aimed at reducing power requirements, extending communication ranges, and improving the efficient use of available bandwidth. Lynch and Loh[18] present an extensive summary review of the developments in wireless monitoring for SHM. As the research has developed over the years, it became apparent that switching to wireless telemetry would achieve more than a cost reduction associated with the absence of extensive cabling. The embedded computing inherent in each wireless node can be used to process data in a decentralized manner, thereby reducing the computational load on the centralized server and simultaneously improving system scalability to larger nodal counts. With improved scalability comes an increased sensor density, leading to more accurate system ID and improved damage detection capabilities.

WSN for SHM can come in many flavors. Most of the research and methods presented herein consider wireless SHM as the practice of replacing wired communication between transducers and a central data aggregator with a wireless link. The wireless links most often use the industrial, scientific, and medical (ISM) radio frequency (RF) spectrum, as defined by the International Telecommunications Union (ITU) and adopted by the US Federal Communications Commission (FCC). The key benefit of using this spectrum is the ability to transmit without a license, provided local regulations are met. Within the ISM spectrum, many WSNs operate around 2.4 GHz due to high information throughput; however, 900 MHz has been used when an increase in range was required.[18] Cellular data networks, i.e. the networks typically used for mobile phones, have also been used in SHM to transmit data from the small on-site data repository to an offsite server managed by the SHM system operator.[19] Brownjohn *et al.*[20] pioneered a unique form of SHM that eliminates the cabling of traditional systems, but does not transmit any response data wirelessly. Instead, a global positioning system (GPS) signal is used to synchronize the clocks of independent data acquisition systems, from which the data are retrieved periodically by manual means.

Beyond moving to a new type of telemetry, SHM using WSN has introduced other exciting opportunities, such as ad hoc communication, mobile sensors, and in-network computing, all of which increase the viability of SHM. Ad hoc communication allows the communication network to self-heal in case a wireless link fails. Additionally, sensors can be upgraded, augmented, or replaced without having to significantly restructure the network.[21] In all wired SHM systems, the sensors are (semi-) permanently installed and cannot autonomously move to return better SHM results. Taking advantage of the mobile freedom associated with wireless telemetry, Zhu *et al.* proposed and developed an autonomous wireless robot that augments the static WSN on a bridge with mobile excitation and response data.[22,23] With this technology, the special resolution of the transmissibility functions used for system ID is improved without significantly increasing the number of nodes in the network. Although wireless networks have limited communication bandwidth, compared to those that are wired, each wireless node has embedded computing (e.g., a microcontroller (MCU)) that can preprocess the data, thereby reducing the amounts of data that need to be transmitted. Not only does this in-network data processing alleviate bandwidth limitations, it can also reduce data inundation of the site's main server. Traditional system ID algorithms, such as the eigen-system realization algorithm (ERA), stochastic subspace identification (SSI), and frequency domain decomposition (FDD), have been successfully embedded as applications in a WSN, and can be used to lessen the computational load on the server. Zimmerman *et al.*[24–26] have embedded simulated-annealing algorithms for identifying model and state-space structural parameters using only the network's distributed computing capability, and utilized a market-based approach for dynamic computational load balancing across the network. The key to these bandwidth optimizations is the transformation, at the wireless node, of raw time-history data to a sparser domain (e.g., the frequency domain) that is then transmitted wirelessly.

With these aforementioned advantages over wired SHM, it is no wonder that researchers and commercial interests have begun successfully deploying WSN. The large majority of the deployments have been on bridge structures, because of their accountable and transparent governmental owners. In 2005, Pakzad *et al.*[27] measured acceleration on the Golden Gate Bridge in California using 64 MicaZ wireless sensors. A multi-hop pipelining approach was used to wirelessly deliver the data from one end of the bridge to the other, a distance that a single wireless transmission could not cover. A large-scale long-term deployment of a WSN with power harvesting was installed on the Jindo Bridge in South Korea.[28] Similarly, a long-term deployment of a WSN on the New Carquinez Bridge in California was integrated with advanced data management tools implemented upon an extensive cyber-infrastructure to aid the operators in analyzing the extensive amount of data collected.[19] A more complete review of successful wireless SHM installations can be found in Chapter 17.

16.2 Overview of wireless networks

The primary difference between WSNs and wired sensor networks is the medium over which the sensor data are communicated to the site's data aggregator. In order to ensure that the greatest amount of information is sent through the network with minimal delay, certain network management practices must be established. These are especially important in a wireless network, since all nodes share a limited frequency spectrum to transmit data. This is in stark contrast to wired networks, where each node has a direct link to the data aggregator. Before considering the network as a whole, it will be helpful to first consider the communication link between two nodes, since peer-to-peer connectivity is the fundamental building block upon which the network is built.

The mathematical theory of communications used to design network management practices was arguably founded by Shannon in Reference 29, in which he defines the five fundamental components of a communication link (see Table 16.1).

1. The *information* source generates a message and desires to communicate it to the receiver. In sensor networks, the message contains information produced by the transducer, such as acceleration, strain, or force data in the case of structural monitoring.
2. The *transmitter* transforms the message into a signal to be sent over the channel. An example of a transmitter in a wired strain-based SHM system is a device that converts the resistance measured across a strain gage into a voltage sent to the data acquisition system (DAQ). In a WSN, the transmitter typically converts the analog voltage produced by the transducer into a digital value, then buffers and packetizes digital measurements, modulates the digital data on a carrier frequency, and excites an antenna to transmit the data through the air.
3. The *channel* is the medium over which the message is transmitted. Copper cabling is most often used for wired SHM; however, fiber optics are sometimes used. Wireless systems transmit data on an RF over whatever medium is between the transmitter and receiver, whether that be air, soil, water, or building walls. The primary reason for limited communication bandwidth is signal attenuation and the introduction of natural noise occurring in the channel. In wireless networks the signal power is attenuated by the inverse square law (i.e., $\text{power} \propto (\text{distance})^{-2}$)[31] and

Table 16.1 Comparison of wired and wireless communications

	Source	Transmitter	Channel	Receiver	Destination
Wired monitoring system	Transducer		Co-axial cable (1 channel/ wire)	Data acquisition (ADC)	Server
Wireless monitoring system	Transducer	ADC + radio	RF medium (multiple channels in spectrum)	Radio	Server

noise is introduced by all sorts of electro-magnetic (EM) interference (e.g., devices emitting energy on the same frequency band, such as other networks, microwave ovens, and fluorescent lights).[31]

4. The *receiver* acts in the opposite manner to the transmitter. In a wired monitoring system, the receiver is a data acquisition system that includes an analog-to-digital converter (ADC). In a WSN, the receiver decodes the noisy and attenuated signal (i.e., message) obtained from the wireless channel and tries to recover, as closely as possible, the message that the source desired to send via the transmitter.
5. The *destination* is the device for which the message was intended. The ultimate destination for most messages in a monitoring system (wired and wireless) is the site's data aggregator. However, in a WSN a message may have to 'hop' from one node to another if the wireless signal is not strong enough to reach from the source to the final destination.

A wireless communication network is formed when a multitude of sources and destinations establish communication links between each other. Together, these links form a network that can be abstracted and described by the Open Systems Interconnection (OSI) reference model.[32] The OSI reference model was created by the *Organisation Internationale de Normalisation* (ISO) subcommittee on OSI in 1977 as a general model to build future network specifications upon. The OSI model has subsequently been used to define the most popular network protocol architectures used for WSN (e.g., the IEEE 802.15.4[33] and ZigBee™ stack often used in wireless SHM networks). Wireless network standards may only define a few of the seven OSI reference model's protocol layers (i.e., physical, data link, network, transport, presentation, and application layers) in order to remain as flexible as possible, leaving the rest up to the user to define. This division of specification responsibility for ZigBee™ networks is shown in Table 16.2 as an example.

Table 16.2 Common network stacks and development responsibility

OSI layer		Responsible party		
	User application	User defined		
(7)	Application layer	ZigBee	User defined	FTP or HTTP
(6)	Presentation layer			MIME
(5)	Session layer			SSL
(4)	Transport layer			TCP or UDP
(3)	Network layer			IPv4 or IPv6
(2)	Data link layer	IEEE		IEEE
(1)	Physical layer	802.15.4		802.11

A network 'stack' (i.e., the software running on the nodes and server) which uses the OSI reference model comprises seven layers (i.e., groups of similar communication functions) where each layer is served by the layer below and serves the layer above. The layers start at the most fundamental *physical layer* and grow to become more abstract, terminating at the *application layer*. The seven layers and their use in some of the most popular WSN networks are described:

1. The *physical (PHY) layer* defines the method by which data are transferred over the physical media (e.g., RF spectrum of the WSN). Digital wireless communications can modulate the bits of a digital message on a carrier frequency in a variety of ways (e.g., amplitude modulation (AM), frequency modulation (FM), and phase modulation (PM)) in an attempt to make the signal less vulnerable to attenuation and noise.[31] Increasing the carrier frequency (e.g., from 900 MHz to 2.4 GHz) increases the achievable data rate but decreases range especially when traveling through solid obstacles. Designers of wireless SHM networks using the popular IEEE 802.15.4 standard should note their networks will share the same physical layer (i.e., 2.4 GHz spectrum) as IEEE 802.11 wireless local area networks (WLANs) and BlueTooth™. If a WLAN is known to be present on a given channel, then the WSN should, either manually or autonomously, re-configure to use a channel in a less active segment of the shared frequency band (see Fig. 16.1).
2. The *data link layer* establishes the link between nodes in the network using an addressing system and defines how addresses are attached to each message's frame. In IEEE 802.15.4 networks, the data link layer comprises two sub-layers. The upper logical link control (LLC) sub-layer shields upper layers of the stack from the specifics of the underlying physical layer. The lower media access control (MAC) sub-layer, whether defined by a schedule-based (e.g., time-division multiple-access (TDMA)) or contention-based protocol (e.g., clear-channel assessment (CCA)),[31] establishes when nodes are allowed to transmit on the channel. Schematically, the typical IEEE 802.15.4 MAC data frame used in WSNs (Fig. 16.2) contains the source and destination address, packet sequence information, and security details, a payload of up to 102 bytes, and a check sum to ensure data integrity when received.[34]
3. The *network layer* provides routing and switching functionality. In wireless networks, the network layer is built around one of the three main topologies shown in Plate XII in the color section between pages 294 and 295: star, mesh, and hierarchical tree topologies. Star networks are often used when all nodes are within range of the central coordinator and offer high data rates; however, the failure of the coordinator or a change in the RF environment can be catastrophic. Mesh networks work especially

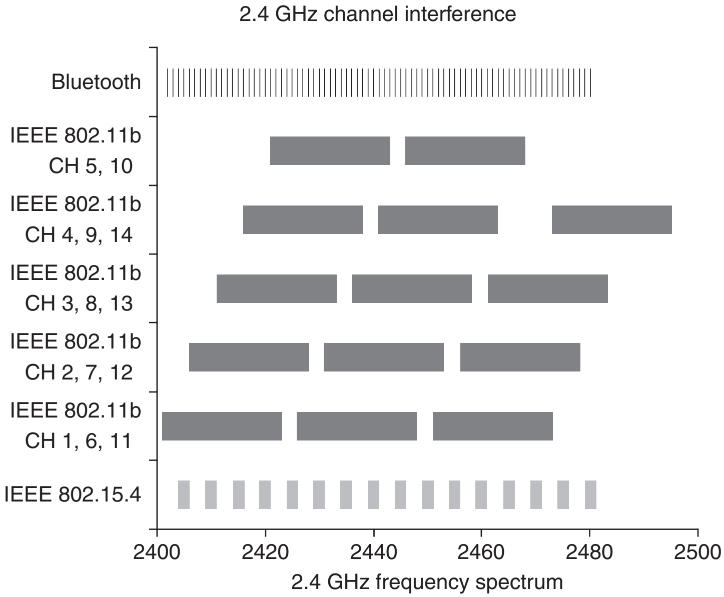

16.1 2.4 GHz channel interference.

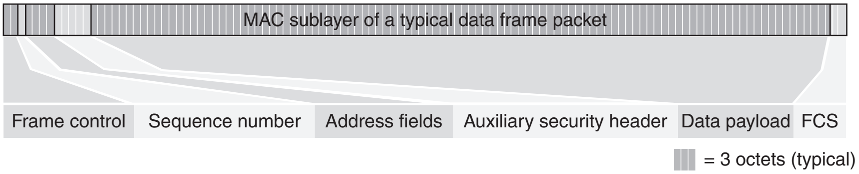
MAC sublayer of a typical data frame packet
Frame control
Sequence number
Address fields
Auxiliary security header
Data payload
FCS
= 3 octets (typical)

16.2 Schematic view of the IEEE 802.15.4 Data Packet MAC sub-layer.[33] (FCS = frame check sum.)

well when the network map is not known *a priori* (e.g., when some nodes are mobile) or when redundant communication paths are required. Due to network management associated with mesh networks, their throughput is limited to low data rate applications. When a heterogeneous set of nodes form the WSN the hierarchical topology may be most appropriate, with the lowest-power devices serving as leaf nodes, and the higher power but more capable nodes as trunk nodes relaying messages at higher data rates, often on another frequency. While the multi-hop topologies (i.e., mesh and hierarchical) increase redundancy and range, the multiple re-transmissions required to get a message from the source to the ultimate destination can significantly reduce network throughput.

4. The *transport layer* provides transparent and reliable data transfer to the upper protocol layers. The important wireless communication tasks

of error control and failed message retransmission are handled by this layer. In WLANs, the two most popular transport layer protocols are the transmission control protocol (TCP) and user datagram protocol (UDP). The transport layer is not specifically defined by the ZigBee™ protocol and is left to the user to define if so desired.

5. The *session layer* controls the binding and unbinding of sessions, i.e., brief amounts of time in which the physical layer is dedicated to data transfer between two specific nodes. Since many network stacks used in WSN are as small as possible in order to fit on a wireless sensor node's limited memory, they do not implement a session layer. Instead, a data-transfer session comprises only a single packet, and transfer of larger amounts of data must be done in multiple packets handled by the application or by network middleware (see Section 16.4).
6. The *presentation layer* creates an abstracted interface to the layers below so higher-level applications may be written regardless of the type of underlying network used. The services provided by this layer include entry, display, and structuring of the data into a message.
7. The *application layer* should be the only layer of the OSI reference model that the user's applications interact with and exchange network-information including network availability (e.g., determining unavailability with a time-out period). The WSN network designer is often left to define this layer; however, popular protocols such as HTTP or FTP can be implemented for this purpose.

The selection of the WSN network stack is an important design decision and should include consideration of the desired data rate, communication range, and power consumption. IEEE 802.15.4 (the foundation for ZigBee) is the preferred stack for low power and low data rate WSN.[18] IEEE 802.11 (the foundation for WiFi) has been used with aggregators in large-scale WSNs where large amounts of data must be transmitted in a short period through a larger network.[35] Finally, 3G and 4G cellular modems are the preferred method for transmitting data from the SHM installation site to the internet, and then to an owner's off site repository.[36]

Plate XIII[30] in the color section between pages 294 and 295 and Table 16.3 explains why these protocols have been used for these different purposes.

Even after selecting the IEEE 802.15.4 physical and data link layers, there are many options available for the remaining layers that lie above in the OSI model. The three most popular are: 60LoWPAN, which implements IPv6, creating an intranet of low-power devices and is ideal when the WSN nodes will be connected to the internet (further design information can be found in Reference 38[38]); the precisely synchronized mesh network WirelessHART protocol was designed to bring wireless connectivity to the HART wired

Table 16.3 Qualitative comparison of wireless standards

OSI Layer	IEEE 802.15.4	Bluetooth	IEEE 802.11
Power consumption	Ultralow	Low	Medium
Battery life	Days to years	Hours to days	Minutes to hours
Cost and complexity	Low	Medium	High

Source: Adapted from Reference 37.

communication standard long used for industrial control systems (further design information can be found in Reference 39); and the low power, low data rate ZigBee protocol has found extensive use in wireless light switches, electrical meters, and other applications where data need to be communicated only intermittently.

16.3 Hardware design and selection

Structural monitoring systems are made up of three main parts: the data acquisition system (Plate XIV in the color section between pages 294 and 295 d through g), the backend data management and analytics system (Plate XIVb), and the user frontend (Plate XIVa). This chapter will focus mainly on the utilization of WSN in the context of the data acquisition system, with discussion on the effects of the data acquisition system architecture on the data management backend and user frontend. For a wireless monitoring system, the data acquisition system contains hardware called wireless sensor nodes (Plate XIVd), also sometimes called 'motes,' which measure physical properties (e.g., structural response to load) and transmit the measurements through a wireless network. These nodes come in many shapes and sizes, but all maintain the same principle parts.

16.3.1 Anatomy of a wireless sensor

Modern wireless sensors (Plate XIVe through g) convert a physical measure into a voltage that is then converted to a digital value, processed, and wirelessly transmitted. The sensing transducer converts the physical measure into an electrical signal that is then typically passed through a signal conditioner and into an ADC. In the node's core (Plate XIVe), the MCU, essentially an extremely small computer, processes measurements, temporarily stores data in external memory, and then packetizes the processed data into a packet, with a destination address and other information, for transmission by a wireless transceiver. The wireless transceiver modulates the packetized data onto a carrier radio wave and transmits it over an antenna to the receiving unit or server. Optionally, wireless nodes may contain a digital-to-analog converter (DAC) that can then be used to excite the structure for active input–output system ID or for structural control.[40] The whole system must be powered by either a wired power source or rechargeable batteries that can be charged using power harvesting techniques.

Low-cost, low-power MCUs have been one of the key enabling technologies for WSN. The MCU, and its embedded firmware (Plate XIVf), handles the node's computation load but also contains a combination of other features including:

- Volatile memory (RAM) for temporary data storage (may also be on an external chip in the node)
- Non-volatile memory (EEPROM or FLASH) for storage of calibration and unit information
- Serial interface (SPI, UART, I2C) to talk to external chips (e.g., external memory, radio, ADC)
- Coprocessors for efficient calculation of fast Fourier transforms (FFTs), floating point operations, or control laws
- Timers for event counting, pulse-width modulation (PWM) generation, or watchdogs to ensure nodes do not 'freeze'
- Internal ADC with simple signal conditioning
- Internal wireless radios (this is becoming more common)
- Programming and debugging support.

The selection of a MCU for a wireless sensor node is a complex task that depends upon the wireless sensor's application. When choosing a commercial wireless sensor, it is sometimes not possible to know which MCU is used, but the node's datasheet will typically contain abstracted specifications (e.g., speed, memory, and power consumption). Therefore, it is important for the designer of a WSN to understand the repercussion of the MCU specifications on overall WSN performance. Since wireless sensors typically run off of batteries, it is important to choose a low-power MCU with sleep modes yielding lower power consumption when a peripheral or computation is not necessary. The most common supply voltages for MCUs are 5 V and 3.3 V, but recently, lower supply voltages of 1.8 V have been growing more common since lower operating voltages generally correlate to lower power consumption. The trade-off most often associated with power consumption is computational power and speed. In other words, higher MCU speeds and computational capabilities require higher power consumption.

The lowest-power MCUs make computations using only 8-bits (i.e., numbers between 0 and 255, or −128 to 127) at a time in a fixed-point manner. Since measurement data are stored in 16-, 32-, or 64-bit variables, many 8-bit operations are required to process each data point at the node, even for simple processing such as scaling and offset correction. Newer 16-bit MCUs are becoming more power efficient, as are 32-bit and 64-bit MCUs, yet greater power is required to operate the wider data busses. The MCU's clock rate determines how long each primitive operation takes and can be anywhere from less than 1 MHz to greater than 500 MHz at the cost of significant power consumption. It is easiest for the user to program data processing algorithms using floating point operations. However, for efficient execution of floating point operations, the MCU should have native hardware floating point capabilities. Otherwise floating point operations must be converted to multiple fixed-point calculations. Floating point numbers stored in 32-bits are sufficient for most SHM applications, but 64-bit calculations may sometimes be necessary.

More and more MCU manufacturers are integrating additional peripherals such as ADCs, larger amounts of memory, and even wireless radio circuitry into their MCU product lines. Each of these can drive down circuit component counts and thereby reduce node costs in addition to making node design simpler. However, off-chip peripherals may still be desired if higher performance is designed (e.g., higher ADC resolution or memory size). Quality documentation, an integrated development environment (IDE), and in-system programming capabilities provided by the manufacturer or design community can further ease the job of a wireless node designer.

Important selection criteria for off-chip ADCs include resolution, speed, and power consumption. Resolutions can range from 8- to 24-bits with most structural monitoring applications using 12- or 16-bit ADCs. High sampling rates are less of an issue for structural applications with low-natural frequencies, but ultrasonic monitoring can require sampling in the MHz range. High sampling rates and resolution require greater amounts of power, and therefore should be chosen as low as possible. Other desirable features that may be available include low-power sleep modes, high data-transfer rates, and a low supply-power voltage. Additionally, a wireless node designer may want to consider ADCs with inputs capable of negative and positive voltages, integrated signal conditioning, and multiple sample-and-hold circuits with multiplexing.

Wireless radio modules (i.e., mountable transceivers) that are easily interfaced with the node's MCU reduce the need for an RF engineer to aid in the wireless node design. These modules most often operate on the 900 MHz or 2.4 GHz ISM license-free radio frequencies using the IEEE 802.15.4 standard for the physical and data link layers. However, radios operating with other standards including IEEE 802.10 (the foundation for Bluetooth) and IEEE 802.11 (the foundation for WiFi) are available. Once again, power is a key selection criterion, which is in a trade-off with transmission range and receiver sensitivity. In fact, the power requirements of the radio are typically the greatest for the entire node. Proper antenna selection can increase communication reliability and range without increased power consumption. 'Smart antenna' designs that can actively control output power and signal direction are an active area of research. Well-timed sleep modes in which the receiver is shut off can save considerable power. A node designer's job can be eased by modules with embedded firmware that automatically implement the lowest levels of the RF stack, relieving the MCU of some computation load.

16.3.2 Wireless sensor families

Application considerations will determine which type of wireless sensor should be used in a wireless structural monitoring system. Power consumption will be less of an issue for short-term deployments of a few days while low power consumption and power harvesting will almost certainly be required for long-term installations. The physical quantity to be measured will also affect sensor selection. While the node can be designed from scratch, it would be most advantageous to use ready-to-deploy, all-in-one commercial units if and only if available devices meet project requirements. More flexible wireless sensor modules, such as the 'mote' family, enable the designer to choose the desired transducer, design the power management circuitry, modify the embedded firmware, and fabricate an assembly enclosure for the specific application. If the greatest amount of flexibility is required, yet the designer wishes to not design a unit from the ground up, academic prototypes may be purchased that bring additional features such as advanced sensing (e.g., piezoelectrics[41,42]), feedback control,[43] and the greatest amount of extensibility. In 2006, Lynch and Loh[18] provided a review of available wireless sensors for structural monitoring at the time, but since technology advances so quickly, newer and more advanced wireless sensor models now exist. Regardless of the family of wireless sensors the user decides to choose from, it will be important that the datasheet of each device being considered is carefully studied. The following datasheet specifications are commonly misread and require intense scrutiny: active versus sleep power consumption along with the time anticipated to be spent active and sleep; maximum theoretical wireless data rate versus the realistic rate at which measurements can be reliably streamed; ADC resolution versus effective resolution including effects by circuit noise; transducer signal bounds, sensitivity, and signal conditioning circuitry; and wireless communication range in environments such as line-of-sight versus lightly or heavily constructed facilities. The remainder of Section 16.3.2 will compare and contrast three main families of wireless sensors currently in use (Fig. 16.3) in an effort to show readers important traits that should be broadly applicable to future generations of devices.

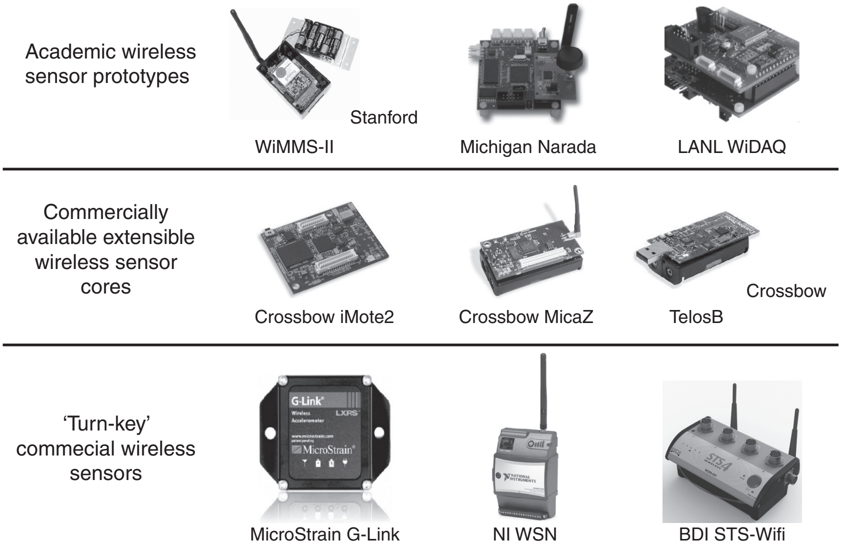
Academic wireless sensor prototypes
Stanford
WiMMS-II
Michigan Narada
LANL WiDAQ
Commercially available extensible wireless sensor cores
Crossbow iMote2
Crossbow MicaZ
Crossbow
TelosB
'Turn-key' commecial wireless sensors
MicroStrain G-Link
NI WSN
BDI STS-Wifi

16.3 Wireless sensor families and selected examples (G-Link photo courtesy of LORD-MicroStrain, NI WSN photo courtesy of National Instruments and BDI STS-WiFi photo courtesy Bridge Diagnostics)

Commercial wireless sensors

Two classes of commercial wireless sensors exist: ready-to-deploy all-in-one units (Plate XIVe through g) and extensible wireless sensor cores (Plate XIVf though g). All-in-one wireless nodes, such as those found in the MicroStrain G/V-Link line,[44] Bridge Diagnostics Inc. (BDI) STS-WiFi – Wireless Structural Testing Systems,[45] National Instrument (NI) WSN line,[46] the Ohm zSeries,[47] and WirelessHART products by companies like Siemens,[48] are robust easily deployed 'turn-key' solutions to wireless monitoring. Each self-contained unit includes a power source, transducer, signal conditioning circuitry, antenna, wireless radio, and computational core. The more popular units have acquired a large user base whose collective experience can be leveraged. In order to maintain an easy-to-use system, many features such as maximum sampling/data rate, in-network data processing, power harvesting capabilities, power management, design flexibility, and multi-hop capabilities are limited. These shortcomings are offset by their ease of use for inexperienced users, and by the large user base whose collective experience can be leveraged by a novice user.

When the user has specific design requirements not met by commercial turn-key solutions, commercially available wireless sensor cores (Plate XIVf though g in colour section between pages 294 and 295) in colour section between pages 294 and 295 can be used to 'jump-start' development of the entire sensor node. These units typically do not include protective housings, transducers, or power management circuitry; as such, peripherals must be designed or selected to bring this functionality. The 'mote' line of devices originating from Berkeley and manufactured by companies such as Intel, Crossbow, and MEMSIC provide the user more flexibility through an open source hardware and software design. The model in this line that has seen the most extensive use in the structural monitoring field is the iMote2,[49] due to its embedded operating system (OS) specifically designed for WSNs, its extensibility through the use of daughter boards (e.g., the SHM-A boards[50] with onboard accelerometer and controllable signal conditioning), and its significant computational capabilities. In the developing field of wireless SHM, commercial units are not always available for immediate purchase to meet a project's needs. As such, the academic community and commercial sector have developed custom nodes, bringing previously unavailable features to the field.

Academic prototypes

Researchers in academia are interested in pushing the vanguard of WSN and have developed nodes with unique features not found in commercial wireless sensors at the time of their development. The costs of working with cutting edge academic prototypes are the smaller user base, required programming skills, and equipment needed for assembly and debugging. The *WiMMS* sensor family developed at Stanford in the late 1990s was one of the earliest wireless sensor families for SHM. WiMMS led to the development of the *Narada* at the University of Michigan. The *Narada* was the first wireless node for civil engineering applications with wireless feedback control capabilities in the original design. Both the *WiMMS Sensor* and the *Narada* featured swappable radio modules so that range, data rate, and power consumption could be tailored to the field application at hand. The wireless node developed by Bennet *et al.*[51] was designed to be embedded into flexible asphalt to measure strain and temperature. Mitchell *et al.*[52] proposed a wireless node with two wireless transceivers; one to talk to low-power nodes in each cluster and the other transceiver to communicate over long distances with other clusters. The WiDAQ developed at Los Alamos National Lab[53] features a unique daughter board capable of measuring the impedance of seven piezoelectric sensors per node. Recently developed at the University of Michigan, the *Martlet* wireless node features a dual core design that allows for real-time data processing or feedback control algorithms to run on a dedicated coprocessor with access to the internal ADC and DAC. This coprocessor leaves the main processor to handle such tasks as collaboration with other nodes. Each of these prototypes has brought something new to the field of wireless SHM, features that will likely be seen in future commercial products. Academic prototypes are similar to commercial devices, e.g. use of the IEEE 802.15.4 communication standard and 16-bit or greater ADCs. The prototype units introduced features such as feedback control, novel transducers, and dual core computations that may eventually find their way into commercial units, as was seen with corrosion sensing.[54]

16.3.3 Wireless sensor peripherals

Besides the node core (Plate XIVf, see colour section between pages 294 and 295), the designer or user of a wireless sensing node needs to consider attached peripherals such as transducers, signal conditioners, and energy harvesters.

Transducers

Transducers convert the physical measurand into an electrical signal that can then be converted to a digital signal. This is true for wired or WSN; as such, WSN can measure the same phenomenon as their wired counterparts, albeit sometimes in a different way as to minimize power consumption. For example, when measuring acceleration, microelectromechanical systems (MEMS) accelerometers are most often used for WSN due to their small size, low cost, and low power requirements. Displacements can be measured with LVDT or potentiometric displacement transducers (e.g., string potentiometers and axial potentiometers). Low power integrated circuits (IC) exist for measuring temperature, humidity, and light levels, often with their own signal conditioning and ADCs. Other transducers that can be interfaced with certain wireless sensors are wind vanes, anemometers, piezoelectrics, strain gages, and proximity detectors. The wide range of low-cost transducers that can be integrated with wireless sensors has led to even greater interest in wireless monitoring systems.

Signal conditioners

The theory behind signal conditioning does not change when using wireless sensors, but new practical considerations arise including power consumption, usable voltage levels, design complexity, and circuit size. Depending upon the type of transducer used, various types of signal conditioning will be required before analog-to-digital conversion. Many transducers now available on the market (e.g., MEMs accelerometers and IC temperature sensors) contain much of the analog signal conditioning required, and output a signal compatible with the most popular ADCs. Even if a transducer such as an accelerometer could be directly integrated, signal conditioning for amplification and anti-alias filtering may be desired and used. If using an older transducer or a newer one without integrated signal conditioning (e.g., metal foil strain gauges), analog circuitry will be required to convert the signal produced by the transducer into a low-noise voltage signal that is within the bounds of the ADC (most commonly 0–3.3 V or 0–5 V). Since wireless sensors are often designed to be as small as possible, the amount of space taken up by signal conditioning on the printed circuit board (PCB) should be minimized. Large analog signal conditioning circuits can often be replaced or minimized by using digital signal processing techniques, such as over sampling, or by using mixed signal ICs (i.e., ICs that process both analog and digital signals) such as the QuickFilter Technologies QF4A512[55] ADC with programmable gain amplifiers, and programmable analog and digital filters. This IC was successfully used on the 'SHM-H sensor board',[56] a peripheral board designed for use with the iMote2, with the capability to measure accelerations with high sensitivity. Less sophisticated boards, but with similar intent, have been created for interfacing strain gages with the MICA Mote,[57] and strain gages and accelerometers with the Tmote Sky wireless sensor core.[58] The designer of a wireless SHM system can simplify the selection process by choosing a commercial wireless node with integrated signal conditioning or can meet their application requirements by designing custom signal conditioning.

Energy management and harvesters

One of the fundamental advantages of WSNs is the absence of wires that transmit signals throughout the network. However, the 'last wire' (i.e., the power supply wire) to each sensor is the most difficult to do away with. In addition to designing a low-power node core, judicious selection of energy harvesters and batteries can extend the uptime of the node, or enable longer sampling periods. The estimates provided in Table 16.4 show general usage scenarios and limitations of commercial energy harvesters and battery chemistries. It should be noted that manufacturers typically specify energy densities with respect to a typical load current and environmental temperature. Large loads and winter temperatures can significantly decrease battery energy capacity.

Aiming to further increase the availability of energy, the research community is pushing the frontiers in two areas: power efficiency and power harvesting. Wireless node energy efficiency can be improved by selecting low-voltage components, selecting components with sleep or low-power modes, and implementing autonomous power switching of high power components (e.g., transducers). Regardless of energy efficiency, long-term deployments of WSNs will require the nodes to be recharged. Since manual replacement of batteries is expensive, the implementation of an energy harvesting system that can power a node directly or can be used to charge rechargeable batteries is preferred. Long-term field deployments of structural monitoring WSN have successfully scavenged power from vibration,[59] wind,[28] light (e.g., solar),[36] and ambient[60] or applied[61] EM energy (i.e., RF). Commercial WSN vendors are beginning

Table 16.4 Energy densities of common WSN power sources

Energy harvesters	Power density	Battery chemistry	Volumetric density $(W\,Hr/L)$
Solar (outdoors)	15 mW/cm^2 (sunny)	Alkaline-MnO$_2$*	347
	0.15 mW/cm^2 (cloudy)	Sealed lead acid	90
Solar (indoors)	0.006 mW/cm^2 (ambient light)	NiCd	80–105
	0.57 mW/cm^2 (task light)	NiMH	175
Vibrations	0.01–0.1 mW/cm^3	Li-ion	200
Acoustic noise	3E-6 mW/cm^2 at 75 dB	Li-polymer	300–415
	9.6 mW/cm^2 at 100 dB		
Applied RF	2–8 mW[61]		

* Non-rechargeable

Source: Adapted from Reference 65.

to market integrated energy harvesting, related products, and consulting services centered on energy management in WSN.[62,63] If the WSN designer must design a custom energy harvesting solution, reference texts such as Beeby and White's *Energy Harvest for Autonomous Systems*[64] provide details on each mode of energy harvesting and design guidelines. By using energy efficient wireless sensors and an appropriately designed energy harvesting system, WSN can be deployed maintenance free for years.

16.4 Wireless sensor network software

There are two types of software running in wireless SHM deployments: the embedded firmware running on the wireless nodes and the software running on the server handling data presentation, processing, and archiving. This section will focus on the embedded firmware because the server-side software for wireless SHM is not much different from the counterpart for wired SHM. Embedded firmware designs can be broken down into three layers (Plate XIVg, see colour section between pages 294 and 295): the OS, middleware, and application software. These layers sit on top of the node hardware. Ideally, these layers should be independent of each other, with well-defined interface abstractions. Delineating embedded firmware in this manner has the benefit of greater amounts of code reuse, reduced development time, and decreased code maintenance costs.

16.4.1 Operating systems (OS)

The software that makes up the OS on a wireless sensor provides system management features and hardware interfaces to the upper middleware and application layers. It should be noted that the OS on a wireless node is significantly different from the OS on a consumer PC (e.g., Windows, MacOS, and Linux) due to the limited memory and computational capability on each node. The design or selection of the OS task scheduler, the software that determines when tasks are executed based on priority and timing, requires careful consideration. Since only one task can run on the processor at any given instant, the OS must be able to preempt tasks (i.e., interrupt a lower priority task to allow a higher priority task to complete) as quickly as possible by moving the current state of the preempted task into temporary memory and allocate resources for the preempting task. This feature allows an MCU to execute higher priority applications quicker in the middle of longer lower priority applications instead of having to wait for the first application to complete. However, task preemption can lead to system failures such as deadlock and task priority inversion. The former causes the processor to 'freeze' and can be mitigated by the strategies outlined in Reference 66. The latter famously led to a failure of the NASA Mars Pathfinder spacecraft; fortunately, the error was discovered and fixed through a remote system upgrade.[67]

A robust task scheduler and the ability to perform remote system upgrades are just two of many features an embedded OS should contain. The OS should be as memory efficient as possible, since MCUs typically used in the design of wireless sensor nodes have limited memory compared to larger computing systems, such as PCs. Just as in hardware design, the software design must always consider power consumption. The processor should go into a low-power idle or sleep state after all tasks in the queue have completed and wake again when an interrupt occurs. The OS is often selected, and not designed, by the designer of the WSN. As such, the OS should be well documented and easy for the WSN designer to implement and/or develop the middleware and application layers. Besides a well-documented application programming interface (API), firmware development time will be shortened if the OS has hardware abstraction layers (HAL) for a wide variety of target processors, a strong community user base, reliable professional support, and the ability to write applications in a popular programming language (e.g., C/C++).

The ubiquity of embedded systems has led to the development of a wide range of embedded OSs. Since nearly instantaneous response to external events such as measurement sampling and radio transmissions are critical for wireless sensors, real-time operating systems (RTOS) have become popular for wireless sensors. An RTOS can guarantee certain capabilities within specified time constraints and should autonomously handle common system failures. FreeRTOS[68] and the Micrium RTOS[69] are open source RTOS that are available for free, allow the user to modify the source code, and have become popular for WSN. A commercial RTOS, such as Keil RTX[70] for ARM processors and Wind River VxWorks[71] developed by Intel, is extensively used in industry and provides professional support and a richer and more robust feature set. All of these embedded RTOSs are multi-threaded. While not considered an RTOS, TinyOS[72] was developed specifically for WSN and is uniquely programmed using the nesC programming language, a derivative of C. Extra care must be taken when using a non-RTOS to ensure data collection is synchronized across the network and time-critical tasks (e.g., interrupts associated with feedback control for structural excitation) are executed with minimum jitter (i.e., small amounts of delay from when the task should have been executed to when it is actually executed). These issues have been addressed with a well-defined middleware[73] in the iMote 2 sensors running TinyOS.[28,50,74] Unfortunately, TinyOS is not multi-threaded, which is another limitation. The complexity, expense, and memory requirements associated with an OS are not always required, in which case a simple interrupt-based state machine along with a HAL can be custom developed. This strategy has been successfully employed on the *Narada* wireless sensor with a low-power 8-bit MCU and only 128 kB of external memory[75] compared to the 32-bit processor on the iMote 2.0 with 64 MB of memory running TinyOS.[76] A state-machine strategy can also be properly designed with interrupts so that the embedded firmware is effectively multi-threaded, yet still capable of real-time operation.

16.4.2 Middleware

Middleware is a software link between the OS and the application layer. It is intended to simplify the job of the application designer and to provide a wide variety of functionality. Wireless boot loaders are desirable because they allow remote firmware upgrades to the WSN, and can even allow software 'agents' to be dynamically distributed throughout.[77,78] Since the IEEE 802.15.4 wireless transmission protocol (see Section 16.2) has no prescribed network layer for handling packet failure, middleware is required to correct these failures in the most efficient way, based on the WSN topology. As has been common to all aspects of WSN discussed in this chapter, middleware can improve energy efficiency, by scheduling the use of low-power 'sleep modes' and duty cycling the radio receiver as discussed in Section 16.2 for TDMA wireless protocols. Additional energy can be saved by reducing the number of bits wirelessly transmitted by compressing the data to be sent using a lossless compression algorithm.[79] Although structural monitoring WSN are relatively static, a method should still exist for new units to be added to the network, or existing units upgraded. Novel techniques for resource allocation include: adaptive fidelity algorithms, in which nodes are near an 'important event' sample with greater resolution than those far away;[80] and dynamic allocation of computation resources using a buyer/seller framework.[81]

Message routing is an important middleware feature because it determines the reliability and efficiency of communications. Message routing in single-hop and multi-hop network architectures is shown in Plate XII. A multi-hop strategy, i.e., one in which the radio output power is reduced so the signal reaches only the closest node in a path to the destination, can be employed to minimize each node's transmission power. The area under the curves in Figure 16.4 are analogous to the amount of power required to transmit over the distance shown for the single-hop configuration (dashed) and multi-hop (dotted). If n transmissions are used to cover a range R, then the reduction in total transmission power is proportional to R^2/n. However, in practice, choosing the correct transmission power, if selectable at all, is a difficult task to accomplish reliably. Additionally, the power saving advantage needs to balance the increased latency associated with each 'hop' the message makes and the exponential decrease in reliability with respect to the number of 'hops,' which would increase power consumption due to many re-transmissions.

Time synchronization of the data collected by all the nodes in the WSN is an inherent challenge with wireless sensors, and is best achieved with effective middleware. In effect, each node maintains its own clock. This is in stark contrast to wired monitoring systems, where the data sampling for all sensors is triggered by the same clock channel. The presence of multiple clocks brings a unique challenge to WSN: a means to synchronize all of the nodal clocks such that an agreement on a common time basis is necessary. De-synchronization can occur on the network level due to network latency and on the hardware level due to gradual drifts of a node's clock commonly provided by a low-cost crystal. Clock drift can be reduced by

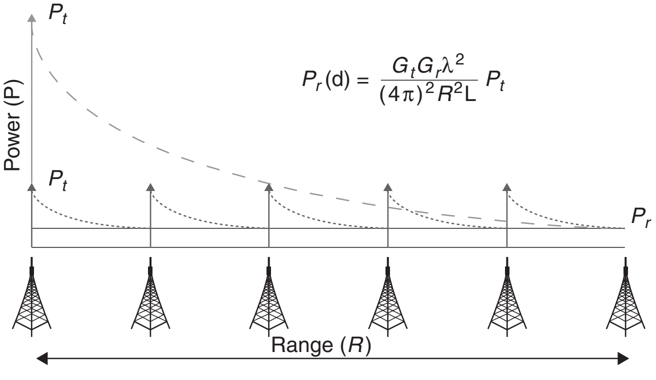
P_t
$P_r(\mathrm{d}) = \frac{G_t G_r \lambda^2}{(4\pi)^2 R^2 \mathrm{L}} P_t$
Power (P)
P_t
P_r
Range (R)

16.4 Power usage in multi-hop networks.

using a more expensive high quality crystal or a thermally corrected crystal that draws additional power. If no ‘hops’ are required to transmit from the network coordinator to all the nodes, a simple beacon can be used to synchronize the network to within $30\ \mu s$.[82] Although synchronized, all the nodes in the network are delayed by an unknown amount from the coordinator’s timing due to radio latency on the order of 10 ms. Multi-hop mesh networks require a more complex strategy such as the flooding time synchronization protocol[83] that quantifies the stochastic delay in each link of the WSN.

The most extensive middle package for SHM was developed by Nagayama, *et al.*[73] for the iMote2 running TinyOS, and includes features such as reliable data transfer, network data aggregation, and sensor synchronization. All of the middleware solutions deployed should share a common application interface so that the application design can effectively utilize the provided features.

16.4.3 Application software

The application software embedded in the WSN is significantly different from the applications that run on a typical PC. While the available computational and memory resources might be equivalent to a PC, they are distributed across all the nodes in the network, as schematically shown in Fig. 16.5; therefore, the applications must also be distributed. Embedded applications must be efficient in terms of processor cycles, memory, and

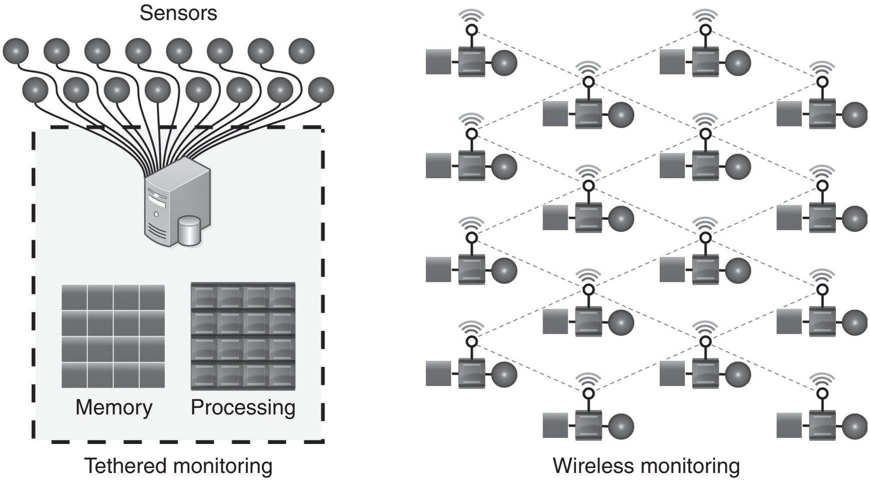

16.5 Comparison of network wide capabilities, wired versus wireless.

energy. Often, only a single application runs on each node due to limited local resources, while a multitude of different applications run simultaneously across the WSN. The ultimate goal of WSN applications is similar to those for wired structural monitoring systems (e.g., data management, damage detection, system ID, and even structural control). The local data processing at the node is a major paradigm shift from wired sensor networks. Important considerations for application designers include accuracy, speed, power efficiency, wireless bandwidth usage, and end-user usability.

In many structural monitoring systems, large amounts of data are collected, but only key characteristics are needed by the user. This disparity necessitates automated methods for data processing and management. For wireless impedance-based SHM the time-history data are converted to the more sparse frequency domain, which is then transferred to the site repository for future processing and analysis.[53] Since the ability to compress data by domain transformations is not always possible, the data repository can direct the method by which the WSN relays the data in real-time depending on whether raw or pre-processed data is required.[84]

When the goal of a wireless SHM installation is damage detection, the analysis can take place autonomously, relaying only the network's prognosis (damage versus undamaged). Automated wireless structural damage detection was first proposed by Straser and Kiremidjian, who used the Arias intensity computed at each node using local acceleration data as an indirect method to detect the energy dissipated as a component in the structure is damaged during an earthquake.[17] Developed for automated damage detection application to situations other than earthquakes, ARX (autoregressive with exogenous input) models have been embedded in a WSN and the magnitude of the residual of the coefficients for nominal can be used to identify the presence of damage.[85] Instead of using global vibration characteristics to detect damage in concrete structures, displacement measurements can be autonomously compared to embedded damage index models to provide estimates of local structural damage.[86]

An entire model of the system can be computed from vibration data using a combination of in-network computing and server-side computing. One realization use a node's local response data to compute Markov parameters, which are then sent to the base station using significantly less bandwidth than would be required to send raw data. The Markov parameters are then input into an ERA.[87] The algorithm successfully identified system parameters of an auditorium balcony using less wireless bandwidth than other strategies. These examples show that many traditional damage detection and system ID algorithms can be distributed across the computational capabilities of the nodes in the wireless network, thus increasing scalability compared to wired systems with central data processing centers.

The lessons learned from developing wireless structural monitoring systems have been extended to wireless feedback control systems. Structural control was first proposed in 1972, but has seen only limited use due to installation costs and reliability concerns.[88] Augmenting these initial control systems with wireless telecommunications has been shown to lead to improved performance over completely decentralized systems, without the added cost of cabling associated with centralized controllers. Due to bandwidth limitations and latency associated with wireless communication, novel distributed control algorithms were developed that utilize the embedded computing available at each node and communicate with other nodes as little as possible.

Wireless control networks are well suited for large systems with many actuators and sensors such as semi-active control, i.e. actuation involves changing stiffness and damping properties of structural elements instead of actively applying a force. Initial research on wireless semi-active control systems considered full measurement feedback at slow sampling rates or fully decentralized control at high sampling rates.[40] Building on existing optimal control theory, the sub-optimal clip-linear quadratic regulator has been an extensive topic of research, along with decentralization of the associated state estimator. One method to strategically utilize wireless bandwidth and achieve performance near that of full state feedback is to use the error between two parallel estimators on each node and request asynchronous measurement updates from other nodes in the network when the error reaches a threshold.[89] The robust H-∞ control law can be applicable by homotopically transforming the feedback matrix to yield sparsity aligned with the sensor sub-networks.[90] In this way, the advantage of feedback is achieved by communicating feedback data on different, non-interfering, wireless channels for each sub-network. Less traditional control techniques, but well-fitting to agent-based wireless networks, are the class of game-theory inspired actuator resource allocation algorithms. These have been experimental validated with large-scale structural-control experiments[91] and can account for the inherent non-linear characteristics of semi-active control devices, a feature not present in clipped-optimal controllers.[92] Most recently, a wireless control and monitoring system has been developed that unifies structural monitoring with feedback semi-active vibration control with a graphical interface for end users[93] for maintenance and management.

Researchers are continuing to develop distributed algorithms for WSN that are inspired by, but different from, those found in parallel supercomputers due to the significant communication latency in wireless networks. Well-developed applications interfaced with the appropriate middleware, OS, and hardware yield a WSN that can perform as well as a comparable wired monitoring system with new features, decreased costs, and reduced installation time.

16.5 Conclusion and future trends

Wireless structural monitoring solutions are rapidly maturing. Early research and development efforts, mainly in hardware development, focused on overcoming the challenge of reliably deploying WSN on structures. These technologies have been tested and deployed in the field on buildings,[94–96] bridges,[28, 97,98] and wind turbines.[99] The early efforts paid off and have led to commercial 'turn-key' solutions for SHM for a limited, yet important, set of applications.

More novel systems require the application of the principles covered in this chapter to design, select, and develop a custom WSN hardware, software, and network. A significant portion of this chapter covered key options and criteria for designing or selecting the network architecture, wireless hardware, and embedded software. Single and multi-hop networks were presented as the main network architectures that supported signals on a variety of different frequencies in the RF spectrum using any number of popular wireless standards. It was shown that the embedded firmware will consist of an OS (or a simple custom solution), middleware to aid with data handling and management, and application software to present meaningful data to the network operator. The development of wireless hardware will also consist of a transducer to measure the desired structural response with appropriate signal conditioning and power management circuitry. This design process can be jumpstarted by using a commercial wireless module. While accuracy, usability, and cost play an important role, the power consumption and data handling will make or break the final design.

Currently, WSN are limited by their effective over-the-air data rates and their strong dependency on batteries. Current and future research efforts aim to exploit the in-network data processing capabilities of WSN to make them even more attractive (i.e., more scalable and power efficient). When considered as an aggregate, the limited computation capabilities of each node are a significant computational resource and can be used to autonomously execute sensor fault detection,[100] data compression,[101] model updating,[24] system ID,[87] and damage detection.[102] Over the past two decades, transistor density, and thereby computation speed and efficiency, has increased at an exponential rate, while battery energy density has hardly increased linearly.[103] As such, development of more efficient energy harvesting systems is a prime area of needed research. Innovative researchers have been able to harvest energy through non-resonant vibration (e.g., traffic)[104] and optimally harvest energy in a distributed manner.[105]

With today's relatively high rate at which data can be processed, feedback control (e.g., using semi-active dampers) and active sensing (e.g., PZT and ultrasonics) are exciting extensions to WSN. In order for all of the developments outlined in this chapter to be used commercially, 'softer' research efforts will have to focus on ease of use of WSN and how to make the advantages of WSN so apparent that the paradigm will shift away from wired sensing and to ubiquitous wireless structural monitoring systems.

16.6 Acknowledgments

The authors of this chapter would like to acknowledge the generous support provided by the National Science Foundation (NSF) through grant numbers CCF-0910765 and CMMI-0846256. The authors would also like to gratefully acknowledge the generous support offered by the US Department of Commerce, National Institute of Standards and Technology (NIST) Technology Innovation Program (TIP) under Cooperative Agreement 70NANB9H9008. This work was supported in part by the US Office of Naval Research (Contracts N00014–05–1-0596 and N00014–09-C0103). Finally, the writing of this chapter was partially supported by the National Research Foundation of Korea Grant funded by the Korean Government (MEST) (NRF-2011–220-D00105(2011068.0)).

16.7 References

1. R. M. Moss and S. L. Matthews (1995), 'In-service structural monitoring a state-of-the-art review', *The Structural Engineer*, vol. **73**, no. 2, pp. 23–31.
2. R. D. Nayeri, S. F. Masri and A. G. Chassiakos (2007), 'Application of structural health monitoring techniques to track changes in retrofitted building based on ambient vibration', *Journal of Engineering Mechanics*, vol. **133**, no. 12, pp. 1311–1325.
3. H. R. Zhou, Y. Q. Ni and J. M. Ko (2006), 'Analysis of structural health monitoring data from the suspension Jiangyin Bridge', in *Third European Workshop on Structural Health Monitoring*.
4. P. Moyo, J. M. W. Brownjohn and P. Omenzetter (2004), 'Highway bridge live loading assessment and load carrying capacity estimation using a health monitoring system', *Structural Engineering & Mechanics*, vol. **18**, pp. 609–626.
5. J. P. Broomfield, K. Davies and K. Hladky (2002), 'The use of permanent corrosion monitoring in new and existing reinforced concrete structures', *Cement and Concrete Composites*, vol. **24**, no. 1, pp. 27–34, February.
6. M. Celebi (2002), 'Seismic instrumentation of buildings (with emphasis on federal buildings)', *Technical Report No. 0–7460–68170*. United States Geological Survey (USGS), Menlo Park, CA.
7. Z. X. Li, T. H. T. Chan and J. M. Ko (2001), 'Fatigue analysis and life prediction of bridges with structural health monitoring data – Part I: Methodology and strategy', *International Journal of Fatigue*, vol. **23**, no. 1, pp. 45–53.

8. D. S. Carder (1937), 'Observed vibrations of bridges', *Bulletin of the Seismological Society of America*, vol. **27**, no. 4, pp. 267–303, October.
9. J. M. W. Brownjohn (2007), 'Structural health monitoring of civil infrastructure', *Philosophical Transactions of the Royal Society A*, vol. **365**, no. 1851, pp. 589–622.
10. C. A. Trutanich, P. B. Echeverria and A. Khorasanee (2011), 'Draft Ordinance Amending Articles 1 and 8 of Chapter IX of the Los Angeles Municipal Code', Los Angeles, CA.
11. B. A. Bolt (2001), 'Seismic instrumentation of bridges and dams: History and possibilities', in *Proceedings of the Instrumental Systems for Diagnostics of Seismic Response of Bridges and Dams*, Consortium of Organizations for Strong-Motion Observation Systems, Richmond, CA, 15 January 2001.
12. R. O. Hamburger (2000), SAC Joint Venture and United States Federal Emergency Management Agency, *A Policy Guide to Steel Moment-Frame Construction*, FEMA, 354. Washington DC.: Federal Emergency Management Agency, p. 36.
13. S. N. Pakzad, G. L. Fenves, S. Kim and D. E. Culler (2008), 'Design and implementation of scalable wireless sensor network for structural monitoring', *Journal of Infrastructure Systems*, vol. **14**, no. 1, pp. 89–101.
14. W. J. Staszewski, C. Boller and G. Tomlinson (2004), *Health Monitoring of Aerospace Structures: Smart Sensor Technologies and Signal Processing*. West Sussex, England: John Wiley & Sons Ltd.
15. P. E. Hess (2007), 'Structural health monitoring for high-speed naval ships', in *6th International Workshop on Structural Health Monitoring*, Stanford, CA, 11–13 September, pp. 3–15.
16. S. B. Slaughter, M. C. Cheung, D. Sucharski and B. Cowper (1997), 'State of the Art in Hull Monitoring Systems', *Report No. SSC-401*. Ship Structure Committee, Washington, DC.
17. E. G. Straser, A. S. Kiremidjian, T. H. Meng and L. Redlefsen (1998), 'Modular, wireless network platform for monitoring structures', in *Proceedings of the 16th Interational Modal Analysis Conference (IMAC)*, vol. **1**, Santa Barbara, CA, February 1998, pp. 450–456.
18. J. P. Lynch and K. J. Loh (2006), 'A summary review of wireless sensors and sensor networks for structural health monitoring', *The Shock and Vibration Digest*, vol. **38**, no. 2, pp. 91–128.
19. Y. Zhang, M. Kurata, J. P. Lynch, G. van der Linden, S. Hassan and A. Prakash (2012), 'Distributed cyberinfrastructure tools for automated data processing of structural monitoring data', in *Proceedings of SPIE 8347, Nondestructive Characterization for Composite Materials, Aerospace Engineering, Civil Infrastructure, and Homeland Security 2012*, San Diago, CA, 26 April 2012, pp. 1–8.
20. J. M. W. Brownjohn, F. Magalhaes, E. Caetano and A. Cunha (2010), 'Ambient vibration re-testing and operational modal analysis of the Humber Bridge', *Engineering Structures*, vol. **32**, no. 8, pp. 2003–2018, August 2010.
21. Y. F. Kao and J. H. Huang (2008), 'Price-based resource allocation for wireless ad hoc networks with multi-rate capability and energy constraints', *Computer Communications*, vol. **31**, pp. 3613–3624.
22. D. Zhu, J. Guo, C. Cho, Y. Wang and K.-M. Lee (2012), 'Wireless mobile sensor network for the system identification of a space frame bridge', *IEEE/ASME Transactions on Mechatronics*, vol. **17**, no. 3, pp. 499–507.

23. D. Zhu, X. Yi, Y. Wang, K.-M. Lee and J. Guo (2010), 'A mobile sensing system for structural health monitoring: design and validation', *Smart Materials and Structures*, vol. **19**, no. 5, p. 055011, May 2010.
24. A. T. Zimmerman and J. P. Lynch (2009), 'A parallel simulated annealing architecture for model updating in wireless sensor networks', *IEEE Sensors Journal*, vol. **9**, no. 11, pp. 1503–1510.
25. A. T. Zimmerman, M. Shiraishi, R. A. Swartz and J. P. Lynch (2008), 'Automated modal parameter estimation by parallel processing within wireless monitoring systems', *ASCE Journal of Infrastructure Systems*, vol. **14**, no. 1, pp. 102–113.
26. A. T. Zimmerman, J. P. Lynch and F. T. Ferrese (2010), 'Market-based resource allocation for distributed data processing in wireless sensor networks', *ACM Transactions on Embedded Computing Systems (TECS)*, vol. **12**, no. 3, pp. 1–28.
27. S. Kim, S. Pakzad, D. Culler, J. Demmel, G. Fenves, S. Glaser and M. Turon (2007), 'Health monitoring of civil infrastructures using wireless sensor networks', *Proceedings of the 6th International Conference on INFORMATION PROCESSING in Sensor Networks*. ACM, Cambridge, Massachusetts, USA.
28. J. W. Park, S. Cho, H.-J. Jung, C.-B. Yun, S. A. Jang, H. Jo, B. F. J. Spencer, T. Nagayama and J.-W. Seo (2010), 'Long-term structural health monitoring system of a cable-stayed bridge based on wireless smart sensor networks and energy harvesting techniques', in *Proceedings of the 5th World Conference of Structural Control and Monitoring*, Tokyo, Japan, 7 March 2010, pp. 1–6.
29. C. E. Shannon (1928), 'A mathematical theory of communication', *Bell Systems Technical Journal*, vol. **27**, pp. 379–423, 623–656.
30. D. K. Sohraby, D. Minoli and T. Znati (2007), *Wireless Sensor Networks*. Hoboken, NJ: John Wiley & Sons, Inc. p. 307.
31. Cisco Systems Inc.(2007), '20 Myths of Wi-Fi Interference: Dispel Myths to Gain High-Performing and Reliable Wireless', San Jose, CA.
32. H. Zimmermann (1980), 'OSI reference model–the ISO model of architecture for open systems interconnection', *Communications, IEEE Transactions on*, vol. **28**, no. 4, pp. 425–432.
33. LAN/MAN Standards Committee of the IEEE Computer Society (2006), 'IEEE Standard for Information technology – Telecommunications and information exchange between systems- Local and metropolitan area networks – Specific requirements–Part 15.4: Wireless MAC and PHY Specifications for Low-Rate WPANs', New York, NY.
34. IEEE (2006), '802.15.4: Standard for Information technology–Telecommunications and information exchange between systems–Local and metropolitan area networks–Specific requirements Part 15.4: Wireless Medium Access Control (MAC) and Physical Layer (PHY) Specification.' IEEE Standards Association, New York, NY.
35. V. A. Kottapalli, A. S. Kiremidjian, J. P. Lynch, E. Carryer, T. W. Kenny, K. H. Law and Y. Lei (2003), 'Two-tiered wireless sensor network architecture for structural health monitoring', in *Proceedings of the International Symposium on Smart Structures and Materials*, San Diego, CA, 2 March 2003.
36. M. Kurata, J. Kim, J. P. Lynch, G. W. Van Der Linden, H. Sedarat, E. Thometz, P. Hipley and L. -H. Sheng (2012), 'Internet-enabled wireless structural monitoring systems: Development and permanent deployment at the New Carquinez Suspension Bridge', *Journal of Structural Engineering*, vol. **139**, pp. 1688–1702.

37. B. Peters (2005), ‘Sensing without wires’, *Machine Design*, Cleveland, OH, January 2005.
38. Z. Shelby, C. Bormann and W. online Library (2009), *6LoWPAN the Wireless Embedded Internet*. Chichester, U.K.: John Wiley.
39. D. Chen, M. Nixon, A. Mok and S. (Online Service) (2010), *WirelessHART™ Real-Time Mesh Network for Industrial Automation*. Boston, MA: Springer Science+Business Media, LLC.
40. C. H. Loh, J. P. Lynch, K. C. Lu, Y. Wang, C. M. Chang, P. Y. Lin and T. H. Yeh (2007), ‘Experimental verification of a wireless sensing and control system for structural control using MR dampers’, *Earthquake Engineering and Structural Dynamics*, vol. **36**, no. 10, pp. 1303–1328.
41. E. Ihler, H. Zaglauer and U. Herold-Schmidt (2000), ‘Integrated wireless piezoelectric sensors’, in *Proceedings of SPIE 3991, Smart Structures and Materials 2000: Industrial and Commercial Applications of Smart Structures Technologies, 44*, vol. **3991**, pp. 44–51.
42. T. G. S. Overly, G. Park, K. M. Farinholt and C. R. Farrar (2008), ‘Development of an extremely compact impedance-based wireless sensing device’, *Smart Materials and Structures*, vol. **17**, no. 6, p. 065011.
43. S. Seth, J. P. Lynch and D. M. Tilbury (2005), ‘Wirelessly networked distributed controllers for real-time control of civil structures’, in *American Control Conference, 2005. Proceedings of the 2005*, pp. 2946–2952 vol. **4**.
44. Microstrain Inc., ‘Wireless System Networks | Microstrain’ (2012) Online. Available: http://www.microstrain.com/wireless/systems.
45. Bridge Diagnostics Inc. (2012), ‘*STS WiFi Wireless Structural Testing System*’, Bridge Diagnostics datasheet, Boulder, CO.
46. National Instruments Inc. (2012), ‘Wireless Measurement Device Selection Guide’ (Online). Available: http://sine.ni.com/np/app/main/p/ap/global/lang/en/pg/1/sn/n24:Wireless/fmid/2988/.
47. Omega Engineering Inc. (2012), ‘Wireless Sensors, Transmitters, Receivers, Meters & Controllers’, (Online). Available: http://www.omega.com/toc_asp/subsectionsc.asp?book=DAS&subsection=K01.
48. Siemens A. G. (2012), ‘WirelessHART – Innovation for the process industry’ (Online). Available: http://www.automation.siemens.com/w1/automation-technology-wirelesshart-18957.htm.
49. Crossbow Technology (2007), ‘Imote2 Datasheet, Document Part Number: 6020–0117–02 Rev A’, vol. **2009**, no. 8 October 2007.
50. J. A. Rice and B. F. Spencer Jr. (2008), ‘Structural health monitoring sensor development for the Imote2 platform’, in *Proceedings of the SPIE 6932, Sensors and Smart Structures Technologies for Civil, Mechanical, and Aerospace Systems 2008*, San Diego, CA, 9 March 2008.
51. R. Bennett, B. Hayes-Gill, J. A. Crowe, R. Armitage, D. Rodgers and A. Hendroff (1999), ‘Wireless monitoring of highways’, in *Smart Systems for Bridges, Structures, and Highways*, Newport Beach, CA, March 1-2, Proccedings of the SPIE, Vol. 3671, pp. 173–182.
52. K. Mitchell, N. Dang, P. Liu, V. S. Rao and H. J. Pottinger (2001), ‘Web-controlled wireless network sensors for structural health monitoring’, in *Smart Structures and Materials – Smart Electronics and MEMS*, Newport Beach, CA, March 5-7, Proccedings of the SPIE, Vol. 4334, pp. 234–243.

53. S. G. Taylor, K. M. Farinholt, G. Park, C. R. Farrar, E. B. Flynn, D. L. Mascarenas and M. D. Todd (2009), 'Wireless impedance device for electromechanical impedance sensing and low-frequency vibration data acquisition', *Proceedings of SPIE 7292, Sensors and Smart Structures Technologies for Civil, Mechanical, and Aerospace Systems 2009*, vol. **7292**, pp. 729228–729228–12, March 2009.
54. D. Inaudi and L. Manetti (2009), 'Reinforced Concrete Corrosion Wireless Monitoring System', in *4th International Conference on Structural Health Monitoring on Intelligent Infrastructure (SHMII-4) 2009*, Zurich, Switzerland, 22–24 July 2009, pp. 1–10.
55. Quickfilter Technologies (2009), 'QF4A512 Datasheet.' Quickfilter Technologies Inc., Allen, Texas, p. 67.
56. H. Jo, S. Sim, T. Nagayama and J. B. F. Spencer (2012), 'Development and application of high-sensitivity wireless smart sensors for decentralized stochastic modal identification', *Journal of Engineering Mechanics,* vol. **138**, no. 6, pp. 683–694.
57. L. Liu and F. G. Yuan (2008), 'Wireless sensors with dual-controller architecture for active diagnosis in structural health monitoring', *Smart Materials and Structures*, vol. **17**, no. 2, p. 025016, April 2008.
58. M. J. Whelan and K. D. Janoyan (2008), 'Design of a robust, high-rate wireless sensor network for static and dynamic structural monitoring', *Journal of Intelligent Material Systems and Structures*, vol. **20**, no. 7, pp. 849–863, November 2008.
59. J. Mccullagh, R. L. Peterson, T. Galchev, R. Gordenker, Y. Zhang, J. Lynch and K. Najafi (2012), 'Short-term and long-term testing of a vibration harvesting system for bridge health monitoring', *Proceedings of PowerMEMS*, pp. 109–112.
60. A. Mita and S. Takahira (2004), 'Damage index sensor for smart structures', *Structural Engineering and Mechanics*, vol. **17**, no. 3, pp. 1–23.
61. D. L. Mascarenas, E. B. Flynn, M. D. Todd, T. G. Overly, K. M. Farinholt, G. Park and C. R. Farrar (2010), 'Experimental studies of using wireless energy transmission for powering embedded sensor nodes', *Journal of Sound and Vibration*, vol. **329**, no. 12, pp. 2421–2433, June 2010.
62. Microstrain Inc. (2012), 'MicroStrain Energy Harvesting' (Online). Available: http://www.microstrain.com/energy-harvesting/harvesters.
63. National Instruments Inc. (2012), 'Using Energy Harvesting Devices with National Instruments Wireless Sensor Networks (WSN)'.
64. S. Beeby and N. White (2010), *Energy Harvesting for Autonomous Systems*. Norwood, Mass: Artech House, p. ix, 292 p.
65. M. A. M. Vieira, J. Coelho, C.N., J. da Silva, D.C. and J. M. da Mata (2003), 'Survey on wireless sensor network devices', in *Emerging Technologies and Factory Automation, 2003. Proceedings. ETFA '03. IEEE Conference*, Vol. 1, 16–19 September, pp. 537–544.
66. E. G. J. Coffman, M. J. Elphick and A. Shoshani (1971), 'System deadlocks', *Computing Surveys*, vol. **3**, no. 2, pp. 67–78.
67. G. E. Reeves (1998), 'What Really Happened on Mars?', Pasadena, Calif.
68. Real Time Engineers Ltd. (2012), 'FreeRTOS',. (Online). Available: http://www.freertos.org/.
69. I. Micrium (2012), 'Micrium – RTOS' (Online). Available: http://micrium.com/page/products/rtos.

70. ARM Ltd. (2012), 'Keil Real-time Kernels and Operating Systems' (Online). Available: http://www.keil.com/rtos/.
71. a subsidiary of I. Wind River, 'Wind River VxWorks RTOS', 2012. (Online). Available: http://www.windriver.com/products/vxworks/.
72. Tiny OS Alliance (2012), 'TinyOS Home Page' (Online). Available: http://www.tinyos.net/.
73. T. Nagayama, B. Spencer Jr, K. Mechitov and G. Agha (2009), 'Middleware services for structural health monitoring using smart sensors', *Smart Structures and Systems*, vol. **5**, no. 2, pp. 119–137.
74. T. Nagayama, B. F. Spencer Jr. and J. A. Rice (2007), 'Structural health monitoring utilizing Intel's Imote2 wireless sensor platform', *Proceedings of SPIE–Sensors and Smart Structures Technologies for Civil, Mechanical, and Aerospace Systems 2007*, vol. **6529**, no. 2, p. 6592943.
75. R. A. Swartz, D. Jung, J. P. Lynch, Y. Wang, D. Shi and M. P. Flynn (2005), 'Design of a wireless sensor for scalable distributed in-network computation in a structural health monitoring system', in *5th International Workshop on Structural Health Monitoring,* Stanford, CA, 12–14 September 2005.
76. Crossbow Technology (2012), 'iMote 2 datasheet' (Online). Available: http://bullseye.xbow.com:81/Products/Product_pdf_files/Wireless_pdf/Imote2_Datasheet.pdf.
77. C. Fok, G. Roman and C. Lu (2005), 'Rapid development and flexible deployment of adaptive wireless sensor network applications', in *Proceedings of the 25th IEEE International Conference on Distributed Computing Systems. ICDCS 2005,* 6-10 June, pp. 653–622.
78. B. F. Spencer, M. E. Ruiz-Sandoval and N. Kurata (2004), 'Smart sensing technology: opportunities and challenges', *Journal of Structural Control and Health Monitoring*, vol. **11**, no. 4, pp. 349–368.
79. J. P. Lynch, A. Sundararajan, K. H. Law, A. S. Kiremidjian and E. Carryer (2003), 'Power-efficient data management for a wireless structural monitoring system', in *4th International Workshop on Structural Health Monitoring*, Stanford, CA, 15–17 September 2003, pp. 1177–1184.
80. D. Estrin, J. Heidemann, S. Kumar and M. Rey (1999), 'Next century challenges: Scalable coordination in sensor networks', in *Proceedings of the ACM/IEEE International Conference on Mobile Computing and Networking*, pp. 263–270.
81. A. T. Zimmerman, J. P. Lynch and F. T. Ferrese (2009), 'Market-based computational task assignment within autonomous wireless sensor networks', in *IEEE International Conference on Electro/Information Technology*, Windsor, ON, 7–9 June 2009, pp. 23–28.
82. R. A. Swartz, A. T. Zimmerman, J. P. Lynch, J. Rosario, T. Brady, L. Salvino and K. H. Law (2010), 'Hybrid wireless hull monitoring system for naval combat vessels', *Structure and Infrastructure Engineering*, vol. **8**, no. 7, pp. 621–638.
83. M. Maróti, B. Kusy, G. Simon and Á. Lédeczi (2004), 'The flooding time synchronization protocol', in *Proceedings of the 2nd International Conference on Embedded Networked Sensor Systems*, Baltimore, MD, 3–5 November 2004.
84. D. W. Allen (2004), '*Software for Manipulating and Embedding Data Interrogation Algorithms into Integrated Systems*', Virginia Polytechnic Institute and State University, Blacksburg, VA.

85. J. P. Lynch, A. Sundararajan, K. H. Law, A. S. Kiremidjian, T. W. Kenny and E. Carryer (2003), 'Embedment of structural monitoring algorithms in a wireless sensing unit', *Structural Engineering and Mechanics*, vol. **15**, no. 3, pp. 285–297.
86. T.-C. Hou, J. P. Lynch and G. Parra-Montesinos (2005), 'Local-based damage detection of cyclically loaded bridge piers using wireless sensing units', *Proceedings of SPIE*, vol. **5768**, pp. 85–96.
87. J. Kim and J. P. Lynch (2012), 'Autonomous decentralized system identification by markov parameter estimation using distributed smart wireless sensor networks', *Journal of Engineering Mechanics*, vol. **138**, no. 5, pp. 478–490.
88. B. F. Spencer (1997), 'Controlling buildings: a new frontier in feedback', *IEEE Control Systems Magazine*, vol. **17**, no. 6, pp. 19–35.
89. R. A. Swartz and J. P. Lynch (2009), 'Strategic network utilization in a wireless structural control system for seismically excited structures', *Journal of Structural Engineering*, vol. **135**, no. 5, pp. 597–608.
90. Y. Wang and K. H. Law (2011), 'Structural control with multi-subnet wireless sensing feedback: experimental validation of time-delayed decentralized H_∞ control design', *Advances in Structural Engineering*, vol. **14**, no. 1, pp. 25–39, February.
91. R. A. Swartz, Y. Wang, J. P. Lynch, K. H. Law and C. Loh (2010), 'Experimental validation of market-based control using wireless sensor and actuator networks', *Relation*, vol. **10**, no. 1.59, p. 5825.
92. M. B. Kane, J. P. Lynch and K. Law (2011), 'Market-based control of shear structures utilizing magnetorheological dampers', in *American Control Conference (ACC), 2011*, pp. 2498–2503.
93. G. Heo and C. Kim (2012), 'Designing a unified wireless system for vibration control', *Soil Dynamics and Earthquake Engineering*, vol. **38**, pp. 72–80, July.
94. C. McDonald (2008), 'Performing Structural Health Monitoring of the Olympic Venues Using NI LabVIEW and CompactRIO', *National Instruments Case Study*. (Online). Available: http://sine.ni.com/cs/app/doc/p/id/cs-11279.
95. G. Moschioni, 'Meazza Stadium Uses NI CompactRIO to Usher in a New Frontier in Structural Monitoring', *National Instruments Case Study*. (Online). Available: http://sine.ni.com/cs/app/doc/p/id/cs-10917.
96. M. Ceriotti, L. Mottola, G. Picco, A. Murphy, S. Guna, M. Corra, M. Possi, D. Zonta and P. Zanon (2009), 'Monitoring heritage buildings with wireless sensor networks: The Torre Aquila deployment', in *IPSN '09 Proceedings of the 2009 International Conference on Information Processing in Sensor Networks*, pp. 277–288.
97. M. Kurata, J. P. Lynch, T. Galchev, M. Flynn, P. Hipley, V. Jacob, G. van der Linden, A. Mortazawi, K. Najafi, R. L. Peterson, L.-H. Sheng, D. Sylvester and E. Thometz (2007), 'A Two-Tiered Self-Powered Wireless Monitoring System Architecture for Bridge Health Management', in *Nondestructive Characterization for Composite Materials, Aerospace Engineering, Civil Infrastructure, and Homeland Security 2010*, 2010, San Diego, CA, December 2007.
98. M. V Gangone, M. J. Whelan, M. P. Fuchs and K. D. Janoyan (2007), 'Performance monitoring of a single-span integral-abutment bridge using a dense wireless sensor network', in *Sensor Systems and Networks: Phenomena, Technology and Applications, SPIE International Symposium on Smart Structures and Materials*

& Nondestructive Evaluation and Health Monitoring, San Diego, CA, 18 March 2007, pp. 1–6.

99. R. Swartz, J. Lynch and B. Sweetman (2010), 'Structural monitoring of wind turbines using wireless sensor networks', *Smart Structures and Systems*, vol. **6**, no. 3, pp. 1–8.
100. L. Paradis and Q. Han (2007), 'A survey of fault management in wireless sensor networks', *Journal of Network and Systems Management*, vol. **15**, no. 2, pp. 171–190, March.
101. N. Kimura and S. Latifi (2005), 'A survey on data compression in wireless sensor networks', in *International Conference on Information Technology: Coding and Computing (ITCC'05) – Volume II*, Las Vegas, NV, 4–6 April 2005, pp. 8–13.
102. T. Nagayama, J. B. F. Spencer and J. A. Rice (2009), 'Autonomous decentralized structural health monitoring using smart sensors', *Structural Control & Health Monitoring*, vol. **16**, pp. 842–859.
103. J. A. Paradiso (2005), 'Energy scavenging for mobile and wireless electronics', *Pervasive Computing, IEEE*, vol. **4**, no. 1, pp. 18–27.
104. T. Galchev, J. McCullagh, R. L. Peterson and K. Najafi (2011), 'Harvesting traffic-induced bridge vibrations', in *Solid-State Sensors, Actuators and Microsystems Conference (TRANSDUCERS), 2011 16th International*, no. Figure 1, pp. 1661–1664.
105. J. T. Scruggs (2009), 'An optimal stochastic control theory for distributed energy harvesting networks', *Journal of Sound and Vibration*, vol. **320**, no. 4–5, pp. 707–725.

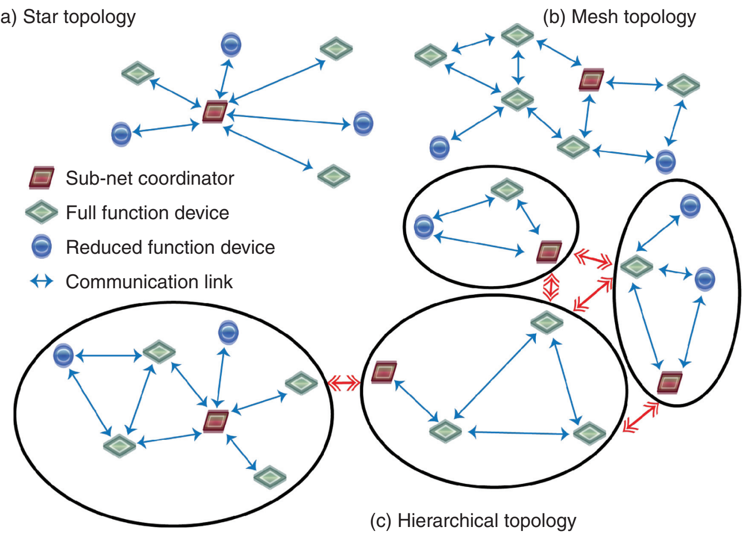
(a) Star topology
(b) Mesh topology
Sub-net coordinator
Full function device
Reduced function device
Communication link
(c) Hierarchical topology

Plate XII (Chapter 16) Typical WSN topologies (*Source*: Adapted from LAN/MAN Standards Committee of the IEEE Computer Society (2006), 'IEEE Standard for Information technology – Telecommunications and information exchange between systems. Local and metropolitan area networks – Specific requirements – Part 15.4: Wireless MAC and PHY Specifications for Low-Rate WPANs', New York, NY.)

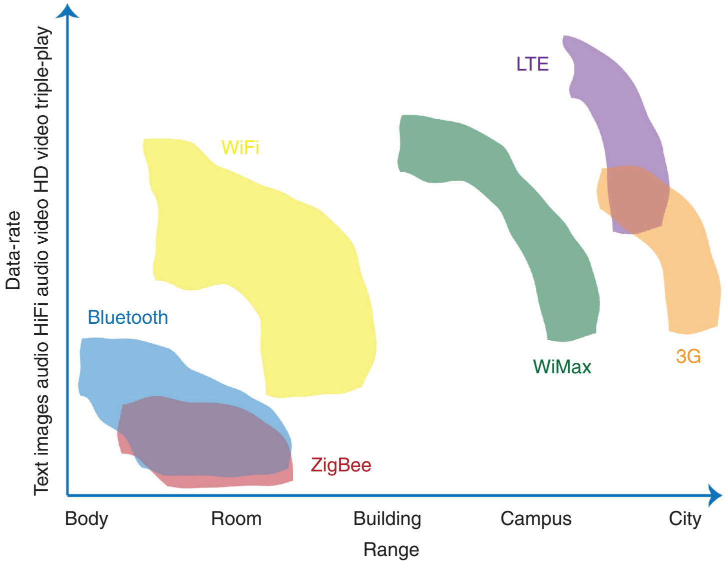

Plate XIII (Chapter 16) Range and data rate of wireless standards (*Source*: Adapted from D. K. Sohraby, D. Minoli and T. Znati (2007), *Wireless Sensor Networks*. Hoboken, NJ: John Wiley & Sons, Inc. p. 307.)

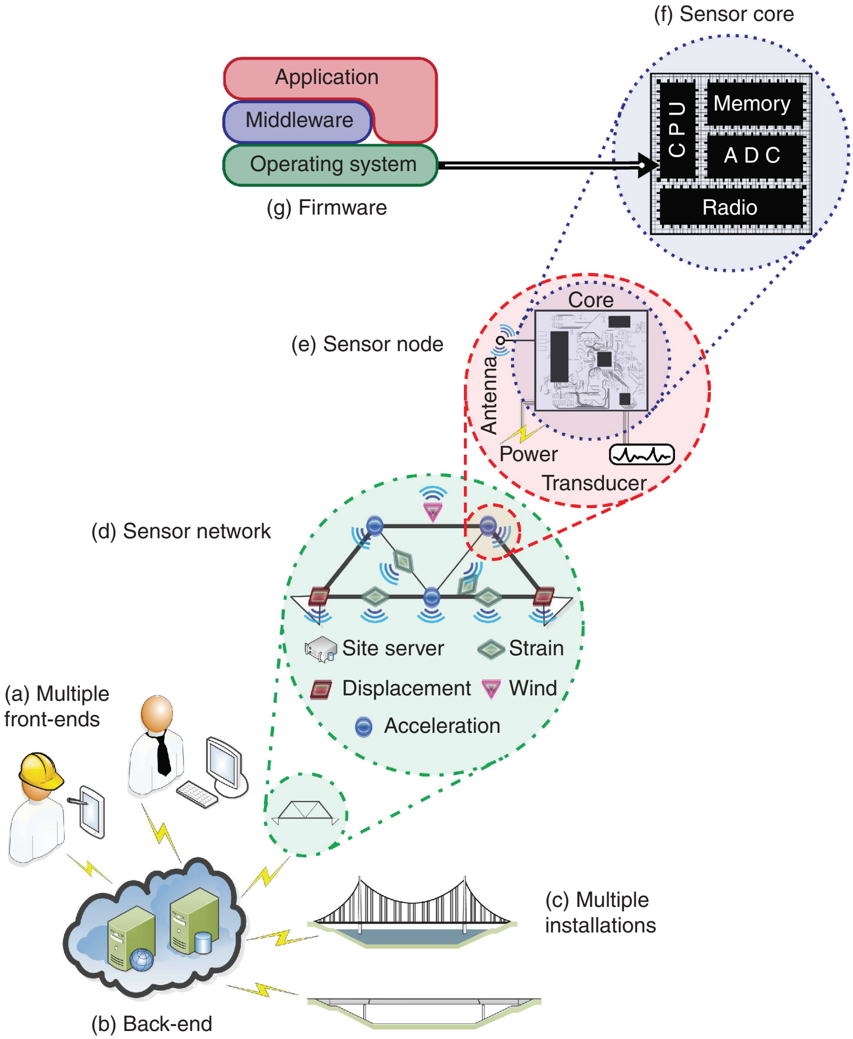
(f) Sensor core
Application
Middleware
Operating system
(g) Firmware
CPU
Memory
ADC
Radio
(e) Sensor node
Core
Antenna
Power
Transducer
(d) Sensor network
Site server
Strain
Displacement
Wind
Acceleration
(a) Multiple front-ends
(c) Multiple installations
(b) Back-end

Plate XIV (Chapter 16) Overview of the wireless structural monitoring system architecture.

17

Permanent installation of wireless structural monitoring systems in infrastructure systems

C. A. PECKENS, M. B. KANE, Y. ZHANG and J. P. LYNCH,
University of Michigan, USA

DOI: 10.1533/9780857099136.480

Abstract: Over the last several decades, wireless sensing technologies have arisen as an inexpensive and robust method of data collection, used in a variety of structural monitoring applications for various types of infrastructure systems. In comparison with their natural counterparts (i.e., cabled monitoring systems), wireless monitoring systems offer low-cost and low-power communication between a large number of sensing devices. However, successful implementation of such technologies is highly dependent on several factors, such as constant power supply, reliable communication, and dependable data collection strategies. These can often be challenging to achieve in real-world applications, due to harsh environmental conditions and overall limitations of the current technology. While numerous studies have effectively overcome such challenges in a variety of infrastructure systems, bridges have had numerous successful deployments of wireless sensor networks. As such, this chapter focuses on four particular cases that demonstrate successful long-term deployment of wireless sensor networks on bridges for structural monitoring purposes.

Key words: structural monitoring, bridge applications, wireless sensors.

17.1 Introduction

Critical infrastructure systems (e.g., bridges, pipelines, roads, buildings) are vital to the economic success of today's society. However, such structures are extremely susceptible to degradation and deterioration due to aging effects or extreme loading scenarios, such as earthquakes or high wind loads. Additionally, due to their extensive daily use, the condition of many infrastructure systems in developed nations such as the United States is dire. For example, 26% of all bridges in the United States have been reported as structurally deficient or functionally obsolete in 2003 by the Federal Highway Administration.[1] Current federal law mandates that all bridges

© 2014 Woodhead Publishing Limited

be visually inspected on a bi-annual basis, but these inspections can be extremely subjective in nature, very costly, and largely insufficient, as the majority of structural defects often lie beneath the surface of the structure.[2] Other infrastructure systems face similar challenges. Therefore, alternative methods of accurately assessing a structure's integrity and detecting key problem areas are needed.

Recently, numerous civil engineering structures across the world have been instrumented with long-term wired monitoring systems, thus allowing for real-time data collection.[3] While offering reliable communications and accurate data collection, wired monitoring systems can be time consuming to install. Additionally, such systems are often extremely expensive, with one sensing node costing several thousand dollars.[4] As a result, due to financial constraints, such monitoring systems often lack high spatial density of sensors across the networks. This has motivated the structural monitoring community to seek alternative methods to traditional wired systems that would allow for a dense deployment of sensors with greater affordability. Wireless sensing technology has risen as one possibility, thus replacing the coaxial cables of wired systems with wireless communication at a fraction of the installation cost. See Chapter 16 for a full overview of wireless sensor technologies as they relate to civil infrastructure.

Since its initial proposal in 1998,[5] the utilization of wireless sensor networks (WSNs) has become increasingly popular for both academic and commercial use, with a particular emphasis on bridge monitoring applications.[6,7] Deploying wireless sensors on bridges presents its own unique challenges for the sensor community. Careful consideration must be given to specific factors before any installation can occur, such as power supplies and the reliability of wireless communication, given current environmental conditions. While the removal of cables relieves much of the manual labor required for installation of monitoring systems, it also eliminates a reliable power source. As a result, WSNs must rely on batteries or other non-traditional energy sources as their primary source of power. If not carefully considered, this factor may severely inhibit the longevity of the overall network. Additionally, in eliminating cables as the avenue for data transmission, WSNs must be able to develop reliable communication at long distances in order to truly be applicable for most monitoring applications. However, such reliability is often achieved at the expense of increased power consumption. Therefore, by removing the cables, successful deployments of WSNs now depend on a careful balance between power constraints and communication ranges. Additionally, such monitoring systems on bridges are highly exposed to harsh environmental conditions, such as wind, snow, and rain. Before any deployment of a WSN, these factors must be considered and extra precautions must be taken to protect system components without inhibiting communication range or the ability to perform data acquisition tasks.

While wireless sensing technologies have emerged as a viable alternative to the traditional tethered systems for civil infrastructure systems, they have many challenges that must be addressed to be useful in real-world applications. This chapter covers four major deployments of WSNs on long-span bridges using various wireless sensing systems. Each case study carefully addresses the aforementioned technical challenges of WSN. This chapter focuses on bridges largely because wireless sensors have seen greatest use in these infrastructure system types. However, the lessons learned from these studies can be generalized for any large, complex infrastructure system. This chapter is not intended to be an exhaustive review of WSNs deployed on bridge systems; rather, a select number of field validation studies offering the most valuable lessons learned have been selected for illustrative purposes. The first case study is the Golden Gate Bridge, where a short-term WSN was installed for monitoring purposes. The remaining three case studies are the Stork Bridge, the Jindo Bridge, and the New Carquinez Bridge, which are all permanent, long-term system deployments.

17.2 Case study I – The Golden Gate Bridge, San Francisco, California, USA

One of the first full-scale deployments of a WSN on a long-span bridge was conducted by Pakzad *et al.*[8] on the Golden Gate Bridge, in San Francisco, California, USA (Fig. 17.1). The WSN was deployed on 14 July 2006, and the study lasted for approximately two months on the bridge, before removal on 22 September 2006. The Golden Gate Bridge was chosen for the wireless

17.1 Golden Gate Bridge, San Francisco, California, USA.[38]

sensor system because Abdel-Ghaffer and Scanlan[9,10] had conducted previous studies on this bridge with tethered data acquisition systems, thus allowing for a comparison between the wired and wireless systems. Completed in 1937, the steel suspension bridge has a main span of 1280 m and two side spans of 343 m. Additionally, two towers separate the main span from each side span, each rising 210 m above sea level.

During the study, 64 wireless sensing nodes were deployed across the bridge (Fig. 17.2), with 56 nodes on the main span measuring transverse and vertical acceleration, and eight nodes on the east tower measuring transverse and longitudinal acceleration. Of the 56 nodes on the main span, 53 were deployed on the west side of the bridge deck during the primary installation phase, and three were deployed on the east side of the bridge deck during a second installation phase. Due to communication constraints, the units were typically placed 30 m apart but in the presence of obstructions this distance was limited to 15 m.

17.2.1 Wireless sensing unit

The MICAz mote[11] was chosen as the wireless sensing node in this study, due to its open source operating system, TinyOS, as well as its reliable communication protocol. The mote operates on the Atmel AVR ATMega128L microprocessor with 512 kB FLASH memory, thereby enabling storage of approximately 250 000 two-byte (16-bit) values prior to data transmission. For data collection, the MICAz interfaces with an external sensor board that monitors four channels of acceleration, as well as one temperature channel. The board uses two types of accelerometers: a high level sensor, Analog Device ADXL202, with a measurement range of ± 2 g and a noise floor of 1 mg at 25 Hz, and a high sensitivity sensor, Silicon Design 1221L, with a scaled measurement range of ± 0.1 g, and noise floor of 10 μg. Each accelerometer channel is equipped with an on-board anti-aliasing filter with a cut-off frequency of 25 Hz, which prefaces a 16-bit analog-to-digital converter (ADC). For data transmission, the MICAz mote interfaces with a 2.4 GHz IEEE 802.15.4 compliant radio transceiver, thus providing reliable in-field communication for distances up to 30 m.

Power is of particular concern for the deployment of wireless sensing networks, and therefore the consumption of each component should be carefully considered. During a preliminary analysis of the sensing node, Kim *et al.*[12] found that the sensor board, including the accelerometers, anti-aliasing filters, and ADC, has a power draw of 240 mW when using a 9 V power source. This is over twice the draw of the MICAz, which draws 118 mW at the same power source in its idle state. However, when operating as a combined unit and performing routine tasks, the entire sensing node draws a

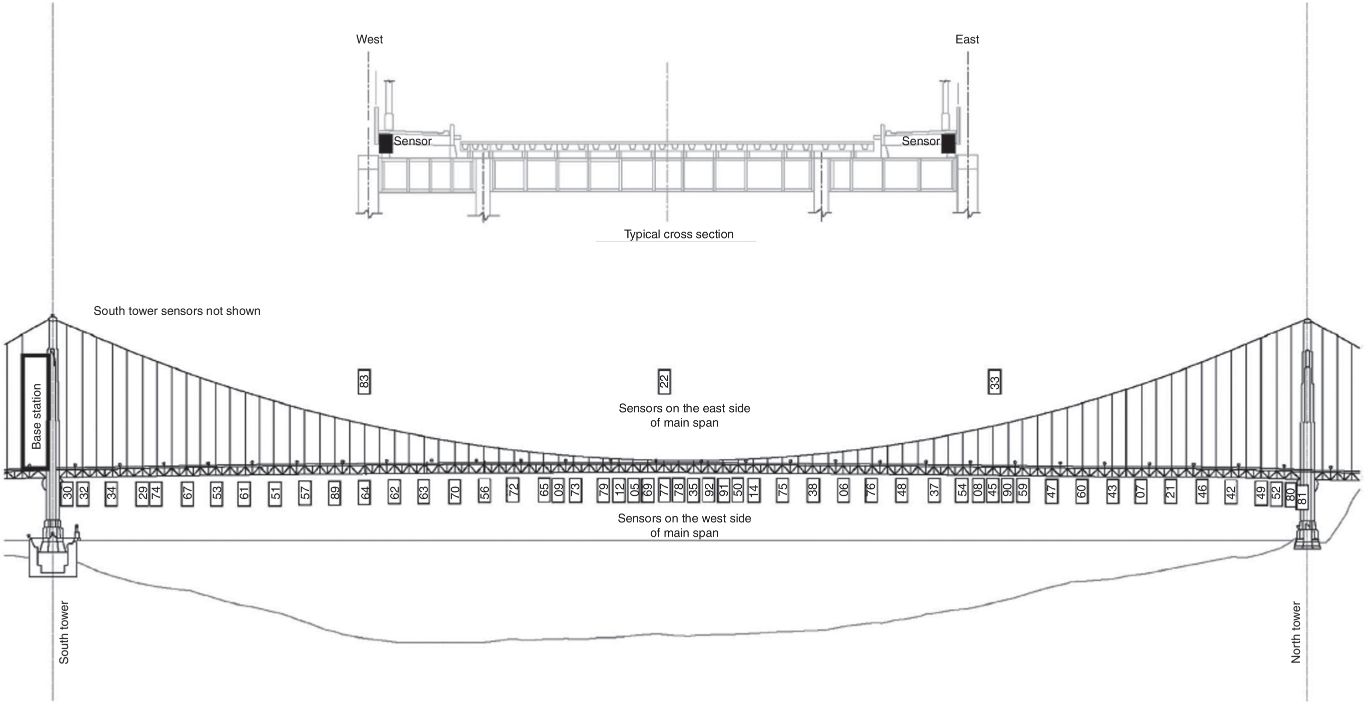
West
East
Sensor
Sensor
Typical cross section
South tower sensors not shown
Base station
83
22
33
Sensors on the east side of main span
30 32 34 29 74 67 53 61 51 57 89 64 62 63 70 56 72 65 09 73 79 12 05 69 77 78 35 92 91 50 14 75 38 06 76 48 37 54 08 45 90 59 47 60 43 07 21 46 42 49 52 80 81
Sensors on the west side of main span
South tower
North tower

17.2 Schematic of bridge instrumentation. (*Source*: used with permission from ASCE Reference 8.) Each numbered box denotes an individual MICAz mote used for acceleration measurements.

maximum of 672 mW at 9 V. Through this brief study, it was acknowledged that more sophisticated methods of power management, such as implementing sleep modes for components, was required for full-scale implementation of wireless sensing networks during long-term or permanent installations.

17.2.2 Communication scheme

While wireless communication is one of the greatest benefits of these new sensor networks, it also poses one of the greatest challenges, due to limited radio bandwidths and short communication ranges. The nodes used in this study have a maximum communication range of 30 m, which is significantly less than the total length of the bridge. Therefore, some units were not able to communicate directly with the base station and alternative methods had to be employed. As a result, the WSN relied on the use of a multi-hop communication scheme whereby data is transferred from distant nodes to the base station through the use of intermediary nodes. While hopping enables communication between all nodes and the base station, it does pose additional constraints to the network design, because each node must find a reliable path that allows for data transfer to the base station, without overlapping the transmission from another unit. Additionally, the unit must be able to dynamically adapt its path in the event that one of its intermediary nodes falls out of the network or exhibits poor reliability.

For the deployment of sensor nodes on the Golden Gate Bridge, Pakzad *et al.*[8] made use of pipelining, first proposed by Kim *et al.*[12] to optimize the communication bandwidth across the multi-hop network. In pipelining, the network organizes data transmission such that several nodes can simultaneously transmit data across the network without interference. In this way, the overall network is able to communicate higher rates of data and the effective bandwidth of radio communication is increased. Even with this method there is a risk of packet loss or radio interference. A balance between the number of hops permitted within the network and the amount of data lost due to interference must be found. For the Golden Gate Bridge network, Pakzad *et al.*[8] found that using five hops between transmitting nodes resulted in reliable data transmission rates of 550 bytes/s, with packet loss rates of 2.5% or lower, which was adequate for their sensing requirements.

In conjunction with multi-hop communication, Pakzad *et al.*[8] also made use of the Scalable Thin and Rapid Amassment Without Loss (STRAW) protocol, first proposed by Kim *et al.*[12] to regulate reliable communication across the network. STRAW is a negative-acknowledgment (NACK) collection protocol, in which the receiver always initiates data collection from the network nodes. Once data transfer has started, the receiver tracks the received packets from each node and sends a list of missed packets to the sender. Based on this list, the sender then retransmits any missed packets. Communication continues between the node and the receiver until all data have been received by the receiver. In this way, reliable communication can be achieved, even with the added risk of multi-hop communication.

The final factor that can prohibit successful communication and data collection in WSNs is time synchronization. To maximize the information that can be extracted from the network, it is important that all units in the network are synchronized. In a single-hop network units can easily be aligned, because each unit can receive a beacon directly from the base station. For a multi-hop network, however, all units cannot communicate with the base station and therefore, delays will be introduced in the network as intermediary nodes relay messages. To overcome this, Pakzad *et al.*[8] employed the Flooding Time Synchronization Protocol (FTSP) first proposed by Maroti *et al.*[13] and readily available in TinyOS. In FTSP, a global timestamp is passed across the network through a series of handshakes until all units are on the same 'time zone,' and hence time synchronized.

17.2.3 Field deployment

Pakzad *et al.*[8] deployed their wireless sensing network on 14 July 2006. Each unit was bonded to the bridge with temporary connections, such as c-clamps, zip ties, and duct tape, all of which proved to be adequate for the two month

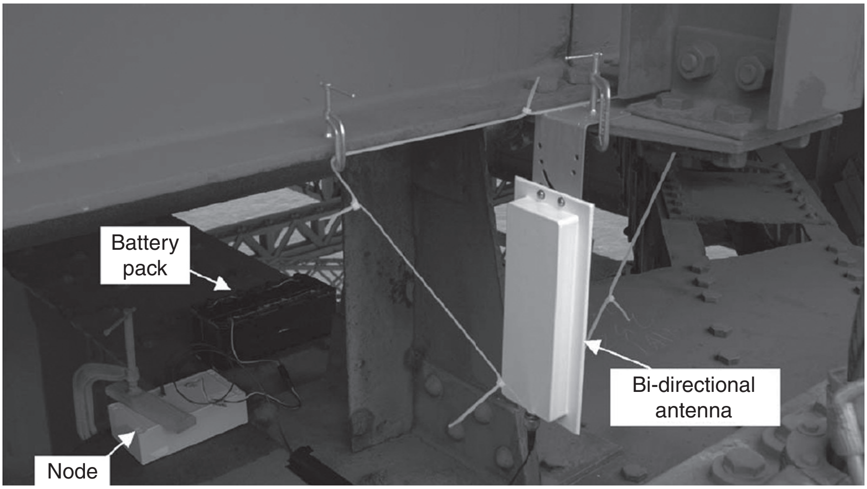

17.3 Wireless sensing unit – mote (denoted as node), battery pack, and antenna. (*Source*: Used with permission from ASCE Reference 8.)

testing scheme (Fig. 17.3). Once the network was installed, vibration time histories were collected at a 50 Hz sampling frequency for 1600 s, resulting in 20 MB of data collected across the entire network. Using the multi-hop communication scheme, it took approximately 9 h to collect data from the entire network. Once data were collected, it was used in an off-line analysis to estimate the modal properties of the Golden Gate Bridge. Through the analysis, it was demonstrated that as more nodes were included in the analysis, higher order modes could be identified with greater accuracy, thereby validating the need for dense networks of sensing nodes on complex civil infrastructure systems.

17.2.4 Case study conclusions

This deployment on the Golden Gate Bridge marked the first successful large-scale deployment of WSNs on a long-span bridge. Through the study, Pakzad *et al*.[8] validated multi-hop communication with the use of pipelining and time synchronization techniques. As such, networks of sensing nodes were not limited to the communication ranges of their radios, but instead could scale according to the requirements of the structure. Additionally, Pakzad *et al*.[8] successfully executed off-line modal analysis, thereby demonstrating the need for dense sensor networks. Thus, the study on the Golden Gate Bridge addressed some of the initial concerns of deploying WSNs on civil infrastructure and presented future areas for exploration.

17.3 Case study II – The Stork Bridge, Winterthur, Switzerland

Shortly following the study on the Golden Gate Bridge, Feltrin *et al.*[14–16] installed a wireless sensing network on the Stork Bridge (Fig. 17.4), a cable-stay bridge located in Winterthur, Switzerland.[14–16] Built in 1996, the Stork Bridge was the first carbon-fiber cable-stayed bridge in the world. Comprising two spans, one 63 m in length and the other 61 m in length, the Stork Bridge has 24 cables, of which two are carbon fiber and the remainder are traditional steel tendon. WSNs are ideal for data acquisition on cable-stayed bridges, due to their ease of application thereby enabling rapid deployment. On 16 January 2007, Feltrin *et al.*[14] deployed six wireless sensors on the cables of the Stork Bridge (Figs 17.5 and 17.6) for a long-term study that has continued to the time of this book's publication.

17.3.1 Wireless sensing unit

Due to its low-power consumption, the commercially available Tmote Sky wireless sensing unit was chosen for this study.[17] The Tmote Sky uses the

17.4 Stork Bridge, Winterthur, Switzerland. (*Source*: Used with permission from Reference 39.)

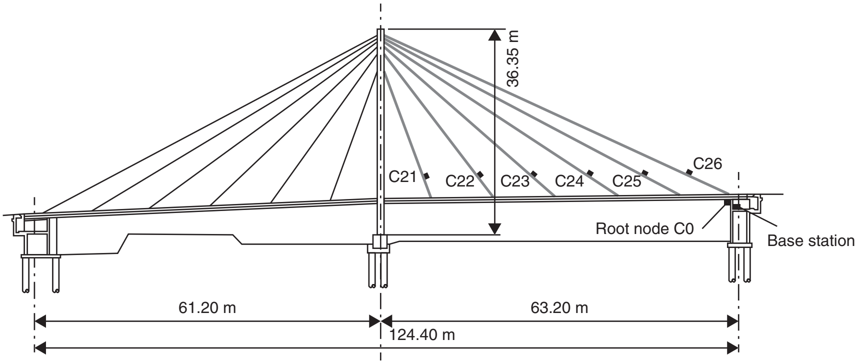
36.35 m
C21
C22
C23
C24
C25
C26
Root node C0
Base station
61.20 m
63.20 m
124.40 m

17.5 Schematic of bridge instrumentation. (*Source*: Used with permission from Reference 14.)

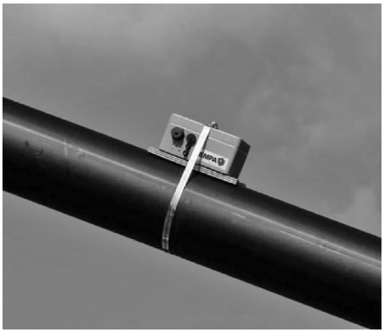

17.6 Sensor mounted to stay cable. (*Source*: Used with permission from Reference 14.)

low-power 16-bit Texas Instruments microprocessor, MSP430F1611, which provides 10 kB of RAM and 48 kB of FLASH memory, while running the TinyOS operating system. The mote interfaces with a 2.4 GHz IEEE 802.15.4 Chipcon wireless transceiver, thereby enabling radio communication for distances of 30–40 m. The Tmote Sky is equipped with eight 12-bit ADC channels, each with a maximum sampling frequency of 200 Hz, thus allowing a variety of sensors (e.g., accelerometers, strain gages) to be integrated into the data acquisition system. For this study, Feltrin *et al.*[14] used one ST Microelectronics LIS2L06 MEMS accelerometer per mote, with a measurement range of ± 2 g, sensitivity of 0.6 V/g and a noise floor of 0.2 mg with a 50 Hz bandwidth. Each analog signal was pre-processed with a low-pass filter having a cut-off frequency of 20 Hz and a low-power signal amplifier. Additionally, the ambient temperature and air humidity were also measured using the Sensirion SHT11 chip. The entire system was packaged in a durable aluminum box, thus protecting it from the harsh outdoor environment (Fig. 17.7).

Throughout the study, the system designers were cognizant of the overall power consumption of the network, and therefore carefully chose each component of the wireless sensing unit according to this constraint. The Tmote Sky consumes 5.4 mW of power in idle mode and 65 mW in full operational mode (at a 3 V referenced power source). Additionally, the signal processing board and accelerometer draw 5 mW of power, while the temperature and humidity sensor consumes 0.5 mW of power. Once the network was deployed, Feltrin *et al.*[14] continually modified the network so as to minimize the energy consumption of the network. They

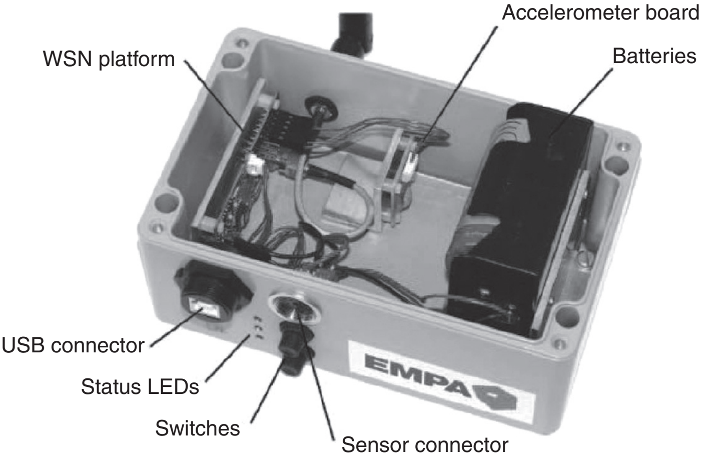

17.7 Hardware packaging for wireless sensors units. (Used with permission from Reference 14.)

Table 17.1 Energy consumption for field deployment of Tmote

Radio duty cycle (%)	Estimated battery life (days)
40	60
10	180
2	450

found that by decreasing the duty cycle of the radio (i.e., the time that the radio is on – for example, a 40% duty cycle corresponds to the radio being on for 40% of the time) they could significantly increase the battery life of their system (see Table 17.1).

17.3.2 Communication scheme

Due to the geometry of the bridge, as well as the availability of a stable AC power supply, the root node, which communicates information between the base station and all other wireless sensor nodes, was installed on the abutment underneath the bridge deck. This location offered no line-of-sight connection with the other wireless sensor nodes. Therefore, the wireless link between the root node and the sensor nodes on the cable-stays was established through reflectivity, thus reducing the overall communication range. As a result, the two sensor nodes that were closest to the mid-span could not directly communicate with the root node, thereby requiring a multi-hop communication scheme. Because there were only six nodes in the network, these two nodes could communicate with the root node by employing one additional hop of the data to any of the four other nodes. These nodes periodically assessed their link quality with adjacent nodes and chose the most reliable one for the hopped transmission. Similar to the Golden Gate Bridge case study, due to the multi-hop communication time synchronization was a concern across the network and a method similar to FTSP was employed. The root node transmitted a global timestamp every 30 s and, upon receiving the timestamp, a sensor node rebroadcast the message. This process continued until the entire network had received the global timestamp and each sensor had updated its local clock.

17.3.3 Data management

In terms of power consumption, WSNs, in general, consume less energy through data processing, as opposed to data transmission.[18] One large benefit of wireless sensing nodes is that they are capable of performing local computations and, as a result, can transmit small bandwidths of processed data, as opposed to large bandwidths of raw data, thus saving radio transmission time. Cable-stay bridges are ideal for localized data processing, as forces in the cables are often monitored through natural frequency estimations that can be extracted from the measured vibrations in each cable.[19] Each cable can be analyzed independently of the others, resulting in a completely decentralized data processing architecture. By converting acceleration time histories to the dominant natural frequencies and transmitting only these values, Feltrin *et al.*[16] found that the transmitted data was reduced by a factor of 500. This resulted in a dramatic reduction in energy consumption due to decreased radio use, as well as decreased likelihood of data loss during transmission between nodes.[14] The ambient vibrations were sampled at 50 Hz for 20.5 s. Each round of sampling took less than 1 s to extract the first eight dominant frequencies.[16] Once the data were analyzed, they were transmitted to the root node and temporarily stored at the base station. The base station was linked through a secure mobile cellular connection to a remote control center that was used for long-term data storage and off-line analysis.

17.3.4 Network stability

One of the largest challenges in deploying a WSN is ensuring network stability over a long period of time. Nodes may fall out of the network for a variety of reasons, including insufficient battery power, lack of reliable communication, or microprocessor inundation due to localized data processing. Throughout their study, Feltrin *et al.*[14] focused on optimizing network stability through various means. They first divided their frequency algorithm into two separate threads, thus improving the node's availability for communication and limiting the likelihood of complete node inundation. They next made improvements to their system management techniques at the node, base station, and control center. Even with these improvements, however, only 4.2 nodes, on average, were responsive throughout an 80 day test period. Therefore, this study clearly highlights the difficulties that arise with a field deployment of WSNs, specifically in terms of long-term network stability.

17.3.5 Case study conclusions

This study demonstrated the successful long-term deployment of a WSN on a cable-stayed bridge. During this time, Feltrin *et al.*[14–16] focused heavily on the reduction of energy consumption across the network, specifically through the optimization of radio usage. They highlighted the benefit of decreased radio use by reducing the duty cycle usage of each node and simultaneously increasing the battery life of the network. Additionally, by performing localized data processing, they were able to significantly minimize the bandwidth of transmitted data, thereby reducing the active time of the radio while paying a minimal price in data processing. Finally, this field deployment demonstrated the difficulties of ensuring network stability over a long time period while offering suggestions for system improvement.

17.4 Case study III – Jindo Bridge, Haenam/Jindo, South Korea

In 2009, as part of a joint collaboration between the University of Illinois at Urbana-Champaign (UIUC, USA), the Korean Advanced Institute of Science and Technology (KAIST, South Korea) and the University of Tokyo (Japan), a full-scale sensor network was deployed on one of the Jindo Bridges in South Korea.[20] The Jindo Bridges are twin cable-stayed bridges that connect the mainland of South Korea, in the city of Haenam, to the Jindo islands (Fig. 17.8). Each bridge comprises three continuous spans, with a main span of 344 m and two 70 m side spans. The first bridge was constructed in 1984 and the second bridge was constructed in 2006. The newer bridge was chosen for the wireless sensing system installation due to the availability of construction and design drawings, as well as access to a pre-existing wired monitoring system, thus allowing for direct comparison between the wired and wireless systems. The wired monitoring system included 15 thermometers, 15 strain gages, four biaxial inclinometers, two string pots, two laser displacement meters, 24 fiber Bragg grating sensors, 20 uniaxial capacitive accelerometers, two biaxial force-balance accelerometers, and three tri-axial seismic accelerometers.[20]

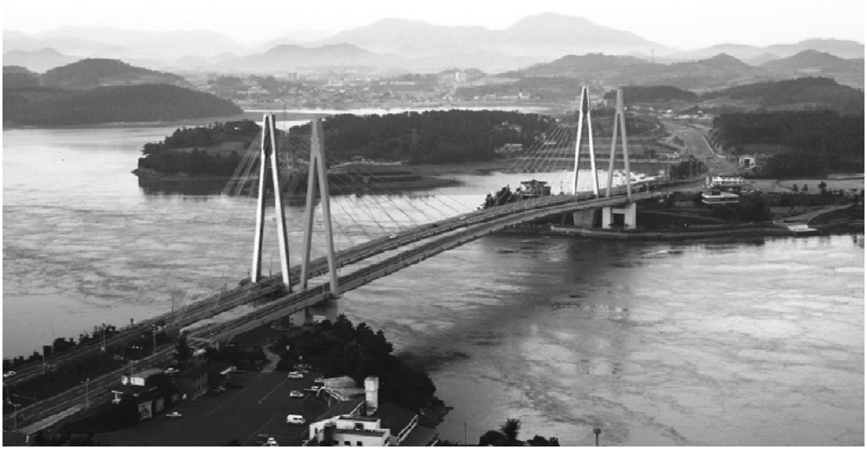

17.8 Jindo Bridge, South Korea. (*Source*: Used with permission from Reference 21.)

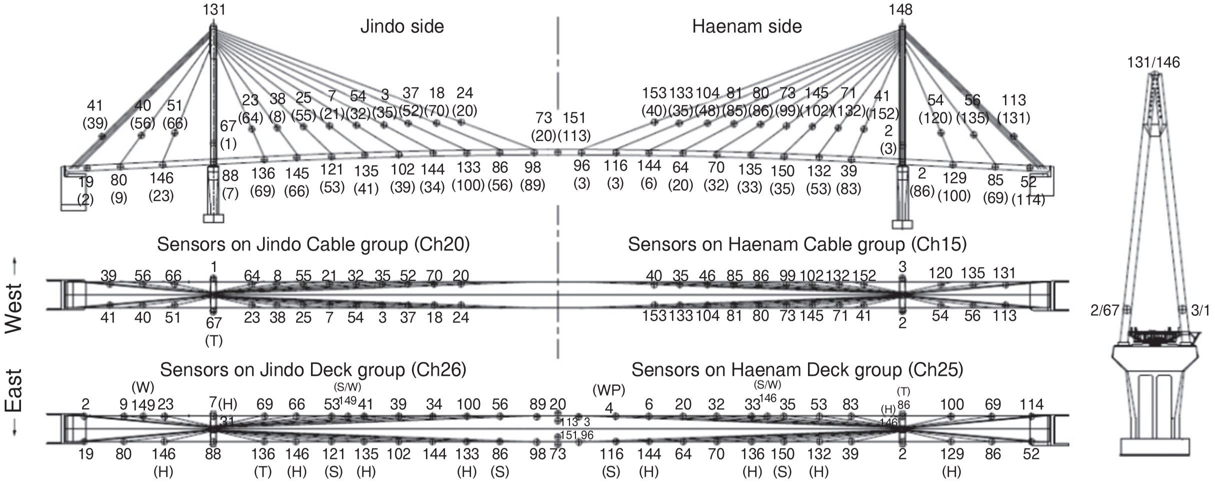

131
Jindo side
148
Haenam side
131/146
41 (39)
40 (56)
51 (66)
67 (1)
23 (64)
38 (8)
25 (55)
7 (21)
54 (32)
3 (35)
37 (52)
18 (70)
24 (20)
73 (20)
151 (113)
153 (40)
133 (35)
104 (48)
81 (85)
80 (86)
73 (99)
145 (102)
71 (132)
41 (152)
2 (3)
54 (120)
56 (135)
113 (131)
19 (2)
80 (9)
146 (23)
88 (7)
136 (69)
145 (66)
121 (53)
135 (41)
102 (39)
144 (34)
133 (100)
86 (56)
98 (89)
96 (3)
116 (3)
144 (6)
64 (20)
70 (32)
135 (33)
150 (35)
132 (53)
39 (83)
2 (86)
129 (100)
85 (69)
52 (114)
Sensors on Jindo Cable group (Ch20)
Sensors on Haenam Cable group (Ch15)
West
East
39 56 66 1 64 8 55 21 32 35 52 70 20
41 40 51 67 (T) 23 38 25 7 54 3 37 18 24
40 35 46 85 86 99 102 132 152 3 120 135 131
153 133 104 81 80 73 145 71 41 2 54 56 113
2/67
3/1
Sensors on Jindo Deck group (Ch26)
Sensors on Haenam Deck group (Ch25)
2 9 (W) 149 23 7 (H) 31 69 66 53 (S/W) 149 41 39 34 100 56 89 20
19 80 146 (H) 88 136 (T) 146 (H) 121 (S) 135 (H) 102 144 133 (H) 86 (S) 98 73
113 3 151 96
(WP) 4 6 20 32 33 (S/W) 146 35 53 83 (H) 146 (T) 86 100 69 114
116 (S) 144 (H) 64 70 136 (H) 150 (S) 132 (H) 39 2 129 (H) 86 52

1. (S/W) values for West-side nodes
2. (H) means SHM–H node
3. (S) means Sentry node
4. (W) means Wind node (anemometer)
5. (T) means external Temperature node
6. (WP) means Wind Power node (wind turbine)

17.9 Schematic of bridge instrumentation. (*Source*: Used with permission from Reference 21.)

With its initial deployment in 2009, the wireless sensing system consisted of 70 nodes (Fig. 17.9), with 33 nodes installed on the half of the bridge closest to the Jindo island (22 nodes on the deck, three on the pylon, and eight on cables) and 37 nodes were installed on the Haenam side (26 nodes on the deck, three on the pylon, and seven on the cables).[20] In 2011, the network was expanded to include a total of 113 sensor nodes,[21] with additional motes added to the previously monitored cables, as well as the deck. Of these 113, three nodes measured temperature, three nodes measured wind characteristics (direction and speed), and the remaining nodes measured acceleration. The system was implemented as a full-scale long-term deployment project without an identified end date.

17.4.1 Wireless sensing unit

Each wireless sensing unit was comprised of the Crossbow Imote2 (now sold by MEMSIC), an IBB2400CA battery board and the SHM-A multiscale sensor board.[22] The commercially available Imote2[23] (Fig. 17.10) was chosen as the wireless sensor unit for this study, due to its high level of adaptability as well its established support system. The mote uses the Intel PXA271 Xscale microprocessor, which runs the TinyOS operating system. It has significant memory capacity with 256 kB SRAM, 32 MB FLASH, and 32 MB SDRAM, thereby enabling longer periods of data collection. The unit is powered from three 1.5 V batteries. The Imote2 is designed to interface with additional data acquisition boards, thereby enhancing its overall functionality. Initially, the SHM-A and SHM-W (a modified

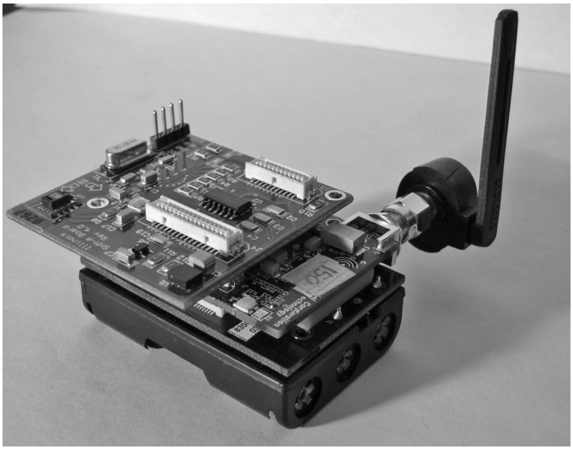

17.10 Imote2 with antenna, stacked on battery board, and with the SHM-A sensor board.

version of SHM-A) were interfaced with the Imote2 for data collection purposes[20] and the SHM-H was later implemented for monitoring low-level ambient vibrations.[21]

By using any of the three sensor boards (SHM-A,[24] SHM-H,[21] or SHM-W[25]), the Imote2 is able to more effectively monitor civil infrastructure systems. The SHM-A board was developed at the University of Illinois as a fully equipped sensing board containing an on-board 3-axis ST Microelectronics LIS344ALH accelerometer with a measurement range of ± 2 g, a sensitivity of 0.66 V/g, a noise floor of 0.3 mg for the x- and y-axes, and a noise floor of 0.7 mg for the z-axis. The acceleration signals are conditioned by the Quickfilter QF4A512[26], which passes the signal through a programmable anti-aliasing filter prior to a 12-bit ADC, with user-selectable sampling rates (pre-programmed at 10, 25, 50, or 100 Hz). The resolution of the ADC can be increased to 16-bits through oversampling but at the penalty of increased power consumption. The SHM-A sensor board also features the Sensirion SHT11 chip, which features on-board digital humidity and temperature sensors. The SHM-H is similar to the SHM-A in design but features an on-board low-noise accelerometer (Silicon's Design SD1221L-002) with a measurement range of ± 2 g, a sensitivity of 2 V/g, and a noise floor of 0.05 mg at 20 Hz.

Due to the location of the bridge and its susceptibility to high winds, it was also important to monitor wind speeds. Therefore, the ADC connection on the SHM-A board was modified, and renamed SHM-W such that it contained three 0–5 V channels that could be used for an anemometer (measuring wind speed), a wind vane (measuring horizontal and vertical wind directions), and an accelerometer. The SHM-W board was interfaced with the RM Young Model 81000 anemometer, chosen because of its high resolution and durability in harsh environments. All units were packaged in water-tight PVC enclosures, thus protecting them from environmental factors (Fig. 17.11) and mounted to the bridge using magnets (for the units

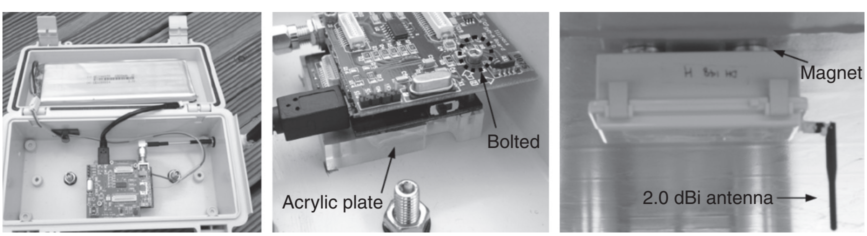

17.11 PVC enclosure for sensing unit (a), sensor mounting (b) and installation to bridge deck (c). (*Source*: Used with permission from Reference 21.)

on the deck or pylons) or U-bars and mounting plates (for the units on the cables), thereby permitting easy and non-obtrusive installation of the units.

17.4.2 Power consumption

As with most field deployments of WSNs, Jang *et al.*[20] were very aware of the power consumption of their network. It was estimated that when using three 1.5 V D-cell batteries a sensing unit would operate for 2 months. To alleviate the issue of periodically replacing batteries, Jang *et al.*[20] also deployed solar panels on eight nodes (five were located on the cables, two on the pylons, and one under the deck). With periodic assessment, they found that the majority of the nodes maintained voltage levels at 4.15 V, which was sufficient to power the units indefinitely, and therefore provided motivation for deployment of more solar charging systems on future network upgrades. The one unit under the deck, however, was not able to properly recharge its batteries. As a result, wind power was also explored as an energy source and was successfully demonstrated as a viable alternative for such nodes.[27]

Additionally, Jang *et al.*[20] found that the network could conserve power by forcing the units to be in sleep mode (all components on the mote are powered down except for the clock) for long periods of time, a form of duty cycling that was first proposed by Ye *et al.*[28]. A unit in sleep mode consumes only 2.25 mW of power as compared to the 756 mW when not in sleep mode (at a 4.5 V referenced power source).[24] To ensure that the network is still responsive to sensing commands, each unit periodically wakes and listens for messages from the base station. If it is desired for the entire network to collect data, the base station continuously sends a wake-up message to all of the units until each unit has verified that it is awake and ready for its task. For deployment on the Jindo Bridge, the units slept for 15 s and woke for 750 ms, resulting in a 4.8% duty cycle of the unit and radio.

17.4.3 Communication scheme

The unit was equipped with an Antenova gigaNova Titanis 2.4 GHz external antenna, which enabled a communication range of approximately 200 m. Because the bridge is almost 500 m in length a single base station would not be able to communicate to all the nodes without the use of multi-hopping. Instead, the system was broken down into two sub-networks with a base station located on the concrete piers of each steel pylon of the first Jindo Bridge. As such, one base station could communicate with the nodes on the half of the bridge closest to the Jindo side and another base station could communicate with the remaining nodes on the other half of the bridge closest to the Haenam side.

17.4.4 Data collection and management

The network employed two data collection strategies, which not only ensured that data were collected at regular intervals but also that low frequency, long duration critical events, such as high winds, were captured by the sensing system. To do this, a small subset of the WSN is designated as sentry nodes and sample more frequently. If a sentry node detects a critical event, as indicated by exceeding a threshold value, then the remaining nodes are woken up and perform routine sampling.[24] The sentry nodes on the Jindo Bridge monitor both wind and acceleration so as to adequately respond to the prevalent environmental factors of the region.[20] If no critical event is detected, the network is designed to sample one time per day, when normal operating thresholds are exceeded.[29] Once collected, data are sent from the base station to a remote server via the Internet.[20] Similar to the aforementioned analyses performed on the Stork Bridge, the collected data were used to perform on-line decentralized cable tension monitoring. Additionally, the data were also used to determine mode shapes, both using off-line centralized processing techniques as well as on-line decentralized processing algorithms. All analyses were consistent with the wired system response.[21]

17.4.5 Case study conclusions

With the installation of this sensor network, Jang *et al*.[20] demonstrated a successful long-term deployment of a dense sensor network using the Imote2. The effective use of alternative energy sources was demonstrated through the successful implementation of solar panels, thus providing motivation for further investigation into the area of energy sources for WSNs. Additionally, Jang *et al*.[20] eliminated the need for a multi-hop communication scheme by creating sub-networks within the entire network. Finally, possible data analyses were demonstrated both on-line and off-line, alluding to greater processing requirements and data management with the deployment of such a large data acquisition system.

17.5 Case study IV – New Carquinez Bridge, Vallejo/Crockett, California, USA

In October 2010, a wireless sensing network was deployed on the New Carquinez (Alfred Zampa Memorial) Bridge, with a strong motivation for further addressing the limitations and challenges found from previous WSN deployments.[30] In particular, this study had a specific focus on the management of the large amounts of data that are collected through dense WSNs, thereby enabling more effective information extraction

17.12 New Carquinez Bridge, California, USA.

by the system end-user. The New Carquinez Bridge is a steel suspension bridge that was constructed in 2003 to cross the Carquinez Strait, thus providing a connection between Vallejo, California and Crockett, California (Fig. 17.12). It is 1024 m in length, with a main span of 728 m; its two concrete towers rise 120 m above sea level. It has a permanent wired monitoring system installed by the California Strong Motion Instrumentation Program, which collects 70 channels of acceleration data from force-balance accelerometers installed along the bridge girder and the link beams of the two concrete towers. Additionally, an anemometer installed at the bridge center span monitors the wind profile of the bridge, and relative longitudinal displacement of the girder is monitored through sensors installed on the girder.[30]

The WSN contains 33 sensing nodes with 23 measuring acceleration (19 on the main girder, two on the south tower, and two on the north tower), three measuring girder displacement from potentiometers, three measuring climate, such as wind speed, temperature, and humidity (two on the main girder, one on the north tower) and four measuring the strain of the continuous girder box at the maximum strain location, as determined by finite element analysis (Fig. 17.13). In total, the network was capable of collecting 104 channels of data at any given time. The system was implemented as a full-scale, long-term deployment without a specified end date.

17.5.1 Wireless sensing unit

The Narada wireless sensing node, developed at the University of Michigan,[31] was chosen as the data acquisition unit for this study, due to its compact design as well as having been tailored specifically for structural monitoring applications (Fig. 17.14). Narada has also been successfully used to monitor bridges,[32] wind turbines,[33] ships,[34] and buildings [35] in the past. The Narada

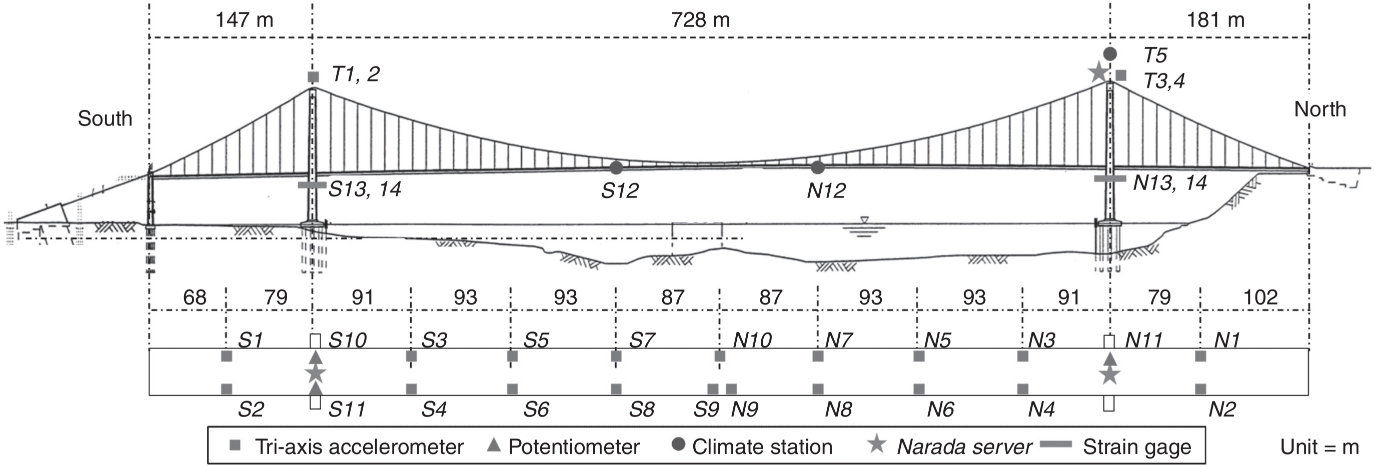
147 m
728 m
181 m
T1, 2
T5
T3,4
South
North
S13, 14
S12
N12
N13, 14
68
79
91
93
93
87
87
93
93
91
79
102
S1
S10
S3
S5
S7
N10
N7
N5
N3
N11
N1
S2
S11
S4
S6
S8
S9
N9
N8
N6
N4
N2
■ Tri-axis accelerometer
▲ Potentiometer
● Climate station
★ *Narada server*
▬ Strain gage
Unit = m

17.13 Schematic of bridge instrumentation on New Carquinez Bridge.

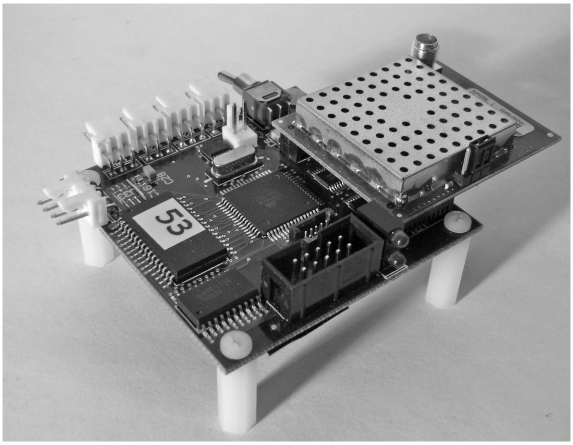

17.14 Narada wireless sensing unit with power-amplified radio.

utilizes the Atmel AVR ATMega128 microprocessor and is enhanced with 128 kB of external SRAM memory capabilities. The Narada directly interfaces with a mounted radio using the Chipcon CC2420 transceiver chip operating on the 2.4 GHz IEEE 802.15.4 standard. The radio's typical communication range is 100 m; however, by using a power-amplified transceiver, the communication range increases to over 500 m.[32]

Narada contains four data acquisition channels, thus enabling data collection from any 5V sensor, which feeds directly into an on-board 16-bit ADC. In this study, the tri-axial MEMSIC CXL02TG03 accelerometer was used to measure the ambient vibrations of the bridge. Vertical and transverse accelerations were tracked on the main girder, while nodes on the towers measured acceleration in the longitudinal and transverse directions.

Units between the wind tongue of the girder and the tower shear key measured longitudinal displacements using Celesco SP2–50 potentiometers. Units on the box girders at both towers used Tokyo Sokki FLA-6–11–3LT gages to measure the strain at both the top (longitudinal and transverse directions) and the bottom of the girder (longitudinal direction only). Finally, units designated as climate sensors measured wind speed using a NRG Systems 40H anemometer, wind direction with the NRG Systems 200P wind vein, temperature with the National Semi-Conductor LM35DT solid-state temperature sensor, and humidity with the TDK Corporation CHS-UPS humidity sensor. All units were enclosed in a polycarbonate NEMA-rated waterproof enclosure, such that all electrical components were protected from harsh environmental effects (Fig. 17.15).

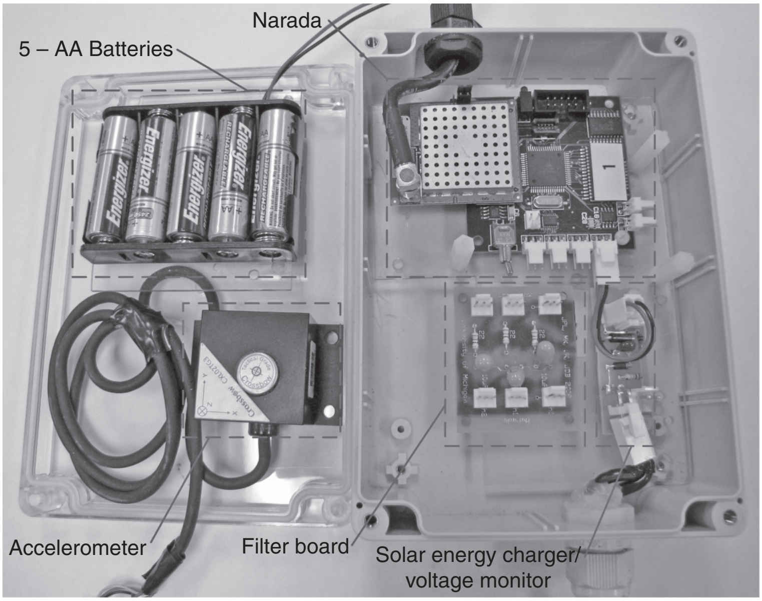

17.15 Polycarbonate enclosure for wireless sensing unit.

17.5.2 Power consumption

Kurata *et al.*[30] optimized their power consumption through the use of alternative energy sources, as well as low-power sleep modes for the wireless sensor. Each sensing unit relied on solar power energy to recharge its battery pack, comprising five AA NiMH rechargeable batteries, thereby alleviating the constraints placed on traditional battery-powered systems. The panel was a mono-crystalline solar panel with a power rating of 3.3 W and a maximum power voltage of 9 V. Each Narada unit could also measure the battery pack voltage, thus ensuring that each solar panel was working properly.

Similar to the previous case studies, Kurata *et al.* also optimized the networks energy consumption by introducing sleep modes to the sensor units.[30] By powering down the microcontroller, but still leaving the radioactive, the Narada consumes 215 mW in sleep mode (at a 5 V regulated power source), as compared to the 375 mW consumed in active mode, resulting in a modest, but important, reduction in energy consumption. By leaving the radio enabled, the unit is still able to receive commands from the system server, thereby still allowing fast response of a unit. In this way, the network is able to be revived very quickly, allowing it to respond to critical events such as earthquakes.

17.5.3 Communication scheme

When equipped with the power-amplified transceiver, the sensing units were capable of communicating over 500 m. The bridge, however, extends more than 1000 m in length, thus prohibiting the use of a single network without implementing a multi-hop communication scheme. To bypass this form of slow communication, Kurata *et al.*[30] employed three sub-networks, each relying on a single-hop communication scheme and communicating to their own unique server station. The 14 nodes on the north side of the bridge operate as one network, the 14 nodes on the south side of the bridge operate as a second network, and the five nodes at the top of the towers operate as the third network. Each sub-network was internally time synchronized through the beacon method, in which all units are synchronized through a single packet sent from the server. The sub-networks were time synchronized through the remote network server that was used to manage and store data, using the network time protocol (NTP) native to Linux.[30]

17.5.4 Data collection and management

As this is a fairly young bridge, the wireless sensing system was not installed as a means of detecting structural deterioration or health. Instead, the system was used to understand the bridge's response to daily use, as well as to understand how bridge behavior varies with the external environment (e.g., wind, temperature). Additionally, data that are collected are also used to verify and update finite element models (FEMs) developed by the bridge owner. Due to the bridge being situated in a seismic region, the bridge owner uses the FEM as a means of checking the bridge condition immediately following a large earthquake by inputting measured ground time

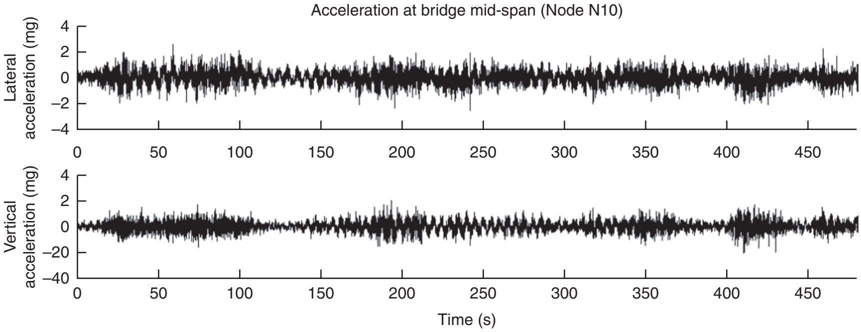

17.16 Time history profiles from accelerometers located at the bridge mid-span.

histories collected from the bridge foundation into the model. As a result of these two motivators for data collection, any data that are collected by the WSN are stored by a remote server where they can be further analyzed and used later, resulting in a high volume of both raw and processed data.

Typically, data are collected from all sensors every 4 h for 8 continuous minutes at 20 Hz, resulting in acceleration (Fig. 17.16), strain (Fig. 17.17), wind (Fig. 17.18), and temperature time histories. This information can be synthesized in post-processing to extract important bridge characteristics and behaviors. For example, using stochastic subspace identification[36] with acceleration data from normal traffic flow, the operational frequencies can be extracted (Fig. 17.19), thereby highlighting important bridge behaviors that can be compared with FEM results through model updating. Numerous other post-processing algorithms can be employed to allow for information integration for the end-user thereby enabling more effective structural monitoring.

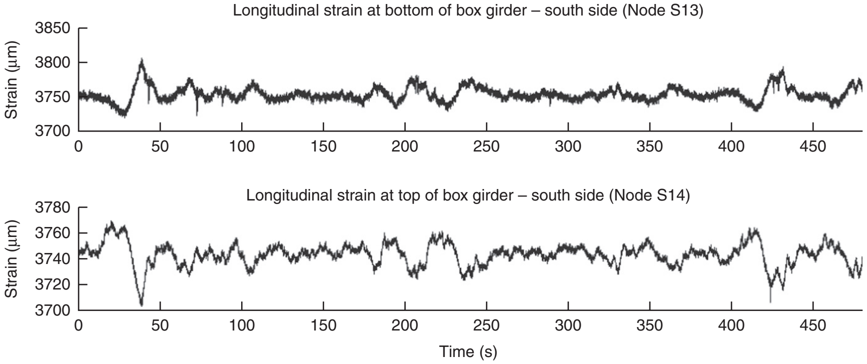

17.17 Time history profiles from strain gages located on the bridge box girder.

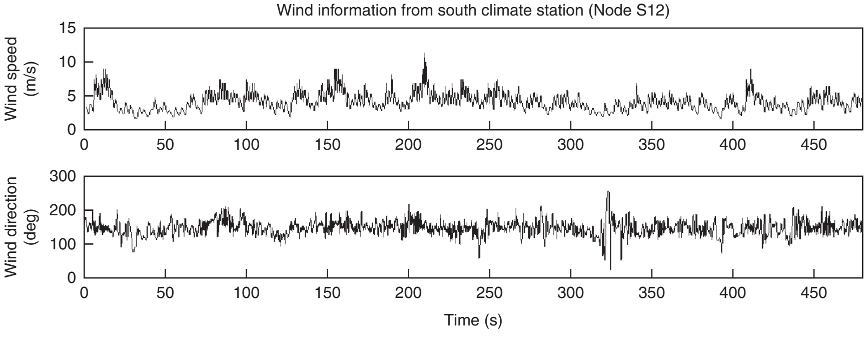

17.18 Time history profiles of wind speed and direction at the south climate station.

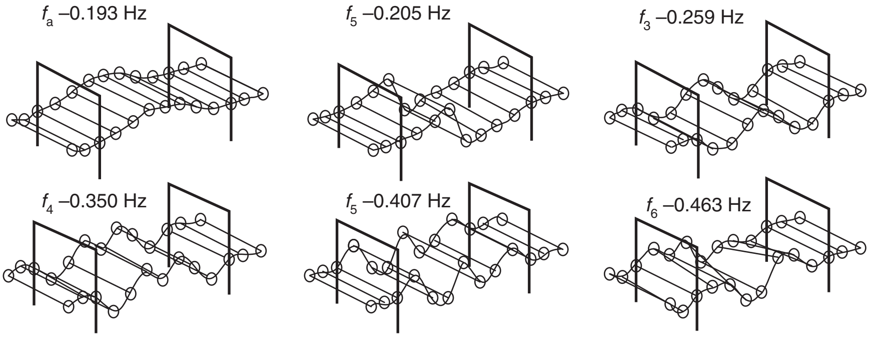
f_a –0.193 Hz
f_5 –0.205 Hz
f_3 –0.259 Hz
f_4 –0.350 Hz
f_5 –0.407 Hz
f_6 –0.463 Hz

17.19 Operating frequencies and mode shapes for the New Carquinez Bridge as derived from acceleration time histories.

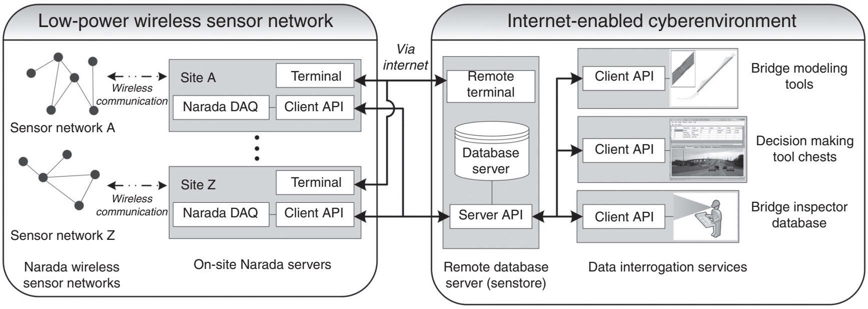
Low-power wireless sensor network
Internet-enabled cyberenvironment
Via internet
Wireless communication
Site A
Terminal
Narada DAQ
Client API
Sensor network A
Site Z
Terminal
Narada DAQ
Client API
Wireless communication
Sensor network Z
Narada wireless sensor networks
On-site Narada servers
Remote terminal
Database server
Server API
Remote database server (senstore)
Client API
Bridge modeling tools
Client API
Decision making tool chests
Client API
Bridge inspector database
Data interrogation services

17.20 Two-tiered wireless sensing network. (API = application program interface and DAQ = data acquisition.)

One of the largest contributions of this study was the implementation of a two-tiered wireless sensing network (Fig. 17.20). The lower tier is the network of low-power sensor nodes (i.e., the Narada units), which performs the data collection across the bridge. The upper tier represents a complete cyber-infrastructure framework with a remote database server called SenStore.[37] Data that are collected from the lower tier are transmitted to the database through a cellular modem where they are archived and stored. Additionally, SenStore stores bridge metadata (i.e., bridge geometric details, structural details, sensor information, etc.) in a separate database, thus allowing easy access by the end-user for modeling or decision-making use. In this way, the end-user is able to access the database at any time, thereby enabling complete information integration.

17.5.6 Case study conclusions

In this study, Kurata *et al.*[30] demonstrated the successful long-term deployment of a WSN on the New Carquinez Bridge. They were able to significantly reduce power concerns through the implementation of solar panels for recharging each wireless sensor unit's battery pack. Additionally, Kurata *et al.* refined the data collection process by creating sub-networks of sensing nodes, each reporting to its own base station, thus eliminating the need for multi-hop communication. Such a network, however, creates large amounts of data that must be stored for further analysis. As such, in this study it was demonstrated the need for, as well as the successful integration of, a database that is capable of storing information that can be easily accessed. These data may be stored in raw form, or may be processed off-line such that they are more useful to the end-user.

17.6 Conclusion

Four case studies were presented in this chapter as a means of providing a representative view of the challenges encountered during full-scale deployment of WSNs on civil infrastructure, in particular bridges. From the studies, it is evident that power consumption, reliable communications, and environmental impact are large concerns that must be addressed for successful implementation. By incorporating software enhancements, such as sleep times for sensing units or streamlining algorithms, as well as integrating alternative energy sources into the network, it is possible to overcome the power constraints of the network. Additionally, by utilizing long range radios and also carefully deploying the network such that all units can be accessed by a server station either directly or through multi-hops, reliable communication can be ensured. Finally, by carefully packaging the units and by performing routine maintenance, the units can be protected against environmental factors that may inhibit the longevity of the network. As such, by overcoming these network constraints, WSNs will become increasingly common for civil infrastructure and, as they do, it is important to develop mechanisms for dealing with the enormous amounts of data that can be extracted from the network. Therefore, as proposed by Kurata *et al.*,[30] in order for such monitoring systems to be truly successful, future work should focus on developing appropriate database systems for data collection that allow for ease of access by the end-user and full integration with existing models and decision-making tools.

17.7 Acknowledgments

The authors of this chapter would like to acknowledge the generous support provided by the National Science Foundation (NSF) through grant numbers CCF-0910765 and CMMI-0846256. The authors would also like to gratefully acknowledge the generous support offered by the US Department of Commerce, National Institute of Standards and Technology (NIST) Technology Innovation Program (TIP) under Cooperative Agreement 70NANB9H9008. Finally, preparation of the chapter was partially supported by the National Research Foundation of Korea Grant funded by the Korean Government (MEST) (NRF-2011–220-D00105 (2011068.0)).

17.8 References

1. S. B. Chase (2005), 'The Role of Sensing and Measurement in Achieving FHWA's Strategic Vision for Highway Infrastructure', in *Sensing Issues in Civil Structural Health Monitoring*, F. Ansari, Ed. The Netherlands: Springer, pp. 23–32.
2. M. Moore, B. Phares, B. Graybeal, D. Rolander and G. Washer (2000), '*Reliability of Visual Inspection for Highway Bridges, Volume 1: Final Report*', NDE Validation Center, Office of Infrastructure Research and Development, McLean, VA.
3. J. M. Ko and Y. Q. Ni (2005), 'Technology developments in structural health monitoring of large-scale bridges', *Engineering Structures*, vol. **27**, no. 12, pp. 1715–1725.
4. M. Celebi (2002), '*Seismic Instrumentation of Buildings* (*with Emphasis on Federal Buildings*)', United States Geological Survey (USGS), Menlo Park, CA.
5. E. G. Straser, A. S. Kiremidjian, T. H. Meng and L. Redlefsen (1998), 'Modular, wireless network platform for monitoring structures', in *16th International Modal Analysis Conference (IMAC)*, vol. **1**, pp. 450–456.
6. J. P. Lynch and K. J. Loh (2006), 'A summary review of wireless sensors and sensor networks for structural health monitoring', *The Shock and Vibration Digest*, vol. **38**, no. 2, pp. 91–128.
7. B. F. Spencer, M. E. Ruiz-Sandoval and N. Kurata (2004), 'Smart sensing technology: Opportunities and challenges', *Journal of Structural Control and Health Monitoring*, vol. **11**, pp. 349–368.
8. S. N. Pakzad, G. L. Fenves, S. Kim and D. E. Culler (2008), 'Design and implementation of scalable wireless sensor network for structural monitoring', *Journal of Infrastructure Systems*, vol. **14**, no. 1, pp. 89–101.
9. A. M. Abdel-Ghaffar and R. H. Scanlan (1985), 'Ambient vibration studies of Golden Gate Bridge: I. Suspended structures', *Journal of Engineering Mechanics*, vol. **111**, no. 4, pp. 463–482.
10. A. M. Abdel-Ghaffar and R. H. Scanlan (1985), 'Ambient vibrations studies of Golden Gate Bridge: II. Pier-tower structure', *Journal of Engineering Mechanics*, vol. **1111**, no. 4, pp. 483–499.
11. C. Technology (2012), 'MICAz Datasheet, Document Part Number: 6020–0060–04 Rev A'. Online. Available: http://www.openautomation.net/uploadsproductos/micaz_datasheet.pdf.
12. S. Kim, S. Pakzad, D. Culler, J. Demmel, G. Fenves, S. Glaser and M. Turon (2007), 'Health monitoring of civil infrastructures using wireless sensor networks',

Proceedings of the 6th International Conference on Information Processing in Sensor Networks. ACM, Cambridge, Massachusetts, USA.

13. M. Maroti, B. Kusy, S. Gyula and A. Ledeczi (2004), 'The flooding time synchronization protocol', in *SenSys '04 2nd International Conference on Embedded Networked Sensor Systems*, pp. 39–49.
14. G. Feltrin, J. Meyer, R. Bischoff and M. Motavalli (2009), 'Long-term monitoring of cable stays with a wireless sensor network', *Structure and Infrastructure Engineering: Maintenance, Management, Life-Cycle Design and Performance*, vol. **6**, no. 5, pp. 535–548.
15. J. Meyer, R. Bischoff, G. Feltrin and M. Motavalli (2010), 'Wireless Sensor Networks for Long Term Structural Monitoring', *Smart Structures and Systems*, vol. **6**, no. 3, pp. 263–275.
16. G. Feltrin, O. Saukh, R. Bischoff, J. Meyer and M. Motavalli (2011), 'Structural monitoring with wireless sensor networks: Experiences from field deployments', in *First Middle East Conference on Smart Monitoring Assessment and Rehabilitation of Civil Structures*.
17. Moteiv Corporation (2006), 'Tmote Sky: Datasheet, Online. Available: http://www.eecs.harvard.edu/~konrad/projects/shimmer/references/tmote-sky-datasheet.pdf.
18. J. P. Lynch, A. Sundararajan, K. H. Law, A. S. Kiremidjian and E. Carryer (2004), 'Embedding damage detection algorithms in a wireless sensing unit for operational power efficiency', *Smart Materials and Structures*, vol. **13**, pp. 800–810.
19. J. R. Casas (1994), 'A combined method for measuring cable forces: The cable-stayed Alamillo Bridge, Spain', *Structural Engineering International*, vol. **4**, no. 4, pp. 235–240.
20. S. Jang, H. Jo, S. Cho, K. Mechitov, J. A. Rice, S.-H. Sim, H.-J. Jung, C.-B. Yun, B. F. J. Spencer and G. Agha (2010), 'Structural health monitoring of a cable-stayed bridge using smart sensor technology: Deployment and evaluation', *Smart Structures and Systems*, vol. **5**, no. 6, pp. 439–459.
21. H. Jo, S.-H. Sim, K. A. Mechitov, R. Kim, J. Li, P. Moinzadeh, B. F. J. Spencer, J. W. Park, S. Cho, H.-J. Jung, C.-B. Yun, J. A. Rice and T. Nagayama (2011), 'Hybrid wireless smart sensor network for full-scale structural health monitoring of a cable-stayed bridge', in *Proceedings of SPIE – Sensors and Smart Structures Technologies for Civil, Mechanical and Aerospace Systems*.
22. J. A. Rice and B. F. Spencer Jr. (2008), 'Structural health monitoring sensor development for the Imote2 platform', in *Proceedings of the SPIE Smart Structures/NDE 2008*, San Diego, CA.
23. Crossbow Technology (2007), 'Imote2 Datasheet, Document Part Number: 6020–0117–02 Rev A', Online.. Available: http://www.xbow.com/Products/Product_pdf_files/Wireless_pdf/Imote2_Datasheet.pdf.
24. J. A. Rice, K. Mechitov, S.-H. Sim, T. Nagayama, S. Jang, R. Kim, B. F. J. Spencer, G. Agha and Y. Fujino (2010), 'Flexible smart sensor framework for autonomous structural health monitoring', *Smart Structures and Systems*, vol. **5**, no. 6, pp. 423–438.
25. T. Nagayama, H.-J. Jung, B. F. J. Spencer, S. Jang, K. A. Mechitov, S. Cho, M. Ushita, C.-B. Yun, G. A. Agha and Y. Fujino (2010), 'International collaboration

to develop a structural health monitoring system utilizing wireless smart sensor network and its deployment on a cable-stayed bridge', in *5th World Conference on Structural Control and Monitoring*.

26. Quickfilters Technologies (2009), 'QF4A512: 4-channel programmable signal converter. Online. Available: http://www.quickfiltertech.com/files/QF4A512-revD8.pdf.
27. J. W. Park, S. Cho, H.-J. Jung, C.-B. Yun, S. A. Jang, K. Jo, B. F. J. Spencer, T. Nagayama and J.-W. Seo (2010), 'Long-term structural health monitoring system of a cable-stayed bridge based on wireless smart sensor networks and energy harvesting techniques', in *5th World Conference on Structural Control and Monitoring*.
28. W. Ye, J. Heidemann and D. Estin (2002), 'An energy-efficient MAC protocol for wireless sensor networks', in *21st Annual Joint Conference on the IEEE Computer and Communication Societies*, pp. 1567–1576.
29. S. Cho, S. A. Jang, H. Jo, K. A. Mechitov, J. A. Rice, H.-J. Jung, C.-B. Yun, B. F. J. Spencer, T. Nagayama and J. Seo (2010), 'Structural health monitoring system of a cable-stayed bridge using a dense array of scalable smart sensor network', in *Proceedings of SPIE – Sensors and Smart Structures Technologies for Civil, Mechanical and Aerospace Systems*.
30. M. Kurata, J. P. Lynch, G. W. van der Linden, H. Sedarat, E. Thometz, P. Hipley and L.-H. Sheng, 'Internet-enabled wireless structural monitoring systems: Development and permanent deployment at the New Carquinez suspension bridge', *Journal of Structural Engineering*, vol. **139**, no. 10, pp. 1688–1702..
31. R. A. Swartz, D. Jung, J. P. Lynch, Y. Wang, D. Shi and M. P. Flynn (2005), 'Design of a wireless sensor for scalable distributed in-network computation in a structural health monitoring system', in *5th International Workshop on Structural Health Monitoring*.
32. J. Kim, R. A. Swartz, J. P. Lynch, C. G. Lee and C. B. Yun (2010), 'Rapid-to-deploy reconfigurable wireless structural monitoring systems using extended-range wireless sensors', *Smart Structures and Systems*, vol. **6**, no. 5, pp. 505–524.
33. R. A. Swartz, J. P. Lynch, S. Zerbst, B. Sweetman and R. Rolfes (2010), 'Structural monitoring of wind turbines using wireless sensor networks', *Smart Structures and Systems*, vol. **6**, no. 3, pp. 183–196.
34. R. A. Swartz, A. T. Zimmerman, J. P. Lynch, J. Rosario, T. Brady, L. Salvino and K. H. Law (2012), 'Hybrid wireless hull monitoring system for naval combat vessels', *Structure and Infrastructure Engineering*, vol. **8**, no. 7, pp. 621–638.
35. J. Kim and J. P. Lynch (2012), 'Autonomous decentralized system identification by markov parameter estimation using distributed smart wireless sensor networks', *Journal of Engineering Mechanics*, vol. **138**, pp. 478–490.
36. B. Peeters and G. De Roeck (1999), 'Reference-based stochastic subspace identification for output-only modal analysis', *Mechanical Systems and Signal Processing*, vol. **13**, no. 6, pp. 855–878.
37. Y. Zhang, M. Kurata, J. P. Lynch, G. W. van der Linden, H. Sadarat and A. Prakash (2012), 'Distributed cyber-infrastructure tools for automated data

processing of structural monitoring data', in *Proceedings of SPIE – Nondestructive Characterization for Composite Materials, Aerospace Engineering, Civil Infrastructure and Homeland Security*.

38. R. J. Niewiroski (2007), 'The Golden Gate Bridge', *Wikimedia Commons*. Online. Available: http://www.projectrich.com/gallery.
39. Decent Lab (2012), 'Stork Bridge in Winterthur', Applications: Structural Monitoring. Online. Available: http://www.decentlab.com/index.php?id=50.

18

Energy harvesting for infrastructure sensing systems

J. T. SCRUGGS, University of Michigan, USA

DOI: 10.1533/9780857099136.510

Abstract: This chapter gives an overview of some of the fundamental design issues arising in vibration energy harvesting systems for sensing applications. We focus primarily on piezoelectric and electromagnetic transducers. Linear dynamical models for these systems are presented and discussed. Impedance matching theory is discussed, and its application to monochromatic energy harvesting is explained. Fundamental limits on power generation are presented for monochromatic disturbances, and analogous limits for stochastic disturbances are briefly presented. Passive tuning techniques are discussed, for reactive power compensation.
A number of basic electronic circuits for extracting power from harvesters are described, including the standard diode bridge rectifier, DC/DC converters, and synchronized switch harvesting inductor (SSHI) circuits. Applicability and tradeoffs between these circuits are discussed. The article closes with some comments about current research trends in small-scale vibration energy harvesting.

Key words: vibration, energy harvesting, impedance matching, power electronics.

18.1 Introduction

In many wireless sensing applications, power availability issues pose some of the most daunting challenges. These sensors are intended for use over the service life of a structure, which implies decades of operation. On-board battery storage systems present obstacles toward the achievement of this objective for a few reasons. In general, they must be periodically replaced or recharged as their energy is depleted. This requirement of routine maintenance may be undesirable in many applications. For example, it limits usage of the sensor to applications in which the unit (or at least its energy storage subsystem) can be easily accessed. This prohibits such sensors from being truly embedded in smart structures, and also may prohibit their reliable use in remote and hostile environments. Moreover, it is a well-known fact that the energy and power density of power storage technology has grown at a much slower rate than the energy and power requirements of small-scale intelligent systems.[1] These issues have motivated a considerable amount of

© 2014 Woodhead Publishing Limited

research activity over the last decade, toward the development of autonomous technologies to harvest energy for wireless sensors, from physical phenomena in proximity to the sensor.

There are indeed a variety of localized energy sources that may be tapped to power wireless sensors. In applications where sensors are mounted to the exterior of a structure, or where they are exposed to ambient lighting, solar energy collection is arguably the most straightforward technology. Integration of small solar panels into wireless sensing units has been demonstrated, and such systems are actually available commercially. Energy may also be harvested from temperature differentials, through a variety of thermal power conversion techniques. In applications where significant fluid flows exist, microturbines can be used to convert this flow energy into electricity, or it can be extracted from deliberately induced turbulence, through a variety of means. In other applications in which a structure or material is subjected to slowly varying (i.e., quasi-static) stresses, piezoelectric materials can be used to harvest a resultant strain-induced charge. Furthermore, there are also opportunities in many applications to wirelessly transmit radio frequency (RF) energy.

All the above techniques, and especially solar energy systems, have been widely explored in the context of wireless sensing nodes. The recent survey by Sudevalayam and Kulkarni[2] provides an excellent recent snapshot of where these technologies are, both in terms of the vanguard of research and development, as well as for readily available commercial units. For solar energy harvesting in particular, a number of plug-and-play devices and development boards can now be purchased for wireless sensor applications, including products from Texas Instruments, Cymbet Corporation, MicroStrain, EnOcean, Solarcraft, Midé, and several others.

It is often argued that for many structural systems, the most pervasive type of energy available to embedded and inaccessible sensors is low-level vibratory energy. This energy manifests itself in the form of machinery vibrations, vehicular traffic, pedestrian activity, etc. Because of the ubiquity of the resource, vibratory energy harvesting (VEH) technology has been the subject of considerable research, with applications spanning the fields of civil, aerospace, transportation, and biomedical engineering. Also for this reason, VEH systems are the focus of this chapter. Many surveys have been written recently, which give snapshots of the status of the technology in this field.[3–8] It is not the purpose of this chapter to provide such a survey, which would inevitably become out-of-date after a short time. Instead, this chapter will concentrate on establishing the theoretical basis for VEH systems, and will illustrate how their technological particulars translate into fundamental engineering problems.

In order to harvest vibratory energy, it must be converted to electricity via some mode of transduction. Typically this transduction is embedded in a resonant electromechanical system that we will call the *harvester*, which is mounted on a larger vibrating structure. The larger structure is assumed to be massive in comparison to the harvester, such that its acceleration can be assumed to be unaffected by the dynamic behavior of the harvester. (This assumption is not necessary in order to analyze and design energy harvesters, but it does simplify the analysis and is valid in many applications.) A harvester is typically tuned such that its natural frequency is within the disturbance passband. At the μW-mW scale, there are three general modes of transduction that have historically been dominant in applications: electromagnetic, piezoelectric, and electrostatic transduction.

Electromagnetic transducers are typically coupled to a single degree-of-freedom (SDOF) sprung mass, as shown in Fig. 18.1a. The transducer simply comprises a moving magnet in a coil, as shown. Speaking broadly, one of the challenges posed by this type of transduction is that it is generally difficult to generate useful voltage levels as the scale becomes small. This is because an electromagnet generates a voltage in proportion to its velocity, with the constant of proportionality growing with the strength of the magnet and the number of coil windings. It is therefore quite difficult to design electromagnetic harvesters with acceptable voltage levels, as the size requirements become more restrictive. However, a number of researchers have demonstrated impressive small-scale prototypes.[9]

Piezoelectric transduction can be embedded into several different types of resonant harvesters, but one of the more common approaches is to bond a layer of piezoceramic material (such as lead zirconate titanate, or PZT) to a flexible beam, which is mounted on the vibratory surface as shown in Fig. 18.1b. This particular configuration is called a *bimorph* configuration, because the material is bonded to both sides of the beam, with the top and

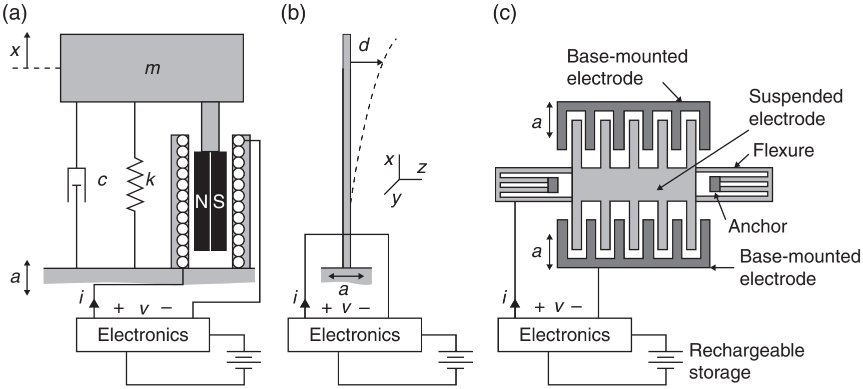

18.1 Harvesters with electromagnetic (a), piezoelectric (b), and electrostatic (c) transduction.

bottom electrodes connected, either in series or parallel. Piezoelectric transducers are arguably the most prevalent at small scale, and have been implemented by many researchers.[4,6] When properly designed, they are capable of generating useful voltages even when strains are very small, and they are easier to fabricate at small scale than electromagnetic transducers. However, as we will discuss in Section 18.4, these advantages do come at a price, in the form of more complicated power processing circuitry.

For applications at the micro-electromechanical systems (MEMS) scale, electrostatic transducers may be a more viable transduction mode. These devices, illustrated in Fig. 18.1c, consist of comb-shaped electrodes, connected through a flexible linkage. The outer electrode is mounted to a base, while the central electrode remains suspended. When the base is shaken, this causes the suspended electrode to resonate, thus causing its teeth to oscillate in and out of those of the base electrode. This has the effect of varying the capacitance between the two electrodes. If the voltage between the electrodes is controlled in coordination with these oscillations in capacitance, this results in energy conversion. Electrostatic harvesters have been successfully demonstrated for use in MEMS systems.[10,11] Although they do scale down very well for MEMS integration, they also require the most sophisticated electronics of the three transduction modes discussed.[12] Additionally, we note that piezoelectric transduction has also been successfully implemented at MEMS scales.[13]

In this chapter, we will focus on electromagnetic and piezoelectric harvesters, which can be analyzed using similar techniques, and which have been demonstrated to be viable sources of power for a multitude of sensor applications.

A number of VEH systems are commercially available, although it must be said that at the present time most products operate at vibration power levels and base acceleration levels that are far in excess of what is typical for sensing applications in civil engineering. A few of the VEH modules currently available off-the-shelf (i.e., as a system, including the transducer, power electronics, and in some cases, local storage) are given in Table 18.1. Many of these products were originally developed for applications with strong vibratory signatures, such as machine and heating, ventilation and air conditioning (HVAC) monitoring, as well as aerospace and defense applications. Some of these companies (such as Midé) have demonstrated their devices to be scalable well below their ratings. Beyond the companies listed in this table, several more (such as Smart Material, PowerCast) offer customizable energy harvesting evaluation kits, which provide modular components for power conversion and storage, but which also allow for considerable customization. Many other companies, (such as MicroStrain and Ambio Systems, to name just a few), provide wireless sensing motes that afford plug-and-play compatability with VEH transducers.

Table 18.1 A sampling of commercially available VEH systems

Model	Company	Type	Weight	Rating
VEH 460	Ferro solutions	EM	0.43 kg	0.3 mW at 25 mg, 60 Hz
PMG FSH	Perpetuum	EM	1.075 kg	0.43 mW at 25 mg, tunable frequency
MVEH	MicroStrain	EM	216 g	4 mW at 0.2 g, 20 Hz
PVEH	MicroStrain	PE	185 g	30 mW at 1.5 g, 1 kHz
Volture	Midé	PE	–	1.45 mW at 1 g, 120 Hz, no tip mass 9.2 mW at 1 g, 40 Hz, 15.6 g tip mass
Harvestor	Advanced Cerametrics	PE	–	0.4 mW at 3 g, 30 Hz 0.81 mW at 3 g, 220 Hz
VH-1	KCF	PE	134 g	> 0.7 g, no power/frequency rating

Techniques to scale the technology down have been demonstrated in the literature (see, e.g., References 13 and 14), but at present these have not fully crossed the threshold into wide availability, commercially. As such, applications with smaller power scales presently require at least some custom design. Scaling the technology down to lower power levels constitutes a significant challenge, especially in regards to the electronics design. We will touch on some of these challenges later in the chapter.

18.2 Harvester dynamic modeling

In this section we present the basic dynamic models for electromagnetic and piezoelectric harvesters, followed by a system-theoretic discussion of more general properties common to the dynamic models of many energy harvesting technologies.

18.2.1 Electromagnetic transducers

Harvesters with electromagnetic transduction, such as the one in Fig. 18.1a, convert power via Faraday's law, by the equations

$$f(t) = K_e i(t) \qquad v(t) = K_e \dot{x}(t) \tag{18.1}$$

where K_e is an electromagnetic conversion constant that is a function of the geometry of the coil, number of turns, and the magnetic field of the magnets. The specific functional dependency of K_e is typically linear in the field intensity and number of turns, while the dependency on the geometry depends on the configuration of the coil relative to the magnets.[11,15] The expressions in Equation [18.1] constitute the linearized version of what is always, to one degree or another, a nonlinear phenomenon exhibiting hysteretic and other losses.

The harvester dynamics are governed by the standard second-order differential equation

$$m\ddot{x}(t) + c\dot{x}(t) + kx(t) = -ma(t) + K_e i(t) \qquad [18.2]$$

In the Laplace domain, voltage v is a consequence of dynamic system inputs a and i, as

$$\hat{v}(s) = G_a(s)\hat{a}(s) + G_i(s)\hat{i}(s) \qquad [18.3]$$

where

$$G_a(s) = \frac{-K_e ms}{k + cs + ms^2} \qquad [18.4]$$

$$G_i(s) = \frac{K_e^2 s}{k + cs + ms^2} \qquad [18.5]$$

18.2.2 Piezoelectric transducers

We assume a composite beam such as the one shown in Fig. 18.1b, in which piezoelectric material is bonded to a substrate material (such as aluminum). It is not necessarily the case that the cross-sectional properties of the beam are constant; indeed, there is some benefit to making the beam become progressively more slender as it extends from the root, as this makes strain deformations more uniform in the fundamental mode. It is also not necessarily optimal to bond the transducer patch over the entire extent of the beam, as is depicted in the figure. Rather, in many designs the patch extends from the root only a fraction of the beam length. This is advantageous because by placing the transducer only where the strain is high, the voltages produced can be higher. Finally, it is often the case that a proof mass is attached to the end of the beam. This can be used to tune the resonant frequency of the beam, as well as having other advantages.

In Reference 16, the electromechanical dynamics of a beam with multiple bimorph piezoelectric transducers were derived. Here, we merely provide an overview, specializing to the single-transducer case. Let $\rho(x,y,z,t)$ denote the density at location $\{x,y,z\}$ in the substrate–piezo composite. Let $S(x,y,z,t) \in \Re^6$ and $T(x,y,z,t) \in \Re^6$ denote the Voigt (i.e., vector) form of the strain and stress tensors, and let $E(x,y,z,t) \in \Re^3$ and $D(x,y,z,t) \in \Re^3$ denote the electric field and displacement vectors. Then for small deformations and small fields, we can assume the linear, coupled constitutive law relating $\{S,E\}$ to $\{T,D\}$, i.e.,

$$\begin{bmatrix} T(x,y,z,t) \\ D(x,y,z,t) \end{bmatrix} = \begin{bmatrix} c(x,y,z,t) & -e^T(x,y,z,t) \\ e(x,y,z,t) & \varepsilon(x,y,z,t) \end{bmatrix} \begin{bmatrix} S(x,y,z,t) \\ E(x,y,z,t) \end{bmatrix} \qquad [18.6]$$

where c is the modulus of elasticity at zero field, ε is the dielectric constant matrix at zero strain, and e is the coupling coefficient matrix. (Note that in the substrate material, e and ε are zero.)

Assuming the classical Bernoulli-Euler assumptions for the beam deformation, define $d(x,t)$ as the transverse deflection of the beam centroid, and then it follows that

$$S(x,y,z,t) = yd''(x,t) \begin{bmatrix} \hat{e}_x \\ 0 \end{bmatrix} \qquad [18.7]$$

A standard Galerkin approximation is typically used for $d(x,t)$, i.e.,

$$d(x,t) = \sum_{i=1}^{N} \phi_i(x) r_i(t) = \phi^T(x) r(t) \qquad [18.8]$$

where $r(t)$ is the vector of generalized displacements, and $\phi(x)$ is the vector of Galerkin shape functions for each generalized displacement. Electric field E is assumed to be constant inside each patch, zero in the substrate, and oriented in the $\hat{e}_y$ direction everywhere; i.e.,

$$E(x,y,z,t) = \hat{e}_y \psi(y) v(t) \qquad [18.9]$$

where $\hat{e}_y$ is the unit vector on the y direction, $\psi(y)$ is a function of the patch thickness and beam geometry.

With these assumptions, the differential equations for the reduced-order system are found as

$$M\ddot{r}(t) + C\dot{r}(t) + Kr(t) + \Theta v(t) = Ga(t) \qquad [18.10]$$

$$C_p\dot{v}(t) + R_p^{-1}v(t) - \Theta^T\dot{r}(t) = i(t) \qquad [18.11]$$

where $\{M, K, \Theta, G, C_p\}$ are found through the standard Rayleigh-Ritz projection. These terms are, respectively, the generalized mass and stiffness matrices, the coupling factor matrix, disturbance input matrix, and piezocapacitance. Generally, mechanical damping matrix C is found after the fact e.g., through a Rayleigh damping assumption. The dielectric leakage resistance R_p, is extremely high for typical designs, and is often assumed to be infinite.

As with the case of the electromagnetic harvester, the Laplace domain characterization of the above is

$$\hat{v}(s) = G_a(s)\hat{a}(s) + G_i(s)\hat{i}(s) \qquad [18.12]$$

but where in this example the above transfer functions are

$$G_a(s) = \begin{bmatrix} 0 \\ 0 \\ 1 \end{bmatrix}^T \begin{bmatrix} sI & -I & 0 \\ M^{-1}K & sI + M^{-1}C & M^{-1}\Theta \\ 0 & -C_p^{-1}\Theta^T & sI + C_p^{-1}R_p^{-1} \end{bmatrix}^{-1} \begin{bmatrix} 0 \\ M^{-1}G \\ 0 \end{bmatrix} \qquad [18.13]$$

$$G_i(s) = \begin{bmatrix} 0 \\ 0 \\ 1 \end{bmatrix}^T \begin{bmatrix} sI & -I & 0 \\ M^{-1}K & sI + M^{-1}C & M^{-1}\Theta \\ 0 & -C_p^{-1}\Theta^T & sI + C_p^{-1}R_p^{-1} \end{bmatrix}^{-1} \begin{bmatrix} 0 \\ 0 \\ C_p^{-1} \end{bmatrix} \qquad [18.14]$$

18.2.3 General properties

Transfer function $G_i(s)$ is the input impedance of the transducer. One can think of it as the driving-point impedance of an electric circuit that is equivalent to the true system from the vantage point of the harvesting electronics. Because harvesters are passive systems (i.e., they typically have no internal energy sources), this equivalent network will also be passive, i.e., it can be built from ideal resistors, inductors, capacitors, transformers, and gyrators. Because of this, one can always assume that $G_i(s)$ is positive real, i.e.,

$$\mathrm{Re}\{G_i(j\omega)\} > 0,\ \forall\omega \in [-\infty,\infty] \qquad [18.15]$$

This property turns out to be important, in the determination of the maximum power generation for energy harvesters.

18.3 Power availability and the optimal harvesting admittance

This section is concerned with the determination of how much power one can expect to generate from a given disturbance, using a given harvester. Specifically, we derive upper limits on the available power, by assuming the electronics are very efficient. This assumption is never completely justifiable, and invariably gives overly optimistic estimates of available power. On the other hand, the analysis is still useful because if the power levels derived here are insufficient for a given application, it can be determined immediately that there is no hope of a given disturbance/harvester combination meeting a design specification. We will keep the discussion general to all linear harvesters, although the results here do specialize on many of the more specific cases derived in the literature (such as in Reference 17 for piezoelectric devices).

18.3.1 Classical impedance matching theory

Consider the case in which $a(t)$ is a finite-energy signal, i.e., one for which $\int_0^\infty a^2(t)dt$ is finite, and let $\hat{a}(s)$ be its Laplace transform. Similarly, let $\hat{i}(s)$ and $\hat{v}(s)$ be the Laplace transforms for the corresponding current and voltage, which we also assume to have finite signal energy. The total amount of energy absorbed from the transducer by the electronics is

$$E_{\text{abs}} = \int_0^\infty -v(t)i(t)dt \qquad [18.16]$$

By the Plancharel theorem, we have that this energy is equivalent to

$$E_{\text{abs}} = \frac{1}{2\pi}\int_{-\infty}^\infty -\hat{v}(-j\omega)\hat{i}(j\omega)d\omega \qquad [18.17]$$

Substituting Equation [18.12], we have

$$E_{\text{abs}} = \frac{1}{2\pi}\int_{-\infty}^\infty -\left(G_a(-j\omega)\hat{a}(-j\omega) + G_i(-j\omega)\hat{i}(-j\omega)\right)\hat{i}(j\omega)d\omega \qquad [18.18]$$

Now, consider that at each ω we can find the $\hat{i}(j\omega)$ maximizing E_{abs}. Performing this maximization, with the constraint that $\hat{i}(-j\omega)$ is the complex conjugate of $\hat{i}(j\omega)$, gives the optimal current as

$$\hat{i}(j\omega) = -\frac{G_a(j\omega)}{G_i(j\omega)+G_i(-j\omega)}\hat{a}(j\omega) \qquad [18.19]$$

Correspondingly, the voltage $\hat{v}(j\omega)$ with the optimal $\hat{i}(j\omega)$ imposed, is

$$\hat{v}(j\omega) = \frac{G_i(-j\omega)G_a(j\omega)}{G_i(j\omega)+G_i(-j\omega)}\hat{a}(j\omega) \qquad [18.20]$$

and the optimized absorbed energy is

$$E_{\text{abs}} = \frac{1}{2\pi}\int_{-\infty}^{\infty}\frac{G_i(j\omega)\,|\,G_a(j\omega)\hat{a}(j\omega)\,|^2}{(G_i(j\omega)+G_i(-j\omega))^2}\,d\omega \qquad [18.21]$$

Recognizing that $\operatorname{Im}\{G_i(j\omega)\} = -\operatorname{Im}\{G_i(-j\omega)\}$ and $\operatorname{Re}\{G_i(j\omega)\} = \operatorname{Re}\{G_i(-j\omega)\}$, the above is equivalent to

$$E_{\text{abs}} = \frac{1}{2\pi}\int_{-\infty}^{\infty}\frac{|\,G_a(j\omega)\hat{a}(j\omega)\,|^2}{4\operatorname{Re}\{G_i(j\omega)\}}\,d\omega \qquad [18.22]$$

Note that the integrand above is real and positive at all frequencies, and constitutes the spectrum of optimized energy.

In the Laplace domain, the optimal $\hat{i}(s)$ may be expressed as a feedback function of $\hat{v}(s)$ as

$$\hat{i}(s) = -Y(s)\hat{v}(s) \qquad [18.23]$$

where

$$Y(s) = G_i^{-1}(-s) \qquad [18.24]$$

is called the *impedance matched* feedback law. However, unlike our usual conventions for feedback, $Y(s)$ above would need to be anticausal (i.e., anticipatory) in order for the closed-loop system to be stable. (In the time domain, this fact would be evident from the impulse response of $Y(s)$ being left-handed, rather than right-handed.) As such, we can say that in general, in order for an VEH system to maximize the physically-available power, it must make power generation decisions based on future disturbance information.

18.3.2 Power availability and tuning for monochromatic disturbances

Now, consider the case in which $a(t)$ is monochromatic, i.e.,

$$a(t) = a_0 \cos \omega_0 t \qquad [18.25]$$

for time-invariant a_0 and ω_0. In this case, it turns out that an analogous optimization can be done, again arriving at the same matching condition in Equation [18.24]. However, in this case, $\hat{a}(j\omega)$ is zero at all frequencies except $\omega = \omega_0$, and it is therefore only necessary for a feedback law $Y(s)$ to satisfy Equation [18.24] at $s = j\omega_0$. At all other frequencies, $Y(j\omega)$ can be chosen arbitrarily, or to meet other design considerations. It is always possible to satisfy the matching condition $Y(j\omega_0) = G_i^{-1}(-j\omega_0)$ with a causal and stable feedback law, and often this feedback law is made equivalent to a simple two-component electric circuit that shunts the transducer, the admittance of which equals $Y(s)$. Two such circuits are shown in Fig. 18.2. A feedback law equivalent to an inductor L in parallel with a resistor R would be

$$Y(j\omega_0) = R^{-1} - j(\omega_0 L)^{-1} \qquad [18.26]$$

which, through choice of R and L, can be made any magnitude, and any phase in the range $[-\pi/2, 0]$. Similarly, a feedback law equivalent to a capacitor C in parallel to a resistor R would be

$$Y(j\omega_0) = R^{-1} + j\omega_0 C \qquad [18.27]$$

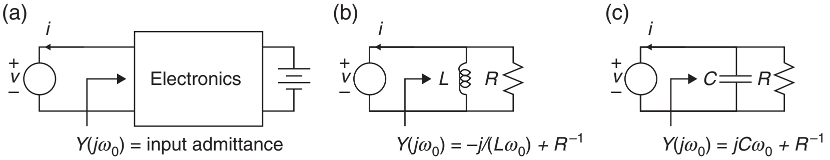
(a)
i
+
v
−
Electronics
$Y(j\omega_0)$ = input admittance
(b)
i
+
v
−
L
R
$Y(j\omega_0) = -j/(L\omega_0) + R^{-1}$
(c)
i
+
v
−
C
R
$Y(j\omega_0) = jC\omega_0 + R^{-1}$

18.2 Equivalent circuits of matched impedances for monochromatic disturbances: general (a), inductive (b), and capacitive (c).

which, through choice of R and C, can be made any magnitude, and any phase in the range $[0, \pi/2]$. Because $G_i(s)$ is positive real, it is known that its phase at all frequencies is in the range $[-\pi/2, \pi/2]$ and therefore, one of the above two cases always results in a matching circuit for any ω_0.

Suppose that the electronics are designed such that their dynamics relate i to v through some causal and stable transfer function, as in Equation [18.23], but not necessarily for the optimal $Y(s)$. Then the closed-loop system is described in the frequency domain, by

$$\hat{v}(j\omega) = H_a(j\omega)\hat{a}(j\omega) \tag{18.28}$$

$$\hat{i}(j\omega) = -Y(j\omega)H_a(j\omega)\hat{a}(j\omega) \tag{18.29}$$

where

$$H_a(j\omega) = \frac{G_a(j\omega)}{1 + G_i(j\omega)Y(j\omega)} \tag{18.30}$$

For the case in which $a(t)$ is characterized by Equation [18.25], the voltage and current in the time domain are

$$v(t) = a_0 \,|\, H_a(j\omega_0) \,|\, \cos(\omega_0 t + \phi_v), \;\; \phi_v = \angle(H_a(j\omega_0)) \tag{18.31}$$

$$i(t) = -a_0 \,|\, Y(j\omega_0) \,||\, H_a(j\omega_0) \,|\, \cos(\omega_0 t + \phi_i), \;\; \phi_i = \phi_v + \angle(Y(j\omega_0)) \tag{18.32}$$

The instantaneous absorbed power is $P_{\text{abs}}(t) = -v(t)i(t)$. Substituting the above, and using some trigonometric identities, we have that

$$P_{\text{abs}}(t) = P\left[1 + \cos(2(\omega_0 t + \varphi_v))\right] + Q\sin(2(\omega_0 t + \varphi_v)) \tag{18.33}$$

where P and Q are the so-called *real* and *reactive* energy flows, defined as

$$P = \tfrac{1}{2} a_0^2 \,|\, H_a(j\omega_0) \,|^2 \, \text{Re}\{Y(j\omega_0)\} \tag{18.34}$$

$$Q = -\tfrac{1}{2} a_0^2 \,|\, H_a(j\omega_0) \,|^2 \, \text{Im}\{Y(j\omega_0)\} \tag{18.35}$$

Note that on average, the reactive power oscillates about zero, while the real power has a mean value of P. This is the average power generation in monochromatic response.

Evaluating the value of P at the optimized $Y(j\omega) = G_i^{-1}(-j\omega)$ gives the physical limit on generated power, as

$$P_{\text{opt}} = \frac{|G_a(j\omega_0)|^2}{8\,\text{Re}\{G_i(j\omega_0)\}} a_0^2 \qquad [18.36]$$

This is the fundamental limit on power generation for monochromatic disturbances. Meanwhile, the reactive power with the optimal feedback is

$$Q_{\text{opt}} = -\frac{|G_a(j\omega_0)|^2 \ \text{Im}\{G_i(j\omega_0)\}}{8\,\text{Re}\{G_i(j\omega_0)\}^2} a_0^2 \qquad [18.37]$$

From Equation [18.33], we see that if $|Q|$ is large, this implies that for each oscillatory cycle a significant amount of energy oscillates back and forth between the harvester and the electronics. If Q is zero, on the other hand, energy always flows from the harvester to the electronics. This is advantageous for a few reasons. Firstly, if it is only necessary for the electronics to facilitate energy flow in one direction, the processing circuitry can be simplified. Secondly, even if processing circuitry with bidirectional energy flow is used, the above analysis does not account for the conductive loss in the circuit, and this loss is minimized for a given P, by designing the system such that Q is zero. For this reason, it is often desirable to design the harvester to achieve $Q = 0$ in the development above by tuning the hardware parameters such that

$$\text{Im}\{G_i(j\omega_0)\} = 0 \qquad [18.38]$$

In other words, the harvester is tuned such that $v(t)$ and $i(t)$ are in phase at the excitation frequency.[18,19]

One way to accomplish this is through mechanical tuning design. For example, consider the SDOF electromagnetic harvester in Fig. 18.1a. In this case, we have that

$$P_{\text{opt}} = \frac{m^2 a_0^2}{8c} \qquad [18.39]$$

$$Q_{\text{opt}} = \frac{m^2 a_0^2 \left(m\omega_0^2 - k\right)}{8c^2 \omega_0} \qquad [18.40]$$

Interestingly, P_{opt} does not depend on k at all, and thus the stiffness can be chosen so as to make $Q_{\text{opt}} = 0$. This is done by tuning the harvester so that $\omega_n = \sqrt{k/m} = \omega_0$. So doing, the optimal $Y(j\omega_0)$ is

$$Y(j\omega_0) = \frac{c}{K_e^2} \qquad [18.41]$$

Thinking back to the 'equivalent circuit' interpretation of the harvesting feedback law, we see that the tuned harvester is equivalent to a resistor (i.e., with no capacitor or inductor in parallel).

To increase P_{opt} for the SDOF electromagnetic harvester, either c must be decreased, or m must be increased. Indeed, P_{opt} can theoretically be made arbitrarily large by designing the harvester to have arbitrarily small damping. This is the reason why most energy harvesters are deliberately designed to have very low damping. However, in actuality there are often other constraints that limit power generation, requiring $Y(s)$ to be different from its theoretically optimal value. For example, for the SDOF electromagnetic harvester, a displacement constraint $|x(t)| \leq x_0$ may impose a tighter limit on power generation. Using Lagrange multipliers, it can be shown that with this constraint imposed the optimal feedback law is modified to

$$Y(j\omega_0) = \frac{c+\lambda}{K_e^2} + j\frac{k - m\omega_0^2}{K_e^2\omega_0} \qquad [18.42]$$

where

$$\lambda = \max\left\{0\,, \frac{ma_0}{\omega_0 x_0} - 2c\right\} \qquad [18.43]$$

is an added term that enforces the closed-loop amplitude constraint $|x(t)| \leq x_0$ The resultant constrained optimal power generation is

$$P_{\text{opt}} = \frac{m^2 a_0^2 (c+\lambda)}{2(2c+\lambda)^2} \qquad [18.44]$$

This expression tells us a lot about the harvesting potential of SDOF systems. Note that for small a_0 and nonzero c, the stroke limit is not saturated, and the available power is the ideal limit. For $c \to 0$, the stroke limit is always saturated, and the available power is $\frac{1}{2} m\omega_0 a_0 x_0$. This is also an upper limit on the power generation, when c is finite.

Sometimes it is difficult or impossible to redesign the mechanical parameters of a VEH system to bring about $\mathrm{Im}\{G_i(j\omega_0)\} = 0$. In many circumstances, an appealing alternative is to bring this condition about via insertion of the equivalent capacitor or inductor in Fig. 18.2 across the terminals of the transducer. So doing, the new $G_i(j\omega_0)$ with this inserted component absorbed into the harvester model has zero phase at the excitation frequency, and consequently the optimized $Y(j\omega_0)$ is equivalent to a resistor. Indeed, this approach is often much easier than mechanical tuning techniques. Its primary disadvantage is that sometimes the particular value of L or C necessary to bring about the matching condition is simply unrealistic. This is true, for example, in piezoelectric applications, in which the value of L can be in the thousands of henries. One clever workaround to address this issue is the SSHI circuit, discussed in Section 18.4.4.

18.3.3 Fundamental power generation limits for stochastic disturbances

When $a(t)$ is stochastic, analogous causal limits can be found for the average power generation in stationary response. However, the mathematics associated with these limits is more complicated, and involves optimal control theory.[20] Nonetheless, there is one very simple but conservative limit that can be stated here, which is useful in sizing harvesters. Suppose that $a(t)$ is extremely broadband, and can justifiably be modeled as white noise with spectral intensity Φ_a. Then it is a fact that the optimal average power generation is bounded from above by

$$P_{\mathrm{opt}} = \frac{1}{2} m\Phi_a \qquad [18.45]$$

where m is the total mass of the harvester. It turns out that this limit holds irrespective of the harvester type; i.e., it can be a piezoelectric beam, an SDOF electromagnetic system, or even a harvester with significant nonlinearities such as an electrostatic transduction system. Furthermore, it is true whether the feedback law is linear or nonlinear, and is insurpassable irrespective of the circuitry used.

This simple limit illustrates a rather uncompromising truth about harvesting energy from broadband stochastic disturbances. The only way to raise the limit is to add mass. However, it is also worth noting that most harvesters, when excited by broadband disturbances, would fall well short of this upper limit, due to internal dissipation in the harvester as well as dissipation in the circuitry. Design of stochastic VEH technologies that come anywhere near reaching the above limit is generally quite challenging.

18.4 Power extraction circuits

The theory derived in the previous section constitutes the idealized situation, in which the electronics that interface the transducer with the energy storage can be designed to absorb energy like a linear admittance $Y(s)$. We showed that for a monochromatic disturbance at frequency ω_0, it is only necessary for the electronics to have this input admittance at $s = j\omega_0$. This makes it easy to design the optimal linear admittance as a combination of a resistor with a reactive component (either an inductor or capacitor, depending on the transducer technology and shaking frequency), as illustrated in Fig. 18.2. However, we have not talked about what the energy harvesting electronics actually constitute, or discussed the way in which practical issues complicate matters.

In order to discuss these issues more concisely from an electrical point of view, equivalent circuit representations of harvesters are helpful. Figure 18.3 shows the Thévenin equivalent circuit for an arbitrary harvester, in which $e(t)$ is called the *open-circuit voltage*. For monochromatic disturbances, it is equal to

$$e(t) = |G_a(j\omega)|\, a_0 \cos(\omega_0 t) = e_0 \cos(\omega_0 t) \qquad [18.46]$$

and the electrical impedance $Z(s) = G_i(s)$, as defined in the previous section. If a reactive component has been added to the terminals of the harvester to tune its response, as discussed in the previous section, we assume that this component has been absorbed into the models for G_a and G_i. We refer to a VEH system which has been designed to bring about $\mathrm{Im}\{G_i(j\omega_0)\} = 0$ as a *tuned* system.

18.4.1 Resistive loads

By far, the most convenient situation in energy harvesting would be where the power generated by the harvester is consumed by a resistive load, with a resistance that can be chosen freely. In this case, the designer would first electrically tune the harvester, if it is not already tuned mechanically, and then simply choose the load resistance to be the optimal R derived from the previous section.

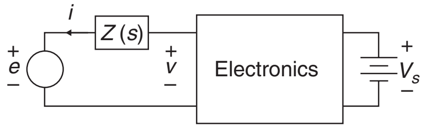

18.3 Thévenin equivalent circuit for an arbitrary VEH system.

However, the reality of an energy harvesting application is usually much more complicated than this scenario. To start with, it is hardly ever the case that the subsystems for which power is being generated consume this power like a simple resistance, and even less common that the resistance may be treated as a design parameter. For sensing applications, harvested energy is usually delivered to a storage subsystem, consisting of a supercapacitor, rechargeable battery, or some combination of both. Typically, sensing systems operating on harvested energy will spend the majority of the time in a sleep mode, where they consume very little power, during which time the storage bus is trickle charged. Then, periodically, the sensor will come online, conduct measurement, computation, and broadcasting tasks, before returning to sleep mode. As such, the sensing system consumes energy in short bursts of activity, during which time the electronics must maintain a constant voltage on the power bus.

In this context, our energy harvesting analysis from the previous section really pertains to the behavior of the system during the 'sleep mode' periods, when the primary objective is to replenish energy storage. During this time, the electronics must facilitate energy transferral from an oscillatory voltage (i.e., e) to the storage device, which typically will possess a positive voltage V_S that rises as a slowly varying parameter as the stored energy increases.

18.4.2 The diode bridge rectifier

The simplest (and by far the most prevalent) recharge circuit is a simple full-bridge diode rectifier. This circuit is shown in Fig. 18.4a. Full-bridge rectifiers conduct current when the transducer voltage magnitude $|v(t)|$ exceeds the bus voltage V_S plus the diode conduction voltage V_d, and disconnects the transducer from storage otherwise. Assuming V_S is a slowly varying parameter, the rectifier imposes a nonlinear relationship between voltage and current, governed by

$$\begin{array}{lcl} |v(t)| < V_S + V_d & : & i(t) = 0 \\ |v(t)| = V_S + V_d & : & i(t) \neq 0 \end{array} \qquad [18.47]$$

As such, the rectifier imposes an amplitude saturation on $v(t)$, and draws the current $i(t)$ necessary to ensure this condition. This is illustrated in Fig. 18.4b.

In using a diode bridge rectifier, one would ideally use a capacitor or inductor to tune the harvester. Then, using the method of harmonic balance, an approximately equivalent input resistance R_{eq} (i.e., a resistance which absorbs the same energy per cycle) can be found for the electronics,

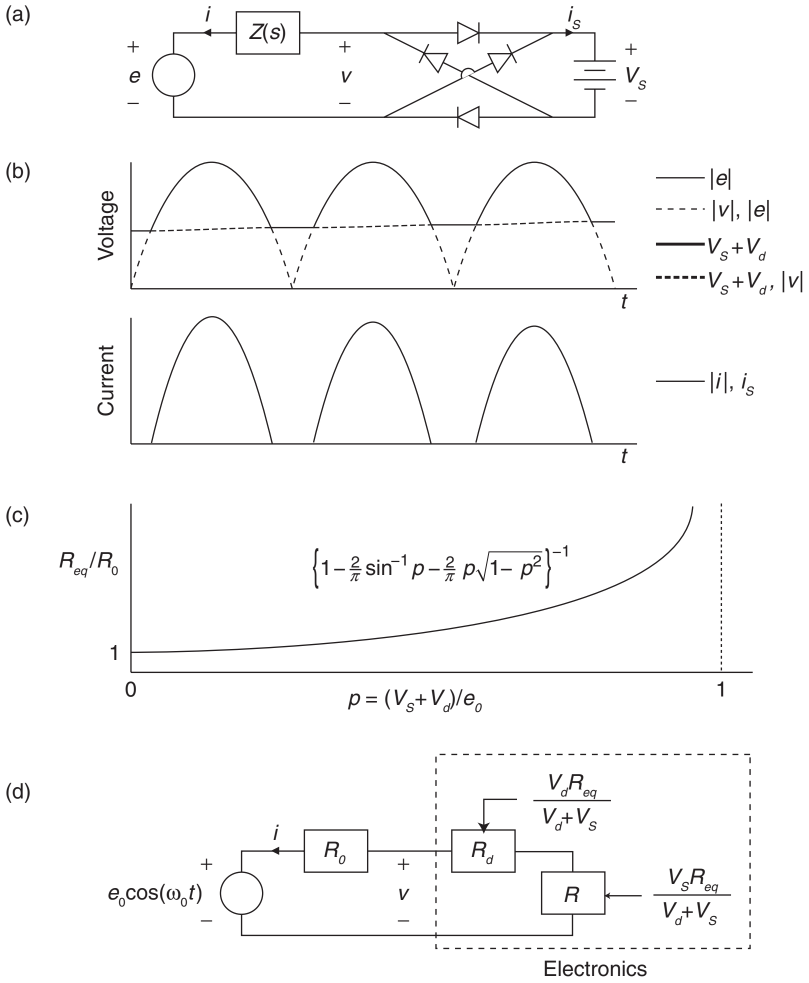
(a)
i
Z(s)
i_s
+
e
–
+
v
–
+
V_S
–
(b)
Voltage
t
|e|
|v|, |e|
V_S+V_d
V_S+V_d, |v|
Current
t
|i|, i_s
(c)
R_{eq}/R_0
$\left\{1-\frac{2}{\pi}\sin^{-1}p-\frac{2}{\pi}p\sqrt{1-p^2}\right\}^{-1}$
1
0
1
$p=(V_S+V_d)/e_0$
(d)
$\frac{V_dR_{eq}}{V_d+V_S}$
i
R_0
R_d
+
$e_0\cos(\omega_0 t)$
–
+
v
–
R
$\frac{V_SR_{eq}}{V_d+V_S}$
Electronics

18.4 Passive full-bridge diode rectifier (a), voltage and current waveforms for a tuned harvester (b), the corresponding equivalent input resistance of the rectifier (c), and an approximate equivalent circuit for the electronics (d).

which is shown in Fig. 18.4c. The specific expression for R_{eq} is complicated, but the general behavior is that R_{eq} for a tuned harvester depends on the ratios $(V_S + V_d)/e_0$ and $R_0 = Z(j\omega_0)$. As shown in Fig. 18.4d, a fraction of this equivalent resistance (R_d) accounts for the power dissipated by the current as it is transmitted through the rectifier. The remainder of the resistance (R) represents the power absorbed by the storage system. For a tuned harvester, power transferral is optimized with the matching condition

$$R = R_0 + R_d \qquad [18.48]$$

The problem with the diode bridge rectifier is that R_{eq} varies over time, as V_S rises, and cannot be controlled. For example, consider the scenario in which the recharge process is initiated at $V_S \approx 0$, and assume a_0 is sufficiently large such that $e_0 > V_S + V_d$ (otherwise, the rectifier will not conduct at all). Then over time, as V_S rises due to the recharge operation, R_{eq} will increase from a low initial value at $V_S \approx 0$, to infinity when $V_S = e_0 - V_d$. This has two specific drawbacks:

- The rate at which energy is delivered to storage is much lower than the optimal power P_{opt} derived in the last section, because R_{eq} will be far from the optimal value for most of the recharge duration. This implies longer recharge times for a desired amount of energy, and inefficient use of the harvester.
- The value of V_S will never exceed e_0, no matter how much time the system is given to recharge. Thus, the recharged bus voltage and recovered energy are limited by the level of shaking. For example, if the energy storage device is a supercapacitor with capacitance C_S, the stored energy is limited to $E_S = \frac{1}{2} C_S e_0^2$.

These drawbacks can limit the usage of the diode bridge rectifier as a recharge circuit. However, for a given application, it makes sense to first assess the typical magnitudes of e_0, and the desired recharge rate, and to see if the diode bridge rectifier will be sufficient. It may also be worth considering a redesign of the harvester, expressly to better cope with these limitations. This is because, even though its performance is limited, the full-bridge rectifier does have the distinct advantage of simplicity. In particular, it has no transistors, and does not require control. As such, it is definitely the preferred option for applications where its limitations can be tolerated.

18.4.3 Pulse-width-modulation (PWM)-controlled DC/DC converters

Various techniques have been proposed to overcome the aforementioned drawbacks of the full-bridge rectifier. The central issue is the desire for a recharge circuit with an input impedance that looks like the optimal equivalent resistance R derived in the previous section. Then, by placing a passive reactive component (i.e., an inductor or capacitor) in parallel with this recharge circuit, the input admittance of electronics will look equivalent to one of the circuits in Fig. 18.2, resulting in optimal absorption.

One way to accomplish this is to insert a switch-mode DC/DC converter between the bridge rectifier and the storage bus.[21,22] One example of such an implementation, shown in Fig. 18.5a, consists of a MOSFET and diode, together with an inductor, and two capacitors for current filtering. It is controlled by switching the MOSFET on and off, in a PWM cycle. When the MOSFET is switched on, it conducts current, while the diode does not. Alternatively, when the MOSFET is switched off, it appears as an open circuit, and the inductor current flows through the diode. The idea is that by switching the MOSFET on and off periodically at frequency $f_s = 1/t_s$, and with duty ratio d, the converter pumps energy from the transducer to the storage bus, using the inductor as an intermediary. Standard procedure is to operate the circuit at a switching frequency which is much higher than the frequency of excitation.

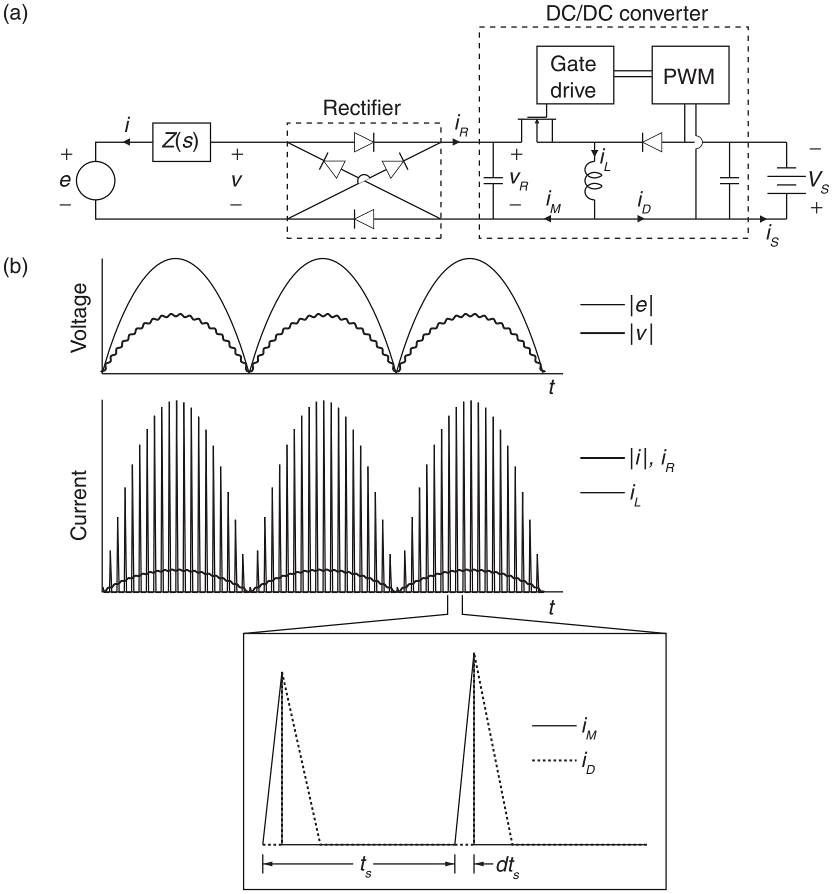

18.5 Buck-boost DC/DC converter power extraction circuit (a), and illustration of discontinuous conduction PWM cycle (b).

The particular converter shown is called a 'buck-boost' converter, because it can transfer power from V_R to V_S, irrespective of which voltage is the larger. This converter is particularly useful for energy harvesting because, when it is operated in the discontinuous conduction regime (i.e., when the inductor current drops to zero before the end of each PWM cycle), its input impedance is approximately linear and resistive at frequencies well below f_s[23]. More specifically, it turns out that at the excitation frequency, ω_0, the input impedance from the point of view of transducer can be expressed approximately as

$$R_{\text{eq}} \approx \frac{r}{d^2} \qquad [18.49]$$

where r is a constant that depends primarily on f_s and L, but is highly insensitive to V_S. As such, the input resistance of the converter can be specified indirectly through proper choice of d, and stays approximately constant as the storage system recharges.[24]

The use of a DC/DC converter allows for power to be absorbed from the harvester in a manner consistent with the theory in the previous section, i.e., like a resistance. Consequently, the use of such converters in parallel with a tuned inductor or capacitor effectively realizes the linear input admittances in Fig. 18.2. The conductive losses in the MOSFET and diodes can also be taken into account in a manner similar to the way they were for the diode bridge rectifier in the previous subsection, to optimize R_{eq}.

However, there are also disadvantages to using DC/DC converters. Most significantly, every time the MOSFET is switched on, its gate capacitance must be charged, and this requires a small amount of energy. Generally, it is not easy to recover this energy when the MOSFET is switched off again. Thus, the gate drive circuit must draw power off of the power bus to run the switching circuit, at a rate that increases with f_s. Consequently, f_s cannot be too high or else the gating losses become prohibitively high. On the other hand, f_s must be kept well above the bandwidth of the harvester in order for the system to operate as intended. As P_{opt} is made smaller, this tradeoff becomes tighter and tighter, and there is ultimately a critical power level below which a given converter is no longer viable. However, the power level where this occurs depends heavily on the specifics of the hardware used, and significant progress is still being made to scale down DC/DC converters to ever-lower power levels for VEH systems.[25,26]

18.4.4 Synchronized switching circuits

Piezoelectric harvesters possess a significant internal capacitance, and consequently a supplemental inductor L must be attached to the harvester terminals to electrically tune it such that $\mathrm{Im}\{G_i(j\omega_0)\} = 0$. Often, the magnitude of L can be prohibitively large, with values in the hundreds or even thousands of henries. This makes passive electrical tuning of the harvester impossible. There are several approaches that could be used to address this issue. One is to use a power-electronic converter with bidirectional energy flow capability, in which case both the real and reactive energy flows are facilitated by the converter.[27] This approach is theoretically advantageous, but the converter circuitry (and its control) are more complicated and exhibit higher parasitic losses. Another approach is to realize the inductor artificially, using a gyrator circuit. Such circuits use operational amplifiers and capacitors to create the illusion of an inductor. However, it is difficult to make such circuits acceptably efficient at small power scales. A third option, which has received significant attention for energy harvesting applications, involves the use of a synchronized switching circuit.

Figure 18.6 illustrates the insertion of a synchronized switch between a piezoelectric transducer and the DC/DC converter circuit discussed in the previous subsection. This particular circuit is called a parallel synchronized switch harvesting inductor (SSHI) circuit, which was originally proposed for these types of applications in Reference 28. Typically, the inductor used in this circuit is very small, many orders of magnitude lower than that necessary to electrically tune the harvester. The switch in the circuit is realized with a MOSFET and diode. Unlike the PWM-controlled switch used in the DC/DC converter, the switch in the SSHI switch is only triggered twice in a vibratory period of the harvester. Each time, it induces a near-instantaneous polarity reversal in v, thus causing it to have zero crossings at desired times. Through

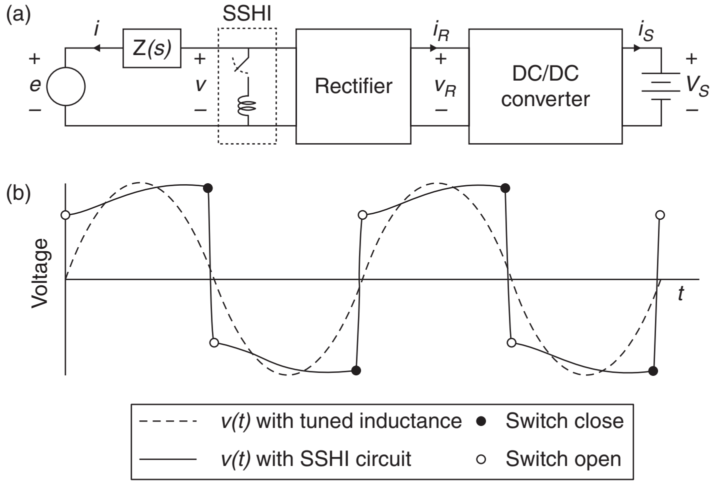

18.6 SSHI circuit (a), and its influence on the voltage (b).

proper switch timing, the phase of the fundamental harmonic of $v(t)$ can be forced to be the same as it would with passive tuning techniques.

Synchronized switching circuits have been shown to be highly effective at greatly enhancing the power generation from monochromatically-excited piezoelectric harvesters.[29–33] Especially near resonance, the optimal switch trigger times are nearly coincident with the displacement peaks of the harvester, and consequently, the switching actions can be instigated using a displacement sensor and a simple peak-detection circuit. In contrast to the PWM-controlled switches, the gating losses associated with the SSHI circuits are negligible, because they are only triggered twice in a vibratory cycle. Meanwhile, they have two drawbacks that can in some circumstances reduce their efficiency. First, they conduct current in a short-period pulse each time the switch is triggered, and this can lead to significant conductive dissipation. Second, they introduce significant harmonics into the periodic response, and much of the energy transferred to these higher frequencies is not recovered. More detailed modeling of the losses in SSHI systems can be used to compensate for these losses.[32]

18.5 Ongoing advancements and future directions

VEH technology continues to be a thriving area of research. We close this chapter with a short (and, to be sure, incomplete) list of three interesting issues currently under investigation by the research community.

18.5.1 Frequency-robust monochromatic energy harvesting

Consider again the optimal power generation limit for a monochromatically-excited SDOF harvester, from Equation [18.39]. As we have discussed, this limit is raised by making c as small as possible, resulting in the general practice of making harvesters very lightly-damped. However, when passive techniques are used to tune the harvester (either mechanically or electrically) this also makes the harvester's power generation capability extremely narrowband, which can have undesirable ramifications if the frequency ω_0 is uncertain. One remedy for this is to deliberately introduce conservative nonlinearities (such as nonlinear stiffnesses) into the electromechanical dynamics of the harvester. If done properly, this can have the effect of creating high-amplitude open-circuit voltages over a wider range of ω_0 values. This has led to a flurry of recent activity on nonlinear energy harvesting, as recently summarized in Reference 34.

Rather than engineer mechanical nonlinearities into a harvester to maintain high power levels as ω_0 is varied, it can be alternatively done by adapting $Y(j\omega)$ such that the condition $Y(j\omega_0) = G_i^{-1}(-j\omega_0)$ is maintained as ω_0

slowly varies. This has been investigated recently in Reference 35. Because the reactive power is actively regulated by the electronics, the rectifier and DC/DC converter shown in Fig. 18.5 cannot be used, and must be replaced with a bidirectional converter. This is challenging because bidirectional converters require more elaborate switching control, and generally exhibit higher parasitic losses.

For piezoelectric applications employing SSHI circuits, adaptive tuning can be achieved merely by adapting the phase angle at which the switch is triggered. This has recently been examined in Reference 36.

18.5.2 Broadband stochastic energy harvesting

In many applications, the disturbance a cannot be presumed to be monochromatic, and is much more appropriately modeled as a stochastic process, possibly with a low quality factor. For such cases, determination of the optimal energy harvesting circuit is more challenging because the system must harvest energy from a continuous band of frequencies *simultaneously*. It should be noted that this problem is fundamentally different from the aforementioned problem in which the disturbance is assumed to be monochromatic but with uncertain frequency. Indeed, it may be the case that a system optimized for one of the two problems performs poorly when applied to the other. A number of recent studies[37,38] have investigated stochastic analogies of the development presented here, in which an equivalent circuit for $Y(s)$ is assumed to be a simple $R-C$ and $R-L$ shunt, and a is assumed to be white noise.

However, it has also been shown in Reference 20 that for white-noise-excited harvesters, the optimal power generation is achievable only with active control, i.e., with a bidirectional converter such as a standard H-bridge drive. Furthermore, the determination of the optimal power extraction can be framed as a feedback optimization problem, with the optimal feedback being determined via the solution to an associated linear-quadratic-Gaussian (LQG) control problem. In Reference 39, this analysis is generalized to the case in which $a(t)$ is colored noise of arbitrary quality factor.

18.5.3 More efficient power electronics

It is almost beyond debate that in the near future, the innovations that will have the largest impact on the state-of-the-art in VEH systems will be those that enhance the efficiency of recharge circuits. This is especially true for power levels below about 100 μW. Efficiency improvements may be made by finding ways to reduce the dissipation of energy as it flows from the transducer terminals to storage, especially in the semiconductor components of the circuit. For example, one simple and well-known technique for reducing conductive losses is to replace the rectifier diodes with MOSFETs which are actively switched to behave like diodes. Although some power is required to actively switch these MOSFETs, they dissipate much less energy than diodes at low current levels, and as such, the net energy consumption is reduced. Another well-known approach to reduce losses is to use DC/DC converters that exhibit soft switching, i.e., MOSFETs that are only switched on or off when their current is zero. This reduces the transition losses associated with switching, actions. There are also opportunities to reduce losses in the gate drive circuits for MOSFETs, through the recapture and reuse of the gating energy. This enables the effective use of DC/DC converters at much lower power levels.

Beyond these ideas, which may be viewed as incremental advancements on existing electronics topologies, it is also likely that in very low-power regimes, custom solid-state converter topologies and transmission techniques will be required. For example, energy harvesting circuits at MEMS scale can be built using CMOS-switched capacitors and without inductors (i.e., charge pumps), which can greatly reduce conduction losses. There has been significant advancement in this area over the last ten years, which is summarized in a recent survey by Chao.[14] These results suggest that the next decade will see a dramatic expansion in the spectrum of power scales over which VEH systems are viable.

18.6 References

1. J. A. Paradiso and T. Starner (2005), 'Energy scavenging for mobile and wireless electronics', *Pervasive Computing*, pp. 18–27, January–March.
2. S. Sudevalayam and P. Kulkarni (2011), 'Energy harvesting sensor nodes: survey and implications', *IEEE Communications Surveys & Tutorials*, vol. **13**, no. 3, pp. 443–461.
3. S. P. Beeby, M. J. Tudor and N. M. White (2006), 'Energy harvesting vibration sources for microsystems applications', *Measurement Science and Technology*, vol. **17**, pp. R175–R195.
4. S. R. Anton and H. A. Sodano (2007), 'A review of power harvesting using piezoelectric materials (2003–2006)', *Smart Materials and Structures*, vol. **16**, pp. R1–R21.
5. K. A. Cook-Chennault, N. Thambi and A. M. Sastry (2008), 'Powering MEMS portable devices – a review of non-regenerative and regenerative power supply systems with special emphasis on piezoelectric energy harvesting systems', *Smart Materials & Structures*, vol. **17**, 043001 (33 p).
6. S. Priya and D. J. Inman, Eds. (2009), *Energy Harvesting Technologies*, Springer, New York.
7. R. J. M. Vullers, R. van Schajik, I. Doms, C. Van Hoof and R. Mertens (2009), 'Mircopower energy harvesting', *Solid-State Electronics*, vol. **53**, pp. 684–693.
8. A. Harb (2011), 'Energy harvesting: state-of-the-art', *Renewable Energy*, vol. **36**, pp. 2641–2654.

9. S. P. Beeby and T. O'Donnell (2009), 'Electromagnetic energy harvesting', in *Energy Harvesting Technologies*, S. Priya and D. J. Inman, Eds., pp. 129–161. Springer-Verlag, Berlin.
10. S. Roundy, P. K. Wright and J. Rabaey (2002), 'A study of low level vibrations as a power source for wireless sensor nodes', *Journal of Computer Communications*, vol. **26**, pp. 1131–1144.
11. P. D. Mitcheson, P. Miao, B. H. Stark, E. M. Yeatman, A. S. Holmes and T. C. Green (2004), 'MEMS electrostatic micro-power generator for low frequency operation', *Sensors Actuators*, vol. **A115**, pp. 523–529.
12. B. H. Stark, P. D. Mitcheson, P. Miao, T. C. Green, E. M. Yeatman and A. S. Holmes (2006), 'Converter circuit design, semiconductor device selection and analysis of parasitics for micropower electrostatic generators', *IEEE Transactions on Power Electronics*, vol. **21**, no. 1, pp. 27–37.
13. L. M. Miller, E. Halvorsen, T. Dong and P. K. Wright (2011), 'Modeling and experimental verification of low-frequency MEMS energy harvesting from ambient vibrations', *Journal of Micromechanical Engineering*, vol. **21**, 045029 (13 p).
14. P. C.-P. Chao (2011), 'Energy harvesting electronics for vibratory devices in self-powered sensors,' *IEEE Sensors Journal*, vol. **11**, no. 12, pp. 3106–3121.
15. P. Glynne-Jones, M. J. Tudor, S. P. Beeby and N. M. White (2004), 'An electromagnetic, vibration-powered generator for intelligent sensor systems', *Sensors and Actuators A*, vol. **110**, pp. 344–349,.
16. N. W. Hagood, W. H. Chong and A. von Flotow (1990), 'Modelling of piezoelectric actuator dynamics for active structural control', *Journal of Intelligent Materials Structures and Systems*, vol. **1**, pp. 327–354.
17. Y. C. Shu and I. C. Lien (2006), 'Analysis of power output for piezoelectric energy harvesting systems', *Smart Materials & Structures*, vol. **15**, pp. 1499–1512.
18. N. G. Stephen (2006), 'On energy harvesting from ambient vibration', *Journal of Sound and Vibration*, vol. **293**, pp. 409–425.
19. S. W. Ibrahim and W. G. Ali (2012), 'A review on frequency tuning methods for piezoelectric energy harvesting systems', *Journal of Renewable and Sustainable Energy*, vol. **4**, 062703 (29 p).
20. J. T. Scruggs (2009), 'An optimal stochastic control theory for distributed energy harvesting networks', *Journal of Sound and Vibration*, vol. **320**, pp. 707–725.
21. G. W. Taylor, J. R. Burns, S. A. Kammann, W. B. Powers and T. R. Welsh (2001), 'The energy harvesting eel: a small subsurface ocean/river power generator', *IEEE Journal of Oceanic Engineering*, vol. **26**, pp. 539–547.
22. G. K. Ottman, H. F. Hofmann and G. A. Lesieutre (2003), 'Optimized piezoelectric energy harvesting circuit using step-down converter in discontinuous conduction mode', *IEEE Transactions On Power Electronics*, vol. **18**, pp. 696–703.
23. E. Lefeuvre, D. Audigier, C. Richard and D. Guyomar (2007), 'Buck-boost converter for sensorless power optimization of piezoelectric energy harvester', *IEEE Transactions on Power Electronics*, vol. **22**, pp. 2018–2025.
24. N. Kong, D. S. Ha, A. Erturk and D. J. Inman (2010), 'Resistive impedance matching circuit for piezoelectric energy harvesting', *Journal of Intelligent Material Systems and Structures*, vol. **21**, pp. 1293–1302.
25. A. Tabesh and L. G. Frechette (2010), 'A low-power stand-alone adaptive circuit for harvesting energy from a piezoelectric micropower generator', *IEEE Transactions on Industrial Electronics*, vol. **57**, pp. 840–849.

26. M. Lallart and D. J. Inman (2010), 'Low-cost integrable tuning-free converter for piezoelectric energy harvesting optimization', *IEEE Transactions on Power Electronics*, vol. **25**, no. 7, pp. 1811–1819.
27. P. D. Mitcheson, T. T. Toh, K. H. Wong, S. G. Burrow and A. S. Holmes (2011), 'Tuning the resonant frequency and damping of an electromagnetic energy harvester using power electronics', *IEEE Transactions on Circuits and Systems II – Express Briefs*, vol. **58**, pp. 792–796.
28. A. Badel, D. Guyomar, E. Lefeuvre and D. Richard (2005), 'Efficiency enhancement of a piezoelectric energy harvesting device in pulsed operation by synchronous charge inversion', *Journal of Intelligent Material Systems and Structures*, vol. **16**, pp. 889–901.
29. K. Makihara, J. Onoda and T. Miyakawa (2006), 'Low energy dissipation electric circuit for energy harvesting', *Smart Materials & Structures*, vol. **15**, pp. 1493–1498.
30. I. C. Lien, Y. C. Shu, W. J. Wu, S. M. Shiu and H. C. Lin (2010), 'Revisit of series-sshi with comparisons to other interfacing circuits in piezoelectric energy harvesting', *Smart Materials & Structures*, vol. **19**, #125009.
31. A. M. Wickenheiser and E. Garcia (2010), 'Power optimization of vibration energy harvesters using passive and active circuits', *Journal of Intelligent Material Systems & Structures*, vol. **21**, pp. 1343–1361.
32. J. R. Liang and W. H. Liao (2011), 'On the influence of transducer internal loss in piezoelectric energy harvesting with sshi interface', *Journal of Intelligent Material Systems & Structures*, vol. **22**, pp. 503–512.
33. D. Guyomar and M. Lallart (2011), 'Recent progress in piezoelectric conversion and energy harvesting using nonlinear electronic interfaces and issues in small scale implementation', *Micromachines*, vol. **2**, pp. 274–294.
34. L. Tang, Y. Yang and C. K. Soh (2010), 'Toward broadband vibration-based energy harvesting', *Journal of Intelligent Material Systems & Structures*, vol. **21**, pp. 1867–1897.
35. A. Cammarano, S. G. Burrow, D. A. W. Barton, A. Carrella and L. R. Clare (2010), 'Tuning a resonant energy harvester using a generalized electrical load', *Smart Materials & Structures*, vol. **19**, #055003.
36. C. Luo and H. F. Hofmann (2011), 'Wideband energy harvesting for piezoelectric devices with linear resonant behavior', *IEEE Transactions on Ultrasonics, Ferroelectrics, and Frequency Control*, vol. **58**, no. 7, pp. 1294–1301.
37. E. Halvorsen (2009), 'Energy harvesters driven by broadband random vibrations', *Journal of Microelectromechanical Systems*, vol. **17**, no. 5, pp. 1061–1071.
38. S. Adhikari, M. Friswell and D. J. Inman (2009), 'Piezoelectric energy harvesting from broadband random vibrations', *Smart Materials & Structures*, vol. **18**, AN 115005.
39. J. T. Scruggs (2010), 'On the causal power generation limit for a vibratory energy harvester in broadband stochastic response', *Journal of Intelligent Material Systems and Structures*, vol. **21**, pp. 1249–1262.

Index

- absolute impedance amplitude, 369
- AC circuit theory, 367–8
- academic prototypes, 461–2
- acceleration, 62–4
  - capacitive, 63
  - force-balance, 62–3
  - piezoelectric, 63–4
- accelerometer, 58, 71–7, 279–81
  - cantilever design using piezoresistive or piezoelectric transduction and capacitive gap change, 280
  - changes in input-output models, 76–7
  - changes in modal parameters, 71, 74–6
    - schematic of the Z24 Bridge, 74
  - changes in time response based models, 77
  - damage identification algorithms, 72–3
  - examples of piezoresistive MEMS accelerometers in literature, 281
- acoustic emission (AE), 103–4
  - duration, 162
  - fundamentals
    - AE process, 161
  - monitoring, 377
  - technique, 103–4
    - fundamentals, 160–1
- acoustic emission (AE) sensor, 281–2
  - AE equipment technology, 169–71
    - capacitive polymer sensor constructed using micro-stereolithography, 170
    - concept of capacitive MEMS resonator, 171
    - out-of-plane and in-plane sensor, Plate IV
  - AE localisation methods, 162–6
    - 1-D source localisation, 164
    - 2-D source localisation, 165
    - normalised cross-correlation function, 164
  - assessment and monitoring civil infrastructures, 159–76
    - field applications and structural health monitoring, 171–5
    - fundamentals of AE technique, 160–1
    - future challenges, 175–6
    - severity assessment, 166–8
  - field applications and structural health monitoring, 171–5
    - bridge wireless application, 173
    - crack location, 173
    - energy vs X crack position under low cycle fatigue loading, 174
  - interpretation of AE signals, 161–2
    - signal and parameters of AE techniques, Plate III
- Acoustic Emission Array Processing, 103–4
- acoustic nonlinearity, 183
- acoustic source localisation, 175
- acoustic waves, 187
- acousto-elasticity, 181–2
- active fibre composite (AFC), 95
- active sensors, 6
- actuator resource allocation algorithms, 470
- adhesive bonding degradation, 283
- aerospace structures, 107–8
  - applications, 107
- air, 217
- air-launched antennas, 221–2

airborne radar applications
    see synthetic aperture radar (SAR)
Akaike Information Criterion (AIC), 163
alkali-silica reaction (ASR), 187–8
American Composites Manufacturers Association (ACMA), 303
American National Standards Institute (ANSI), 351
amplitude modulation (AM), 453
amplitude-splitting, 333
analog-digital converter (ADC), 420–1, 452, 483
analog filtering, 42
analog-to-digital conversion, 34–9
Analogue Device ADXL202, 483
anemometers, 64–5
anodic reactions, 361
application layer, 455
application programming interface (API), 465
application software, 468–71
ARX models, 469
Atmel AVR ATmega 128L microprocessor, 483
atom-atom collision approach, 332
atomic system, 329
attenuation spectrum, 126
auto-regressive, exogenous input (ARX) model, 74
automated data interpretation software, 209
automated file transfer, 386
automated wireless structural damage detection, 469
automatic onset time determination, 175
autonomous robots, 421
autoregressive process, 163
auxiliary counter electrode, 366–7
avalanche photodiode (APD), 51–2
Avalanche transistors, 221
Avogadro constant, 329–30
axial tension, 131

b-value, 168
back scattering, 148
Bayesian finite element model, 75
Bernoulli-Euler assumptions, 516
Bersoft Image Measurement (BIM), 388
Bessel function, 37
Bill Emerson Memorial Bridge, 79
binary coded decimal, 34
binary coding, 33–4
biocular-vision-based measurement system, 387–8
BlueTooth, 453
Bode plot, 369–72
Boltzmann constant, 329–30
Boltzmann's equation, 329
bonding effects, 97–8
  bonding layer between a piezoelectric transducer and host structure, 98
Borehole antennas, 221–2
Bragg gratings (FBG), 128–9
bridge cable tension measurements, 348
bridge cable test, 399, 401–3
  displacement time histories of cable segment from camcorders, Plate XI
  field measurement of cable vibration, 402
  images of cable segment recorded by two camcorders, 403
  schematic diagram of inclined cable, 401
bridge structures, 106–7
  applications, 106
Brillouin scattering distributed sensors, 142–5
Brillouin scattering systems, 129
broadband piezoceramic transducers, 169
broadband stochastic energy harvesting, 533
buck-boost converter, 530
buffers, 44
bulb thermometer, 28
bulk micromachining, 270–1
Burj Khalifa Tower, 78
buses, 43
bytes, 34

C4 probe, 375
cables, 130

California Strong Motion Instrumentation Program, 3
camera calibration, 389–92
  pinhole camera model, 389
  plane-based camera calibration, 392
  steel building frame with targets for camera calibration and tracking, 391
camera movement, 395–6
capacitance, 273, 274–5
capacitive accelerometer, 63
carbon fibre reinforced polymer (CFRP), 102
  composites, 303–4
carbon nanomaterials
  properties, 296–9
    illustration of SWNT represents of single sheet of graphene rolled, 297
    various types of carbon nanotubes sold by different companies, 298
carbonation induced corrosion, 360
Cartesian coordinates, 268
Cartesian reference system, 389–90
case study
  data collection and management, 502–4
    operating frequencies and mode shapes for New Carquinez Bridge, 504
    time history profiles from strain gages located on bridge box, 503
    time history profiles of wind speed and direction at south climate station, 503
    two-tiered wireless sensing network, 504
  field deployment, 486–7
    wireless sensing unit, 486
  Golden Gate Bridge, San Francisco, California, USA, 482–7
    communication scheme, 485–6
    image, 482
    schematic of bridge instrumentation, 484
    wireless sensing unit, 483–5
  Jingo Bridge, Haenam/Jindo, South Korea, 492–7
    communication scheme, 496
    data collection and management, 497
    image, 492
    power consumption, 496
    schematic of bridge instrumentation, 493
    wireless sensing unit, 494–6
  New Carquinez Bridge, Vallejo/Crockett, California, USA, 497–505
    communication scheme, 502
    image, 498
    power consumption, 501
    schematic of bridge instrumentation, 499
    wireless sensing unit, 498, 500–1
  Stork Bridge, Winterthur, Switzerland, 487–92
    communication scheme, 490
    data management, 490–1
    image, 488
    network stability, 491
    schematic of bridge instrumentation, 488
    sensor mounted to stay cable, 488
    wireless sensing unit, 487, 489–90
cathodic reactions, 361
Celesco SP2–50 potentiometers, 500
cementitious-based composites, 299–303
  mechanical reinforcement, 302–3
  smart concrete fabrication and nanomaterial dispersion, 300–1
  strain sensing, 301–2
    measured resistance time history of self-sensing CNT/cement composite, 322
    smart concrete modified MWNT for traffic monitoring applications, Plate VII
cementitious materials, 300
central processing unit (CPU), 43
channel, 451–2
charge amplifier, 25
charge-coupled device (CCD), 333
chemical vapour deposition, 270

chloride induced corrosion, 359–60
chloride ions, 359–60
civil infrastructure
  acoustic emission sensors for assessment and monitoring, 159–76
    AE equipment technology, 169–71
    AE localisation methods, 162–6
    field applications and structural health monitoring, 171–5
    fundamentals of AE technique, 160–1
    future challenges, 175–6
    interpretation of AE signals, 161–2
    severity assessment, 166–8
  associated algorithms, 69–78
    accelerometers, 71–7
    displacement sensors, 69–70
    environmental measurements, 77–8
    strain gages, 70
  commonly used sensors and their algorithms, 57–80
    continuous monitoring systems, 78–9
    future trends, 79–80
  corrosion sensing for assessment and monitoring, 357–78
    corrosion evaluation techniques, 361–72
    field monitoring, 372–7
    future trends, 377–8
    principles of corrosion, 358–61
  electromagnetic sensors for assessment and monitoring, 238–62
    eddy current, 258
    future trends, 262
    magnetic sensory technologies, 245–9
    magnetoelastic stress sensors for tension monitoring of steel cables, 253–6
    magnetoelasticity, 242–5
    removable or portable elastomagnetic stress sensor, 259–61
    role of microstructure in magnetisation and magnetoelasticity, 249–53
    temperature effects, 256–8
  energy harvesting for sensing systems for assessment and monitoring, 510–34
    harvest dynamic modelling, 514–18
    ongoing advancements and future directions, 532–4
    power availability and optimal harvesting admittance, 518–24
    power extraction circuits, 525–32
  fibre optic sensors for assessment and monitoring, 121–50
    common optical fibre sensors, 130–45
    future trends, 145–9
    properties of optical fibres, 123–30
  laser-based sensing for assessment and monitoring, 327–52
    civil infrastructure applications, 348–50
    laser digital shearography, 335–7
    laser Doppler vibrometry, 339–42
    laser interferometry or electronic speckle pattern interferometry, 333–5
    laser principles, 329–32
    laser safety, 351
    laser scanning photogrammetry, 337–9
    laser-ultrasound, 342–6
    other techniques, 346–8
  micro-electro-mechanical-systems (MEMS) for assessment and monitoring, 265–87
    application examples, 284–5
    future trends, 286–7
    long term technical challenges, 285–6
    MEMS sensors for SHM, 279–84
    sensor characteristics, 273–8
    sensor materials and micromachining techniques, 266–73
  multifunctional materials and nanotechnology for assessment and monitoring, 295–317
    cementitious-based composites, 299–303
    fibre-reinforced polymer composites, 303–6

  future trends, 316–17
  polymer-based thin films, 306–16
  properties of carbon nanomaterials, 296–9
nonlinear acoustic methods and ultrasound methods for assessing and monitoring, 179–97
  fundamentals of nonlinear acousto-ultrasound techniques, 181–2
  future trends, 196–7
  harmonic and subharmonic generation, 182–5
  nonlinear resonance ultrasound spectroscopy, 191–5
  nonlinear wave modulation, 185–91
piezoelectric transducers for assessment and monitoring, 86–113
  applications, 105–10
  bonding effects, 97–8
  future trends, 110–12
  limitations, 98–9
  piezoelectric materials and fabrication, 92–5
  principle of piezoelectricity, 87–92
  SHM applications, 95–7
  SHM techniques, 99–105
radar technology for assessment and monitoring, 201–34
  brief history of ground penetrating radar (GPR) systems, 203–8
  current challenges and state of the art systems, 208–9
  electromagnetic interactions with materials, 217–19
  fundamentals of operation, 209–17
  future trends, 232–4
  laboratory and field studies, 227–32
  radio frequency, interferometric, millimetre wave and terahertz sensors, 201–34
  signal processing, 224–7
  transmitter and receiver design, 219–24
robotic sensing for assessment and monitoring, 410–39
  future trends, 436–9
  remote robotic sensing for structural health monitoring (SHM), 419–24
  vibration-based mobile wireless sensors, 424–36
  vision-based for structural health monitoring (SHM), 414–19
sensing technologies, 58–68
  acceleration, 62–4
  displacement, 59–60
  environment, 64–5
  prevalence of commonly used sensors in SHM systems, 65–8
  strain, 60–2
vision-based sensing for assessment and monitoring, 383–406
  applications, 396–405
  important issues for vision-based measurement techniques, 388–96
  vision-based measurement techniques for civil engineering applications, 386–8
wireless structural monitoring systems design and selection, 446–72
  future trends, 471–2
  hardware, 456–64
  overview of wireless networks, 450–6
  wireless sensor network software, 464–71
cladding modes, 125
classical impedance matching theory, 518–20
clear-channel assessment (CCA), 453
clipping, 38
closed-loop system, 519–20
co-linear wave mixing method, 188–9
cognitive radar system concepts, 233–4
coherence length, 134
coherent interferometers, 131–4
  intensity signals as function of interferometer phase difference for two sensor signals, 134
  schematic of Mach-Zehnder interferometer, 132
  schematic of Michelson interferometer, 133
collapse voltage, 275–6

commercial wireless sensors, 460–1
communication scheme, 485–6, 490, 496, 502
complementary metal oxide semiconductor (CMOS), 271–2, 387–8
complex reactive index mixture (CRIM), 219
compliance matrix, 92
computer-aided speckle pattern interferometry (CASPI) *see* laser interferometry
concrete, 192–3
concrete multi-depth sensor, 373–4
connectors, 130
constitutive equations, 90–2
construction monitoring, 348
continuous-wave radar system, 219
control module, 23, 25–6
copper sulfate electrode (CSE), 362–3
corrosion
  principles, 358–61
    carbonation induced corrosion, 360
    chloride induced corrosion, 359–60
    mechanism of corrosion in reinforced concrete, 360–1
    Pourbaix diagram for Fe-H_2O at 25°C, 358
    products of iron, 359
corrosion evaluation techniques, 361–72
  cyclic polarisation, 372
  electrochemical impedance spectroscopy (EIS), 367–72
  equipment with guard ring, 366–7
  galvanostatic pulse technique, 365–6
    schematic illustration of equation, 367
    schematic illustration of galvanostatic pulse results, 366
  half-cell potential technique, 362–3
    apparatus described in ASTM C876 to measure surface potential, 362
  linear polarisation resistance (LPR), 363–5
    schematic illustration of linear polarisation curve, 364
  potentiostatic linear polarisation resistance, 365
corrosion mechanism, 360–1
corrosion monitoring, 246
corrosion potential, 361
corrosion-related magnetic (CMR) field, 247
corrosion sensing, 8
  assessing and monitoring civil infrastructures, 357–78
    corrosion evaluation techniques, 361–72
    future trends, 377–8
    principles of corrosion, 358–61
  field monitoring, 372–7
    electrochemical sensors, 372–5
  other sensors, 375–7
    circuit diagram for corrosion sensor based on inductance, 376
corrosion sensor, 283
CorrWatch multi-sensor, 374
cost-cutting development, 172
coupling coefficient, 138
  matrix, 516
covariance-driven method, 349
cross-axis sensitivity, 29
crystal anisotropy, 242–3
crystallography, 268
Curie temperature, 94–5, 283–4
custom solid-state converter topologies, 534
cyclic polarisation, 372

3D laser scanning system, 338
damage detection, 10
damage index method, 74
damage indicator (DI), 432
damage locating vector method, 75
dark current, 50
data acquisition, 23
data acquisition system, 41–7
  analog signal considerations, 41–5
    central bus architecture, 43
  digital communications, 45–7
    DAQ system plug-and-play architecture, 45
  schematic diagram, 41
data acquisition unit, 255
data collection, 497, 502–4
data-driven method, 349
data link layer, 453

data management, 10, 490–1, 497, 502–4
Debye expression, 218
deformation, 8
degrees of freedom (DOF), 77
deposition, 266, 270
destination, 452
dielectric, 217–18
dielectric constant, 216–17
  matrix, 516
differential-ended connections, 42
diffusion, 270
digital-analog converter (DAC), 456–7
digital surface models (DSM), 337
digital terrain models (DTM), 337
digital-to-analog conversion, 39–40
  schematic diagram, 40
diode bridge rectifier, 526–8
direct ADCs *see* flash ADCs
direct stiffness calculation method, 75–6
discrete Fourier transform (DFT), 30–2
discrete-time methods, 395–6
displacement, 59–60
  linear variable differential transformers, 59–60
  potentiometers, 60
displacement sensors, 69–70
dithering, 38
Doppler effect, 340
Doppler frequency, 340
doublet, 220
dry etching, 270
durability demonstrations, 287
dynamic analysis, 349
dynamic magnetic signal, 246
dynamic modulus, 189
dynamic random access memory (DRAM), 44–5
dynamic range, 29

eddy current, 258, 376
  simulation of average longitudinal induction intensity, 260
  simulation of classical eddy current and magnetic induction in steel, 260
edge-emitting diodes (ELEDs), 49
eigensystem realisation algorithm (ERA), 436, 449–50
eigenvalue realisation algorithm (ERA), 349
elastomagnetic stress sensor
  removable or portable, 259–61
    calibration curves of U-shaped stress sensor at different temperatures, 261
    magnetostatic simulation of induction in magnetic circuit of yoke and steel rod, 261
electric charge, 87
electric displacement, 90
electrical impedance tomography (EIT), 314–15
electrically-erasable programmable read-only memory (EEPROM), 44
electrochemical impedance, 101
electrochemical impedance spectroscopy (EIS), 367–72
  data interpretation, 369–72
    Bode plot for simple electrochemical system, 371
    equivalent circuit for simple electrochemical system, 370
    Nyquist plot for simple electrochemical system, 371
  relationship between sinusoidal AC current and rotating vector representation, 368
electrochemical sensors, 372–5
  examples, 373–5
    concrete multi-depth sensor, 373–4
    CorrWatch multi-sensor, 374
    embedded corrosion instrument (ECI), 373
    Interek-CAPCIS probes, 375
    SensCore corrosion sensor, 374
electrochemical techniques, 361–2
electromagnetic interference, 137
electromagnetic sensors, 9
  assessing and monitoring civil infrastructure, 238–62
    eddy current, 258
    future trends, 262
    magnetic domain in non-magnetised ferromagnetic sample, 240

electromagnetic sensors (*cont.*)
  magnetic hysteresis curves for typical ferromagnetic materials, 241
  magnetic sensory technologies, 245–9
  magnetoelastic stress sensors for tension monitoring of steel cables, 253–6
  magnetoelasticity, 242–5
  removable or portable elastomagnetic stress sensor, 259–61
  temperature effects, 256–8
 role of microstructure in magnetisation and magnetoelasticity, 249–53
  hardness of various carbon and alloy steels, 251
  hysteresis of piano steel having undergone different heat treatment, 251
  initiative magnetisation curves of various steels, 250
  permeability vs stress up to yield point for piano steel rod, 253
  relative permeability measurements for piano steel during initial magnetisation, 252
  relative permeability of piano steels undergone different heat treatments, 251
  relative permeability under technical saturation vs tension of different steel rods, 252
electromagnetic transducers, 514–17
electronic speckle pattern interferometry (ESPI), 333–5
electronics integration, 287
electroplating method, 270
electrostatic force, 309–10
electrostatic load, 276
embedded corrosion instrument (ECI), 373
embedded firmware, 464
emission limits, 207–8
energy, 162
energy harvesting, 109–10, 172
 ongoing advancements and future directions, 532–4
  broadband stochastic energy harvesting, 533
  frequency-robust monochromatic energy harvesting, 532–3
  more efficient power electronics, 533–4
 sensing systems for assessing and monitoring civil infrastructures, 510–34
  harvest dynamic modelling, 514–18
  harvesters with electromagnetics, 512
  power availability and optimal harvesting admittance, 518–24
  power extraction circuits, 525–32
  sampling of commercially available VEH systems, 514
energy management, 463–4
engineered cementitious composites (ECC), 299
environment, 64–5
 anemometers, 64–5
 measurements, 77–8
 thermocouples and resistive thermometers, 65
epipolar plane, 395
epitaxy, 270
epoxy moulding, 309
equivalent isotropically radiated power (EIRP), 207–8
etching, 266, 270
evaporation, 309
exposure limits, 351
extrinsic Fabry-Pérot interferometer (EFPI), 136

Fabry-Pérot interferometers, 128–9, 134, 136–7
 piezometers, embeddable strain sensors, spot-weldable strain and displacement sensor, 137
 schematic overview for strain, pressure and displacement, 136
Fabry-Perot tunable filter, 52
Faraday' law, 514–17
fast Fourier transforms (FFTs), 457

Federal Communications Commission (FCC), 207, 449
feedback law, 520
Felicity effect, 166–7
ferroelectricity, 88
fibre Bragg grating (FBG), 137–42, 377
  combined WDM and TDM for FBG sensor network, 140
  multi-axis loading applied to FBG sensor written into bowtie PM fibre, 141
  optical FBG sensor, 138
  response of FBG embedded in compact tension specimen, 141
  theoretical transmission spectrum for long period FBG, 142
fibre optic sensors
  assessing and monitoring civil infrastructures, 121–50
    common optical fibre sensors, 130–45
    future trends, 145–9
    properties of optical fibres, 123–30
    types, 122
fibre-reinforced concrete (FRC), 299
fibre-reinforced polymer (FRP), 299, 345
fibre-reinforced polymer (FRP) composites, 303–6
  improving FRP electromechanical properties, 305–6
    FRPs modified with CNTs exhibit great promise for strain sensing and SHM, 306
  manufacturing, 304–5
    wet layup and VARTM FRP composites manufacturing techniques, 305
field application, 7
field deployment, 486–7
finite difference time domain (FDTD), 216–17
finite element (FE) models, 342
finite element model (FEM), 314–15, 502–3
flash ADCs, 39
flash memory (ROM), 44
flip-chip method, 278
Flooding Time Synchronisation Protocol (FTSP), 486
force-balance accelerometers, 62–3
Fourier analysis, 342
Fourier transform, 220
Fourier transformation, 186–7
Fourier's theorem, 211–12
fractional bandwidth (FBW), 206
fracture-critical element, 173
free real-time operating system (RTOS), 465–6
frequency domain decomposition (FDD), 449–50
frequency modulation (FM), 453
frequency response function (FRF), 76, 431
frequency-robust monochromatic energy harvesting, 532–3
full-scale sensor network, 492
fundamental matrix, 395
fundamental mode, 125
fundamental power generation limits, 524
fused silica fibres, 126

Galerkin approximation, 516
galvanic corrosion, 247
galvanostatic pulse technique, 365–6
GalvaPulse, 367
game theory, 470
gauge factor, 273
Gauss bell, 220
Gauss-hermite functions, 220
Gaussian beams, 211–12
GECOR, 367
general purpose interface bus (GPIB), 46–7
Geophysical Survey System Inc. (GSSI), 203–4
glass fibre reinforced polymer (GFRP), 102, 305
global positioning system (GPS), 337
  signal, 449
Golden Gate Bridge, 2
good thermal matching, 270
grating spectrum distortion, 140–1
Green's function, 165–6
ground-coupled antennas, 221–2

ground penetrating radar (GPR), 9
  brief history, 203–8
    EM wave interactions with concrete bridge deck, 203
    EM wavelengths as function of frequency for different media, 206
    FCC15.209 emission limits, 208
    maximum average emission limits for frequency bands above 960 MHz, 208
    maximum average emission limits using resolution bandwidth of no less than 1KHx, 208
guard ring electrode, 366–7
  schematic plan of GalvaPulse, Plate X
guided wave techniques, 99–101
  principle of phased array technique, 101
  pulse-echo mode and pitch-catch mode, 100
guided wave tomography, 100
guided waves, 99

half-cell potential technique, 362–3
Hall accelerometers, 2
hall-effect sensors, 429–30
harmonic generation, 182–5
  harmonic ratio as function of water-to-cement content, 184
  illustration, 183
  physical explanation of CAN, Plate V
Harris corner detection methods, 392–3
harvest dynamic modelling, 514–18
  electromagnetic transducers, 514–17
  general principles, 517–18
  piezoelectric transducers, 515–17
harvesters, 463–4
HERMES system, 204–5
high-birefringence fibres, 125–6
high frequency harmonics local nature, 196
high-performance fibre-reinforced cementitious composites (HPFRCC), 299
high power, 197
high-precision control applications, 109
high-strain piezoelectric transducers, 111
high temperature piezoelectric transducers, 110
Hilbert-Huang transform method, 349
historic index (HI), 167
historical structures limit analysis, 350
holey fibres, 146
Hooke's law, 182
hostile environments, 175
hyperbolic nonlinearity, 226

IBM 7700 data acquisition system, 2–3
IBM 1710 personal computer, 2
image-based deformation measurement technique, 386
image based integrated measurement (IBIM), 386
image-based visual serving (IBVS) technique, 422
imaginary current, 369
imaging system, 207
Imote2, 495
impact modulation method, 190
impedance matched feedback law, 519–20
impedance matching, 223
impedance techniques, 101–3
impulse radar system, 219
in-network computing, 469
industrial, scientific and medical (ISM) radiofrequency (RF) spectrum, 449
infinity models, 216
information source, 451
infrared (IR) spectrum, 351
infrared lamp tracking systems, 415–16
infrastructure systems
  permanent installation of wireless structural monitoring systems, 480–505
    case study I of Golden Gate Bridge, San Francisco, California, USA, 482–7
    case study II of Stork Bridge, Winterthur, Switzerland, 487–92
    case study III of Jindo Bridge, Haenam/Jindo, South Korea, 492–7

    - case study IV of New Carquinez Bridge, Vallejo/Crockett, California, USA, 497–505
- instantaneous absorbed power, 521
- instantaneous-time methods, 395–6
- insulators, 270
- integrated circuits (IC) technology, 266
- integrated development environment (IDE), 458
- integration with optic-based SHM techniques, 111
- intelligent data acquisition, 287
- intensity losses, 148
- interchannel delay, 42
- Interek-CAPCIS probes, 375
- interferometry
  - radar technology and radio frequency, millimetre wave and terahertz sensors, 201–34
    - assessment and monitoring civil infrastructures, 201–34
    - brief history of ground penetrating radar (GPR) systems, 203–8
    - current challenges and state of the art systems, 208–9
    - electromagnetic interactions with materials, 217–19
    - fundamentals of operation, 209–17
    - future trends, 232–4
    - laboratory and field studies, 227–32
    - signal processing, 224–7
    - transmitter and receiver design, 219–24
- International Telecommunication Communication (ITU), 449
- ion implantation, 270
- ion milling, 270–1
- iWitness photogrammetry software system, 388

- Kaiser effect, 166–7
- Keil RTX, 465–6

- laboratory steel portal frame, 430–1
- Lamb waves, 164, 343
- Lamé constants, 342–3
- Landau theory, 192–3
- Langrange multipliers, 523
- Laplace domain, 515
- Laplace operator, 342–3
- large-scale steel building frame test, 397–9
  - displacement responses, 399
- laser, 329
- laser-acoustic-emission (laser-AE) technique, 346–7
- laser amplifying medium, 329
- laser-based sensing, 8
  - assessing and monitoring civil infrastructures, 327–52
    - civil infrastructure applications, 348–50
    - laser digital shearography, 335–7
    - laser Doppler vibrometry, 339–42
    - laser interferometry or electronic speckle pattern interferometry, 333–5
    - laser principles, 329–32
    - laser safety, 351
    - laser scanning photogrammetry, 337–9
    - laser-ultrasound, 342–6
  - other techniques, 346–8
    - laser diffraction grafting, 346
    - laser infrared (IR) photothermal radiometry (PTR), 347
- laser-based ultrasound *see* laser-ultrasound
- laser-based wireless power transmission, 422–4
  - laser targeting on orthogonal ceiling, 424
  - prototype of laser targeting mobile robot system, 423
- laser beam pointing tracking system, 415–16
- laser diffraction grafting, 346
- laser digital shearography, 335–7
  - illustration, 336
- laser Doppler vibrometry, 339–42
  - types of LDV, 339
- laser holographic interferometry, 333–5
- laser infrared photothermal radiometry (laser IR-PTR), 347

Laser Institute of America (LIA), 351
laser interferometry, 333–5
  in-plane measurement, 334
  laser holographic interferometry, 333–5
    phase shifting illustration, 335
  out-of-plane measurement, 334
laser photoacoustic spectroscopy, 347
laser principles, 329–32
  optical amplification of lights in medium, 331–2
    properties of selected lasers, 332
  stimulated emission and thermal radiation, 329–31
    energy absorption and emission, 330
    ratio of stimulated emission rate to spontaneous emission rate, 331
    three energy states in laser, 330
laser range finder (LRF), 350
laser safety, 351
laser scanning photogrammetry, 337–9
  laser scanning vs photogrammetry, 338
  principle of 2D laser scanning, 337
laser-ultrasound, 342–6
  laser-acoustic technique for detecting subsurface debonding and cracking, 345
  types of mechanical waves, 344
layer-by-layer (LbL) fabrication, 309–10
leakage, 32
Lifschitz theory, 192–3
LIGA process, 272
light-emitting diode (LED), 332, 415–16
light pulses, 144
light reflection, 376
light source, 132
linear polarisation resistance (LPR), 363–5
linear-quadratic-Gaussian (LQG) control, 533
linear variable differential transformer (LVDT), 59–60, 349–50, 448
Linux, 502
lithography, 266, 270
logical link control (LLC), 453
long period grating (LPG), 125
long term technical challenges, 285–6
Los Angeles Amendment Building Code, 448
lossy dielectric, 218
Love waves, 343
low-coherence interferometers, 134–6
  example of SOFO sensor installed in rebar and SOFO readout unit, 135
  schematic overview of SOFO system, Plate I
low pressure chemical vapour deposition (LPCVP), 269

M3 probe, 375
M9 probe, 375
Mack-Zehnder interferometer, 132
macro-cell corrosion, 360
macro-fibre composite (MFC), 95
magnetic anisotropy, 242–3
  sensory approach, 248
magnetic anisotropy and permeability system (MAPS), 247–8
magnetic method, 245–6
magnetic permeability, 250
magnetic sensory technologies, 245–9
  distribution of residual principal stresses on longitudinal top surfaces of rail, 248
  indicative corrosion-related magnetic field on ship, 248
  indicative drawing of magnetic anisotropy sensor, 249
  magnetic sensors to indicate various classes of defects in steel rope, 246
magnetic stress anisotropy, 243
magnetisation, 245, 249–53
magnetisation behaviour, 244
magneto-hydrodynamics theory, 246
magnetocrystalline anisotropy, 242–3
magnetoelastic stress sensors, 249–50
  tension monitoring of steel cables, 253–6
    EM sensor and load cell measurements for0.6 in. steel strand, 257
    indicative configuration, 254

    - magnetoelastic characteristics of piano steel cables with different sizes, 256
- magnetoelasticity, 242–5, 249–53
  - hysteresis curves at descending stages for piano steel cable under various stress level, 244
- magnetorestrictive sensors, 248–9
- mapping, 247–8
- Markov parameters, 469
- Martlet wireless node, 461–2
- Massachusetts Institute Technology, 95
- master sensor, 163
- mathematical theory, 451
- maximum permissible exposure (MPE), 351
- Maxwell equations, 247
- Maxwell's equation, 209–10
- mechanical reinforcement, 302–3
- mechanical response power (MRP), 104–5
- mechanical tuning design, 522
- media access control (MAC), 453
- memory, 44
- metal-metal oxide (MMO), 372–3
- metallic reflective, 218
- metals, 270
- Mexican hat function, 220
- MICAz mote, 483
- Michelson interferometer, 132
- Micrium real-time operating system (RTOS), 465–6
- micro-cell corrosion, 360
- micro-electro-mechanical systems (MEMS), 341
  - process, 170
- micro-electro-mechanical-systems (MEMS)
  - application examples, 284–5
    - MEMS sensors in monitoring civil structures, 285
  - assessing and monitoring civil infrastructures, 265–87
    - future trends, 286–7
    - long term technical challenges, 285–6
    - sensor characteristics, 273–8
    - sensor materials and micromachining techniques, 266–73
  - sensors for SHM, 279–84
    - accelerometer, 279–81
    - acoustic emission sensor, 281–2
    - corrosion sensor, 283
    - strain sensor, 282–3
    - ultrasonic sensor, 283–4
- micro-embossing fabrication technique, 282
- micro-mechanical systems, 109–10
- micro-optical-electromechanical systems (MOEMS), 341
- micro-stereolithography, 169–70
- microelectromechanical systems (MEMS), 3, 15
- micromachining methods, 270–3
  - process flows of three methods to create a freely moving microstructure layer, 271
  - profilometer measurements of capacitive sensor designs, Plate VI
- micropower impulse radar (MIR), 204–5
- Microstrain G/V-Link line, 460
- microstructured optical fibre sensors, 146–8
  - SEM image of end of photonic crystal fibre, 147
- microwave-based wireless power transmission, 421
- middleware, 466–8
- migration radar, 225–6
- Miller indices, 267–8
- millimetre wave
  - radar technology and radio frequency, interferometric and terahertz sensors, 201–34
    - assessment and monitoring civil infrastructures, 201–34
    - brief history of ground penetrating radar (GPR) systems, 203–8
    - current challenges and state of the art systems, 208–9
    - electromagnetic interactions with materials, 217–19
    - fundamentals of operation, 209–17
    - future trends, 232–4
    - laboratory and field studies, 227–32
    - signal processing, 224–7
    - transmitter and receiver design, 219–24

mobile sensing nodes, 436
mobile sensor network, 427–36
  design of magnet-wheeled mobile sensing node, 429–30
    mobile sensor components, accelerometer attachment and corner negotiation, 428–9
  field validation experiments for vibration modal analysis, 435–6
    3D illustration of five measurement configurations for mobile sensing nodes, 435
    first three mode shapes with significant vertical components, 438
    image of mobile sensing nodes during field testing, 437
    image of space frame bridge on Georgia Tech campus, 435
  laboratory validation experiments for structural damage detection, 430–5
    DIs for three damage scenarios, 434
    laboratory steel portal frame for damage detection using two mobile sensing nodes, 431
    three damage scenarios on laboratory frame structure, 433
modal analysis, 314, 349
monocular-vision-based measurement system, 387–8
monocyle, 220
MOSFET, 529
multi-frequency diffraction tomography, 225–6
multi-functional piezoelectric sensing, 112
multi-hop network, 485
1-D multi-layered model, 210
multi-mode fibre, 125
multi-user micro-electro-mechanical systems (MUMPS) process, 170
multi-user polysilicon (MUMPs) process, 282–3
multi-walled carbon nanotubes (MWNT), 297–8
multicore fibre sensors, 146
  cross-section of multicore fibre illuminated with white light and principle of curvature measurement, 147
multifunctional materials, 7
  nanotechnology for assessing and monitoring civil infrastructures, 295–317
    cementitious-based composites, 299–303
    fibre-reinforced polymer composites, 303–6
    future trends, 316–17
    polymer-based thin films, 306–16
    properties of carbon nanomaterials, 296–9
multiple bimporph piezoelectric transducers, 515–16
multiplexing unit, 25
multisensory data fusion methods, 234

nano-piezoelectric transducers, 111–12
nanoelectromechanical systems (NEMS), 341
nanomaterial dispersion, 300–1
nanotechnology
  multifunctional materials for assessing and monitoring civil infrastructures, 295–317
    cementitious-based composites, 299–303
    fibre-reinforced polymer composites, 303–6
    future trends, 316–17
    polymer-based thin films, 306–16
    properties of carbon nanomaterials, 296–9
Narada, 461–2, 498
NASA Langley Research Centre, 95
National Centre for Research on Earthquake Engineering, 397
National Instrument (NI) WSN line, 460
Navier equation, 342
negative-acknowledgement (NACK) collection protocol, 485–6
network layer, 453–4
network stability, 491
network time protocol (NTP), 502

Newton and Sykes equation, 366
noise filter, 25
non-contact technologies, 196
nondestructive detection techniques, 4
nondestructive evaluation (NDE), 245, 345
  methods, 12, 14
nondestructive testing (NDT), 105
nonlinear acoustic methods
  ultrasound methods for assessing and monitoring civil infrastructures, 179–97
    fundamentals of nonlinear acousto-ultrasound techniques, 181–2
    future trends, 196–7
    harmonic and subharmonic generation, 182–5
    nonlinear resonance ultrasound spectroscopy, 191–5
    nonlinear wave modulation, 185–91
nonlinear acousto-ultrasound techniques, 181–2
nonlinear behaviour, 187
nonlinear bulk waves, 183–4
nonlinear coefficients, 185
nonlinear effect, 196
nonlinear elastic coefficient, 182
nonlinear imaging, 196
nonlinear impact resonance acoustic spectroscopy (NIRAS), 193–4
nonlinear mesoscopic elastic (NME), 185
nonlinear resonance methods, 191–2
nonlinear resonance ultrasound spectroscopy (NRUS), 191–5
  experiment for damaged sample, 193
  nonlinear parameter as function of exposure temperature for P mode with S mode, 194
  nonlinearity reference vs testes samples for highly reactive S2 mixture at 55 days, 195
  resonance frequency vs drive amplitude of intact and damaged sample, 192
nonlinear wave equation, 182
nonlinear wave modulation, 185–91
  correlation between variation of compressive strength and nonlinearity parameter, 191
  linear and nonlinear modulation effect, 186
  linear and nonlinear ultrasonic methods on thermally damaged concrete, 189
  location before heating and same location after heating and permeable pore vs nonlinearity, 190
  material with crack and amplitude modulation of probe and vibration and ultrasonic signal, 187
  parameters measured at three locations in thick and thinner sample, 188
nonlinear wave modulation spectroscopy (NWMS), 185
novel sensor design, 287
nuclear energy, 108–9
nuclear power plants, 108–9
Nyquist filter, 25
Nyquist frequency, 32, 42
Nyquist plot, 369–72

offset binary code, 34
Ohm zSeries, 460
Ohm's law, 368
open circuit potential, 361
open-circuit voltage, 525
open systems interconnection (OSI) reference model, 452
operating frequency, 207
operating systems (OS), 464–6
Optech ILRIS 3-D, 338
optical amplification, 331–2
optical fibre concepts, 123–6
  common fibre index of retraction profiles, 125
  cross-section of step-index fibre, 124
  material attenuation losses as function of wavelength for fused silica, 126

optical fibres, 376
  properties, 123–30
    cables, connectors and splicing, 130
    optical fibre concepts, 123–6
    sensing mechanisms, 126–9
    sensor packaging, 129–30
optical microscopy, 190–1
optimal harvesting admittance, 518–24
Øresund Bridge, 78–9
Organisation Internationale de Normalisation, 452
output module, 23, 25
oxidation, 270

packaging, 277–8
parallel SSHI circuit, 531–2
parametric acoustic array (PAA), 345
Particle Image Velocimetry, 386
passive film formation, 358–9
pavement texture characterisation, 350
pedestrian bridge test, 404–5
  displacement along X, Y and Z axes and rotations about X, Y and Z axes, 405
  pedestrian bridge and set-up of test, 404
peripheral component interconnect (PCI), 47
permanent installation
  wireless structural monitoring systems in infrastructure systems, 480–505
    case study I of Golden Gate Bridge, San Francisco, California, USA, 482–7
    case study II of Stork Bridge, Winterthur, Switzerland, 487–92
    case study III of Jindo Bridge, Haenam/Jindo, South Korea, 492–7
    case study IV of New Carquinez Bridge, Vallejo/Crockett, California, USA, 497–505
permanently installed transducers performance, 196–7
permittivity matrix, 91
phase array technique, 100–1
phase modulation (PM), 453
phase shifts, 132
phase velocity, 189
photodetectors, 49–52
  PIN and avalanche photodiode cross-sections, 51
photodiodes, 48–9
  surface-emitting and edge-emitting diode light source, 50
Photometrix, 388
photonic crystal fibres, 146
photovoltaic cavity converter system, 422
physical layer, 453
physical models, 196
physical vapour deposition, 270
Physik Instrumente Inc., 109
piezoceramic resonant transducers, 169
piezoelectric accelerometers, 63–4
  schematic diagram, 64
piezoelectric ceramics
  fabrication, 93–5
piezoelectric coefficients, 91–2
piezoelectric elements, 9
piezoelectric equations, 274
piezoelectric harvesters, 530–1
piezoelectric materials, 93
  illustration, 93
  typical properties of piezoelectric ceramics, 94
piezoelectric (PZT) crystal, 335
piezoelectric (PZT) device, 169
piezoelectric thin films, 274
piezoelectric transducer self-diagnosis techniques, 104–5
piezoelectric transducers, 515–17
  applications based SHM, 105–10
    aerospace structures, 107–8
    bridge structures, 106–7
    nuclear power plants, 108–9
    pipeline structures, 108
    wind turbines, 109
  assessing and monitoring civil infrastructures, 86–113
    bonding effects, 97–8
    future trends, 110–12
    limitations, 98–9
    piezoelectric materials and fabrication, 92–5

    - principle of piezoelectricity, 87–92
  - other fields of applications, 109–10
    - high-precision and vibration control, 110
  - SHM techniques, 99–105
    - acoustic emission techniques, 103–4
    - guided wave techniques, 99–101
    - impedance techniques, 101–3
    - piezoelectric transducer self-diagnosis techniques, 104–5
  - structural health monitoring (SHM) applications, 95–7
    - paint sensor and smart aggregate, 97
    - properties of piezoelectric materials at 20°C, 97
    - various transducers, 95
- piezoelectricity, 273
  - constitutive equations of materials, 90–2
    - typical piezoelectric material sheet, 91
  - definition and categorisation, 87–9
    - categorisation, 88
    - direct piezoelectric and converse piezoelectric effect, 87
    - polarisations of dielectric vs ferroelectric materials under varying electric field, 89
  - operational principle of materials, 89–90
    - longitudinal, transverse and volume effects, 89
  - principle, 87–92
- piezoresistive accelerometers, 279
- piezoresistive strain, 60–1
- piezoresistivity, 273
- piezoresistivity coefficient, 268
- pin photodiode, 50–1
- pinhole model, 389
- pipeline structures, 108
- pipelining, 485
- Plancharel theorem, 518
- Planck constant, 330
- Planck radiation formula, 330
- plane-based calibration process, 387–8
- plane-based method, 390
- plasma-coupled device (PCD), 346
- plasma etching, 270–1
- platinum, 65
- Poisson ratio, 126, 248–9, 273, 343–4
- polarisation, 361–2
  - behaviour, 88
  - scan rate, 372
- polarisation maintaining (PM) fibres *see* high-birefringence fibres
- poling process, 94–5
- polycrystalline silicon (polysilicon), 269
- polymer-based piezoelectric paint sensor, 96
- polymer-based thin films, 306–16
  - layer-by-layer (LbL) fabrication, 309–10
    - schematic of LbL fabrication methods for assembling CNT-PE thin films, 313
  - mechanical properties of LbL nanocomposites, 310, 313
  - sensing skins for spatial damage detection, 314–16
    - carbon nanotube sensing skin coated with aluminium plate, Plate VIII
    - photosynthesis-inspired CNT-based multifunctional thin films, Plate IX
    - schematic illustration of procedure for solving EIT inverse problem, 315
  - strain sensing, 313–14
    - resistance time history response of SWNT-PE LbL thin film, 314
  - thin film fabrication, 307–9
    - electrical properties of carbon nanotube-polymer nanocomposites, 310
    - electrical properties of CNT buckypapers, 307
    - mechanical properties of carbon nanotube-polymer nanocomposites, 311
    - mechanical properties of CNT buckypapers, 308
    - SEM images of surface and cross-section of LbL SWNT-based thin film, 312

polymer casting, 309
polymer optical fibre sensors, 148–9
  measured true stress-strain curves for single-mode PMMA doped core POF, 149
  single-mode POF during loading with uniform visible light attenuation, Plate II
Polytec PSV 300, 341
Polytec PSV 400 3D-M, 341
Polytec PSV 400 system, 341
polyvinylidene fluoride (PVDF), 96
portable laser photogrammetric sensor, 338
post-tensioning process, 256
potentiometers, 60
potentiostatic linear polarisation resistance, 365
Pourbaix diagram, 358
power, 483, 485
power availability, 518–24, 520–4
  monochromatic disturbances tuning, 520–4
    equivalent circuits of matched impedances for monochromatic disturbances, 520
power consumption, 496, 501
power extraction circuits, 525–32
  diode bridge rectifier, 526–8
    passive full-bridge diode rectifier, 527
  pulse-width-modulation (PWM)-controlled DC/DC converters, 528–30
    buck-boost DC-DC converter power extraction circuit, 529
  resistive loads, 525–6
  synchronised switching circuits, 530–2
    SSHI circuit and influence on voltage, 531
  Thevenin equivalent circuit for arbitrary VEH system, 525
power storage, 175–6
Preisach-Mayergoyz space representation, 181
presentation layer, 455
principal component analysis (PCA), 10, 76, 342
printed circuit board (PCB), 462–3
propagating light-wave, 129
propagation factor, 212
proportional-integral-derivative (PID), 417–18
pulse repetition frequency (PRF), 206
pulse-width modulation (PWM), 457
pulse-width-modulation (PWM)-controlled DC/DC converters, 528–30

quantitative Lamb wave map, 100
quantization, 35–8
  voltage by 3-bit digitizer, 37
quantization error, 35–8
  signal-to-noise ratio as a function of A/D word-length capacity, 38
quantum cascade laser (QCL), 347
quartz crystal tuning fork (QCTF), 347
Quickfilter QF4A512, 495

Radar Review Panel, 206
RADAR technique, 144
radar technology, 7
  fundamentals of operation, 209–17
    2-D geometry of moving monostatic antenna and hyperbolic nonlinear distortion, 214
    B-scan of aluminium bar suspended in air with hyperbolic nonlinearity, 215
    hyperbolic nonlinearity that results from moving an antenna relative to fixed reflector, 214
    various models of EM wave propagation, 210
  laboratory and field studies, 227–32
    ability of terahertz imaging system to detect corrosion under Space Shuttle TPS, 232
    B-scan of Bostwick Road Bridge with reinforcing bar hyperbolas, 232
    B-scan of concrete slab after 7 months of accelerated corrosion testing, 230
    B-scan of concrete slab after 6 months of curing and before accelerated corrosion test, 229

    B-scan of Turkey Lane Bridge showing distinct hyperbolas of reinforcing bars, 231
    direction and path of scan on Bostwick Road Bridge, Shelburne, VT, USA, 231
    GPR measurements with2.3 GHz handheld antenna on concrete slab specimen, 227
    reflected signal vs time for two 38 mm slabs stacked with 1mm gap, 228
    salt water ponding as part of accelerated corrosion test on reinforced concrete slab, 229
    scanning the deck of Turkey Lane Bridge, Hinesburg, VT, USA, 230
  radio frequency, interferometric, millimetre wave and terahertz sensors, 201–34
    assessment and monitoring civil infrastructures, 201–34
    brief history of ground penetrating radar (GPR) systems, 203–8
    current challenges and state of the art systems, 208–9
    electromagnetic interactions with materials, 217–19
    future trends, 232–4
    generic EM structural sensing system, 202
    signal processing, 224–7
  transmitter and receiver design, 219–24
    detail of impedance-matching low-loss antenna apex connection, 223
    full waveform digitisation of 1 ns impulse with sampling at 20 GHz by gang of ADC, 220
    Gaussian impulses and derivatives as Gauss-Hermite functions, 221
    high-speed ground-coupled GPR system, 222
    image of horn antenna before mounting and encasement, 222
radio frequency
  radar technology and interferometric, millimetre wave and terahertz sensors, 201–34
    assessment and monitoring civil infrastructures, 201–34
    brief history of ground penetrating radar (GPR) systems, 203–8
    current challenges and state of the art systems, 208–9
    electromagnetic interactions with materials, 217–19
    fundamentals of operation, 209–17
    future trends, 232–4
    laboratory and field studies, 227–32
    signal processing, 224–7
    transmitter and receiver design, 219–24
rail track evaluation, 349
Raman scattering distributed sensors, 142–5
  distributed sensor cables examples, 145
  light scattering in optical fibres and use for strain and temperature sensing, 143
  schematic example of distributed strain and temperature measurement, 144
ramp converter ADC, 39
ray tracing methods, 213
Rayleigh-Lamb equation, 343
Rayleigh-Ritz projection, 517
Rayleigh scattering distributed sensors, 149
Rayleigh waves, 343
reactive energy flows, 521
reactive ion etching (RIE) sputtering, 270–1
read-only memory (ROM), 44
real current, 369
real energy flows, 521
real-time operating system (RTOS), 465–6
receiver, 452
reference-free techniques, 99–100
reflection coefficient, 215
refractive index, 211
region of interest (ROI), 394
reinforced concrete, 360–1
remote digital photography, 386

remote robotic sensing
  structural health monitoring (SHM), 419–24
    laser-based WPT, 422–4
    microwave-based WPT, 421
    wireless, 420–1
    wireless sensing and wireless power transmission (WPT), 419–20
repetitive cycling, 286
residual stress characterisation, 247–8
resistive loads, 525–6
resistive thermometers, 65
resolution, 29
responsivity, 50
Reynolds number, 276–7
Richter scale, 167–8
rise time, 162
RM Young Model 81000 anemometer, 495–6
robotic sensing
  assessing and monitoring civil infrastructures, 410–39
    future trends, 436–9
    remote robotic sensing for structural health monitoring (SHM), 419–24
    vibration-based mobile wireless sensors, 424–36
    vision-based for structural health monitoring (SHM), 414–19
Robug IV prototype, 426–7
robust task scheduler, 465
Roma2 model prototype, 426–7
rotational velocity, 340

sacrificial layers, 270
sag effect, 402
sampling criteria, 30–3
  5 Hz sinusoid waveform, 31
  5 Hz waveform and DFT, 33
  discrete Fourier transform (DFT), 31
sampling frequency, 30
saturated permeability, 255
Scalable Thin and Rapid Amassment Without Loss (STRAW), 485–6
scanning angular resolution, 338
scanning laser Doppler vibrometer (SLDV), 104, 341
SDOF electromagnetic harvester, 523
second-order differential equation, 515
SensCore corrosion sensor, 374
sensing
  future trends, 13–17
    damage models for structural health assessment, 15–16
    data inundation and information extraction, 16–17
    displacement measurement, 15
    sensors for monitoring of material processes, 14–15
  structural performance assessment and health monitoring, 1–17
    application to operational structure, 11–13
    overview, 5–9
    sensor data interrogation and decision making, 9–11
sensing equation, 92
sensing hardware, 5
sensing mechanisms, 126–9
  output signals of optical fibre sensors, 127
  sensor interrogation schemes, 128
sensing module, 26–30
  piezoelectric accelerometer cut-away vs second-order spring/mass/damper dynamic system representation, 27
sensing skins, 314–16
sensing systems
  energy harvesting for assessing and monitoring civil infrastructures, 510–34
    harvest dynamic modelling, 514–18
    ongoing advancements and future directions, 532–4
    power availability and optimal harvesting admittance, 518–24
    power extraction circuits, 525–32
sensing transducer, 5–6
Sensirion SHT11 chip, 489
sensitivity, 27, 29
  extraneous measurands, 29
sensor characteristics, 273–8
  packaging, 277–8
    ceramic package and plastic moulded package, 278
  squeeze film damping, 276–7

  - stiction and collapse voltage, 275–6
    - intended microstructure and consequence of stiction, 276
  - thin film residual stress, 277
    - profilometer measurements of capacitive sensor designs, Plate VI
  - transduction principles, 273–5
    - SEM images of capacitive gap change design and out-of-plane and in-plane motion, 275
- sensor data acquisition systems, 23–56
  - analog-to-digital conversion, 34–9
    - architectures, 38–9
    - quantization and quantization error, 35–8
    - simple switch, 35
  - concepts in signals and digital sampling, 30–4
    - digitization and encoding, 33–4
    - sampling criteria, 30–3
  - data acquisition system, 41–7
  - digital-to-analog conversion, 39–40
  - future trends, 54–6
    - schematic of sensor and data acquisition taxonomic evolution, 55
  - general measurement system, 24–6
    - schematic diagram, 24
  - optical sensing DAQ system, 47–53
    - fiber optic measurement system, 48
    - photodetectors, 49–52
    - photodiodes, 48–9
    - tunable optical filters, 52–3
  - sensing module, 26–30
- sensor materials, 266–70
  - insulators, 270
  - mechanical and electrical properties of MEMS microstructure vs structural steel, 267
  - metals, 270
  - polycrystalline silicon (polysilicon), 269
  - sacrificial layers, 270
  - silicon, 267–9
    - wafer indicating primary flat and directions, 268
  - silicon carbide, 269–70
  - typical materials and purposes, 267
- sensor module, 23, 25, 26–30
- sensor order, 26
- sensor packaging, 129–30
  - design, 130
- sensors
  - used for civil infrastructures, 57–80
    - associated algorithms, 69–78
    - continuous monitoring systems, 78–9
    - future trends, 79–80
    - sensing technologies, 58–68
- server-side computing, 469
- server-side software, 464
- session layer, 455
- severity assessment, 166–8
  - example of intensity chart, 168
  - Kaiser effect, 166
- severity index, 167
- shape anisotropy, 242–3
- shunt circuits, 41
- sigma-delta ADCs, 39
- signal conditioners, 462–3
- signal conditioning module, 23, 25
- signal processing, 224–7
  - flowchart of synthetic aperture algorithm, 225
  - geometry of wavenumbers associated with synthetic aperture imaging, 226
  - image of rebars and defects inside of concrete slab by Mast and Johansson, 224
- signal-to-noise ratio, 100–1, 284–5
- silicon, 267–9
- silicon carbide, 269–70
- single crystal silicon, 267–8
- single-ended connections, 42
- single-mode fibre, 125
- single-walled carbon nanotubes (SWNT), 297–8
- singular value decomposition (SVD), 342
- slow dynamics, 192–3
- small-scale building model test, 396–7
  - comparative results of videogrammetric measurement and shake table input, 398
  - displacement responses of 3-storey building model under 1940 El Centre earthquake, 398

small-scale building model test (*cont.*)
  experimental set-up of 3-storey building model, 397
smaller robot prototype, 427
smart aggregate, 97
smart concrete fabrication, 300–1
smart layer, 96
sol-gel technique, 274
SolidWork, 342
spatial damage detection, 314–16
spatial variations, 76
speckle image intensity, 336
spin coating, 309
splicing, 130
spontaneous emission, 49
spraying, 309
sputtering, 270
squeeze film damping, 276–7
ST Microelectronics LIS2L06 MEMS accelerometer, 489
standard telecom connectors, 130
static random access memory (SRAM), 44–5
static sensitivity, 27
steady-state stress, 280
step-frequency radar system, 219
step-index optical fibre, 123
step recovery diodes (SRD), 204–5
Stern-Geary equation, 364
StickyBot, 427
stiction, 275–6
stimulated emission, 329–31
stochastic disturbances, 524
stochastic subspace identification (SSI), 449–50
stone aggregates image segmentation, 349
Stonecutters Bridge, 78
straight binary code, 34
strain, 60–2
  piezoresistive, 60–1
  vibrating-wire, 61–2
strain gages, 70
strain sensing, 301–2, 313–14
strain sensor, 282–3
street mapping, 350
stress effective field, 243
stress-strain curves, 181
stress-strain matrices, 92
stress-strain nonlinear model, 192
structural health monitoring (SHM), 3, 160, 171–5, 279–84, 349–50, 447
  acoustic emission techniques, 103–4
    overview illustration, 103
  applications, 95–7
  guided wave techniques
    principle of phased array technique, 101
  guided wave tomography, 100
  impedance techniques, 101–3
    scheme illustration, 102
  piezoelectric transducer self-diagnosis techniques, 104–5
    illustration based on TRP for PZT debonding detection, 105
  prevalence of commonly used sensors, 65–8
    literative of health monitoring systems, 67–8
    sensor layout for Stonecutters Bridge, 66
  remote robotic sensing, 419–24
  sensing, 1–17
    application to operational structure, 11–13
    future trends, 13–17
    overview, 5–9
    sensor data interrogation and decision making, 9–11
  techniques, 99–105
  vision-based robotic sensing, 414–19
  wireless, 420–1
    functional elements of wireless sensor, 420
subharmonic generation, 182–5
successive approximation ADC, 39
surface acoustic waves (SAW), 343–4
surface-emitting diodes, 49
surface micromachining, 271–2
Surveillance d'ouvrages par senseurs à fibres optiques (SOFO) sensors, 134
swept-wavelength interferometry (SWI), 149
switch register, 35
synchronised switching circuits, 530–2
synthetic aperture radar (SAR), 204–5
system operators, 207

Tafel constants, 364
target
  correspondence, 392–5
    epipolar geometry for two-camera image acquisition system, 396
    schematic illustration of optical flow method, 395
    target point extraction, 393
    target point tracking by correlation-based method, 394
television holography *see* laser interferometry
temperature effects, 256–8
  dependence of initial magnetisation curve on temperature variation, 258
  temperature dependence of permeability, 259
tensile stress monitoring, 249
terahertz sensors
  radar technology and radio frequency, interferometric and millimetre wave, 201–34
    assessment and monitoring civil infrastructures, 201–34
    brief history of ground penetrating radar (GPR) systems, 203–8
    current challenges and state of the art systems, 208–9
    electromagnetic interactions with materials, 217–19
    fundamentals of operation, 209–17
    future trends, 232–4
    laboratory and field studies, 227–32
    signal processing, 224–7
    transmitter and receiver design, 219–24
terrestrial laser scanning (TLS) system, 349–50
thermal protection system (TPS), 230–2
thermal radiation, 329–31
thermocouples, 65
Thevenin equivalent circuit, 525
thin film fabrication, 307–9
thin film residual stress, 272, 277
time constant, 27
time-division multiple-access (TDMA), 453
time-division multiplexing (TDM), 133–4
time domain, 521
time of arrival (TOA), 163
time-of-flight, 148
time-of-flight (TOF) laser scanner, 350
time reversal acoustic method, 165–6
time reversal process (TRP), 99–100
time synchronisation, 467–8
time-varying electric currents, 213
timing skew, 47
TinyOS, 465–6, 483
Tmote Sky, 489
transducer-based feature tracking systems, 415–16
transducers, 462
transduction principles, 273–5
transistor-transistor logic, 35
transmissibility function analysis, 431
transmission coefficient, 215
transmission control protocol (TCP), 454–5
transmission techniques, 534
transmitter, 451
transport layer, 454–5
transportation system, 12
transverse electric (TE) polarised wave, 215
transverse magnetic (TM) polarised wave, 215
triangular method, 392–3
Tsing Ma Bridge, 78
tunable optical filters, 52–3
  etalon-based tunable Fabry–Pérot optical filter and transfer function, 53
tunnel liner inspection, 348–9
two-camera image acquisition system, 395

U-shaped yoke, 260–1
ultrasonic sensor, 283–4
ultrasound methods
  nonlinear acoustic methods for assessing and monitoring civil infrastructures, 179–97
    fundamentals of nonlinear acousto-ultrasound techniques, 181–2
    future trends, 196–7

ultrasound methods (*cont.*)
    harmonic and subharmonic generation, 182–5
    nonlinear resonance ultrasound spectroscopy, 191–5
    nonlinear wave modulation, 185–91
ultraviolet (UV) spectrum, 351
ultrawideband (UWB), 204–5
unmanned aerial vehicles (UAV), 421
U.S. Department of Labour, Occupational Safety and Health Administration (OSHA), 351
USB, 46
user datagram protocol (UDP), 454–5

vacuum, 217
vacuum-assisted resin-transfer moulding (VARTM), 304
vacuum packaging, 278
van der Waals force, 309–10
vector field equations, 210
vector wave equations, 211
Versatile Onboard Traffic-Embedded Roaming Sensors (VOTERS) project, 11
vibrating-wire strain, 61–2
vibration-based mobile wireless sensors, 424–36
  case study of development and validation of mobile sensor network, 427–36
  literature review on climbing robots and mobile sensors, 426–7
  static sensor networks vs mobile sensor networks, 426
vibration control, 109
vibration modal analysis, 435–6
video holography *see* laser interferometry
videogrammetric technique, 387–8
vision-based measurement techniques
  civil engineering applications, 386–8
vision-based robotic sensing
  structural health monitoring (SHM), 414–19
    vision-based structural displacement monitoring, 415–19
  vision-based structural crack detection, 414–15
    schematic diagram of Bridge Inspection Robot Development Interface, 415
vision-based sensing
  assessing and monitoring civil infrastructures, 383–406
    applications, 396–405
    important issues for vision-based measurement techniques, 388–96
    vision-based measurement techniques for civil engineering applications, 386–8
vision-based structural crack detection, 414–15
vision-based structural displacement monitoring, 415–19
  configuration of conventional SL, 417
  diagram of 6-DOF displacement estimation method using three laser range finders, 419
  process of visually servoed paired structured light system, 418
  schematic diagram of visually servoed paired structured light system, 417
visually servoed paired (ViSP), 416–17
voltage standard wave ratio (VSWR), 223

water intrusion, 227
water-to-cement ratio, 185
wave velocity, 175
wavefront-splitting, 333
wavelength-division multiplexing (WDM), 139–40
wavelet transform method, 349
web-based reporting system, 386
wet etching, 270
Wheatstone bridge, 65
WiDAQ, 461–2
Wind River VxWorks, 465–6
wind tunnel bridge sectional model test, 399
  measured responses at Target A and B, 400

  - wind tunnel test for bridge sectional model, 400
- wind turbines, 109
- wire bonding method, 278
- wired sensor technologies, 172
- wireless communication, 13, 485
- wireless control networks, 470
- wireless HART, 460
  - protocol, 455–6
- wireless local area networks (WLAN), 453
- wireless networks
  - overview, 450–6
    - 2.4 GHz channel interference, 454
    - common network stacks and development responsibility, 452
    - qualitative comparison of wireless standards, 456
    - range and data rate of wireless standards, Plate XIII
    - schematic view of IEEE 802.15.4 Data Packet MAC sub-layer, 454
    - wired vs wireless communications, 451
    - WSN topologies, Plate XII
- wireless power transmission (WPT), 347–8, 419–20
- wireless radio modules, 458–9
- wireless sensing nodes (WSN), 419–20, 483
- wireless sensing unit, 487, 489–90, 494–6, 498, 500–1
  - Golden Gate Bridge, San Francisco, California, USA, 483–5
  - Jindo Bridge, Haenam/Jindo, South Korea, 494–6
    - Imote2 with antenna, stacked on battery board with SHM-A sensor board, 494
    - PVC enclosure for sensing unit, 495
  - new Carquinez Bridge, Vallejo/Crockett, California, USA, 498, 500–1
    - Narada wireless sensing unit with power-amplified radio, 500
    - polycarbonate enclosure, 501
  - Stork Bridge, Winterthur, Switzerland, 489–90
    - energy consumption for field deployment of Tmote, 490
    - hardware packaging for wireless sensors units, 489
- wireless sensor, 8–9
  - anatomy, 456–9
  - families, 459–62
    - academic prototypes, 461–2
    - commercial wireless sensors, 460–1
    - peripherals, 462–4
    - selected examples, 460
- wireless sensor network software, 464–71
  - application software, 468–71
    - network wide capabilities of wired vs wireless, 468
  - middleware, 466–8
    - power usage in multi-hop networks, 467
    - WSN topologies, Plate XII
  - operating systems (OS), 464–6
- wireless sensor networks, 425–6
- wireless sensor peripherals, 462–4
  - energy management and harvesters, 463–4
    - energy densities of common WSN power sources, 464
  - signal conditioners, 462–3
  - transducers, 462
- wireless structural health monitoring, 420–1
- wireless structural monitoring systems
  - design and selection for civil infrastructures, 446–72
    - future trends, 471–2
    - overview of wireless networks, 450–6
    - state of practice, 447–8
    - state of the art, 449–50
    - wireless sensor network software, 464–71
  - hardware design and selection, 456–64
    - anatomy of wireless sensor, 456–9

wireless structural monitoring systems (*cont.*)
    overview, Plate XIV
    wireless sensor families, 459–62
  permanent installation in infrastructure systems, 480–505
    case study I of Golden Gate Bridge, San Francisco, California, USA, 482–7
    case study II of Stork Bridge, Winterthur, Switzerland, 487–92
    case study III of Jindo Bridge, Haenam/Jindo, South Korea, 492–7
    case study IV of New Carquinez Bridge, Vallejo/Crockett, California, USA, 497–505
Wireless Structural Testing Systems, 460
words, 34

X-ray resist, 272–3
X-ray source, 272

Young modulus, 182, 248–9, 273–4, 310, 313, 343–4

zero resistance ammeter (ZRA), 373–4
ZigBee, 452